L-Università ta' Malta
Faculty of Engineering

DOCTOR OF PHILOSOPHY IN ENGINEERING DISSERTATION

Nanoindentation of Graphene Membranes using Atomic Force Microscopy and Molecular Dynamics Simulations

BY

ANTHEA AGIUS ANASTASI

DEPARTMENT OF METALLURGY AND MATERIALS ENGINEERING
FACULTY OF ENGINEERING
UNIVERSITY OF MALTA

A dissertation submitted to the Faculty of Engineering in partial fulfilment of the requirements for the research-based degree of Doctor of Philosophy in Engineering

February 2021

Copyright Notice

ABSTRACT

This study focuses on the mechanical properties of graphene – a carbon allotrope consisting of a single layer of atoms arranged in a two-dimensional hexagonal lattice. Given the massive scientific research interest that graphene generated during the last few years, work directed at fully understanding its material properties and in turn its expected behaviour under different conditions has proved key to its wider utilisation. Specifically, understanding the mechanical response of graphene under different loads is deemed central in the design of graphene-based devices such as filtration membranes. This work focuses on the measurement of the elastic modulus of graphene, particularly for pristine and defective membranes using point-loading nanoindentation via atomic force microscopy.

Few-layer and multi-layer graphene membranes prepared in-house via mechanical exfoliation as well as single-layer CVD-grown graphene membranes deposited on pre-fabricated microsieves were considered. Atomic force microscopy was the primary tool used to indent the graphene membranes and thereby measure the elastic modulus of graphene. While generally nanoindentation is considered a suitable technique for accurate modulus determination, this work reveals that testing parameters such as the spring constant of the cantilever used and the depth to which the membranes are indented affect the measurements obtained. The work presented emphasises the dependency of the measurements obtained on the exact methodology adopted. This points towards the need for an established set of guidelines to be followed such that the results across multiple research groups and testing platforms can be comparable. This work provides preliminary guidelines for this scope.

Some applications, such as graphene-based filtration devices, exploit the presence of defects in the crystalline lattice of graphene to tailor its performance. In this work, gallium ion irradiation was used to introduce defects in the graphene membrane. Similar nanoindentation of the treated membranes revealed no clear trend as to whether the elastic modulus is affected by the applied treatment when compared to the untreated material.

Finally, molecular dynamics simulations were performed to support and provide insight to the experimental work carried out. The results confirm the ability for simulations to replicate experimental results. As a significant contribution, this work highlights the limitations of the mathematical model used to calculate the elastic modulus from the obtained indentation curves. The use of mathematical methods to ascertain whether experimental results obtained are accurate is suggested.

This one’s for me.

ACKNOWLEDGMENTS

This thesis would not have been possible without a few individuals who have offered their support in one way or another.

First and foremost, I would like to express my sincere gratitude for my main supervisor Prof. Ing. Glenn Cassar for the continuous support of my Ph.D. study and related research, for his patience, motivation, and knowledge. His guidance helped me throughout the research and writing of this thesis.

My appreciation extends to my co-supervisor Dr. Matthew K. Borg who has assisted me to learn computer simulation and has offered his support and patience throughout the years. I am grateful for him enabling me to visit the School of Engineering at The University of Edinburgh and learn from his students. Chapter 6 is dedicated to all of them.

I am forever grateful for the assistance offered by Dr. Andrea Valsesia, Dr. Pascal Colpo, and their colleagues at the Joint Research Centre in Ispra that made Chapter 5 of this dissertation possible. Meeting them, visiting and accessing their nanotechnology laboratories was a very humbling experience which I will never forget.

I also wish to send my regards to Prof. Luciano Mule Stagno who gave me access to his laboratories at the Institute for Sustainable Energy, University of Malta.

This research would not have been possible without the funding provided by ENDEAVOUR Scholarship Scheme. Part of this research has been carried out using computational facilities procured through the European Regional Development Fund, Project ERDF-080 'A Supercomputing Laboratory for the University of Malta' (http://www.um.edu.mt/research/scienceeng/erdf_080).

A special mention should go to the technical staff at the Department of Metallurgy and Materials Engineering. Ing. James Camilleri, Ing. Mary Grace Micallef, Mr. Nicholas Gingell, Mr. Noel Tonna, Mr. Daniel Dimech, and Mr. Andrew Agius – thank you for all your help throughout these last 6 years. My sincere appreciation goes to all the hours spent helping me fix the ICF equipment – an endless battle which would have been impossible without your technical assistance. Your morale support was invaluable during my days spent at the lab and for that, I am forever indebted. I would also like to thank all the academic staff at DMME; Prof.

Ing. Maurice Grech, Prof. Ing. Bertram Mallia, Prof. Ing. Joseph Buhagiar, Dr. Daniel Vella, Dr. Ing. Ann Zammit, and Dr. Ing. Stephen Abela. Thank you for accepting me as your colleague and offering your wisdom and academic support whenever needed. I would like to thank Ms. Antonella Sammut and Ms. Elise Ann Mifsud for processing all my purchase orders throughout this journey.

Last but not least, I would like to thank the handful of individuals who have supported me through thick and thin. Thank you mum and dad for believing in me since I was a young child, even when I didn't believe in myself. I wouldn't have been here without your endless love, patience, encouragement, and financial support. I wouldn't have made it through the last few years without my fiancé, Antonino. Thank you for loving me when I was the weakest and rejoicing with me when we were the strongest. Last but not least, a special furry thanks goes to all the cats in my life who have given me their best cuddles in time of need. You have been purrfect.

TABLE OF CONTENTS

Abstract i

Acknowledgments iii

Table of Contents v

List of Figures x

List of Tables xxvii

List of Abbreviations and Symbols xxxi

Chapter 1 Introduction 1

1.1 Graphene 1

1.1.1 Mechanical Properties of Graphene 3

1.1.2 Defects in the Graphene Crystal 3

1.1.3 Graphene-Based Applications 5

1.1.4 Enabling Nanotechnologies 6

1.2 Motivation and Scope of Research 8

Chapter 2 Literature Review 10

2.1 Graphene Synthesis 10

2.1.1 Mechanical Exfoliation 11

2.1.2 Chemical Vapour Deposition 13

2.1.3 Other Techniques 15

2.1.4 Graphene Modification Methods 18

2.1.5 Substrate Preparation 21

2.1.6 Summary 21

2.2 Characterisation of Graphene 22

2.2.1 Optical Microscopy 22

2.2.2 Scanning Electron Microscopy 23

2.2.3 Raman Spectroscopy 24

2.2.4 Summary 28
2.3 Atomic Force Microscopy 28
2.3.1 Nanoindentation of Graphene 32
2.3.2 Summary 42
2.4 Molecular Dynamics Simulations 43
2.4.1 Uniaxial Tensile Loading 45
2.4.2 Point Loading Nanoindentation 49
2.4.3 Simulations Investigating Defect Formation 53
2.4.4 Summary 54
2.5 Nanoporous Graphene 55
2.5.1 Permeability of Graphene Membranes 56
2.5.2 Effect of Defects on the Mechanical Properties 59
2.5.3 Effect of Nanopores on the Mechanical Properties 63
2.5.4 Summary 64
2.6 Conclusions 65
2.7 Research Questions and Objectives 67
2.7.1 Objectives 68
Chapter 3 Sample Preparation 70
3.1 Introduction 70
3.2 Characterization Methodology 72
3.2.1 Optical Microscopy 72
3.2.2 Atomic Force Microscopy (AFM) 72
3.2.3 Raman Spectroscopy 73
3.2.4 Scanning Electron Microscopy 74
3.3 Mechanically Exfoliated Graphene 74
3.3.1 Preparation of Patterned PAA/Si Substrate 75
3.3.2 Preparation of the PDMS Stamp 79

3.3.3 Mechanical Exfoliation and Deposition....79
3.3.4 Results....80
3.3.5 Concluding Remarks....101
3.4 Chemical Vapour Deposition (CVD) Grown Graphene....103
3.4.1 Supported Graphene on SiO_2/Si....103
3.4.2 Suspended Graphene on TEM Grids....106
3.4.3 Suspended Graphene on Patterned PAA/Si Substrate and Silicon Nitride Microsieves....110
3.4.4 Concluding Remarks....118
Chapter 4 Nanoindentation using Atomic Force Microscopy....120
4.1 Introduction....120
4.2 Background and Theory....121
4.2.1 Tip-Sample Interaction Theory....121
4.2.2 Static Contact Mode....123
4.2.3 Dynamic Non-Contact Mode....124
4.2.4 Force Spectroscopy....124
4.2.5 General Description of the AFM Set-Up....126
4.2.6 The AFM Probe....127
4.3 Static Mode Imaging....131
4.3.1 Calibration of the Piezo Scanners....132
4.3.2 Nonidealities....133
4.4 Force-Distance (FD) Curves....134
4.4.1 System Nonidealities....136
4.4.2 Calibration of the Sensor Sensitivity Factor....139
4.4.3 Calibration of the Cantilever Spring Constant....142
4.5 Indentations on As-Deposited Mechanically Exfoliated Graphene....150
4.5.1 Case Study 1 – Flake D....151

4.5.2 Case Study 2 – Flake C 165
4.5.3 Discussion 169
4.6 Indentations of As-Deposited CVD Graphene 172
4.6.1 Results 173
4.6.2 Discussion 184
Chapter 5 Focused Gallium Ion Beam Bombardment 194
5.1 Introduction 194
5.2 Effect of Ion Bombardment on Raman Spectra 195
5.2.1 Characterization Methods 197
5.2.2 Results 198
5.2.3 Discussion 221
5.3 Effect of Ion Bombardment on Elastic Modulus 230
5.3.1 Results 231
5.4 Conclusion 235
Chapter 6 Molecular Dynamics Simulations 236
6.1 Introduction 236
6.2 Molecular Dynamics 237
6.3 A Simplified Model for Graphene on OpenFOAM 239
6.3.1 Methodology 240
6.3.2 Results and Discussion 243
6.3.3 Conclusion 255
6.4 AIREBO Via LAMMPS 256
6.4.1 Potential Functions 257
6.4.2 Validation Study 258
6.4.3 Nanoindentation 265
6.5 Conclusion - Comparing Experimental with Molecular Dynamics Results 294
Chapter 7 Conclusions 296

7.1 Future Work 300

References 302

Appendix A Raman Post-Processing Script 318

Appendix B TEM Grid Sample Holder Drawing 323

Appendix C Probe Holder Drawing 326

Appendix D Spring Constant Calibration Script 327

Appendix E 2D Raman Spectral Maps 330

Appendix F Raman Peak Parameters 332

F.1 Treated Suspended CVD Graphene Membranes on Silicon Nitride Microsieves 332

F.2 Treated Mechanically Exfoliated Graphene Membranes on PAA/Si Substrate 333

F.2.1 Flake F - 1.33×10^{-14} C/μm^2 Patterning Method 333

F.2.2 Flake G – 3.30×10^{-15} C/μm^2 Imaging Method 334

F.2.3 Flake H – 3.30×10^{-15} C/μm^2 Imaging Method 335

F.2.4 Flake C – 6.60×10^{-16} C/μm^2 Imaging Method 336

F.2.5 Flake I – 6.60×10^{-16} C/μm^2 Imaging Method 337

F.2.6 Flake J – 6.60×10^{-16} C/μm^2 Imaging Method 338

Appendix G AIREBO MD Script 339

LIST OF FIGURES

Figure 1.1: A model of a graphene sheet showing the bond length (1.42 Å), bond angle (120°), and direction notation (armchair, AC, and zigzag, ZZ, directions). 2
Figure 1.2: Atomic configurations of (a) single vacancy, (b) adatom, (c) foreign atom, and (d) grain boundary [26, 27].....4
Figure 2.1: Mechanical exfoliation of graphene using the Scotch tape method; (a) The tape is pressed onto bulk graphite, (b) the top graphite layers are peeled off, (c) the graphite adhered to the tape is pressed against the substrate, and (d) the tape is peeled off, leaving single or few layer graphene on the substrate [62]. 12
Figure 2.2: Production of reduced graphene oxide via the production of graphene oxide and the subsequent reduction by hydrazine [105]. 16
Figure 2.3: Trapping of a graphene nanoplatelet under the graphene monolayer after ion bombardment; 3D STM images of graphene structure with side view illustrations of the defect creation in the graphene, before (left) and after (right) ion irradiation [115]. 20
Figure 2.4: Production of graphene nanoribbons using REI and V_2O_2 nanowires as a mask [69]. 21
Figure 2.5: Raman spectra of (top) pristine, and (bottom) defected single-layer graphene [125]. 24
Figure 2.6: Atomic displacements in the breathing mode that activates the D peak [125]. 26
Figure 2.7: Evolution of the 2D peak with the number of layers using (a) 514 nm and (b) 633 nm excitation wavelengths. (c) The four components of the 2D peak in bilayer graphene [122]. 26
Figure 2.8: Typical friction force microscopy data. (A) Topographic and (C) friction force images of the surface of the copper foil partially covered by graphene islands, (B) topographic and (D) lateral force line profile along the white dashed line marked in (A) and (C), respectively, (E) friction force profile along the same line shows that graphene reduces friction by a factor of 17 compared to Cu, (F) friction force versus load plot for graphene and copper acquired in a single region spanning the graphene-Cu boundary (indicated by the blue square in (C)) [76]. 30
Figure 2.9: The (a) Peak Force behaviour and (b) Peak Force Tunnelling AFM current when the tip is brought close to the sample [143]. 31

Figure 2.10: Imaging the first water adlayers on mica using an AFM tip at ambient conditions. (A) A schematic of graphene covering the water adlayers, (B) the structure of ice, (C, D, F) AFM images of monolayer graphene on mica, and (E, G) height profiles showing the thickness of the water islands [64].....32
Figure 2.11: Indentation at the centre of the suspended graphene membrane via AFM. 33
Figure 2.12: Force-displacement curve obtained experimentally via nanoindentation, fitted to Equation 2.1 [8]. 34
Figure 2.13: Schematic of the AFM tip at different positions on the sample; the dashed lines represent the shape of the membrane at the corresponding contact point, the solid line represents the acquired tip trajectory and thus the obtained AFM topography image [134]...38
Figure 2.14: Pristine graphene sheet modelled in tensile loading; the C atoms on the left (in red) are fixed, while the C atoms on the right (in red) are constrained to move at a pre-defined velocity [166]. 44
Figure 2.15: Crack propagation in graphene sheets under a tensile load along different orientation angles; (a) 0° (AC), (b) 6.6°, (c) 8.2°, (d) 16.1°, (e) 23.4°, and (f) 30° (ZZ) [174]. 48
Figure 2.16: Fracture process upon loading in the (a, b) AC, and (c, d) ZZ directions (a, c) [166], (b, d) [167].....49
Figure 2.17: Wrinkling of a circular graphene membrane under point loading [185].....52
Figure 2.18: Use of nanoporous graphene as a molecular sieve that only allows water molecules from saline water to pass through under a pressure difference (Image courtesy: Matthew K. Borg). 56
Figure 2.19: (a – c) Atomistic models illustrating the bond rotation in a Stone-Wales defect, and (d, e) TEM images of the Stone-Wales defect [29]. 59
Figure 3.1: (a) Schematic representation of graphene on a perforated substrate to create a drum-like membrane. (b) Cross-sectional view of the graphene membrane. 70
Figure 3.2: Schematic of the procedure for the fabrication of holey PAA/Si substrate. (a) Oxygen plasma cleaning of the Si wafer, (b) deposition of a PDDA layer, (c) deposition of the polystyrene (PS) microbeads, (d) annealing of microbeads, (e) deposition of the PAA layer, and (f) the dissolution of the annealed PS beads in toluene. 75
Figure 3.3: Micrographs showing the various stages of the PAA/Si substrate fabrication. (a) Deposition of PS beads on PDDA-modified silicon wafer. (b) PS beads after annealing at 100°C for 2 minutes. (c) The sample after PAA deposition and 5 minutes of ultrasonication in

toluene. (d) The sample after 120 minutes of ultrasonication in toluene. (e) A typical circular hole. (f) Optical micrograph of the final PAA/Si substrate. 77
Figure 3.4: (a) A 3D AFM topography micrograph of a typical hole in the PAA/Si substrate. (b) A section view of the sample through the hole as depicted by the black line in (a). 78
Figure 3.5: Typical Raman spectra obtained from the PAA/Si substrate using (a) 532 nm, and (b) 633 nm excitation wavelengths. The red curves denoted as 'Back. Sub.' refer to the background subtracted data..... 78
Figure 3.6: Schematic of the procedure for the mechanical exfoliation and deposition of graphene membranes on the PAA/Si substrates. (a) Cleaving of the HOPG, (b) deposition of a smaller graphite flake onto one of the PDMS stamps, (c) mechanical exfoliation of the graphite flake between two PDMS stamps, (d) loading of the graphene-loaded PDMS stamp onto the PAA/Si substrate, (e) final deposition of graphene membranes on the substrate after removal of the PDMS stamp. 80
Figure 3.7: (a, b) Typical optical micrographs of mechanically exfoliated graphene flakes deposited on the patterned PAA/Si substrate. In (b), the solid arrows mark Flakes A, X, Y and Z, while the dashed arrows indicate folding of the flakes. 82
Figure 3.8: Optical micrographs of (a) Flake B and (b) Flake C. 83
Figure 3.9: Static contact mode AFM (a) height, (b) frictional, and (c) normal force micrographs of Flake A. (d) Section views showing the 2D topographical profiles along line 'A' and line 'B' in (a). The direction of the section lines 'A' and 'B' shown in (a) is from left to right. 84
Figure 3.10: (a) Optical micrograph and (b, c) collated AFM height image of Flake B for visualisation. (c) shows the various areas with different thicknesses labelled B1 to B6, and the covered holes labelled BH1 to BH4..... 85
Figure 3.11: (a) Static contact mode AFM height micrograph of Flake B showing areas B3 and B4, and hole BH3. (b) and (c) Section views showing the topographical height along the black line (A), blue line (B), red line (C), and green line (D) in (a), taken from left to right, or up to down..... 87
Figure 3.12: Static contact mode AFM height micrograph of Flake B showing areas B2 and B3, and holes BH2, BH3 and partial BH4. 87
Figure 3.13: (a) Static contact mode AFM height micrograph of Flake B showing area close to hole BH2 (just to the right of the image). (b) Section views showing the topographical height along the black line (A), and blue line (B) in (a), taken from left to right..... 88

Figure 3.14: (a) Static contact mode AFM height micrograph of Flake B showing hole BH1. (b) and (c) Section views showing the topographical height along the black line (A), blue line (B), and red line (C) in (a), taken from left to right. 88
Figure 3.15: (a) Static contact mode AFM height micrograph of Flake B showing hole BH1. (b) Section view showing the topographical height along the black line (A) in (a), taken from left to right..... 89
Figure 3.16: (a) Static contact mode AFM height micrograph of Flake B showing area B1. (b) Section views showing the topographical height along the black line (A), and blue line (B) in (a), taken from left to right, or up to down. 89
Figure 3.17: (a) Static contact mode AFM height micrograph of Flake B showing areas B2, B5 and B6, and hole BH4. (b) Section views showing the topographical height along the black line (A), blue line (B), red line (C), and green line (D) in (a), taken from left to right. 90
Figure 3.18: (a) Static contact mode AFM height micrograph of Flake C. (b) Section view showing the topographical height along the black line (A), blue line (B), red line (C), and green line (D) in (a), taken from left to right. 91
Figure 3.19: (a) Static contact mode AFM height micrograph of Flake C. (b) Section view showing the topographical height along the black line (A), blue line (B), and red line (C) in (a), taken from up to down. 91
Figure 3.20: Typical Raman spectra obtained from mechanically exfoliated graphene flakes on PAA/Si substrate using (a) 532 nm, and (b) 633 nm excitation wavelength. In both cases, an appropriate baseline was fitted and subsequently subtracted from the raw data (Base. Sub. in legends). 92
Figure 3.21: The locations labelled A1 to A3 from where the Raman spectra were obtained from Flake A. 92
Figure 3.22: 2D Raman spectral maps of the sum of parts of the spectrum depicting the intensity of the (a) 2D, (b) G, and (c) D peaks of Flake A, at each pixel. 95
Figure 3.23: Flake A after 2D Raman mapping using the 532 nm laser, clearly showing a damaged area as circled in white. 95
Figure 3.24: 2D Raman spectral maps of the sum of parts of the spectrum depicting the intensity of the (a) 2D, (b) G, and (c) D peaks of Flake B, at each pixel. 96
Figure 3.25: Averaged Raman spectra obtained from the areas within Flake B as labelled in Figure 3.10 (c) using the 633 nm excitation wavelength. The baseline is not subtracted in any of the presented spectra. 96

Figure 3.26: The peak position P, intensity I, width F, and area A, of the D, G, D+D'', 2D and 2D' bands, and the intensity and width ratios between the D and G bands (I_D/I_G, F_D/F_G), and the 2D and G bands (I_{2D}/I_G, F_{2D}/F_G) with an increasing flake thickness of Flake B. 98
Figure 3.27: The evolution of the 2D peak with an increase in flake thickness. 99
Figure 3.28: 2D Raman spectral maps of the sum of parts of the spectrum depicting the intensity of the (a) 2D, (b) G, and (c) D peaks of Flake C, at each pixel. 99
Figure 3.29: Scanning electron micrographs of mechanically exfoliated graphene on the patterned PAA/SiO_2 substrate using a (a, c) secondary electron detector and (b, d) Inlens detector. In (a), Flake A is circled for reference. 100
Figure 3.30: Scanning electron micrographs of Flake B using the secondary electron detector. 101
Figure 3.31: (a) Optical micrograph of the CVD graphene supported on the SiO_2/Si substrate with locations A1 – A4 from where the Raman spectra in (b and c) were obtained using the 532 nm excitation wavelength, without baseline subtraction. 104
Figure 3.32: Scanning electron micrograph of supported CVD graphene on Si/SiO_2 105
Figure 3.33: The design of the TEM grid sample holder; (a) labelled components, (b) assembly. 107
Figure 3.34: Scanning electron micrographs of suspended CVD graphene on a TEM grid. 108
Figure 3.35: (a – c) Static contact mode, and (d) dynamic non-contact mode AFM micrographs showing the (a) normal force, (b) lateral force, (c) topography, and (d) phase signals of the CVD graphene membranes on TEM grids. 109
Figure 3.36: Raman spectra of various areas within the CVD graphene suspended on TEM grids using the 633 nm laser, without baseline subtraction. 110
Figure 3.37: Schematic of the procedure to transfer the Easy Transfer graphene. (a) As-received sacrificial layer/graphene/polymer sandwich, (b) detachment of sacrificial layer and graphene from the polymer support using deionized water, (c) deposition on substrate of choice, and (d) removal of the top sacrificial layer to expose the graphene. 111
Figure 3.38: Optical micrographs of the Easy Transfer CVD graphene deposited on the patterned PAA/Si substrate. (a) Before and (b) after removal of the top sacrificial layer. 112
Figure 3.39: Optical micrographs of the Easy Transfer CVD graphene deposited on the silicon nitride microsieves with pore diameter of 0.45 μm. (a) Before and (b) after removal of the top sacrificial layer. 112
Figure 3.40: Static contact mode AFM topography micrograph of the CVD graphene membranes deposited over the 0.45 μm pores in the microsieve. 113

Figure 3.41: Raman spectra of various areas within the CVD graphene, deposited on the patterned PAA/Si substrate using the 532 nm laser, (a) before and (b) after subtraction of baseline. 115
Figure 3.42: Raman spectra of various areas within the CVD graphene on silicon nitride microsieve using the 532 nm laser, (a) before and (b) after subtraction of baseline. 115
Figure 3.43: Scanning electron micrographs of suspended CVD graphene on the patterned PAA/Si substrate using (a) a secondary electron detector and (b – d) Inlens detector. (a) and (b) show the same area of the sample using different detectors. 117
Figure 3.44: Scanning electron micrograph of suspended CVD graphene on a 0.45 μm silicon nitride microsieve..... 118
Figure 4.1: The (a) potential energy and (b) interaction force between two bodies as they are brought closer to each other. 122
Figure 4.2: Simple illustrations of the tip motion relative to the sample surface during (a) static contact, and (b) dynamic non-contact AFM modes. 123
Figure 4.3: Theory of force-distance curves. (a) Labelled positions of the tip with respect to the sample during indentation. (b) A typical force-distance curve with the labels referring to the tip-positions in (a). 125
Figure 4.4: (a) The RHK UHV 750 AFM/STM chamber (enclosed in a dashed white box) within the Integrated Characterisation Facility (ICF) available at DMME, UM. (b) The Beetle^{TM} scanning head and sample holder. (c) A simplified schematic of the AFM set-up working in contact mode. 127
Figure 4.5: Rendered images of the designed and machined probe holder together with the AFM cantilever mount and the AFM probe in (a) exploded and (b) assembly views..... 130
Figure 4.6: (a) A topography image of the XYZ calibration nanogrid circular structure. (b) A section view through the white line shown in (a). 133
Figure 4.7: Topography images of the calibration nanogrid with the highly ordered structures showing the manifestation of hysteresis and creep through the distortion of the arrays; (a) circular structures with a pitch size of 500 nm (reverse scan), (b) linear structure with a pitch size of 5 μm (reverse scan), and (c) the forward and reverse scans of the section view across the white line shown in (b)..... 134
Figure 4.8: An indentation curve obtained from a silicon sample surface prior processing showing the curve corrected for creep (red) calculated by subtracting the baseline (dotted blue) from the raw data (black) and shifted such that the point of contact is at the origin. 137

Figure 4.9: An indentation curve obtained from a silicon sample surface prior processing showing the approach (black) and retract (red) curves showing a hysteresis loop between them. 137
Figure 4.10: Force-distance curves against a silicon sample surface prior processing. (a) The raw PSD voltage [V] against Z Scanner distance [nm] data showing a slope i.e. Sensor Sensitivity Factor of 0.00115 V/nm. (b) The resulting Cantilever Deflection [nm] against Z Scanner [nm] upon dividing the PSD by the Sensor Sensitivity Factor to obtain a slope of 1. 140
Figure 4.11: Representative calibration indentation curves obtained from the XYZ calibration nanogrid using Tap190DLC, showing both the approach and retract curves for maximum pre-set indentation depths of 19.3 nm and 95.3 nm. 141
Figure 4.12: (a) The variability of the sensor sensitivity factor with pre-set indentation depth using three different types of cantilevers. (b) A representative relationship between the sensor sensitivity factor using an FM50 probe (k = 2.6 N/m) upon increasing (ramp-up) and decreasing (ramp-down) the indentation depth, showing a fit to the relationship $Ss = adb$. 142
Figure 4.13: SEM micrographs of a Tap190DLC probe showing how the (a) length, l, widths, $w1$, $w2$, and (b) thickness, tC, were measured.....146
Figure 4.14: (a) Optical micrograph and (b, c) AFM topographical images of the graphene membrane investigated in Case Study 1. The circular graphene membrane as well as several folding of the graphene layers are indicated. 151
Figure 4.15: SEM images of the FM50 (a, b) cantilever and (c, d) tip (c) before and (d) after use. 152
Figure 4.16: SEM images of the Tap190DLC (a, b) cantilever and (c, d) tip (c) before and (d) after use. 152
Figure 4.17: SEM images of the DT NCLR (a, b) cantilever and (c, d) tip (c) before and (d) after use……..153
Figure 4.18: Representative calibration indentation curves obtained from the XYZ calibration nanogrid using Tap190DLC, showing both the approach and retract curves for maximum indentation depths of 19.3 nm and 95.3 nm. 153
Figure 4.19: The sensor sensitivity factor, Ss, as measured from the slope of the approach curves for (a) FM50, (b) Tap190DLC and (c) DTNCLR tips. 154

Figure 4.20: Representative FD curve showing the approach and retract curves for a single indentation prior post-processing. 156
Figure 4.21: Representative FD curves obtained from the same graphene membrane using the Tap190DLC probe during (a) ramp-up (when the indented depth is increased from the previous indentation), and (b) ramp-down (when the indented depth is decreased from the previous indentation); (c) presents all the curves. 156
Figure 4.22: The true indented depth against the pre-set indentation depth upon indenting the graphene membrane using the (a) FM50, (b) Tap190DLC, and (c) DTNCLR probes. All obtained FD curves were calibrated using both a fixed sensor sensitivity factor, F. Ss, and a variable sensor sensitivity factor, V. Ss. 157
Figure 4.23: The maximum indentation force against (a, c, e) the pre-set indentation depth, and (b, d, f) the indented depth using the FM50 (a, b), Tap190DLC (b, c), and DTNCLR (e, f) probes. 159
Figure 4.24: The calculated elastic modulus against (a, c, e) the pre-set indentation depth, and (b) the indented depth using the (a, b) FM50, (c, d) Tap190DLC, and (e, f) DTNCLR probes. 160
Figure 4.25: The average calculated elastic modulus, E, using both a fixed Ss and variable Ss, for all three probes used. The error bars represent the standard deviation. 161
Figure 4.26: The (a, c, e) reduced chi-square and adjusted R-square, and (b, d, f) standard error of parameter B of the fitting procedure, against the pre-set indentation depth using the (a, b) FM50, (c, d) Tap190DLC, and (e, f) DTNCLR probes. 162
Figure 4.27: The average calculated elastic modulus, E, using a variable Ss, and a pre-set indentation depth of between 40 nm and 80 nm, for all three probes. Error bars represent the standard deviation. 163
Figure 4.28: Calculated elastic modulus, E, against indented depth using all three probes. . 164
Figure 4.29: The maximum indentation force at maximum indented depth for every FD curve obtained on the same graphene membrane using the FM50, Tap190DLC, and DTNCLR tips, calibrated with the variable Ss. 164
Figure 4.30: (a) Optical micrograph and (b) AFM topographical image of the graphene membrane investigated in Case Study 2. Two circular graphene membranes, M01 and M02, are indicated. 165
Figure 4.31: SEM images of the FM50 (a, b) cantilever and (c, d) tip (c) before and (d) after use. 166

Figure 4.32: SEM images of the Tap190DLC (a, b) cantilever and (c, d) tip (c) before and (d) after use. 166
Figure 4.33: The sensor sensitivity factor, Ss, as measured from the slope of the approach curves for (a) FM50 and (b) Tap190DLC. 167
Figure 4.34: Results from indentations carried out using the Tap190DLC probe on graphene membranes M01 and M02. (a) Representative FD curves, (b) the true indented depth of the graphene membranes upon indentation against the pre-set indentation depth, (c, d) the maximum indentation force against (c) the pre-set indentation depth, and (d) the indented depth, and (e, f) the calculated elastic modulus against (e) the pre-set indentation depth, and (f) the indented depth. 168
Figure 4.35: (a) Indented depth against pre-set indentation depth, and (b) elastic modulus, (c) maximum force, (d) standard error of the cubic term, and (e) reduced chi-squared and adjusted R-square against indented depth, for a representative graphene membrane using a FM50 probe with $ktrapezoidal$ of 2.6 N/m. 174
Figure 4.36: (a) Indented depth against pre-set indentation depth, and (b) elastic modulus, (c) maximum force, (d) standard error of the cubic term against indented depth, and (e) reduced chi-squared and adjusted R-square for two representative graphene membranes using two Tap190DLC probes with $ktrapezoidal$ of 48 N/m and 48.8 N/m. 175
Figure 4.37: (a) Indented depth against pre-set indentation depth, and (b) elastic modulus, (c) maximum force, (d) standard error of the cubic term, and (e) reduced chi-squared and adjusted R-square against indented depth, for a representative graphene membrane using a DTNCLR probe with k of 54 N/m. 176
Figure 4.38: Values for the elastic modulus with the respective standard error against the indented depth, measured using the (a) DTNCLR, (b) Tap190DLC, and (c) FM50 probes. k is the spring constant of the cantilever used in N/m while M01, M02 etc. refer to different membranes. Note that each membrane is only indented with one probe. 177
Figure 4.39: Values for the pretension against the indented depth, measured using the (a) DTNCLR, (b) Tap190DLC, and (c) FM50 probes. k is the spring constant of the cantilever used in N/m while M01, M02 etc. refer to different membranes. Note that each membrane is only indented with one probe. 179
Figure 4.40: Values for the elastic modulus against the pretension, measured using the (a) DTNCLR, (b) Tap190DLC, and (c) FM50 probes. k is the spring constant of the cantilever

used in N/m while M01, M02 etc. refer to different membranes. Note that each membrane is only indented with one probe. 180
Figure 4.41: Values for the pretension against the elastic modulus, measured using the (a) DTNCLR, (b) Tap190DLC, and (c) FM50 probes. k is the spring constant of the cantilever used in N/m while M01, M02 etc. refer to different membranes. Note that each membrane is only indented with one probe. 181
Figure 4.42: Average value of the elastic modulus omitting values obtained from indentation depths lower than 25 nm, against the spring constant of the probe used. The error bars represent the standard error. 182
Figure 4.43: Histograms and log-normal distribution curves of the obtained values of the elastic modulus for all indented depths using the (a) DTNCLR, (b) Tap190DLC, (c) FM50, and (d) all probes. 183
Figure 4.44: A comparison of the distribution curves for the elastic moduli obtained at all indentation depths using the DTNCLR, Tap190DLC, and FM50 probes, in red, blue, and green respectively. (a) and (b) have different scales. 183
Figure 4.45: (a – c) Tapping mode AFM images obtained in ambient conditions using a Tap190DLC probe (k = 24 N/m using the Sader method) of the CVD-graphene membranes. (d) Cross-sectional height data across two typical graphene membranes. 186
Figure 4.46: The average measured elastic modulus as measured using the DTNCLR, Tap190DLC and FM50 probes. The error bars represent the standard error. 187
Figure 4.47: Typical FD curve obtained using Tap190DLC with Equation 4.5 being fit to different indented depths. 189
Figure 5.1: Treated supported CVD graphene patterned via a focused gallium ion beam. (a) SEM image. (b-e) 2D Raman spectral maps of the sum of parts of the spectrum depicting the intensity of the (b) G and D, (c) D, (d) G, and (e) 2D peaks. 199
Figure 5.2: Representative Raman spectra from the supported CVD graphene treated with a dose of 1×10^{-12} C/μm^2 (T1), 5×10^{-13} C/μm^2 (T0.5), and 1.8×10^{-13} C/μm^2 (T0.18). 200
Figure 5.3: The position of the Lorentzian D band (P_D) and Lorentzian G band (P_G) in the damaged supported graphene. 201
Figure 5.4: The 2D band in the damaged supported graphene. 201
Figure 5.5: The (a) intensity, (b) FWHM, and (c) position of the Gaussian D and Gaussian G bands in the damaged supported graphene. (d) The intensity of the Lorentzian D band (I_D) and the intensity ratio between the Lorentzian D band and Lorentzian G band (I_D/I_G) in the damaged supported graphene. 202

Figure 5.6: The intensity of the Lorentzian D band (I_D) and the intensity ratio between the Lorentzian D band and Lorentzian G band (I_D/I_G) in the damaged supported graphene.....203
Figure 5.7: The intensity ratio between the Gaussian and Lorentzian D band (I_{DG}/I_{DL}) and the intensity ratio between the Gaussian and Lorentzian G band (I_{GG}/I_{GL}) in the damaged supported graphene.....204
Figure 5.8: The Raman spectrum at $DT = 40$ μm showing the D peak (1327.4 cm^{-1}), 'Gaussian G' peak (1530.1 cm^{-1}), Lorentzian G peak (1590.0 cm^{-1}), D' peak (1620.68 cm^{-1}) and 2D peak (2637.7 cm^{-1}).....204
Figure 5.9: (a) The position and intensity of the Lorentzian 2D peak, and (b) the intensities of the Lorentzian D and G peaks, in suspended graphene. 205
Figure 5.10: The position of the Lorentzian and Gaussian (a) D peak, and (b) G peak, in suspended graphene. 205
Figure 5.11: (a) The FWHM and integrated area of the Lorentzian 2D peak, and (b) the intensity ratio I_D/I_G and FWHM ratio F_D/F_G, in suspended graphene. 206
Figure 5.12: The Lorentzian D peak against ion beam incidence angle.....206
Figure 5.13: The FWHM and integrated area of the Lorentzian G peak against ion beam incidence angle.....207
Figure 5.14: The intensity ratio I_D/I_G and the FWHM ratio F_D/F_G against the incident angle. 207
Figure 5.15: Optical micrographs of the CVD graphene on the silicon nitride microsieve (a) before, and (b) after removal of the sacrificial layer, showing the ion irradiated areas in (b). 208
Figure 5.16: Raman spectra obtained of the CVD-graphene on the silicon nitride microsieve in the untreated (UT) and treated (T) regions. The spectra were (a) averaged and normalised, and (b) subtracted from the baseline.....208
Figure 5.17: 2D Raman spectral maps of the sum of parts of the spectrum depicting the intensity of the (a, d) 2D, (b, e) G, and (c, f) D peaks of Flake E, (a – c) before and (d – f) after ion bombardment. 210
Figure 5.18: Raman spectra obtained from Flake E (a, b) before, and (c) after ion bombardment. In all spectra, an appropriate baseline was fitted and subsequently subtracted from the raw data. 210
Figure 5.19: Optical micrograph of Flake F (a) before, and (b) after irradiation. 211

Figure 5.20: 2D Raman spectral maps of the sum of parts of the spectrum depicting the intensity of the (a, d) 2D, (b, e) G, and (c, f) D peaks of Flake F, (a – c) before and (d – f) after ion bombardment. 212
Figure 5.21: Raman spectra obtained from Flake F before (dashed), and after (solid) ion bombardment. 212
Figure 5.22: Representative 2D peak from the untreated Flake F. 213
Figure 5.23: (a) Optical micrograph, and (b) AFM height micrograph of Flake G. 214
Figure 5.24: 2D Raman spectral maps of the sum of parts of the spectrum depicting the intensity of the (a, d) 2D, (b, e) G, and (c, f) D peaks of Flake G (a – c) before and (d – f) after ion bombardment. 214
Figure 5.25: Raman spectra obtained from Flake G before (dashed), and after (solid) ion bombardment. 215
Figure 5.26: Optical micrograph of Flake H. 216
Figure 5.27: 2D Raman spectral maps of the sum of parts of the spectrum depicting the intensity of the (a) 2D, (b) G, and (c) D peaks of Flake H, after ion bombardment. 216
Figure 5.28: Raman spectra obtained from Flake H after ion bombardment. 216
Figure 5.29: 2D Raman spectral maps of the sum of parts of the spectrum depicting the intensity of the (a, d) 2D, (b, e) G, and (c, f) D peaks of Flake C, (a – c) before and (d – f) after ion bombardment. 217
Figure 5.30: Raman spectra obtained from Flake C before (dashed), and after (solid) ion bombardment. 218
Figure 5.31: Optical micrograph of Flake I. 218
Figure 5.32: 2D Raman spectral maps of the sum of parts of the spectrum depicting the intensity of the (a, d) 2D, (b, e) G, and (c, f) D peaks of Flake I, (a – c) before and (d – f) after ion bombardment. 219
Figure 5.33: Raman spectra obtained from Flake I before (dashed), and after (solid) ion bombardment. 219
Figure 5.34: Optical micrograph of Flake J. 220
Figure 5.35: 2D Raman spectral maps of the sum of parts of the spectrum depicting the intensity of the (a) 2D, (b) G, and (c) D peaks of Flake J, after ion bombardment. 220
Figure 5.36: Raman spectra obtained from Flake J after ion bombardment. 221
Figure 5.37: The evolution of the intensity ratio between the Lorentzian D and D' bands ($I_D/I_{D'}$) and the intensity ratio between the Lorentzian D' and G bands ($I_{D'}/I_G$). 223

Figure 5.38: The evolution of (a) the intensity ratios I_{DG}/I_{DL} and I_{GG}/I_{GL}, and (b) the total integrated area A_D and A_G in suspended graphene. 225
Figure 5.39: The peak parameters with increasing dose. Every data point represents the average obtained from one entire flake, with the error bars signifying the standard deviation. 228
Figure 5.40: Average value of the elastic modulus before (UT) and after (T) treatment, against the spring constant of the probe used. The error bars represent the standard error. 232
Figure 5.41: The average measured elastic modulus as measured using the FM50, Tap190DLC, and DTNCLR, probes before (UT) and after (T) treatment. The error bars represent the standard error. 232
Figure 5.42: (a) The calculated elastic modulus against the indented depth, and (b) the average calculated elastic modulus, E, using a pre-set indentation depth of between 40 nm and 80 nm, before (UT) and after (T) ion bombardment. 233
Figure 5.43: (a) The calculated elastic modulus against the indented depth, and (b) the average calculated elastic modulus, E, using a pre-set indentation depth of between 40 nm and 80 nm, using two Tap190DLC probes on both graphene membranes M01 and M02, before (UT) and after (T) ion bombardment. 234
Figure 6.1: A flow chart showing the velocity Verlet algorithm in a typical MD simulation timestep. 239
Figure 6.2: Schematics of (a) the Morse bond length rij, (b) the bond angle θjik, (c) the torsion angle $\phi jikl$, and (d) the Lennard-Jones pair interaction distance rij, where the highlighted region indicates the 1–2 and 1–3 atom interactions which are excluded for an arbitrary atom i. 241
Figure 6.3: (a) A schematic illustration of a graphene sheet showing the edge atoms constrained (shaded in grey) for the application of the pre-defined strain-rate. (b) and (c) illustrate the loading direction of an armchair (AC) and zigzag (ZZ) sheet, respectively. 243
Figure 6.4: Results for elastic modulus, fracture stress and fracture strain for AC- oriented graphene (red solid circles) and ZZ-oriented graphene (blue inverted triangles) with increasing sheet size for two different temperatures: (a – c) 0 K, and (d – f) 300 K. The dashed lines represent bulk mechanical properties. 245
Figure 6.5: (a) Stress-strain plot of AC (red) and ZZ (blue) graphene sheets. All simulations were run at 300 K except the ones marked otherwise. Results from other simulations for sheets with a single vacancy (SV) defect, and nanoporous sheets with 7% defect density are also

presented. (b) and (c) illustrate the resolved forces along selected covalent bonds during AC and ZZ loading, respectively.....247
Figure 6.6: Fracture process of a pristine AC graphene sheet with a diagonal length of 14.63 nm at 300 K. (a – f) show snapshots of the sheet at different times of the simulation during the occurrence of fracture. 248
Figure 6.7: Fracture process of a pristine ZZ graphene sheet with a diagonal length of 14.84 nm at 300 K. (a – f) show snapshots of the sheet at different times of the simulation during the occurrence of fracture. 248
Figure 6.8: Results for (a) elastic modulus, (b) fracture stress, and (c) fracture strain of AC (red solid circles) and ZZ (blue inverted triangles) graphene sheets (LD=14.7 nm), varying with sheet temperature. 249
Figure 6.9: (a) Plot showing the increase in rippling in the z-direction with an increasing sheet temperature in AC and ZZ graphene sheets. The effective thickness has been normalized with respect to the original thickness of the pristine graphene sheets at 0 K i.e. $z0K$ = 0.335 nm. (b) and (c) illustrate a side view of pristine graphene sheets at 0 K and 1100 K, respectively, to highlight the rippling effect in the z-direction at higher temperatures. 250
Figure 6.10: Graphs showing elastic modulus, fracture stress and fracture strain for AC- (red solid circles) and ZZ-loaded (blue inverted triangles) graphene sheets at 300 K with increasing defect density distributed (a – c) randomly, and (d – f) uniformly. The dashed lines represent bulk mechanical properties. 252
Figure 6.11: The increase in rippling in the z-direction with an increasing (a) random and (b) ordered defect density in AC and ZZ graphene sheets. The effective thickness has been normalized with respect to the original thickness of the pristine graphene sheets at 0 K. (c) A side view of a pristine graphene sheet at 0 K. (d, e) Side views of ZZ graphene sheets with a (d) random and (e) ordered defect density of 12% after 37 ps of relaxation. 253
Figure 6.12: Fracture process of an AC graphene sheet with a diagonal length of 14.63 nm at 300 K and with a single vacancy defect at its centre; (a – f) show snapshots of the sheet at the corresponding time in picoseconds (ps) after initiation of loading.....254
Figure 6.13: Fracture process of a ZZ graphene sheet with a diagonal length of 14.84 nm at 300 K and with a single vacancy defect at its centre; (a – f) show snapshots of the sheet at the corresponding time in picoseconds (ps) after initiation of loading.....254
Figure 6.14: Fracture process of a ZZ graphene sheet with a diagonal length of 14.48 nm at 300 K and with 5.5% of the original atoms selected randomly and removed as vacancy defects; (a

– f) show snapshots of the sheet at the corresponding time in picoseconds (ps) after initiation of loading. 255
Figure 6.15: Fracture process of a ZZ graphene sheet with a diagonal length of 13.67 nm at 300 K and with 5% of the original atoms being removed as vacancy defects and distributed uniformly; (a – f) show snapshots of the sheet at the corresponding time in picoseconds (ps) after initiation of loading. 255
Figure 6.16: A schematic illustration of a graphene sheet showing the edge atoms constrained (shaded in grey) for the application of the pre-defined strain-rate. 259
Figure 6.17: Representative strain energy against strain curves of the uniaxially loaded ZZ graphene sheets at 1 K (black) and 300 K (red), and strain rate of 2.56×10^{8} s^{-1} (solid lines) and 8.55×10^{9} s^{-1} (dashed lines). 261
Figure 6.18: Strain energy against strain of the uniaxially loaded ZZ graphene sheet, together with the corresponding cubic fits. 261
Figure 6.19: The average (a) elastic modulus, (b) failure stress, and (c) failure strain obtained from uniaxial loading at the four loading conditions. The error bars represent the standard deviation across three repeated readings. 262
Figure 6.20: (a) Perspective and (b) side views of the system geometry of the nanoindentation simulations showing the hemispherical diamond indenter (red), graphene membrane (black), and the porous substrate (blue). 266
Figure 6.21: Force-distance curve for the benchmark case. 269
Figure 6.22: Force-distance curves for indentation velocities of 3 m/s, 10 m/s and 100 m/s. 271
Figure 6.23: The dependency of the time-steps computed per second, and the total computational time with an increase in the total number of simulated atoms. 273
Figure 6.24: (a) Force-distance curves and (b) force/membrane radius vs distance/membrane radius curves for membrane radii of 5, 6.5, 8, 9.5, 15, and 50 nm. 274
Figure 6.25: (a) Force-distance curves and (b) force/membrane radius vs. distance/membrane radius curves for indentation velocities of 100 m/s and 10 m/s, and membrane radius of 5 nm and 22.5 nm, respectively. 274
Figure 6.26: Force-distance curve and change in temperature of the graphene sheet with indentation distance. 276
Figure 6.27: Force-distance curves for membrane radius of 50 nm, with fitting ignoring the data points within the peaks marked in red. 276

Figure 6.28: Illustration of the effect of periodic boundaries whereby one simulation box is a unit cell which is repeated in the adjacent cells. 277
Figure 6.29: Force-distance curves for membrane radius of 5 nm at an indentation velocity of 100 m/s, with an $a:L$ ratio of 0.417 (black line) and 0.0123 (red lime). 278
Figure 6.30: Force-distance curves as obtained using the Berendsen and Nosé-Hoover thermostats, both at 300 K. 279
Figure 6.31: A series of snapshots during indentation with a dynamic substrate. Only a slice through the middle of the graphene membrane system of 13 Å width is shown. 280
Figure 6.32: (a) Perspective and (b) side views of the system geometry of the nanoindentation simulations using a spring-loaded tip to simulate the effect of a flexible cantilever with a known spring constant, k. The hemispherical diamond indenter is coupled to a cylindrical cantilever by a virtual spring. 283
Figure 6.33: Force-distance curves of simulations utilizing different spring constants, k (eV/Å^2), and cantilever-to-indenter distance, d (Å). 283
Figure 6.34: Force-distance curves of simulations utilizing different methods of calculating the force. 284
Figure 6.35: A series of snapshots obtained during indentation of the graphene membrane using the spring-loaded indenter with k = 3.12 eV/Å^2, d = 23.13 Å. (a) Before indenter-to-graphene contact, (b) during indentation, (c) when the virtual spring is fully compressed such that the cantilever atoms are in contact with the indenter atoms, and (d) after graphene membrane failure. 285
Figure 6.36: Wrinkling in a 15 nm radius membrane without periodic boundaries. 287
Figure 6.37: Force-distance curves for similar 15 nm radius membranes indented with an indentation velocity v of 100 m/s (black) and by a step-wise displacement d of 0.2 Å (red). 287
Figure 6.38: (a) Force-distance curves, and (b) force/membrane radius vs distance/membrane radius curves for membrane radii of 5, 15, and 25 nm. Simulation a = 25 nm* was performed with longer equilibration time between indentation steps. 287
Figure 6.39: Force-distance curves of simulations utilizing different spring constants, k (eV/Å^2), with the same cantilever-to-indenter distance of 63.13 Å; (a) raw data, (b) smoothed, and (c) shifted in the x-direction such that the curves overlap at higher indentation depths. 289
Figure 6.40: Elastic moduli as measured using different spring constants, and fitted to the entire force curve vs. to indentation depths higher than 4 nm. 291

Figure 6.41: (a) Cumulative-fitting of the force distance curve to different indentation distances. (b) The resulting elastic moduli obtained for different indentation distances.....292
Figure 6.42: The values of elastic modulus obtained via cumulative fitting of the force curve. The x-axis is represented by the normalized displacement δ/a.....292
Figure 6.43: (a) F vs. $\delta/a3$ showing examples of the rolling-average data set represented by M, and (b) the resulting elastic modulus at different indentation depths. M is not drawn to scale. 293
Figure 6.45: Selected F/a vs δ/a curves obtained via MD simulations and experimental AFM indentations. The elastic moduli in the legends were obtained by fitting Equation 6.23 to the entire force-curve. 295
Figure 6.46: The elastic modulus at different indentation depths for selected force curves obtained via MD simulations and experimental AFM indentations. (a) using the cumulative fitting for increasing δ/a, and (b) using rolling average at different $\delta/a3$. 295
Figure E.0.1: 2D Raman spectral maps of the suspended graphene treated with a dose of 4.86×10^{-4} C/μm^2. The intensity colour of each map represents the intensity of the (a) D, (b) G, (c) 2D, and (d) G + D peaks.....330
Figure E.0.2: 2D Raman spectral maps of the suspended graphene treated with a dose of 5.28×10^{-5} C/μm^2. The intensity colour of each map represents the intensity of the (a) D, (b) G, (c) 2D, and (d) G + D peaks.....330
Figure E.0.3: 2D Raman spectral maps of the suspended graphene treated with a dose of 3.27×10^{-3} C/μm^2 at an incidence angle of 83°. The intensity colour of each map represents the intensity of the (a) D, (b) G, (c) 2D, and (d) G + D peaks.....331

LIST OF TABLES

Table 2.1: Published values for the elastic modulus of graphene membranes prepared via mechanical exfoliation. 38
Table 2.2: Published values for the elastic modulus of graphene membranes prepared via other preparation methods. 39
Table 2.3: Mechanical properties of graphene measured under uniaxial tensile loading in MD. 46
Table 3.1: The materials used for the preparation of the graphene samples and/or substrates. 71
Table 3.2: The graphene-substrate combinations investigated. 71
Table 3.3: The approximate thickness of locations B1 to B6, and membranes covering holes BH1 to BH4, as measured by static contact mode AFM. Note that the stated thicknesses may vary by ± 2.5 nm. 90
Table 3.4: The relative shift (P) and the full width at half maximum (F) of the D, G, D+D'', 2D and 2D' peaks obtained from various locations in Flake A as shown in Figure 3.21. 93
Table 3.5: The intensity (I) and width (F) ratios between the D and G peaks, and the 2D and G peaks obtained from various locations in Flake A as shown in Figure 3.21. 93
Table 3.6: The relative shift (P) and the full width at half maximum (F) of the D, G, D+D'', 2D and 2D' peaks obtained from various locations in the CVD graphene on SiO_2/Si substrate as shown in Figure 3.31, using the 532 nm excitation wavelength. 105
Table 3.7: The intensity (I) and width (F) ratios between the D and G peaks, and the 2D and G peaks obtained from various locations in the CVD graphene on SiO_2/Si substrate as shown in Figure 3.31, using the 532 nm excitation wavelength. 105
Table 3.8: The relative shift (P) and the full width at half maximum (F) of the D, G, D+D'' and 2D peaks obtained from various locations in the CVD graphene on TEM grid. 110
Table 3.9: The intensity (I) and width (F) ratios between the D and G peaks, and the 2D and G peaks obtained from various locations in the CVD graphene on TEM grid. 110
Table 3.10: The relative shift (P), full width at half maximum (F), and intensity (I) and ratios between the G and 2D peaks obtained from various locations across the Easy Transfer graphene on 0.45 μm microsieve as shown in Figure 3.42. 116

Table 4.1: The AFM probe types used together with the tip material, nominal tip radius, nominal spring constant, $knominal$, and nominal resonance frequency, $f0$, as provided by the manufacturer. 131
Table 4.2: The cantilever length, l, width, w, and thickness, t, are given in μm, the spring constant, k, is given in N/m, and the resonance frequency, $f0$, and the 1st order harmonic, $f1$, are given in kHz. 149
Table 4.3: The AFM probes used together with the nominal spring constant, $knominal$, and the calculated spring constants, $ktrapezoidal$. 151
Table 4.4: Statistical analysis of the elastic moduli as obtained using the three different types of probes. 182
Table 5.1: Patterning Focused Gallium Ion Beam Treatments on Supported CVD Graphene on SiO_2/Si, and Suspended CVD Graphene on TEM Grids. 196
Table 5.2: Imaging Focused Gallium Ion Beam Treatments on Suspended CVD Graphene on Silicon Nitride Microsieves. 197
Table 5.3: Focused Gallium Ion Beam Treatments on Mechanically Exfoliated Multi-layer Graphene on patterned PAA/Si Substrate. 197
Table 5.4: Focused Gallium Ion Beam Treatments on Mechanically Exfoliated Multi-Layer Graphene indented via AFM. 231
Table 6.1: Parameter constants for the potential functions. [270] 241
Table 6.2: Measured mechanical properties of pristine bulk graphene. Note that the error bars of the 0 K graphene sheet are negligible and have not been included. 246
Table 6.3: Parameter constants for the AIREBO potential functions. [263] 258
Table 6.4: Simulation parameters and results obtained by uniaxial loading a ZZ graphene sheet with $LD = 16.4$ nm. The errors represent the standard deviation across three repeated readings. 262
Table 6.5: Simulation dimensional parameters compared to the AFM experimental set-up. 268
Table 6.6: Simulation dimensional parameters to investigate the size-effect. All simulations were performed using the 4-core CPU using a 100 m/s indentation velocity, unless otherwise noted. 273
Table 6.7: The results comparing the elastic modulus, E, and breaking strength, σm, using different membrane radii, a. r is the indenter radius in nm while v is the indentation velocity. 275

Table 6.8: The results comparing different spring constants, k, and cantilever-to-indenter distance, d. The membrane radius is 5 nm, indenter radius 0.7 nm, temperature 300 K, and indentation velocity 100 m/s. 284
Table 6.9: The results comparing the elastic modulus, E, and breaking strength, σm, using different membrane radii, a. r is the indenter radius equal to 0.5 nm, and an indenter displacement of 0.2 Å was used. 288
Table 6.10: The results comparing different spring constants, k. The cantilever-to-indenter distance is 63.12 Å, membrane radius 25 nm, indenter radius 0.7 nm, temperature 300 K, indentation step-wise displacement of 0.1 Å and 2000 time-steps equilibration after each indentation step. 289
Table 6.11: The results comparing different spring constants, k upon fitting Equation 6.23 to the entire force curve or to indentation depths, δ > 4 nm. 291
Table F.0.1: The relative shift (P) and the full width at half maximum (F) of the D, G, and 2D peaks obtained from untreated (UT) and irradiated (T) membranes. 332
Table F.0.2: The intensity (I) and width (F) ratios between the D, G and 2D peaks obtained from untreated (UT) and irradiated (T) membranes. 332
Table F.0.3: The relative shift (P) and the full width at half maximum (F) of the D, G, and D' peaks obtained from various locations in Flake F, before (UT) and after (T) irradiation. 333
Table F.0.4: The relative shift (P) and the full width at half maximum (F) of the $2D^1$ and $2D^2$ peaks obtained from various locations in Flake F, before (UT) and after (T) irradiation. 333
Table F.0.5: The intensity (I) and width (F) ratios between the D, G and D' peaks obtained from various locations in Flake F, before (UT) and after (T) irradiation. 334
Table F.0.6: The relative shift (P) and the full width at half maximum (F) of the D, G, D' and D+D'' peaks obtained from various locations in Flake G, before (UT) and after (T) irradiation. 334
Table F.0.7: The relative shift (P) and the full width at half maximum (F) of the $2D^1$, $2D^2$ and 2D' peaks obtained from various locations in Flake G, before (UT) and after (T) irradiation. 334
Table F.0.8: The intensity (I) and width (F) ratios between the D, G, and D' peaks obtained from various locations in Flake G, before (UT) and after (T) irradiation. 335
Table F.0.9: The relative shift (P) and the full width at half maximum (F) of the D, G, and D' peaks obtained from various locations in Flake H after (T) irradiation. 335

Table F.0.10: The relative shift (P) and the full width at half maximum (F) of the $2D^1$ and $2D^2$ peaks obtained from various locations in Flake H after (T) irradiation. 335
Table F.0.11: The intensity (I) and width (F) ratios between the D, G and D' peaks obtained from various locations in Flake H after (T) irradiation. 335
Table F.0.12: The relative shift (P) and the full width at half maximum (F) of the D, G, D' and D+D'' peaks obtained from various locations in Flake C, before (UT) and after (T) irradiation. 336
Table F.0.13: The relative shift (P) and the full width at half maximum (F) of the $2D^1$, $2D^2$ and 2D' peaks obtained from various locations in Flake, before (UT) and after (T) irradiation. .336
Table F.0.14: The intensity (I) and width (F) ratios between the D, G and D' peaks obtained from various locations in Flake C, before (UT) and after (T) irradiation. 336
Table F.0.15: The relative shift (P) and the full width at half maximum (F) of the D, G, D' and D+D'' peaks obtained from various locations in Flake I, before (UT) and after (T) irradiation. 337
Table F.0.16: The relative shift (P) and the full width at half maximum (F) of the $2D^1$, $2D^2$ and 2D' peaks obtained from various locations in Flake I, before (UT) and after (T) irradiation. 337
Table F.0.17: The intensity (I) and width (F) ratios between the D, D' and G peaks obtained from various locations in Flake I, before (UT) and after (T) irradiation. 337
Table F.0.18: The relative shift (P) and the full width at half maximum (F) of the D, G, D' and D+D'' peaks obtained from various locations in Flake J, after (T) irradiation. 338
Table F.0.19: The relative shift (P) and the full width at half maximum (F) of the $2D^1$ and $2D^2$ peaks obtained from various locations in Flake J, after (T) irradiation. 338
Table F.0.20: The intensity (I) and width (F) ratios between the D, G, and D' peaks obtained from various locations in Flake J, after (T) irradiation. 338

LIST OF ABBREVIATIONS AND SYMBOLS

Abbreviation	Definition
2D	Two-dimensional
3D	Three-dimensional
AC	Armchair
AFM	Atomic Force Microscopy
AIREBO	Adaptive Intermolecular Reactive Empirical Bond Order
BLG	Bi-Layer Graphene
CVD	Chemical Vapour Deposition
DC	Direct Current
DFT	Density Functional Theory
DLC	Diamond-like Carbon
DMME	Department of Metallurgy and Materials Engineering
EFM	Electrostatic Force Microscopy
FCC	Face Centred Cubic
FD	Force-Distance
FEA	Finite Element Analysis
FET	Field-effect Transistor
FLG	Few-Layer Graphene
FWHM	Full Width at Half Maximum
GB	Grain Boundary
GNR	Graphene Nanoribbon
GO	Graphene Oxide
HOPG	Highly Oriented Pyrolytic Graphite
ICF	Integrated Characterisation Facility
IPA	Isopropyl Alcohol
LAMMPS	Large-scale Atomic/Molecular Massively Parallel Simulator
LJ	Lennard-Jones
MD	Molecular Dynamics
MEMS	Microelectromechanical Systems
MLG	Multi-Layer Graphene

NEMS	Nanoelectromechanical Systems
NPT	Isothermal-Isobaric Ensemble
NVE	Microcanonical Ensemble
NVT	Canonical Ensemble
NWs	Nanowires
OM	Optical Microscopy
PAA	Plasma-polymerized Polyacyclic Acid
PDDA	Poly(diallyldimethylammonium chloride)
PDMS	Polydimethylsiloxane
PMMA	Poly(methyl methacrylate)
PS	Polystyrene
PSD	Photosesitive Diode
RF	Radio Frequency
rGO	Reduced Graphene Oxide
RIE	Reactive Ion Etching
SEM	Scanning Electron Microscopy
SLG	Single-Layer Graphene
STM	Scanning Tunnelling Microscopy
T	Treated
TEM	Transmission Electron Microscopy
TUNA	Peak Force Tunnelling AFM
UHV	Ultrahigh vacuum
UM	University of Malta
UT	Untreated
ZDP	Zero-Displacement Point
ZZ	Zigzag

Symbol	Meaning	Units
a	Membrane radius	nm
a_{equi}	Equivalent radius of a rectangular graphene sheet	nm
A	Fitting parameter	N/m
A_{ij}	REBO fitting parameter	eV
b	Breadth of sheet	nm
b_{ij}	Bond order	-
B	Fitting parameter	N/m^3
$B_{ij}^{(1),(2),(3)}$	REBO fitting parameters	eV
d	Equilibrium cantilever-indenter distance	Å
d	Cantilever deflection	nm
D	Z Scanner pre-set indentation depth	nm
D_T	Distance from edge of treated area	μm
E	Elastic modulus	TPa
E^{2D}	2D elastic constant	N/m
f_0	Resonance frequency	kHz
f_1	First harmonic of the resonance frequency	kHz
$\boldsymbol{f}_i$	Force vector of atom i	N
f_n	Eigenfrequency of the n^{th} mode	kHz
F	FWHM of peak	cm^{-1}
F	Applied force	nN
F_0	Force at the ZDP	nN
h^{DG}	Initial height if indenter above graphene sheet	nm
h^S	Substrate thickness	nm
h^{SG}	Distance between graphene and substrate	nm
I	Intensity of peak	-
I	Moment of inertia	$kg\ m^2$
k	Cantilever spring constant	N/m
$k_{nominal}$	Nominal spring constant	N/m
$k_{tip-mass}$	Spring constant with tip-mass correction	N/m
$k_{trapezoidal}$	Spring constant with trapezoidal correction	N/m

K_{Cr}	Morse potential force constant	kJ mol^{-1}
$K_{C\theta}$	Bending force constant	kJ mol^{-1}
$K_{C\phi}$	Torsion force constant	kJ mol^{-1}
l	Cantilever length	μm
l_0	Original distance between two atoms	mm
$l_x(t)$	Distance between two atoms at time t	mm
L	Length of sheet	nm
L_D	Diagonal length of sheet	nm
m	Mass of cantilever	kg
m_i	Mass of atom i	kg
M	Number of data points for rolling-average	-
N	Number of atoms	-
P	Raman shift, or position of peak	cm^{-1}
PSD	PSD voltage	V
q	Dimensionless constant	-
Q_{ij}	REBO fitting parameter	Å
r	Indenter tip radius	nm
r_C	Equilibrium bond length	Å
r_{cut}	Cut-off radius	nm
$\boldsymbol{r}_i$	Position vector of atom i	nm
r_{ij}	Morse bond length	nm
SE	Standard error	-
S_s	Sensor sensitivity factor	V/nm
t	Time	s
t_C	Cantilever thickness	μm
t_G	Thickness of membrane	nm
T	Temperature	K
U	Strain energy	J
v	Velocity	m/s
$\boldsymbol{v}_i$	Velocity vector of atom i	m/s
V_0	Original volume	nm^3
$\mathcal{V}_{ij}^A$	Attractive contribution	J

$\mathcal{V}^{AIREBO}$	AIREBO potential	J
$\mathcal{V}_{jik}^{BA}$	Harmonic bending angle potential	J
$\mathcal{V}_{ij}^{LJ}$	Lennard-Jones potential	J
$\mathcal{V}_{ij}^{M}$	Morse stretching potential	J
$\mathcal{V}^{MORSE}$	Morse potential	J
$\mathcal{V}(r)$	Force field	J
$\mathcal{V}_{ij}^{R}$	Repulsive contribution	J
$\mathcal{V}^{REBO}$	REBO potential	J
$\mathcal{V}_{jikl}^{T}$	Torsion potential	J
w	Cantilever width	µm
w_1	Cantilever back side width	µm
w_2	Cantilever tip side width	µm
w_{ij}	Bond-weighting factor	-
Z	Corrected displacement	nm
z_D	Effective thickness for defect density D	nm
z_T	Effective thickness at temperature T	nm
α_1	Eigenvalues of the Euler-Bernoulli equation	-
α_2	Eigenvalues of the Euler-Bernoulli equation	-
α_{ij}	REBO fitting parameter	$Å^{-1}$
α_n	Eigenvalues of the Euler-Bernoulli equation	-
$\beta_{ij}^{(1),(2),(3)}$	REBO fitting parameters	$Å^{-1}$
γ	Morse potential constant	$Å^{-1}$
δ	Deflection of membrane	nm
δ_0	Displacement at the ZDP	nm
Δt	Time-step	fs
ε	Strain	-
ε_f	Failure strain	-
ϵ_{CC}	Characteristic energy of Lennard-Jones potential	kJ mol^{-1}
ϵ_{DG}	Characteristic energy of Lennard-Jones potential	eV
ϵ_{SG}	Characteristic energy of Lennard-Jones potential	eV
θ_C	Equilibrium C-C angle	°

θ_{jik}	Bond angle	°
μ	Ratio between tip mass and cantilever mass	-
ν	Poisson's ratio	-
ρ	Density	kg m^{-3}
σ	Stress	GPa
σ_0^{2D}	Pre-tension	N/m
σ_m^{2D}	Maximum fracture stress	N/m
σ_{CC}	Characteristic length of Lennard-Jones potential	Å
σ_{DG}	Characteristic length of Lennard-Jones potential	Å
σ_f	Failure stress	Pa
σ_{SG}	Characteristic length of Lennard-Jones potential	Å
ϕ_C	Equilibrium out-of-plane torsion angle	°
τ_T	Relaxation time	ps
ϕ_{jikl}	Torsion angle	°

To raise new questions, new possibilities, to regard old problems from a new angle, requires creative imagination and marks real advance in science.

~ Albert Einstein

Chapter 1 INTRODUCTION

Advances in nanotechnology has led multi-disciplinary scientific researchers to discover new exciting phenomena and invent breakthrough materials and technologies. One such notable discovery includes the successful synthesis of graphene [6, 7], a strictly two-dimensional (2D) carbonaceous material possessing remarkable electrical [8, 9], thermal [10, 11], chemical [12] and mechanical [13] properties. With such exceptional properties and the establishment of a large research investment [14], it is expected that graphene will markedly improve a number of existing technologies and become the enabling technology of new products and processes. Nonetheless, the proper understanding of graphene's properties and the ability to measure and predict them will truly allow for graphene-based technologies to be successful.

1.1 GRAPHENE

The 2D layers that make up graphite have been theoretically studied in the mid-20th Century [15, 16]. Such 2D structures were only used as theoretical models since it was generally believed that individual 2D layers are physically unstable due to large thermal fluctuations [17, 18]. However, in 2004, experimentation revealed the possibility of creating stable free-standing graphene [6] – a single hexagonal layer of sp^2-hybridized carbon (C) atoms. The atomic structure of graphene is illustrated in Figure 1.1; multiple graphene sheets stacked one on top of the other form the 3D bulk graphite. The discovery of graphene landed Novoselov and Geim a Nobel Prize in Physics in 2010 [19] and opened up research on other 2D materials such as hexagonal boron nitride, stanene and phosphorene [20, 21]. Apart from the widely researched monolayer graphene (or single-layer graphene (SLG)), two stacked layers of graphene (bilayer graphene (BLG)), few-layer graphene (FLG), and multi-layer graphene (MLG) have also been identified and produced.

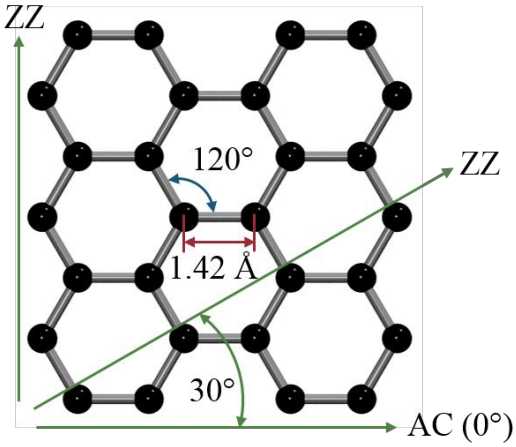

Figure 1.1: A model of a graphene sheet showing the bond length (1.42 Å), bond angle (120°), and direction notation (armchair, AC, and zigzag, ZZ, directions).

Following its breakthrough discovery, numerous investigations on the properties and behaviour of graphene when exposed to different conditions were, and are still being, carried out. Perhaps one of the most researched areas is the electrical properties of graphene. Its single-atom thickness and very high electron mobility allow the use of graphene in nanoelectromechanical systems (NEMS) and microelectromechanical systems (MEMS), even possibly replacing the widely-used silicon in the micro and nano-electronics industry with smaller and more efficient transistors.

On the other hand, the mechanical properties of graphene have been studied to a lesser extent compared to its electrical and electronic counterpart. The design of graphene-based technologies that rely on the mechanical performance of graphene requires extensive knowledge on its mechanical properties for its use in that specific application. Early experiments demonstrated that graphene possesses a very high breaking strength, coupled with an elastic modulus comparable to that of diamond and graphite along the basal plane [13]. These promising results were followed by other experimental, theoretical, and simulation studies geared towards the measurement and/or calculation of such properties and their response to a change in system conditions (such as temperature and the quality of the graphene sheet). The permeability of graphene sheets was also studied, concluding that while pristine graphene is impermeable to even one of the smallest atoms, helium [22], the controlled introduction of nanopores in the graphene membrane renders the nanomaterial selectively permeable [23], that is, only atoms or molecules smaller than the nanopores would be able to pass through the graphene membrane. Such characteristics permit graphene to be exploited in new, exciting applications.

1.1.1 MECHANICAL PROPERTIES OF GRAPHENE

Since its discovery, the peculiar properties of graphene have entranced numerous researchers into a wide-spread drive to study the full potential of graphene. Studies exploring the mechanical properties of graphene have indeed revealed extraordinary mechanical behaviours.

For instance, pristine graphene exhibits a modulus of elasticity of around 1 TPa, a value which has been found using both experimental techniques [13, 22], and computer simulation [24]. It was revealed that graphene exhibits a nonlinear elastic response, with computer simulations indicating that the maximum stress and strain sustained before fracture are anisotropic. It was noted that monolayer graphene loaded in the zigzag (ZZ) direction sustains stresses of around 107 to 130 GPa and strains of around 0.23 [13, 24], while in the armchair direction, the maximum stress at fracture is around 90 GPa at 0.13 strain [24]. The range of values reported for the fracture stresses, strains and elastic moduli is typically attributed to (i) the accuracy of the experimental testing system or simulation model, (ii) the different conditions in which the graphene was mechanically loaded, or (iii) the crystalline quality of the graphene. In fact, work on establishing the relationship between the measured mechanical properties with system temperature [25-28], graphene sheet size [24, 25], and the crystalline quality of the initial graphene sheet (or the presence of defects) [25, 28-30], amongst others, has been initiated.

1.1.2 DEFECTS IN THE GRAPHENE CRYSTAL

Graphene crystals are seldom two-dimensional pristine hexagonal lattices, but instead are often riddled with various defects within their structure. To this end, one of the advantages of nanomaterials in general is that the probability of the nanomaterial to have a defect can be substantially lowered due to the lower number of atoms making up the nanocrystalline material.

Nonetheless, several types of defects in the graphene crystal have been identified [4]. Amongst the most commonly found are (i) vacancies in which one or more C atoms are missing from the lattice (Figure 1.2 (a)), (ii) adatoms whereby extra C atoms covalently bond to the hexagonal lattice in the third dimension creating a case where the bottom C atoms within the graphene sheet are bonded to four atoms rather than three (Figure 1.2 (b)), (iii) other atoms or functional groups[1] replacing a C atom or otherwise attached to the graphene sheet either

[1] Functional groups are groups of atoms chemically attached to the graphene sheet that alter the chemical properties of the system.

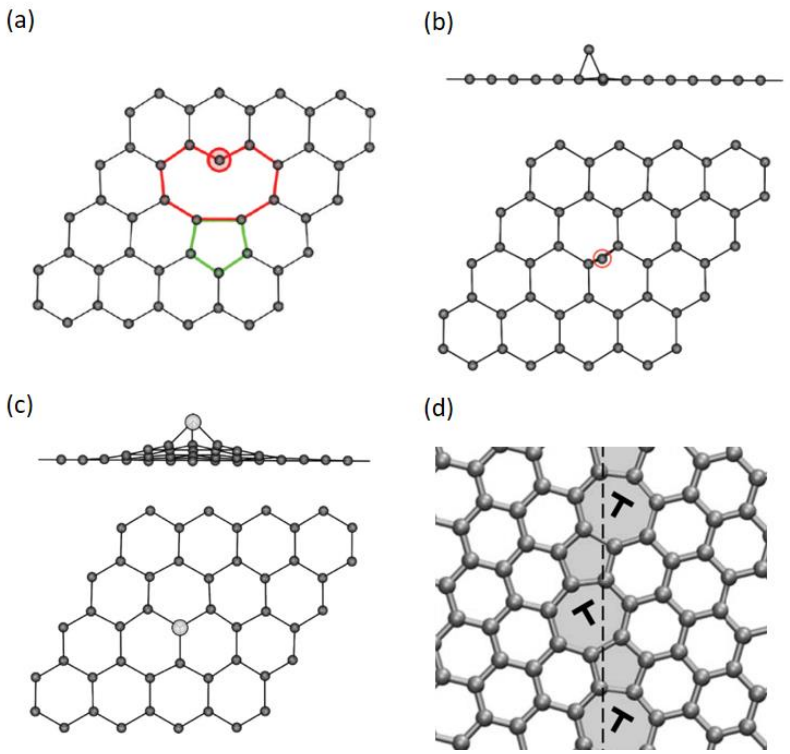

Figure 1.2: Atomic configurations of (a) single vacancy, (b) adatom, (c) foreign atom, and (d) grain boundary [4, 5].

above/below the plane or at the edges (Figure 1.2 (c)), and (iv) grain boundaries marking a change in the crystal orientation from one domain, or grain, to another (Figure 1.2 (d)).

While significant research has been geared towards developing various synthesis techniques to isolate or produce graphene, it was found that different synthesis routes tend to produce graphene with different crystalline quality. For instance, the condition of the graphite from which the graphene is mechanically exfoliated, the structural quality of the substrate onto which graphene is deposited, the chemicals used in other synthesis routes and/or the graphene growth and deposition parameters, highly determine the crystalline quality of the graphene produced. In the case of mechanically exfoliated graphene, although in general the graphene samples have a high degree of order, defects present typically include vacancies or Stone-Wales defects[2]. On the other hand, graphene grown via chemical vapour deposition tends to contain an appreciable number of grain boundaries that separate domains of different orientations [31]. Furthermore, graphene produced by the chemical reduction of graphene oxide tends to contain a significant amount of functional groups. Defects can also be intentionally introduced by energetic particle irradiation [4, 32] or oxygen plasma techniques

[2] Stone-Wales (SW) defects involve the reconfiguration of the C-C bond to form non-hexagonal polygons.

[33]. The energetic electrons or ions are capable of locally disrupting the crystalline structure of the graphene and even sputtering carbon atoms from the hexagonal structure upon collision to create point defects.

It was shown that these defects have the potential of altering the properties of graphene, with different types of defects affecting different aspects of the graphene's electrical, chemical, and mechanical properties. With reference to the mechanical properties, the presence of single point defects (such as vacancies or Stone-Wales defects) reduces the strength of the graphene sheet [25, 28, 29, 34], while an increased defect density causes a significant drop in fracture stress and fracture strain [25, 28, 35]. It is still debatable whether a closely-controlled defect density can, in special cases, increase the elastic modulus of graphene [94], as opposed to the typical observed behaviour of a reduction in modulus with an increase in defect density [25, 30]. Focused electron and ion beams have been used to introduce point defects or nanopores, and nanopattern graphene structures. These nanostructures are in turn of great interest for use in next-generation filtration or desalination membranes whereby the nanoporous graphene can act as a filtration membrane [36, 37], and nanoelectronics, which often require graphene to be nanopatterned in specific geometries [38].

The ability to alter the graphene crystal lattice by introducing the desired defects offers the capability of tailoring the properties of graphene for the intended application. As such, understanding the nature of defects in graphene and the techniques used for creating and characterizing such defects is key to the effective integration of graphene in several dedicated applications.

1.1.3 Graphene-Based Applications

Graphene's exceptional electron mobility and mechanical flexibility are very attractive properties for the electronics industry, especially in the development of flexible electronics [39, 40]. Its sensitive electronic properties towards a change in chemical structure or surrounding conditions also makes graphene an attractive candidate material for use in sensors, most particularly biosensors [41]. Amongst the most recent and temporally relevant applications of graphene in this respect is the use of graphene-coated field-effect transistor-based devices to detect COVID-19 (SARS-CoV-2) in clinical samples [42].

Due to the high-strength and high-stiffness to weight ratios, graphene has also been integrated in composite materials to enhance the material's properties [43]. The addition of graphene nano-platelets to an epoxy-based vinyl ester polymer matrix has been shown to increase the

elastic modulus, the normal hardness, and scratching hardness of the nanocomposite [43]. The addition of partially oxygenated graphene in an epoxy polymer matrix drastically increases the fracture toughness of the matrix by 65% and the fracture energy by 115% [44]. It was also concluded that for the same weight percentage, graphene is more effective in improving the fracture properties of the polymer-based nanocomposite than carbon nanotubes. Other studies indicate the potential use of graphene in bullet-proof armour material as it was found to exhibit excellent impact energy delocalization under a supersonic penetration event [45]. In fact, it was reported that multi-layer graphene sheets performed up to 12 times better than steel under high speed projectile impacts. High speed projectile tests on multi-layer graphene revealed a fracture mechanism that exhibits very effective energy absorption, rendering graphene potentially ideal for body armour vests [45].

The use of graphene in nanocomposite materials is also being investigated in the aviation industry. Electrically and thermally conductive graphene-based nanocomposites used in the aircraft fuselage, while offering high strength-to-weight ratios, are capable of effectively dissipating the sudden and extreme electrical current from lightning strikes, thereby minimizing the severe localized damage incurred on the structure [46, 47].

Finally, the selective permeability of porous graphene opens doors for innovative, efficient and cost-effective filtration and desalination membranes. Studies revealed an anticipated 15% reduction of energy consumption in reverse osmosis plants with the installation of the proposed graphene-based membranes [48].

Regardless of the application, the mechanical behaviour of the graphene is crucial for the design of the device. The strength, stiffness, and structural integrity under different environmental and mechanical loading conditions are essential pieces of information which allow for the graphene-based device to be designed, produced, and effective in application.

1.1.4 Enabling Nanotechnologies

Enabling technologies comprising both experimental techniques and computer simulation are essential for the understanding of the material's behaviour under various conditions.

Research on the properties and behaviour of nanomaterials is multidisciplinary and can be generically addressed from two main fronts. In the field of nanomaterials, theoretical scientists can predict the behaviour of a nanomaterial in a set of pre-defined conditions. At the early stages of development, theoretical analysis is capable of determining the stability of new

materials. Such principles can be further adapted to create a model of the atomic structure and configuration of the material, and thereby calculate the predicted material properties. However, the complexity of the model and thus the capability of simulating a scenario that fully replicates real life conditions is often constrained due to the limitations imposed by the computational power required to apply all of the governing equations. As such, simulation models are often categorized by the particular set of theories that are adopted, and thus the extent of properties that can be studied, as well as the scale of the model, that is respective to the dimensional envelope and the time-scale of the simulation. For instance, depending on the system model and complexity chosen for the computer simulation, the time and length-scale of the observed phenomena may vary from the atomic-scale, typical with the use of molecular dynamics (MD) and density functional theory (DFT), up to the macro-scale, with the use of finite element modelling.

On the other hand, experimental scientists may use the hypotheses outlined by their theoretical counterparts to test the material's behaviour in a controlled environment. While certain scenarios can be replicated in an experimental setup, these atomistic studies of nanomaterials still need highly specialised equipment. As such, the advancements in dedicated and precise characterisation techniques are essential for the study of nanomaterials. Most importantly amongst these techniques, the development of scanning probe microscopy such as atomic force microscopy (AFM) has largely facilitated the study of nanomaterials at the nano and atomic scales. The technique broadly uses a nanometric probe to interact with the surface of the nanomaterial sample in study.

The ability to adopt graphene for many new applications lies in the capability to use both experimentation and computer simulation to account for processes that occur over multiple time and length scales. Quantifying the inherent uncertainty in both approaches is key to realise the limitations and strengths of both approaches. Sometimes, the ease with which novel graphene systems can be modelled opens up doors to the discovery of phenomena which would not have been possible with current state-of-the-art experimental technologies. On the other hand, the ability to experimentally test and use the nanomaterial in the desired application can be the ultimate goal of such research. As such, the two approaches are complementary to each other.

1.2 MOTIVATION AND SCOPE OF RESEARCH

At the time of writing, graphene would have been first discovered sixteen years ago. Compared to most other materials which have been studied and used for at least a number of decades, graphene research is still in its infancy. Yet, the exponential growth in the research interest on this nanomaterial shown by the scientific community in the last few years is testament to the unparalleled promise that this material holds.

The novelty of graphene has driven research from across multi-disciplinary fields to investigate graphene. Needless to say that the fundamental phenomena surrounding graphene as well as the technology adopted for its synthesis, characterization, engineering, and integration in application-based devices still require extensive investigation. For instance, the literature review in Chapter 2 will present a number of synthesis and manipulation techniques that have since been explored. Yet, none of such methods have been sufficiently developed to result in the reliable and repeatable synthesis of graphene with known pre-defined morphologies, yields, structural quality, and material properties.

Similarly, the use of various characterization techniques to assess the desired properties of the produced graphene is still being explored. For the scope of this work which aims at investigating the mechanical properties of graphene, the lack of an established methodology for the measurement of the elastic modulus of graphene, which includes guidelines accepted and adopted by the scientific community, is evident. This calls for continued research on such methodologies until a well validated method that provides reliable and repeatable results emerges.

While the above is ordinary for most bulk-materials, with published standards and specifications covering all key aspects of the material, it is clear that more work is needed for the development of equivalent methods for graphene. The extended use of graphene to many engineering applications depends on the availability of a sound body of knowledge about graphene and the respective synthesis routes, characterisation methods, and testing procedures. Methods and procedures can only be established and widely accepted by the research community after said methods have been tested by numerous research groups. Repeatability of the results across different laboratories will support establishing the use of graphene in various applications.

These requirements set the overall aim of this study; to reproduce methods for the preparation and modification of graphene samples, and subsequent testing of their mechanical properties. For the latter, nanoindentation studies using both atomic force microscopy and molecular dynamics simulations are to be used to measure the elastic modulus and failure strength of graphene. Ion bombardment technology will also be used to introduce defects in the graphene samples to allow evaluation of the mechanical properties of the treated non-pristine graphene membranes. The results generated will thereby contribute towards establishing a set of guidelines or methods that can be followed for the attainment of the desired repeatable results.

This dissertation is structured as follows. Chapter 2 presents a literature review of the relevant studies undertaken with respect to graphene synthesis, characterisation, mechanical testing, and modification by ion bombardment. The chapter ends with an outline of the work conducted. Chapter 3 will address the sample preparation routine of the required graphene membranes for subsequent experimentation, as well as the results obtained from the characterization techniques employed. Chapter 4 is dedicated to atomic force microscopy. A theoretical overview of AFM and nanoindentation is provided, and then followed by the calibration procedures to be adopted for the available AFM set-up. Secondly, nanoindentations carried out on the prepared graphene samples and the measured elastic modulus are presented. Chapter 5 describes the methods used to introduce defects in the graphene samples and to characterize the damaged graphene, and the results obtained after nanoindentation of the damaged membranes. The theory behind molecular dynamics simulations is given in Chapter 6, together with the use of two different graphene models to simulate the mechanical behaviour of graphene, and the results obtained used to support the experimental findings. Finally, Chapter 7 presents the conclusions that can be drawn from this study, and scope for future work.

Chapter 2 LITERATURE REVIEW

Chapter 1 introduced graphene as a recently discovered nanomaterial which sparked global research interest and accompanying market value in a variety of industries. A thorough understanding of the behaviour and response of graphene under various loading conditions is paramount to the successful integration of this nanomaterial in the myriad of promising applications. The response of graphene to a mechanical load, and hence the study of its mechanical properties, is one of the facets that needs to be explored in detail in order to allow graphene-based devices to be realised.

This chapter aims at reviewing the relevant literature concerning graphene and specifically focuses on its mechanical properties. Section 2.1 starts the discussion on the main routes that have thus far been established to synthesize graphene. Various characterization techniques which are often used to analyse the prepared graphene are presented in Section 2.2. Section 2.3 is dedicated entirely to atomic force microscopy – the principal testing method adopted for this work. Section 2.4 provides an overview of molecular dynamics simulation studies on graphene. Section 2.5 gives an overview of the work that has been done with reference to nanoporous graphene, whereby the permeability of pristine and nanoporous graphene as well as the effects that defects and nanopores in graphene's crystalline structure have on the mechanical properties are discussed. Finally, Section 2.6 summarises the literature reviewed in this chapter and outlines the aim of this work, research questions, and objectives of this work.

2.1 GRAPHENE SYNTHESIS

One of the most central aspects in nanomaterial experimentation is how to deal with synthesising and producing the nanomaterial – in this case graphene. The production route chosen tends to greatly influence the quality, and of course the cost, of the graphene produced. As will be discussed in more detail in Section 2.5, the properties of graphene are highly dependent on the quality of the lattice. That is, the introduction of defects such as grain boundaries, vacancies, pores and functional groups tend to alter the mechanical, physical, electrical and chemical properties of the graphene, making the defective graphene either unsuitable for certain applications or otherwise ideal for other specific applications. Thus, it must be ensured that economically feasible synthesis processes are developed in order to produce the required quality of graphene for the intended application.

There are four main production routes commonly used to obtain graphene. The two top-down approaches are; (1) mechanical exfoliation and (2) chemical reduction, and the other two bottom-up approaches are; (3) chemical vapour deposition (CVD) and (4) epitaxial growth. This review will mainly discuss the simplest route – mechanical exfoliation and the most large-scale-production-friendly synthesis technique – CVD. Other niche methods are also discussed at the end of this section. A more detailed review on the different top-down and bottom-up approaches to graphene production with the advantages and disadvantages of both routes is available in [49, 50].

2.1.1 MECHANICAL EXFOLIATION

The first ever produced samples of graphene were prepared via mechanical exfoliation by Novoselov et al. [6, 8]. Due to its simplicity in terms of the equipment and materials required, this technique was subsequently widely adopted by other research groups [13, 33, 38, 51-64] to synthesise graphene for laboratory-scale research. This method fundamentally involves the mechanical peeling, or exfoliation, of a single layer of graphene from the bulk 3D graphite. Thus, this top-down technique revolves around the ability to disrupt the weak van der Waals forces that hold the individual hexagonal carbon planes together in graphite to isolate individual graphene sheets. In their work, Novoselov et al. [8] start with 1 mm thick platelets of commercially available highly oriented pyrolytic graphite (HOPG). After dry etching in oxygen plasma to form 5 μm high graphitic stacks, the structured surface is stuck to a glass substrate with photoresist. This allows the bulk of the HOPG to be cleaved and leave the thin stacks attached to the substrate. Scotch tape is then used to peel off flakes of graphite from the stacks to obtain few-layer graphene (FLG) and single-layer graphene (SLG) flakes. Due to the use of the adhesive tape, this approach is also referred to as the Scotch-tape method. The graphene flakes are finally deposited on silicon wafers or similar substrates. This technique proved to be very reliable to produce FLG films of up to 10 μm in size, and even thicker flakes of up to 100 μm across [8]. The main steps involved in the Scotch-tape method to mechanically exfoliate graphene are shown in Figure 2.1. Novoselov et al. [6] have also successfully modified the mechanical exfoliation technique to produce different 2D crystallites (graphene, BN, MoS_2, $NbSe_2$, $Bi_2Sr_2CaCu_2O_x$) by rubbing a fresh surface of the bulk layered crystal against the oxidized silicon wafer, in a process similar to writing with chalk. Similar rubbing techniques have also been used to deposit graphene on silicon wafers with an oxide layer of

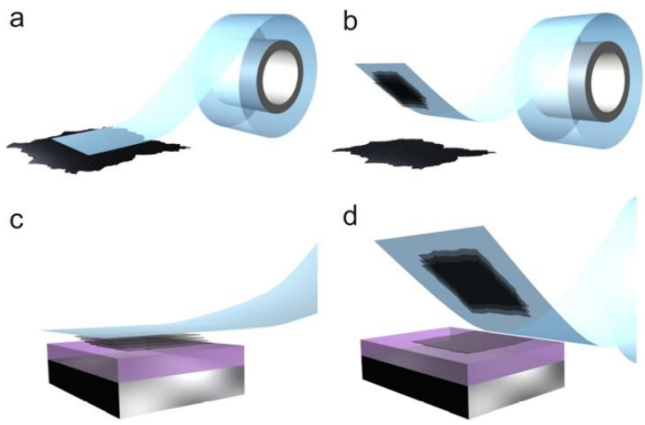

Figure 2.1: Mechanical exfoliation of graphene using the Scotch tape method; (a) The tape is pressed onto bulk graphite, (b) the top graphite layers are peeled off, (c) the graphite adhered to the tape is pressed against the substrate, and (d) the tape is peeled off, leaving single or few layer graphene on the substrate [3].

260 to 330 nm from freshly cleaved Kish graphite[3] [51, 52]. The graphite flakes are attached to a probe and, acting like a pencil, it is rubbed across the silicon oxide substrate.

The mechanical exfoliation process is dependent on a number of parameters which need to be selected carefully in order to obtain high quality single-layer graphene samples. To start with, the bulk graphite should have a high crystalline quality, hence the popular choice of either HOPG [6, 8, 45, 56, 57] or Kish graphite [2, 13, 51, 52, 65-68]. Secondly, the substrate onto which the graphene layers are deposited determines the ease of locating the graphene flakes. It was determined that graphitic films thinner than 50 nm are visible via optical microscopy on specific substrates, namely silicon oxide of thickness between 260 nm to 330 nm on top of a silicon wafer [8], or other substrates with comparable optical properties [69]. On these substrates, FLG and SLG are visible under optical microscopy, essential for the fast location of graphene flakes amongst the more abundant and much thicker graphite flakes [6, 69]. Graphene prepared by mechanical exfoliation has also been deposited on silicon oxide thicknesses of 100 nm [54, 70] and (001) muscovite mica [2, 67]. Mechanical exfoliation has also been adapted to produce thin layers of muscovite mica [71] and MoS_2 [72, 73].

Mechanical exfoliation is known to produce graphene samples of high crystalline order, yet limited to samples of micrometre dimensions [8]. Hence, such technique is ideal to prepare pristine samples for research purposes, whereby the quality of the graphene can be easily controlled with relatively inexpensive methods.

[3] Kish graphite is high-quality flake graphite obtained from the steel-making waste material.

2.1.2 CHEMICAL VAPOUR DEPOSITION

A bottom-up approach to produce graphene uses chemical vapour deposition (CVD) of carbon on a metallic substrate. In contrast to mechanical exfoliation, CVD requires more advanced equipment but is able to produce larger graphene samples. In fact, CVD has been thus far the most successful method for commercial large scale production of graphene [50].

Most commonly, graphene is grown on copper foil substrates [37, 74-84]. The copper foils, with thickness varying from 12.5 μm to 50 μm [74, 78, 82, 83], are first sonicated in acetic acid for 5 minutes to remove the oxide layer [77] and subsequently rinsed with deionized water. The copper foils are then introduced in a vacuum furnace and annealed at 600°C [75] to 1050°C [77] for 20 to 90 minutes under an Ar/H_2 flow. After annealing, the temperature is gradually increased to 900°C to 1057°C, the Ar/H_2 flow suspended and methane (CH_4) introduced at controlled pressures for 30 to 40 minutes [35-37]. At high temperatures, the methane decomposes and carbon is deposited on both sides of the copper foil, forming monolayer graphene. The graphene can then be transferred onto another substrate using an intermediate transfer material, most commonly poly(methyl methacrylate) (PMMA) [37, 74, 76, 80, 81, 83-86].

Graphene can also be grown on different substrates, such as iridium Ir(111) [87], nickel Ni(111) [88], rhodium Rh(111) [89], or thin Ir films on YSZ/Si [90]. The FCC crystal substrates and their (111) plane have been shown to better accommodate the formation of the graphene on the surface [91]. Different carbon precursors can also be used such as ethylene [89], acetylene [88], ethanol [90], benzene, and polycyclic aromatic hydrocarbons [50]. Similar to common practices employed when depositing other films via CVD, the substrate surface preparation can significantly affect the crystal quality of graphene; for instance clean surfaces with very low surface roughness tend to promote uniform nucleation and less structural defects within the graphene layer [92-94]. This will in turn affect the properties of the graphene produced [88, 93]. For example, electropolishing of the copper foil before deposition has been noted to improve the electrical transport properties of the grown polycrystalline graphene [93]. It was also found that graphene grown on Ni(111) has its electronic structure altered due to the strong graphene-Ni interaction [88]. To restore its electronic structure, Na intercalation can be used in which Na atoms adsorbed on the graphene surface spontaneously penetrate below the graphene layer at room temperature hence separating the graphene from the Ni substrate. The

Na layer can then be easily oxidized such that the graphene is supported on an insulating layer [88].

The final physical properties of the grown graphene are also dependant on the temperatures, pressures, and gas flow rates used, and the duration of each step of the CVD process [78, 95]. Hence such properties need to be carefully controlled for the desired graphene samples. Several studies have been published on the effect of the growth temperature on the resultant graphene product, its grain size and its electronic properties [89, 96, 97]. It is claimed that high quality single grain graphene layers can only grow at temperatures higher than ~827°C [89], however some research has been published suggesting that growth temperature – and hence costs of this synthesis technique – can be reduced further [98].

The transfer process from the metallic substrate onto which the graphene was originally grown, to the substrate of choice for the required application also determines the final quality of the graphene layer. A wet transfer process is often used; this involves the initial deposition of a thin polymeric film, such as PMMA or polydimethylsiloxane (PDMS), on one side of the graphene to act as intermediate transfer material [74, 76, 80, 82, 83, 85, 86]. The bottom exposed graphene layer is etched away by air or oxygen plasma [78, 83] and the metallic substrate removed with aqueous etchants such as iron nitrate [74], ferric chloride [37, 83, 85, 86], or ammonium persulfate [78, 82, 84] for copper substrates. The graphene/polymer stack is then rinsed in deionized water and deposited onto the desired substrate with the graphene in contact with the substrate. The overlying polymer is finally removed via thermal [78, 81, 82, 86] or chemical means, with organic solvents such as acetone [37, 83-85] being the most popular. Annealing can also be used after dissolution of the PMMA to remove any residues [80, 83, 84]. This lengthy process inevitably introduces a number of defects in the graphene membrane – the use of chemical baths can attack the graphene membrane and add functional groups to the otherwise pristine graphene. Moreover, the physical transfer of the graphene stack from one substrate to another, often over a water bath, can result in wrinkling of the final deposited graphene sheet due to the fragility of the thin polymeric transfer medium [83].

Presently, the typical CVD output comprises of a relatively large area of graphene having grain boundaries dividing differently oriented grains. The production of large amounts of high quality graphene, single grain films is still in its infancy. The transfer process has also been improved with certain commercial groups preparing CVD-grown graphene in an easy-to-transfer ‘sandwich’ to facilitate the process [99].

2.1.3 OTHER TECHNIQUES

In addition to the above mentioned graphene synthesis routes, other graphene production routes have been developed. For example, a chemical route which involves the chemical reduction of graphene oxide is also often adopted. Other 'unconventional' graphene production methods have also been explored, some of which will be outlined hereunder.

2.1.3.1 Chemical Reduction of Graphene Oxide

Another top-down technique involves the chemical reduction of graphene oxide (GO) to produce graphene. The initial GO is typically prepared from graphite using the Hummers method [100]. Graphite flakes are mixed with sodium nitrate (or nitric acid) and sulphuric acid in an ice bath at 0°C and stirred continuously for 15 minutes [101]. While maintaining vigorous agitation, potassium permanganate is added to the suspension over 15 minutes, making sure that the temperature of the mixture is kept below room temperature. The temperature is then increased gradually to around 35°C for about 30 minutes as the mixture turns brown in colour. Distilled water is then added slowly while keeping the temperature at 98°C for 15 to 30 minutes. The suspension is further diluted with warm (40°C) distilled water and hydrogen peroxide to reduce the residual permanganate and manganese dioxide to manganese sulphate. The addition of the hydrogen peroxide turns the solution to a bright yellow colour which is then filtered, washed with distilled water and finally dried in vacuum at 60°C for 24 hours to obtain GO.

The oxygen functional groups of GO make the graphene oxide soluble in water with sonication. The presence of -OH, -O, and/or -COOH functional groups in GO increases the interlayer spacing between the individual graphite oxide layers hence weakening the van der Waals interlayer forces [102]. In turn, the reduction in interlayer interaction facilitates exfoliation via sonication. Graphene oxide nanosheets can thus be obtained by ultrasonicating and hence exfoliating the GO [103]. The prepared solution can then be deposited over the desired substrate, such as Si/SiO_2 wafer, and reduced by hydrogen plasma treatments to yield graphene monolayers with lateral dimensions of 0.1 to 5 μm [104]. Several other reduction techniques can be used to reduce GO to graphene. Stankovich et al. [105] used hydrazine hydrate to reduce GO in an oil bath at 100°C under a water-cooled condenser for 24 hours, in a similar process presented in [106] illustrated in Figure 2.2. Pomegranate juice has also been used to reduce the GO via the reducing agent anthocyanin present in the juice [101].

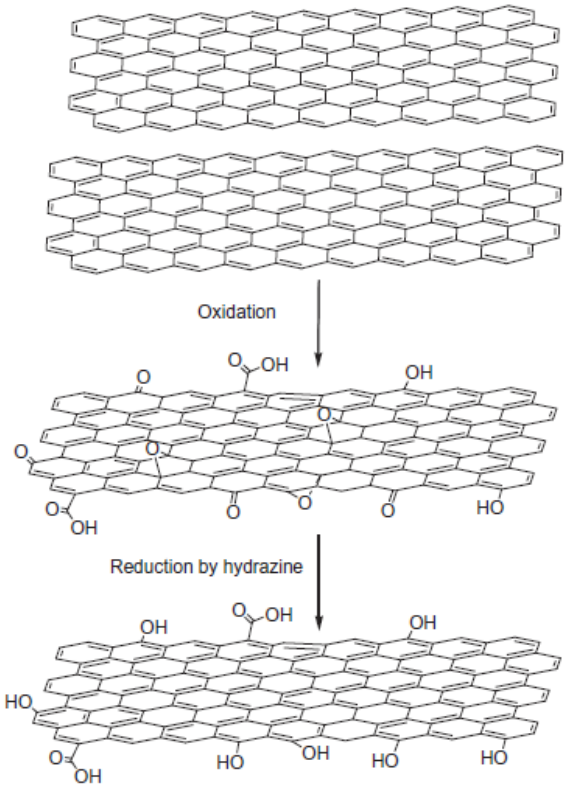

Figure 2.2: Production of reduced graphene oxide via the production of graphene oxide and the subsequent reduction by hydrazine [106].

Su et al. [107] presented a study on impermeable barrier films and protective coatings based on graphene obtained via GO reduction. After preparing GO using the Hummer's method, the authors [107] report three methods of reduction; (1) thermal reduction at 300°C in Ar/H_2 mixture for 4 hours, (2) exposure to hydrochloric acid vapour at 90°C for 5 to 30 minutes with the samples rinsed repeatedly with ethanol to remove residual acid, and (3) immersion in vitamin C/water solution at 90°C for 1 hour. The permeation properties of the GO and reduced GO were then investigated, concluding that the reduced GO is generally less permeable than the GO.

While GO is soluble in water, reduced GO is not; chemical reduction removes the oxygen functionality of graphene oxide and reduces the water dispersability, causing the graphene layers to aggregate and precipitate. In order to produce water soluble graphene, Si et al. [102] suggest the introduction of a small number of *p*-phenyl-SO_3H groups into the GO before it is fully reduced. In this method, the graphene oxide is first partially reduced using sodium borohydride at 80°C for 1 hour, followed by sulfonation with the aryl diazonium salt of sulfanilic acid in an ice bath for 2 hours, and finally treated with hydrazine at 100°C for 24 hours to remove the remaining oxygen functionality. Upon reduction, the graphene oxide

flakes slightly reduced in their lateral size from dimensions of several micrometres to several hundreds of nanometres, whilst their thicknesses appeared to increase slightly from 1 nm to 1.2 nm, which is thought to be due to the undulations of the reduced graphene's surface on the substrate. Overexposure to sonication resulted in an increase in defects and decrease in lateral dimensions.

Unfortunately, when reduced, graphene oxide tends to produce graphene with some functional groups still attached to it, due to the incomplete reduction of the oxide and the use of chemicals, some of which may chemically bond with graphene [105]. Such functional groups tend to alter the properties of graphene, and can in fact be considered as defects in certain applications. The choice of the chemicals used, the concentrations of the chemicals, the reaction time and temperatures, all determine the chemical and physical nature of the produced graphene sheets.

2.1.3.2 Shear Exfoliation

Similar to mechanical exfoliation by peeling, graphene can be derived from graphite using shear exfoliation with the help of intercalation [108]. Briefly, intercalation involves the introduction of molecules between the graphite layers to weaken the inter-layer van der Waals forces and hence facilitate exfoliation.

However, Paton et al. [108] argue that fabrication time of graphene via shear mixing and exfoliation can be reduced by eliminating the intercalation step. In this method, graphite is mixed with the solvent N-methyl-2-pyrrolidone and/or aqueous surfactant solutions and shear mixed using a kitchen blender (as long as a local shear rate exceeding 10^4 s^{-1} can be achieved). After centrifugation of the shear-mixed suspension, large quantities of high-quality graphene nanosheets and monolayers are obtained. The authors claim that such method is a scalable one, capable of producing relatively large quantities of defect-free graphene, as opposed to the previous technique.

2.1.3.3 Epitaxial Graphene by Graphitization

Another bottom-up technique involves the graphitization of a carbide surface. Similar to CVD, it was reported that epitaxial growth of graphene via SiC graphitization has the potential for realistically achieving large-scale fabrication of graphene [109, 110].

Si-terminated surfaces of silicon carbide 4*H*-SiC(0001) or 4*H*-SiC($000\bar{1}$) wafers are first hydrogen etched to produce atomically flat surfaces, and annealed in ultrahigh vacuum (UHV) at temperatures above 1200°C up to 1600°C for 10 minutes [110, 111]. At these high temperatures and low pressures, graphitization occurs whereby the silicon evaporates and

leaves a continuous carbon layer behind. The resulting graphene thickness and coverage is controlled by both the graphitization temperature and annealing time [110, 111]. According to Rutter et al. [110], temperatures above 1200°C produced graphene sheets ranging from 1 to 3 layers in thickness with graphitization temperatures dictating different graphene morphologies.

Sublimation of Si-terminated SiC surfaces was also performed at temperatures as high as 2000°C in Ar at a pressure of 1 atm [112, 113] without prior hydrogen etching. This modified graphitization technique produced monolayer graphene covering up to 40% of the total wafer area, and multi-layer graphene covering less than 2% of the area [113].

While typical SiC graphitization processes yield large-area graphene, Au and Si implantation in selected areas of the SiC substrate before graphitization enables the formation of graphene nanoribbons and other nanometre structures. Tongay et al. [114] presented a method for selective forming of graphene on 4H- and 6H-SiC. In their experiment, gold and silicon ions were first implanted at 30 kV with fluences ranging from 1×10^{16} to 1×10^{17} Au ions/cm^2 and 5×10^{14} to 5×10^{17} Si ions/cm^2 into the SiC surface in areas where graphene growth was desired. Gold and silicon lower the graphitization temperature in the implanted areas from 1300°C to 1200°C allowing selective graphitization if the annealing is carried out at this range of temperature. As with normal SiC graphitization, the quality of the SiC surface determines the quality of the nanoribbons formed. Also, it was noted that graphene growth is not self-limiting and hence, the annealing time has to be carefully controlled to limit graphene growth to the size desired. The selection of optimal ion species, implantation energy, ion dose, sample temperature and quality of the original SiC could ultimately lower the graphitization temperatures and improve the graphene crystalline order.

2.1.4 Graphene Modification Methods

As mentioned in the introduction, defects within the graphene sheet have the potential to alter the properties exhibited by the nanomaterial. As such, several studies have aimed at introducing defects in the graphene in a controlled manner to systematically study the effects of such defects on the relevant properties [33]. Furthermore, some applications require the graphene to have a particular shape, size and structure. For instance, the electronics industry often requires pristine graphene in the form of high aspect-ratio nanoribbons instead of sheets. On the other hand, the introduction of size-controlled pores is required for the manufacturing of graphene molecular sieving membranes. In order to introduce defects and modify the structure of graphene, bombardment with energetic particles [4, 32] or an oxygen plasma [33] can be used.

The energetic electrons or ions are capable of locally disrupting the crystalline structure of the graphene and even ejecting carbon atoms from the hexagonal structure upon collision to create point defects. This section reviews some of the methods that have been adopted to modify graphene.

Ultraviolet-induced oxidative etching was used to introduce sub-nanometre-sized pores within mechanically exfoliated graphene membranes [66]. The suspended pristine membranes were first pressurized from one side with pure hydrogen up to 200 kPa above ambient pressure to form a blister. A series of 30-second UV etches were performed, followed by imaging to assess the blister size. This allowed for the leak rate and hence the gas permeability of the membranes to be calculated. It was found that exposing the graphene membranes to such UV etches enabled selective molecular sieving [66].

Zandiatashbar et al. [33] used a benchtop radio frequency oxygen plasma cleaner to introduce defects in suspended mechanically exfoliated graphene membranes. To control the etch rate and defect formation, the graphene sample was shielded from direct exposure to plasma by sandwiching the sample between two glass slides and placing it Si-side up. It was noted that disorder in the graphene structure increases with an increase in oxygen plasma exposure time. The defects formed were mainly of an sp^3 nature at shorter exposure times. Following longer exposure times, vacancies were introduced [33].

Similar mechanically exfoliated graphene membranes were also exposed to argon ion (Ar^+) bombardment [57, 61, 62, 115]. Ar^+ ions with an energy of 90 eV at a bombardment dose of 10^{11} Ar^+/cm^2 up to 10^{15} Ar^+/cm^2 were used [57], with the highest doses leading to full amorphization of the graphene. Ar^+ ions with a higher energy of 140 eV and at an ionic bombardment rate of $\sim 3 \times 10^{-8}$ Ar^+/cm^2 were used for treatment times ranging from 10 seconds to 3 minutes [61, 62, 115]. Such treatment introduced randomly distributed mono- and di-vacancies in the membrane [61, 62] with no sp^3 type defects [115].

A scanning helium ion microscope was used for imaging and etching graphene flakes on a 300 nm SiO_2 substrate [56]. He^+ ions at 30 kV and 1 pA beam current was used at lower doses for imaging ($\sim 1.87 \times 10^{15}$ He^+/cm^2) with little damage to the graphene, while an increased dose of 6.24×10^{17} He^+/cm^2 was able to etch a 35 nm wide line in the graphene with measureable damage in the graphene as far as 250 to 300 nm away from the etched line. Lower doses between 4×10^{12} ions/cm^2 and 1×10^{15} ions/cm^2 [63] still retained the predominant sp^2 bonding character indicating that amorphization does not occur.

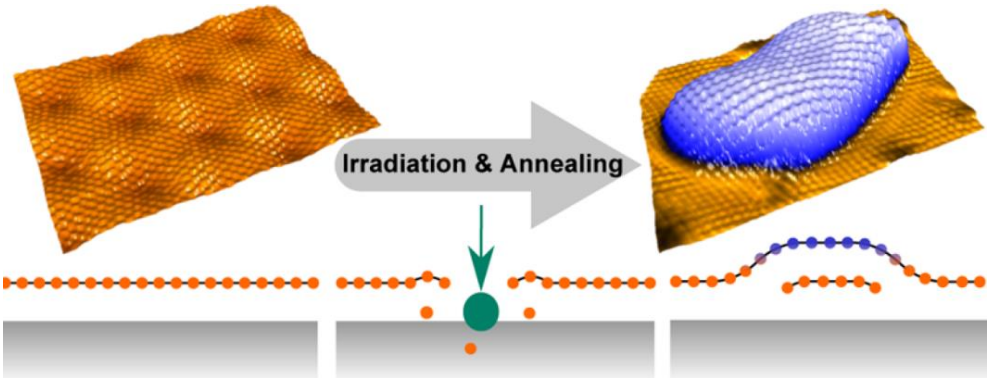

Figure 2.3: Trapping of a graphene nanoplatelet under the graphene monolayer after ion bombardment; 3D STM images of graphene structure with side view illustrations of the defect creation in the graphene, before (left) and after (right) ion irradiation [116].

Among the several studies investigating the creation of defects when graphene is exposed to ion bombardment, the fate of the detached carbon atoms after the supported graphene is irradiated was also investigated in [116]. A high-quality graphene layer was first grown on Ir(111) by adsorption and subsequent thermal decomposition of ethylene. The grown graphene was then ion irradiated using He^+, Ne^+, Ar^+ and Xe^+ having energies ranging from 100 eV to 5 keV at room temperature. Each irradiation step was followed by annealing and imaging to assess the created defects. It was found that some of the detached C atoms were trapped at the interface between the original graphene layer and the Ir(111) substrate, in a process similar to that illustrated in Figure 2.3. Variation of the ion irradiation parameters (ion mass, energy, radiation duration and number of radiation-annealing cycles) resulted in the formation of different structures of the trapped graphene nanoplatelets.

Apart from its typical use in graphene research to etch wells in Si/SiO_2 wafers, reactive ion etching (RIE) has also been used to directly etch graphene. Kim [70] reports an efficient method of producing aligned graphene nanoribbons on a large scale, with the help of RIE. Graphene was first mechanically exfoliated and deposited on a 100 nm SiO_2/Si substrate. A solution of V_2O_5 was carefully sprayed onto the deposited graphene to form V_2O_5 nanowires (NWs). The V_2O_5 NWs act as a mask material protecting the underlying graphene during the RIE process (60 W, 2 minutes) which tends to etch any unprotected graphene. The V_2O_5 NWs were then dissolved in HCl to uncover the graphene nanoribbons (GNRs). The aligned GNRs were later used to create FETs after the deposition of Au and Pd films as contacts. A schematic of this procedure is shown in Figure 2.4. This process yielded graphene nanoribbons of average width of 30 nm, 80% of which aligned along the original direction of V_2O_5 flow, with a deviation of less than 10%.

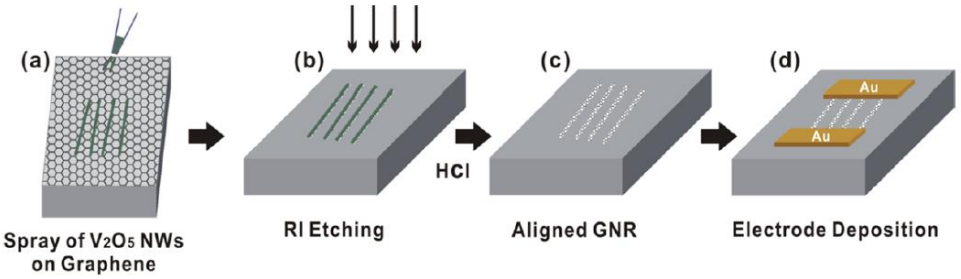

Figure 2.4: Production of graphene nanoribbons using REI and V_2O_2 nanowires as a mask [70].

2.1.5 SUBSTRATE PREPARATION

In order to study suspended graphene, the Si/SiO_2 wafers can be modified to allow the deposited graphene flakes to be suspended over wells. Typically, reactive ion etching is used to etch pre-defined circular wells (or trenches) with diameters ranging from 0.5 µm to 7 µm [33, 52, 117, 118] and depths of 100 nm to 500 nm [117, 118]. The etching process starts with spin-coating a 300 nm to 350 nm thick layer of photoresist on the Si/SiO_2 wafers and baking for 2 minutes at 115°C [118]. The circular well pattern is transferred from a photomask to the photoresist using photolithography. After developing the photoresist, the pits are etched using RIE in O_2/CHF_3 radio frequency (RF) plasma for 3 to 4 minutes. The photoresist is dissolved and a layer of poly(methyl methacrylate) (PMMA) is spin-coated on the wafers as protection before dicing the wafers into smaller chips. Finally, the chips are cleaned with solvents, deionized water, piranha solution (H_2O_2 and H_2SO_4) and oxygen plasma. The exfoliated graphene sheets are then deposited over the etched wells, whereby the graphene membrane adheres to the exposed Si/SiO_2 surface via van der Waals forces. It was found that the sheets tend to be in tension [13] with the graphene also adhering to the vertical Si/SiO_2 hole walls down to about 2 to 10 nm [117, 118]. Applying a DC bias between the graphene and the silicon substrate further increases the tension [52].

2.1.6 SUMMARY

The synthesis routes reviewed in this section require different methodologies varying in complexity, advancements in the equipment used, and produce graphene with different levels of crystalline quality at different yield rates. For example, the mechanical exfoliation of HOPG or Kish graphite using the Scotch tape method has been described as a relatively simple and economical technique, yet able to produce very good quality (pristine) graphene. However, yield rates tend to be low and thus limiting its use for small-scale research purposes only. On the other hand, CVD grown graphene requires higher-end equipment and yields graphene of a

lesser quality, but is capable of producing larger amounts of graphene. Therefore, more research on possible synthesis routes which are able to produce graphene with good parameter control at low costs and high yield rates is needed to be able to integrate graphene in commercial applications.

2.2 CHARACTERISATION OF GRAPHENE

Throughout the synthesis process and following its preparation, characterization is indispensable in order to analyse the quality of the graphene structure and thereby assess the suitability of the prepared material for the desired application. Specialized characterization techniques are often required in order to image and examine the graphene samples. The most commonly used include optical microscopy (OM), atomic force microscopy (AFM), scanning tunnelling microscopy (STM), Raman spectroscopy, scanning electron microscopy (SEM), and transmission electron microscopy (TEM).

This section will discuss the use of optical microscopy, scanning electron microscopy, and Raman spectroscopy. Section 2.3 is then dedicated solely to atomic force microscopy and its use in graphene characterization.

2.2.1 OPTICAL MICROSCOPY

Albeit seemingly impossible to image a single atomic thin graphene layer with a typical optical microscope, this tool may be the most common piece of equipment which is used in graphene research. Optical microscopy is in fact the simplest characterisation technique suitable for large-scale analysis of graphene [7]. While other specialised and advanced techniques may provide more information on the graphene sample as will be discussed in the following sections, optical microscopy allows the user to quickly scan the sample to identify the presence of graphene. This is especially useful for mechanically exfoliated graphene samples whereby SLG or FLG are often present at very low yields amongst a large number of other MLG or graphite flakes.

In fact, initial sorting of graphite flakes and few-layer graphene is often done with optical microscopy as different graphene thicknesses exhibit different optical properties when supported on a substrate [6, 119]. A literature survey on the use of optical microscopy for the characterisation of graphene found that the visibility of graphene depends on both the optical properties of the substrate as well as on the wavelength of light used for imaging [69].

Mechanically exfoliated graphene is often deposited on an oxidised silicon wafer with a 300 nm thick SiO_2 layer as the latter allows for optimal optical contrast when imaging [69]. However, it was found that slightly altering the oxide thickness by even 15 nm significantly lowers the optical contrast of SLG on the substrate [7]. The use of monochromatic illumination in the optical microscope – achieved with the use of narrow-band filters – improves contrast irrespective of substrate thickness and also allows for identification of SLG on different substrates such as PMMA [69].

Graphene can also be made optically visible directly on the copper substrate by thermally annealing the sample [78]. Although graphene does not offer good contrast against the copper substrate, thermally annealing the graphene-on-copper sample oxidizes the uncovered copper substrate while leaving the graphene-coated copper intact. This drastically improves optical contrast between areas of oxidised copper, and areas of graphene which have protected the underlying copper from oxidation [78].

Optical microscopy has also been successfully used to image the grain boundaries of CVD-grown graphene while still on the Cu substrate [120]. However, in order to be able to visualise the graphene grain boundaries and distinguish them from the grain boundaries of the copper substrate, the sample was exposed to an ultraviolet oxidation treatment which chemically modified the graphene. This chemical modification coupled with some morphological changes at the grain boundaries creates the required contrast in the optical image [120].

2.2.2 Scanning Electron Microscopy

Electron microscopy is another characterisation technique which has grown increasingly central to materials science research. The technique has been studied extensively over the last half a century since its first commercialisation in the 1960s [121]. SEM offers the ability to image a wide variety of specimens and features with improved resolution. It follows that researchers studying the nanomaterials field have adapted the well-known SEM techniques to image graphene. In general, the use of low accelerating voltages allows imaging of graphene on insulating substrates, with a voltage of 3 kV being found to be optimal [85].

As already mentioned, both mechanical exfoliation and CVD can produce graphene having different number of layers within the same sample. While the colour contrast achieved with optical microscopy may give an indication to the number of layers present in thin FLG or SLG, it was found that the use of SEM can facilitate this distinction. In particular, an Inlens secondary electron detector was successfully used to quantitatively determine the approximate thickness

of the graphene sample imaged [85]. The authors [85] attribute this ability to the attenuation of secondary electrons emitted from the underlying substrate by each graphene layer further reducing the number of secondary electrons that reach the detector.

2.2.3 RAMAN SPECTROSCOPY

Raman spectroscopy is a characterization technique often used to obtain a unique spectral fingerprint for molecules. In this technique, the inelastic scattering of the photons emitted by a monochromatic laser source, known as Raman scattering, exposes the vibrational modes of the molecules being characterized and can thus be used to distinguish between different molecular structures.

Since the first isolation of graphene, Raman spectroscopy has been successfully adapted to characterise and positively identify the presence of graphene [13, 122, 123]. The presence of defects within the graphene crystal/molecule was also noted to affect the resulting Raman spectrum. In fact, Raman spectroscopy can be used to study the extent and type of defects present in graphene [56-58, 123-129], as well as determine the number of carbon atom layers in the graphene sample [122, 123]. The Raman spectra of pristine and defected single-layer graphene is shown in Figure 2.5. As labelled in Figure 2.5, the three main Raman peaks in graphene are the G peak, the 2D peak, and the D peak; the latter is only present for defected graphene. These peaks are also present in the other carbon allotropes and aromatic hydrocarbons having a similar hexagonal carbon ring structure [125]. As shown in Figure 2.5, other smaller peaks may also be present which are often more significant in the presence of defects; these include the D', D+D'', D+D', and 2D' peaks [54, 55, 57, 127].

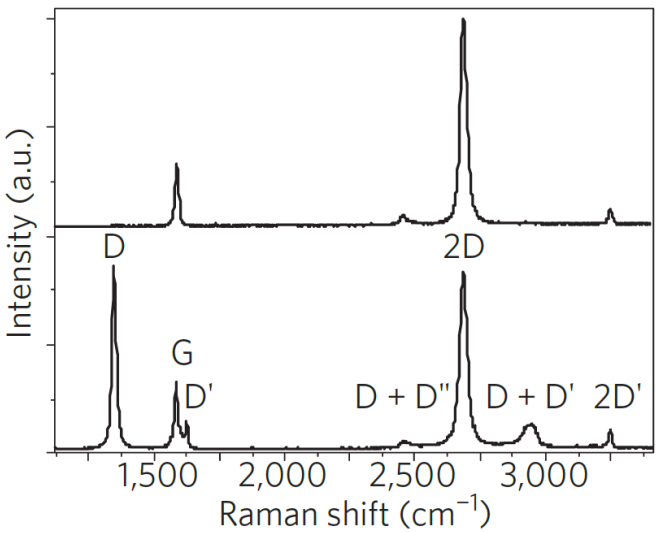

Figure 2.5: Raman spectra of (top) pristine, and (bottom) defected single-layer graphene [126].

The following presents a descriptor of the Raman peaks exhibited by graphene, and their changes with respect to the graphene quality or number of layers.

1. **G peak**: The G peak is found at a Raman shift of around 1560 – 1587 cm^{-1} and is brought about by the in-plane vibrational mode involving the sp^2-hybridized carbon atoms [122, 125]. It has been shown that the exact Raman shift, or position, of the G peak as well as its intensity are sensitive to the number of layers of the graphene; the peak translates to a lower Raman shift [130] and increases in intensity [131] with an increase in the number of layers. Temperature, doping of the graphene sample, and strain within the graphene sheet can also affect the G peak [122]. For example, an upshift of 8 cm^{-1} [131] was reported following annealing at 300°C, with the shift being attributed to hole doping of the graphene by molecular oxygen [132]. Functionalization of SLG has also shown to upshift and broaden the G peak [133].

2. **D peak**: The D peak, found at a Raman shift of around 1360 cm^{-1}, is associated with the presence of defects within the graphene. Although there are conflicting reports about the exact origin of the D peak [125], it is generally accepted that this peak reflects the breathing mode of the hexagonal carbon ring (Figure 2.6) [122]. However, in order for this mode to be active, a disorder, or defect, has to be present next to the 'breathing' ring [122]. As such, the intensity of the D peak is closely related to the defect density in the graphene [55, 57, 122, 133].

3. **2D peak**: The 2D peak is perhaps the most important peak in the Raman spectrum of graphene, found at around 2700 cm^{-1} [125]. It is the second order, or overtone, of the D peak, yet it does not need a defect to be activated, unlike the D peak [122]. As shown in Figure 2.7, the 2D peak is significantly affected by the number of layers in the graphene sample; pristine SLG has a single sharp peak with a full width at half maximum (FWHM) of around 30 cm^{-1} [37, 122, 134] and is around 2 to 4 times more intense than the G peak [37, 55, 122, 125]. The latter ratio may depend on the substrate such as thickness of the SiO_2 layer [53]. As the number of graphene layers is increased, the 2D peak is observed to broaden and consist of multiple components [60, 134], as shown for BLG in Figure 2.7 (c) [123]. Oxygen doping of the graphene via annealing also upshifts the 2D peak [54, 132] by around 12 cm^{-1} [131] and decreases its intensity [54]. In other work, it was found that exposing BLG to oxygen plasma transforms the

4-component 2D peak into one which resembles that of SLG. This is accompanied by an increase in its FWHM attributed to the loss of the AB-stacking configuration [134].

As previously mentioned, both the G and the 2D peak are also present in graphite. However, the intensity ratio between the two peaks, I_{2D}/I_G, changes drastically from the strictly 2D material, to BLG, FLG, MLG, and graphite. The I_{2D}/I_G was also observed to decrease from 1.9 in as-deposited mechanically exfoliated SLG to 1.4 upon annealing at 300°C for 2 hours [131]. A similar decrease was recorded after carbon ion irradiation [54], gallium ion irradiation [68], and increased plasma etching [33, 55]; the incorporation of defects through these different routes further reduces the I_{2D}/I_G ratio.

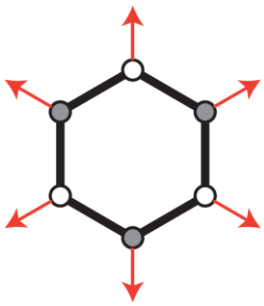

Figure 2.6: Atomic displacements in the breathing mode that activates the D peak [126].

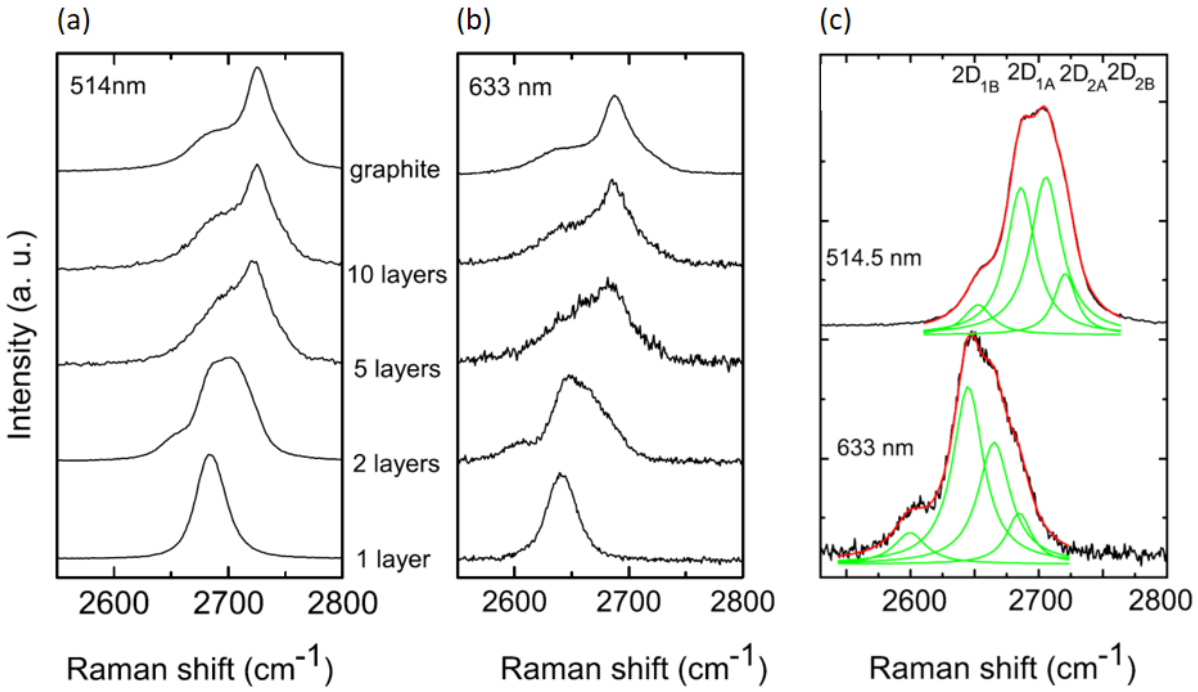

Figure 2.7: Evolution of the 2D peak with the number of layers using (a) 514 nm and (b) 633 nm excitation wavelengths. (c) The four components of the 2D peak in bilayer graphene [123].

Since the D peak is only detected when there are defects in the graphene, the I_D/I_G ratio is often used to indicate the defect density within the graphene. Most notably, it was shown that the I_D/I_G ratio exhibits a non-monotonic dependence on the average distance between the defects or defect density [57]. This relationship was first reported by Lucchese et al. [57] by bombarding mechanically exfoliated SLG using low energy argon ions with an energy of 90 eV at doses ranging from 10^{11} Ar^+/cm^2 (corresponding to one defect per 4×10^4 C atoms) up to 10^{15} Ar^+/cm^2 (corresponding to the limit of full disorder in graphene). In this non-monotonic trend, at low defect densities, the I_D/I_G is seen to increase to around 3.5 due to enhanced elastic scattering. When the average distance between the defects reduces to below 5 nm, the G and D' peaks start to overlap and both D and G peaks broaden significantly. Here, the increased ion bombardment causes the amorphization of the graphene. In turn, all of the Raman peaks are attenuated and hence the I_D/I_G is seen to decrease [57].

A similar non-monotonic dependence of the I_D/I_G on the defect density was also observed after exposing the graphene to a high energy electron beam [55], oxygen plasma [33, 55], and to a gallium ion beam [68]. Further damage to the graphene, for example following annealing in an argon atmosphere, broadens the D and G peaks considerably such that the Raman spectrum resembles that obtained from carbon black [132]. Upon bombarding SLG, FLG and MLG using C^+ ions at an exceedingly larger bias of 500 keV, the I_D/I_G was observed to increase for all three graphene variants with the ratio in SLG being consistently higher than that in FLG and MLG for the same ion dose [54]. Graphene oxide [135] and other thin carbonaceous membranes with significantly reduced crystalline order [136, 137] were also characterised by large broad D and G peaks.

At the lower defect densities before the D' peak becomes indiscernible from the G peak, it was also found that the $I_D/I_{D'}$ ratio can indicate the type of defects present in the graphene [127]. An $I_D/I_{D'}$ of around 13 was found for sp^3-hybridized defects, a ratio of around 7 for vacancy-like defects, while a lower $I_D/I_{D'}$ of around 3.5 stems from boundary-like defects.

For graphene, the 514 nm [57, 58, 127], 532 nm [33, 56, 82, 138], 633 nm [54, 58, 131], and 785 nm [58] Raman excitation wavelengths are often chosen. It is worth noting that the position and shape of the D peak can change with the use of different laser wavelengths [122]. This dependence of the peak position on the laser wavelength is called ‘dispersion’ [122]. It was also found that the non-monotonic trend of the I_D/I_G with defect density is more pronounced and has a larger I_D/I_G maximum when using higher Raman excitation wavelengths [58].

As reviewed in the above, the dependence of the Raman spectrum on the defects present within graphene allows for Raman spectroscopy to be used to study the effect of different energetic particle beam parameters on supported graphene [38, 54, 56-58, 132, 139].

While the effect of different energetic particle beam parameters on supported graphene has been studied by Raman spectroscopy [38, 54, 56-58, 132, 139], the effects of such energetic particle bombardment on suspended graphene, i.e. unsupported graphene in the form of membranes has received little attention [37, 80, 140]. Furthermore, the immediate area surrounding the location directly irradiated by the beam may also be of significant interest due to the resulting damage profile created from the area of attack radiating away from it [56].

2.2.4 SUMMARY

This section reviewed three of the most commonly used techniques which are being adopted to characterise graphene, with each technique being capable of providing varying degrees of information on the sample. The use of optical microscopy and scanning electron microscopy allow for a quick assessment on the presence, location, and morphology of any single-layer graphene flakes amongst other few-layer or multi-layer graphene. On the other hand, Raman spectroscopy is capable of determining with more certainty the number of layers in the graphene sample, as well as its crystalline quality and hence defect density. Section 2.3 focuses on the use of atomic force microscopy to characterise graphene.

2.3 ATOMIC FORCE MICROSCOPY

Atomic force microscopy is one of the most commonly used scanning probe microscopy techniques in graphene characterization. The technique involves the use of a sharp tip mounted on a flexible cantilever to sense the presence of the sample. The interaction forces present between the tip and the sample are strong enough to bend the cantilever. The extent of deflection of a cantilever of known stiffness, or spring constant, reflects the magnitude of these interaction forces. This can then be translated to information about the sample surface, in this case graphene.

In most cases, AFM is first used to 'image' the sample to obtain information on the topography of the sample surface. There are a number of imaging modes that can be used, the most common being (i) static contact mode in which the AFM tip touches the sample and is dragged across the surface, (ii) dynamic non-contact mode in which the AFM tip is oscillated above the sample

surface such that the tip is always held a few nanometres away from the sample surface, and (iii) tapping mode in which the AFM tip intermittently touches the sample during similar oscillation of (ii), but is not in relative motion during the contact part of the cycle, as in (i). The thin and thus fragile nature of graphene dictates that topographic imaging is often performed in non-contact mode [13, 33, 52, 104, 105, 117], or tapping mode [2, 22, 60, 141, 142] to avoid or at least minimise damaging the graphene sample with the tip.

Theoretically, the change in height between the substrate surface and the graphene surface can determine the thickness and hence, the number of layers of the graphene flake. However, it was found that this method, while providing adequate qualitative data for comparison across a batch of samples, is less able to provide absolute measurements [52, 119]. This led researchers to resort to Raman spectroscopy to determine the number of graphene layers.

When AFM is operated in static contact mode, frictional forces between the tip and graphene surface often lead to torsional or lateral bending in the cantilever. This lateral bending can be measured to investigate the different friction properties of graphene compared to those of other materials, mostly the substrate material [76]. Friction measurements can also be used to assess the thickness of graphene layers. Frictional force microscopy shows that mechanically exfoliated graphene exhibits higher friction with a reduced number of layers [20]. The higher friction of SLG is attributed to the low bending stiffness of the thin layer causing the SLG to bunch up ahead of the AFM tip resulting in stick-slip motion [20]. Additionally, while it can be challenging to detect the atom-thick SLG on relatively non-flat substrates with topographic images, such as in Figure 2.8 (*A*), significant changes in the frictional properties between the graphene and the substrate can create greater contrast, such as in Figure 2.8 (*C*). By scanning the same area multiple times, using different normal loads, frictional data can be extracted for a given graphene-substrate system [77, 117]. The friction forces can then be calculated as the average of the difference between the lateral forces measured during sliding in the forward and backward directions, as shown in Figure 2.8 [77].

Static contact mode imaging was also used to manipulate functionalized graphene sheets deposited over freshly-cleaved HOPG substrates [143]. Schniepp et al. [143] report of actively folding the graphene sheets with an AFM probe of cantilever spring constant of 0.32 N/m, operated at a normal force setpoint of 1 nN. Analysis of the folded region allowed for a study on the bending rigidity of functionalised graphene.

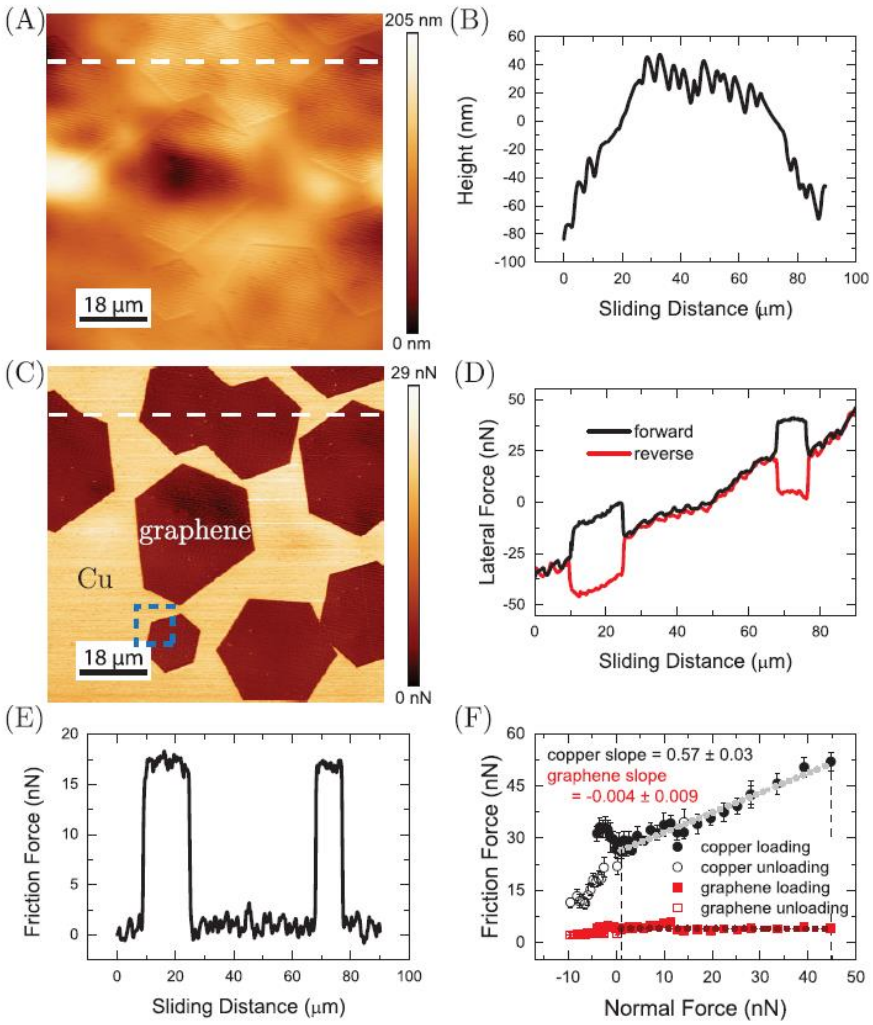

Figure 2.8: Typical friction force microscopy data. (A) Topographic and (C) friction force images of the surface of the copper foil partially covered by graphene islands, (B) topographic and (D) lateral force line profile along the white dashed line marked in (A) and (C), respectively, (E) friction force profile along the same line shows that graphene reduces friction by a factor of 17 compared to Cu, (F) friction force versus load plot for graphene and copper acquired in a single region spanning the graphene-Cu boundary (indicated by the blue square in (C)) [77].

Adhesion forces can also be analysed by bringing the tip and sample into contact, and slowly moving the tip away from the graphene sample until contact is lost, measuring the required pull-off force [67]. Typically, the tip-to-sample distance at which contact is lost is larger than the tip-to-sample distance at which contact is initiated due to adhesion forces.

Using the same principle, another AFM operating mode used for graphene imaging is the Peak Force mode [1]. From Figure 2.9, in the Peak Force mode, the AFM tip is lowered towards the sample. At the critical value of the tip-sample attractive force, that is, as the stiffness/magnitude

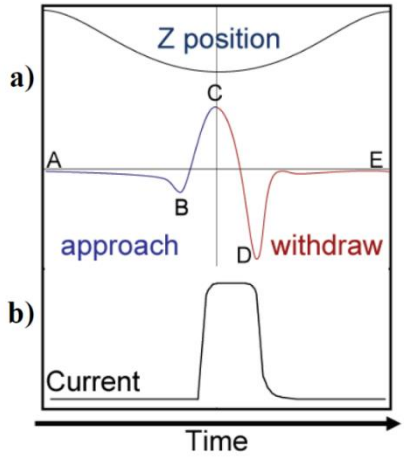

Figure 2.9: The (a) Peak Force behaviour and (b) Peak Force Tunnelling AFM current when the tip is brought close to the sample [1].

of the tip-sample force becomes larger than the cantilever stiffness, the tip snaps into contact with the sample surface (at B in Figure 2.9). When the tip is subsequently retracted, the cantilever snaps back out of contact (at D in Figure 2.9) at the higher attractive force. The snap-in force and snap-out force can be measured to obtain specific parameters.

While AFM techniques detect short-range tip-sample forces originating from either repulsive contact forces or attractive van der Waals forces, long-range forces such as electrostatic forces can be measured with other probe techniques called electrostatic force microscopy (EFM). Similar to dynamic non-contact mode AFM, in EFM the tip is oscillated at a slightly larger lift height of approximately 16 nm and a DC bias is often applied to amplify the electrostatic forces. Burnett et al. [113] developed an amplitude modulation EFM technique which enables the identification of the number of layers in graphene, without necessarily requiring the measurement of the distance between each layer. With this technique, the authors [113] claim that they have successfully monitored the phase shift as a function of the electrostatic DC bias applied concluding that the phase shift is correlated to the number of graphene layers.

Peak Force Tunnelling AFM (TUNA) mode – a variant of the tapping mode – also makes use of long(er) range forces [1]. Due to the presence of an electric field, tip-sample contact may result in a contact current, which can be measured during Peak Force Tapping mode. Thus, the Peak Force TUNA mode is used to map the conductivity of the graphene with very high sensitivities.

Although AFM can be used to study the topography and properties of graphene itself, the 2D nanomaterial has also been used to study other structures which would have been otherwise

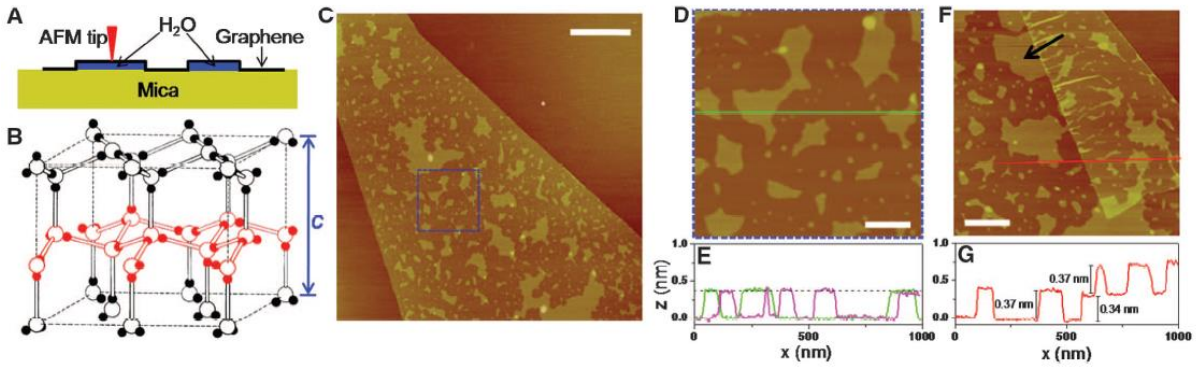

Figure 2.10: Imaging the first water adlayers on mica using an AFM tip at ambient conditions. (A) A schematic of graphene covering the water adlayers, (B) the structure of ice, (C, D, F) AFM images of monolayer graphene on mica, and (E, G) height profiles showing the thickness of the water islands [2].

impossible to image without graphene acting as an intermediary surface. As shown in Figure 2.10 [2], pristine graphene was successfully used as an ultrathin coating covering the water adlayers on mica. This allowed imaging of the otherwise unstable water adlayer structures beneath the graphene membrane. Tapping mode AFM was performed at ambient conditions at a relative humidity ranging from 2% to 40% in order to reveal humidity-dependent water structures, including the development of ice-like structures in the first water adlayers.

2.3.1 Nanoindentation of Graphene

Apart from imaging the topography of graphene samples, the response of a supported graphene layer or a suspended graphene membrane under a point load is valuable information for the realization of a variety of graphene-based applications. With current available technologies, this field can be investigated at three different length scales; the micro, nano, and atomistic length scales. Since at the nano scale most phenomena tend to be size dependent, the behaviour of graphene at all length and time scales is important.

Using relatively standard nanoindentation experimental setups, a diamond Berkovich indenter has been used to study the mechanical and tribological properties of supported graphene on SiO_2 wafers [144] and graphene-polymer nanocomposites [43]. Due to the relatively large scale of indentation depths in the order of hundreds of nanometres – compared to the thickness of graphene [144], indentation speeds in the order of hundreds of nanometres per second and normal loads of hundreds of nanonewtons [43], it was found difficult to obtain mechanical properties of pure graphene; the testing parameters are likely to generate a response by a significant portion of the substrate system thus affecting the results obtained for the graphene layer at the surface [144].

Conversely, an AFM tip can be used to indent a graphene sample and assess the response of graphene to nanoindentation by limiting the scale of interaction [13, 33, 117, 145, 146]. This method is broadly known as force spectroscopy but is often referred to as *nanoindentation via AFM* when applied to graphene studies. In this technique, graphene is typically first suspended over a well within the substrate to create a drum-like membrane in a set-up illustrated in Figure 2.11. Once the graphene membrane is properly located and imaged with AFM, the same tip is used to apply load and hence indent the membrane. As the AFM tip is lowered into the sample, the force being applied to the graphene membrane is recorded to obtain a force-distance (FD) curve. This force curve can then be used to extract the elastic properties of the graphene. For such indentations, the tip is often centred in the middle of the membrane and pushed slowly into the graphene. Indentation velocities ranging from 0.23 μm/s and up to 0.5 μm/s were used in literature reports [13, 52, 61, 104, 117]. Having established the stiffness or spring constant of the cantilever via a calibration procedure, a graph of interaction force against the indentation depth is plotted, the slope of which represents the elastic stiffness of the graphene membrane. The theory behind the force curves is detailed in Chapter 4.

In earlier works [52, 145], the tip was operated in dynamic mode during the approach, resulting in the loss of free amplitude of tip oscillation once the tip comes in contact with the graphene. With this technique, Frank et al. [52] noted that the spring constant of graphene membranes suspended over 1 μm wide trenches rises by a factor of 2 nearer the clamped edges, while it remains stable as long as the tip is within 100 nm of the centre of the suspended sheet. The authors report an elastic modulus of 0.5 TPa for mechanically exfoliated FLG with thicknesses ranging from 2 to 8 nm. Similarly, Gomez-Navarro et al. [104] suspend chemically-derived SLG on trenches to create rectangular beams. Upon indenting the centre of the suspended graphene, the authors highlight the nonlinearity in the elastic response of material especially for large deflections >10 nm.

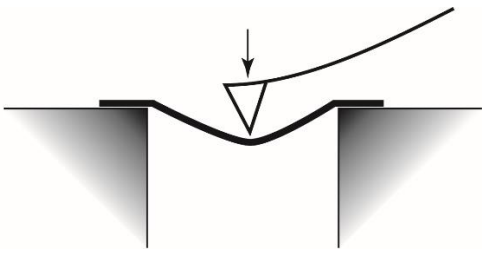

Figure 2.11: Indentation at the centre of the suspended graphene membrane via AFM.

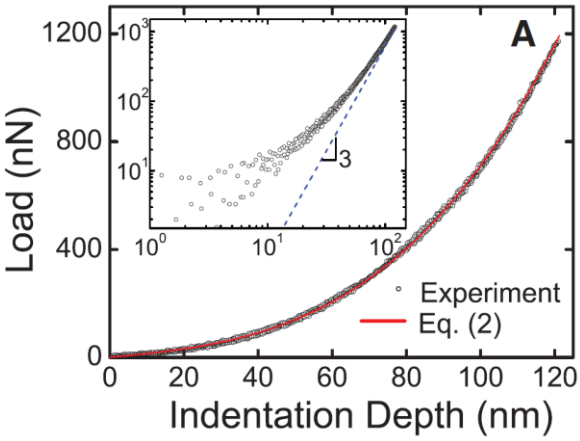

Figure 2.12: Force-displacement curve obtained experimentally via nanoindentation, fitted to Equation 2.1 [13].

Perhaps the most prominent work in this regard was that carried out by Lee et al. [13, 117]. The authors derive a mathematical model from first principles to describe the behaviour of a circular graphene membrane under AFM nanoindentation. This model allows for the determination of the elastic modulus of graphene. In their work, monolayer and multi-layer graphene membranes were suspended over open holes of 1 µm and 1.5 µm radius and nanoindentation was performed using a diamond tip of radius 15 to 30 nm. Indentation depths of 20 to 100 nm were achieved at a constant displacement rate of 0.23 to 1.3 µm/s. Once a pre-set depth was reached the membrane was further loaded up to failure.

Analysis of the force-displacement behaviour shown in Figure 2.12 and comparison to a finite-element-analysis-derived model concluded that the nonlinear elastic response of the graphene membrane can be approximated to a clamped circular membrane of linear isotropic material loaded at the membrane centre as in Equation 2.1 [13].

$$F = \sigma_0^{2D}(\pi a)\left(\frac{\delta}{a}\right) + E^{2D}(q^3 a)\left(\frac{\delta}{a}\right)^3 \qquad \textit{Equation 2.1}$$

where F is the applied force, δ is the deflection of the membrane at the centre point, a is the graphene membrane radius, σ_0^{2D} is the pre-tension[4] of the membrane, E^{2D} is the 2D elastic constant, and q is taken as 0.98 [147, 148] derived from a function of the Poisson's ratio ν, taken as 0.165, ($q = \frac{1}{1.05-0.15\nu-016\nu^2}$). It was determined that for a tip radius r, much smaller than the graphene membrane radius a, the force-displacement behaviour is insensitive to the tip radius and to the precise position of the tip relative to the circular membrane – within one

[4] The pre-tension of the membrane refers to the tension in the graphene membrane prior indentation. The magnitude of the pre-tension depends on the deposition method and/or any applied stress.

tenth of the membrane radius off the membrane centre. Based on a continuum model, the maximum stress, σ_m^{2D} sustained by a graphene membrane indented by a tip of radius r can be found using Equation 2.2 [13, 117]. Unlike the force-displacement behaviour during elastic response, it was noted that the breaking force is a function of the tip radius, yet it shows no dependence on membrane size because of the extreme stress concentration under the indenter tip [13, 117].

$$\sigma_m^{2D} = \sqrt{\frac{FE^{2D}}{4\pi r}} \qquad \textit{Equation 2.2}$$

With this methodology, the authors [13] reported for the first time an experimentally-derived 2D elastic modulus of 340 ± 50 N/m, equivalent to 1.0 ± 0.1 TPa for 0.335 nm thick graphene. The film pre-tension was noted to vary from 0.07 to 0.74 N/m. Loading membranes up to breaking point resulted in large membrane deflections before failure, in excess of 100 nm and forces of around 1.8 μN to 2.9 μN. An average breaking strength of 42 ± 4 N/m at failure strain of 0.25 was found. Since the films close to the tip are taken as defect free, the maximum stress should represent the intrinsic strength. However, the authors acknowledge that this is an overestimation since the model in Equation 2.2 ignores nonlinear elasticity.

Equation 2.1 and Equation 2.2 have since been repeatedly adopted in later studies [33, 63, 64, 81-84, 86, 149, 150] to measure the elastic and fracture properties of graphene using AFM, with some studies suggesting minor changes to the fitting constants [61, 83, 86].

The same model was used to measure the elastic properties of CVD-grown graphene whereby the average modulus was found to be 0.979 ± 0.045 TPa, marginally lower than that of pristine mechanically exfoliated graphene [82]. It was also noted that while the grain boundaries do not seem to largely affect the modulus, they have a detrimental effect on the fracture strength [82]. In fact, Equation 2.2 was used to measure the breaking strength of CVD-graphene reporting an average breaking stress of around 35 GPa, around 16% lower than that found for mechanically exfoliated graphene [13].

On the other hand, the elastic modulus of monolayer graphene oxide was reported to be between 0.21 TPa [135] and up to 0.34 TPa [150], significantly lower than that of mechanically exfoliated and CVD-grown graphene.

Ruiz-Vargas et al. [86] modify Equation 2.1 to Equation 2.3 to take into consideration the radius of the indenter, r.

$$F = \frac{2\pi\sigma^{2D}\delta}{\ln\frac{a}{r}} + \frac{E^{2D}(q\delta)^3}{a^2} \qquad \textit{Equation 2.3}$$

With this model, the authors [86] report an elastic modulus of 0.16 TPa with a distribution FWHM of 0.15 TPa for CVD-grown SLG, significantly lower than that found in [13] and [82]. An average pre-tension of 0.085 N/m was reported [86]. As will be discussed in Section 2.3.1.1, the authors [86] attribute the low elastic modulus to the presence of wrinkling in the CVD-grown graphene membranes. Equation 2.3 was also used by Storch et al. [151] reporting an elastic modulus of 0.657 TPa for CVD-grown graphene, significantly higher than that found in [86] yet still lower than that found for both mechanically exfoliated graphene [13] and CVD-grown graphene [82] using Equation 2.1.

To enhance both the modulus and the breaking strength, Ruiz-Vargas et al. [86] deposit two graphene membranes, one on either side of the perforated substrate to create BLG membranes. It was highlighted that such BLG membranes do not fail catastrophically upon loading.

A similar model to Equation 2.1 was derived for thin membranes of muscovite mica and MoS_2 shown in Equation 2.4 [71-73].

$$F = \left[\frac{4\pi E}{3(1-\nu^2)}\left(\frac{t_G^3}{a^2}\right)\right]\delta + (\pi\sigma)\delta + \left(\frac{q^3 E t}{a^2}\right)\delta^3 \qquad \textit{Equation 2.4}$$

where t_G is the thickness of the membranes. Equation 2.4 was then adapted for mechanically exfoliated graphene membranes, once again using a Poisson's ratio of 0.165, to obtain an elastic modulus of 1.12 TPa for SLG and ~ 3.3 TPa for BLG and FLG [60].

Force-curves obtained from mechanically exfoliated graphene membranes were also approximated to the Schwering-type equation shown in Equation 2.5 [61, 62, 64, 115]. Although similar to Equation 2.1, the constant q is omitted. With this equation, an elastic modulus of 0.75 to 1.07 TPa [61] or 1.045 ± 0.090 TPa [64] was obtained for mechanically exfoliated graphene and 0.15 ± 0.03 TPa for graphene oxide [62].

$$F = \sigma_0^{2D}\pi\delta + \frac{E^{2D}}{a^2}\delta^3 \qquad \textit{Equation 2.5}$$

Lin et al. [83] further modified Equation 2.1 to account for changes in the zero-displacement point (ZDP)[5], as shown in Equation 2.6.

[5] The significance of the zero-displacement point will be discussed in Chapter 4.

$$F = F_0 - \sigma_0^{2D}\pi\delta_0 - \frac{E^{2D}q^3\delta_0^3}{a^2} + \left(\sigma_0^{2D}\pi + \frac{3E^{2D}q^3\delta_0^2}{a^2}\right)Z - \frac{3E^{2D}q^3\delta_0}{a^2}Z^2 + \frac{E^{2D}q^3}{a^2}Z^3 \qquad \textit{Equation 2.6}$$

where F_0 and δ_0 refer to the force and displacement values of the ZDP, and $Z = \delta + \delta_0$.

Storch et al. [151] also compare different loading conditions; point loading during AFM nanoindentation versus uniform loading by applying a bias across the membrane. The elastic modulus obtained by uniform loading was measured at only 0.152 TPa. They attribute this discrepancy to the fact that the strain is highly localized under point loading as opposed to uniform loading.

To avoid such localized strain, other techniques to measure the elastic modulus of graphene membranes using AFM yet without point-loading the membrane with the tip were also developed [22, 135, 137].

For example, in the bulge test technique [22], a pressure difference is applied across the graphene membrane to create a concave or convex membrane. In initial works by Bunch et al. [22], pristine graphene was determined to be impermeable to all standard gases including helium. Therefore, after applying a pressure difference, the bulging of the graphene sheet can be imaged with AFM and the change in topography of the membrane can be used to extract the elastic properties of the stretched graphene membrane.

AFM static contact mode imaging was also used directly to measure the elastic properties of graphene oxide [135] and amorphous carbon [137] membranes. During imaging, the AFM tip is in reality continuously indenting the graphene membrane at low normal loads. Thus, the topography image obtained reflects the indented depth of the graphene membrane at each location of the AFM tip, as shown schematically in Figure 2.13.

Table 2.1 and Table 2.2 collate the main experimental variants and results obtained by principal research groups.

Figure 2.13: Schematic of the AFM tip at different positions on the sample; the dashed lines represent the shape of the membrane at the corresponding contact point, the solid line represents the acquired tip trajectory and thus the obtained AFM topography image [135].

Table 2.1: Published values for the elastic modulus of graphene membranes prepared via mechanical exfoliation.

Graphene Preparation Method	Number of Layers	Equation	Spring Constant (N/m)	Indentation Depth (nm)	Membrane Diameter (μm)	Elastic Modulus (TPa)	Ref.
Mechanically Exfoliated	1	Equation 2.1	-	100	1, 1.5	1.02 ± 0.15	[117]
			0.4	350	8	1.04 ± 0.149	[149]
			3	35	0.5 – 3	1.045 ± 0.090	[64]
			40	50 – 80	1	1.06 ± 0.32	[63]
			73.5	50 – 200	0.5 – 5	~ 1	[33]
			44.8, 58.8	20 – 100	2.5	1.0 ± 0.1	[150]
		Equation 2.4	2.8	120	3.8	1.12	[60]
		Equation 2.5	33	80	0.5 – 3	0.746 – 1.075	[61, 62]
	2	Equation 2.1	-	50	1, 1.5	1.04	[117]
			40	50 – 80	1	1.040 ± 0.046	[63]
		Equation 2.4	2.8	80	3.8	3.25	[60]
	3	Equation 2.1	-	50	1, 1.5	0.98	[117]
		Equation 2.4	2.8	60	3.8	3.25	[60]
	5	Equation 2.1	40	50 – 80	1	1.036 ± 0.037	[63]
		Equation 2.4	2.8	50	3.8	3.43	[60]
	2 – 8 nm	Other	2	15	-	0.5	[52]
	8 – 100 nm	Other	2, 42	Within linear regime	1	0.02 – 3	[59]
	1	Other	0.4	-	8	1.04 ± 0.149	[149]
		Other	-	-	-	1.16 ± 0.06	[22]

Table 2.2: Published values for the elastic modulus of graphene membranes prepared via other preparation methods.

Graphene Preparation Method	Number of Layers	Equation	Spring Constant (N/m)	Indentation Depth (nm)	Membrane Diameter (μm)	Elastic Modulus (TPa)	Ref.
CVD-grown	1	Equation 2.1	-	-	1, 1.5	0.979 ± 0.045	[82]
			27	130	2.2	0.540 ± 0.033 up to ~ 0.8	[83]
		Equation 2.3	3	-	2	0.16	[86]
			70	-	42	0.657	[151]
rGO	1	Other	1 – 50	-		0.25 ± 0.15	[104]
GO	1	Equation 2.1	34.24	80 – 120	2.5	0.384 ± 0.031	[150]
		Equation 2.5	30	-		0.15 ± 0.03	[62]
		Other	0.07	-		0.208 ± 0.023	[135]
	2	Other	0.07	-		0.445 ± 0.025	[135]
	3	Other	0.07	-		0.666 ± 0.035	[135]
Strained	1	Other	200	-		1.25	[152]
~0.3% Strained	1	Equation 2.1	30	-		~2	[64]
Amorphous Carbon	3.7 ± 0.08 nm	Other	-	-		0.179 ± 0.032	[137]
	6.8 ± 0.12 nm	Other	-	-		0.193 ± 0.02	[137]
	10.4 ± 0.17 nm	Other	-	-		0.211 ± 0.045	[137]

2.3.1.1 Wrinkles in the graphene membrane

In the work by Lee et al. [13], non-contact imaging revealed that mechanically exfoliating and depositing graphene on a 300 nm SiO_2 substrate with 1 μm to 1.5 μm diameter wells results in tautly stretched graphene membranes which adhered to the vertical walls of the substrate hole for 2 to 10 nm. Similarly, mechanically exfoliated graphene over 4.75 × 4.75 μm square wells in SiO_2 were observed to adhere to the sides of the wells to ~17 nm due to the strong van der Waals interaction between the graphene and the SiO_2 [22]. Amorphous carbon membranes on silicon nitride grids have also been observed to attach to the side walls by 1 to 5 nm, with thicker membranes adhering less [137].

Conversely, it was found that CVD-grown graphene membranes are often characterised by wrinkles of amplitudes in the order of a few nanometres within the sheet and significant surface roughness (rms) of around 3 nm [86]. It is believed that such wrinkles may originate from the roughness of the copper substrate during growth [86, 153], and may be increased during the transfer process to the second substrate. It was also suggested that due to a mismatch in the expansion coefficients of the copper substrate and the graphene, compressive strains are introduced in graphene upon cooling from the growth-temperature. The formation of wrinkles releases such strains [153].

It is understood that any wrinkles in both exfoliated and CVD-grown graphene membranes lower the elastic modulus of the graphene [154]. Less energy would be required to flatten out a rippled sheet before the elastic response of the graphene sheet is initiated [86]. The softening due to these wrinkles may be significant enough to reduce the elastic modulus down to 0.06 TPa [154]. As such, it was suggested that by controlling the magnitude of these wrinkles, the elastic modulus of the graphene can be adjusted [86]. Furthermore, by applying a pressure difference across mechanically exfoliated membranes with no visible wrinkles, Lopez-Polin et al. [64] enhanced the elastic modulus of these membranes. It is believed that the applied pressure difference introduces strain within the membrane and thereby suppresses thermal fluctuations which are always present at room temperature [64].

2.3.1.2 Variation in methodologies adopted

AFM has been frequently used to indent graphene membranes to measure graphene's elastic modulus. Table 2.1 and Table 2.2 reveal that for a given sample preparation method and mathematical model used, the elastic modulus results appear to be comparable [33, 63, 117, 150]. However, most research groups adopt different methodologies. In this section, two parameters central to AFM nanoindentation – yet often overlooked in literature – are discussed. These are (i) the spring constant of the cantilever used, and (ii) the depth of indentation. Both of these parameters are also listed in Table 2.1 and Table 2.2.

2.3.1.2.1 Spring constant

As described in Section 2.3, AFM uses a tip attached to the end of a flexible cantilever. In AFM nanoindentation, the stiffness, or spring constant, of the cantilever is used to convert the deflection of the cantilever during indentation, into quantitative values of the indentation force being applied to the sample. This allows for the force-displacement curves to be obtained.

The studies discussed in Section 2.3.1 indicate that (i) a significantly wide range of spring constants were used, from 0.4 N/m up to 73.5 N/m, and (ii) there is no apparent correlation between the spring constant used and the elastic modulus obtained (Table 2.1 and Table 2.2). To this end, the rationale behind the choice of the AFM cantilever spring constant used is not always made clear in published reports on graphene, and to the best of the author's knowledge, the effect of the spring constant on the results has not been investigated systematically yet.

The vast majority of the published reports [33, 52, 60, 62, 63, 71-73, 81-83, 86, 117, 143, 150, 151] present values for the elastic modulus of graphene membranes obtained using a single type of cantilever. Others [61, 64, 104, 149] use cantilevers with different spring constants to indent the graphene membranes, yet report no dependency of the results on the probes used. For example, Lopez-Polin et al. [61] indent mechanically exfoliated graphene using a range of cantilevers with spring constants varying from 2 to 40 N/m. Upon the introduction of defects, the authors [61] note that the E^{2D} of the flakes increases no matter what cantilever is used; however, the authors do not relate this effect on the modulus obtained using various cantilevers and associated spring constants.

On the other hand, some authors have often highlighted that the spring constant of the cantilever has to be chosen to closely match the expected stiffness of the sample material. Heurberger et al. [155] emphasise that in order to probe the elastic properties of a sample, a cantilever that will produce a larger deflection in the sample than the lower limit of detection of the bending cantilever should be used. More recently, Kaman et al. [156] investigated the effect of the choice of spring constant relative to the elastic modulus of hydrogen ions-irradiated PDMS. The authors determine that using stiffer cantilevers will produce values for the measured elastic modulus that are more stable around the bulk value at a large range of indentation depths. On the contrary, for a very flexible cantilever the force-displacement slope will be equal to 1 for an infinitely rigid substrate (refer to Chapter 4, Section 4.4) since the force-curve will be dominated by the bending of the cantilever rather than the elastic deformation of the sample. In such cases, the elastic modulus is underestimated at low indentation depths, and only at high indentation depths does the elastic modulus reach the bulk value [156].

In the case of free-standing graphene, Frank et al. [52] also stress the need to choose an AFM probe with a spring constant close to that of the graphene sheets. The authors [52] point out that if the cantilever is too stiff, the cantilever deflection is minimal possibly below the detectable limit of the instrument. As a result, at low indentation depths the cantilever starts

indenting the graphene membrane before it can start to bend. In this case, the cantilever is not sufficiently sensitive to truthfully detect the point of contact and initial indentation. On the other hand, if the cantilever is too flexible the graphene membrane will appear to be too rigid and no meaningful information can be extracted; that is, the cantilever will bend too much with limited or no indentation of the graphene membrane. For their studies, Frank et al. [52] used a 2 N/m cantilever spring constant to indent 1 μm long graphene beams.

The above evidently indicates the importance of selecting the best suited cantilever, yet no clear guidelines are provided in literature especially with direct reference to indenting graphene membranes.

2.3.1.2.2 Indentation Depth and Membrane Radius

As described earlier, graphene exhibits a nonlinear elastic behaviour. In fact, the force-displacement curve is often modelled by (i) a linear term to account for any pre-tension in the membrane, and (ii) a cubic term that reflects the elastic modulus of the graphene as can be seen in Equation 2.1, Equation 2.3, Equation 2.4, and Equation 2.5.

As shown in Table 2.1 and Table 2.2, different research groups indent graphene membranes to different indentation depths. In turn, these do not correlate the measured elastic modulus to this parameter.

In terms of membrane size, most groups use membranes having different diameters, with most lying in the range of 0.5 μm to 3.8 μm [33, 59-64, 82, 83, 86, 117, 150]. This has been determined to be inconsequential to the elastic modulus measured [33, 61, 62, 64, 82, 117, 150].

2.3.2 SUMMARY

The extensive use of atomic force microscopy to study and characterise graphene is evident from this section. Indeed, AFM was successfully used multiple times to image the graphene sample and thus obtain different types of information such as its topography, friction properties, and adhesive properties. In Section 2.3.1, the use of AFM to perform nanoindentation on freely-suspended graphene membranes was presented. While this technique was the first method used to experimentally measure the mechanical properties of graphene and confirm the theoretically-derived elastic modulus of 1 TPa, its continued use by various research groups indicates the need for further study and standardization of the method with respect to graphene characterization. Some of the methodological variants that have been used which might have

affected the reported results were highlighted and discussed in Section 2.3.1.2. Nonetheless, a robust systematic study on the methodology parameters, such as cantilever spring constant, membrane size, and indentation depths, is yet to be conducted.

Section 2.4 reviews the use of molecular dynamics simulations to circumvent some of the experimental challenges highlighted above while providing new understanding of the phenomena observed.

2.4 MOLECULAR DYNAMICS SIMULATIONS

Experimental studies on nanomaterials, although often imperative to observe key material phenomena, often require a high level of expertise in the production, handling and characterisation techniques adopted. As reviewed in Sections 2.2 and 2.3, material characterisation requires specialized equipment and highly skilled personnel able to master the required techniques, such as Raman spectroscopy and atomic force microscopy. Moreover, the possible scale of phenomena to be studied is limited by the ability of current cutting-edge technologies to probe at the nano and sub-nano scale. Even though these probing capabilities are continuously being improved through improved spatial resolutions and advancement of other techniques, such limitations, together with the manifestation of inevitable experimental errors, tend to inhibit widespread experimentation on graphene.

The development of powerful computers and complex algorithms have made simulations based on *ab initio* models and/or empirical data more feasible. Due to the rigorous calculations performed during the simulations, especially in atomistic simulations where each atom and bond is individually modelled, certain phenomena can be observed and studied in greater detail. For example, processes which occur in fractions of a second will be easier to investigate in computer simulations. In contrast, experimental techniques are often too slow in their measurement techniques being limited by the intrinsic delays and constraints of the mechanical and electrical systems. Computer simulations are however limited to geometries and problem times in the nanoscale; running simulations of larger scales can be too computationally expensive. An increase in the scale of study requires coarser computer models, such as continuum mechanics or finite element analysis (FEA), that tend to over-simplify the underlying mechanisms in nanomaterials.

Indeed, computational and theoretical methods have been used to predict and calculate the mechanical behaviour and properties of graphene under various conditions. Among the most

common techniques used is molecular dynamics (MD) simulation whereby every carbon atom and C-C covalent bond in the graphene lattice is individually modelled. The atoms' motion is calculated using Newton's equations of motion, with the inter- and intra-molecular forces being derived from the atomic force fields or potential functions. For graphene, the adaptive intermolecular reactive empirical bond order (AIREBO) [24, 30, 34, 63, 115, 148, 157-165] and Tersoff-Brenner [29, 166, 167] potentials are reportedly the most accurate and hence widely adopted models. The Morse bond potential coupled with the angular, torsion, and Lennard-Jones (LJ) potentials have been shown to match the accuracy of the former models [25, 168]. Background theory on molecular dynamics and the role of the potential functions to model graphene is given in Chapter 6.

While MD simulations have to be restricted to a relatively small number of atoms (on the order of a few million atoms), this limitation ensures that the model is carefully designed such that only the phenomenon of interest is simulated. In fact, in most MD simulation platforms, the user is free to model any form of graphene by pre-defining the initial position of every atom involved in the simulation. Furthermore, the environment in which the graphene is simulated and the loads applied to it can be difficult to implement experimentally, yet can produce accurate results on the behaviour of graphene itself in MD. For instance, as shown in Figure 2.14 [166], most simulations intended for the investigation of the mechanical properties of graphene tend to commence with a perfectly square or rectangular sheet of pristine graphene. The edge atoms are then constrained such that they are fixed in space or moved at a pre-defined velocity to simulate uniaxial tensile loading. This is experimentally challenging to replicate, yet allows for precise relationships to be formed between the mechanical behaviour of the graphene and the sheet size, aspect ratio, loading orientation, loading velocity, temperature etc. A review of such relationships reported in literature is given in Section 2.4.1.

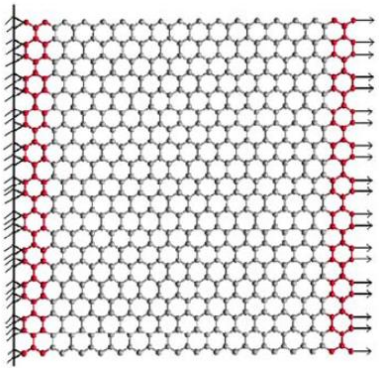

Figure 2.14: Pristine graphene sheet modelled in tensile loading; the C atoms on the left (in red) are fixed, while the C atoms on the right (in red) are constrained to move at a pre-defined velocity [166].

2.4.1 UNIAXIAL TENSILE LOADING

Measuring the elastic modulus and fracture strength of a material under uniaxial tensile loading is common practice in material science given that the material can be formed into a standard macro test specimen. Using a similar tensile testing strategy to load an atomically-thin material is problematic given that the scale dictates that the jigs that hold the nanomaterial, and the actuators and sensors required to apply the strain and measure the force need to be reimagined to allow use at such small scale. The use of molecular dynamics simulation circumvents these experimental difficulties and instead simulate tensile loading of graphene as a nanomaterial.

As shown in Table 2.3, under such loading conditions using MD, several research groups [24, 30, 34, 158, 166-170] obtained values for the elastic modulus, fracture stress, and fracture strain of pristine graphene which are in good agreement with experimental measurements [13]. Table 2.3 further lists the loading orientation, sheet size, temperature, and strain rate used in the corresponding simulations.

2.4.1.1 Loading orientation and Anisotropy

Simulating uniaxial tensile loading has enabled researchers to observe that graphene exhibits anisotropic mechanical behaviour. A graphene sheet loaded in the ZZ direction was found to exhibit up to 25% higher fracture stress and up to 69% higher fracture strain than when loaded in the AC direction [24, 25, 34, 167, 170].

Less agreement is found when comparing various studies for the elastic modulus of graphene along different directions; some simulation work has shown isotropy for the elastic modulus [24, 169, 170], while other authors either claim that the AC loading direction is stiffer than the ZZ direction or vice versa [157, 166]. The anisotropy is attributed to the alignment of the individual C-C bonds to the loading direction and the resulting variation in the C-C bond lengths and bond angles when loading in either direction [24, 166].

Table 2.3: Mechanical properties of graphene measured under uniaxial tensile loading in MD.

Potential	Temperature (K)	Strain Rate	Sheet size (nm × nm)	Elastic modulus (TPa)		Fracture Stress (GPa)		Fracture Strain		Ref.
				AC	ZZ	AC	ZZ	AC	ZZ	
AIREBO	300	10^9 s^{-1}	10 × 10 periodic	1.01 ± 0.03	-	90	107	0.13	0.20	[24]
	300	5×10^9 s^{-1}	4.26 × 4.92	-	-	90	105	0.13	0.22	[34]
	300	10^9 s^{-1}	12.64 × 11.07	1.090 ± 0.003	-	90.8	-	0.137	-	[30]
	300	10^8 s^{-1}	-	-	-	93	117	0.179	0.257	[160]
	0	10^9 s^{-1}	100 × 30	-	-	100	120	-	-	[158]
Tersoff-Brenner	300	10^8 s^{-1}	4.15 × 4.15	1.13	1.05	180	210	0.33	0.44	[166]
	300	2.45×10^8 s^{-1}	4.8 × 6.1	0.790	0.807	123	127	0.23	0.22	[167]
REBO	1800	-	-	-		46.9	51.2	-	-	[171]
	1	-	1.95 × 7.95	0.907	0.907	86.55	86.55	0.135	0.135	[169]
Morse	0	2.6×10^8 s^{-1} up to 0.026×10^8 s^{-1}	20.0 × 20.3	0.853	-	-	-	-	-	[168]
	-	-	9.35 × 7.96	1.3	1.3	100	125	-	-	[170]

2.4.1.2 Sheet size and Aspect ratio

The relationships between the elastic and fracture properties with sheet size and aspect ratio were also investigated in some literature sources [24, 157, 161, 166, 172, 173], but some disagreement is found as to how the mechanical properties change with the overall dimensions of a graphene nanoribbon.

Simulations indicate that as the aspect ratio of the nanoribbon is increased, the fracture stress decreases while the fracture strain increases [161, 172, 173]. The elastic modulus was also observed to increase with an increase in aspect ratio [157].

However, for the same aspect ratio, Zhao et al. [24] claim that the elastic modulus increases with an increase in sheet size, until it reaches the value for bulk graphene at a diagonal length of approximately 10 nm. On the contrary, Tserpes et al. [170] reported that the elastic modulus and tensile strength decrease with an increase in sheet size with the mechanical properties stabilizing beyond a sheet size of 9.35 × 7.96 nm. Ni et al. [166] find that the elastic modulus is not affected by the sheet size ranging from a 2.0 × 2.0 nm sheet up to a 8.4 × 8.4 nm sheet.

2.4.1.3 Temperature

It is generally accepted that the fracture stress and fracture strain decrease, sometimes linearly, with an increase in system temperature [34, 171-177].

The elastic modulus was found to be insensitive to change in temperature in some studies [171], yet was found to marginally decrease with an increase in temperature up to 1000 K in others [157, 177].

2.4.1.4 Strain rate

The applied strain rate may also affect the simulation results. If the strain rate is too large, atoms do not have the time necessary to redistribute the stress, or relax, while if it is too slow, the computational time is inevitably increased. Using a time step of 1 fs, varying the strain rate from approximately 2.4×10^7 up to 2.4×10^8 s^{-1} indicates that the rate does not significantly affect the stress-strain curves, yet slightly affects the fracture point [166]. Le and Batra [168] report that the strain rate varied from 2.6×10^6 up to 2.6×10^8 s^{-1} does not affect the tensile deformations but only affect the fracture behaviour.

2.4.1.5 Wrinkling

Similar to what has been observed experimentally, MD simulations also report fluctuations or wrinkling within the graphene sheet, prior to any load being applied. In fact, Ni et al. [166]

note that at 300 K, the first 4% of strain is only used to flatten out the wrinkled sheet. Zhao et al. [24] report out-of-plane fluctuations of around 0.576 Å at 300 K. The magnitude of these ripples were observed to be directly proportional to the temperature [178].

2.4.1.6 Fracture behaviour

Apart from the elastic properties and quantitative fracture parameters of graphene, the mode in which graphene sheets fail qualitatively due to a variety of loading systems is also important. The fracture behaviour of pristine and defected graphene was analysed in numerous works [29, 35, 166, 174, 179, 180] with the use of different computational and theoretical techniques. In general, it is agreed that pristine graphene exhibits a brittle failure with no or insignificant plastic deformation when subjected to a tensile load [159]. A brief overview is provided hereunder. A more detailed review on the fracture of graphene can be found in [181].

Due to its hexagonal lattice structure, the way in which the crack propagates in graphene also shows anisotropy. It was found that irrespective of the direction of loading, a crack in pristine graphene tends to favour the ZZ lattice direction, as shown in Figure 2.15 [174]. If the sheet is loaded along the AC direction, the crack travels perpendicular to the loading direction, as shown in Figure 2.16 (a, b), with some simulations showing a number of pentagon-heptagon defects forming just ahead of the crack tip [166]. On the other hand, if the sheet is loaded in the ZZ direction, the crack travels at 60° from the loading direction, as shown in Figure 2.16 (c, d) [29, 166, 167]. TEM imaging of a torn graphene sheet indicates that the preferred directions are both the AC and ZZ direction, as opposed to other chiral directions [182].

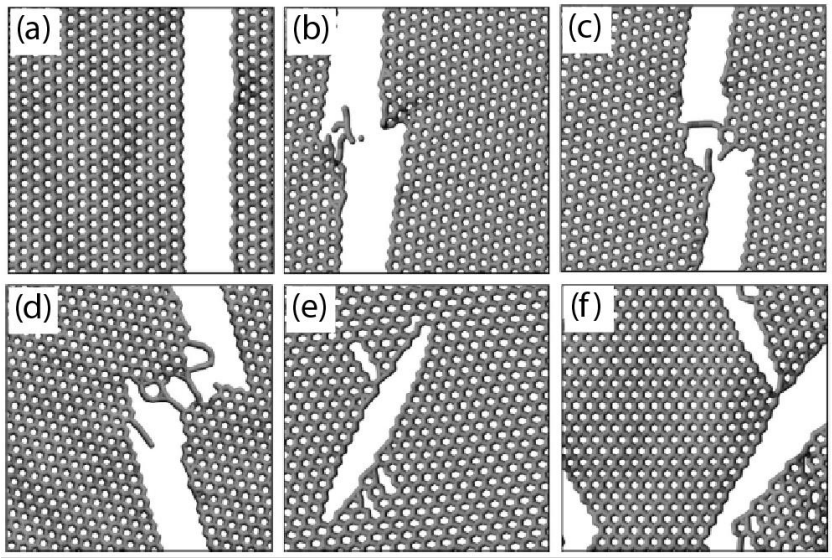

Figure 2.15: Crack propagation in graphene sheets under a tensile load along different orientation angles; (a) 0° (AC), (b) 6.6°, (c) 8.2°, (d) 16.1°, (e) 23.4°, and (f) 30° (ZZ) [174].

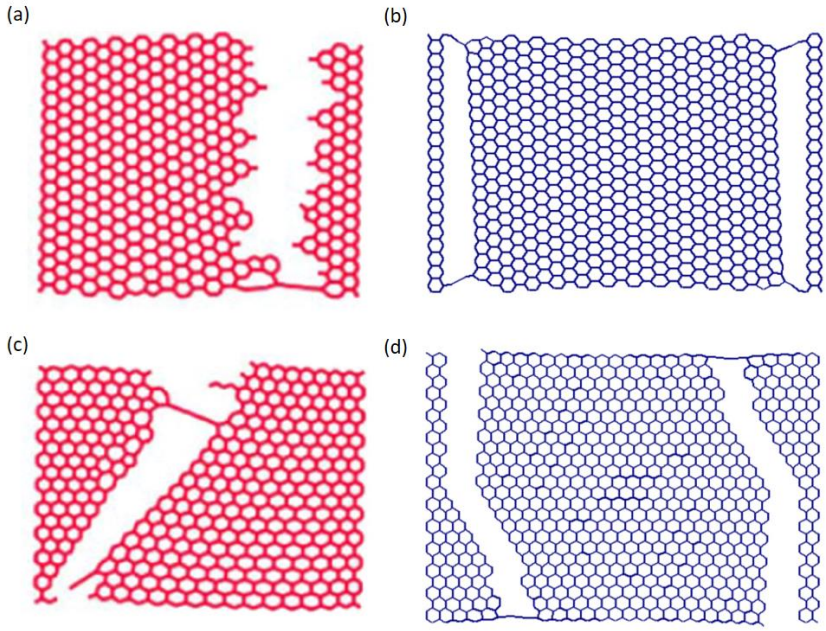

Figure 2.16: Fracture process upon loading in the (a, b) AC, and (c, d) ZZ directions (a, c) [166], (b, d) [167].

2.4.2 Point Loading Nanoindentation

As presented in Section 2.4.1, it is physically challenging to apply a uniaxial tensile load to a perfectly rectangular pristine graphene sheet to measure the elastic and fracture properties of graphene. In fact, to circumvent this limitation, nanoindentation of a circular graphene membrane using an AFM probe has been used as reviewed in Section 2.3.1. Nonetheless, simulating point loading of a circular graphene membrane to replicate AFM nanoindentation is still of interest to confirm the applicability of the mathematical models used in the experimental scenarios, as well as to understand in depth the behaviour of graphene under such loading conditions on an atomic scale.

In fact, Zandiatashbar et al. [33] point out that the properties obtained by nanoindentation with an AFM tip are often spatially averaged values, hence atomistic defects and size dependent features are often overlooked. It was also pointed out by Fair et al. [183] that the model derived in [13, 117], i.e. Equation 2.1, assumes that: (i) the bending rigidity of the graphene membrane can be ignored, (ii) that graphene is isotropic in all three directions (disputed in [157, 166, 167]), and (iii) the induced stresses are isotropic, that is, they are independent from the radial distance from the membrane centre.

To circumvent the above assumptions and be able to analyse the behaviour of graphene at atomistic level, density functional theory (DFT) [145, 183] and MD simulations [147, 148, 183-187] have been performed. As previously mentioned, simulations also permit more control

on the system conditions, in this case the graphene membrane size, number of layers in the graphene membrane, tip size and morphology, indentation speeds and depths, temperature, etc. This enables a thorough understanding of the response of graphene under different circumstances. It is worthwhile noting that due to the computational costs and current processing abilities, typical MD system scales describe graphene sheets of only a few tens of nanometres, indentation depths of a few nanometres, and indentation speeds of tens of meters per second (i.e. significantly higher than possible in experimental setup).

In MD, point loading is often applied by simulating a small indenter to replicate the very tip of the AFM probe [147, 148, 162, 165, 184, 185, 187, 188]. The indenter is often modelled as a spherical [148, 165, 185], hemispherical [147, 162, 187], or pyramidal [184] diamond, with the Lennard-Jones potential [147, 148, 184, 185, 187, 188] to model the long-range van der Waals interaction forces between the indenter and the graphene. A square-based pyramidal indenter with platinum atoms in an FCC crystal lattice was also used [184, 188], yet no dependence was found on the material of the indenter and the behaviour of the graphene membrane [184].

The graphene sheet is usually modelled as a free-standing circular sheet with the circular boundary atoms fixed in 3D space [147, 165, 188]. The boundary atoms have also been fixed in the sheet's out-of-plane direction but are able to move freely within its plane [185].

To obtain a force-distance curve similar to that in Section 2.3.1 Figure 2.12, the indentation depth can be obtained from the position of the bottom-most atoms in the indenter, while the force applied is often calculated as the average force in the normal direction exerted in the tip by the graphene membrane [162, 165]. The FD curve is then fit to a polynomial of the form shown in Equation 2.7 [148, 165, 184, 188]. The fitting parameters A and B are then used to extract the elastic properties of the simulated graphene membrane. For example, upon indenting rigidly clamped circular SLG and BLG membranes with radii ranging from 12 to 25 nm with a square-based pyramidal platinum indenter, Neek-Amal et al. [184, 188] used the analytical solution in Equation 2.8 [189] to obtain the elastic modulus E.

$$F = A\delta + B\delta^3 \qquad \textit{Equation 2.7}$$

$$B = \frac{\pi E t_G}{4a^2 G(\nu)} \qquad \textit{Equation 2.8}$$

where $G(\nu)$ is a function of the Poisson's ratio and varies from 0.65 to 0.9. The authors find that for deflections smaller than 1 nm, the linear term of Equation 2.1 is sufficient to model the force-distance curve, yet the cubic term would be required for deflections larger than 1 nm.

Tan et al. [147] also investigate the effect of tip (r) to sheet radius (a) in MD simulation. For sheet radius, a, ranging from 7.5 to 9 nm and a hemispherical tip of radii, r, 1.6 to 3 nm, the authors note that the resultant $\frac{r}{a}$ ratio requires a correction factor of $\left(\frac{r}{a}\right)^{\frac{1}{4}}$ to the cubic term for $\frac{r}{a} < 0.03$ [13, 117]. In their work, Tan et al. [147] further differentiate between a point load model and a sphere load model for different indentation depths. While for smaller indentation depths (< 2.5 nm), the point load model is appropriate since the graphene-indenter contact area is very small, for larger indentation depths whereby the graphene-indenter area is increased, the spherical model i.e. with the addition of the correction factor, becomes more suitable.

Wang et al. [148] indent a square graphene membrane and fit the force-distance curve to a polynomial – Equation 2.7. The authors assess whether the aspect ratio of the membrane affects the resultant modulus. In fact, a change in the aspect ratio of the graphene sheet did not result in a change in the elastic modulus and fracture stress. Since $\frac{r}{a_{equi}} < 0.1$ where $a_{equi} = \sqrt{\frac{Lb}{\pi}}$, the equivalent radius of the rectangular graphene sheet with dimensions L and b, a similar correction factor to that used in [147] is necessary. In agreement with experimental results, the simulations resulted in an elastic modulus of 1.05 TPa and maximum stress 205.13 GPa. Furthermore, for a given squarish membrane indented at an indentation velocity of 0.20 Å/ps using indenters with radii varying from 1, 2 and 3 nm, it was found that with an increase in indenter radius, the indentation depth, maximum load sustained, and the elastic modulus increase [148].

In earlier works, Wang et al. [185] simulated a simply supported 16 nm radius graphene membrane indented using a 0.27 nm radius spherical diamond indenter. Using the Tersoff-Brenner potential for the graphene membrane at 300 K, the authors report that upon indenting the membrane to a critical depth of 0.7 nm, radial wrinkles within the graphene membrane emerge as shown in Figure 2.17. Such wrinkling suggests that graphene under nanoindentation cannot in fact be modelled as a membrane with zero bending stiffness. Similar wrinkling, increasing with graphene membrane diameter, was observed using a quasi-continuum model which reduces the computational cost compared to MD simulations [190].

Overall, the effect of wrinkling within the graphene membrane on the measured elastic modulus by nanoindentation seems to reduce the elastic modulus of the graphene [86, 191].

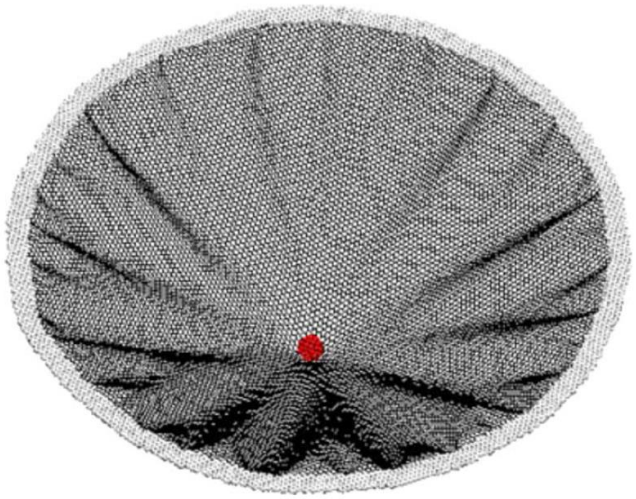

Figure 2.17: Wrinkling of a circular graphene membrane under point loading [185].

Nanoindentation of a rectangular graphene sheet similar to the geometry used in the experimental work by Frank et al [52], discussed in Section 2.3.1, was carried out by Fang et al. [187] with the Tersoff empirical potential energy function. Snap-to-contact and snap-out-of-contact phenomena were observed in their simulations whereby the graphene sheet was observed to make contact with the hemispherical diamond tip due to attractive forces when the tip was just above the graphene sheet. Several indentation depths ranging from 0 to 0.6 nm were simulated, with higher indentation depths leading to more graphene atoms being in contact with the indenter, and hence produce a larger snap-out-of-contact height upon unloading. Furthermore, the strong adhesion forces during unloading caused Stone-Wales and vacancy defects to nucleate in the graphene sheet.

Similar to what was discussed in Section 2.4.1.4, the indentation velocity – and thus the strain rate – may have an effect on the mechanical behaviour of graphene. It was found that no observable changes in the FD curves were noted up to indentation speeds of 20 m/s [148]. At loading speeds higher than 20 m/s, the maximum load sustained was noted to increase rapidly together with a significant reduction in the critical indentation depth [148]. Similarly, for indentation velocities ranging from 25 m/s up to 100 m/s, it was noted that higher indentation velocities result in higher sustained loads for the same indentation depths, thus higher elastic moduli, and lower snap-out-of-contact height [187]. However, in other works [162], no significant dependence of the FD curves on the indentation speeds varying from 25 m/s to 100 m/s was found.

Finally, in agreement with other MD simulations of graphene under uniaxial tensile loading [34, 171-177], MD nanoindentation simulations revealed that at higher temperatures, less energy would be required to indent the graphene membrane since high temperatures increases the kinetic energy of atoms which decrease the bond strength [187].

2.4.3 Simulations Investigating Defect Formation

Analogous to the experimental techniques which have been adopted to modify and introduce defects in the graphene structure (Section 2.1.4), MD simulations have also been used to study the phenomena involved. Most simulations revolve around bombarding graphene freely-suspended [63, 163, 164] or supported on a substrate [164] with energetic particles. These studies have studied the effect of the incident ions, their energy, fluence, incidence angle, and effect of the substrate [164]. In most cases, the electronic excitation caused by the impact of charged ions on the graphene is neglected due to graphene's excellent electrical and thermal conductance [163, 164].

The use of carbon, silicon, and gold ions for the creation of nanopores in graphene membranes was investigated by Li et al. [163]. It was found that an ion fluence of 4.24×10^{15} ions/cm^2 is required to create a nanopore with smooth edges. The heavier ions of gold and silicon were found to be more efficient than carbon ions to remove the C atoms from the graphene. Furthermore, it was observed that lower ion energies were more effective at creating the desired nanopores – for heavier ions, higher ion energies can be used. The authors report that the number of sputtered atoms increases linearly with number of ions irradiated with the overall sputtering yield, i.e. the average sputtered atoms per incident ion, experiencing a progressively faster growth. Eventually, the increase in sputtering becomes very slow and nearly saturates. All these three stages were observed for any of the incident ions simulated, yet occur at different rates.

With regards to the incidence angle, in general, the number of sputtered atoms increases slightly as the incidence angle is increased from 0 to 75° [163]. This result is attributed to the fact that at larger incidence angles, the effective thickness of graphene is larger which enables more kinetic energy to be transferred to the graphene.

Argon ions were also used to create nanopores [164]. It was noted that while a nanopore was formed in both suspended and supported graphene at the optimal parameters, the pore in the supported graphene has worse quality with irregular structure and larger size. In supported graphene, vacancies were also created in the vicinity of the nanopore. Furthermore, apart from

sputtering the graphene atoms, the Ar ions also lead to sputtering of the substrate atoms which backscatter towards the graphene. The sputtered substrate atoms induce secondary sputtering of graphene and vacancies in the rest of the graphene sheet. Due to this secondary sputtering, the authors note that the dose required to manufacture the nanopore is lower for supported then in suspended graphene.

MD simulations of argon ion irradiation on 5-layer graphene revealed the formation of cross-linking between the graphene sheets, strengthening the interaction between the different layers [164]. An increase in the number of graphene layers required higher ion energies for optimal nanopore creation [164].

Simulations using helium ion irradiation created the formation of mono-, di-, and larger vacancies clusters, Stone-Wales defects, and interlayer cross-linking in 5-layer graphene [63]. Similar to what was observed in [164], as the He ion hits the first graphene layer, it scatters several C atoms creating different types of defects, with the C atoms becoming trapped. The collision leads to a wave pulse in the graphene layers and a cascade of damages. This wave is eventually damped and relaxed via thermal fluctuation forming interlayer links, which might explain the strengthening effect as opposed to other defects. It is expected that the interlinking can be used to an advantage. Interlinking may prevent sliding between layers and hence increase bending rigidity. The links may enable load distribution between the layers, serving to blunt or halt crack propagation, and thus increase toughness. Interlayer linking may also pin the thermal ripples of the layers, effectively increasing the elastic modulus.

2.4.4 SUMMARY

Molecular dynamics simulations have been used in several studies to analyse the behaviour of graphene under mechanical loading and hence measure the elastic and fracture properties of graphene [24, 26, 29, 30, 166, 168, 192, 193]. The results obtained have been directly compared to the results from experimental studies with good agreement. However, it is worthwhile noting that the length scales of MD and experiments are sometimes prohibitive to allow such direct comparison.

As reviewed in this section, although the mechanical properties of graphene have received significant attention by the research community, few have investigated the fracture behaviour and mechanical properties of graphene under various conditions while validating simpler, computationally cheaper potentials such as the Morse bond potential.

As reviewed in Section 2.4.2, MD simulations have also been used to replicate nanoindentation of circular graphene membranes [147, 148, 162, 184, 185, 187, 188] to validate the use of the mathematical model often used in experiments (Equation 2.1). As with uniaxial tensile loading, agreement with the experimental results was common.

Finally, in Section 2.4.3, literature investigating the formation of defects and creation of nanopores with the use of energetic ion bombardment via MD was briefly outlined.

Section 2.5 will delve further into the invaluable role of MD simulations for understanding the effect of closely controlled defects in the graphene membrane on its behaviour.

2.5 NANOPOROUS GRAPHENE

The shortage of clean water resources calls for the development of efficient technologies for effective waste water reclamation, sea water desalinization and water decontamination. More effective, low-cost technologies to desalinate, decontaminate and disinfect water for point-of-use (POU) purposes are needed, especially in rural regions [194].

Current state-of-the-art technologies typically involve the use of semi-permeable polymeric membranes in reverse osmosis systems. This technology is based on the diffusion of water molecules through the membrane which is somewhat slow and requires high pressures and hence energy input [195]. Polymeric membranes also tend to suffer from fouling. Nanomaterials are being investigated for their potential use in desalination and decontamination applications, with the aims of miniaturizing advanced devices while rendering them more efficient and economic. Research efforts are being directed at developing systems which increase water throughput via the use of porous nanostructured membranes that sieve water molecules from the larger salt ions and contaminants. Suggested nanomaterials include carbon nanotubes [191] and zeolites [196], however, the expected increase in efficiency is counteracted by the increase in manufacturing costs of such membranes [197].

Nanoporous graphene has also been identified as a promising nanomaterial for desalination membranes. As already mentioned in previous sections, pristine graphene is impermeable to all substances, including helium [22], while exhibiting remarkably high elastic modulus and fracture stress of around 1 TPa [13] and 100 GPa [24], respectively. The introduction of nanopores in the graphene sheet by the removal of multiple atoms via UV-induced oxidative etching [66], electron [198] or ion [36] beam irradiation, or otherwise [33, 199, 200], renders

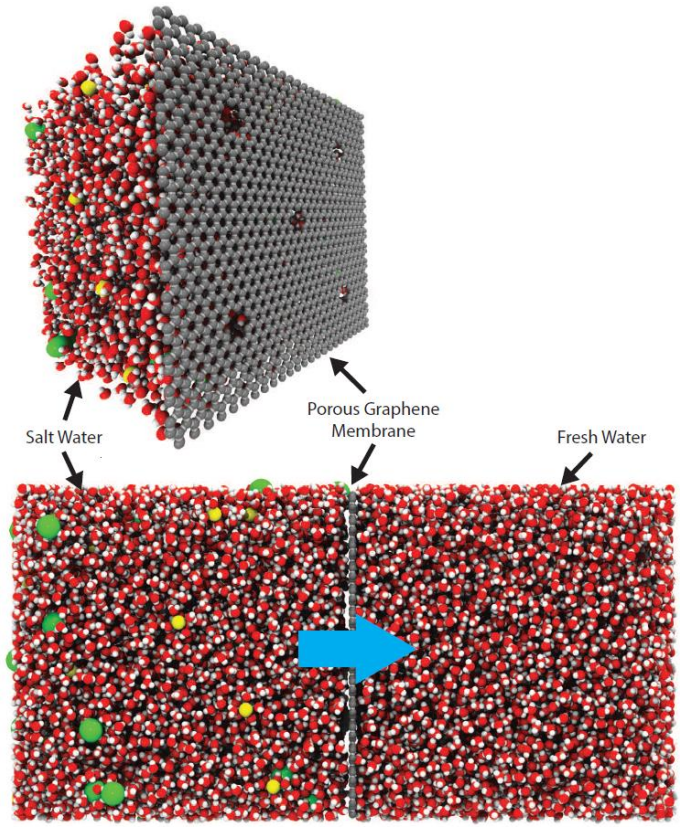

Figure 2.18: Use of nanoporous graphene as a molecular sieve that only allows water molecules from saline water to pass through under a pressure difference (Image courtesy: Matthew K. Borg).

the 2D membrane permeable, sometimes selectively. Hence, it is anticipated that porous graphene will be used as semi-permeable membranes in desalination and decontamination nanofilters, using the phenomenon of molecular sieving rather than diffusion, as illustrated in Figure 2.18. Moreover, due to its chemical structure, porous graphene can also be potentially used for gas storage applications [199, 201].

A brief overview of the permeability studies that have been done on nanoporous graphene membranes is given in the following section.

2.5.1 Permeability of Graphene Membranes

Bulge-test experimental techniques using mechanically exfoliated monolayer graphene sheets were first adopted by Bunch et al. [22]. These tests confirm the impermeability of pristine membranes to standard gases including helium. Furthermore, through *ab initio* calculations and molecular dynamics simulations, Leenaerts et al. [202] conclude that small defects such as Stone-Wales and monovacancy defects do not destroy the impermeability of graphene sheets. Permeability to helium atoms is obtained with the introduction of larger defects.

In contrast, CVD graphene grown on copper foil and transferred onto porous polymeric membranes may enable selective molecular transport via the intrinsic defects that originate during synthesis, as explained in [203]. Furthermore, the introduction of controlled, sub-nanometer pores in CVD graphene has been successfully achieved in [200]. The authors use oxidative etching to selectively etch previously nucleated reactive defects via ion bombardment. The resulting pores increase in size with treatment time and have a maximum diameter of 0.4 nm, presumably being ideal for nanofiltration applications due to the high transport selectivity shown for Allura Red dye and potassium chloride solutions.

The transport mechanisms of water molecules through porous graphene has been studied by Suk and Aluru [204]. The authors modelled monolayer graphene with nanopores of various diameters ranging from 7.5 to 27.5 Å. The water flow through the nanoporous graphene membrane was then analysed using MD simulations. The effects of pore size, pore functionalization and applied pressure on the desalination dynamics were also investigated in [48]. Molecular dynamics simulations enabled a systematic approach for the investigation to be taken, and preliminary conclusions have been draw regarding the optimal conditions for desalination. Namely, it was shown that hydrogenated pores, i.e. pores having edges functionalized with hydrogen atoms, reduce the water flow due to the pore hydrophobicity, yet hydroxyl (-OH) functionalization improves the salt rejection. Konatham et al. [205] confirm the superior salt rejection and hence effectiveness for desalination when using -OH functionalized pores, when compared to those pristine or functionalized with COO^- and NH_3^+. In both cases of pristine and -OH functionalized pores, the optimum effective pore diameter was found to be 7.5 Å [205]. The MD simulations were performed with the carbon atoms in graphene being modelled as stationary Lennard-Jones spheres.

In [36], quasi-defect free CVD graphene was transferred on porous SiN_x to create supported membranes and subsequently subjected to gallium or helium focused ion beams to drill nanopores of diameters between 7.6 nm and 1 μm. The obtained porous graphene membranes having approximately 10^3 to 10^6 pores per 4 μm membrane diameter are reported to withstand pressures of up to 2 bar. In their work, Celebi et al. [36] found that although water permeation through such membranes is superior to conventional ultrafiltration membranes when both sides of the membrane are wet, the porous graphene membrane does not allow water permeation to occur even under a few bars of pressure if one side of the membrane is dry. Yet, water vapour and other gases still permeate in such cases. This suggests the potential use of porous graphene in efficient waterproof yet highly breathable membrane materials.

Studies on the use of graphene-based materials as electrodes in capacitive deionization have also been carried out in [206]. The use of a reduced graphite oxide resol-like material for the electrodes proved to enhance the performance of NaCl removal [206]. Both MD simulations and experiments on micrometre thick graphene oxide membranes were carried out in [207], showing how such membranes allow water together with small species of contaminants to permeate through, yet restrict flow to larger species.

Furthermore, to explore the applicability of porous graphene membranes for atmospheric filtering, other researchers investigated the possibility of selectively separating gaseous species. Jiang et al. [208] used first principles DFT calculations to study the permeability of graphene having passivated pores of approximately 3 Å in diameter to hydrogen and methane molecules. Similarly, Blankenburg et al. [209] and Schrier et al. [210] included several other gases – helium, oxygen, nitrogen, carbon monoxide, carbon dioxide, ammonia, neon and argon – in the modelled atmosphere and conclude that graphene is highly selective towards hydrogen and helium. Separation of ^{3}He and ^{4}He isotopes was predicted when using graphene membranes having nitrogen passivated nanopores [211].

Molecular dynamics simulations were also devised by Du et al. [212], concluding that regularly distributed pores of approximately 3.725 Å in diameter result in 100% separation of hydrogen from nitrogen. Sun et al. [23] confirmed the ability of porous graphene to separate hydrogen and helium from nitrogen and methane with a pore consisting of 10 vacancies using MD simulations. The authors [23] investigated how the flux changes with the pore size. A study on the mechanisms of molecular transport through the nanoporous membrane and how they are affected by the molecule mass, kinetic diameter and interaction strength with graphene, and functionalization of the pore was also presented [23].

Experiments using porous bilayer graphene were also carried out by Koenig et al. [66] to measure the transport dynamics of hydrogen, carbon dioxide, argon, nitrogen, methane and sulphur hexafluoride gases through such membranes.

Studies on the potential use of porous graphene in hydrogen and carbon dioxide gas storage applications have been carried out by Du et al. [201] and Dong et al. [199]. The latter used microwave-assisted reduction of graphene oxide to produce porous graphene capable of absorbing high percentages of hydrogen and carbon dioxide at specific temperature and pressure conditions.

Although, nanoporous graphene is clearly a very promising membrane-material for desalination or liquid or gas filtering applications, the implementation of such membranes requires more studies targeted towards the production of reliable nanoporous graphene membranes using a cost-effective method. Other than the permeability properties, it is also necessary to investigate the mechanical properties of porous graphene to ensure enough structural rigidity is exhibited for the required system operating conditions.

Section 2.5.2 and Section 2.5.3 discuss the effects of crystalline defects and nanopores on the mechanical properties of graphene, respectively.

2.5.2 Effect of Defects on the Mechanical Properties

As mentioned in Section 2.1, while pristine graphene is reasonably easy to prepare, certain synthesis routes tend to produce graphene with a lesser crystalline quality with different types of defects within the graphene crystal. The condition of graphite from which the graphene is mechanically exfoliated, the structural quality of the substrate onto which graphene is deposited, be it via CVD, epitaxial growth or another method, and the graphene growth and deposition parameters, highly determine the crystalline quality of the graphene produced.

In the case of mechanically exfoliated graphene, although in general the graphene samples have a high degree of order, defects present typically include vacancies or Stone-Wales defects (a reconfiguration of the C-C bond to form non-hexagonal polygons, as shown in Figure 2.19). On the other hand, CVD graphene tends to contain a significant number of grain boundaries that separate grains of different orientations [31]. Furthermore, graphene produced by the chemical reduction of graphene oxide tends to contain a significant amount of functional groups (groups of atoms attached to the graphene sheet that alter the chemical properties of the system), that might also be considered as imperfections in the crystalline structure.

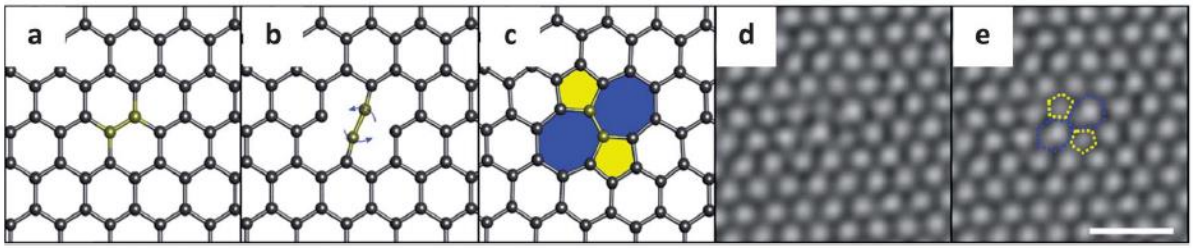

Figure 2.19: (a – c) Atomistic models illustrating the bond rotation in a Stone-Wales defect, and (d, e) TEM images of the Stone-Wales defect [32].

The presence of these defects often alter the electrical, chemical, and mechanical properties of the graphene. As such, several methods have been devised to introduce the desired defects in a controlled manner to tailor graphene's properties for a particular application; a few of such modification methods were reviewed in Section 2.1.4 and Section 2.4.3. These methods allow for the relationships between such defects and the properties in question to be studied systematically.

While the effects of the introduced defects on the Raman spectrum of graphene have been reviewed in Section 2.2.3, Section 2.3 has mostly dealt with pristine or as-deposited/as-grown graphene. In fact, Table 2.1 and Table 2.2 present the elastic moduli obtained via AFM nanoindentation of pristine or as-grown CVD graphene. The results obtained from molecular dynamics simulation reviewed in Section 2.4 are also applicable to pristine graphene. This section aims at reviewing the effects of different defects on the mechanical properties of graphene, in particular its elastic modulus and breaking strength. The presence of defects in the graphene sheet with respect to the mechanical properties can be investigated more clearly using computer simulations [167, 169, 213]. Such simulations allow for specific defects to be introduced at their exact desired density and distribution.

In earlier experimental works [33], it was reported that the elastic modulus of graphene is not affected by low oxygen plasma treatment times that produce sp^3 hybridization defects. However, it was noted that the modulus starts to decrease with increasing treatment times. This results from vacancy-type defects with a mean distance between defects of 5 nm. Such vacancy defects reduce the elastic modulus by ~ 70% at the maximum exposure time investigated. It is reported that the breaking load shows greater sensitivity to the oxygen plasma treatment regardless of the exposure time and hence defect type; the breaking strength was noted to reduce from ~ 35 N/m for the pristine membranes, to ~ 30 N/m for the longest treatment time. The authors note that similar to pristine graphene, defective graphene fractures directly beneath the AFM tip.

Similar behaviour was reported by Liu et al. [63] whereby the elastic modulus was found to be insensitive to the presence of defects caused by low doses of high energy helium ion irradiation ($<10^{13}$ He^{2+}/cm^2). With higher irradiation doses ($>10^{13}$ He^{2+}/cm^2), the modulus was reported to decrease. This behaviour was attributed to the fact that the high density of defects starts to weaken the average atomic bond in the graphene. At ~ 3×10^{14} He^{2+}/cm^2, the modulus significantly decreases by up to 20%, after which the elastic modulus shows an abnormal

increase, yet never exceeding that of pristine graphene. Such increase in the modulus was attributed to the fact that at such high doses, the contamination layer formed on top of the membrane upon irradiation becomes too thick to effectively clean with static mode AFM imaging. This layer in turn provides the extra rigidity. The authors also note that the reduction in the elastic modulus was mostly pronounced in SLG, and was less evident in BLG and MLG. This was attributed to the ability of MLG to passivate the defects inside the layers via interlayer linking. As such, the elastic modulus of MLG shows enhanced resistance to radiation damage.

However, Lopez-Polin et al. [61, 62] claim to increase the elastic modulus of SLG by introducing defects via low energy argon ion irradiation. With STM, the authors observed that such irradiation introduces mono or di- vacancies, and some vacancies saturated by small atoms, similar to the defects created via oxygen plasma at the high doses in [33]. However, as opposed to [33, 63], in this case the authors report that the elastic modulus increases with increasing irradiation reaching around 1.45 ± 0.07 TPa with 0.2% defect content, equivalent to a mean distance of 5 nm between defects. They only note a reduction in the modulus with higher defect contents beyond ~1.5%. However, in agreement with [33], the breaking strength was observed to rapidly decrease from 30 N/m to 18 N/m at a mean distance between defects of 10 to 15 nm. Notably, the authors [62] report that crack propagation is restricted in partially amorphous membranes, with the tearing length being strongly dependent on the density of atomic scale defects.

The introduction of Stone-Wales defects, single, double and larger vacancies, and grain boundaries was also studied using MD simulation work, most of the defects resulting in a general reduction in fracture stress [28, 29, 35, 161, 179, 214].

In simulations, vacancy defects were found to reduce the fracture strength by up to 12.2% due to a single vacancy defect [167], by 37.3% for a sheet with a 3-vacancy defect (3 missing atoms next to each other) [34], and by 50% for a defect density of 4.5% [170]. However, a single vacancy only resulted in a 0.8% reduction of the elastic modulus, with a higher density of single vacancies further reducing the modulus [28, 29, 35, 170, 213].

The location of the vacancies was noted not to affect the elastic modulus [213], yet having the vacancies closer to each other significantly reduced the fracture stress [29]. Larger vacancy defects that create nanopores also reduce the elastic modulus and fracture strength [30].

Stone-Wales defects were found to reduce the fracture strength less significantly than vacancy defects [167]. This is attributed to the fact that unlike in vacancy defects, the number of bonds

in SW defects is maintained. The fracture strength was noted to reduce by 10.81% with a SW defect – compared to 12.19% for a single vacancy.

BLG with sp^3 interlayer bonding was also modelled using the REBO potential at 1 K [169]. It was noted that the shear modulus is significantly enhanced with the presence of the sp^3 interlayer bonding [169]. While the elastic modulus of pristine BLG was found to be 0.872 TPa, the modulus was shown to linearly decrease with increasing sp^3 defect density, with a decrease of 11.4% with 5.8% sp^3 bonds. The tensile strength also reduces with increased sp^3 defects, reducing by 16.64% at 5.8% defects. A similar reduction in strain from 0.184 to 0.125 was reported [169].

The tilt angle of grain boundaries (GB) and their effect on the strength of polycrystalline graphene has been investigated by carefully structuring the atomic configuration through both molecular dynamics simulations and continuum mechanics [158, 215]. It was found that such boundaries can both increase and decrease the strength depending on the tilt angle, the pentagon-heptagon arrangements along the boundary, and the loading direction [158, 171]. However, experimental work on CVD-grown graphene claims that the mechanical strength of the polycrystalline graphene is not dependent on the tilt angle of the GBs however still report significant scatter in the results varying the fracture stress from ~ 50 GPa to ~ 90 GPa [84].

Furthermore, an increase in temperature reduces significantly the fracture strain and fracture strength of graphene with grain boundaries [171, 215], while an increased strain rate only increases slightly the fracture properties [215].

It is still debatable whether and how the presence of grain boundaries and defects affect crack propagation. For single or a few defects such as vacancies, nanopores, or reconstructions in an otherwise pristine graphene sheet, failure tends to start from the defect and propagate through the rest of the sheet [25, 29, 216]; the crack often passes through other nearby defects even if it is not the shortest path to the edge. Moreover, the presence of additional defects has the potential of confining crack propagation as experimentally studied in [62]. It was shown that for larger graphene sheets with a relatively high defect or grain boundary density and a rather large hole in the middle, the crack does not nucleate from the central large defect, but from the surrounding defects [159]. This phenomenon is known as flaw insensitivity and is contrary to pristine graphene with a single large vacancy, from where the crack is shown to initiate [30]. In polycrystalline graphene, some studies showed that cracks tend to initiate from the junctions between different grains [217-219], yet there is a disagreement on whether larger grains

decrease or increase the strength of the graphene. The elastic modulus was reported to decrease significantly with a decrease in grain mean size i.e. increase in GB density [160]

The fracture behaviour was also seen to transition from a brittle one to a ductile one at higher defect densities [35], yet is reported to be still brittle for nanocrystalline graphene [160]. In fact, following a significant decrease in the fracture strain with the introduction of defects, the fracture strain was observed to increase back to the pristine value at defect densities between 7 to 12% [35].

Sha et al. [162] simulate nanoindentation of polycrystalline graphene membranes with an average grain size of 28.2 nm. The authors [162] investigate the dependence on the fracture stress in relation to the grain boundaries within the membrane and find that significant scattering in the results can be attributed to the different position of the GB in relation to the indentation location. In the case of grain boundaries, membranes tend to fail from the nearest grain boundary even if the indentation location is in the middle of the grain.

2.5.3 Effect of Nanopores on the Mechanical Properties

Despite extensive work being carried out on the permeability and dynamics of different fluids across porous graphene sheets, the mechanical properties of these membranes have not yet been widely investigated. Although the effects of single and double vacancies have been studied in [26, 29, 30, 220], and reviewed in Section 2.5.2, the effects of larger pores and ordered arrays of such pores on the elastic modulus and fracture stresses of graphene sheets still need to be explored. Such information is crucial to the application of porous graphene membranes in real filters.

The critical pressure at which both pristine and porous graphene membranes fracture was investigated by Song et al. [221]. The blister test with single-layer graphene as the membrane was modelled using MD simulations, with the pressure being applied by a piston pushing down on argon atoms. The graphene membrane size and the pore size were systematically studied. For pristine membranes, it was observed that the critical pressure decreases with increasing sheet size, starting at 118.6 GPa and decreasing to 4.3 GPa for membrane diameters of 2.7 nm and 19.9 nm, respectively. As expected, the critical pressure further drops with the introduction of pores in the membrane – the shape of the hole also having an effect on the strength of the graphene sheet. Preliminary work looking into multiple pores shows that the presence of multiple pores does not have a much larger impact when compared to the presence of a single pore of the same size.

In a more extensive approach, Cohen-Tanugi and Grossman [222] investigated the mechanical properties of nanoporous graphene membranes under a water pressure via molecular dynamics simulations and continuum fracture mechanics. The authors conclude that the mechanical integrity of such membranes depends on the size of the substrate pores, with larger pores reducing the critical pressure under which the membrane fails. Relationships between the pore radius, pore separation and porosity, and fracture stress, elastic modulus and Poisson's ratio were established, interestingly claiming that some increase in graphene porosity might increase the critical maximum pressure.

Molecular dynamics simulations of graphene with 2 nm nanopores under tensile loading revealed that a single 2 nm nanopore drastically reduces the fracture stress and fracture strain by 36% and 45%, respectively [164]. Furthermore, the fracture properties are not much further affected with the addition of up to 5% single vacancy defects in the vicinity of the 2 nm nanopore. The mechanical properties significantly deteriorate with the addition of single vacancy defect densities higher than 5%.

Molecular dynamics simulations of graphene with periodic circular nanopores creating a ‘nanomesh’ under nanoindentation have been recently carried out [165]. With the pore centre-to-centre distance kept constant, the authors found that the elastic modulus decreases with an increase in pore size [165].

2.5.4 SUMMARY

The potential use of nanoporous graphene for filtration or desalination applications is evident from the literature outlined in this section. Section 2.5.1 presented some of the experimental studies and computer simulations conducted to investigate the filtering abilities of defective or nanoporous graphene. In order to render the graphene membrane permeable, some defects or nanopores need to be introduced. The effects of smaller crystalline defects and larger nanopores on the mechanical properties of graphene are discussed in Section 2.5.2 and Section 2.5.3, respectively. As will be further highlighted at the end of this chapter, in Section 2.6, more work needs to be done when it comes to investigating the mechanical limitations of nanoporous graphene membranes.

2.6 CONCLUSIONS

Expectedly, since its first successful isolation in 2004, scientific communities from diverse fields of research have embarked on exploring graphene and its potential use in a myriad of applications. As mentioned in Chapter 1, initial studies found that graphene exhibits a wide variety of exceptional material behaviours – from excellent electrical and thermal conductivities, and chemical and thermal robustness, to the possibility of tailoring the same material properties by modifying the graphene molecular structure. The allure of graphene is further fortified by its exceptionally stable atomic thickness and a complementary set of remarkable mechanical properties. This literature review has highlighted some of the emerging fields of research concerning graphene's mechanical properties.

As necessary to initiate any experimentation on graphene, the first section of this review presented some of the most commonly adopted synthesis methods to produce this nanomaterial. In this review, mechanical exfoliation of graphite and chemical vapour deposition to grow single-layer graphene were presented. As the first method used by Novoselov and Geim to produce graphene, mechanical exfoliation remains the synthesis method which is repeatedly used for laboratory-scale research. Irrespective of its simplicity, mechanical exfoliation is well able to produce high quality graphene – albeit with small yields. As expected from an almost entirely manual process, this technique is heavily dependent on the skill and experience of the researcher to exfoliate the graphitic flakes down to single layer, and subsequently find the few SLG amongst the more plentiful MLG and graphitic flakes. On the other hand, advances in chemical vapour deposition, some of which highlighted in this review, allow for the synthesis of large-scale single-layer graphene sheets. Ongoing studies are aiming towards mass-production of defect-free CVD-grown graphene with substantial control on the nature and density of the grain boundaries which often plague the grown graphene. Methods of transferring the CVD-grown graphene from the copper foil substrate to the desired substrate for subsequent experimentation have also been explored to some extent. To this end, further systematic experimentation is required to establish a reliable method such that the graphene's quality is preserved and no additional morphological or topographical defects are introduced.

While structural defects are often undesirable in most applications since they tend to detrimentally affect the otherwise exceptional properties of graphene, understanding their role may be crucial for a number of other applications. This review revealed some of the techniques which have been explored to actively introduce defects in the graphene, mostly involving

exposing the graphene to incident energetic particles. It is believed that this field of research is still in its infancy wherein several other techniques and types of energetic particles can potentially be used to introduce such defects, with each methodology offering different degrees of control and efficiency. It was shown that computer simulations are also enabling the understanding of the phenomena involved when an ion is incident on the graphene. These simulations have been found to complement well experimentation, especially in their ability to precisely control the nature and quantity of defects, and carefully assess their effect on the mechanical properties of graphene.

Subsequent to synthesis, characterization of the produced graphene is essential to verify the presence and quality of the graphene yield. In this literature review, a few of the most commonly used characterization techniques were outlined, namely optical microscopy, scanning electron microscopy, Raman spectroscopy, and atomic force microscopy. Particular emphasis was placed on Raman spectroscopy which has been shown to confirm the presence of graphene and its crystalline quality. In fact, developments in Raman spectroscopy have allowed the quantification of the density of defects in the graphene, and is therefore an indispensable technique when investigating the effects of defects on the mechanical properties of graphene.

A brief review on the use of atomic force microscopy to image the topography and morphology of the prepared graphene sheets preceded a detailed account on the use of AFM to measure the mechanical properties of graphene. This review aims at acknowledging the numerous studies which indent graphene membranes using the AFM probe to measure the elastic modulus, fracture strength, and fracture strain of graphene. While most experimental studies claim that the measured mechanical properties are in agreement with the established values, this review highlighted the different methods adopted by such research groups which led to differences in the results obtained. Furthermore, the rationale behind the choice of one experimental variant of the method in place of another is not often clear in the published literature reports. For instance, the rationale behind the choice of the AFM cantilever's spring constant used is not always evident, and to the best of our knowledge, the effect of the cantilever's spring constant on the results has not been investigated systematically yet. Similarly, no guidelines have been established regarding the depth to which graphene membranes should be indented to reliably measure the correct elastic modulus.

The overview of the AFM nanoindentation computer simulations given in this review further highlights the changes in the measured mechanical properties exhibited upon loading the graphene membrane under different conditions. This disputes the claim made by some experimental reports that their measurements are necessarily in agreement with other experimental work.

As mentioned in the above, the use of molecular dynamics simulations to model graphene and its mechanical behaviour under various conditions can be invaluable to support experimental work. However, the limited length-scales for computationally feasible simulations compared to the relatively larger systems in experimental work tends to limit the ability to directly compare the results across both domains. This limitation is particularly problematic since graphene, like most other nanomaterials, was shown to exhibit size-dependency.

2.7 RESEARCH QUESTIONS AND OBJECTIVES

As described in Chapter 1, the principal objective of this research work is to investigate the mechanical behaviour of graphene using both atomic force microscopy and molecular dynamics simulations. The following research questions will be addressed.

Research Question 1

> *To what extent can nanoindentation via atomic force microscopy be used to accurately and repeatably measure the elastic modulus, fracture stress, and fracture strain of freely-suspended graphene membranes?*

In the absence of standardized testing protocols, minor variations in the quality of the graphene samples produced, and the differences in the AFM set-up, probes and indentation methods may cause variations in the measured mechanical properties. As such, the first aim of this study is to understand the extent of such variations and thereby the applicability of the use of nanoindentation via atomic force microscopy to measure the elastic modulus of graphene.

Research Question 2

> *How does the introduction of defects in graphene affect its elastic modulus?*

The type, energy, and dose of energetic particles used to bombard graphene is expected to determine the type and density of defects created within the graphene. The second aim of this study is therefore to analyse the effect of such defects on the elastic modulus of graphene.

Research Question 3

> *Can molecular dynamic simulations adequately simulate the mechanical behaviour of graphene under nanoindentation?*

The selected potential functions and system conditions for the molecular dynamics simulations are expected to affect the results obtained. The third aim of this study is to test the ability of molecular dynamics simulations to reproduce the mechanical behaviour of graphene under nanoindentation, and thereby support the experimental results obtained.

2.7.1 OBJECTIVES

In order to address the abovementioned research questions, the following specific objectives need to be achieved.

1. To prepare freely-suspended graphene membranes and subsequently characterise the samples produced.

The first objective in this research work dealing with experimental testing of graphene requires the successful imaging and characterization of graphene samples using optical microscopy, scanning electron microscopy, atomic force microscopy, and Raman spectroscopy. The aim is to establish the best practices and parameters for such characterization methods to enable further studies to take place on the graphene samples.

Different graphene synthesis routes are to be explored and the simplest and effective used. The first method to be adopted to produce graphene is through mechanical exfoliation of HOPG graphite using the Scotch tape technique as it is reportedly the most economic route while producing monolayer graphene samples of high crystalline quality. The use of CVD-grown graphene will also be explored.

The measurement of the elastic modulus through force-displacement curves necessitates nanoindentation on suspended single-layer and multi-layer graphene membranes. Thus, following the successful production of graphene, a suitable robust technique for the deposition of the graphene samples on the desired substrates needs to be established. Graphene needs to be deposited on various porous substrates, some of which are not commercially available and need to be prepared in-house. The use of commercial silicon nitride microsieves can also be investigated, possibly resulting in a more economical, reliable and effective substrate as a

supporting structure for graphene membranes. This is a significant step forward towards the achievement of graphene-based filtration and desalination membranes.

2. To establish a method to calibrate the AFM, and post-process the acquired force-distance curves.
3. To compare the elastic modulus of different graphene samples using different AFM probes and AFM indentation parameters.
4. To experimentally introduce defects in graphene and subsequently analyse any changes in the elastic modulus.

The use of ion irradiation for the creation of controlled defects will be explored. The treated graphene samples are then characterised and nanoindented to correlate the measured mechanical rigidity to that found for as-deposited or pristine graphene.

5. To use molecular dynamics simulations to measure the elastic modulus of graphene.

Different potential functions and simulation platforms will be used to allow for comparison of the results. The adopted graphene models are to be validated under uniaxial tensile loading to confirm the mechanical behaviour of the graphene. The best model will be subsequently used to simulate nanoindentation and the results compared to those obtained experimentally.

Chapter 3 SAMPLE PREPARATION

3.1 INTRODUCTION

The main aim of this work is to investigate the mechanical properties of graphene. In order to proceed with the experimental work, particularly the indentation of graphene membranes, the first set of objectives included the preparation of the graphene samples that allow such indentation studies to be carried out. Concurrently, the characterisation methods that can be used to confirm the presence of graphene and determine the quality of the samples prepared were established.

In this work, graphene was initially synthesised via mechanical exfoliation from a highly ordered pyrolytic graphite (HOPG) crystal. Due to the limitations imposed by the mechanical exfoliation technique, the use of graphene grown via chemical vapour deposition (CVD-grown graphene) was also investigated.

For indentation studies of very thin materials using AFM, it is ideal to have a freely suspended layer of material in order to be able to accurately differentiate between the properties of the thin layer – in this case graphene – and those of the substrate. In order to be able to physically handle the material and allow for subsequent indentations, the graphene needs to be suspended over a hole to create a drum-like membrane, as schematically shown in Figure 3.1.

To allow for the preparation of the drum-like membrane structures, the suitability of three different substrates was investigated. Each substrate explored offered different hole sizes, hole distributions, surface flatness, and degrees of rigidity and robustness of the entire sample. A novel substrate with wells fabricated into its surface, denoted as 'Patterned PAA/Si Substrate'

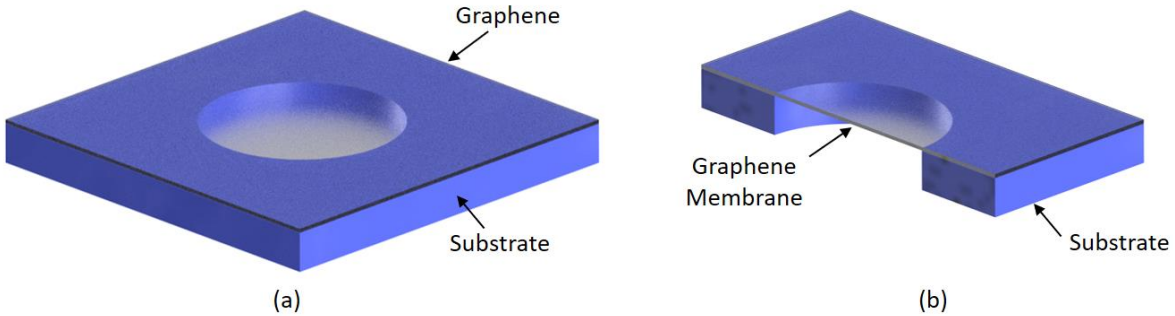

Figure 3.1: (a) Schematic representation of graphene on a perforated substrate to create a drum-like membrane. (b) Cross-sectional view of the graphene membrane.

was initially prepared. The suitability of commercially available TEM Quantifoil® grids and silicon nitride microsieves to act as the perforated substrates was also considered. Table 3.1 lists the materials sourced for the preparation of the graphene samples and/or substrates. The graphene-substrate combinations studied and discussed in this chapter are listed in Table 3.2.

Table 3.1: The materials used for the preparation of the graphene samples and/or substrates.

Graphene Source and/or Substrate	**As-received Materials**
Mechanically Exfoliated Graphene	Highly ordered pyrolytic graphite (HOPG) *(Agar Scientific Ltd., Essex, UK)*
	Polydimethylsiloxane (PDMS) Sylgard 184 Silicone Elastomer Kit *(Dow Corning, Michigan, USA)*
Patterned PAA/Si Substrate	Silicon wafer Si(100) *(ITME, Warsaw, Poland)*
	Poly(diallyldimethylammonium chloride) (PDDA)
	Carboxylate-modified polystyrene (PS) microbeads *(Polysciences Europe GmbH, Hirschberg an der Bergstraße, Germany)*
	Polycyclic acid (PAA)
CVD-Grown Graphene on SiO_2/Si Wafer	CVD-grown single-layer graphene on SiO_2/Si substrates *(Nano Carbon Sp. z o.o., Warsaw, Poland)*
CVD-Grown Graphene on TEM Quantifoil® Grid	Suspended Monolayer Graphene on Quantifoil® TEM grids *(Agar Scientific Ltd., Essex, UK)*
'Easy Transfer' CVD-Grown Graphene	Easy Transfer: Monolayer Graphene on Polymer Film *(Graphenea Semiconductor SLU, San Sebastián, Spain)*
Silicon Nitride Microsieve	High-Porosity Silicon Nitride Microsieves *(Aquamarijn Micro Filtration BV, Zutphen, The Netherlands)*

Table 3.2: The graphene-substrate combinations investigated.

Graphene Source	**Substrate**
Mechanically Exfoliated Graphene	Patterned PAA/Si Substrate
CVD-Grown Graphene	SiO_2/Si Wafer
	TEM Quantifoil® Grid
'Easy Transfer' CVD-Grown Graphene	Patterned PAA/Si Substrate
	Silicon Nitride Microsieve

For each graphene sample prepared, a number of characterisation techniques were used to confirm the deposition of graphene as well as to assess the morphological and crystalline quality of the graphene produced. For such purpose, optical and electron microscopy, Raman spectroscopy, and atomic force microscopy were used.

In this chapter, a brief overview of the technical specifications of the characterization techniques used and the accompanying methodology adopted is first given in Section 3.2. Section 3.3 presents the methodology implemented for the mechanical exfoliation of graphene together with the characterisation results of the prepared samples. Similarly, the use of CVD-grown graphene is explored in Section 3.4.

3.2 CHARACTERIZATION METHODOLOGY

Several characterization techniques were employed in order to assess and study the graphene samples after their preparation. Optical microscopy was first used for preliminary imaging and identification of possible areas of few or single-layer graphene. Atomic force microscopy (AFM) allowed for a more detailed analysis of the topography of the graphene membranes. The use of Raman spectroscopy verified the presence of graphene and its crystalline quality and thickness, and finally, scanning electron microscopy (SEM) was used for higher magnification imaging. AFM was also used for the study of the mechanical properties via force-distance curves. This will be discussed in detail in Chapter 4.

In this section, a brief outline of the methodology employed for the characterization techniques used throughout this work is presented.

3.2.1 OPTICAL MICROSCOPY

Preliminary characterization of the prepared substrates and samples was carried out by an optical microscope. The optical microscope used for the majority of the work was a Nikon Optiphot-100 employing a tungsten filament lamp as its light source and Nikon CF Plan ∞/0 BD D/C lenses, a Leica DFC295 (Leica Microsystems Ltd.) camera, and a NCB11 colour conversion filter.

3.2.2 ATOMIC FORCE MICROSCOPY (AFM)

Following optical microscopy, the graphene samples were imaged using static contact mode AFM at a chamber pressure of around 3×10^{-9} mbar. In order to locate a particular feature area,

the prepared sample, or a specific graphene flake with the AFM probe (as in Section 3.3.4.2), an imaging system integrated within the Integrated Characterization Facility (ICF) was used. The camera (DMK 41AU02 Monochrome Camera, The Imaging Source Europe GmbH, Germany) together with two lens extenders with each doubling the focal length (EX2C, Computar, US) integrated within the ICF was used to view the sample. A fine ink mark which could be located by the imaging system was placed in the vicinity of the feature to be imaged to aid the positioning of the AFM probe over the area of interest. The AFM probe was scanned to identify the area of interest, however, the maximum area that the AFM can scan at any one time is 6 × 6 μm in size, with each scan taking more than 10 minutes. This necessitated the imaging of various locations in and around the broad region located under low magnification via optical imaging until one or more reference features were identified and used to locate the AFM probe more accurately.

3.2.3 RAMAN SPECTROSCOPY

The graphene samples prepared were analysed via Raman spectroscopy. By analysing the spectra generated by Raman spectroscopy, a number of important characteristics could be determined, particularly the number of layers present in the graphene/multi-layer graphene sample [122, 123, 223], and the amount of defects or crystalline disorder present in the crystal lattice [57, 80, 123, 127]. Throughout this study, two Raman spectroscopes were used; a Witec Alpha300 at an excitation wavelength of 633 nm (1.9587 eV), using a 60x objective, and a 600 g/mm grating, and a Horiba Xplora Plus with an excitation wavelength of 532 nm, using a 50x or 100x objective, and a 1200 g/mm grating.

The following is an overview of the methods used to obtain the Raman spectra from the graphene samples and the required post-processing of the data to allow for numerical analysis. A comparison of the spectra obtained with the use of both excitation wavelengths is presented in Section 3.3.4.3.

For each graphene sample analysed, both single spectra and 2D spectral maps were gathered. For the single spectra, an integration time of 10 seconds was used for a total of 10 accumulations using the 633 nm excitation wavelength, and an integration time of 3 seconds for 3 accumulations using the 532 nm excitation wavelength. For the 2D spectral maps, the 633 nm excitation wavelength was used with an integration time of 5 seconds and an acquisition step size varying from 0.1 to 0.5 μm. For each map, sets of ten consecutive spectra obtained from circular areas of freely suspended graphene (i.e. graphene membranes), and

hence those featuring minimal substrate-generated background noise, were selected and averaged.

In order to eliminate background noise caused by fluorescence of the substrate, a 2nd order polynomial for supported graphene (i.e. where the graphene is in direct contact with the substrate), or a 3rd order polynomial for suspended graphene (graphene membrane), was fitted using the modified polyfit method outlined in [224] after manually removing sporadic spikes associated with cosmic rays from the raw spectra. An additional weighting function was added to the fitting procedure to improve the polynomial fit and better represent the less-active regions, namely < 1000 cm^{-1}, between 1600 cm^{-1} and 2500 cm^{-1}, and > 2750 cm^{-1}. A script was developed using Matlab (The MathWorks Inc., MA, USA) to process all the Raman spectra efficiently. The script used is available in Appendix A.

After background subtraction, the Peak Analyzer function in OriginPro 9.0.0 software was used to fit the peaks in the Raman spectra. The majority of the fits had a χ^2 value smaller than 3×10^{-3} and an adjusted R^2 value larger than 0.9. For clarity, the peak Position or frequency, Intensity, Full width at half maximum (FWHM), and integrated Area will be denoted by P, I, F, and A, respectively, while subscripts indicate the peak i.e. D, G or 2D.

3.2.4 Scanning Electron Microscopy

Field emission scanning electron microscopy (SEM) (Carl Zeiss Merlin Gemini, Jena, Germany) was used to study the topography and morphology of the substrates and the graphene samples. Accelerating voltages of 1.5 to 5 kV, probe currents of ~80 pA and a working distance of 3 to 7 mm were used throughout the study. Both an Everhart Thornley secondary electron detector (SE2) and an Inlens secondary electron detector (Inlens) were used. With the use of the conventional SE2 detector, information from the subsurface of the sample in the form of both secondary electrons as well as some backscattered electrons is often detected and imaged. On the other hand, the configuration of the Inlens detector allows that only the surface features are imaged. As such, the Inlens detector is capable of imaging surface features that are otherwise invisible to the SE2 detector [225].

3.3 Mechanically Exfoliated Graphene

The use of mechanically exfoliated graphene was initially investigated in view of the fact that such graphene tends to contain minimal to no defects within its structure. For in-house

mechanical exfoliation and subsequent deposition of graphene, a suitable substrate which would allow the graphene to form suspended membranes needed to be prepared. The procedure is explained in Section 3.3.1. The preparation for the transfer medium used for the exfoliation process is outlined in Section 3.3.2, while the actual exfoliation and deposition process is described in Section 3.3.3. The characterisation results and observations made on the suitability of mechanical exfoliation for the scope of this study are presented in Section 3.3.4 and Section 3.3.5, respectively.

3.3.1 Preparation of Patterned PAA/Si Substrate

Graphene is often deposited on a layer of SiO_2 which has been thermally grown on silicon to an approximate thickness of 300 nm. This is done to improve the optical visibility of the graphene flakes and hence facilitate their detection. In this work, Si wafers were also selected as the primary substrates due to their high degree of flatness and robustness. The fabrication of circular holes cut into the substrate were necessary such that the graphene membranes could then be suspended atop these 'wells'. In order to do this, a novel approach was developed. This method allowed for the preparation of a high density of well-dispersed, sharply-defined, circular holes in the substrate.

The procedure adopted to prepare a suitable substrate onto which mechanically exfoliated graphene or the CVD-grown graphene can be deposited forming drum-like graphene membranes is illustrated in Figure 3.2.

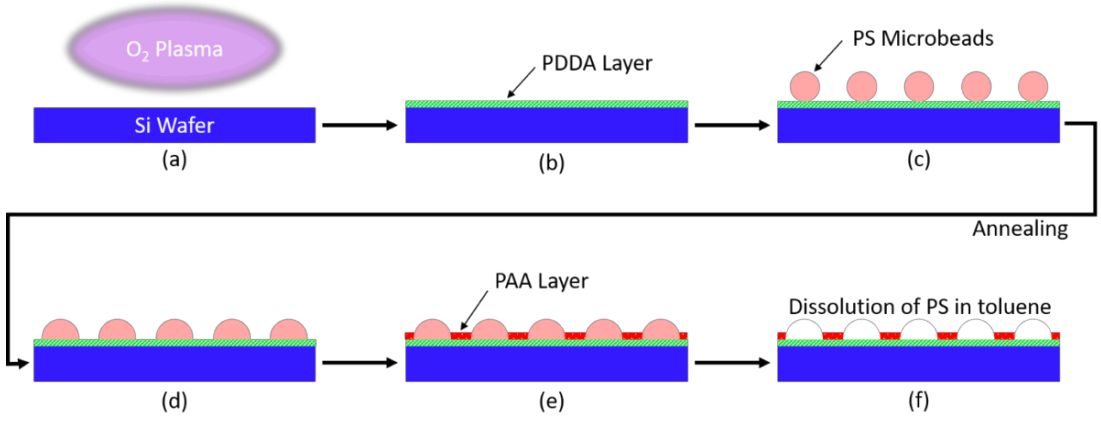

Figure 3.2: Schematic of the procedure for the fabrication of holey PAA/Si substrate. (a) Oxygen plasma cleaning of the Si wafer, (b) deposition of a PDDA layer, (c) deposition of the polystyrene (PS) microbeads, (d) annealing of microbeads, (e) deposition of the PAA layer, and (f) the dissolution of the annealed PS beads in toluene.

A silicon wafer (Si(100) supplied by ITME, Warsaw, Poland) was first washed with ethanol, then water and finally dried under a stream of nitrogen. To further clean and activate the surface, the Si wafer was put in an inductively coupled oxygen plasma operated at 140 W at a working pressure of 0.0133 mbar and an O_2 flow rate of 25 SCCM for 5 minutes (Figure 3.2 (a)). Following this, the surface-activated silicon wafer was incubated for 20 minutes in a Poly(diallyldimethylammonium chloride) (PDDA) 2% solution in purified water for the self-assembly deposition of the positively charged PDDA polyelectrolyte layer [226] (Figure 3.2 (b)), after which it was thoroughly rinsed with purified water and dried under nitrogen flow.

Carboxylate-modified polystyrene (PS) microbeads with a 1 μm diameter (Polysciences Europe GmbH, Hirschberg an der Bergstraße, Germany) were used to create a mask for the holes. The PDDA/Si wafer was incubated in a suspension of the PS microbeads diluted to a 1/100 solution of purified water for 25 minutes to allow the deposition of an even layer of randomly distributed and well-separated PS beads onto the PDDA/Si surface, as shown in Figure 3.2 (c). Following rinsing in purified water and drying under a nitrogen stream, the sample was annealed at a temperature of 100°C on a hot-plate for 2 minutes. This partially melted the PS beads into semi-spherical domes on the surface, as shown schematically in Figure 3.2 (d). The final layer of plasma-polymerized polycyclic acid (PAA) with a thickness of approximately 120 nm was deposited at a bias power of 400 W for 10 minutes onto the modified substrate and around the annealed beads [226] (Figure 3.2 (e)). Acrylic acid was used as the precursor gas at a pressure of 21.3 mbar. Finally, the PS microbeads were dissolved by ultrasonication in toluene for approximately 120 minutes.

Just before use, the PAA/Si substrate was diced into 1 cm × 1 cm sections, rinsed with isopropyl alcohol (IPA) and deionized water, and dried under a nitrogen stream.

3.3.1.1 Results

Figure 3.3 shows a series of micrographs representing the fabrication of the patterned PAA/Si substrate at various stages of the procedure. Figure 3.3 (a) shows the deposited PS beads over the PDDA-modified Si wafer. During preliminary experimentation, the pH of the PS suspension applied to the PDDA surface-modified silicon was varied, however, it was concluded that the optimal surface coverage of the surface with the PS beads with minimal agglomeration was obtained with a neutral pH of 7. The PDDA layer was also noted to improve the adhesion of the PAA layer to the silicon substrate.

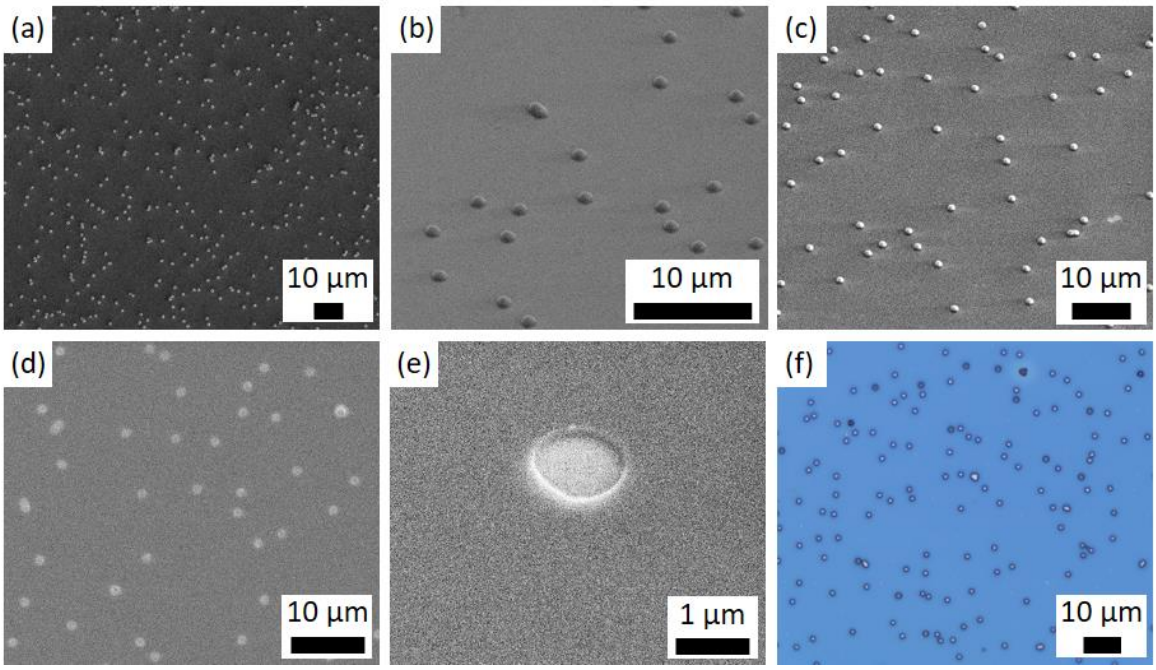

Figure 3.3: Micrographs showing the various stages of the PAA/Si substrate fabrication. (a) Deposition of PS beads on PDDA-modified silicon wafer. (b) PS beads after annealing at 100°C for 2 minutes. (c) The sample after PAA deposition and 5 minutes of ultrasonication in toluene. (d) The sample after 120 minutes of ultrasonication in toluene. (e) A typical circular hole. (f) Optical micrograph of the final PAA/Si substrate.

Figure 3.3 (b) shows a micrograph of the molten PS beads following annealing at 100°C for 2 minutes to create dome-like structures. These process parameters were determined following a series of experiments utilising various annealing temperatures and times. A duration of 2 minutes at 100°C was found to be optimal as the PS beads form dome-like structures without over-melting.

Figure 3.3 (c) displays the sample after the deposition of the PAA and following a 5-minute ultrasonication in toluene. This shows that after only 5 minutes of ultrasonication, not all the PS beads have been removed. It was determined that ultrasonication in toluene at room temperature for a total of 120 minutes was needed to fully lift off the PS microbeads without damaging the rest of the deposited PAA layer, as shown in Figure 3.3 (d).

Ultimately, the removal of the PS beads created well-dispersed, abundant, and well-defined, circular holes of approximately 1.2 µm in diameter, as shown in Figure 3.3 (e). This was confirmed via optical microscopy, which served to document the appearance of the patterned holes in the PAA/Si substrates, as shown in Figure 3.3 (f). The PAA/Si substrate was rinsed in deionized water before storing, and rinsed in IPA and deionized water just before use.

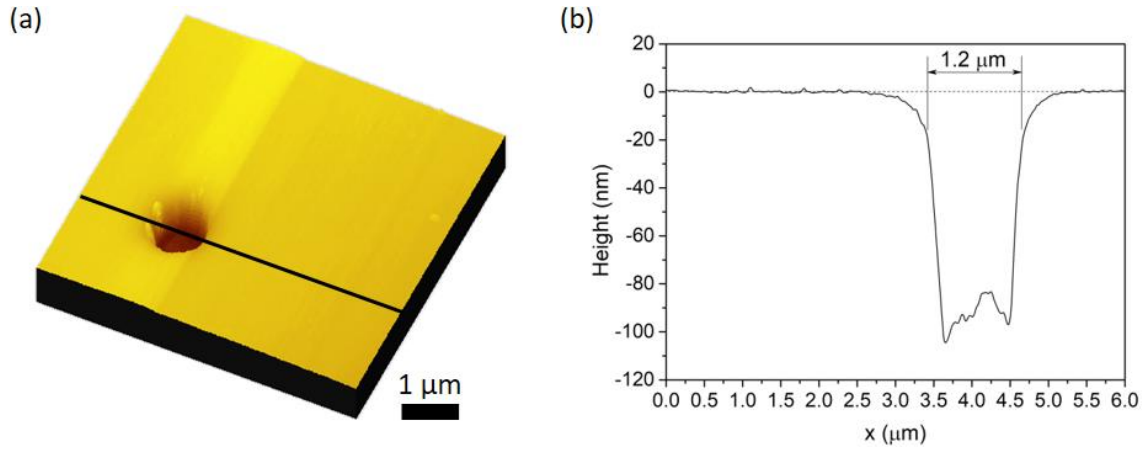

Figure 3.4: (a) A 3D AFM topography micrograph of a typical hole in the PAA/Si substrate. (b) A section view of the sample through the hole as depicted by the black line in (a).

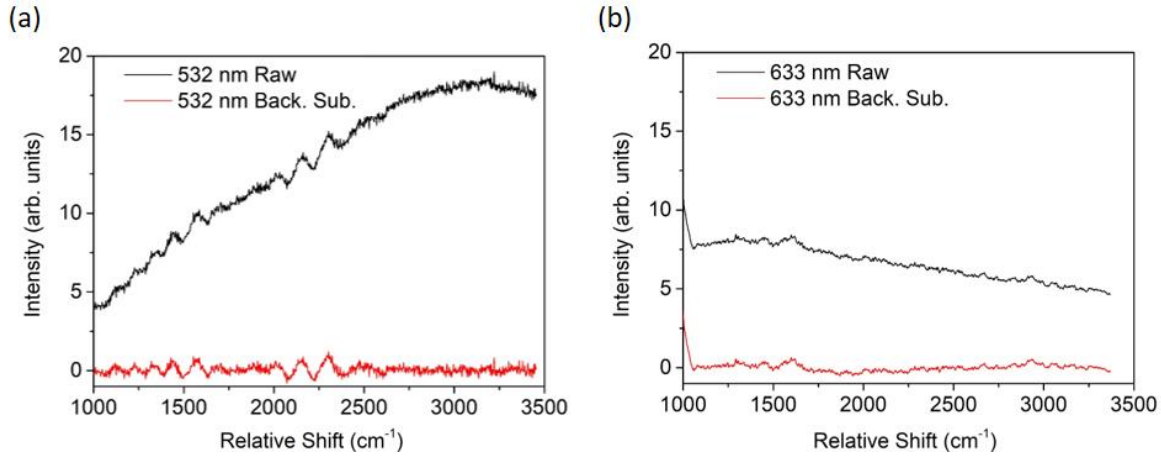

Figure 3.5: Typical Raman spectra obtained from the PAA/Si substrate using (a) 532 nm, and (b) 633 nm excitation wavelengths. The red curves denoted as 'Back. Sub.' refer to the background subtracted data.

Atomic force microscopy was used in static contact mode to map the topography of the resulting holes with higher accuracy and resolution. Figure 3.4 shows a height image displayed in 3D (Figure 3.4 (a)) obtained using an Arrow^{TM} Force Modulation Mode (FM50) AFM probe by NanoWorld AG. Figure 3.4 (b) shows a cross-sectional view of the representative hole having a diameter of around 1.2 µm and depth of around 100 nm. This hole geometry was deemed to be suitable for the purpose of this work.

Raman spectra of the resulting PAA/Si substrate obtained using both the 532 nm and 633 nm excitation wavelengths are shown in Figure 3.5. The PAA/Si material was observed to fluoresce more under the 532 nm wavelength. Nonetheless, an appropriate polynomial baseline was fitted and subsequently subtracted from both spectra, denoted by 'Back. Sub.' in Figure

3.5. These were then used during the analysis of the Raman spectra obtained from the graphene deposited on the PAA/Si substrate.

3.3.2 Preparation of the PDMS Stamp

For the exfoliation process, a polydimethylsiloxane (PDMS) stamp was fabricated. Sylgard 184 Silicone Elastomer Kit supplied by Dow Corning, Michigan, USA was used with a weight ratio of 10:1. The mixture was thoroughly mixed and poured into 2 cm × 2 cm styrene containers to a thickness of around 5 mm. The mixture was lightly tapped against a hard surface and left to stand for around 30 minutes to remove all the air bubbles trapped during mixing. The mixture was then cured at 60°C for 4 hours.

Before use, the stamps were cut in half to produce two 1 cm × 2 cm stamps and cleaned via ultrasonication in an acetone bath at a temperature of 60°C for 12 minutes. The stamps were rinsed in acetone and dried under nitrogen flow just before use. The stamps were re-used a number of times with cleaning in between uses until progressive degradation of surface adhesion necessitated replacement.

3.3.3 Mechanical Exfoliation and Deposition

The procedure adopted to mechanically exfoliate and deposit graphene membranes over the prepared PAA/Si substrate is illustrated in Figure 3.6 and explained hereunder.

A 10 mm × 10 mm × 2 mm HOPG with a mosaic angle of 3.5° ± 1.5° supplied by Agar Scientific Ltd., Essex, UK was used as the precursor of the graphene. The HOPG was freshly cleaved using Scotch® Magic™ tape (Figure 3.6 (a)), subsequently pressed onto and finally lifted off from the flat side of one of the PDMS stamps to deposit a smaller graphitic flake, as shown in Figure 3.6 (b). The second clean PDMS stamp was subsequently pressed onto and quickly separated from the graphite-loaded PDMS stamp for a number of times until a light grey film was observed on the surface of both stamps, as illustrated in Figure 3.6 (c). This process exfoliated the graphite flake into thinner graphene flakes.

Once a light grey film could be seen on the PDMS stamps, these were pressed gently onto the freshly-cleaned PAA/Si substrates and left overnight under a load of ~300 g (Figure 3.6 (d)). After 24 hours, the PDMS stamps were gently removed from the substrates to reveal that some of the graphene flakes have been deposited from the PDMS surface to the substrate, as shown in Figure 3.6 (e).

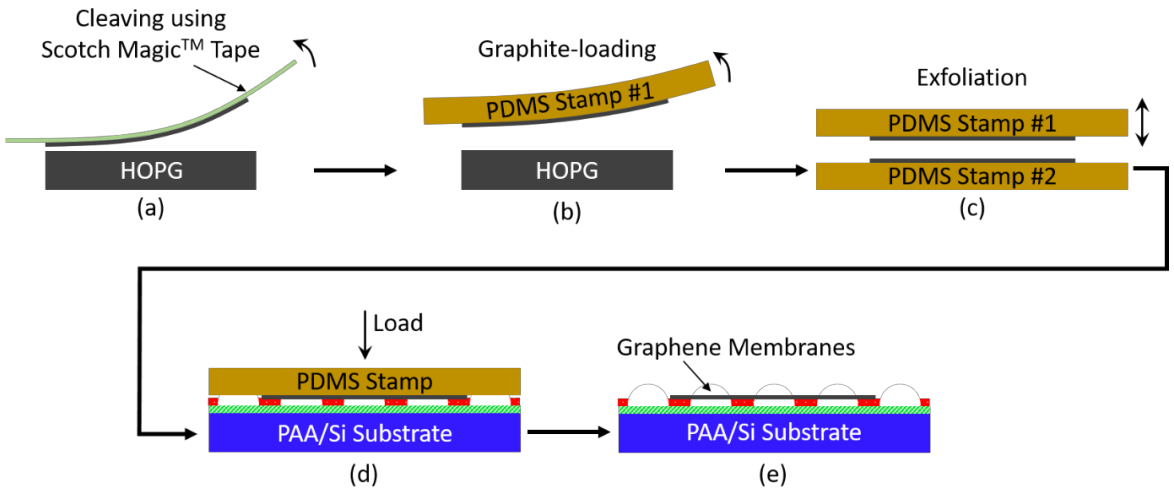

Figure 3.6: Schematic of the procedure for the mechanical exfoliation and deposition of graphene membranes on the PAA/Si substrates. (a) Cleaving of the HOPG, (b) deposition of a smaller graphite flake onto one of the PDMS stamps, (c) mechanical exfoliation of the graphite flake between two PDMS stamps, (d) loading of the graphene-loaded PDMS stamp onto the PAA/Si substrate, (e) final deposition of graphene membranes on the substrate after removal of the PDMS stamp.

3.3.4 Results

3.3.4.1 Optical Microscopy

Optical microscopy was first used in order to identify areas of high graphene yield. Since different graphene thicknesses exhibit different optical properties when supported on a substrate [6, 69, 119], the colour of each graphitic/graphene flake was also used to identify thinner flakes which could be subsequently characterized using AFM. This technique also allowed for the determination of whether a particular flake was too thick to be considered as multi-layer graphene. Optical microscopy was also used to identify and document the thinner graphene flakes which appear to cover the holes in the substrate – hence creating the desired circular graphene membranes.

Figure 3.7 shows typical optical micrographs of mechanically exfoliated graphene deposited on the patterned PAA/Si substrate. The images show no residue or other contaminants which can be attributed to the use of the PDMS stamp for exfoliation and subsequent deposition of the graphitic flakes on the substrate. This contrasts with the result of similar deposition methodologies when using an adhesive tape such as Scotch® Magic™ tape [62, 71, 131]. The micrograph shown in Figure 3.7 (a) exhibits the typical yield within a given area. While the procedure for the manual exfoliation process has been improved and optimized in previous preliminary work, one can still note the presence of numerous flakes with varying thicknesses

and lateral dimensions. The progression of the colour of the flake with respect to its thickness is evident in Figure 3.7 (b), which shows four different flakes with different colours and thus thicknesses. On such a blue substrate, the thinner graphene sheets, such as Flake A in Figure 3.7 (b), are nearly invisible with the flakes taking on a whitish hue with increasing thickness. Thicker flakes thus appear to be paler blue to white in colour, as in Flakes X, Y and Z, respectively. As the thickness of the graphitic flakes is further increased, the flakes start to appear increasingly opaque and their colour varying from yellow, brown and finally grey. This further thickness-to-colour progression can be seen in Flakes Y and Z whereby the flakes have folded on themselves (as indicated by the dashed arrows) to create thicker graphitic areas which appear yellow to brown. For the purpose of this study, the palest flakes were identified for further analysis, with the ratio of such promising thin flakes to the rest of the flakes being rather low.

With regards to lateral dimensions, while the largest flakes can be up to 50 to 60 μm across, such large flakes also tend to be thicker flakes, and as such unsuitable for further analysis. On the other hand, the thinner flakes had typical lateral dimensions of around 5 to 20 μm. This limited lateral size further reduced the probability of finding a thin flake which completely covers at least one hole from the substrate. Such an example is in fact Flake A (Figure 3.7 (b)) which was located just between the substrate holes, covering neither.

Figure 3.8 presents optical micrographs of two other relatively thin as-deposited graphene flakes which have been observed to cover multiple holes from the PAA/Si substrate, hereon termed ‘Flake B’ in (a) and ‘Flake C’ in (b).

For simplicity, the use of atomic force microscopy, Raman spectroscopy and scanning electron microscopy to analyse as-deposited mechanically exfoliated graphene will be discussed in relation to Flake A shown in Figure 3.7 (b), and Flake B and Flake C shown in Figure 3.8.

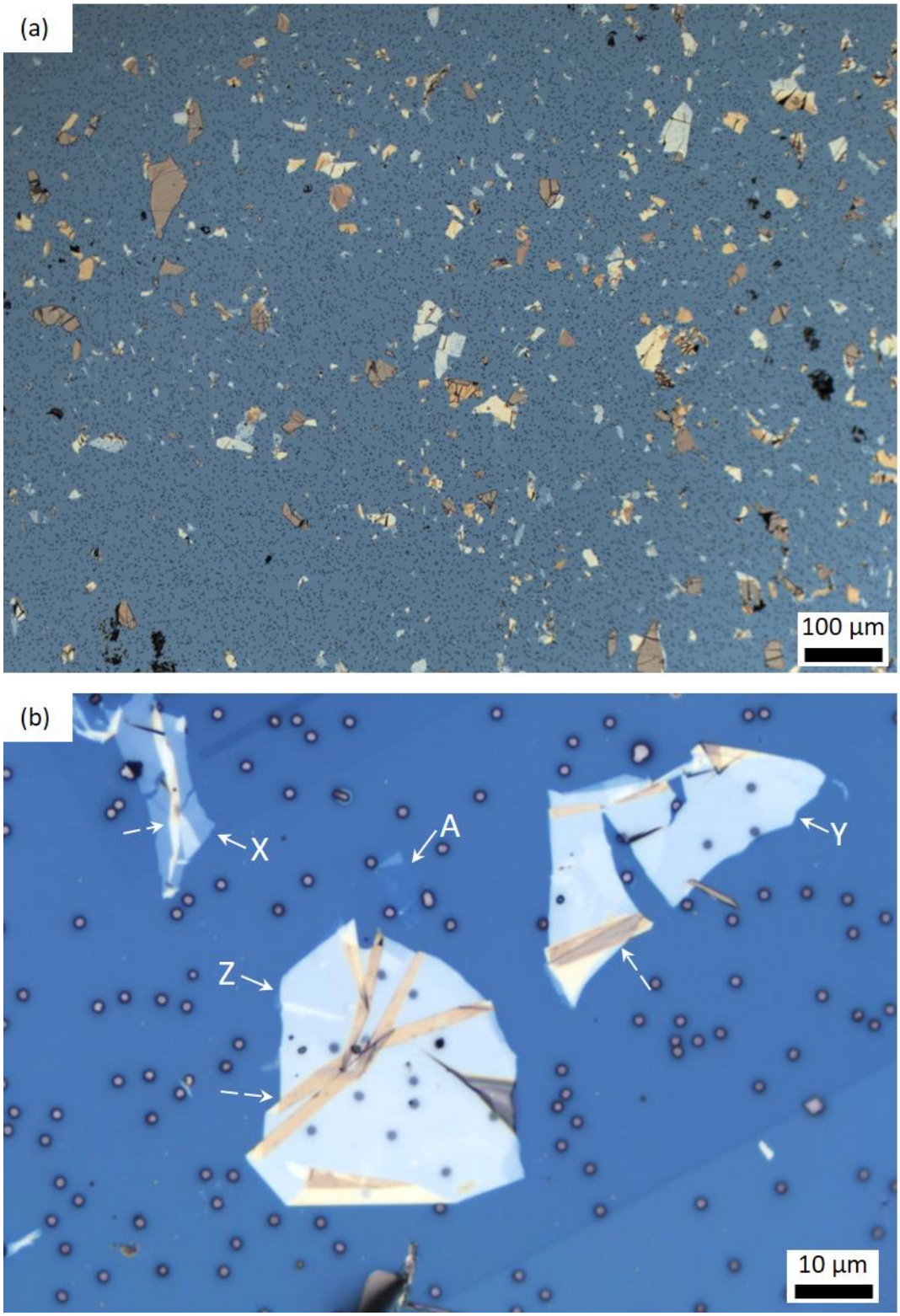

Figure 3.7: (a, b) Typical optical micrographs of mechanically exfoliated graphene flakes deposited on the patterned PAA/Si substrate. In (b), the solid arrows mark Flakes A, X, Y and Z, while the dashed arrows indicate folding of the flakes.

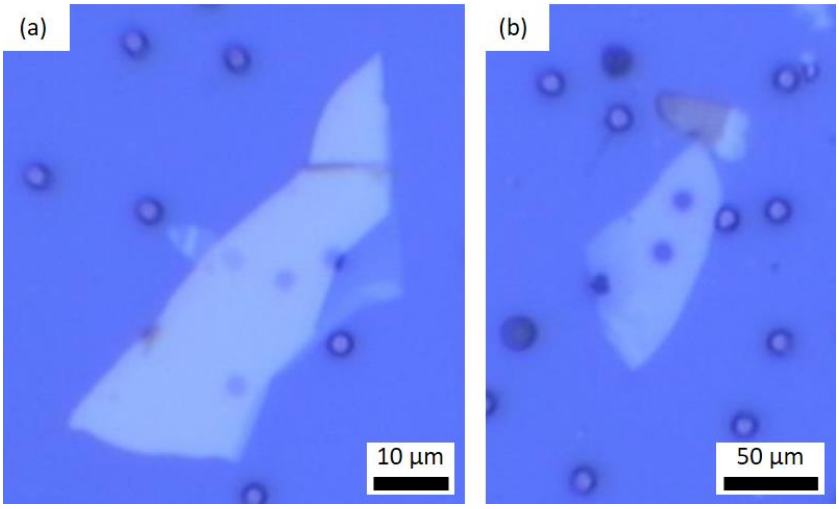

Figure 3.8: Optical micrographs of (a) Flake B and (b) Flake C.

3.3.4.2 Atomic Force Microscopy

Figure 3.9 (a) shows a height image obtained using static contact mode AFM of Flake A. As indicated by the 2D surface profiles (A and B) shown in Figure 3.9 (d), the flake is around 5 nm in thickness. Furthermore, the flake appears to be laterally cleaved in two, with one half of the flake overlapping the other. Although individual scans, such as those shown in Figure 3.9 (d), indicate that the portion of the flake just on top of the other appears to be thicker by around 1.5 nm, this discrepancy is not detected when considering the average height of each area (substrate, flake, and overlapping flakes) across multiple scans.

Figure 3.9 (b) shows the frictional force micrograph of the same flake. A slight difference in friction force is detected between the substrate and the flake. Furthermore, the average root mean square (RMS) of the height data of the substrate representing the roughness of the sample and calculated using Equation 3.1, was measured to be around 3 nm, while that of the flake was measured to be less than 1.5 nm, when using an FM50 probe.

$$RMS\ Roughness = \left[\frac{Z_1^2 + Z_2^2 + \cdots + Z_N^2}{N}\right]^{\frac{1}{2}} \qquad \textit{Equation 3.1}$$

where Z_N is the measured height from each data point N. The frictional force micrograph also highlights the edges and wrinkles of the flake. Finally, Figure 3.9 (c) shows the change in the normal force measured during scanning. The different textures of the substrate and the flake, the edges and wrinkles within the flakes, and other perturbations possibly caused by trapped debris are clearly highlighted with this image.

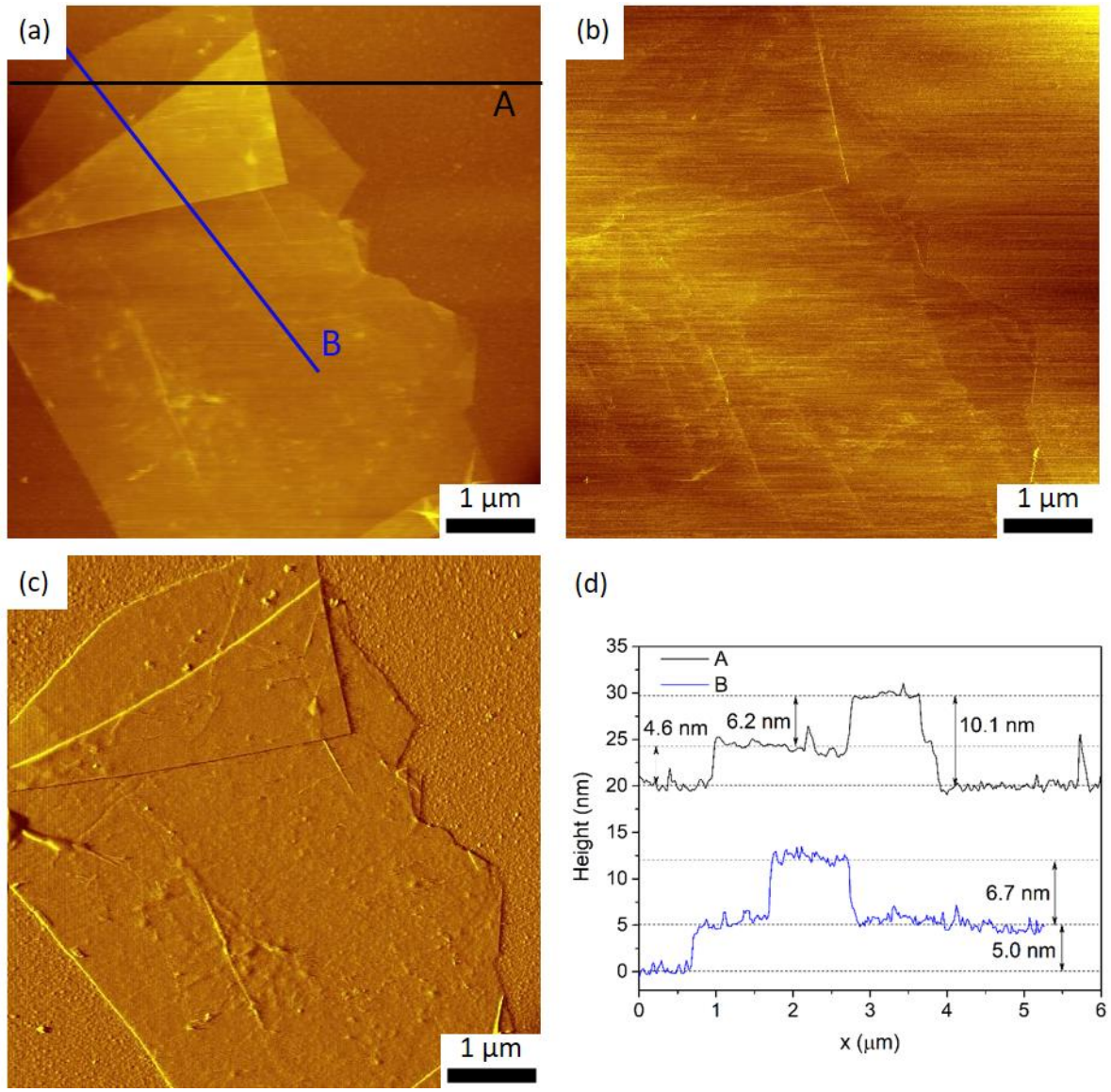

Figure 3.9: Static contact mode AFM (a) height, (b) frictional, and (c) normal force micrographs of Flake A. (d) Section views showing the 2D topographical profiles along line 'A' and line 'B' in (a). The direction of the section lines 'A' and 'B' shown in (a) is from left to right.

Figure 3.10 presents a set of AFM height images of Flake B together with its optical micrograph for reference. Especially from the AFM images (Figure 3.10 (b)), various features are identifiable, such as the fact that the flake itself is multi-layered with areas having more or less layers, the presence of wrinkling within the flake, and the presence of folded areas. Furthermore, Flake B appears to completely cover a total of four holes, each of which being covered with an area of different thicknesses. For simplicity, the main different areas and holes are labelled from B1 to B6, and BH1 to BH4, respectively, Figure 3.10 (c).

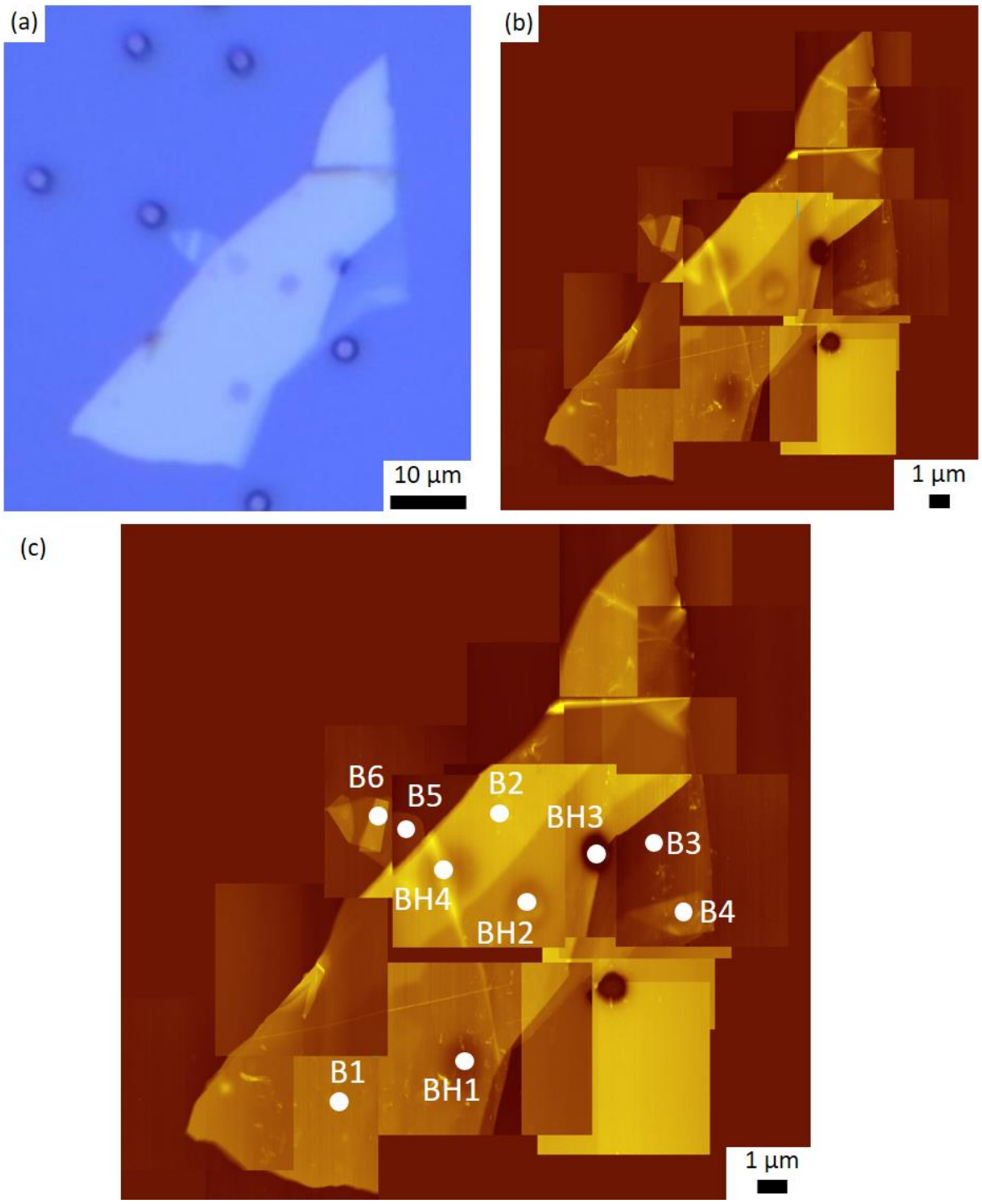

Figure 3.10: (a) Optical micrograph and (b, c) collated AFM height image of Flake B for visualisation. (c) shows the various areas with different thicknesses labelled B1 to B6, and the covered holes labelled BH1 to BH4.

Figure 3.11 to Figure 3.17 show various AFM height micrographs of different locations within Flake B, together with some cross-sectional views used to determine the thickness of the flake in the different locations labelled in Figure 3.10 (c). The approximate measured thicknesses at the different labelled locations are listed in Table 3.3. As evidenced by the presented cross-sections, it can be noted that the thicknesses of the same locations within the flake as measured

by different cross-sections taken from different topographical maps vary by up to 2.5 nm. This is especially true for areas located at the middle of the flake, such as areas BH2 and BH3, which make it difficult to directly measure the thickness of the flake with respect to the substrate datum due to the limited scan size. Conversely, the measured thicknesses are much more accurate when multiple cross-sections of the same areas are taken such that the thickness is always measured with respect to the substrate datum, such as in Figure 3.17.

Figure 3.11 particularly shows the membrane covering hole BH3, having a thickness of around 32 nm. It can be noted that the membrane appears to be dipped inside the hole to around 65 nm at its middle. This can be attributed to the flake conforming to the surface and exhibiting some slack across the hole. Furthermore, these images were obtained in static contact mode, and hence the normal force setpoint of the AFM probe during imaging may cause the probe to indent the membrane at each data acquisition point. Nonetheless, Figure 3.12 shows BH2, BH3, and part of BH4 imaged during the same scan, and hence with the same normal force setpoint, concluding that the membrane at BH3 is in fact much more slack than the other two.

Figure 3.14 and Figure 3.15 both show a particular wrinkle crossing area B1. From both cross-sections, such wrinkle is around 9 to 13 nm higher than the surrounding flake.

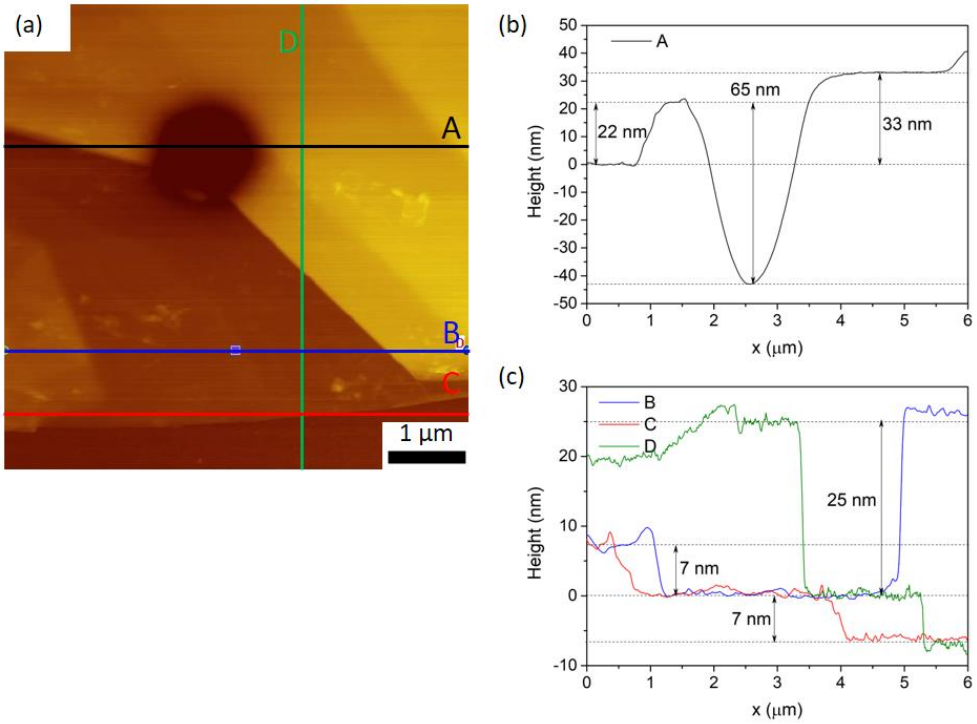

Figure 3.11: (a) Static contact mode AFM height micrograph of Flake B showing areas B3 and B4, and hole BH3. (b) and (c) Section views showing the topographical height along the black line (A), blue line (B), red line (C), and green line (D) in (a), taken from left to right, or up to down.

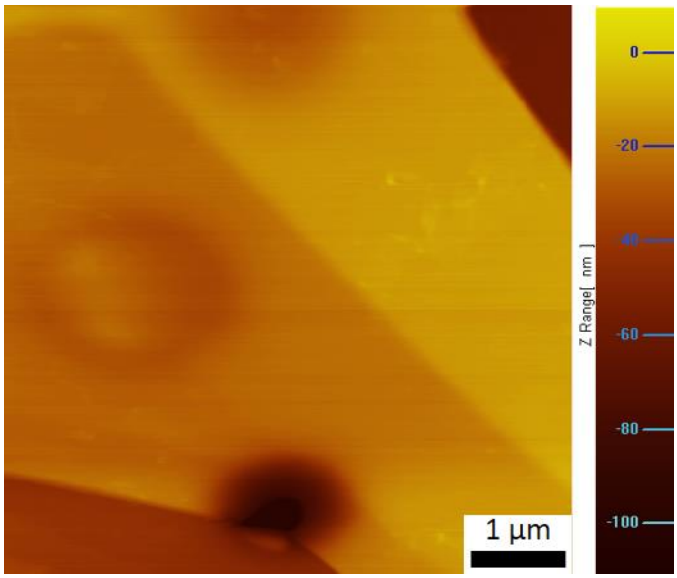

Figure 3.12: Static contact mode AFM height micrograph of Flake B showing areas B2 and B3, and holes BH2, BH3 and partial BH4.

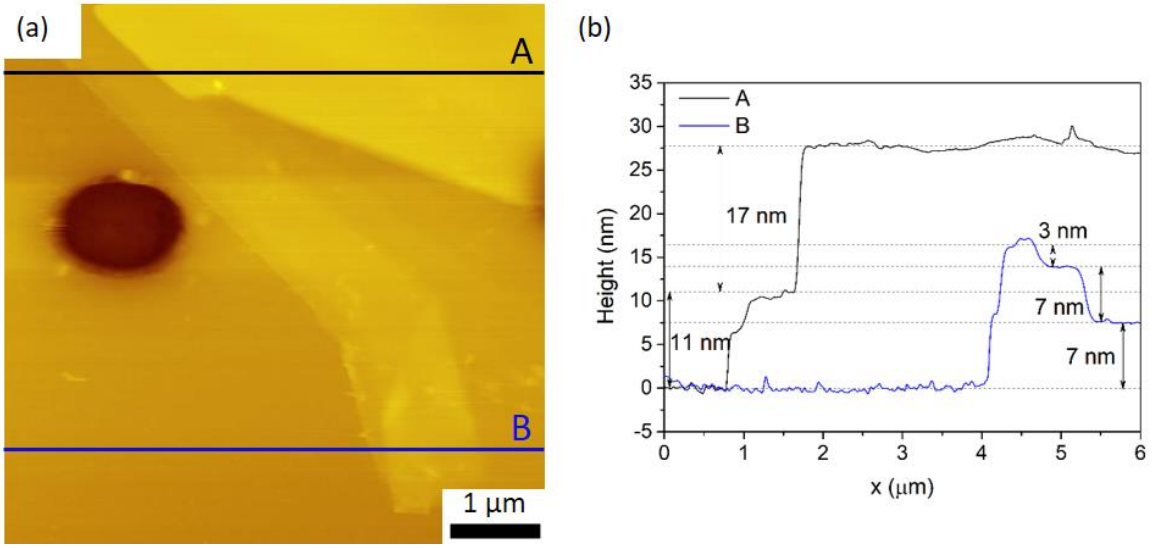

Figure 3.13: (a) Static contact mode AFM height micrograph of Flake B showing area close to hole BH2 (just to the right of the image). (b) Section views showing the topographical height along the black line (A), and blue line (B) in (a), taken from left to right.

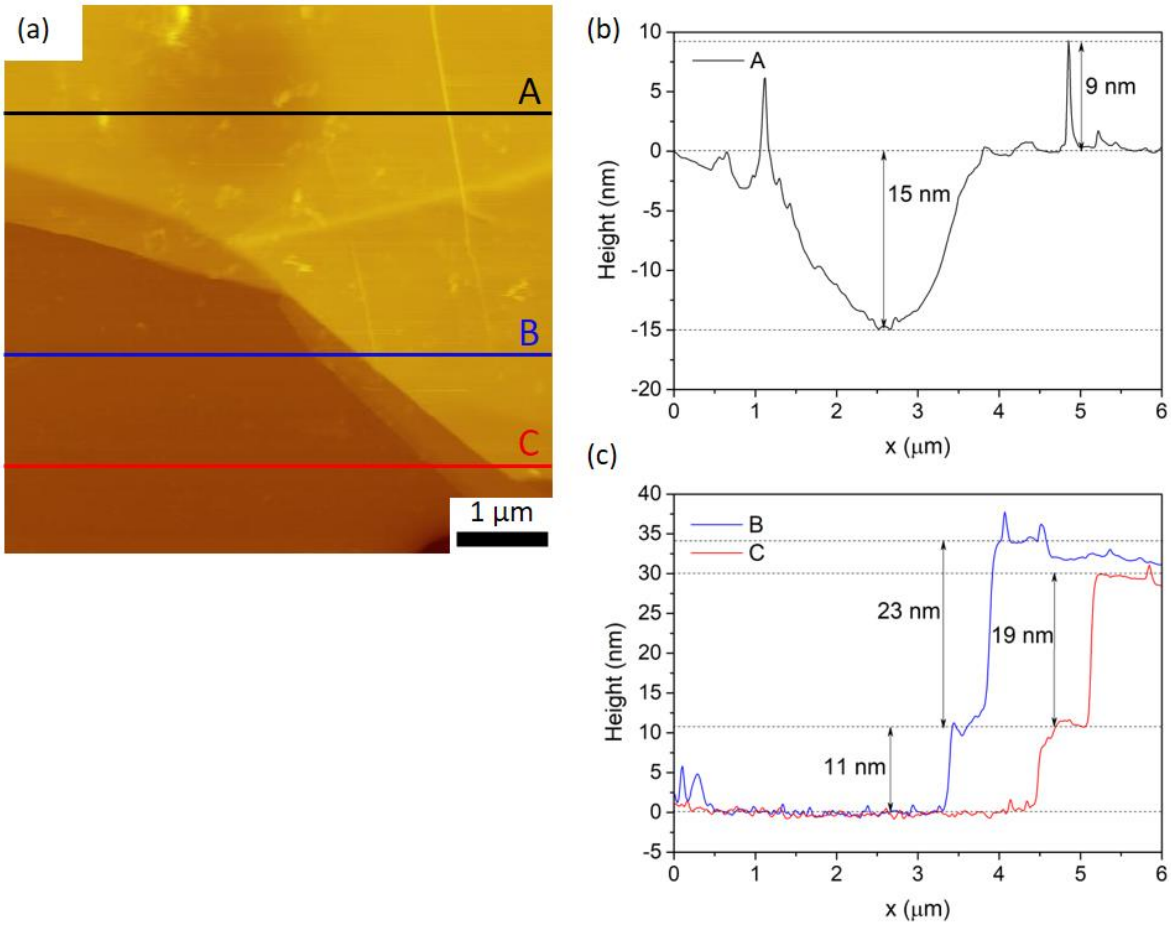

Figure 3.14: (a) Static contact mode AFM height micrograph of Flake B showing hole BH1. (b) and (c) Section views showing the topographical height along the black line (A), blue line (B), and red line (C) in (a), taken from left to right.

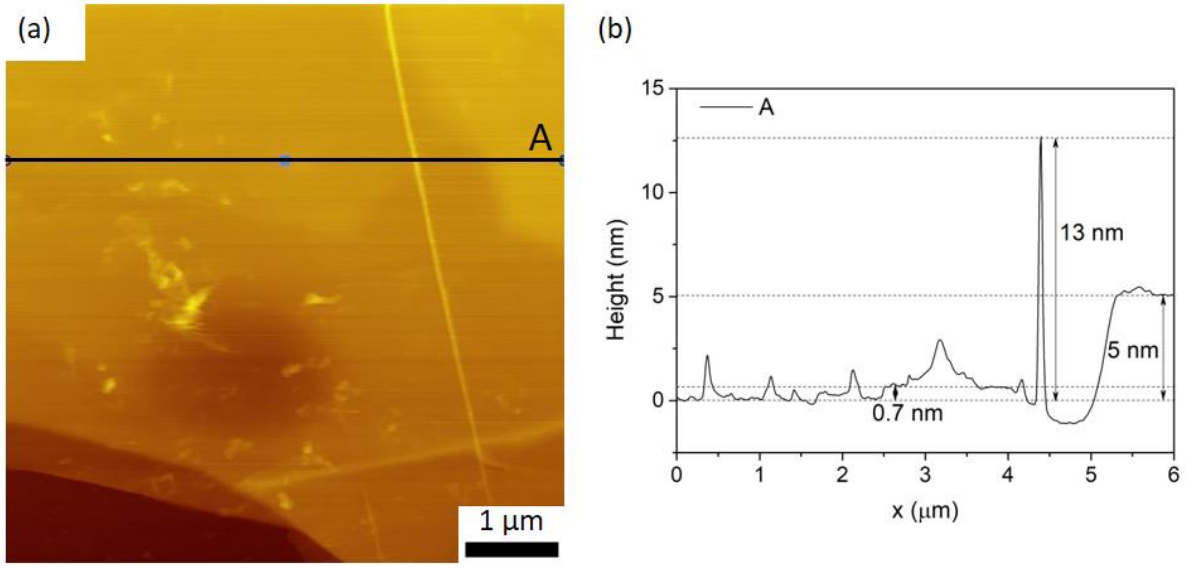

Figure 3.15: (a) Static contact mode AFM height micrograph of Flake B showing hole BH1. (b) Section view showing the topographical height along the black line (A) in (a), taken from left to right.

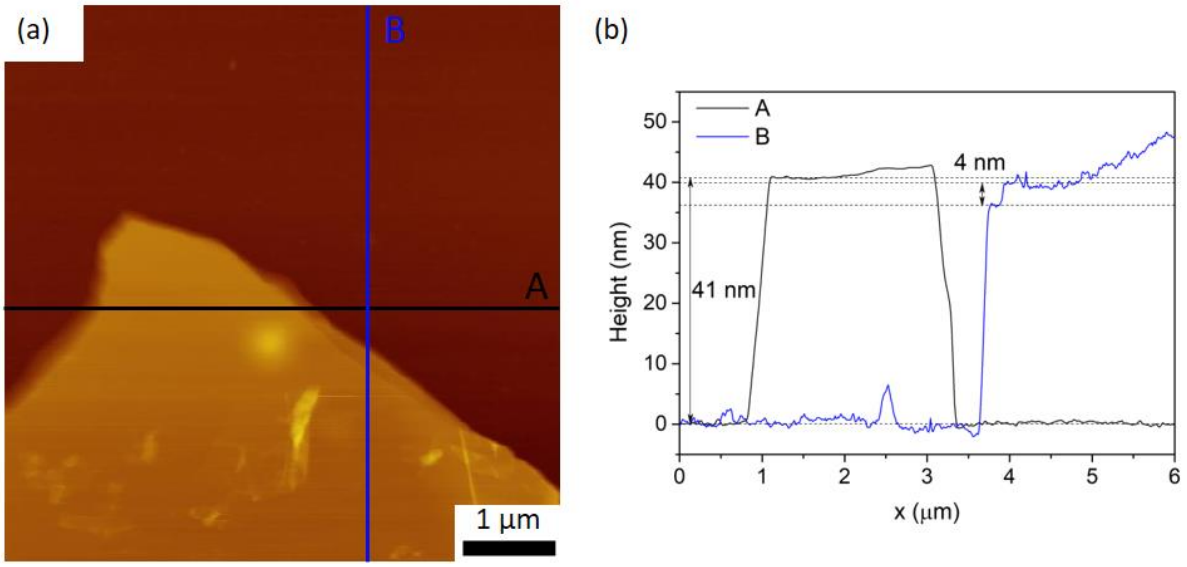

Figure 3.16: (a) Static contact mode AFM height micrograph of Flake B showing area B1. (b) Section views showing the topographical height along the black line (A), and blue line (B) in (a), taken from left to right, or up to down.

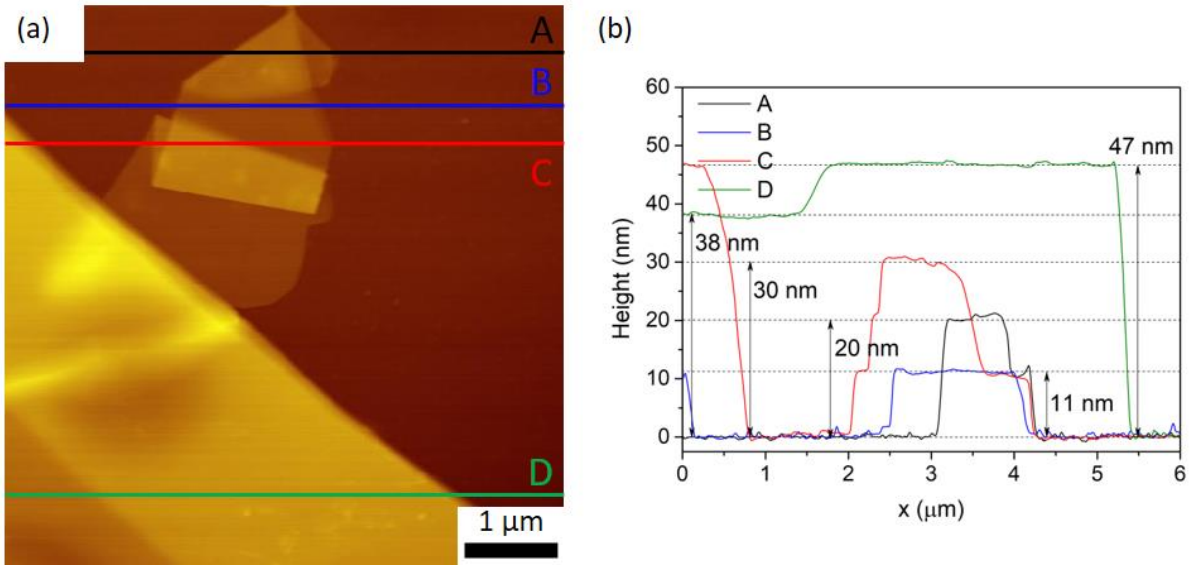

Figure 3.17: (a) Static contact mode AFM height micrograph of Flake B showing areas B2, B5 and B6, and hole BH4. (b) Section views showing the topographical height along the black line (A), blue line (B), red line (C), and green line (D) in (a), taken from left to right.

Table 3.3: The approximate thickness of locations B1 to B6, and membranes covering holes BH1 to BH4, as measured by static contact mode AFM. Note that the stated thicknesses may vary by ± 2.5 nm.

Location	Approximate thickness (nm)	Location	Approximate thickness (nm)
B1	32	BH1	32
B2	47	BH2	40
B3	7	BH3	32
B4	14	BH4	47
B5	11		
B6	30		

Flake C whose optical micrograph (Figure 3.8(b)) and static mode AFM micrographs are presented in Figure 3.18 and Figure 3.19 reveals similar characteristics to the previously studied flakes. The flake appears to be around 25 nm in thickness, with a thinner portion on the left side, as evident from the lighter colour in the optical micrograph (Figure 3.8 (b)). Flake C will be used in the experimentation and studies presented in Chapter 5.

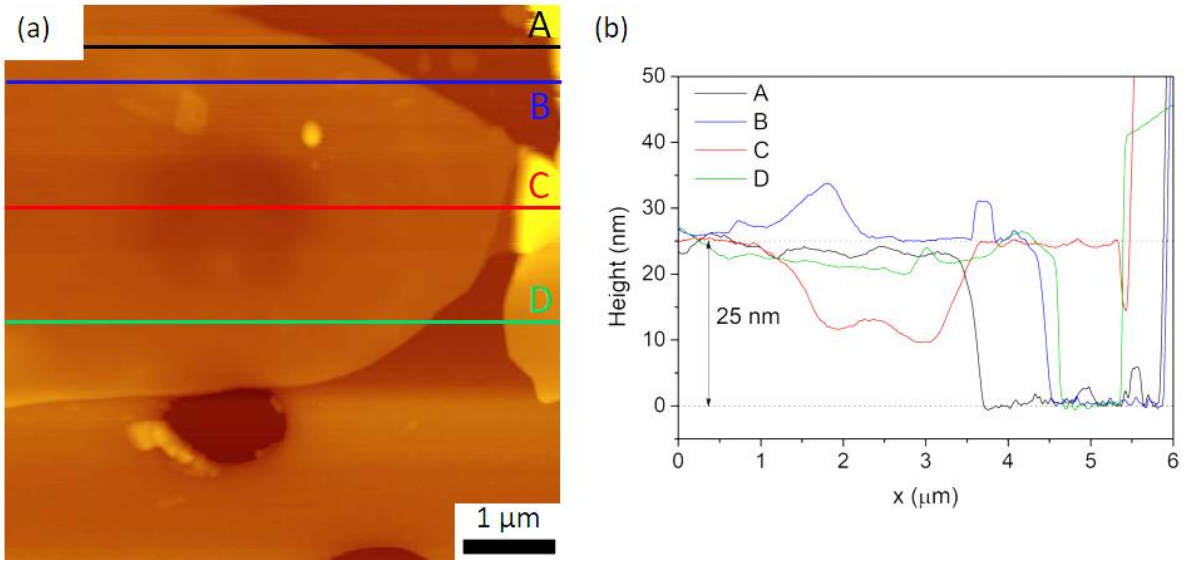

Figure 3.18: (a) Static contact mode AFM height micrograph of Flake C. (b) Section view showing the topographical height along the black line (A), blue line (B), red line (C), and green line (D) in (a), taken from left to right.

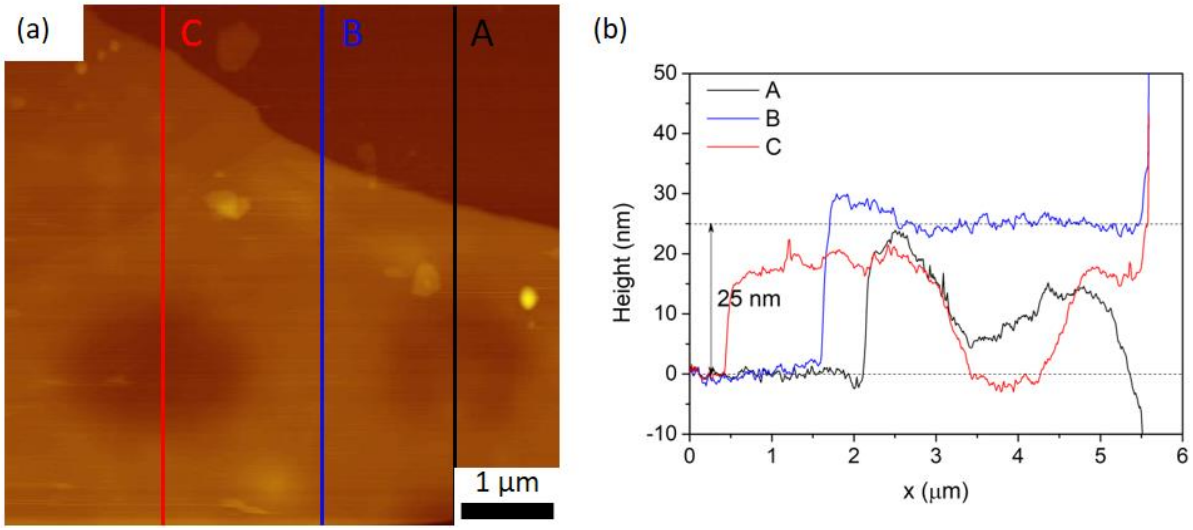

Figure 3.19: (a) Static contact mode AFM height micrograph of Flake C. (b) Section view showing the topographical height along the black line (A), blue line (B), and red line (C) in (a), taken from up to down.

3.3.4.3 Raman Spectroscopy

Figure 3.20 presents typical Raman spectra obtained from the mechanically exfoliated graphene flakes using both 532 nm and 633 nm excitation wavelengths. The raw spectra together with the baseline corrected spectra are presented to highlight the effect that the underlying PAA/Si substrate has on the results. In fact, it can be noted that the baseline is a reproduction of the raw spectra obtained from the clean PAA/Si substrate, while the characteristic peaks of graphene are simply superimposed on top of such baseline. As such, the

pronounced D peak in Figure 3.20 (a), which is in turn not present in Figure 3.20 (b) when using the 633 nm laser, may be the result of the band's coincidence with one of the peaks present in the PAA/Si spectrum at around 1350 cm^{-1} (Figure 3.5 (a)).

Once the baselines were subtracted from the respective spectra and the characteristic graphene D, G, and 2D peaks were fitted to Lorentzian peaks, several parameters such as their relative shift or position, P, their relative intensity, I, and their full width at half maximum (FWHM), F, could be analysed and compared. Such parameters obtained from the areas A1, A2, and A3 within Flake A as marked in Figure 3.21 are recorded in Table 3.4 and Table 3.5.

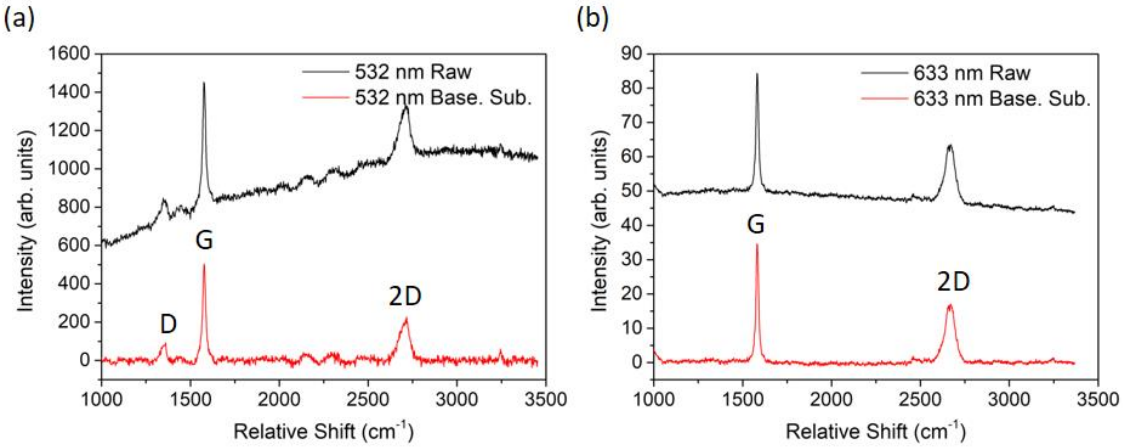

Figure 3.20: Typical Raman spectra obtained from mechanically exfoliated graphene flakes on PAA/Si substrate using (a) 532 nm, and (b) 633 nm excitation wavelength. In both cases, an appropriate baseline was fitted and subsequently subtracted from the raw data (Base. Sub. in legends).

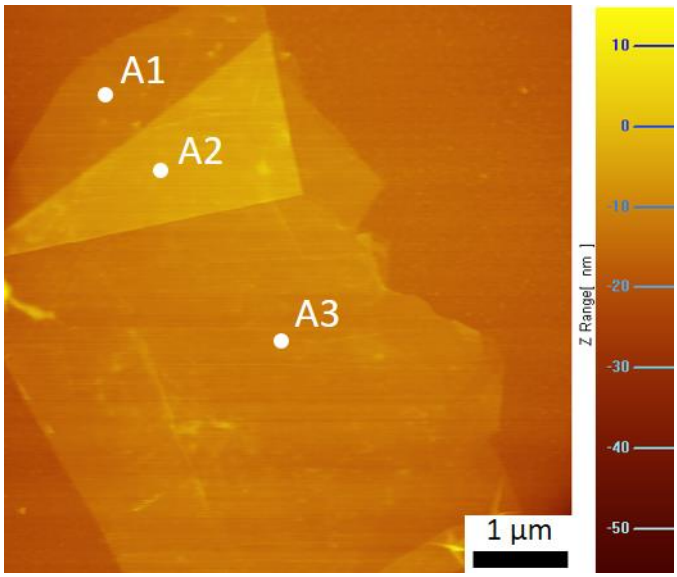

Figure 3.21: The locations labelled A1 to A3 from where the Raman spectra were obtained from Flake A.

Table 3.4: The relative shift (P) and the full width at half maximum (F) of the D, G, D+D'', 2D and 2D' peaks obtained from various locations in Flake A as shown in Figure 3.21.

Location		D Peak (cm^{-1})		G Peak (cm^{-1})		D+D'' Peak (cm^{-1})		2D Peak (cm^{-1})		2D' Peak (cm^{-1})	
		P	F	P	F	P	F	P	F	P	F
532 nm	A1	1349.7	28.0	1577.4	18.7	-	-	2705.3	57.2	-	-
	A3	1350.3	31.0	1577.3	17.5		-	2707.0	56.2	-	-
633 nm	A1	-	-	1581.4	16.6	-	-	2672.1	60.4	-	-
	A2	1326.6	125.5	1581.2	17.6	2464.5	38.7	2673.2	62.0	3240.3	70.9
	A3	1327.9	107.0	1581.9	17.4	2463.3	27.0	2663.3	57.9	3239.2	133.2

Table 3.5: The intensity (I) and width (F) ratios between the D and G peaks, and the 2D and G peaks obtained from various locations in Flake A as shown in Figure 3.21.

Location		I_D/I_G	F_D/F_G	I_{2D}/I_G	F_{2D}/F_G
532 nm	A1	0.2	1.5	0.4	3.1
	A3	0.2	1.8	0.4	3.2
633 nm	A1	-	-	0.4	3.6
	A2	0.0	7.2	0.4	3.5
	A3	0.0	6.1	0.6	3.3

The results presented here indicate that while there are no significant changes in the peak positions at the various locations, the use of different excitation wavelengths shifts the peak positions. For instance, while the D peak appears at around 1350 cm^{-1} using the 532 nm excitation wavelength, the same peak appears around 1327 cm^{-1} using the 633 nm excitation wavelength. A similar downshift is seen in the 2D peak, with its position being recorded at 2706 cm^{-1} using the 532 nm excitation wavelength and around 2670 cm^{-1} using the 633 nm. Conversely, the G peak is upshifted from 1577 cm^{-1} to 1581 cm^{-1}. Apart from the shape of the 2D peak, the ratio between the intensity of the 2D peak and that of the G peak, I_{2D}/I_G, is also used to give an indication on the number of layers that the graphene has [37, 56, 123, 125]. In fact, using both lasers, this ratio was calculated to be around 0.4, signifying that the flake is multi-layered, further evidenced by the 5 nm thickness measured by the AFM.

The most significant peak that changed upon using different excitation wavelengths was the D peak, particularly its intensity relative to the G peak (I_D/I_G) and its FWHM. In fact, the D peak is relatively small to insignificant, with the I_D/I_G calculated to be around 0.03 when using the 633 nm excitation wavelength, while the D peak is significantly more predominant with an I_D/I_G of around 0.16 using the 532 nm excitation wavelength. While the higher D peak with the 532 nm excitation wavelength can be partly attributed to the coinciding peaks and hence a superimposition of their intensity of the underlying PAA/Si substrate, as explained earlier, another factor might be at play. As such, it is worthwhile to note that:

- Using both excitation wavelengths, a 2D Raman map of the flake was obtained, and individual spectra, or an average of some of the spectra, were extracted from the 2D Raman spectra array.
- A 10 × 10 μm area was scanned using the 633 nm excitation wavelength at a pixel resolution of 0.2 μm, while a 5 × 5 μm area was scanned using the 532 nm laser at a pixel resolution of 0.1 μm.
- The power of the 633 nm excitation wavelength at the sample surface was set to around 19 W/m^2, while 1% of the full power of the 532 nm laser was used resulting to 0.5 mW at the sample surface with a spot size of 0.72 μm (1.23×10^9 W/m^2).

With these conditions, while the sample, especially the PAA/Si substrate, appears to be undamaged following Raman mapping using the 633 nm (as shown in Figure 3.7 (b)), damage was visible after mapping with the 532 nm, as shown in Figure 3.22. Thus, it can be concluded that the 532 nm excitation wavelength damaged the graphene flake.

Therefore, while the 532 nm excitation wavelength could be used at the reduced laser power and by employing point spectra rather than 2D mapping to avoid prolonged laser exposure, the 633 nm excitation wavelength at the reduced power was better suited for the majority of the work since this excitation wavelength did not significantly alter the graphene. Therefore, the 633 nm excitation wavelength was mostly used throughout this work.

Figure 3.23 shows the 2D Raman spectral intensity maps of Flake A obtained using the 633 nm excitation wavelength, with the brightness of each pixel corresponding to the intensity of the 2D, G, and D peaks in (a), (b), and (c), respectively. Such maps aid the identification of particular areas which emit a different Raman spectrum. In fact, while the intensity of the G peak in Figure 3.23 (b) is more or less even throughout the flake, the 2D peak seems to be slightly more intense or broad in some areas towards the middle of the flake. These areas

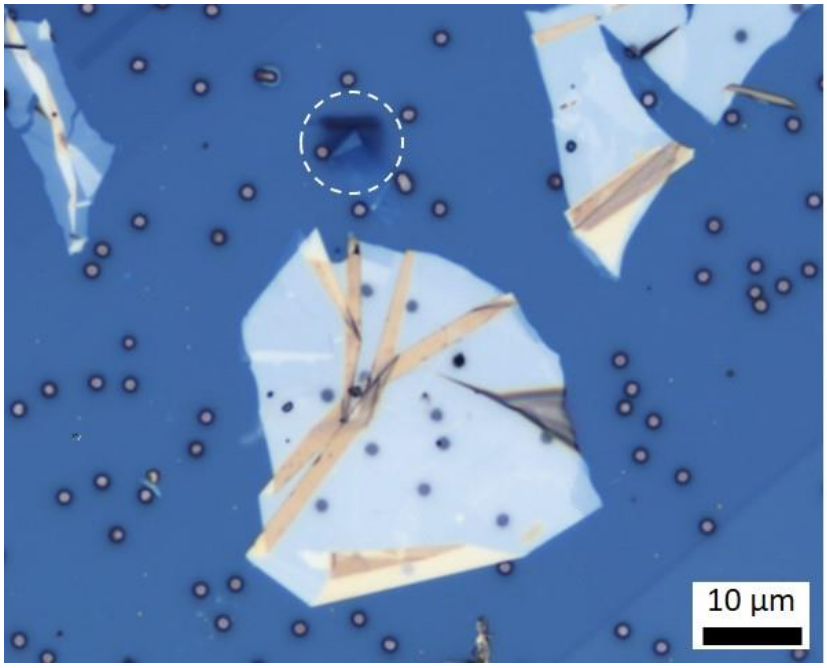

Figure 3.22: Flake A after 2D Raman mapping using the 532 nm laser, clearly showing a damaged area as circled in white.

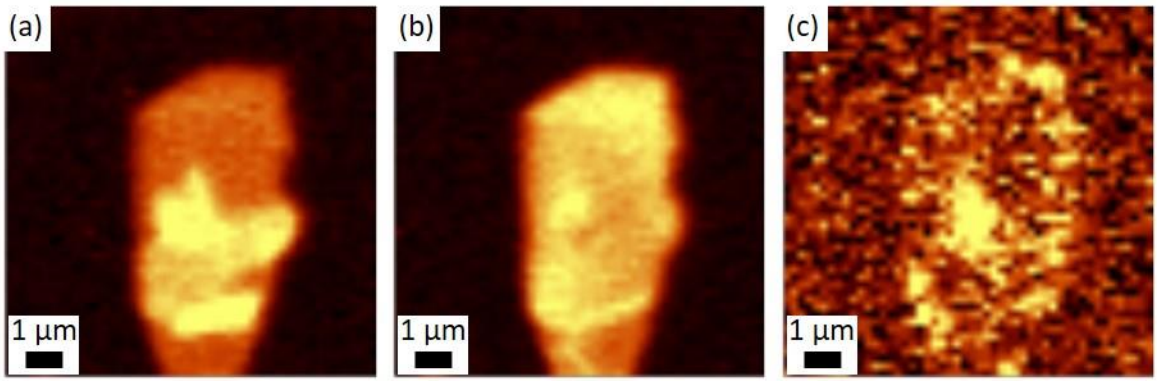

Figure 3.23: 2D Raman spectral maps of the sum of parts of the spectrum depicting the intensity of the (a) 2D, (b) G, and (c) D peaks of Flake A, at each pixel.

correspond to some wrinkles and folding detected from the AFM height images. Notably, Figure 3.23 (c) shows that while the D peak is practically absent throughout the majority of the flake, its intensity is significant towards the middle part of the flake where a wrinkle is visible in the AFM height image (Figure 3.9), and also at the edges of the flake.

Figure 3.24 shows the 2D Raman spectral intensity maps of Flake B as obtained using the 633 nm excitation wavelength with a pixel resolution of 0.2 µm, with the brightness of each pixel corresponding to the intensity of the 2D, G, and D peaks in (a), (b), and (c), respectively. With a better pixel resolution than those obtained for Flake A, the spectral maps of the 2D and G peak intensities (Figure 3.24 (a) and (b)) further confirm that the peak parameters change

with the thickness of the flake. In fact, the various areas and holes labelled earlier are once again distinguishable, with thinner areas generally showing higher intensities – with the exception of the spectra obtained from the holes which is possibly a result of the higher background noise detected. What is particularly evident in the spectral map showing the intensity of the D peak (Figure 3.24 (c)) is that the D peak is significantly higher at the edges of the flake, and nearly absent throughout the rest of the flake, similar to reports by [125].

Figure 3.25 presents the averaged spectra obtained from the differently labelled areas and holes (Figure 3.10 (c)) before subtracting an appropriate baseline from each. These show that spectra acquired from thicker areas, such as B1, B2 and B6, have a lower background noise, as opposed to thinner areas (B3, B4 and B5). As such, it can be concluded that fewer layers of graphene allow the signal from the substrate to be recorded. Further analysis on the individual peaks was done after subtracting the baseline from the spectra.

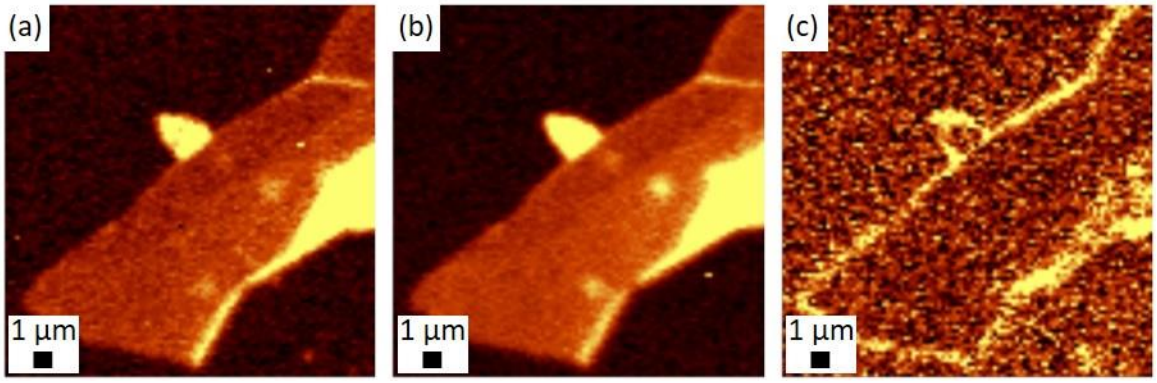

Figure 3.24: 2D Raman spectral maps of the sum of parts of the spectrum depicting the intensity of the (a) 2D, (b) G, and (c) D peaks of Flake B, at each pixel.

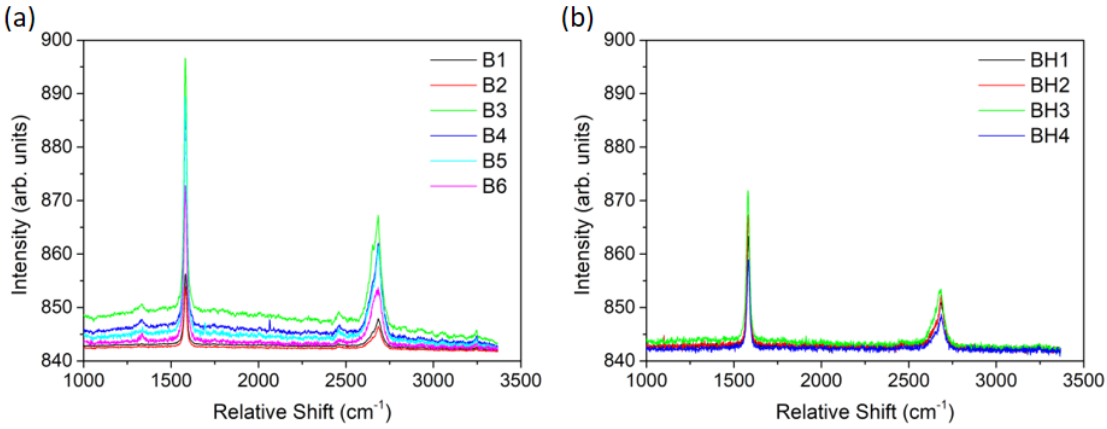

Figure 3.25: Averaged Raman spectra obtained from the areas within Flake B as labelled in Figure 3.10 (c) using the 633 nm excitation wavelength. The baseline is not subtracted in any of the presented spectra.

Figure 3.26 presents some of the peak parameters obtained against the thickness of the flake at a particular location or area. These results show that generally, the entire Raman spectrum is upshifted with an increase in the flake thickness; the D peak is upshifted by 7.5 cm^{-1}, the G peak by just 0.5 cm^{-1}, the D+D'' peak by up to 6.7 cm^{-1}, the 2D peak by around 9 cm^{-1}, and the 2D' peak by around 2 cm^{-1}, in agreement with [123, 125, 126]. This is coupled with a general decrease in peak intensity with an increase in thickness. The 2D peak has shown the most significant changes, with an increase in FWHM and peak area with increasing thickness. The I_{2D}/I_G and the F_{2D}/F_G, the former commonly used to determine the thickness of the graphene sheet being analysed, show a clear linear trend with the thickness, with both ratios decreasing from 0.4 to 0.33 and from 3.7 to 3.1, respectively. On the other hand, while the I_D/I_G increases slightly, the F_D/F_G decreases, meaning that, when present, the D peak appears to be sharper with increasing thickness. Furthermore, it was noted that the 2D peak does not truly have the lineshape of a single Lorentzian peak, as evidenced in Figure 3.27 which shows the evolution of the 2D peak with respect to flake thickness. Nevertheless, while the shape of the 2D peak changes with different measured thicknesses and hence the number of layers in the MLG flake, the shape of the band at each thickness is the same, confirming repeatability of results.

The 2D Raman spectral intensity maps of Flake C as obtained using the 633 nm excitation wavelength with a pixel resolution of 0.2 μm, are shown in Figure 3.28. Similar observations can be made to those for Flake A and Flake B.

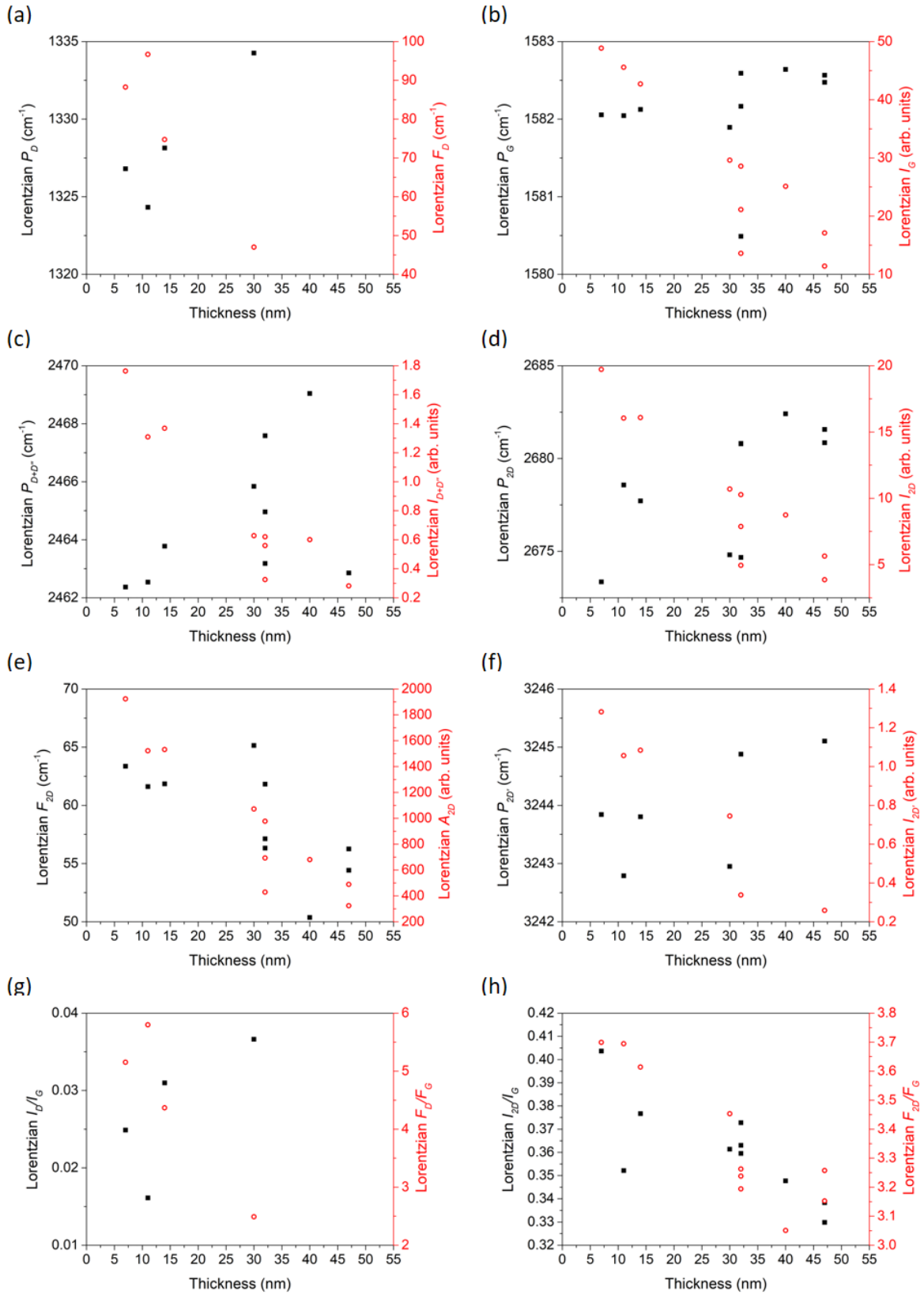

Figure 3.26: The peak position P, intensity I, width F, and area A, of the D, G, D+D'', 2D and 2D' bands, and the intensity and width ratios between the D and G bands (I_D/I_G, F_D/F_G), and the 2D and G bands (I_{2D}/I_G, F_{2D}/F_G) with an increasing flake thickness of Flake B.

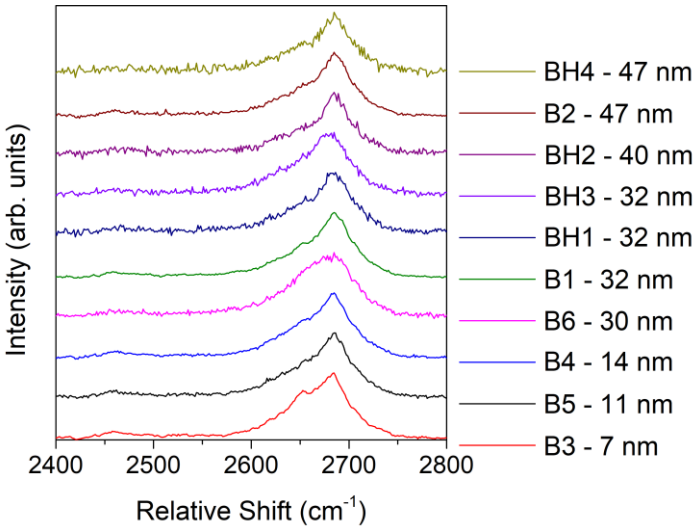

Figure 3.27: The evolution of the 2D peak with an increase in flake thickness.

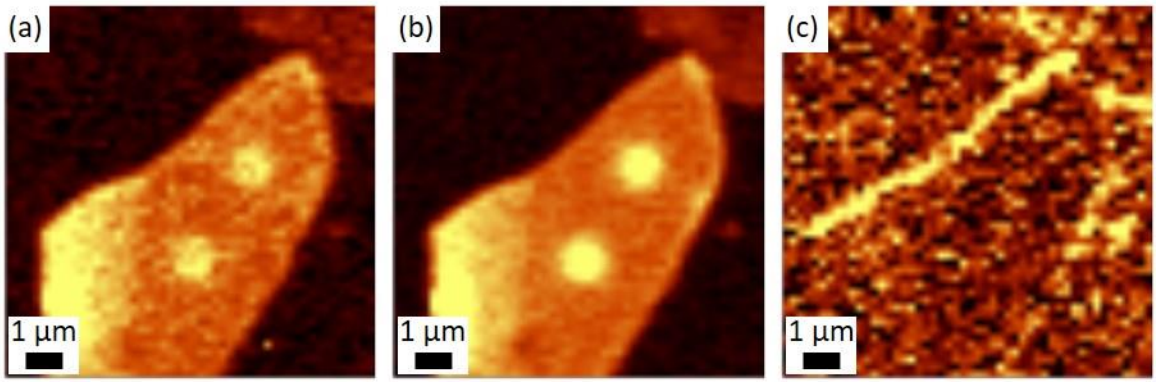

Figure 3.28: 2D Raman spectral maps of the sum of parts of the spectrum depicting the intensity of the (a) 2D, (b) G, and (c) D peaks of Flake C, at each pixel.

3.3.4.4 Scanning Electron Microscopy (SEM)

Figure 3.29 shows Flake A imaged via SEM; while (a) and (c) were obtained using the secondary electron detector, (b) and (d) were obtained using the Inlens detector. It can be noted that while the morphology of the graphene flakes with respect to the wrinkles and folds is particularly evident in the SE2 micrographs, Flake A which is around 5 nm thick, is barely detected (Figure 3.29 (a)). Conversely, Flake A is significantly more predominant in Figure 3.29 (b) with the use of the Inlens detector. At higher magnifications (Figure 3.29 (c, d)), the damage imparted on the sample by the Raman laser can also be observed as lighter regions, especially directly on the PAA/SiO_2 substrate just above Flake A.

Figure 3.30 shows four scanning electron micrographs of Flake B. Such micrographs further reveal the different thicknesses across the entire flake and helps determine more accurately the

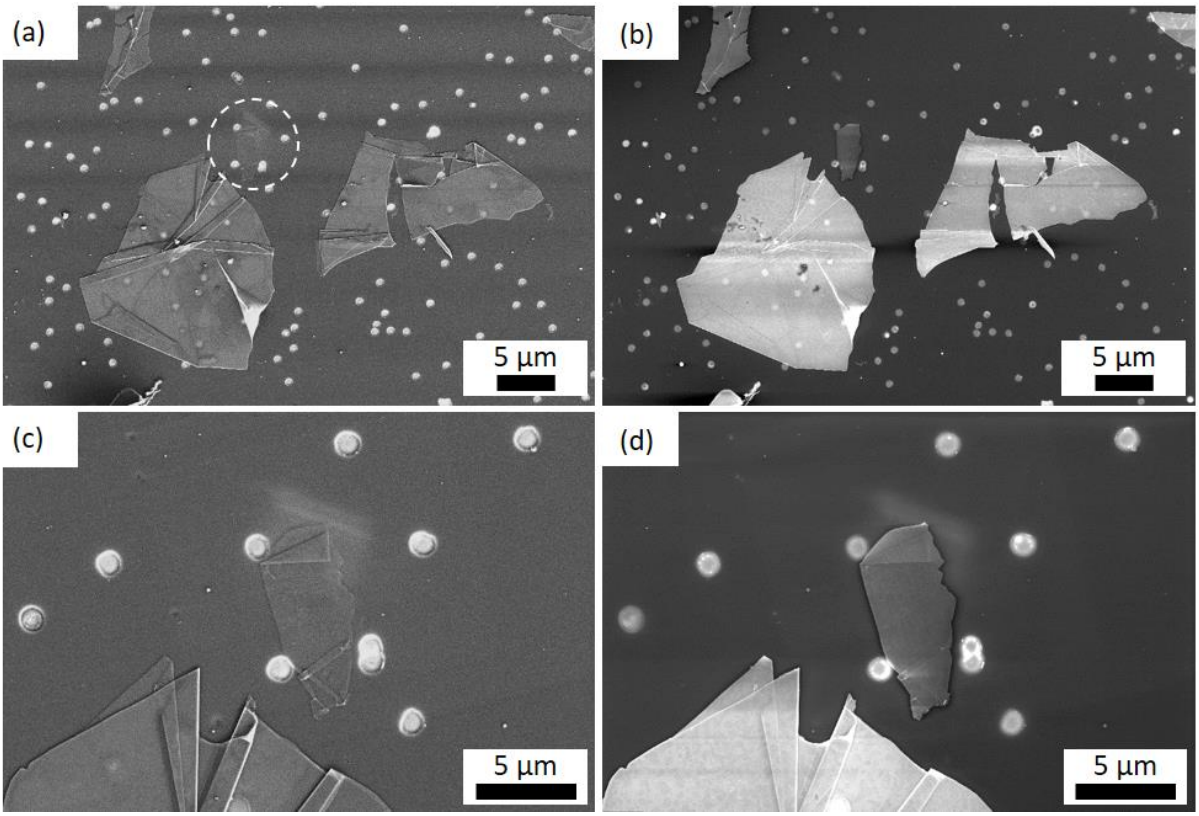

Figure 3.29: Scanning electron micrographs of mechanically exfoliated graphene on the patterned PAA/SiO_2 substrate using a (a, c) secondary electron detector and (b, d) Inlens detector. In (a), Flake A is circled for reference.

morphologies of the wrinkles and overlapping layers. The holes covered by the flake are also partially visible through the MLG, yet with less definition than those which are not covered.

As such, in general, the SE2 detector was used to study the morphology of the graphene flakes since wrinkles and overlapping features are much more visible with such detector. On the other hand, the Inlens detector was capable of differentiating the individual graphene flakes based on their relative thickness to each other, with the thicker flakes appearing much brighter than the thinner flakes. Furthermore, while the thinner graphene flakes were barely visible with the SE2 detector, the Inlens detector offered better imaging capabilities for such thin flakes, especially those having a thickness less than around 5 nm.

In order to mitigate potential damage by electron bombardment, imaging work with SEM was only conducted at the end of the characterisation cycle.

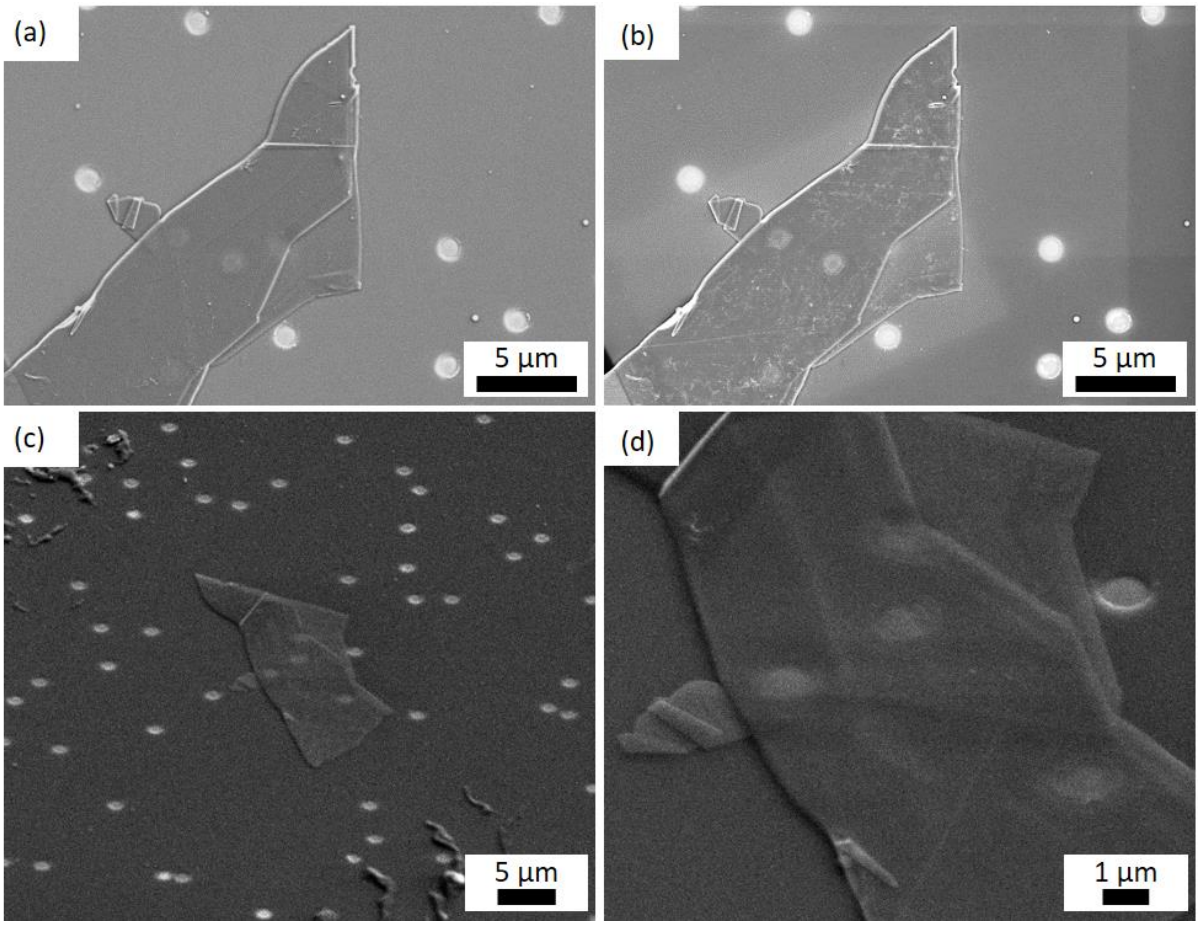

Figure 3.30: Scanning electron micrographs of Flake B using the secondary electron detector.

3.3.5 CONCLUDING REMARKS

Graphene samples were prepared via mechanical exfoliation of HOPG and subsequently deposited on the patterned PAA/Si substrates. The results obtained demonstrate that graphene can be produced via mechanical exfoliation using only minimal tools including; (i) the HOPG as the graphitic precursor, (ii) the adhesive exfoliation and transfer medium, and (iii) the substrate. This made it possible to prepare graphene samples in-house. Furthermore, as evidenced by the very low to negligible D peak in the Raman spectra of the obtained graphene flakes, as shown in Figure 3.20 and Figure 3.25, mechanically exfoliated graphene tends to have good structural quality and low disorder in its crystalline lattice. Nonetheless, a few observations on the graphene samples produced in this work via mechanical exfoliation raise some concern on the suitability of this technique for the preparation of graphene membranes, as discussed below.

1. The graphene flakes produced via mechanical exfoliation have limited lateral dimensions. As shown in the optical micrographs of Figure 3.7 and Figure 3.8, larger

flakes with lateral dimensions of up to 60 μm are significantly thick graphitic flakes, while thinner multi-layer graphene flakes are rarely larger than 20 μm. This limitation creates three major challenges for the scope of this research.

   i. For the hole or 'well' density patterned onto the substrate used, smaller flakes have a lower probability of entirely and securely covering a hole to create the required drum-like membranes.
   ii. Smaller flakes are much more difficult to locate with the AFM making the subsequent characterization and testing phases much more labour intensive.
   iii. For the graphene membranes to be used for filtration purposes, it would be highly desirable to have individual graphene flakes spanning across larger areas, i.e. covering significantly more holes.

2. Since the successful mechanical exfoliation of graphite to single-layer graphene is highly dependent on manual repeated pressing and separation of the two PDMS stamps, little control can be achieved on the thickness of the final deposited flakes. In fact, the thinnest flakes that could be identified from the samples produced were still significantly thick; in excess of 5 nm as measured by AFM scans. The large I_{2D}/I_G ratios of around 0.4 in the Raman spectra of the thinner flakes further indicate the significant thickness compared to single-layer graphene (typical $I_{2D}/I_G > 1$ [37, 55, 122, 125]). Thus, multi-layer graphene was produced rather than single-layer graphene.
3. The graphene flakes often demonstrate morphological defects including large wrinkles, folds and overlapping flakes (such as shown in Figure 3.7 (d) and Figure 3.9 (a, d)), which change the thickness and adhesion to the substrate within the same flake.
4. The manual mechanical exfoliation technique used in this study resulted in a large variety of flakes having different thicknesses, lateral dimensions, and morphologies in terms of wrinkles and overlapping portions. The limited number of flakes of similar thickness that could be identified and located via AFM which also covered a 'well' and without any dominant wrinkles or structural defects within or in the vicinity of the membranes led to restrictions in the repeatability of the subsequent experiments. This will be discussed in Chapter 4.

In order to address some of the limitations imposed by the mechanical exfoliation technique, other graphene synthesis routes were explored, as will be explained in Section 3.4.

3.4 CHEMICAL VAPOUR DEPOSITION (CVD) GROWN GRAPHENE

As discussed in the previous section, the mechanical exfoliation synthesis route proved to be challenging to obtain single-layer graphene with larger lateral dimensions. The latter was deemed to be more important should the produced graphene membranes be used in filtration devices. Chemical vapour deposition (CVD) was considered as a potentially suitable technique which may produce larger, single layer graphene flakes. Each graphene sample was characterized using a combination of optical microscopy, Raman spectroscopy, AFM, and SEM, as was done for the mechanically exfoliated graphene samples.

3.4.1 SUPPORTED GRAPHENE ON SiO_2/SI

Initial familiarisation work was conducted on CVD-grown monolayer graphene pre-transferred on SiO_2/Si. The CVD-grown single-layer graphene with a nominal thickness of 0.345 nm and grain size of 1 mm [227], transferred onto SiO_2/Si substrates were supplied by Nano Carbon Sp. z o.o., Warsaw, Poland.

Figure 3.31 (a) shows an optical micrograph of a representative area of the supported CVD graphene on SiO_2/Si. Raman spectra using the 532 nm excitation wavelength obtained from the areas labelled A1 to A4 are presented in Figure 3.31 (b, c) and the associated peak parameters are listed in Table 3.6 and Table 3.7. Figure 3.32 shows scanning electron micrographs showing the same features as in Figure 3.31 (a).

Within the optical and electron micrographs (Figure 3.31 (a) and Figure 3.32, respectively), various linear and circular areas having a darker shade are visible. These features are attributed to grain boundaries and nucleation sites. Since CVD-grown graphene grows from multiple nucleation sites, it is expected that grain boundaries are created as soon as the individual grain fronts meet. Furthermore, the coverage (total area covered by graphene) and the number of graphene layers grown are closely related to the growth parameters. As such, it is common that total coverage is obtained at the expense of having adlayers - additional areas of bi-layer or few-layer graphene [95].

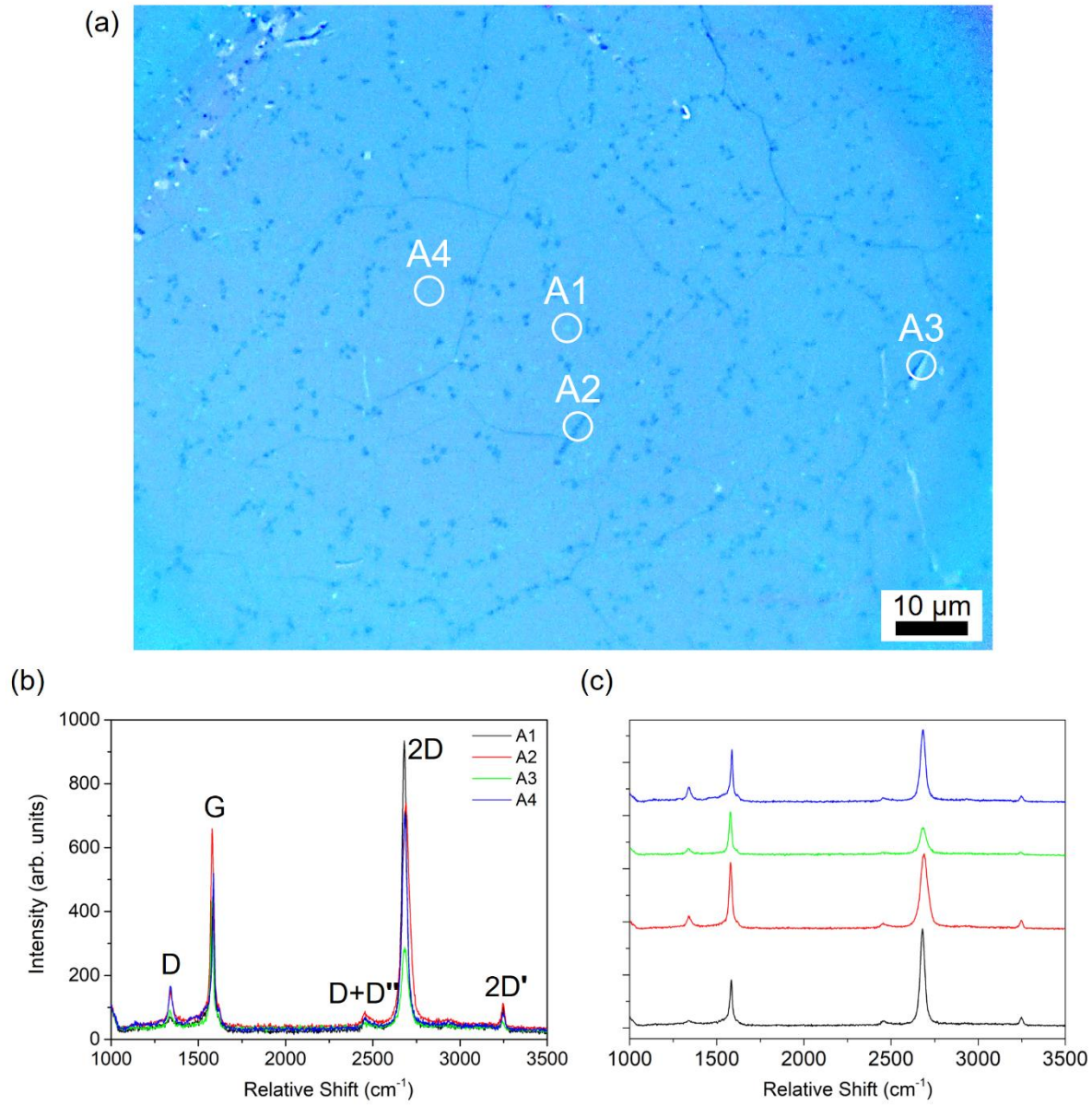

Figure 3.31: (a) Optical micrograph of the CVD graphene supported on the SiO_2/Si substrate with locations A1 – A4 from where the Raman spectra in (b and c) were obtained using the 532 nm excitation wavelength, without baseline subtraction.

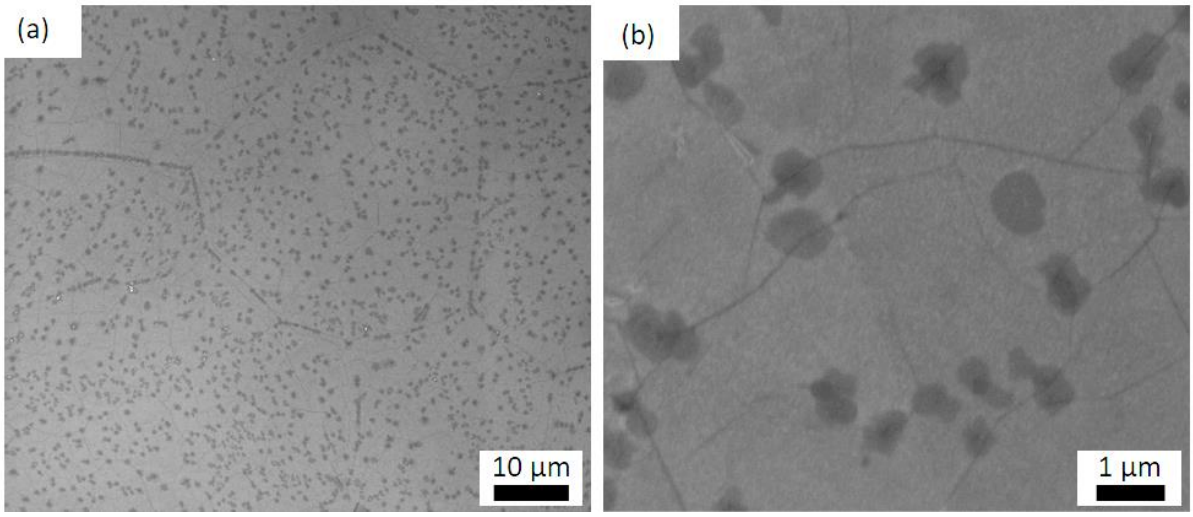

Figure 3.32: Scanning electron micrograph of supported CVD graphene on Si/SiO_2.

Table 3.6: The relative shift (P) and the full width at half maximum (F) of the D, G, D+D'', 2D and 2D' peaks obtained from various locations in the CVD graphene on SiO_2/Si substrate as shown in Figure 3.31, using the 532 nm excitation wavelength.

Location	D Peak (cm^{-1})		G Peak (cm^{-1})		D+D'' Peak (cm^{-1})		2D Peak (cm^{-1})		2D' Peak (cm^{-1})	
	P	F	P	F	P	F	P	F	P	F
A1	1339.7	54.0	1582.4	19.5	2458.5	34.2	2680.4	28.2	3247.7	18.6
A2	1341.4	27.9	1579.4	20.3	2456.7	30.3	2689.3	43.0	3247.0	19.0
A3	1338.6	24.6	1578.1	17.7	2454.2	31.8	2684.3	39.4	3243.3	22.7
A4	1340.9	23.9	1586.1	18.5	2459.1	23.7	2683.0	30.7	3248.0	20.3

Table 3.7: The intensity (I) and width (F) ratios between the D and G peaks, and the 2D and G peaks obtained from various locations in the CVD graphene on SiO_2/Si substrate as shown in Figure 3.31, using the 532 nm excitation wavelength.

Location	I_D/I_G	F_D/F_G	I_{2D}/I_G	F_{2D}/F_G
A1	0.06	2.76	2.34	1.44
A2	0.15	1.37	1.18	2.11
A3	0.12	1.39	0.63	2.23
A4	0.27	1.29	1.57	1.66

All spectra have sharp Lorentzian profiles for the G and 2D peaks; the latter indicates the presence of single layer graphene. The G peak is found at around 1581 cm^{-1} and has a FWHM of ~19 cm^{-1}. The 2D peak is found at ~2684 cm^{-1} with a FWHM of ~35 cm^{-1}.

As opposed to the Raman spectra obtained from the mechanically exfoliated graphene samples, the spectra obtained from the supported CVD graphene on SiO_2/Si using the 532 nm excitation wavelength exhibit a significantly higher I_{2D}/I_G ratio of up to 2.3 (compared to 0.3 for the mechanically exfoliated graphene samples). Such large ratio clearly confirms that the majority of the sample is single-layered [122, 123]. Furthermore, spectra obtained from the darker areas such as A2 and A3 have a smaller I_{2D}/I_G ratio of 1.18 and 0.63, respectively, indicating the presence of bi-layer or few-layer graphene at the grain boundaries and nucleation sites. The latter notion is further supported by the work of Reina et al. [223], suggesting that in few-layer CVD graphene the stacking order typical of highly ordered pyrolytic graphite might not be preserved, hence stacked graphene layers might still have a sharp 2D peak with a single Lorentzian line shape rather than a superposition of multiple peaks [126, 228]. Thus, it has been subsequently determined that the I_{2D}/I_G ratio is indeed a better indication of the number of layers in CVD graphene rather than the profile of the 2D peak, suggesting that an I_{2D}/I_G of ~0.76 corresponds to a stack of around 3 single layers [223].

The D band was found to be satisfactorily low across the graphene sample with an I_D/I_G ratio of around 0.15, yet still higher than that in the mechanically exfoliated graphene ($I_D/I_G < 0.04$). This is also in agreement with studies by Li et al. [95] which suggests that CVD-grown graphene tends to have more disorder in its crystalline structure. The D+D'' peak is also detected at 2457 cm^{-1}. This indicates that the graphene has few defects, most likely limited to grain boundaries and wrinkles often present in CVD graphene. In fact, Figure 3.31 and Figure 3.32 clearly highlight the presence of such grain boundaries and areas of bi- or multi-layer graphene seen as darker linear or circular features, respectively.

Due to the flatness of both the SiO_2/Si substrate as well as the graphene layer on top, the use of atomic force microscopy in static mode imaging did not produce any satisfactory results; the roughness and feature size of the sample was too similar to the noise signal.

3.4.2 Suspended Graphene on TEM Grids

CVD-grown single-layer graphene membranes (nominal thickness and grain size of 0.345 nm and 10 μm, respectively [229]) suspended over Quantifoil® TEM mesh grids with 2 μm

diameter holes, supplied by Agar Scientific Ltd., Essex, UK, were used as the drum-like suspended graphene membranes for subsequent work.

3.4.2.1 Fixation of TEM Grids

Unlike the rigid SiO_2/Si substrates, the TEM grids that support the Quantifoil® are gold-coated copper-based grids with a thickness of only ~8 µm. Furthermore, the Quantifoil® is a second mesh with a nanometric thickness (<30 nm) which supports the graphene. This makes the entire TEM grid very delicate and fragile. As such, to allow manipulation of the membranes on this substrate, a clamp was designed and fabricated. Figure 3.33 (a) shows a schematic of the TEM grid sample holder components, while Figure 3.33 (b) shows the sample holder as assembled with the TEM grid sandwiched between the top and bottom washers. The clamp was machined from aluminium 6061 and silver paste (Electodag 1415, Agar Scientific Ltd., Essex, UK) was used as an adhesive at the mating faces of the top and bottom washers. Detailed drawings of the TEM grid sample holder are presented in Appendix B.

3.4.2.2 Characterisation

Figure 3.34 shows scanning electron micrographs of suspended graphene on TEM grid sample at various magnifications. In Figure 3.34 (a) the larger TEM grid structure is visible together with the Quantifoil® mesh on top. The punctured Quantifoil® on the right hand side of the micrograph evidences the fragility of the mesh. In Figure 3.34 (b) only the Quantifoil® mesh is visible. At higher magnification, Figure 3.34 (c, d), graphene is much more visible as a transparent grey membrane. SEM imaging is able to reveal wrinkles and areas of multi-layered graphene as shown in Figure 3.34 (c). On the other hand, the membrane in Figure 3.34 (d) is significantly compromised with the graphene layer draping inside the hole.

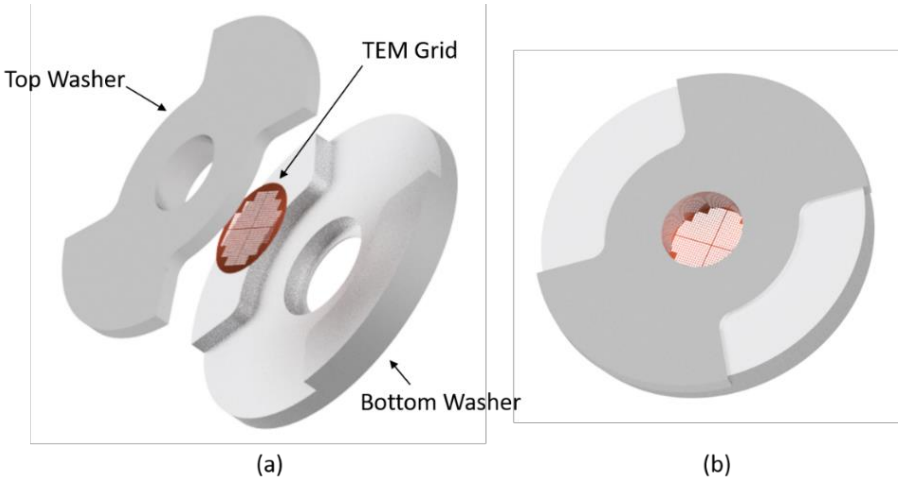

Figure 3.33: The design of the TEM grid sample holder; (a) labelled components, (b) assembly.

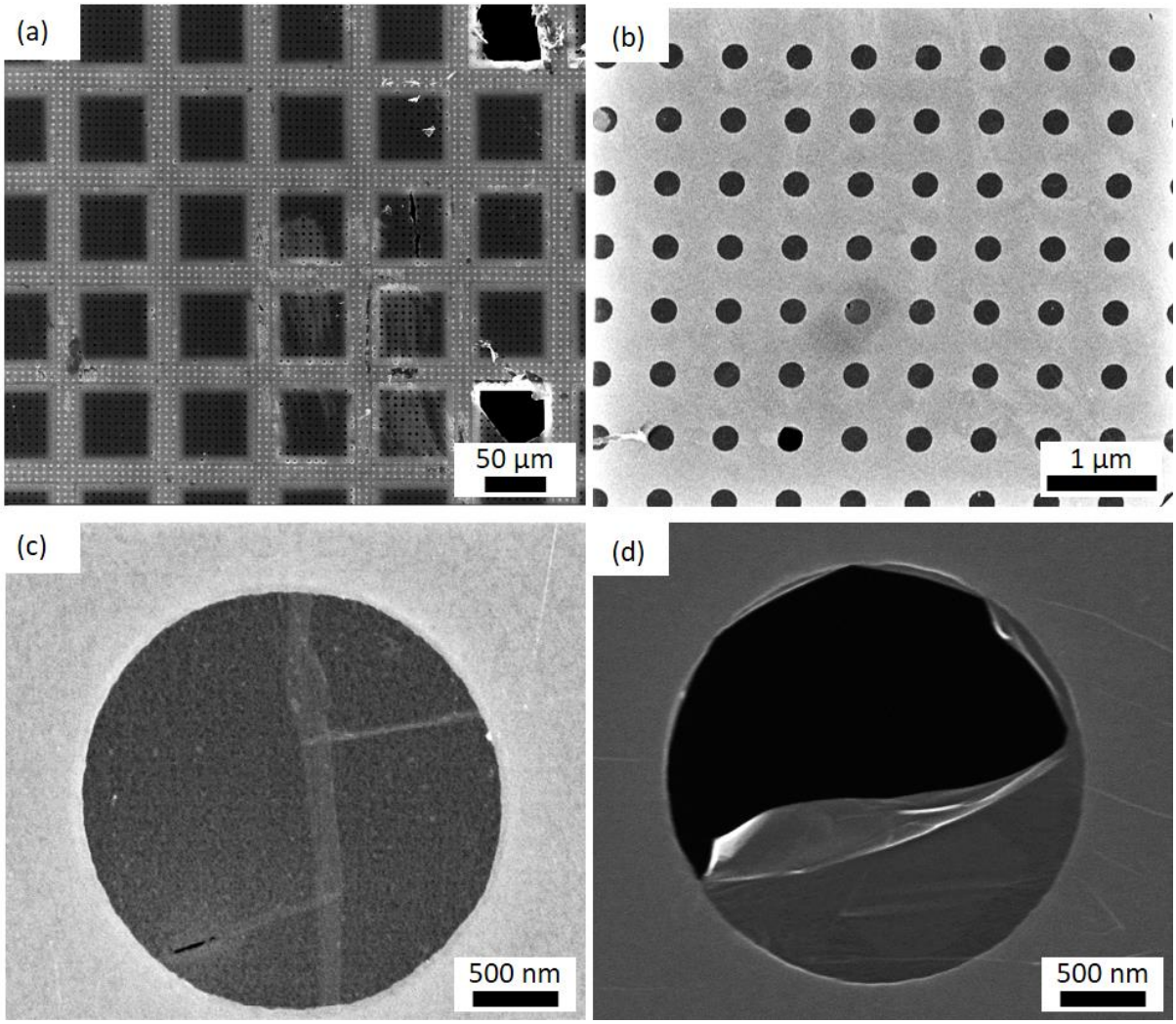

Figure 3.34: Scanning electron micrographs of suspended CVD graphene on a TEM grid.

As shown in Figure 3.35, atomic force microscopy was successfully used to confirm the presence of a membrane over the hole structure of the Quantifoil® mesh. Figure 3.35 (a – c) show the same membrane imaged under static contact mode. The normal force micrograph (Figure 3.35 (a)) highlights the edge of the membrane/hole and a few perturbations on the supported regions. The lateral force micrograph (Figure 3.35 (b)) indicates that the friction coefficient is similar throughout the scan reflecting the fact that graphene covers the entire scan area. The height micrograph (Figure 3.35 (c)) shows a depression in the graphene membrane compared to the supporting substrate. This indicates that the tip is pushing the graphene membrane downwards. Finally, Figure 3.35 (d) shows a dynamic non-contact mode micrograph of another membrane. Under dynamic non-contact mode, the true topography of the membrane without any applied load can be imaged. In fact, Figure 3.35 (d) reveals the presence of multiple ripples across the graphene layer which are significantly higher in

amplitude in the unsupported membrane region. The presence of such wrinkles is in agreement with published studies concerning CVD-graphene [86, 153].

Figure 3.36 shows representative Raman spectra obtained from the suspended regions of the CVD-graphene on TEM grids using the 633 nm excitation wavelength, with the respective Raman peak parameters listed in Table 3.8 and Table 3.9. Once again, the high I_{2D}/I_G ratio of 2.5 to 2.9 indicates the presence of single-layer graphene. However, the D band was significantly higher than that found in the other CVD samples, with an I_D/I_G ratio of 0.57 to 1.21.

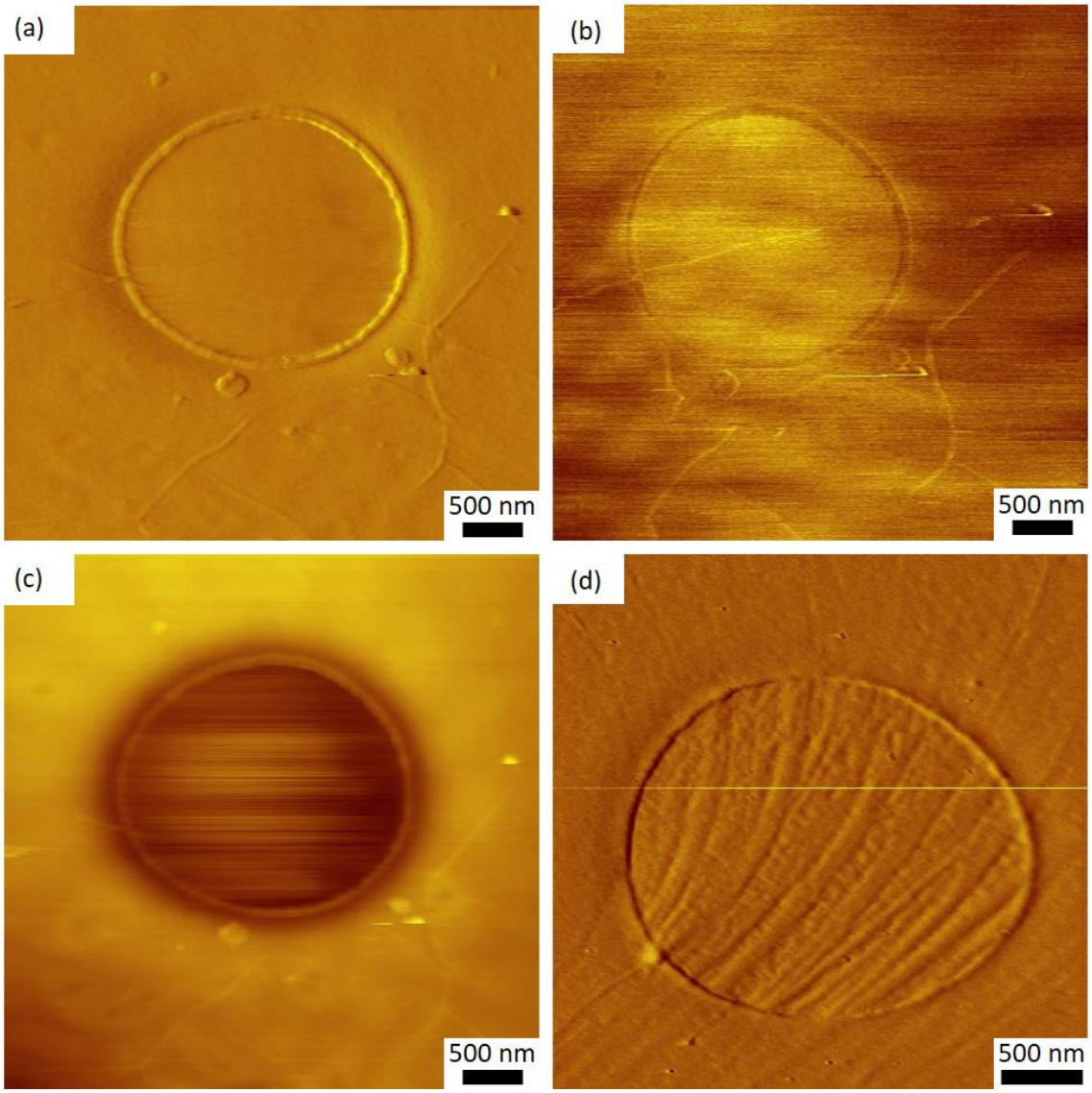

Figure 3.35: (a – c) Static contact mode, and (d) dynamic non-contact mode AFM micrographs showing the (a) normal force, (b) lateral force, (c) topography, and (d) phase signals of the CVD graphene membranes on TEM grids.

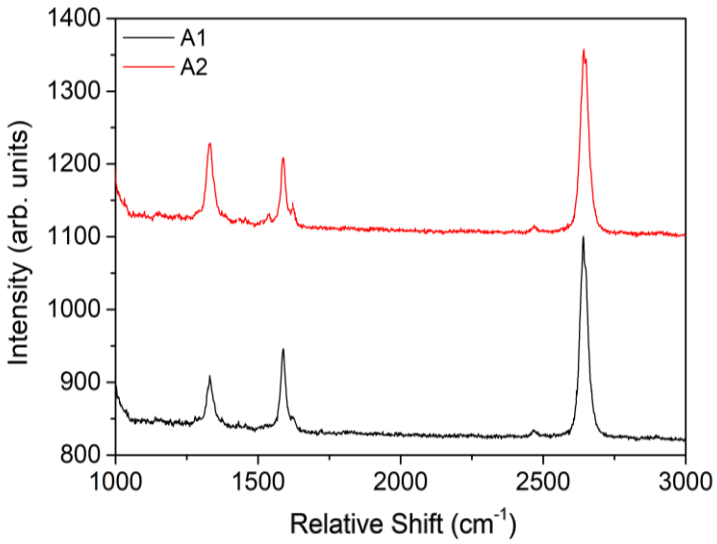

Figure 3.36: Raman spectra of various areas within the CVD graphene suspended on TEM grids using the 633 nm laser, without baseline subtraction.

Table 3.8: The relative shift (P) and the full width at half maximum (F) of the D, G, D+D'' and 2D peaks obtained from various locations in the CVD graphene on TEM grid.

Location	D Peak (cm^{-1})		G Peak (cm^{-1})		D+D'' Peak (cm^{-1})		2D Peak (cm^{-1})	
	P	F	P	F	P	F	P	F
A1	1331.2	27.3	1588.1	20.5	2467.0	13.6	2642.6	28.6
A2	1330.6	27.5	1588.7	23.8	2468.5	14.6	2644.9	29.9

Table 3.9: The intensity (I) and width (F) ratios between the D and G peaks, and the 2D and G peaks obtained from various locations in the CVD graphene on TEM grid.

Location	I_D/I_G	F_D/F_G	I_{2D}/I_G	F_{2D}/F_G
A1	0.57	1.33	2.50	1.40
A2	1.21	1.16	2.91	1.26

3.4.3 Suspended Graphene on Patterned PAA/Si Substrate and Silicon Nitride Microsieves

In order to investigate the high D band intensity exhibited by the CVD-graphene, a second CVD-graphene source was selected for investigation. CVD-grown single-layer graphene with a nominal thickness and grain size of 0.345 nm and 20 µm, respectively [99], sandwiched between a proprietary polymeric support film and a sacrificial layer (Easy Transfer: Monolayer

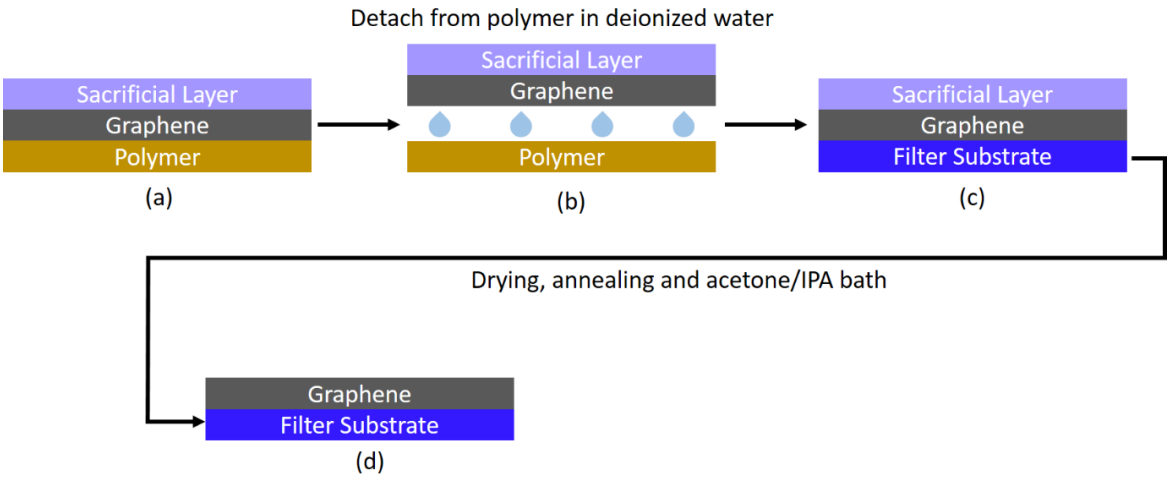

Figure 3.37: Schematic of the procedure to transfer the Easy Transfer graphene. (a) As-received sacrificial layer/graphene/polymer sandwich, (b) detachment of sacrificial layer and graphene from the polymer support using deionized water, (c) deposition on substrate of choice, and (d) removal of the top sacrificial layer to expose the graphene.

Graphene on Polymer) was supplied by Graphenea Semiconductor SLU, San Sebastián, Spain. The Easy Transfer graphene was deposited on both the patterned PAA/Si substrate as prepared in Section 3.3.1 as well as on silicon nitride microsieves (High-Porosity Microsieves, Aquamarijn Micro Filtration BV, Zutphen, The Netherlands) with a pore diameter of 0.45 µm.

Initially, the as-received sample was slowly immersed in a petri dish of deionized water to detach the graphene and sacrificial layer from the polymeric support film, Figure 3.37 [14]. This step causes the sacrificial layer/graphene to float on the water. A freshly cleaned piece of the patterned PAA/Si substrate or a silicon nitride microsieve was then introduced into the deionized water at an angle of around 45°. The floating sacrificial layer and graphene was deposited onto this substrate. The resulting laminate was left to dry in air for 30 minutes, annealed on a hot plate at 150°C for one hour and stored under vacuum for at least 24 hours. The sacrificial layer was then removed by immersing the sacrificial layer/graphene/substrate in acetone for one hour, followed by an isopropyl alcohol bath for another hour. The graphene/substrate was then dried under a nitrogen flow.

3.4.3.1 Optical Microscopy

Due to the simplicity of the technique, optical microscopy was used throughout the deposition process to verify the successful transfer of the CVD graphene from the polymer/sacrificial layer sandwich onto the substrates of choice. As such, optical micrographs of the deposited graphene sheet both before and after removing the top sacrificial layer via the acetone and isopropyl alcohol baths were obtained.

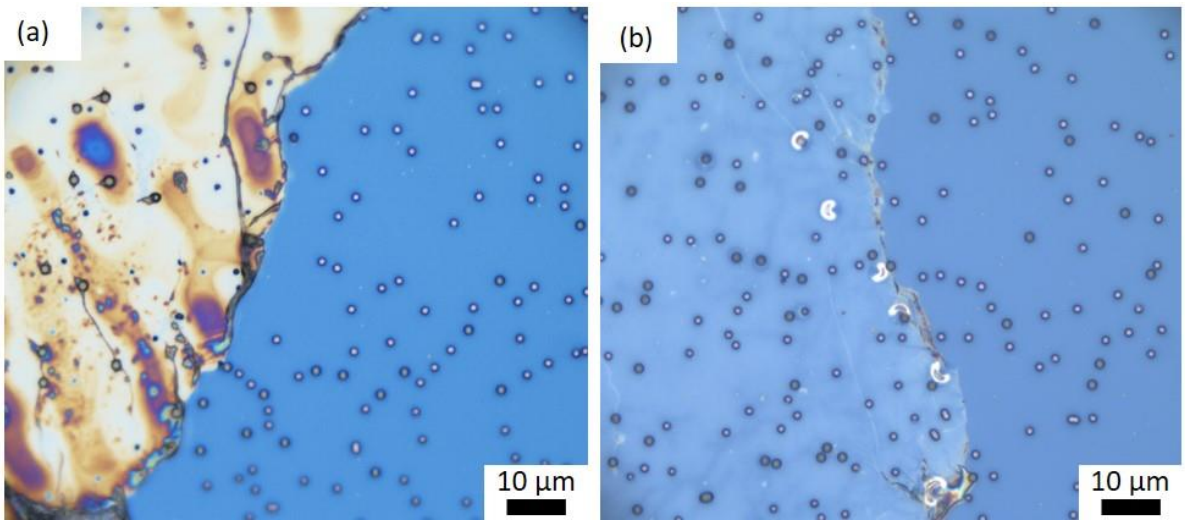

Figure 3.38: Optical micrographs of the Easy Transfer CVD graphene deposited on the patterned PAA/Si substrate. (a) Before and (b) after removal of the top sacrificial layer.

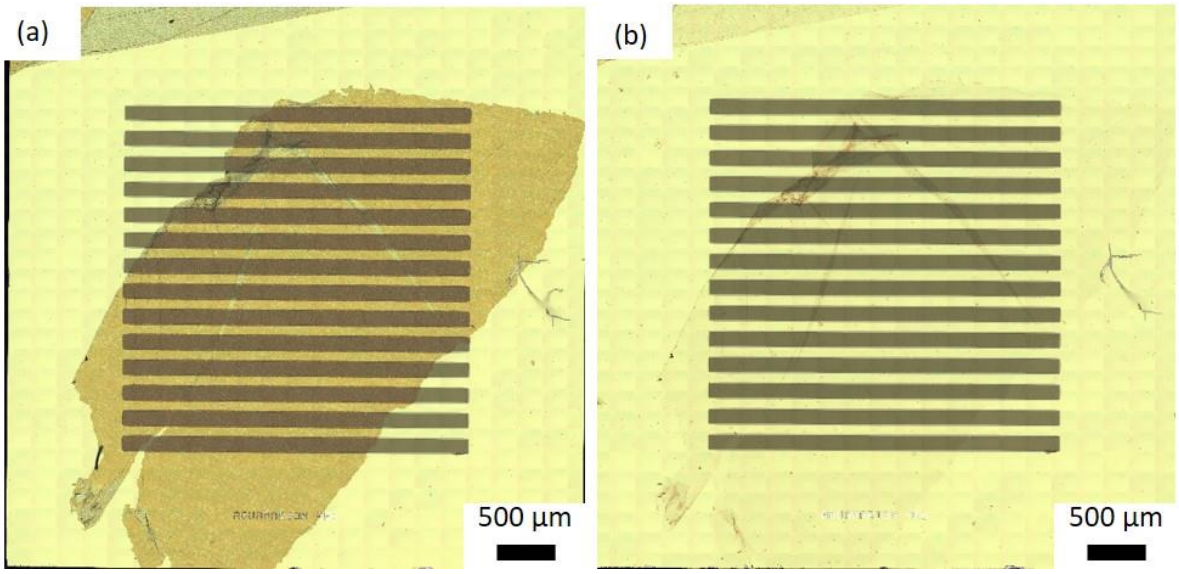

Figure 3.39: Optical micrographs of the Easy Transfer CVD graphene deposited on the silicon nitride microsieves with pore diameter of 0.45 µm. (a) Before and (b) after removal of the top sacrificial layer.

Figure 3.38 and Figure 3.39 show optical micrographs of the deposited CVD graphene onto the patterned PAA/Si substrate and the 0.45 µm silicon nitride microsieve, respectively.

For both types of substrates – the patterned PAA/Si and the silicon nitride microsieve – the graphene sheet is significantly more visible when still covered by the sacrificial layer than after dissolution of the latter. This change in optical contrast confirms that the top sacrificial layer was indeed being removed during the final transfer step. Furthermore, the very low contrast between the areas covered by the graphene sheet and the rest of the substrate after the removal of the sacrificial layer (Figure 3.38 (b) and Figure 3.39 (b)) indicates that the deposited

graphene sheet is indeed much thinner than the mechanically exfoliated flakes. Moreover, the fact that the general morphology of the deposited graphene sheet remained the same before and after the dissolution step confirms that the last dissolution step is not significantly modifying the underlying graphene, such as by delamination.

Comparing the optical micrographs of the transferred Easy Transfer CVD graphene to those of the mechanically exfoliated graphene flakes shown in Section 3.3 reveals a key advantage of using CVD to synthesise graphene as opposed to mechanical exfoliation. While mechanical exfoliation yielded small flakes with widely varying thicknesses and a very low yield of thin graphene flakes, the transfer of CVD-grown graphene yielded a single large sheet covering the majority of the substrate which mostly appears to be uniform and homogeneous in thickness.

3.4.3.2 Atomic Force Microscopy

Since the majority of the substrates were covered by the CVD graphene sheet, imaging and analysis with AFM was greatly facilitated. A representative topography image of the graphene membranes covering the 0.45 µm pores of the silicon nitride microsieve using an FM50 AFM probe is shown in Figure 3.40. This imaging work confirms that the majority of the graphene membranes are intact and cover the pores completely. Only a few of the membranes appear to have a wrinkle or possibly a grain boundary across the pore indicating that the majority of the circular membranes were suitable for further analysis using indentation. In fact, most of the indentation tests were performed on the Easy Transfer CVD graphene on 0.45 µm microsieves due to the larger number of available membranes with the same graphene thickness and crystalline quality.

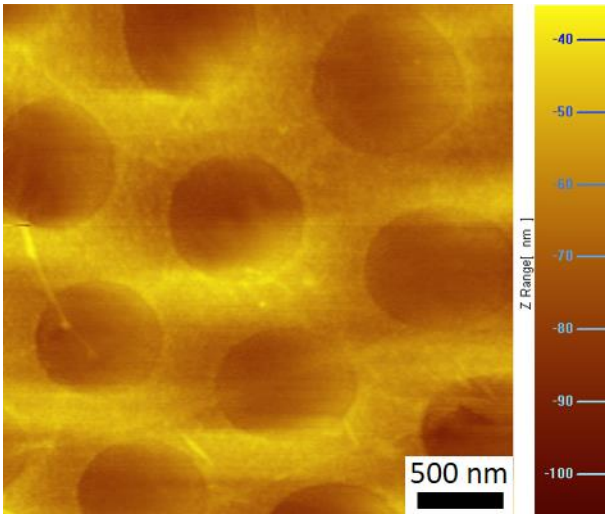

Figure 3.40: Static contact mode AFM topography micrograph of the CVD graphene membranes deposited over the 0.45 µm pores in the microsieve.

Unlike the CVD graphene transferred onto the microsieves, the graphene transferred onto the patterned PAA/Si substrates resulted in less-favourable specimens. Although the sheet appears to be intact and covering the majority of the holes via optical microscopy, AFM imaging of the transferred CVD graphene sheet on the patterned PAA/Si substrate was more problematic, revealing that most of the membranes were ruptured. While rupturing the membranes during the static contact mode imaging is possible when a normal force setpoint is set too high, the low forces used here (<140 nN) suggest a different cause. The transfer process involves submerging the patterned PAA/Si substrate into water over which the graphene/sacrificial layer is floating. The substrate is then pushed upwards under the floating graphene sheet until the graphene sheet makes full contact with the substrate and subsequently adheres to it. Therefore, it is plausible that the wells patterned into the PAA/Si substrate are filled with water and this moisture is then sealed by the impermeable graphene membrane. During the following step when the sample is put under vacuum it is possible that the water-filled wells are forced to expand causing rupture of the membranes. This phenomenon is further supported by the fact that upon inserting the sample in the AFM chamber and the pressure was slowly reduced to the target 3×10^{-9} mbar, the pressure was noted to suddenly increase by multiple orders of magnitude, indicating that the membranes covering the wells have ruptured releasing moisture into the chamber.

3.4.3.3 Raman Spectroscopy

The Easy Transfer CVD graphene sheets transferred onto both the patterned PAA/Si substrate as well as the 0.45 μm silicon nitride microsieve were also analysed via Raman spectroscopy. Figure 3.41 and Figure 3.42 present typical Raman spectra obtained from the CVD graphene on the patterned PAA/Si substrate and the 0.45 μm silicon nitride microsieve, respectively, using the 532 nm excitation wavelength. The raw spectra together with the baseline corrected spectra are once again presented to highlight the effect that the underlying substrate has on the results.

Although the presence of the characteristic Raman peaks of graphene in the spectra obtained from the CVD graphene on the PAA/Si substrate is just observable, the intensity of background noise is sufficient to allow for challenging numerical analysis of the peak parameters. On the other hand, the characteristic G and 2D peaks are much more pronounced in the spectra obtained from the CVD graphene transferred onto the silicon nitride microsieves. Since both pieces of CVD graphene were obtained from the same as-received sheet, it is logical to assume that the crystalline quality of the graphene is similar for both substrate samples.

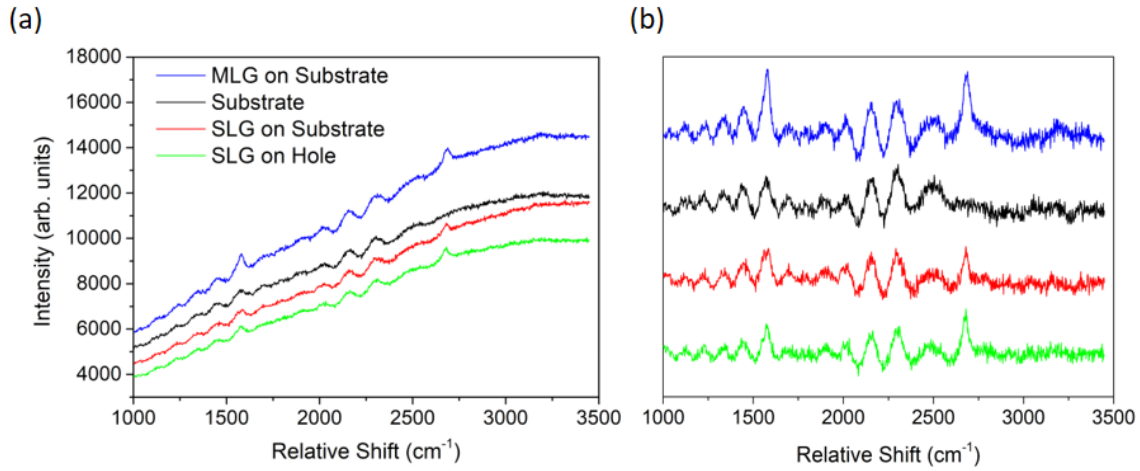

Figure 3.41: Raman spectra of various areas within the CVD graphene, deposited on the patterned PAA/Si substrate using the 532 nm laser, (a) before and (b) after subtraction of baseline.

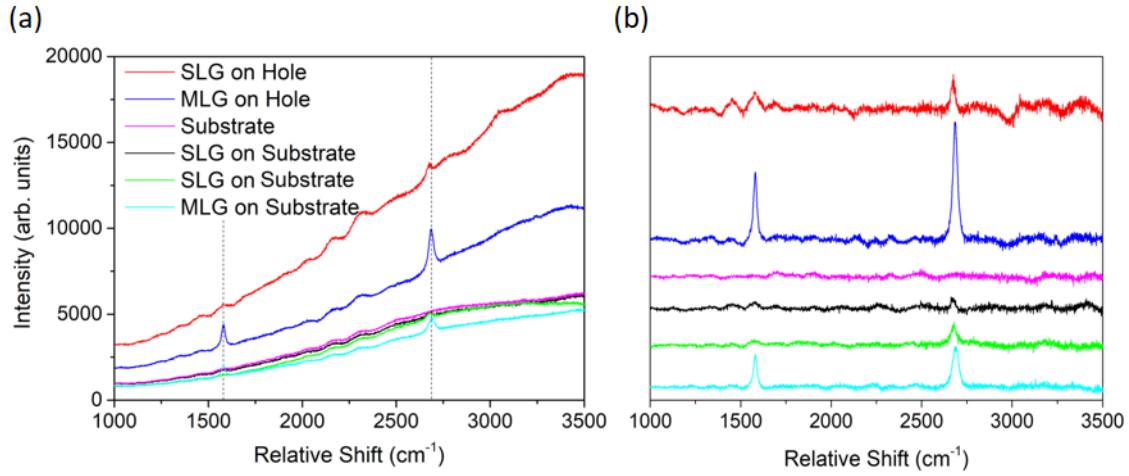

Figure 3.42: Raman spectra of various areas within the CVD graphene on silicon nitride microsieve using the 532 nm laser, (a) before and (b) after subtraction of baseline.

The peak parameters extracted from the Raman spectra shown in Figure 3.42 are listed in Table 3.4. In all of the graphene spectra, it is clear that the 2D peak is more intense than the G peak, with an intensity ratio I_{2D}/I_G of around 1.7, unlike what was observed for the thinner mechanically exfoliated flake in Section 3.3 ($I_{2D}/I_G < 0.6$). This indicates that the transferred CVD graphene is indeed single-layered as claimed by the supplier. Furthermore, the D peak is nearly absent, indicating good quality graphene. Finally, although the spectrum labelled as 'MLG on Hole' in Figure 3.42 was obtained from an area of bi or multi-layer graphene (confirmed via optical microscopy) the 2D peak still appears to be narrow and larger than the G peak. This may be due to the lack of Bernal (ABAB) stacking in randomly overlapping graphene sites, unlike what is expected in MLG derived from HOPG [223].

Table 3.10: The relative shift (P), full width at half maximum (F), and intensity (I) and ratios between the G and 2D peaks obtained from various locations across the Easy Transfer graphene on 0.45 µm microsieve as shown in Figure 3.42.

Sample	G Peak (cm^{-1})		2D Peak (cm^{-1})		I_{2D}/I_G	F_{2D}/F_G
	P	F	P	F		
SLG on Substrate	1575.6	44.6	2671.7	19.2	1.7	0.4
SLG on Hole	1579.2	47.6	2673.3	22.6	1.7	0.5
SLG on Green Area	1581.8	47.6	2677.7	43.3	1.7	0.9
MLG on Substrate	1580.4	20.2	2688.0	35.5	1.7	1.8
MLG on Hole	1580.3	20.2	2685.6	26.9	1.7	1.3

3.4.3.4 Scanning Electron Microscopy

Figure 3.43 shows scanning electron micrographs of the Easy Transfer CVD graphene on the patterned PAA/Si substrate. Figure 3.43 (a) and (b) show the same area imaged using the secondary electron detector and the Inlens detector, respectively. These two micrographs particularly highlight the advantages of both detectors. With the secondary electron detector, the graphene itself is not visible and only the well structures patterned into the PAA/Si substrate are visible as lighter circular structures. Some PS beads which were not removed during ultrasonication in toluene (Section 3.3.1) are also visible. On the other hand, with the Inlens detector the deposited graphene is very visible as a grey film, compared to the darker substrate. While the wells seem to be entirely covered by a graphene membrane, such as shown more clearly in Figure 3.43 (c) and (d), both of which micrographs were obtained using the Inlens detector, some cracking is visible. As shown in both Figure 3.43 (b) and (c), most of the cracks radiate from the PS beads. It is believed that the stresses created during drying and annealing just after deposition of the graphene layer on the substrate cause the tearing of the graphene around the protruding PS beads.

A representative scanning electron micrograph of the Easy Transfer CVD graphene on the silicon nitride microsieves is presented in Figure 3.44. Since the substrate is much flatter than the patterned PAA/Si substrate, much less cracking was exhibited by the single-layer graphene. In fact, most of the holes are completely covered by the graphene membrane and only a few are ruptured similar to what was observed in the TEM grid samples (Figure 3.34). Furthermore, similar features to those observed in the CVD graphene supported on the SiO_2/Si substrates

which are attributed to grain boundaries and nucleation sites are also visible. It is worthwhile to note that less nucleation sites are visible in these samples.

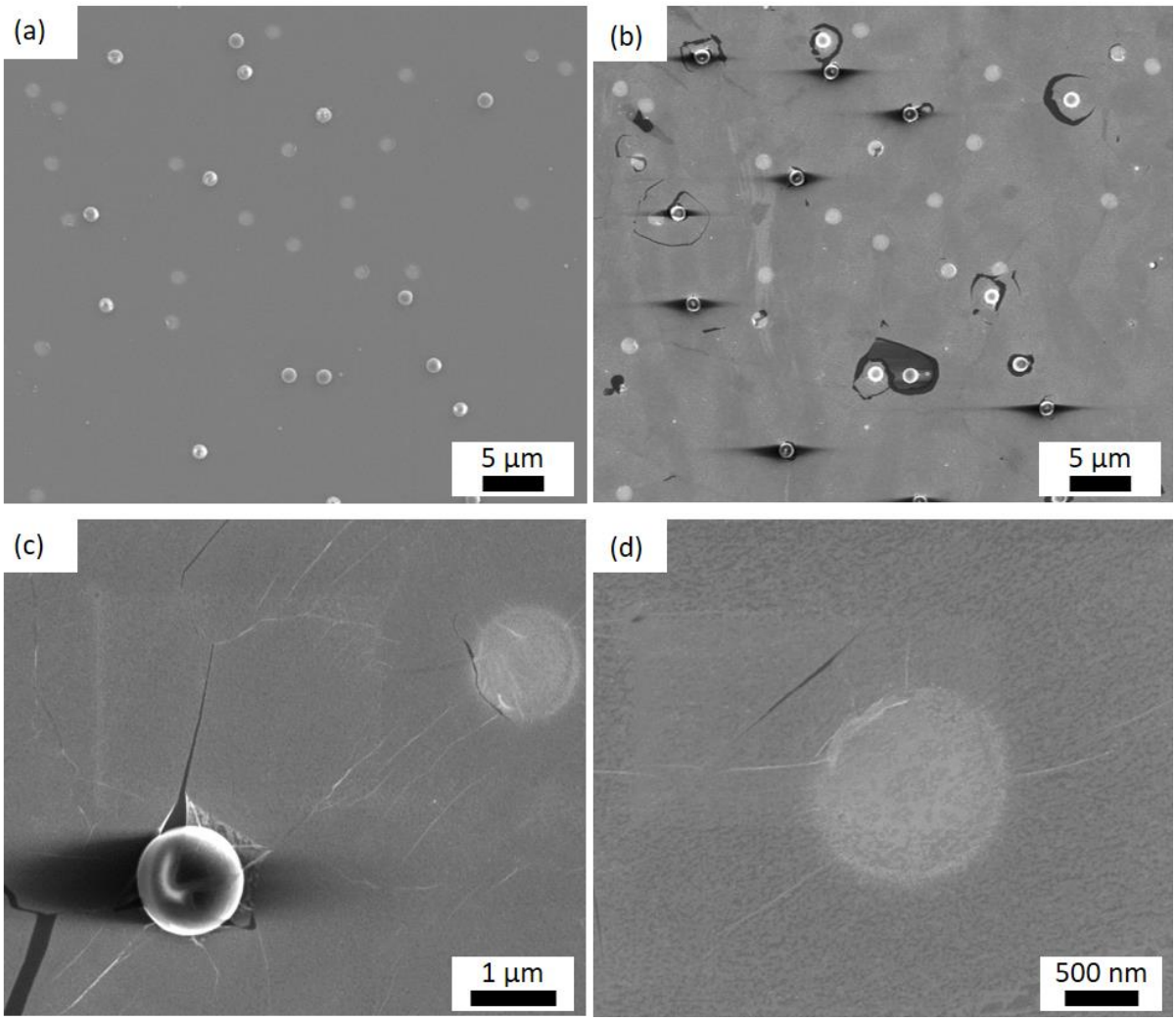

Figure 3.43: Scanning electron micrographs of suspended CVD graphene on the patterned PAA/Si substrate using (a) a secondary electron detector and (b – d) Inlens detector. (a) and (b) show the same area of the sample using different detectors.

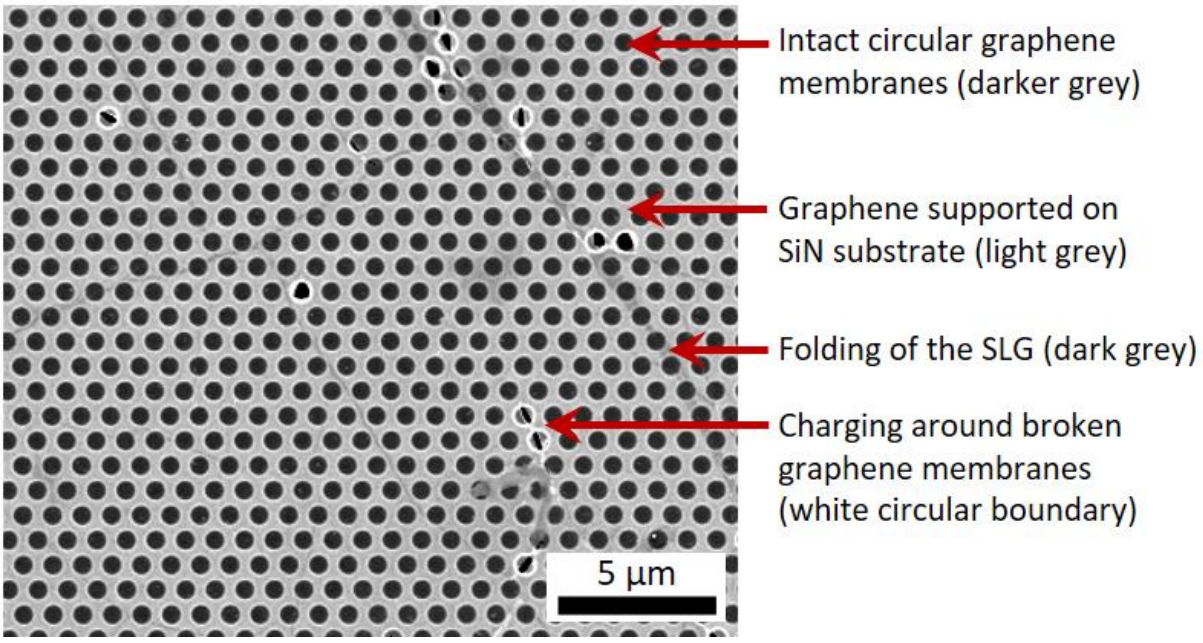

Figure 3.44: Scanning electron micrograph of suspended CVD graphene on a 0.45 µm silicon nitride microsieve.

3.4.4 Concluding Remarks

A total of three sources of CVD-grown single-layer graphene were investigated for their suitability in this work. Although the supported CVD graphene on SiO_2/Si was not suitable for subsequent indentations due to the absence of the required drum-like free-standing graphene membranes, these samples served as a good control during characterisation. The high I_{2D}/I_G ratio of the Raman spectra confirming that the graphene was single-layered validated Raman spectroscopy as a means to detect single-layer graphene. Furthermore, the observation of features attributed to grain boundaries and nucleation sites via both optical and scanning electron microscopy confirmed the ability of these two characterization techniques to image graphene.

As discussed in Section 3.4.2, the as-received SLG on TEM grids proved difficult to handle without damaging the TEM grid and overlying graphene. Furthermore, the excessive variability in the D band measurement caused large scatter in the subsequent experimental results. For these reasons, further experimentation on these samples was limited. Nonetheless, the ability of both SEM and AFM to image the presence of free-standing graphene membranes was noteworthy and encouraging for this work.

Finally, the Easy Transfer CVD graphene was successfully transferred onto both the patterned PAA/Si substrate and even more so on the silicon nitride microsieves. As discussed in Section 3.4.3, the Easy Transfer graphene on the silicon nitride microsieves produced a sample

which was well-suited for subsequent indentation and experimentation. In particular, the presence of a significantly large area of single-layer graphene originating from the same growth and transfer parameters, covering a large array of size-controlled holes means that further experimentation would lead to more repeatable results. Furthermore, AFM imaging confirmed that most of the membranes were without any defects such as significant perturbations, wrinkles or rupture. The only limitation encountered with the use of the silicon nitride microsieves, which will become more evident in Chapter 4, is that the supporting microsieve had an ordered array of holes and no other prominent features which would otherwise allow identification of single specific graphene membranes. This means that it was not possible to perform repeated indentation experiments on exactly the same membrane.

Chapter 4 NANOINDENTATION USING ATOMIC FORCE MICROSCOPY

4.1 INTRODUCTION

For the atomic probe studies carried out in this work, an RHK UHV 750 Variable Temperature Ultra-High Vacuum (UHV) Atomic Force Microscope (AFM) equipped with a Beetle^{TM} scanning head and SPM 100 controller, PLLPro2 Universal AFM Control and PMC 100 controllers (supplied by RHK Technologies Inc., Troy, USA) integrated within the Integrated Characterization Facility (ICF) was used. The AFM was operated at a high vacuum pressure of around 3×10^{-9} mbar. XPMPro 2.0.1.1, PLLproII Front End 0.20.0, and OriginPro 9.0.0 were used for data acquisition and post-processing. The use of the AFM within the ICF offers multiple benefits over the use of simpler AFM set-ups that operate at ambient conditions. Apart from the AFM, the ICF has many other sample preparation and characterisation techniques such as ion sputtering to clean the sample surface, X-ray photoelectron spectroscopy, Auger electron microscopy, low energy electron diffraction and scanning tunneling microscopy, all operating at high vacuum pressure. As such, one would be able to characterize the sample using different techniques without exposing the sample to ambient conditions and hence contaminating the sample.

As described in Chapter 3, the AFM was initially used in the static contact mode for topographic imaging of the graphene samples and membranes. Force spectroscopy was then used to perform indentations on the graphene membranes and obtain the required force-distance (FD) curves.

In Section 4.2, a brief description of the AFM theory and set-up is presented together with the procedure adopted for tip installation and characterization. Section 4.3 and Section 4.4 describe the methods used for static mode imaging and force spectroscopy, respectively. A description of the system nonidealities observed together with the necessary data post-processing, corrections and calibration procedures are included. Finally, Section 4.5 and Section 4.6 present and discuss the results obtained for the indentations performed on the as-deposited

mechanically exfoliated graphene membranes and as-deposited CVD-grown graphene membranes, respectively.

4.2 BACKGROUND AND THEORY

As mentioned in Chapter 2, atomic force microscopy is a versatile technique which is often used to study graphene. This section will present the relevant theoretical background required to understand the physical principles used in AFM. Firstly, the tip-sample interaction forces are described in Section 4.2.1. Two of the main AFM modes which are often used to image the sample surface are the static contact mode and the dynamic non-contact mode. These will be briefly explained in Section 4.2.2 and Section 4.2.3, respectively. Section 4.2.4 presents the theory behind force spectroscopy which is used for the nanoindentations in this work, while the AFM set-up used in this work is explained in Section 4.2.5. Finally, a few notes on the AFM probes to be used together with the characterization methodology required are given in Section 4.2.6.

4.2.1 TIP-SAMPLE INTERACTION THEORY

To understand how the AFM probe is able to feel the presence of the sample, the interactions present between two bodies of condensed matter must first be established. On the atomic scale, the interaction energy present between two neutral atoms can be broadly described by the Lennard-Jones potential, illustrated in Figure 4.1 (a). At large separations (or distances), van der Waals forces exist between the two atoms due to the fluctuations in their polarization whereby the electronic cloud of one atom is attracted towards the nucleus of the other due to their unlike charges. Although the weakest of the interaction forces, van der Waals are significant in the nanoscale and increase substantially as the separation decreases. However, at shorter interatomic distances, the electronic clouds of the two atoms start to overlap and cause repulsion. The Lennard-Jones potential thus represents the net potential energy by considering the competing attractive and repulsive forces. Other possibly stronger long-range forces may exist such as magnetic forces, electrostatic forces and capillary forces. However, for the scope of this work in which the samples and tips are not magnetic and capillary forces are not present due to the ultra-high vacuum conditions used, such additional forces are not considered.

The resulting interaction force present between the two bodies, shown in Figure 4.1 (b), can be obtained by differentiating the potential energy. Due to such mathematical transformation, the

turning point or minimum of the potential energy curve in Figure 4.1 (a) translates to the point of zero force in Figure 4.1 (b).

In AFM, a very sharp tip, with a radius typically ranging from 5 to 50 nm, attached to a flexible cantilever, with typical normal spring constant ranging from 0.1 to 100 N/m, is used to detect such small interaction forces. The change in the forces acting between the sample and the AFM tip are detected during scanning, and can then be analysed in order to obtain qualitative as well as quantitative information on the sample surface such as the topography, elastic stiffness, adhesion and frictional properties.

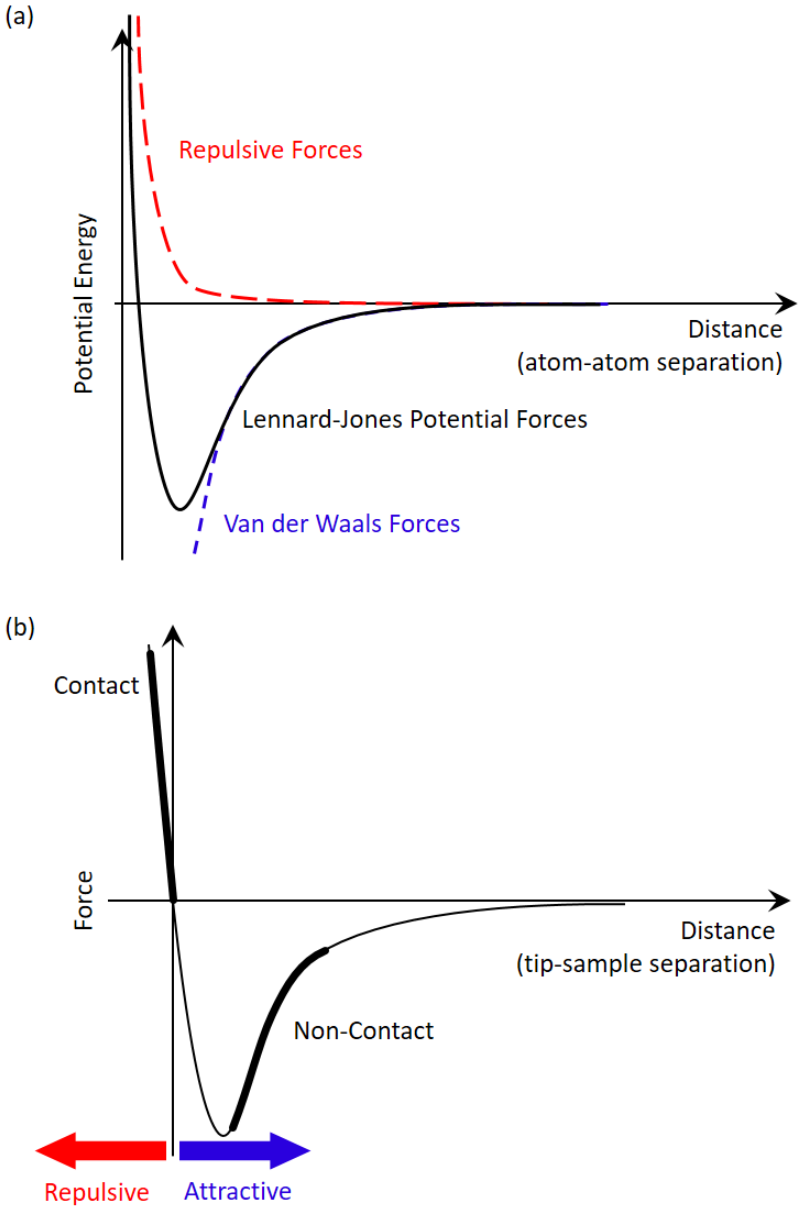

Figure 4.1: The (a) potential energy and (b) interaction force between two bodies as they are brought closer to each other.

4.2.2 STATIC CONTACT MODE

In static contact mode imaging, the tip is in contact with the sample causing repulsive forces to deflect the tip-cantilever assembly. In order to obtain topographic images of the sample, the tip is dragged across the sample as shown in Figure 4.2 (a) in a raster motion and the deflection of the cantilever is monitored. A feedback system is able to maintain a constant force between the tip and the sample, referred to as the normal setpoint force.

For high resolution topographic imaging, static contact mode is typically employed using a soft cantilever (with low normal spring constant) such that the cantilever will be easily bent without causing any damage to the sample or tip during scanning. A variation of this technique, also known as lateral or frictional force microscopy, can be used to study the frictional properties of the sample by appropriately selecting a cantilever with a soft torsional stiffness so that the cantilever will be able to twist along its longitudinal axis during scanning, hence detecting the lateral interaction forces rather than the normal forces. In this technique, rougher surfaces with higher frictional properties will cause the cantilever to twist more. The degree of twisting is then analysed to obtain either comparative data for the same setup, or else quantitative data given that all the parameters are known. In the AFM set-up used in this work, the frictional force data is obtained simultaneously with the normal force data.

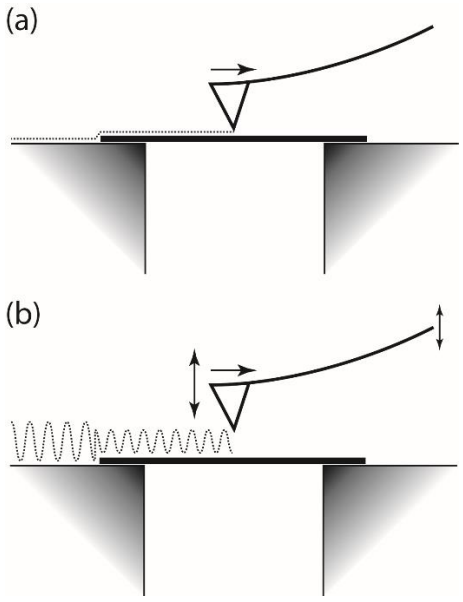

Figure 4.2: Simple illustrations of the tip motion relative to the sample surface during (a) static contact, and (b) dynamic non-contact AFM modes.

4.2.3 Dynamic Non-Contact Mode

In dynamic non-contact mode (Figure 4.2 (b)) the tip is not in contact with the sample, but held approximately 2 to 3 nm away, such that the attractive forces are substantial. In this mode, the cantilever is oscillated at frequencies close to its natural frequency (in the order of tens to hundreds of kHz), with amplitudes in the order of nanometers, with the tip never touching the sample during its oscillation period. Changes in the tip-sample attractive forces lead to a change in resonance frequency of the cantilever and hence amplitude of oscillation; the frequency shift or oscillation amplitude can be used as a measure of sample topography, while the phase shift reflects the sample material's elastic properties.

In contrast to contact mode, non-contact mode is sometimes preferred for softer samples since the tip does not touch the sample and hence would not induce any damage to either the tip or the sample. However, the control system of the dynamic non-contact mode is more complex and hence slower imaging is required. In fact, dynamic non-contact mode was only used to image the graphene membranes and understand the morphology of the wrinkles that form upon depositing the graphene on the well structures of the substrate.

4.2.4 Force Spectroscopy

While the previously mentioned AFM modes are typically used to obtain topographic information of the sample being scanned, the AFM assembly can also be used to investigate the material properties of the sample by indenting the sample and obtaining force-distance (FD) curves. Figure 4.3 (a) illustrates the motion of the tip during indentation as the tip is brought closer towards the sample (A to D) in the approach cycle and then retracted away from the sample surface (E to G). In more detail, the AFM probe is initially positioned away from the sample such that no tip-sample interactions exist. This is labelled as A in Figure 4.3 (a) and represents the flat region in the approach curve in Figure 4.3 (b). As the tip is lowered towards the sample, the attractive forces between the tip and the sample start to increase. If the cantilever is softer than the magnitude of these increasingly attractive forces, snap-to-contact occurs (B) at which point the tip is suddenly attracted towards the sample allowed by the bending of the cantilever. As the piezo actuator continues to lower the cantilever and tip towards the sample, the cantilever curvature increases until it is straight again (C). This is the moment when the attractive forces are equally balanced by the opposing repulsive forces, resulting in zero net forces. Upon further indentation, the tip and sample experience repulsion which causes the cantilever to bend upwards (D), as well as the sample material to be indented.

With appropriate tip-sample interaction models specific for the materials used, this region of the curve can be used to measure the elastic modulus of the sample. The model used for this work is explained in more detail in Section 4.4. Once the desired indentation depth is reached, the tip and cantilever are retracted away from the sample to obtain the retract curve in Figure 4.3 (b). In the ideal scenario, the force curve passes through the origin (zero-force) once again (E). In most cases, the energy required to break contact between the tip and the sample is larger than that required to put them in contact in the first place. This means that in force-distance curves, the tip-sample separation needs to be larger than that required for snap-to-contact until the tip suddenly breaks contact and snap-out-of-contact occurs. Region F in the force curve can be investigated to measure the adhesion properties of the sample. Beyond snap-out-of-contact, the tip-sample forces are once again negligible as illustrated in the flat region labelled G.

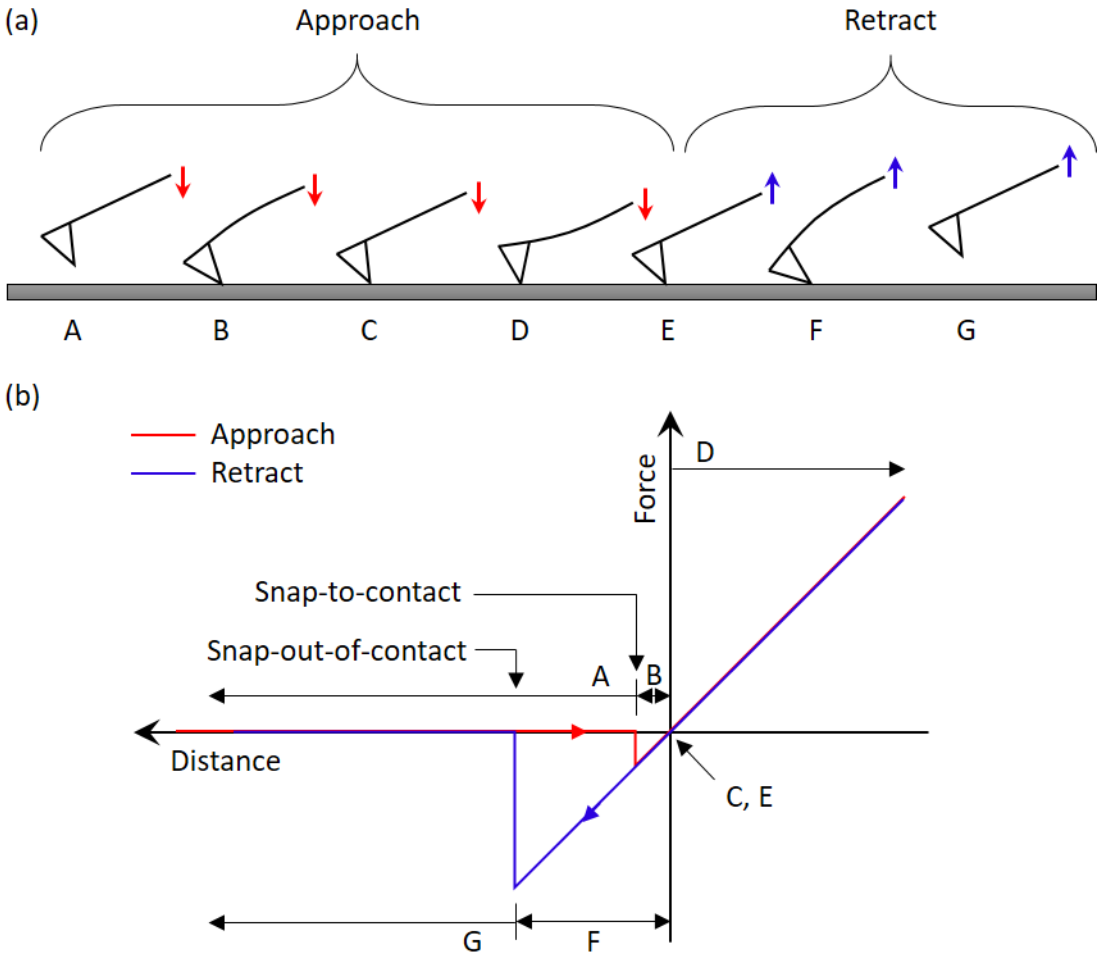

Figure 4.3: Theory of force-distance curves. (a) Labelled positions of the tip with respect to the sample during indentation. (b) A typical force-distance curve with the labels referring to the tip-positions in (a).

The AFM set-up used in this work is only capable of indenting the sample with the AFM probe while plotting the voltage of the photosensitive diode, that is the output of the sensor which detects the deflection of the cantilever, against the pre-set indentation depth, that is the voltage applied to the piezo actuators to lower the cantilever down into the sample surface and back. As such, such curves need to be converted into meaningful force against distance curves using a procedure explained in Section 4.4.

4.2.5 General Description of the AFM Set-Up

Figure 4.4 (a) and (b) show the ICF and AFM equipment used in this work, respectively, while Figure 4.4 (c) is a simplified schematic of the RHK AFM set-up. The three piezo tubes attached to the three outer legs of the scan head act as actuators providing coarse motion of the scan head in the X, Y and Z directions. In the schematic, the positions of the X, Y and Z scanners are modified for simplicity. These are primarily used to coarsely approach the AFM cantilever towards the sample surface and traverse the scan head across the sample surface. These three piezo tubes are also responsible to raster the scan head in the X and Y directions during scanning. In addition, the cantilever mount is coupled to the scan head via another piezo actuator stack which provides the Z motion during static contact scanning and force spectroscopy, referred to as the Z Scanner hereunder.

The RHK AFM is equipped with an optical lever detection system whereby a laser beam is reflected off the back of the cantilever and onto a segmented photosensitive diode (PSD) which detects any change in cantilever deflection and converts it into voltage. In order to get meaningful results, the piezo scanner needs to be calibrated to ensure that the measured dimensions during scanning match the real distance travelled by the scan head and thus the dimensions of the sample, as will be discussed in Section 4.3.1. Furthermore, for force spectroscopy, the Z Scanner needs to move a specified distance towards and away from the sample surface. Once the laser spot is reflected off the back of the cantilever and onto the PSD, the change in voltage recorded has to be converted to a measure of the cantilever deflection (Section 4.4.1). This cantilever deflection, d, can then be converted to the tip-sample interaction force, F, using Hooke's law, $F = kd$, where k is the cantilever spring constant.

This allows for routine calibration prior data acquisition and analysis such as to ensure that the readings measured, typically in volts by the sensors, are faithfully converted to the real heights or forces they represent, as well as to correct for, or at least minimize, the several nonidealities

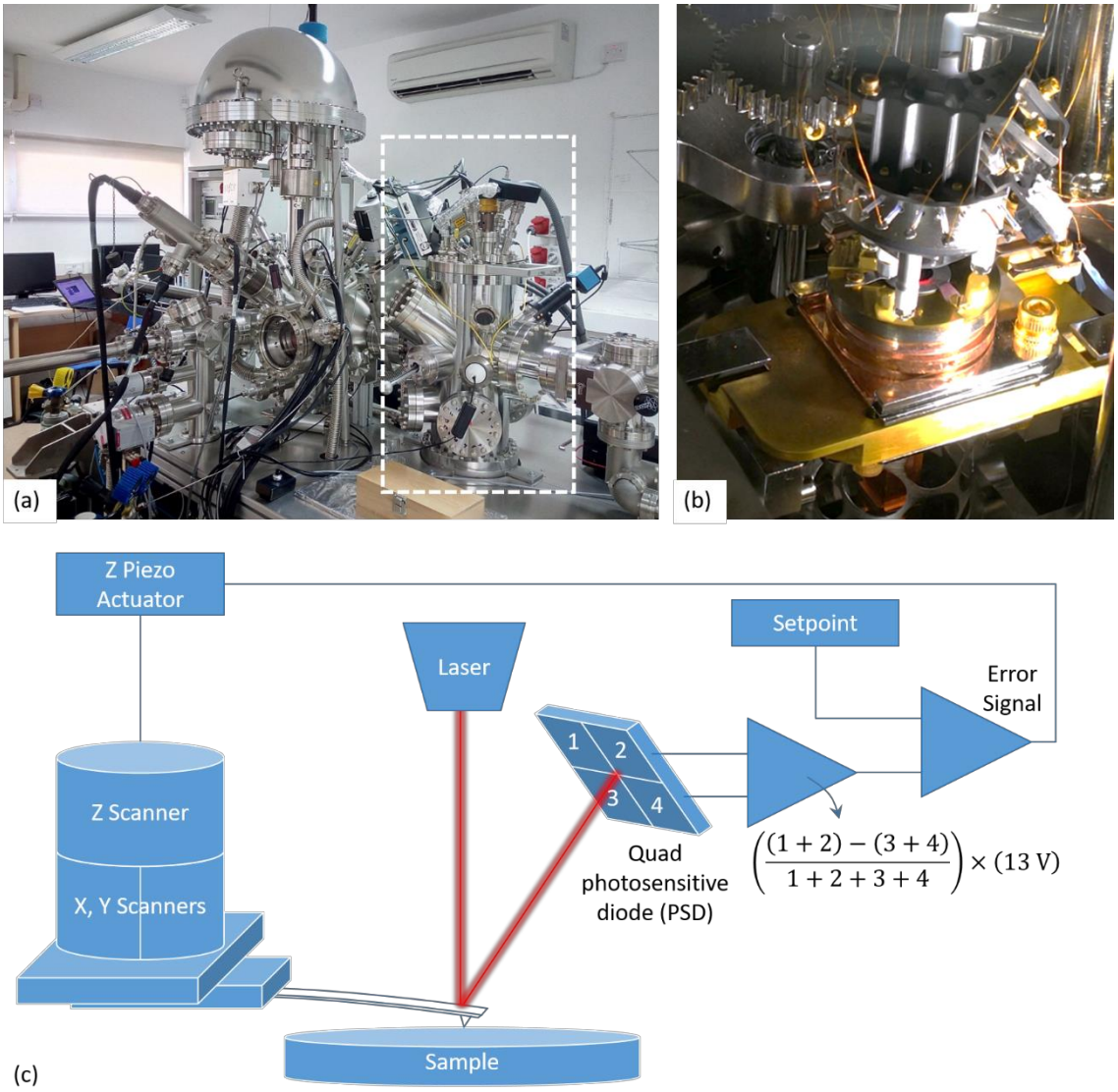

Figure 4.4: (a) The RHK UHV 750 AFM/STM chamber (enclosed in a dashed white box) within the Integrated Characterisation Facility (ICF) available at DMME, UM. (b) The Beetle™ scanning head and sample holder. (c) A simplified schematic of the AFM set-up working in contact mode.

the technique inherently possesses. In the following sections, the settings and calibration methods used are described.

4.2.6 The AFM Probe

4.2.6.1 AFM Probe Parameters

As the main force sensor, the AFM probe, typically consisting of a sharp tip attached to a flexible cantilever, is a key component for high sensitivity and reliable measurements. Since different samples and AFM modes require a different set of probe parameters and characteristics, the selection of the most appropriate AFM probe from the abundant different probes available on the market is logical. The main characteristics and parameters which are

typically considered for the selection and their effect on the operation of the AFM are discussed in the following.

4.2.6.1.1 Spring Constant, k

The spring constant of the cantilever, k in N/m, determines the interaction forces required to bend the cantilever. For topographical imaging, the spring constant needs to be quite low to enable the cantilever to flex with relatively low forces on the order of a few nanometers, such that the sample deformation is kept to a minimum [155]. This will allow the detection of very small forces by a measurable deflection of the cantilever. In fact, for static contact mode and high resolution imaging, a low spring constant is typically chosen to detect the smallest of forces and hence produce highest sensitivity.

On the other hand, the accurate measurement of the spring constant is vital for the accuracy of force-distance curves. In fact, during indentation, as the piezo scanner is lowering the cantilever and tip towards and into the sample, both tip deflection and sample indentation are taking place. The degree to which either of these occur depends on the relative stiffness of the cantilever and the sample material.

Due to the noise on the tip displacement detector i.e. the photosensitive diode (PSD), which tends to limit the depth resolution to 0.1 nm [230], the accuracy of the calculated forces can be on the order of 1 to 10 nN, depending on the cantilever stiffness [231]. Therefore, when obtaining force-distance curves to study the elastic stiffness of the sample, the spring constant has to be chosen to closely match the stiffness of the sample material [231]. If the cantilever is too flexible, the tip will not be able to indent the sample material before the laser spot is reflected off the PSD, and hence no meaningful results can be obtained. Conversely, if the cantilever is too stiff, some information on the initial repulsive regime of the interaction force might be lost. In other words, a stiffer cantilever will be required to measure the elastic modulus of stiffer materials [231].

Heurberger et al. [155] emphasise that in order to probe the elastic properties of a sample, one would need to choose a cantilever that will produce a larger deflection in the sample than the detection sensitivity of the cantilever bending.

4.2.6.1.2 Resonance Frequency, f_0

For static AFM modes, a high resonance frequency of around 10 to 350 kHz is generally desirable in order to minimize the sensitivity to vibrational noise from the building which is

near 100 Hz. The data rate or imaging rate in the AFM is also limited by the mechanical resonance frequency of the cantilever. As such, the AFM cantilever should have a resonance frequency greater than about 10 kHz in order to make the cantilever the least sensitive part of the system. Fast imaging rates are not just a matter of convenience, since the effects of thermal drifts are more pronounced with slow-scanning speeds. The combined requirements of a low spring constant and a high resonant frequency is met by reducing the mass of the cantilever, m, according to Equation 4.1.

$$f_o = \frac{1}{2\pi}\sqrt{\frac{k}{m}} \qquad \textit{Equation 4.1}$$

In fact, typical cantilevers made of silicon or silicon nitride have a rectangular shape with width of around 30 µm, length of around 100 to 400 µm and thickness of around 3 to 5 µm. Triangular cantilevers are also available, with their geometry optimized to achieve similar spring constants and resonance frequencies.

4.2.6.1.3 Tip radius, r

The tip radius should be much smaller than the radii of corrugations in the sample in order for these to be measured accurately. A blunt tip will not be able to detect finer corrugations in the sample surface and hence will produce an image with flatter topography in a phenomenon referred to as the 'tip-broadening effect'.

However, for indentation studies, a tip with a larger radius can be preferred to avoid large stress concentrations in the sample surface just under the tip [232, 233].

4.2.6.2 Characterisation Methodology

AFM probes are generally considered as consumables as the tip is often damaged during use, mainly due to wear or harsh collisions with the sample. Furthermore, in this study, different types of AFM probes were used to investigate the effect of various spring constants on the results obtained. As such, a procedure designed to streamline the handling of each AFM tip for characterisation, use, and subsequent replacement was established as follows.

First, a new AFM probe is mounted onto the AFM cantilever mount via conductive silver epoxy and aligned to optimize the reflected laser spot onto the PSD using the dedicated alignment tool. A two-part conductive silver epoxy (Agar Scientific, Elektron Technology UK Ltd., Stansted, UK) which cures at room temperature after 4 hours, or at 65°C after 10 minutes was used. This long-setting epoxy was selected as it allowed curing at room temperature in a

controlled environment and as such, cantilever and tip contamination was mitigated – particularly when compared to fast, high-temperature setting epoxies which require furnace curing.

To allow for safe manipulation of the cantilever and thus minimise potential damage to both the cantilever and tip, both of which are extremely fragile to the touch during handling and mounting onto the SEM stubs, a dedicated probe holder for the AFM cantilever mount was designed. Rendered images of the design in exploded and assembly views are shown in Figure 4.5 while the detailed drawings are presented in Appendix C.

Therefore, after curing of the silver epoxy, the cantilever mount is installed in the designed probe holder (Figure 4.5) and affixed to an SEM stub for SEM imaging. SEM imaging is used to measure the dimensions of the AFM cantilevers for subsequent calculation of their respective spring constants, as well as imaging of the tip to assess its condition both before and after use. For SEM imaging an accelerating voltage of 5 kV, probe current of around 80 pA and a working distance of 3 to 8 mm were used, together with the secondary electron and the Inlens detectors.

After SEM imaging, the cantilever mount is removed from the probe holder and mounted in the AFM probe exchanger. The probe exchanger is a propriety RHK holder that is used to insert the cantilever into the AFM chamber in preparation for use. After use, the tip is removed from

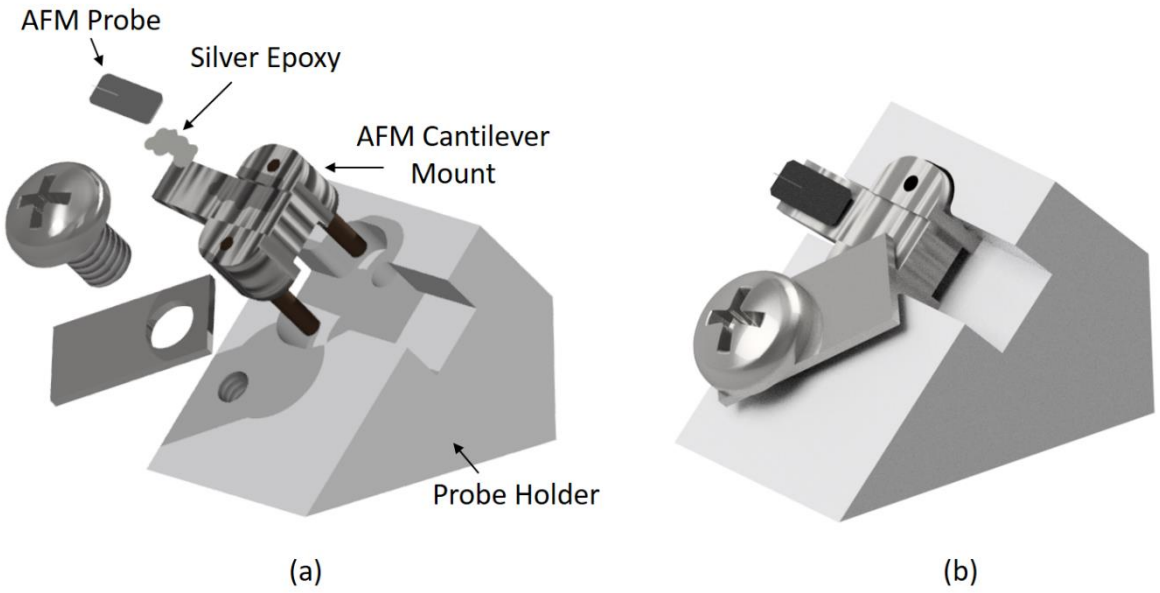

Figure 4.5: Rendered images of the designed and machined probe holder together with the AFM cantilever mount and the AFM probe in (a) exploded and (b) assembly views.

the AFM and once again transferred into the probe holder for SEM imaging. If the latter SEM imaging of the AFM probe indicates that the tip is compromised, the probe is discarded.

As highlighted in Chapter 2, the rationale behind the choice of the AFM cantilever's spring constant used is not always made clear in published reports, and to the best of our knowledge, the effect of the spring constant on the results has not been investigated systematically yet. In this work, three different types of AFM probes were used in order to investigate how probe characteristics can affect the results obtained. Details such as their tip material, nominal tip radius, r, nominal spring constant, k, and nominal resonance frequency, f_0, as provided by the manufacturer, are listed in Table 4.1.

Table 4.1: The AFM probe types used together with the tip material, nominal tip radius, nominal spring constant, $k_{nominal}$, and nominal resonance frequency, f_0, as provided by the manufacturer.

AFM Probe	Designation	Tip Material	Nominal Tip Radius, r	Nominal Spring Constant, $k_{nominal}$	Nominal Resonance Frequency, f_0
NanoWorld PointProbe® Arrow™ Force Modulation probes	FM50	Silicon	< 10 nm	2.8 N/m	75 kHz
BudgetSensors Tap190DLC probes	Tap190DLC	Diamond-like carbon (DLC) coated	< 15 nm	48 N/m	190 kHz
NANOSENSORS™ DT-NCLR probes	DTNCLR	Diamond coated	< 100 nm	72 N/m*	210 kHz

* The DTNCLR probes were obtained with a certificate from the supplier outlining the *individually* calibrated spring constants.

4.3 STATIC MODE IMAGING

Prior to indenting the prepared graphene membranes to obtain the force-distance curves, a topography image of the sample in static contact mode was obtained using a scan speed of around 3 to 9 μm/s. The scan speed was chosen as a compromise between the total acquisition time (typically limited to a maximum of 15 minutes per 6 × 6 μm area) and the quality of the image obtained. The latter is often dependant on the environmental vibration noise, sample

surface roughness, as well as quality of the AFM scanning tip in terms of tip radius and any tip contamination.

A normal cantilever deflection setpoint (as measured by the PSD) of 0.1 to 3 mV was used, equating to normal forces of between 0.1 nN and 140 nN depending on the cantilever spring constant used. The choice of the optimal normal force setpoint for each scan was once again dependant on the surface roughness of the sample, as well as the AFM probe characteristics, such as tip radius, tip material and/or the presence of any contamination on the tip, and cantilever stiffness, all of which effecting the strength of the tip-sample interaction forces. In general, lower force setpoints are preferred since they minimize (i) damage imparted to the graphene due to the sharp tip and (ii) wearing of the tip itself. However, for cantilevers with higher spring constants or blunted or contaminated tips, a lower setpoint often resulted into challenging approach routines during which the tip is falsely detected as being in contact with the sample. Therefore, higher setpoints of around 3 mV were preferred, even though the latter may cause more damage to the tip and sample.

Prior to imaging the graphene samples, the motion of the scan head had to be calibrated in order to ensure that the voltages supplied to the piezo electric actuators to move the scan head in the X, Y and Z directions are faithfully converted to the real distances moved in nanometres. The calibration procedure used is outlined in the following section.

4.3.1 Calibration of the Piezo Scanners

The AFM probe is moved across and normal to the sample surface via a set of piezoelectric actuators. As such, the required voltage supplied to the piezoelectric actuators in order to move the probe a known distance needs to be calibrated.

An XYZ calibration nanogrid (CS-20NG supplied by NanoAndMore GmbH, Wetzlar, Germany) featuring silicon dioxide structure arrays with a pitch size of 500 nm and step height of 21.5 nm on a silicon chip was used to calibrate the piezo scanners in the X, Y and Z directions. The grid was imaged in static mode using an FM50 cantilever, scanning area of 5 × 5 μm and scanning speed of around 9.5 μm/s. The pitch size and step height were measured from the data obtained (Figure 4.6) and the correct voltage-to-distance calibration values for the X, Y and Z Scanner were inputted in the hardware configuration settings. The same grid was imaged again to verify that the measured features conform with the calibration sample.

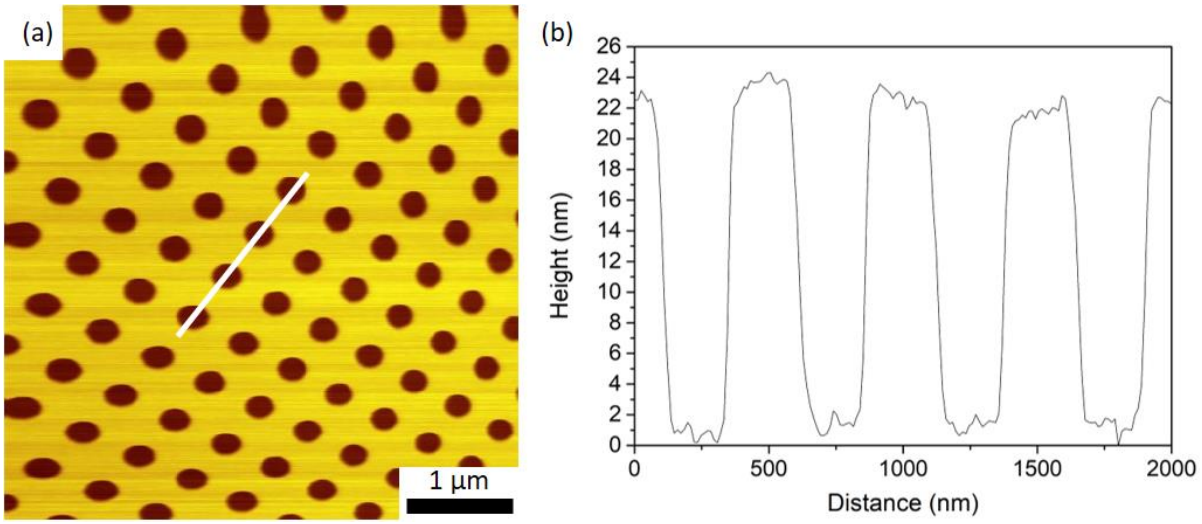

Figure 4.6: (a) A topography image of the XYZ calibration nanogrid circular structure. (b) A section view through the white line shown in (a).

This calibration routine was performed periodically to correct for any aging of the piezo actuators, that is the loss in sensitivity over time [234].

4.3.2 NONIDEALITIES

As with most actuators and sensors, both the piezo actuators and the photosensitive diode used in this AFM setup are inherently nonlinear and exhibit creep and hysteresis [235, 236]. This means that the above described calibration routine is only accurate for a specific set of machine parameters, sample-tip interaction, and system settings.

During X-Y scanning, creep in the X and Y piezo actuators is often manifested in the stretching and distortion of the image produced, as evident from the irregular pattern obtained when imaging the highly precise nanogrid structures shown in Figure 4.7 (a, b). On the other hand, hysteresis is manifested in the difference between the forward and reverse scans shown in Figure 4.7 (c). Since the error produced by such nonidealities would mainly affect scanning in the plane of the sample surface hence affecting the measurements of the lateral dimensions of the graphene flakes, these errors were not deemed to be critical to the major part of this study which revolves around force spectroscopy. As such, since piezo actuators are typically most linear at the centre of their travel range [237], the calibration factors from the calibration procedure outlined in Section 4.3.1 were optimized for the middle 3 × 3 µm area of the image.

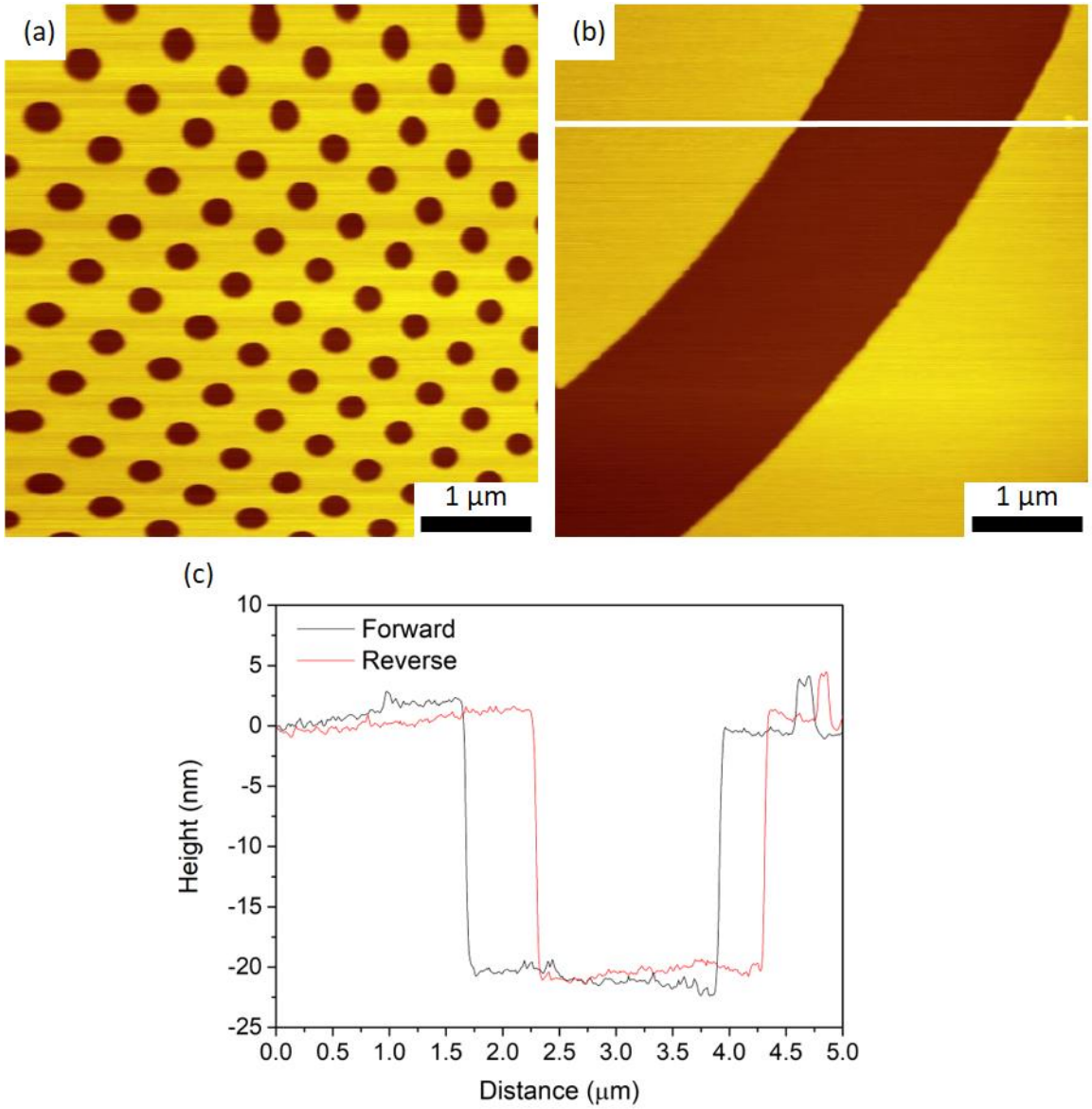

Figure 4.7: Topography images of the calibration nanogrid with the highly ordered structures showing the manifestation of hysteresis and creep through the distortion of the arrays; (a) circular structures with a pitch size of 500 nm (reverse scan), (b) linear structure with a pitch size of 5 µm (reverse scan), and (c) the forward and reverse scans of the section view across the white line shown in (b).

4.4 Force-Distance (FD) Curves

While Section 4.2.4 described the theory behind force spectroscopy including how FD curves are obtained together with a brief description of a typical curve, the following will explain the methodology used to obtain an FD curve and how the latter can be converted to a true tip-sample force against indentation distance curve.

After obtaining topographic images of the sample for which force curves were to be obtained, the tip was then moved to the desired location for indentation. When the FD curve was obtained to analyse the mechanical properties of the circular graphene membranes, the tip was located within ~50 nm of the centre of the membrane – allowing for positioning errors and drift.

For each sample, multiple PSD voltage [V] against Z Scanner pre-set indentation depth [nm] curves were acquired using a set sweep rate of 23 nm/s. The pre-set indentation depth was varied from around 10 nm up to around 100 nm, as discussed in Section 4.5.[6]

The procedure used for converting indentation curves to true tip-sample force against indentation distance is outlined below. The following subsections will describe the various calibration factors and corrections required.

1. In accordance with the procedure which will be explained in Section 4.4.1, each curve was first post-processed for system nonidealities. In brief, for each PSD voltage against Z Scanner pre-set indentation distance curve obtained, the best first-order polynomial was fitted to the baseline and the interpolated polynomial subsequently subtracted from the entire force curve. Subsequently, the point of contact, i.e. zero net interaction force and zero indentation depth, was located manually and set as the new origin of the curve.
2. The PSD voltage [V] was then divided by the sensor sensitivity factor, S_s [V/nm], (Section 4.4.2) to obtain the cantilever deflection, d [nm], using Equation 4.2.

$$d\ [\mathrm{nm}] = \frac{PSD\ [\mathrm{V}]}{S_s\left[\frac{\mathrm{V}}{\mathrm{nm}}\right]} \qquad \textit{Equation 4.2}$$

3. The cantilever deflection, d, was subtracted from the Z Scanner pre-set indentation depth, D, to obtain the true indented depth, δ [nm], using Equation 4.3.

$$\delta\ [\mathrm{nm}] = D\ [\mathrm{nm}] - d\ [\mathrm{nm}] \qquad \textit{Equation 4.3}$$

4. The cantilever deflection, d, was multiplied by the cantilever spring constant, k [N/m] to obtain the tip-sample interaction normal force, F [nN], using Equation 4.4.

$$F\ [\mathrm{nN}] = k\left[\frac{\mathrm{N}}{\mathrm{m}}\right] \times d\ [\mathrm{nm}] \qquad \textit{Equation 4.4}$$

[6] Note that this procedure was also used to indent the XYZ calibration nanogrid for calibration purposes as discussed in Section 4.4.1.

5. Finally, the force, F [nN] was plotted against the indentation distance, δ [nm] to obtain the final FD curve.

The FD curves obtained from circular graphene membranes were then fitted to Equation 4.5 which approximates the indented sample to a clamped circular membrane of linear isotropic material loaded at the membrane centre [13].

$$F = \sigma_0^{2D}\pi\delta + \frac{E^{2D}q^3}{a^2}\delta^3 \qquad \textit{Equation 4.5}$$

where F is the applied force, δ is the deflection of the membrane at the centre point (or the indented depth), a is the graphene membrane radius, σ_0^{2D} is the pretension of the membrane, E^{2D} is the 2D elastic constant and q is a function of the Poisson's ratio and is taken as $q = 0.98$ [13].

4.4.1 System Nonidealities

The Z piezo actuator (or Z Scanner) also exhibits creep and hysteresis. However, unlike for the X and Y piezo actuators, errors in the Z piezo actuator will directly affect the accuracy of the FD curves acquired. As such, it was deemed necessary to investigate the nature and magnitude of these nonidealities.

In force-distance curves, creep and thermal drift is often manifested in the shifting of the FD curves with respect to the zero-force/voltage and zero-distance origin. As such, this can be easily corrected by manually locating the zero-force, zero-distance point (or zero-displacement point, (ZDP)) on the curve and shifting back each FD curve during post-processing [235]. While for force curves obtained from the hard calibration sample the ZDP is often easily identifiable, this post-processing procedure can be more difficult when the point of inflection cannot be clearly identified, and as such, determining this point will introduce undesirable errors.

Furthermore, the plateau region of the curve, also referred to as the baseline, in which the deflection should be close to zero, may be slanted or wavy with respect to the x-axis. This artefact is typically attributed to the non-ideal angle between the incident laser beam and the sample normal [235] and other minute misalignments in the AFM assembly [238]. To correct for the slanting baseline, a linear or first-order polynomial is fitted to the noncontact region, and the interpolated polynomial is subsequently subtracted from the entire force curve to adjust the linear contact region of the curve [238]. An example of this process is shown in Figure 4.8.

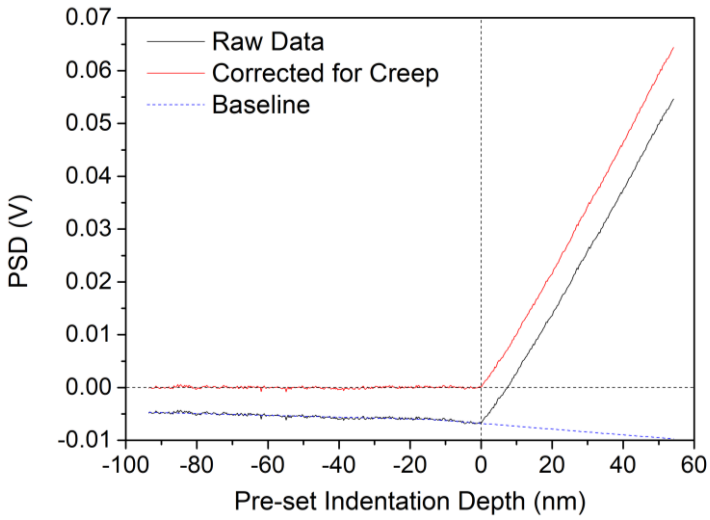

Figure 4.8: An indentation curve obtained from a silicon sample surface prior processing showing the curve corrected for creep (red) calculated by subtracting the baseline (dotted blue) from the raw data (black) and shifted such that the point of contact is at the origin.

Once again, fitting the most suitable first-order polynomial to the baseline relies on the proper identification of the zero-displacement point.

The second type of nonideality which can be observed in force-distance curves is hysteresis which is evident by lack of re-traceability of the approach and retract curves. More specifically, Z Scanner hysteresis is known to produce greater displacement data (more negative in the x-axis) during retraction per unit change of Z voltage [235], as shown in Figure 4.9. Furthermore, hysteresis is more significant when the piezo is actuated through a larger range as clearly visible when comparing curve *A* to *B* in Figure 4.9.

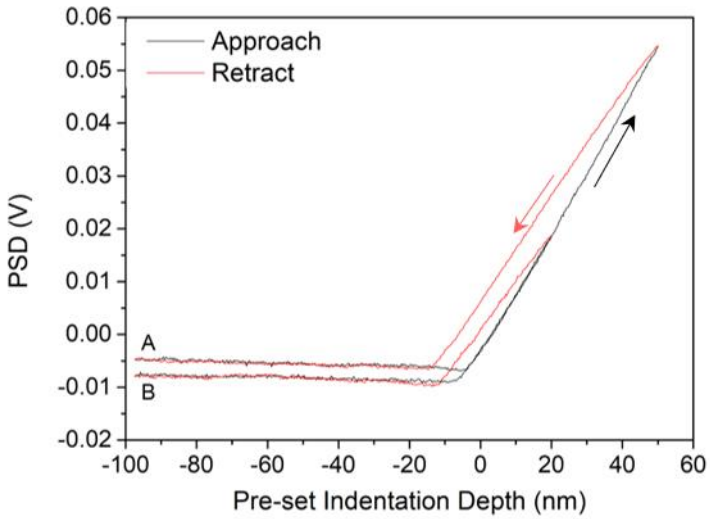

Figure 4.9: An indentation curve obtained from a silicon sample surface prior processing showing the approach (black) and retract (red) curves showing a hysteresis loop between them.

This hysteresis naturally introduces a number of issues when analysing FD curves.

(i) Firstly, if the Z Scanner produces a greater displacement upon retraction, then the zero-displacement point would be different for the approach and retraction curves, as indeed shown in Figure 4.9. Necessarily one curve needs to be selected for creep correction.

(ii) The sensor sensitivity factor, S_s, needs to be determined from the slope of the PSD vs. Z Scanner curve obtained from a hard silicon sample. If the slope of the approach and retraction curves are not the same, then once again one curve must be selected to determine this factor.

(iii) Finally, the S_s can vary with indentation depth because of the difference in hysteresis at different Z Scanner indentation ranges. In fact, indenting the hard silicon sample to different indentation depths (i.e. by varying the Z Scanner range) has been shown to result in different S_s values, as will be discussed in Section 4.4.2.1. Therefore, it should be established to what indentation depth should the calibration curve be performed to determine S_s.

It is worthwhile noting that the above nonidealities of the Z Scanner are measured by the PSD. However, as a sensor, the PSD may also contribute to these nonidealities. As such, the above results may be a combination of the nonidealities present both in the Z Scanner piezo actuator as well as in the PSD sensor. For the scope of this work, the nonidealities of the Z Scanner piezo and the PSD were considered jointly.

In order to limit the nonidealities inherently present in most AFM systems, a number of literature reports [236, 239, 240] attempt at finding a complex mathematical model to correct for these issues. Similarly, "second generation" AFMs integrate a closed-loop feedback system to correct for these nonidealities automatically, however this is obtained at the expense of other system capabilities such as resolution [235]. For AFM systems which do not have such capabilities, such as the RHK AFM used in this work, Haugstad [235] suggests to limit the cantilever deflection so that the nonidealities of the PSD are minimised [234], either by limiting the Z Scanner range or by using stiffer cantilevers – thereby obtaining similar forces at much lower deflections.

Haugstad [235] concludes by emphasising that while these nonidealities may influence absolute values, comparative analysis is still adequate given that the same cantilever and machine setup is used while the sample is the only variable.

4.4.2 CALIBRATION OF THE SENSOR SENSITIVITY FACTOR

For topographic imaging, the cantilever is only allowed to bend slightly such that the PSD senses only a small deflection of the laser (detected by a shift in the voltage) until the feedback system corrects for this via the piezo actuators. Conversely, force-distance curves depend on gross deflection of the cantilever and as such rely on the accuracy and sensitivity of the PSD in converting the motion of laser spot into true cantilever deflection.

To be able to convert the voltage measured by the PSD into cantilever deflection (refer to Equation 4.2), a force-distance curve must be acquired using the cantilever used for the preceding[7] measurements on a hard sample which resists indentation from the tip. To be consistent throughout this study, the same XYZ calibration nanogrid used in Section 4.3.1 was used as the sample to obtain S_s. In preliminary studies, for more flexible substrates such as the TEM Grids, the S_s was obtained both from the XYZ calibration nanogrid as well as from the substrate just next to the graphene membrane being indented. This was done to assess whether any bending or deformation of the substrate during the indentation of the graphene membranes affects the S_s. However, it was found that the difference in the obtained S_s from the two substrates is negligible. Therefore, the XYZ calibration nanogrid was used for all indentations performed to obtain the S_s.

When approaching and indenting a perfectly hard sample with the cantilever/tip, it can be assumed that the entire vertical distance that the Z Scanner is lowered beyond the initial contact between the tip and the sample is entirely translated to cantilever deflection and thus reflected into a PSD voltage. In other words, the resultant curve of cantilever deflection against Z Scanner depth should have a slope of 1. Thus, to convert the PSD voltage data [V] into cantilever deflection [nm] the PSD voltage is divided by the sensor sensitivity factor, S_s [V/nm], which is the slope of the PSD vs Z Scanner curve. Figure 4.10 (a) is an example of a curve acquired to obtain S_s, while Figure 4.10 (b) shows how plotting the obtained cantilever deflection against the Z Scanner will result in a slope of 1.

[7] Since indenting a hard silicon surface with the tip might damage the tip, this procedure is typically done *after* all the data is gathered on the experimental samples.

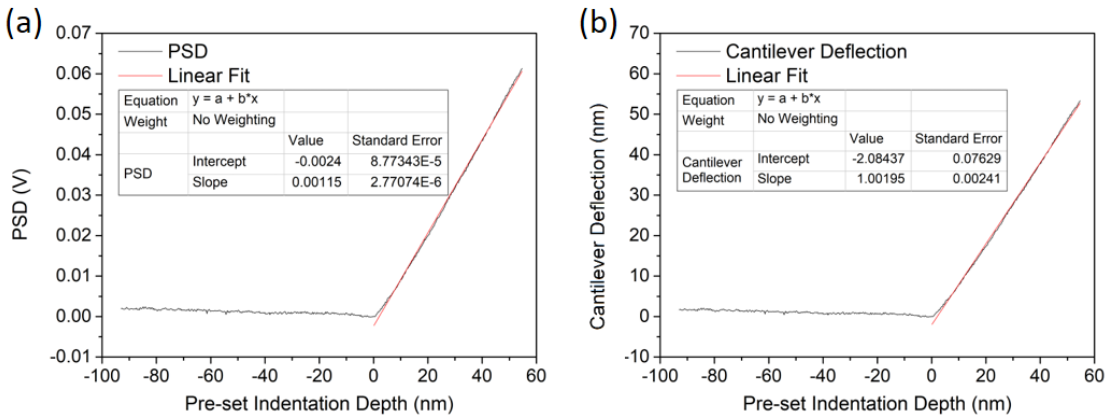

Figure 4.10: Force-distance curves against a silicon sample surface prior processing. (a) The raw PSD voltage [V] against Z Scanner distance [nm] data showing a slope i.e. Sensor Sensitivity Factor of 0.00115 V/nm. (b) The resulting Cantilever Deflection [nm] against Z Scanner [nm] upon dividing the PSD by the Sensor Sensitivity Factor to obtain a slope of 1.

4.4.2.1 Determination of the Sensor Sensitivity Factor

While a solution can be found to correct for most of the nonlinearities described in Section 4.4.1 the precise determination of the sensor sensitivity factor requires a more robust investigation. This section presents the methodology employed for such investigation. The results obtained allow for a set of conclusions to be drawn and for a methodology to be established for determining the S_s throughout the rest of this work.

Figure 4.11 shows representative indentation curves obtained from the XYZ calibration nanogrid, post-processed such that the point of inflection, or the zero-displacement point, of the approach curves coincide with the origin (0,0) of the plot. Both the approach and retract curves are shown, once again highlighting the hysteresis present as discussed in Section 4.4.1. However, while the slopes of the approach curves are visibly different than the slope of the retract curves, the slopes of the two approach curves which were obtained by indenting to different pre-set indentation depths are better aligned.

Standard nanoindentation studies [241] use the retract curves since it is assumed that the hysteresis is caused by plastic deformation of the sample. However, no plastic deformation is expected to happen with the indentation of graphene. Furthermore, results presented in Section 4.5 show that multiple indentation curves obtained from exactly the same location are very repeatable, confirming that the sample/tip/cantilever are only deforming elastically. Therefore, it was decided that the approach curves can be used this study.

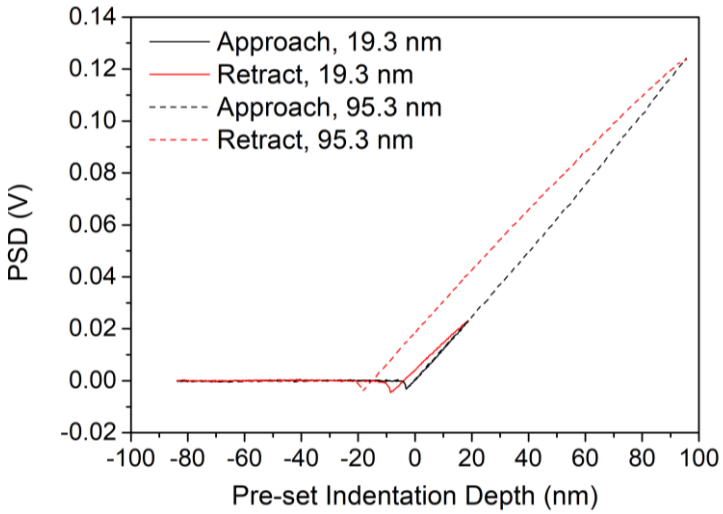

Figure 4.11: Representative calibration indentation curves obtained from the XYZ calibration nanogrid using Tap190DLC, showing both the approach and retract curves for maximum pre-set indentation depths of 19.3 nm and 95.3 nm.

In order to establish a method of determining the correct sensor sensitivity factor using the approach curve which is robust and applicable to different AFM probes, a number of indentations were carried out using the FM50, Tap190DLC, and DTNCLR probes. The pre-set indentation depth (i.e. the distance the Z Scanner piezo lowers the probe into the sample surface) was first ramped-up from 20 nm up to maximum (around 90 nm), and then ramped-down from maximum down to around 20 nm, in steps of around 10 nm. After the post-processing described in Section 4.4.1 to correct the baseline and zero-displacement origin, the slopes of the approach curves were fit to a straight line to obtain the sensor sensitivity factor, S_s, in each case.

The sensor sensitivity factors obtained at each indentation depth using some of the different probes are plotted in Figure 4.12 (a). Although from the two curves presented in Figure 4.11 obtained by the Tap190DLC, the two approach slopes appear to be the same, Figure 4.12 reveals an interesting phenomenon. Ideally, for linear piezo scanners, the sensor sensitivity factor should be the same for any indentation depth; however, as evident from Figure 4.12 (a), the calculated sensor sensitivity factor is in fact dependent on the indentation depth. As a representative example, Figure 4.12 (b) shows how the sensor sensitivity factor, S_s, ranges from ~1.16×10^6 V/m up to ~1.32×10^6 V/m when obtained using the same FM50 cantilever however at different indentation depths. Given that the cantilever deflection is linear according to Hooke's law, this phenomenon shows that it is the relationship between the Z Scanner piezo actuator and the PSD sensor, and hence the sensor sensitivity factor, which is nonlinear.

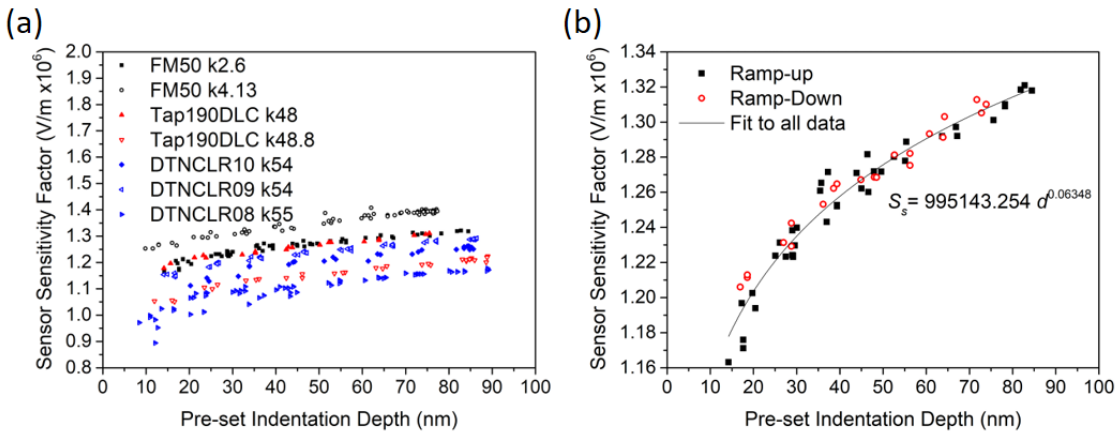

Figure 4.12: (a) The variability of the sensor sensitivity factor with pre-set indentation depth using three different types of cantilevers. (b) A representative relationship between the sensor sensitivity factor using an FM50 probe (k = 2.6 N/m) upon increasing (ramp-up) and decreasing (ramp-down) the indentation depth, showing a fit to the relationship $S_s = ad^b$.

In order to deal with the nonlinearity of the sensor sensitivity factor, two noteworthy observations can be made. Firstly, as evident from Figure 4.12 (a), different probes resulted in different sensor sensitivity factors. As such, the S_s has to be determined for every probe used and the force curves have to be post-processed using the individually found S_s. Secondly, for all probes used, the S_s varies with a similar power-law growth. Therefore, the relationship between the sensor sensitivity factor, S_s, and the pre-set indentation depth, d, can be found by fitting a power-law relationship of the form of $S_s = ad^b$ to the results, where a and b are constants, as shown in Figure 4.12 (b).

In order to determine the effect of the improved methodology for the determination of S_s on the measurement of the elastic modulus of the graphene membranes, the FD curves obtained from select graphene membranes were each calibrated both using a fixed average value for the S_s, (termed "Fixed S_s" hereunder) and by using the obtained $S_s - d$ power-law relationship (termed "Variable S_s"). The results are presented in Section 4.5, specifically Section 4.5.1.5.

4.4.3 Calibration of the Cantilever Spring Constant

In order to be able to convert the cantilever deflection (as measured in volts by the photo-sensitive diode (PSD) and subsequently converted to nanometres using the sensor sensitivity factor, S_s, as explained in Section 4.4.2) to a meaningful force value via Equation 4.4, the spring constant, k, of every cantilever has to be known. While manufacturers specify the nominal spring constant of the cantilevers, a slight variation in the individual cantilever

dimensions results in a large variability of the spring constants [235] rendering the use of the nominal spring constant as provided by the manufacturer not adequate for accurate force-distance data. As such, in absence of an in-built function to measure or calculate the spring constant of the cantilever, a suitable method had to be adopted for finding a more accurate value for the spring constant of every cantilever used.

Amongst the most frequently used methods of calibrating the spring constant of AFM cantilevers are the use of a reference cantilever having a well-known spring constant, the Sader method [242], the thermal tune method [243], and the geometrical methods [244].

Possibly one of the most accurate and theoretically straight-forward methods used to find the spring constant is the reference cantilever method which involves acquiring a force-distance curve with a cantilever of known spring constant (referred to as the reference cantilever) as the sample. However, the cantilever to be calibrated has to be positioned precisely over the reference cantilever, making sure that the tip is located very close to the end of the reference cantilever and centred on its principal axis, with both cantilevers being anti-parallel to each other [235]. With the equipment set-up used in this study, precisely locating the scanning cantilever over the reference cantilever is not possible.

Another well-known method of finding the spring constant is known as the Sader method [242]. This method has to be applied to a cantilever in a viscous fluid (air or water) [245]. Sader et al. [242] note that the resonant frequency of a cantilever depends on the fluid in which the cantilever is, mainly due to inertial effects brought about by the fluid. As such, the Sader method cannot be used under the UHV conditions used in this study [246].

The thermal tune method [243, 247], also considered to be an accurate method of determining the spring constant of the cantilever, requires a spectrum analyser to record the motion of the cantilever under thermal excitation, which is not available on the RHK AFM system.

This leaves the possibility of calculating the spring constant of the individual cantilevers using geometrical methods which require the accurate determination of cantilever dimensions. The most widely used method involves the measurement of the length, l, width, w, and thickness, t_C, of the beam, and calculating the spring constant, k, by assuming a known cantilever elastic modulus, E, with a rectangular cross-section using Equation 4.6:

$$k = \frac{Ewt_C^3}{4l^3} \qquad \textit{Equation 4.6}$$

As an improvement to this method, Poggi et al. [244] cater for the fact that most cantilevers actually have a trapezoidal cross-section rather than a rectangular cross-section which is assumed in Equation 4.6. However, the proposed method, referred to as the 'geometrical method with trapezoidal cross-section correction', still does not consider the mass of the tip which inherently introduces an inaccuracy in the calculated spring constant. The latter deficiency was addressed by Lubbe et al. [246] in the method referred to as the 'geometrical method with tip-mass correction'.

The method with tip-mass correction suggested by Lubbe et al. [246] is based on the work by Cleveland et al. [248] in which known precision weights are added to the end of the cantilever and the change in the resonance frequency is measured to calculate the spring constant of the cantilever. Lubbe et al. [246] measure instead the fundamental frequency and the first harmonic mode of the cantilever oscillation to derive the tip-mass correction that needs to be applied to the regular cross-section cantilever. The relevant theories underlying the calibration methods suggested by both Poggi et al. [244] and Lubbe et al. [246] are presented in Section 4.4.3.1 and Section 4.4.3.2, respectively.

4.4.3.1 Geometrical method with trapezoidal cross-section correction

This method of calculating the spring constant of the AFM cantilever only requires the accurate measurement of the dimensions of the cantilever and the elastic modulus of the material. The geometrical method of calculating the spring constant of the AFM probe with trapezoidal cross-section correction, as suggested by Poggi et al. [244], is based on the Euler-Bernoulli beam theory [249], in which the spring constant, $k_{trapezoidal}$, of a trapezoidal cantilever can be found using Equation 4.7:

$$k_{trapezoidal} = \frac{3EI}{l^3} \qquad \textit{Equation 4.7}$$

where E, l, and I are the elastic modulus ($E_{silicon}$ = 169 GPa [246, 250, 251]), length, and moment of inertia of the cantilever, respectively. Furthermore, the moment of inertia of a beam with a trapezoidal cross-section is given by Equation 4.8:

$$I = \frac{t_C^3(w_1^2 + 4w_1w_2 + w_2^2)}{36(w_1 + w_2)} \qquad \textit{Equation 4.8}$$

where t_C is the thickness of the cantilever, and w_1 and w_2 are the widths of the back side and tip side of the cantilever, respectively.

Following the use of this method, Poggi et al. [244] compare the resonance frequency of the beam based on the calculated spring constant ($k_{trapezoidal}$) to the direct measurement of the resonance frequency, and report an average difference of only 2%. Furthermore, the authors demonstrate a 15% relative uncertainty in their calculated spring constant. This is in contrast to a reported 15 to 25% overestimation of the spring constant measured assuming a rectangular cross-section, and a 21 to 43% overestimation when using Sader's method [244].

4.4.3.2 Geometrical method with tip-mass correction

Lubbe et al. [246] start by noting that the spring constants of a set of AFM cantilevers obtained by the geometrical method assuming a rectangular cross-section and those obtained using the reference cantilever method only deviate by a maximum of 15% between them, thus indicating that the geometrical methods (especially if corrected for the trapezoidal cross-section [244]) are quite accurate.

Nonetheless as an improvement to the above-mentioned method, Lubbe et al. [246] consider the oscillation analysis of the cantilever in vacuum together with the cantilever dimensions. In order to use the natural frequencies of the cantilever to correct for the tip-mass effect, the use of the following equations is suggested. A more detailed derivation is given by Lubbe et al. [246]. With the suggested method, the spring constant, $k_{tip-mass}$, can be found by Equation 4.9:

$$k_{tip-mass} = \frac{36\sqrt{2} f_n^3 \pi^3 l^3 (w_1 + w_2)^2}{\alpha_n^6 \sqrt{(w_1^2 + 4w_1 w_2 + w_2^2}} \sqrt{\frac{\rho^3}{E}} \qquad \textit{Equation 4.9}$$

where f_n is the eigenfrequency of the n^{th} mode, ρ is the density of the cantilever ($\rho_{silicon} = 2331$ kgm^{-3} [246, 252]), and α_n is found by solving numerically Equation 4.10:

$$\cos \alpha_n + \frac{1}{\cosh \alpha_n} + \mu \alpha_n (\tanh \alpha_n \cos \alpha_n - \sin \alpha_n) = 0 \qquad \textit{Equation 4.10}$$

μ is the ratio between the tip mass and the mass of the cantilever beam, and is related to Equation 4.11:

$$\frac{f_1}{f_0} = \frac{\alpha_1^2}{\alpha_0^2}. \qquad \textit{Equation 4.11}$$

Lubbe et al. [246] also provide a MATLAB script to solve for α_0, α_1 and μ given f_0 and f_1, attached in Appendix D. As such, this method requires the direct measurement of only the length and widths of the cantilever, and does away with the measurement of the cantilever

thickness which can be challenging to accurately determine due to alignment issues in the SEM. Yet, the fundamental frequency and its 1st harmonic need to be found.

Lubbe et al. [246] report that this method for calculating the spring constant reduces the uncertainty to only ±7%. However, they note that this method is less applicable to coated cantilevers since any change in the beam's material (via the presence of a coating) will change the parameters that need to be used in the beam model.

4.4.3.3 Determination of the Cantilever Spring Constant

In order to be able to select the most suitable method for the calibration of the cantilever spring constant, both geometrical methods with the trapezoidal cross-section correction as well as with the tip-mass correction were utilized for all the cantilevers used throughout this study. As such, before installing each probe in the AFM, electron microscopy was used to measure the cantilever's length, width and thickness, as shown in Figure 4.13. It should be noted that all the cantilevers had a trapezoidal cross-section. A frequency scan was also performed for all cantilevers inside the UHV AFM chamber to find their resonance frequency, f_0, and its 1st harmonic, f_1. As for the other cantilever parameters required, an elastic modulus of 169 GPa [246] and density of 2331 kgm^{-3} [246] were assumed for the silicon cantilevers.

Table 4.2 presents the cantilevers' dimensions, resonance frequency and spring constant as provided by the manufacturer, and as measured and calculated in this work for all the AFM probes used. First of all, it must be noted that the manufacturers provide quite a significantly large range of the expected cantilever spring constant for the FM50 and Tap190DLC probes. Such error will intrinsically introduce a large error in the calculation of the elastic modulus of the graphene membranes, rendering the rest of the results inaccurate. More specifically, the

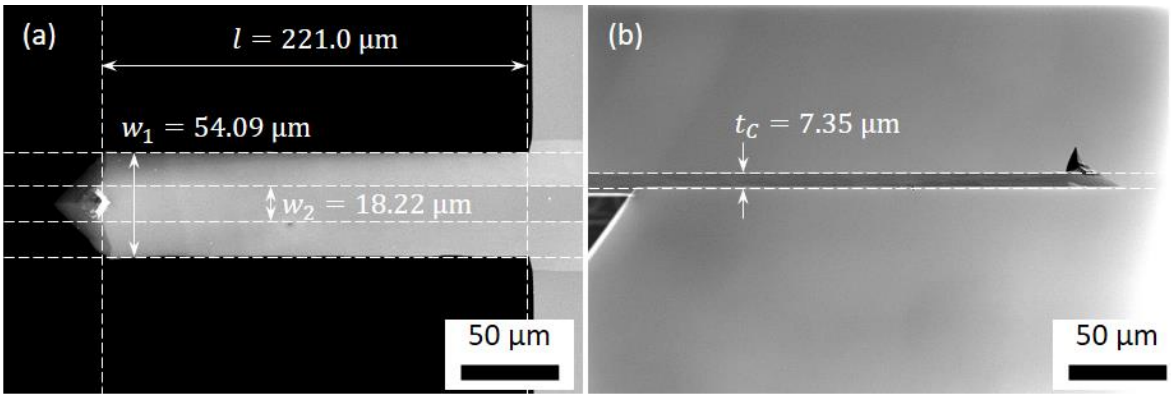

Figure 4.13: SEM micrographs of a Tap190DLC probe showing how the (a) length, l, widths, w_1, w_2, and (b) thickness, t_C, were measured.

equation used to derive the 2D elastic modulus from the force-distance curves (refer to Equation 4.5) shows that the 2D elastic modulus scales proportionally with the force, as in Equation 4.12:

$$F \propto E^{2D}\delta^3 \qquad \textit{Equation 4.12}$$

Since the 2D elastic modulus is directly proportional to the elastic modulus $\left(E = \frac{E^{2D}}{t_G}\right)$, and the force is scaled proportionally by the spring constant ($F = kd$, Equation 4.4), the spring constant, and so the error in the spring constant, is directly proportional to the calculated elastic modulus, as in Equation 4.13:

$$k \propto E \qquad \textit{Equation 4.13}$$

Therefore, an error in the spring constant of +108% and -50% for the FM50 probes as obtained by calculating the percentage error of the minimum and maximum values with respect to the nominal value given in the manufacturers' data as indicated in Table 4.2 (i.e. $\frac{5.8-2.8}{2.8} \times 100$ and $\frac{2.8-1.4}{2.8} \times 100$), will introduce proportionally the same error in the calculated elastic modulus. Thus, for example, for an elastic modulus of 1 TPa, the measured elastic modulus using the nominal spring constant of 2.8 N/m could vary from 0.5 TPa if the actual cantilever spring constant was 1.4 N/m, up to 2 TPa if the actual cantilever spring constant was 5.8 N/m. This highlights the need to individually calibrate the spring constant of every cantilever used.

As shown in Table 4.2, upon calculating the spring constant using the geometrical method with trapezoidal cross-section correction, $k_{trapezoidal}$, it was found that all the spring constants measured are indeed within the range specified by the manufacturers. Except for one FM50 cantilever for which the percentage difference between $k_{trapezoidal}$ (5.31 N/m) and the nominal spring constant (2.8 N/m) was 89%, the average percentage difference for the FM50 probes was 20%, that for the Tap190DLC probes was 17%, while that for the DTNCLR probes was 25%. Furthermore, calculating $k_{trapezoidal}$ for the DTNCLR probes, for which the manufacturer provided individually calibrated spring constants, revealed up to a 30% difference. According to the manufacturer, the spring constants were calibrated using a method based on the cantilever dimensions and thus it is not clear to what the difference between the two spring constants could be attributed. The fact that the manufacturer only provided one width dimension instead of two, which would otherwise completely characterise the trapezoidal cross-section, indicates that the method used assumes a rectangular cross-section.

Moreover, this discrepancy can also be attributed to the presence of the 100 nm thick polycrystalline diamond coating on the tip side of the cantilever which can alter the elastic modulus of the cantilever from that of silicon as used in the calculations.

The spring constant of the cantilevers was also found using the geometrical method with tip-mass correction, $k_{tip-mass}$, the results of which are also presented in Table 4.2. As mentioned previously, the resonance frequency and its 1st harmonic were found for every cantilever using the RHK AFM equipment. The resonance frequency can be easily determined and verified by comparison to the nominal resonance frequency specified by the manufacturer. It is the determination of the 1st harmonic that can be difficult. This is because for some cantilevers, only one peak in the frequency scan can be identified, hence attributed to the resonance frequency f_0 while for other cantilevers, multiple peaks can be detected in addition to the most intense peak at f_0. This causes some uncertainty to which frequency is the 1st harmonic.

In the provided MATLAB script, Lubbe et al. [246] suggest that the ratio of $\frac{f_1}{f_0}$ has to be larger than ~6.3 for the underlying beam theory used to be applicable. This was found not to be the case for most of the measurement obtained in this work. Such instances, found especially for the Tap190DLC cantilevers, resulted in a significant underestimation of calculated spring constant compared to $k_{nominal}$ and $k_{trapezoidal}$, with an average percentage difference from $k_{nominal}$ of 38%. This could be once again attributed to the presence of the 15 nm thick diamond-like-carbon coating on the tip side of the cantilever and a 30 nm thick aluminium coating on the backside of the cantilever which can change the oscillation behaviour.

To conclude, considering the above results, the method with tip-mass correction was deemed not sufficiently robust for this study. Specifically, this method could not be applied to every cantilever due to the difficulties in obtaining the 1st harmonic of the natural frequency, f_1. Therefore, it was decided that the method with trapezoidal cross-section correction was better suited to calibrate the spring constants of the FM50 and Tap190DLC cantilevers, with the average percentage difference between $k_{nominal}$ and $k_{trapezoidal}$ being less than the error given by the manufacturers' wide range of values. Finally, since the DTNCLR probes were calibrated individually by the manufacturer and the calculated $k_{trapezoidal}$ were always between 19% to 31% less than the provided values, it was decided that the manufacturer values were to be used. Furthermore, this was necessary to avoid the introduction of errors caused by the presence of the diamond coating which inevitably affects the beam's elastic modulus but is not accounted for by the geometrical technique.

Table 4.2: The cantilever length, l, width, w, and thickness, t, are given in µm, the spring constant, k, is given in N/m, and the resonance frequency, f_0, and the 1st order harmonic, f_1, are given in kHz.

	Nominal Values					Measured Values							
Probe	l	w	t_C	$k_{nominal}$	f_0	l	w_1	w_2	t_C	f_0	f_1	$k_{trapezoidal}$	$k_{tip-mass}$
FM50	240 ± 5	35 ± 5	3.0 ± 0.5	**2.8 (1.4 - 5.8)**	75 (58 - 97)	218.2	32.63	18.22	3.36	76.69	482.72	**3.82**	**2.29**
						221.0	32.63	17.64	3.20	77.14	-	**3.13**	**-**
						221.2	32.18	18.08	3.06	77.39	-	**2.74**	**-**
						219.9	32.04	17.34	3.82	77.97	487.97	**5.31**	**2.07**
						214.6	32.63	17.93	3.2	76.84	483.41	**3.44**	**2.16**
						211.9	32.33	17.64	3.23	75.00	489.94	**3.63**	**2.78**
						209.9	33.22	17.05	3.00	79.14	496.82	**2.99**	**2.10**
						221.3	33.22	17.05	2.90	79.44	511.79	**2.55**	**3.42**
						219.6	33.22	18.22	3.18	79.54	500.08	**4.13**	**2.58**
Tap190DLC	225 ± 10	38 ± 5	7 ± 1	**48 (28 - 75)**	190 (160 - 220)	226.6	56.44	19.40	7.80	160.72	1002.08	**60.15**	**31.22**
						224.0	55.30	18.67	7.76	159.64	-	**59.66**	**-**
						226.9	54.67	18.96	7.55	159.67	994.20	**57.34**	**29.82**
						224.0	55.26	18.81	7.81	159.05	999.69	**60.97**	**32.23**
						215.8	54.53	18.52	7.96	159.26	-	**71.17**	**-**
						225.2	54.97	18.81	7.91	158.57	987.73	**62.13**	**28.64**
						224.9	54.24	19.11	7.47	159.71	997.85	**52.44**	**28.92**
						224.9	53.50	18.22	7.77	156.27	975.72	**57.44**	**26.55**
						226.3	54.67	19.11	7.35	156.90	-	**42.72**	**-**
						225.8	53.79	18.22	7.06	156.43	186.70	**42.72**	**27.07**
						221.9	53.50	18.52	7.06	157.21	978.00	**45.15**	**26.04**
						215.5	53.50	18.22	7.06	156.56	1882.60	**48.86**	**56.87**
						219.6	53.79	19.11	7.64	157.58	1977.80	**59.96**	**62.19**
						221.9	54.67	18.81	-	156.51	1775.96	**44.86**	**63.50**
						221.0	53.20	18.22	7.30	156.30	975.50	**50.03**	**25.10**
						221.0	54.09	18.22	7.35	157.31	980.27	**51.58**	**25.93**
DTNCLR	225	35	6.4	**54**	189	224.4	53.50	18.22	6.76	193.02	1202.00	**38.08**	**49.70**
	225	35	6.4	**54**	189	219.6	54.38	19.99	6.47	191.93	1852.75	**37.32**	**114.38**
	225	35	6.5	**55**	190	218.1	54.38	18.52	6.80	194.50	1209.29	**42.91**	**47.45**
	225	35	6.6	**59**	194	217.8	54.09	18.22	7.06	192.13	1202.70	**47.76**	**45.22**

4.5 INDENTATIONS ON AS-DEPOSITED MECHANICALLY EXFOLIATED GRAPHENE

As outlined in Chapter 3, a PDMS stamp was used to mechanically exfoliate HOPG and subsequently deposit graphitic flakes onto the patterned PAA/Si substrate. The samples produced were imaged via optical microscopy to identify areas of high yield, and also identify and document thinner graphene flakes when these appear to cover the holes in the substrate – hence creating the desired circular suspended graphene membranes.

Samples with higher yields of such suspended flakes were then imaged using static contact mode AFM. Once a relatively thin graphene flake (typically less than 25 nm in thickness, as measured by AFM) completely covering one of the substrate holes has been located and imaged, the probe was situated in the middle of the circular graphene membrane to obtain a number of force-distance curves. FD curves were obtained both during ramp-up and ramp-down experiments. During ramp-up, pre-set indentation depths were increased from 10 nm up to around 100 nm, in 10 nm increments, whilst obtaining at least three repeated curves at each depth. This was followed by decreasing pre-set indentation depths from the maximum 100 nm down to 10 nm for the ramp-down experiments.

After the required FD curves from the graphene membrane were obtained, the same tip was used to image the XYZ calibration nanogrid and a number of FD curves were obtained for calibration purposes, as discussed in Section 4.4. Analysis of the FD curves, both for calibration purposes, as well as to convert the PSD voltage and Z Scanner pre-set indentation depth into the indentation force and true indented depth, was carried out according to the procedure outlined in Section 4.4.

A total of 12 graphene membranes across 8 mechanically exfoliated graphene flakes were indented and analysed using such procedures. Section 4.5.1 and Section 4.5.2 illustrate two representative case studies which were used to investigate a number of phenomena and relationships between different indentation parameters. A discussion on the results obtained upon indenting the case study membranes and other graphene membranes is presented in Section 4.5.3.

4.5.1 Case Study 1 – Flake D

Figure 4.14 shows an example of an optical micrograph of a graphene flake with a measured thickness of 16 nm together with corresponding AFM topographical images. Three AFM probes, whose details are listed in Table 4.3, were used both for imaging as well as for indentation studies using AFM. SEM images of the cantilevers and tips before and after use are shown in Figure 4.15, Figure 4.16 and Figure 4.17.

A number of FD curves using the Tap190DLC, FM50, and DTNCLR probes were obtained from the circular graphene membrane shown in Figure 4.14. Once again, the pre-set indentation depth was varied from around 10 nm up to the maximum value of 97.5 nm. The pre-set indentation depth was first ramped-up from minimum up to maximum, and then ramped-down from maximum down to the minimum indentation depth, in steps of 10 nm. For each depth, between 2 and 5 repeated readings were obtained.

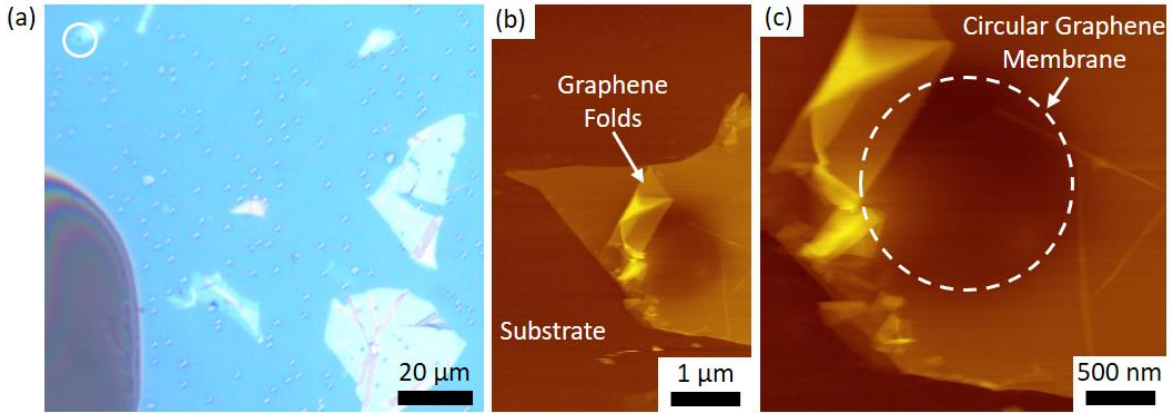

Figure 4.14: (a) Optical micrograph and (b, c) AFM topographical images of the graphene membrane investigated in Case Study 1. The circular graphene membrane as well as several folding of the graphene layers are indicated.

Table 4.3: The AFM probes used together with the nominal spring constant, $k_{nominal}$, and the calculated spring constants, $k_{trapezoidal}$.

Probe	**Nominal Spring Constant, $k_{nominal}$**	**Measured Spring Constant, $k_{trapezoidal}$**
FM50	2.8 N/m	2.74 N/m
Tap190DLC	48 N/m	51 N/m
DTNCLR	54 N/m *	

* As provided by the manufacturer's certificate.

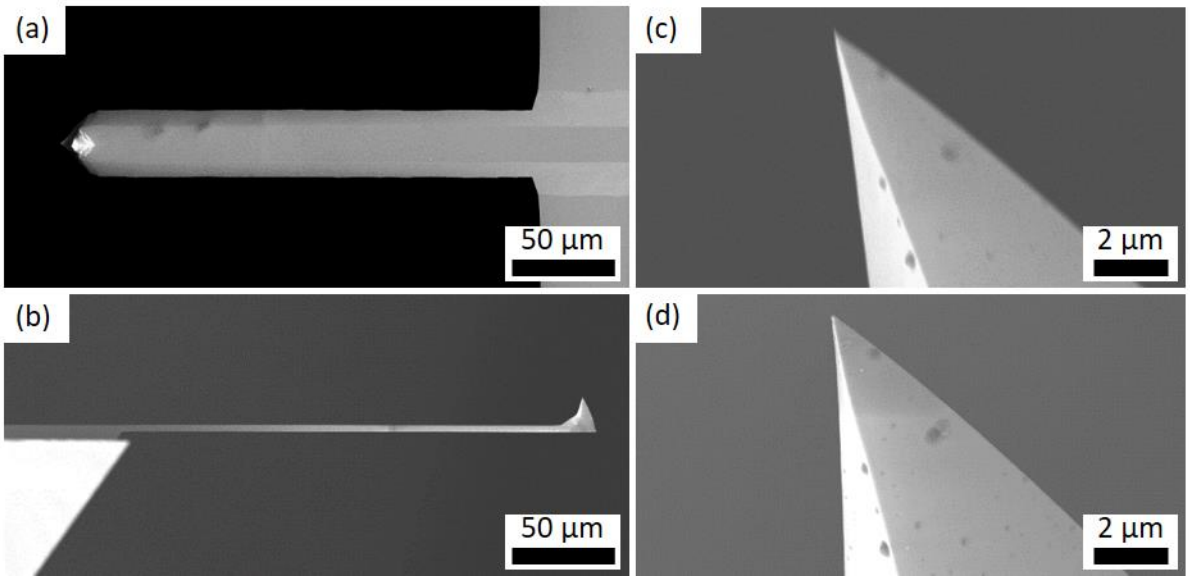

Figure 4.15: SEM images of the FM50 (a, b) cantilever and (c, d) tip (c) before and (d) after use.

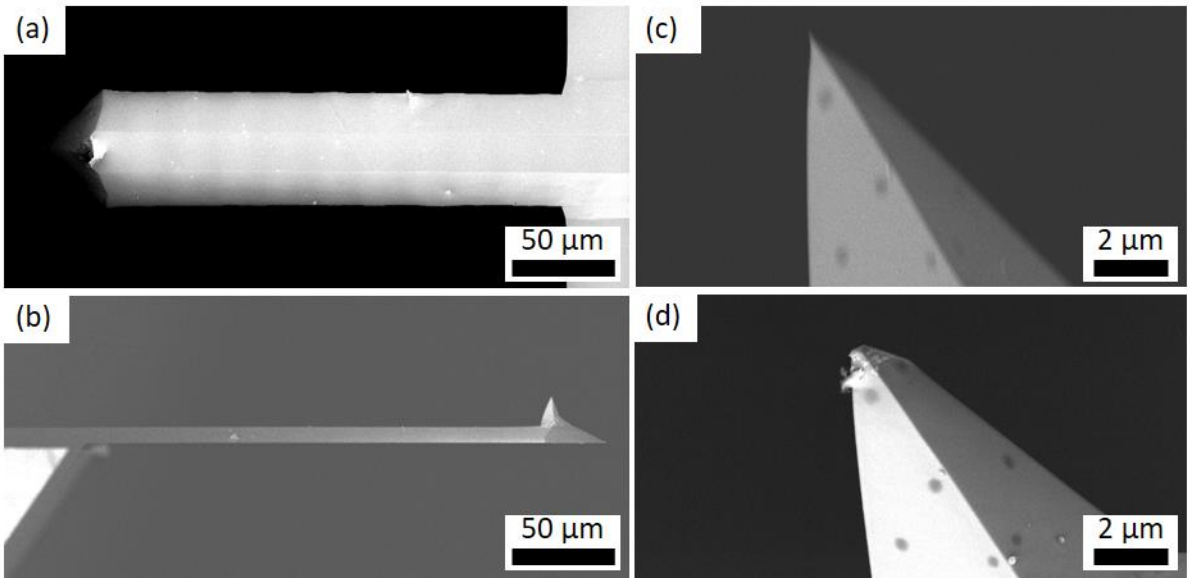

Figure 4.16: SEM images of the Tap190DLC (a, b) cantilever and (c, d) tip (c) before and (d) after use.

To investigate the system nonidealities in depth, a number of indentations were also carried out on the XYZ calibration nanogrid using the FM50, Tap190DLC, and DTNCLR tips. The pre-set indentation depth was first ramped-up from 20 nm up to a maximum of 95 nm, and then ramped-down from maximum down to around 35 nm, in steps of around 10 nm. The slopes of the approach curves were fit to a straight line to obtain the sensor sensitivity factor, S_s, which is required for the post-processing of the FD curves obtained from the graphene membranes.

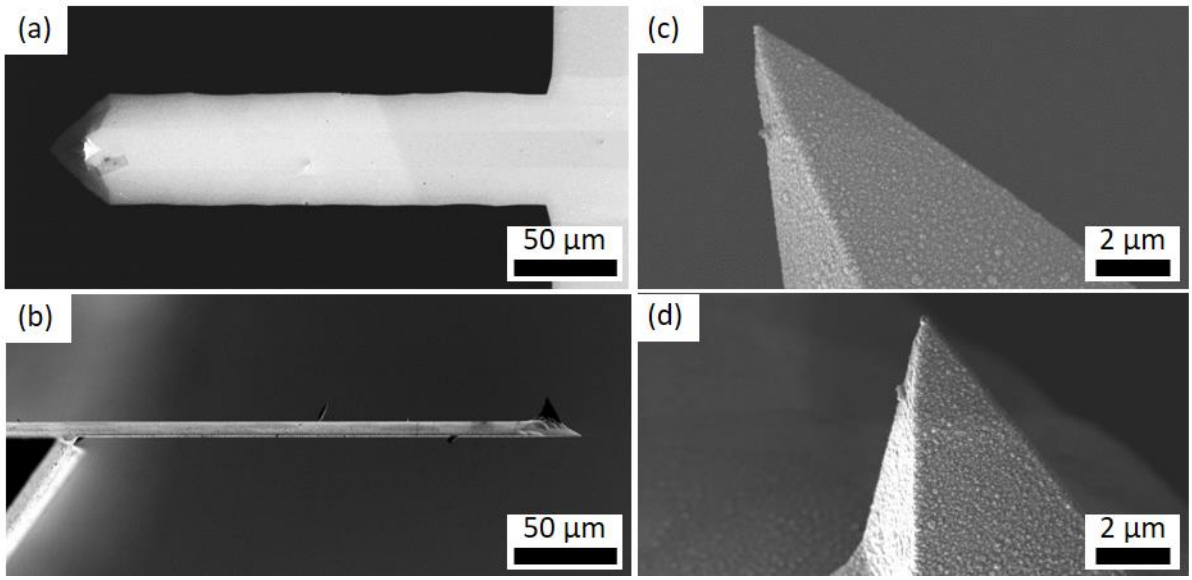

Figure 4.17: SEM images of the DTNCLR (a, b) cantilever and (c, d) tip (c) before and (d) after use.

4.5.1.1 Sensor Sensitivity Factor Calibration

Figure 4.18 shows representative indentation curves obtained from the XYZ calibration nanogrid, post-processed such that the point of contact of the approach curves coincide with the origin (0, 0) of the plot, as described in Section 4.4.1. Both the approach and retract curves are shown, once again highlighting the hysteresis present as discussed in Section 4.4.1.

The sensor sensitivity factors obtained at each indentation depth are plotted in Figure 4.19 (a), (b) and (c) for FM50, Tap190DLC and DTNCLR, respectively. Although from the two curves obtained by the Tap190DLC, presented in Figure 4.18, the slopes of the two approach curves

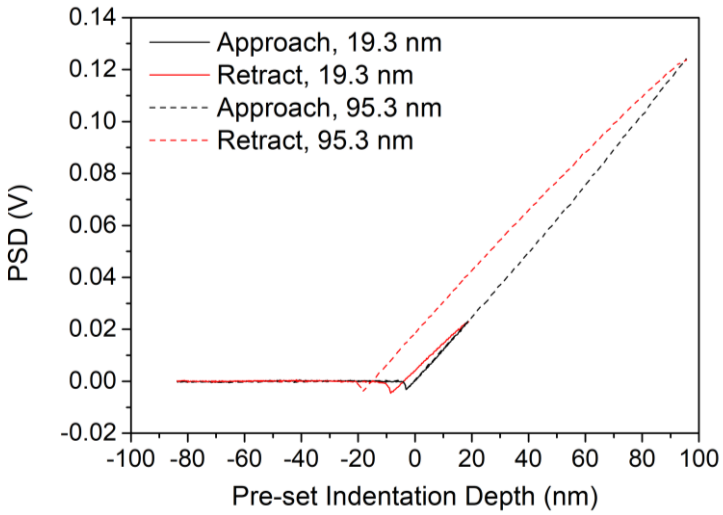

Figure 4.18: Representative calibration indentation curves obtained from the XYZ calibration nanogrid using Tap190DLC, showing both the approach and retract curves for maximum indentation depths of 19.3 nm and 95.3 nm.

appear to be the same in the overlapping region, i.e. up to an indentation depth of 20 nm, Figure 4.19 (b) confirms the nonlinearity of the piezo Z Scanner and/or the PSD sensor as discussed in Section 4.4.1. Specifically, from the data shown in Figure 4.19 (b), the piezo scanner appears to be linear for small indentation depths (up to around 40 nm) resulting in a S_s of around 1.217×10^6 V/m, yet nonlinear for larger indentation depths, increasing the S_s to 1.295×10^6 V/m for an indentation depth of 95.3 nm. A hysteresis loop between the sensitivity factors obtained from ramp-up and ramp-down curves is also indicated. A similar nonlinearity and hysteresis effect was observed using the FM50 cantilever, as shown in Figure 4.19 (a). Unlike the case when using Tap190DLC, the sensor sensitivity factor obtained using both the FM50 and DTNCLR probes was noted to be nonlinear throughout the range of indentation depths. As such, the sensor sensitivity factor was recorded to be as low as 1.076×10^6 V/m for an indentation depth of approximately 23 nm and as high as 1.166×10^6 V/m for an indentation depth of up to 80 nm for the FM50 while the sensor sensitivity factor using the DTNCLR probe varied from 1.134×10^6 V/m up to 1.338×10^6 V/m. Hysteresis between the ramp-up and ramp-down was not evident when using the DTNCLR probe.

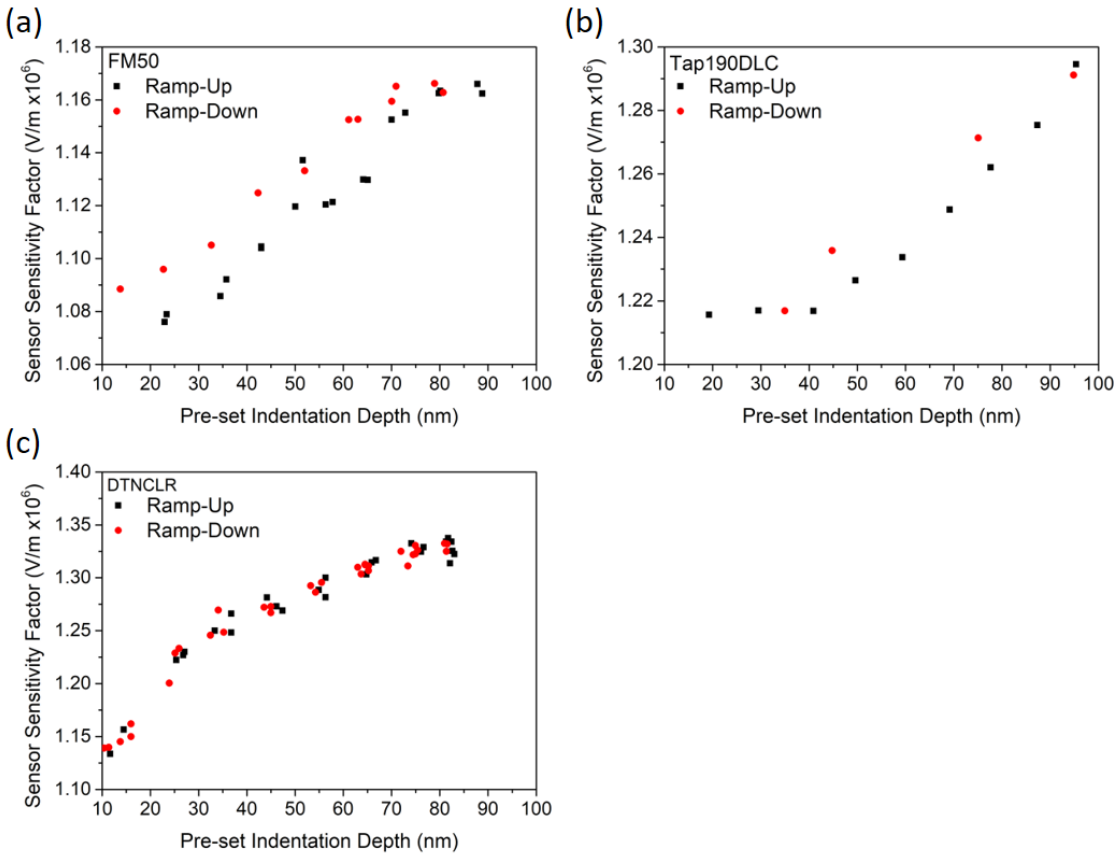

Figure 4.19: The sensor sensitivity factor, S_s, as measured from the slope of the approach curves for (a) FM50, (b) Tap190DLC and (c) DTNCLR tips.

In order to determine by how much the observed nonlinearity affects the final results for the FD curves obtained from the graphene membranes, the FD curves were each calibrated both using a fixed, mid-range S_s of 1.255×10^6 V/m for Tap190DLC, 1.130×10^6 V/m for FM50, and 1.280×10^6 V/m for DTNCLR, as well as an adjusted, variable S_s calculated according to the best function fitted to the data in Figure 4.19, i.e. considering the nonlinearity.

4.5.1.2 Indentation Experiments on the Graphene Membrane

Figure 4.20 shows a representative force curve as acquired from a single indentation, showing both the approach (loading) curve and the retract (unloading) curve. Although the retract curve does not perfectly retrace the approach curve, the hysteresis observed is correlated to the same hysteresis observed on the XYZ calibration grid with 'infinite stiffness', such as in Figure 4.18 (Section 4.4.1). As such, this hysteresis is attributed to nonlinearities of the AFM system rather than to plastic deformation of the sample. Accordingly, only the approach curves were used in the following analysis.

Figure 4.21 shows representative post-processed FD curves obtained from both the ramp-up and ramp-down using Tap190DLC, at different indentation depths. For clarity only the approach curves calibrated using a variable sensor sensitivity factor, S_s, are shown. It is clear that the FD curves obtained are generally very repeatable particularly up to an indented depth of 6 nm. A snap-to-contact phenomenon also occurred for all indentations as evidenced by the dip observed just before the (0,0) contact point. Some variation is noted at higher indented depths especially for the ramp-up curves, while the ramp-down curves overall differed slightly when compared to the majority of the ramp-up curves obtained. Nonetheless, the good repeatability for the obtained FD curves indicates that the graphene membrane is not being damaged by repeated indentation and no slipping is occurring. Similar results were obtained using the FM50 and DTNCLR probes.

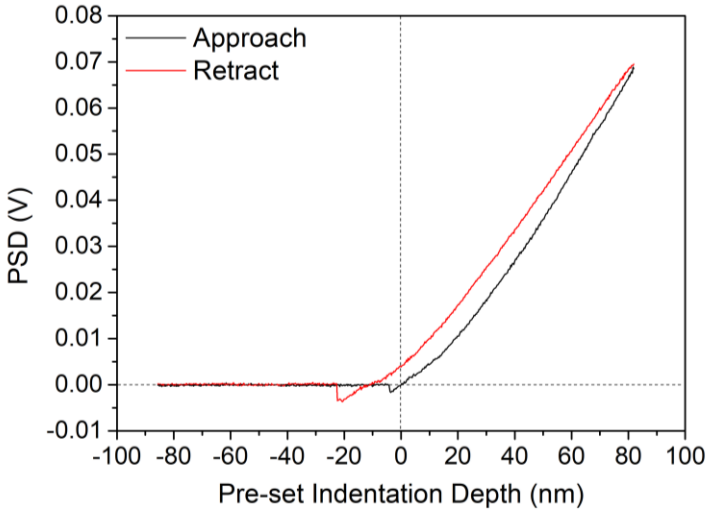

Figure 4.20: Representative FD curve showing the approach and retract curves for a single indentation prior post-processing.

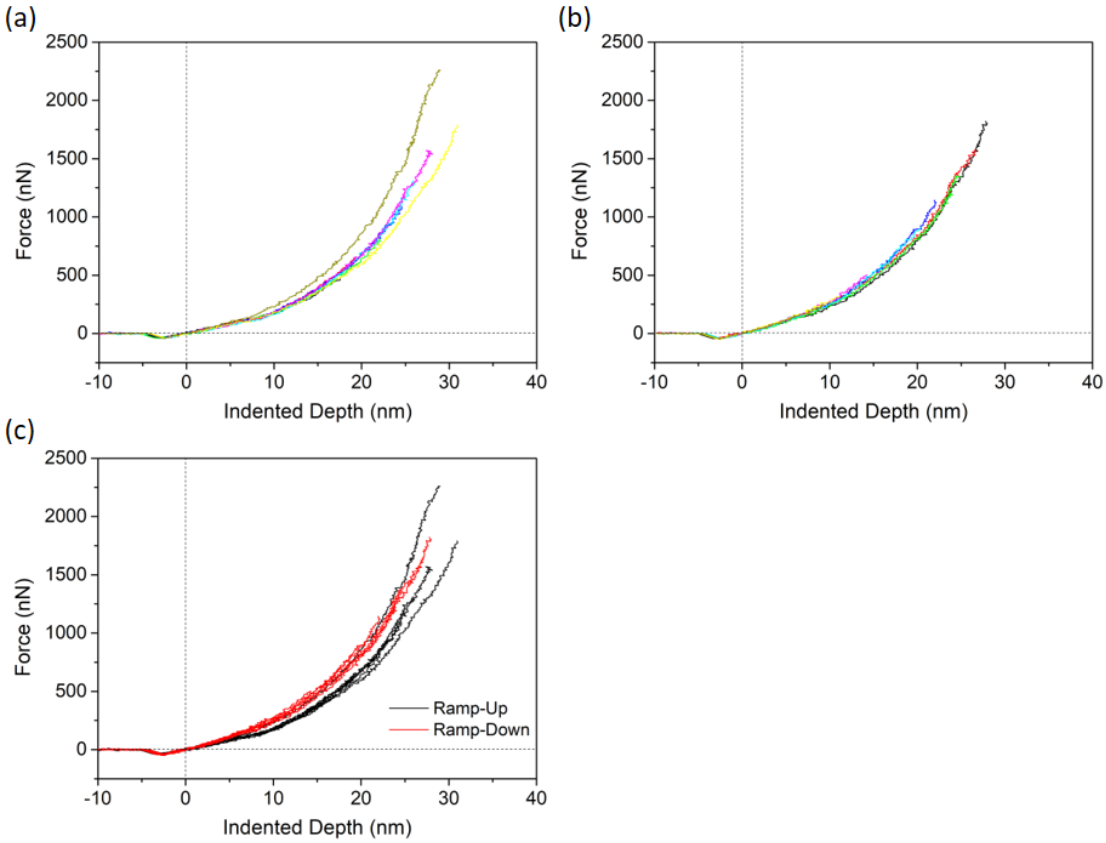

Figure 4.21: Representative FD curves obtained from the same graphene membrane using the Tap190DLC probe during (a) ramp-up (when the indented depth is increased from the previous indentation), and (b) ramp-down (when the indented depth is decreased from the previous indentation); (c) presents all the curves.

4.5.1.3 Pre-Set Indentation Depth vs. True Indented Depth

First, the relationship between the pre-set indentation depth and the true indented depth upon indenting the graphene membranes was investigated. Figure 4.22 presents the true indented depth against the pre-set indentation depth using the FM50, Tap190DLC and DTNCLR probes for the same mechanically exfoliated graphene membrane. In an ideal system, it is expected that the indented depth is linearly proportional to the pre-set indentation depth, that is, increasing the pre-set indentation depth will always lead to a linear and equivalent increase in the indented depth. However, it was noted that the two are non-linearly proportional, especially when using the Tap190DLC. Furthermore, at larger indentation depths (in excess of 90 nm) using Tap190DLC, the real indented depth saturates to around 27 nm with large scatter. Upon closer inspection of the FD curves, this saturation is reflected in the way that the curves assume a quasi-asymptotic nature at large indented depth. Moreover, upon comparing the maximum real indented depth achieved using the three cantilevers, it is evident that a cantilever with the

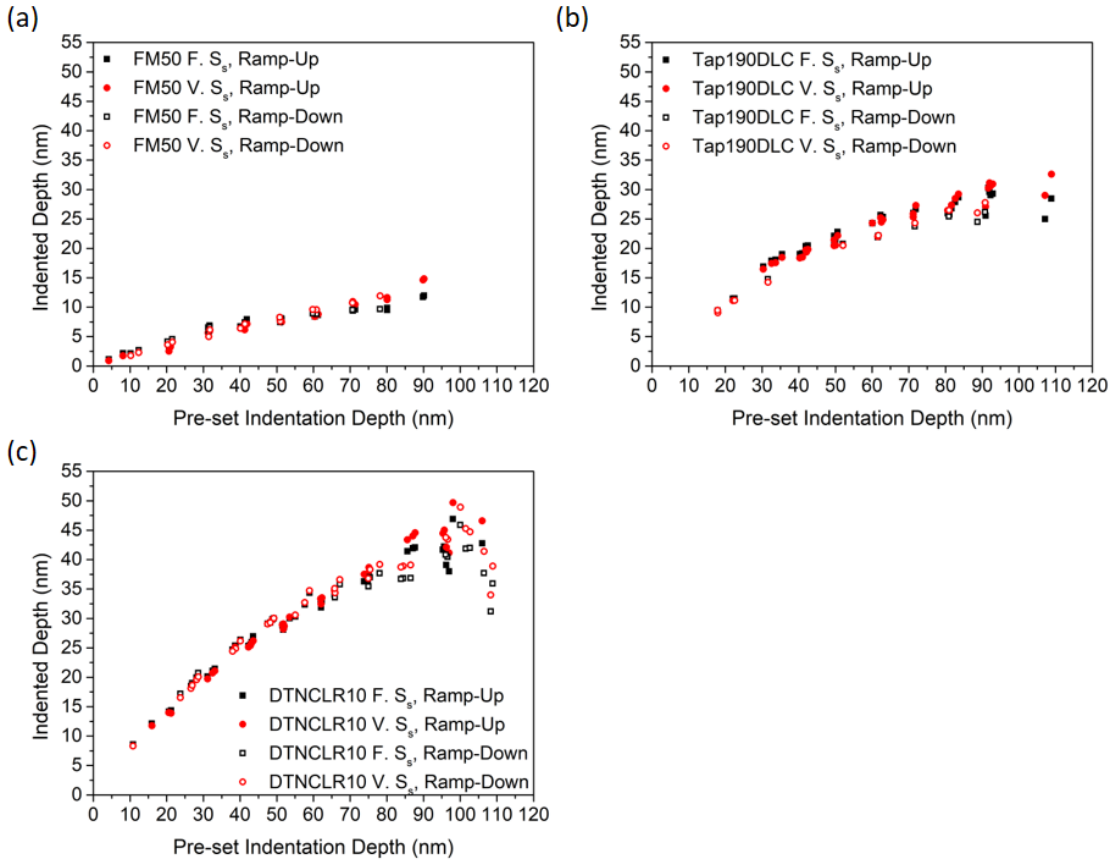

Figure 4.22: The true indented depth against the pre-set indentation depth upon indenting the graphene membrane using the (a) FM50, (b) Tap190DLC, and (c) DTNCLR probes. All obtained FD curves were calibrated using both a fixed sensor sensitivity factor, F. S_s, and a variable sensor sensitivity factor, V. S_s.

lowest spring constant (FM50) is able to indent the graphene membrane less than the cantilever with the highest spring constant (DTNCLR) is able to.

4.5.1.4 Indentation Force vs. Indentation Depth

Figure 4.23 shows the maximum indentation force recorded for every FD curve obtained against the pre-set indentation depth and the real indented depth. While the indentation force is more or less linearly proportional to the pre-set indentation depth, the indentation force is once again non-linearly proportional to the indented depth as is especially evident for Tap190DLC, as shown in Figure 4.23 (d). This can be explained by the fact that, at higher indentation depths (or strain), the graphene membrane deflects less, and in turn causes the cantilever to deflect more. Therefore, this nonlinearity is attributed to the nonlinear response of the graphene membrane under deformation. This is particularly evident when using the Tap190DLC and DTNCLR probes which have higher spring constants and hence are able to indent the graphene membrane to larger extents.

4.5.1.5 Fixed vs. Variable Sensor Sensitivity Factor, S_s

Figure 4.22 and Figure 4.23 also highlight the difference between the results obtained using a fixed S_s and a variable S_s – the black data points obtained using a fixed S_s deviate from the red data points obtained from the same raw FD curves using a variable S_s. The calibrated force-distance curves were used to derive and calculate the elastic modulus of the graphene membrane.

As described in Section 4.4, the approach FD curves, both calibrated using a fixed S_s as well as a variable S_s, were fit to Equation 4.14 (derived from Equation 4.5).

$$F = A\delta + B\delta^3 \qquad \textit{Equation 4.14}$$

Parameter A was used to find the pretension of the membrane, σ_0^{2D}, via Equation 4.15, while parameter B was used to find the 2D elastic constant, E^{2D}, via Equation 4.16, where a is the radius of the circular membrane (675×10^{-9} m) and $q = 0.98$.

$$\sigma_0^{2D} = \frac{A}{\pi} \qquad \textit{Equation 4.15}$$

$$E^{2D} = \frac{Ba^2}{q^3} \qquad \textit{Equation 4.16}$$

In order to obtain the elastic modulus, E, the 2D elastic constant was divided by the measured thickness of the membrane (16×10^{-9} m).

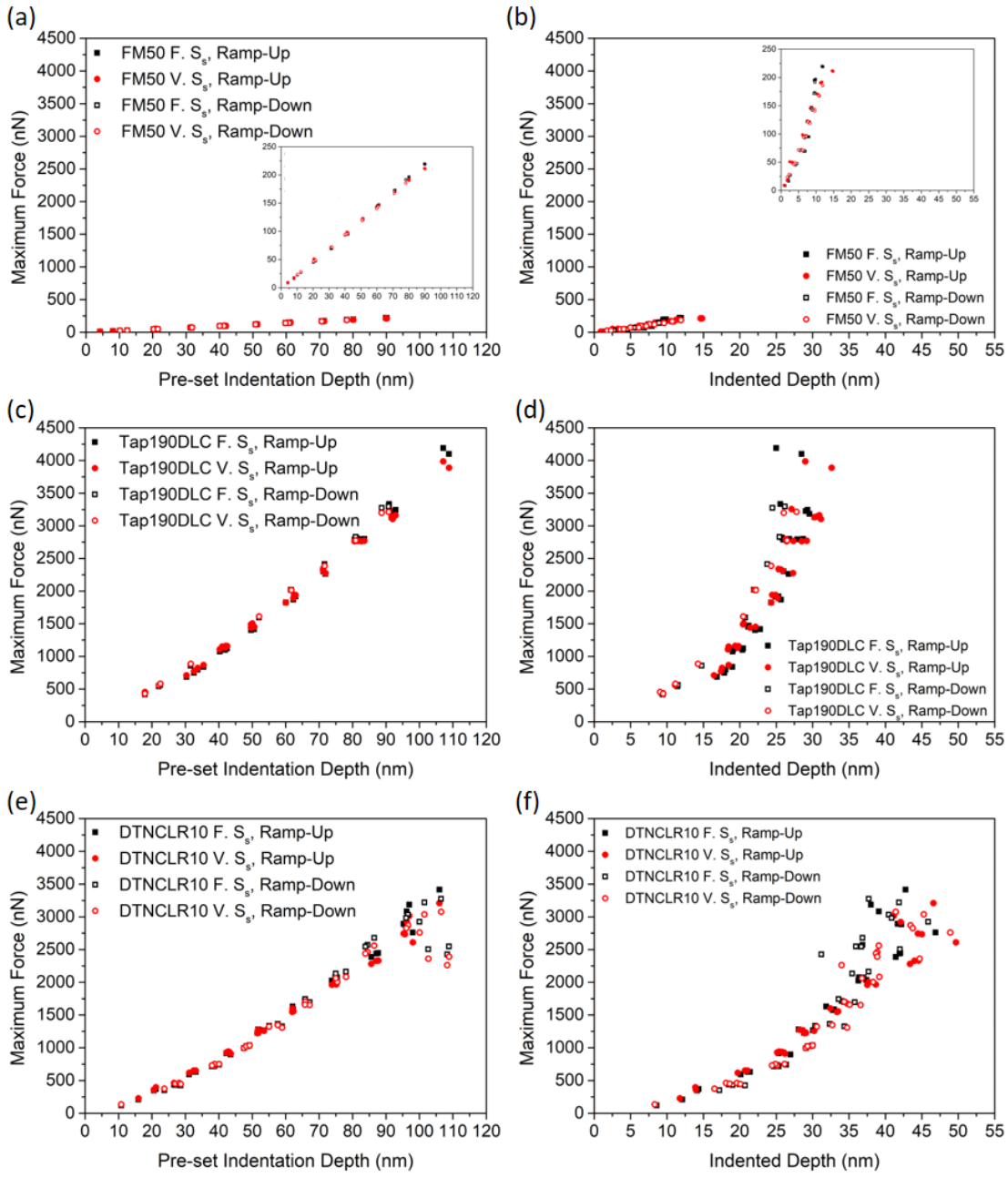

Figure 4.23: The maximum indentation force against (a, c, e) the pre-set indentation depth, and (b, d, f) the indented depth using the FM50 (a, b), Tap190DLC (b, c), and DTNCLR (e, f) probes.

Figure 4.24 shows the calculated elastic moduli as measured using all the three probes, at various indentation depths and post-processed using both the fixed S_s and the variable S_s. Figure 4.25 shows the averages with error bars representing the standard deviation of all the calculated elastic moduli, from the ramp-up and ramp-down measurements, using both the fixed S_s and variable S_s. Note that in Figure 4.25, data obtained from pre-set indentation depths < 20 nm was ignored since, especially using the FM50 cantilever, for indented depths less than

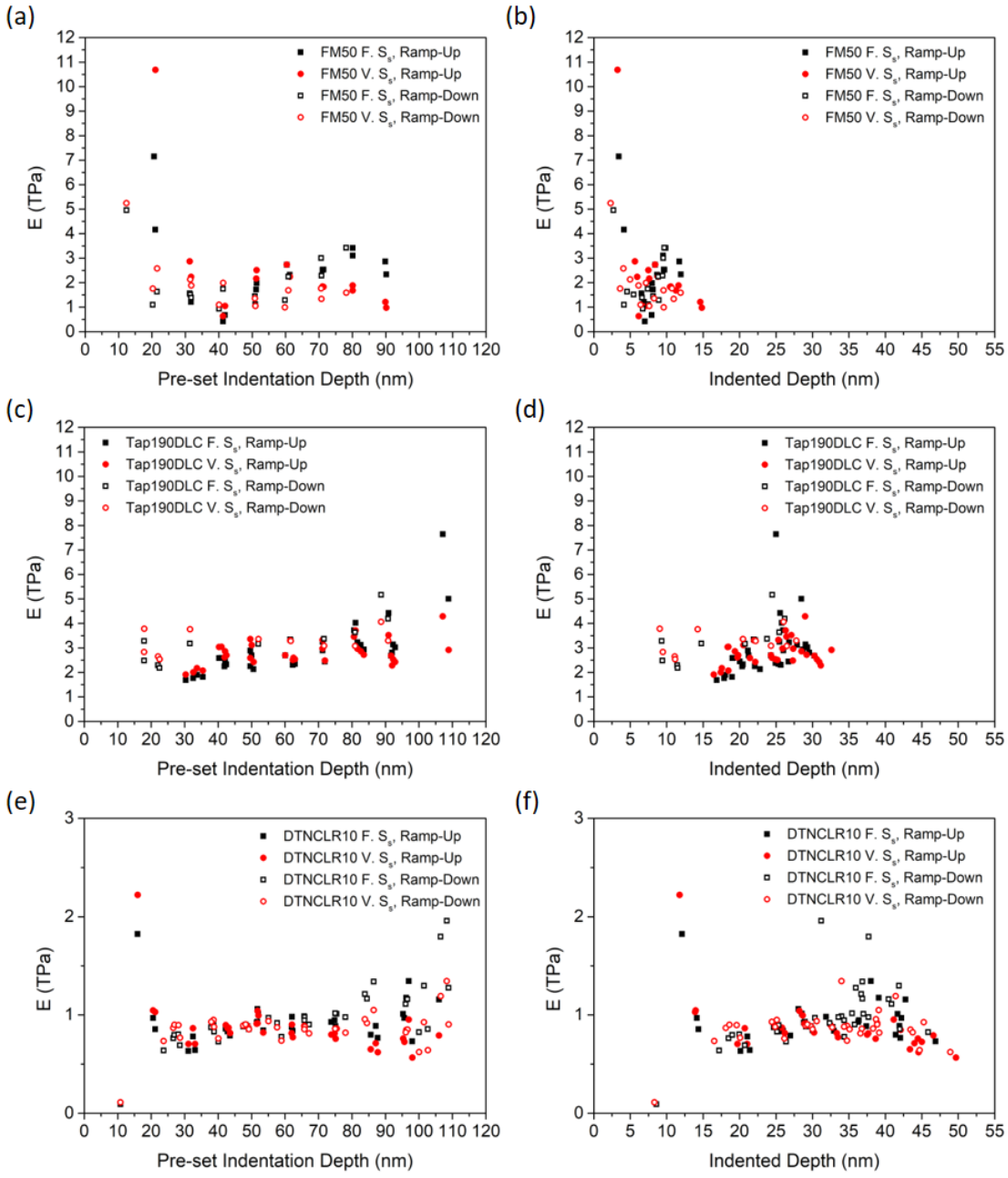

Figure 4.24: The calculated elastic modulus against (a, c, e) the pre-set indentation depth, and (b) the indented depth using the (a, b) FM50, (c, d) Tap190DLC, and (e, f) DTNCLR probes.

around 3.5 nm the calculated values for the elastic modulus varied significantly with unrealistic values.

A closer look at the results and how the calculated elastic modulus changes with the indentation depth and the used sensor sensitivity factor reveals some interesting effects. Studying the data points in Figure 4.24, one can notice that the data using a fixed sensitivity factor has a larger variance or scatter than that from variable sensitivity factors. This is additionally reflected in the smaller error bars for "Variable S_s" compared to "Fixed S_s" in Figure 4.25.

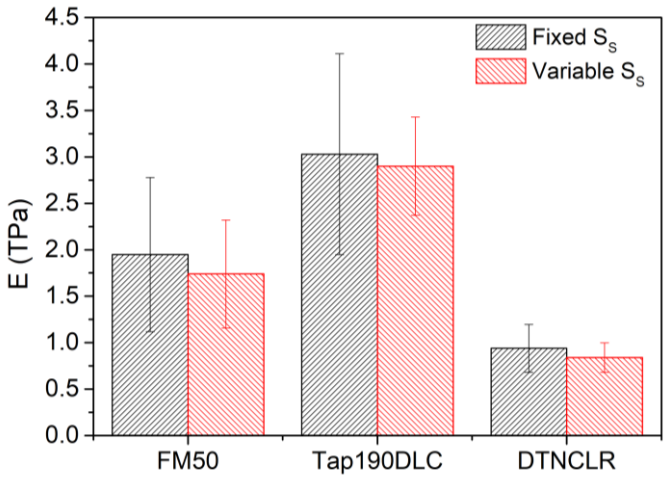

Figure 4.25: The average calculated elastic modulus, E, using both a fixed S_s and variable S_s, for all three probes used. The error bars represent the standard deviation.

Furthermore, while there is a slight trend for an increasing elastic modulus with indentation depth using the fixed S_s, this trend is less evident when using a variable S_s. This indicates that the non-linearity of the Z Scanner, as reflected in a nonlinear sensitivity factor with indentation depth as shown in Figure 4.19, does indeed affect the final calculated elastic modulus. Additionally, the use of a variable sensitivity factor is observed to reduce the nonlinearity in the results, and hence reduce the dependence of the calculated elastic modulus on the indentation depth. The hysteresis in the Z Scanner is still observed, especially at the extremities (i.e. for the lower and higher indentation depths) when comparing the ramp-up with the ramp-down data.

4.5.1.6 Errors at Low and High Indentation Depths

Figure 4.26 shows the reduced chi-squared and adjusted R-square of the fitting procedure and the standard error of parameter B against the pre-set indentation depth, using all three probes.

When using the stiffer Tap190DLC (Figure 4.24 (c)), one can deduce that the nonlinearities of the system are least manifested at mid-range indentation depths, i.e. at pre-set indentation depths of around 40 to 80 nm. This ideal range is also reflected in the quality of fit and standard errors displayed in Figure 4.26 (c, d) – the standard error (Figure 4.26 (c)) is lowest between 40 and 80 nm and is seen to increase significantly at lower and higher pre-set indentation depths. Likewise, the adjusted R-square representing the goodness of fit is closest to a value of 1 with least variance for the same indentation depths.

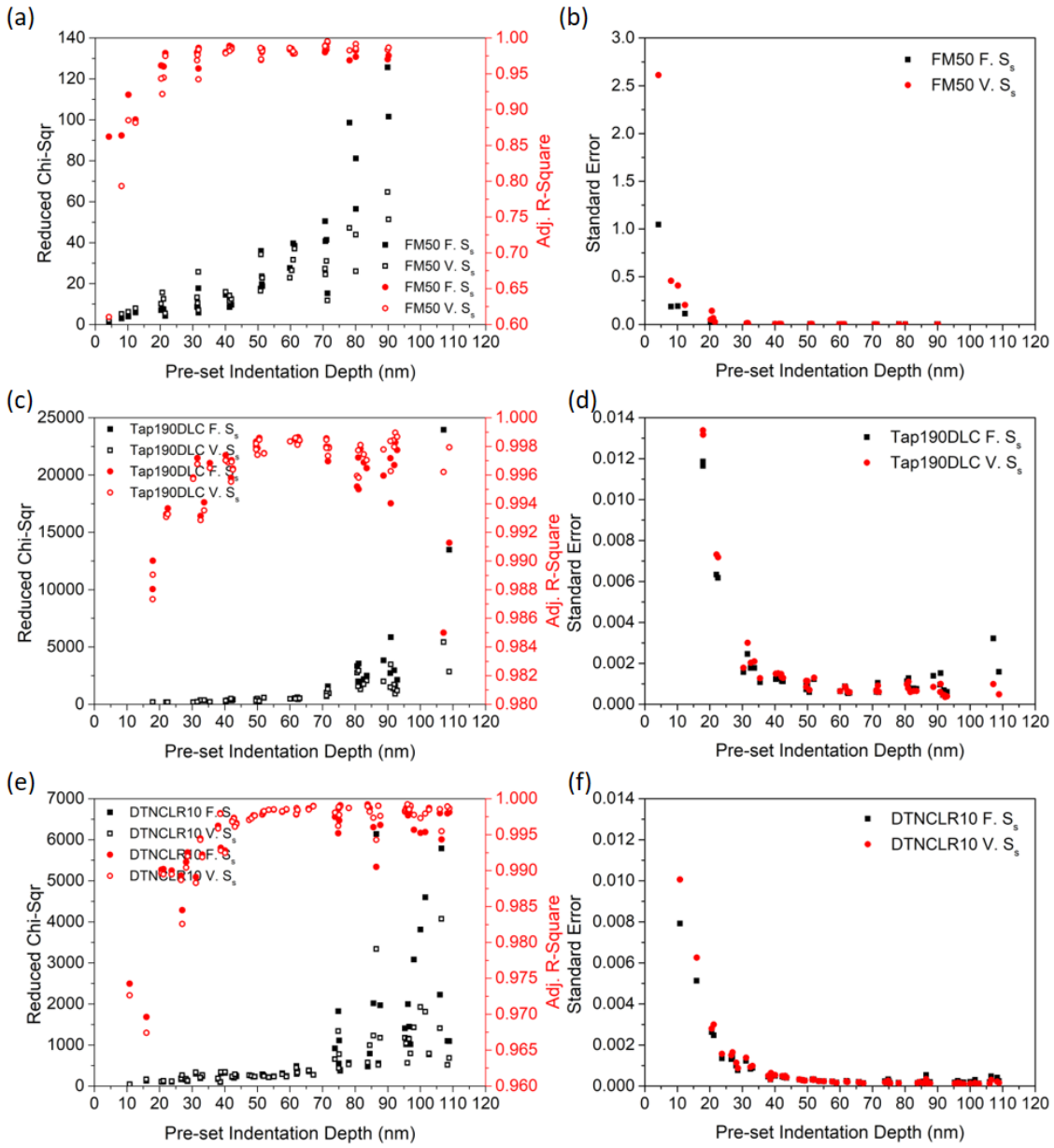

Figure 4.26: The (a, c, e) reduced chi-square and adjusted R-square, and (b, d, f) standard error of parameter B of the fitting procedure, against the pre-set indentation depth using the (a, b) FM50, (c, d) Tap190DLC, and (e, f) DTNCLR probes.

When using the softer FM50 (Figure 4.24 (a)), one can deduce that the nonlinearities of the system are mostly manifested at lower indentation depths, i.e. at pre-set indentation depths of less than around 30 to 40 nm. The pre-set indentation depth range, at which the calculated elastic modulus is more stable, is also seen to apply for FM50 as reflected in the goodness of fit and standard errors displayed in Figure 4.26 (a, b) – the adjusted R-squared (Figure 4.26 (a)) is highest between 40 and 80 nm and is seen to decrease significantly especially at lower pre-

set indentation depths. The same trends and conclusions can be drawn for the results obtained by the DTNCLR probe, shown in Figure 4.24 (e, f) and Figure 4.26 (e, f).

It was also noted that when the indented depth was very low, less than around 3.5 nm, negative values for the elastic modulus was sometimes obtained. This happens because at such low indentation depths, while keeping the same data rate acquisition as the rest of the indentations, the signal to noise ratio can be too small. As such, the fit is very poor and not representative of the general shape of the FD curve.

In conclusion, the method which best reduces the errors and the effects of nonlinearities of the system on the results involves obtaining the function of the sensor sensitivity factor calibration curve (similar to that shown in Figure 4.12 (b)) and using it to adjust the sensitivity factor used for post-processing depending on what pre-set indentation depth is used, i.e. using a variable S_s.

Secondly, the pre-set indentation depth should be kept between 40 and 80 nm. This results in an elastic modulus of 1.66 ± 0.55 TPa using FM50, 2.93 ± 0.34 TPa using Tap190DLC, and 0.86 ± 0.07 TPa using DTNCLR. With these results, it can be noted that the standard deviation indeed reduced. Nevertheless, the average values for the elastic modulus of the same graphene membrane are significantly different when measured using different AFM probes, as shown in Figure 4.27. Moreover, Figure 4.28 plots the individual calculated values for the elastic modulus at all indentation depths.

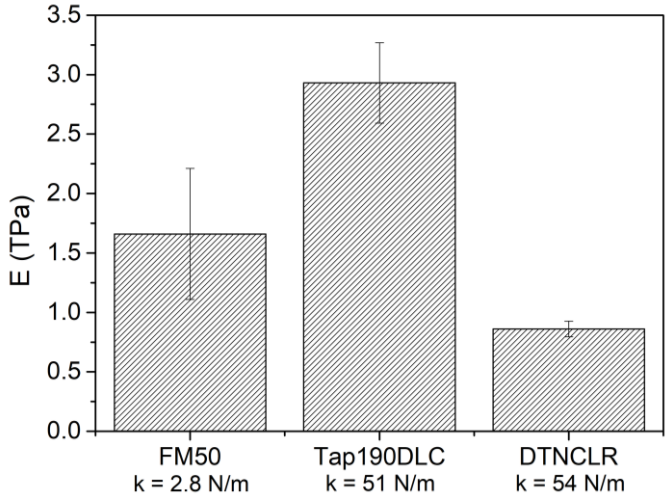

Figure 4.27: The average calculated elastic modulus, E, using a variable S_s, and a pre-set indentation depth of between 40 nm and 80 nm, for all three probes. Error bars represent the standard deviation.

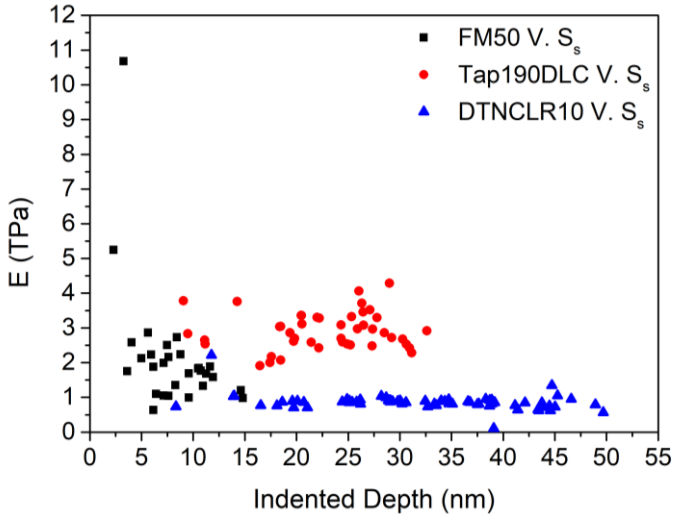

Figure 4.28: Calculated elastic modulus, E, against indented depth using all three probes.

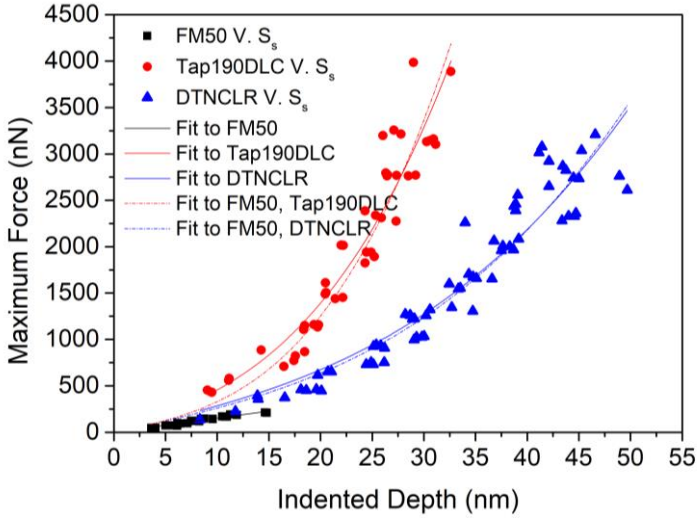

Figure 4.29: The maximum indentation force at maximum indented depth for every FD curve obtained on the same graphene membrane using the FM50, Tap190DLC, and DTNCLR tips, calibrated with the variable S_s.

The end data point for each FD curve (i.e. representing the maximum force applied at the full indented depth) obtained at different indented depths were used to build an FD curve, as shown in Figure 4.29. Fitting Equation 4.14 to the data points acquired using the FM50 probe and DTNCLR probes (dashed blue curve in Figure 4.29), and calculating the elastic modulus reveals an elastic modulus of 0.51 TPa, while an elastic modulus of 2.65 TPa is obtained for the data points acquired using the FM50 and Tap190DLC probes (dashed red curve in Figure 4.29). On the other hand, fitting Equation 4.14 to the data points acquired using the Tap190DLC and DTNCLR probes separately (solid red and blue curves in Figure 4.29), reveals an elastic modulus of 2.42 TPa and 0.53 TPa, respectively.

4.5.2 Case Study 2 – Flake C

The second case study discusses the indentations performed on Flake C from Chapter 3 having an average thickness of 25 nm. An optical micrograph and a corresponding AFM topographical image are presented in Figure 4.30. The two graphene membranes which covered the entire hole in the substrate are labelled M01 and M02. The indentations were performed using similar FM50 and Tap190DLC tips via AFM. The probes, imaged in Figure 4.31 and Figure 4.32, had a calculated cantilever spring constant of 3.82 N/m and 62.13 N/m, respectively. The membranes were indented several times (at least 11 times) with the pre-set indentation depth being again varied from around 20 nm up to around 90 nm. A number of indentation curves were also obtained on the XYZ calibration nanogrid after indenting the graphene membranes to determine the sensor sensitivity factor. The following sections present and discuss the results obtained.

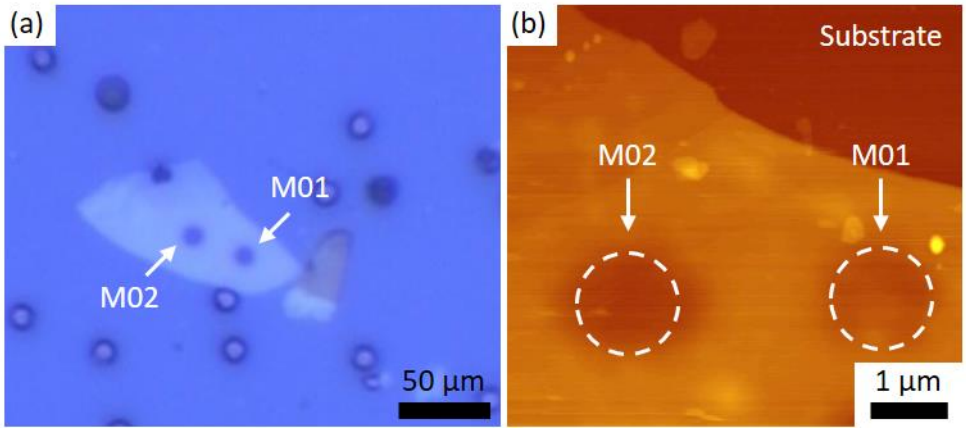

Figure 4.30: (a) Optical micrograph and (b) AFM topographical image of the graphene membrane investigated in Case Study 2. Two circular graphene membranes, M01 and M02, are indicated.

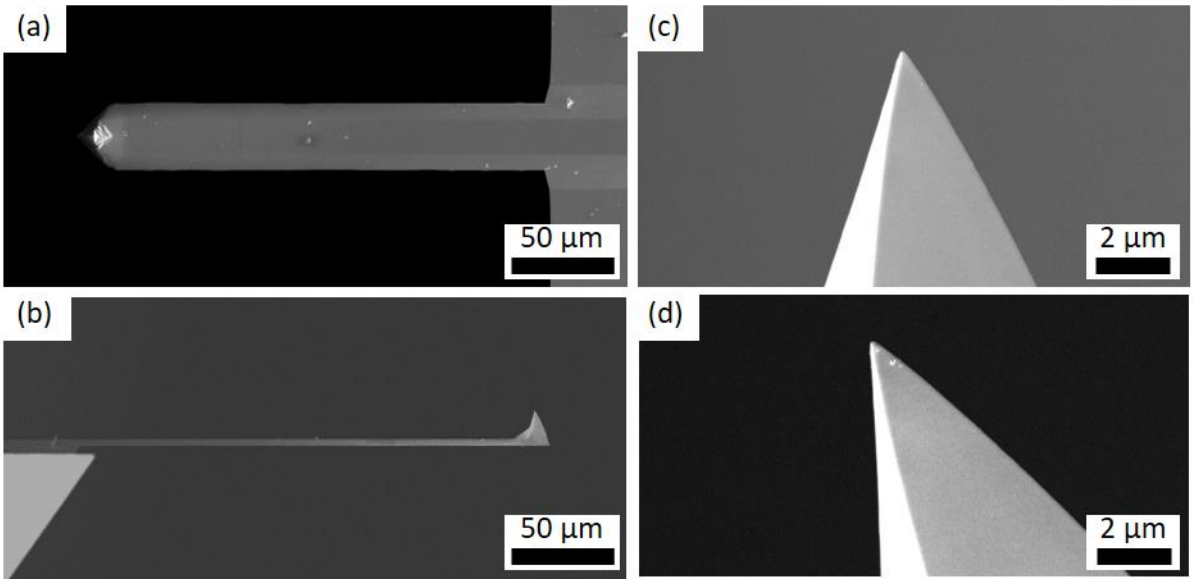

Figure 4.31: SEM images of the FM50 (a, b) cantilever and (c, d) tip (c) before and (d) after use.

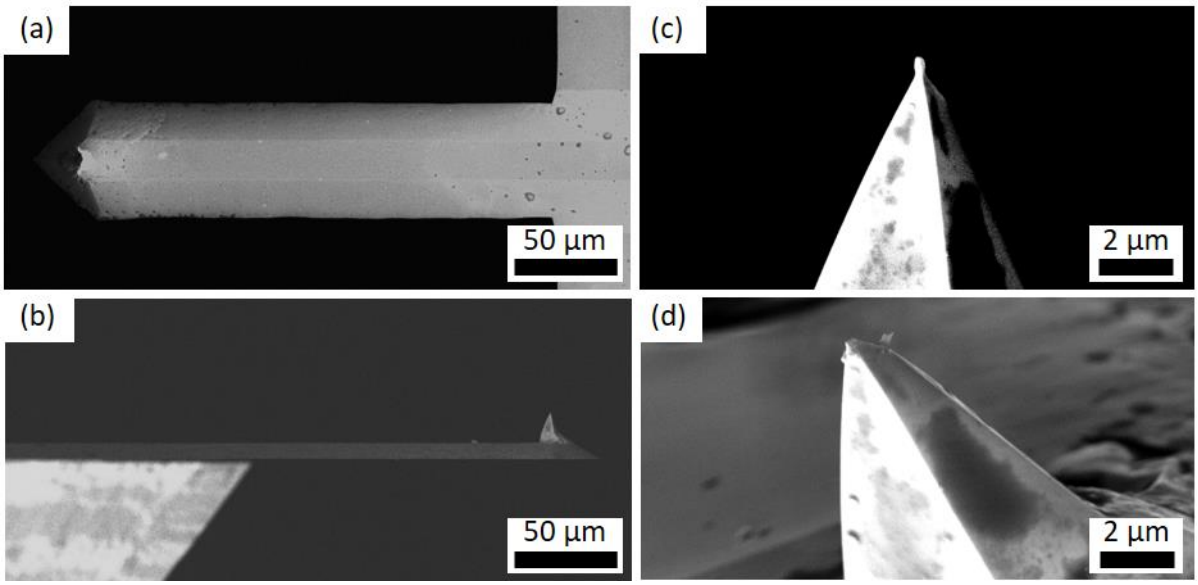

Figure 4.32: SEM images of the Tap190DLC (a, b) cantilever and (c, d) tip (c) before and (d) after use.

4.5.2.1 Sensor Sensitivity Factor Calibration

Figure 4.33 shows the sensor sensitivity factors obtained at various indentation depths using both the FM50 and Tap190DLC probes.

Considering the data presented in Figure 4.33 (a), an average sensor sensitivity factor of 1.1×10^6 V/m was used for the FD curves obtained using the FM50 probe. On the other hand, the FD curves obtained from the Tap190DLC probe were post-processed using a variable sensor sensitivity factor according to the calibration curve fitted in Figure 4.33 (b).

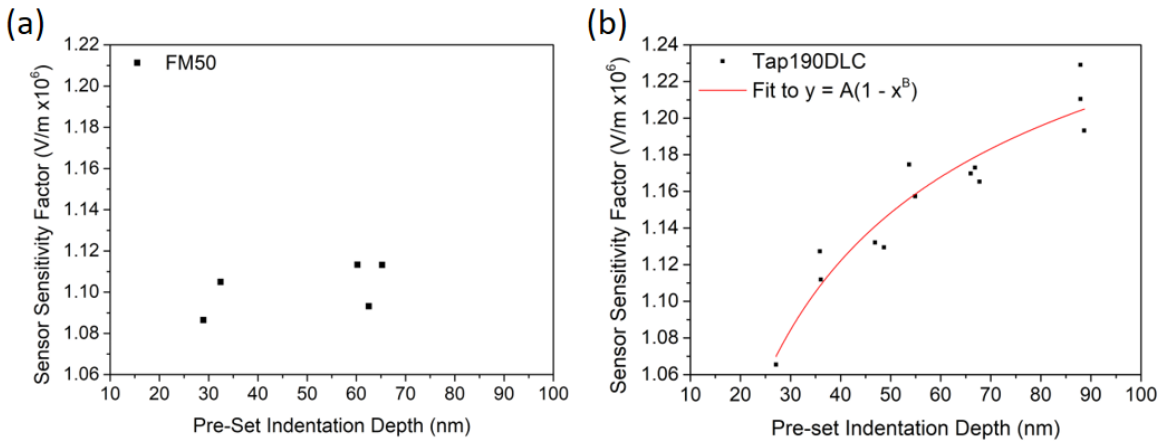

Figure 4.33: The sensor sensitivity factor, S_s, as measured from the slope of the approach curves for (a) FM50 and (b) Tap190DLC.

4.5.2.2 Indentation Experiments on the Graphene Membrane

Upon examining the FD curves obtained using the FM50 probe, it was noted that all the force curves obtained were relatively steep i.e. the force rapidly increased with indentation depth, and while the pre-set indentation depth was increased up to 70 nm, the indented depth was never more than 4 nm. Upon fitting the post-processed force curves to the cubic equation that models the indentation of thin graphene membranes (Equation 4.14), the obtained values for the elastic modulus varied widely from negative values up to 50 TPa. Such unrealistic results are being attributed to the fact that the FM50 cantilever is too flexible with a spring constant of just 3.82 N/m for the relatively thick 25 nm graphene membrane. As such, the cantilever was not sufficiently stiff to indent the graphene and most of the Z Scanner indentation distance was manifested as cantilever deflection rather than graphene membrane deformation.

Figure 4.34 shows all the results obtained from the force curves using the Tap190DLC probe. From the representative force curves in Figure 4.34 (a), it can already be noted that first of all, the curves are somewhat repeatable for the individual membranes, eliminating the possibility of the membranes being damaged or modified during the indentations. Furthermore, the force curves obtained from M02 are generally steeper than those from M01. The same trends with respect to how the maximum indentation force and elastic modulus change with the pre-set indentation depth or true indented depth as those investigated in Case Study 1 are present. Predominantly, the increased elastic modulus as measured from lower indentation depths is evident (Figure 4.34 (e, f)). As suggested in Case Study 1, the average elastic modulus obtained considering pre-set indentation depths of between 40 nm to 80 nm was found to be

2.18 ± 0.28 TPa for M01, and 3.43 ± 0.34 TPa for M02. The standard deviation for both these values is adequately small meaning that the individual results are repeatable.

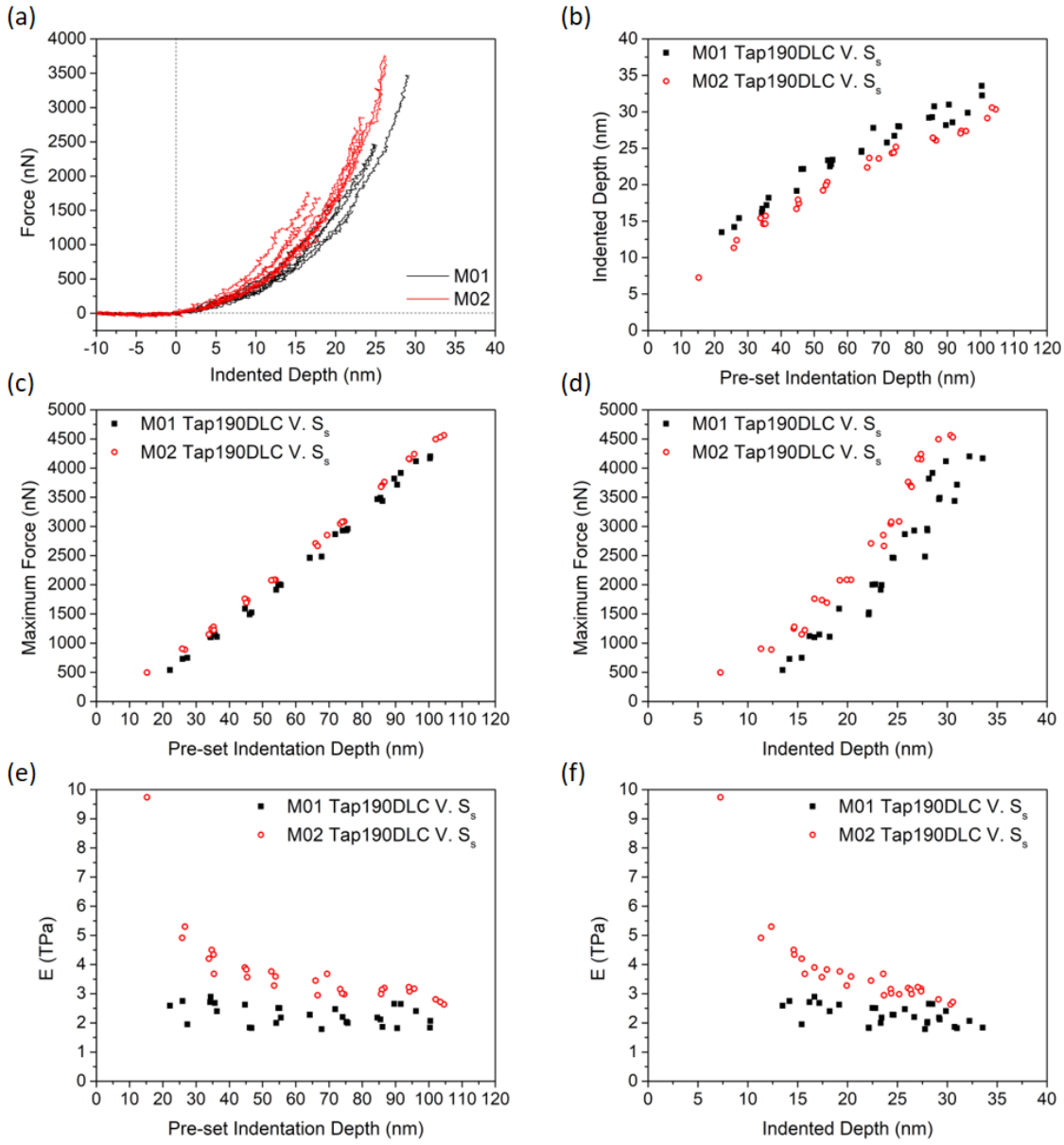

Figure 4.34: Results from indentations carried out using the Tap190DLC probe on graphene membranes M01 and M02. (a) Representative FD curves, (b) the true indented depth of the graphene membranes upon indentation against the pre-set indentation depth, (c, d) the maximum indentation force against (c) the pre-set indentation depth, and (d) the indented depth, and (e, f) the calculated elastic modulus against (e) the pre-set indentation depth, and (f) the indented depth.

4.5.3 DISCUSSION

A total of twelve graphene membranes across eight mechanically exfoliated graphene flakes were indented and analysed using the procedures outlined above. The case studies presented in Section 4.5.1 and Section 4.5.2 were chosen due to their representative nature with respect to the results obtained. Based on both these case studies as well as the other indented graphene membranes, a number of observations can be made.

Primarily, the scope of performing indentations via AFM on graphene membranes is to measure the elastic modulus of the graphene membrane material. However, from the results presented in this section, the values for the elastic modulus of graphene were seen to vary appreciably from an average of 0.53 TPa to an average of 3.43 TPa. Such deviations from the established value of elastic modulus of graphene of 1 TPa as found and reported in literature [13] can be attributed to many factors.

Variability in the measured elastic modulus of the graphene membranes can be ascribed to various factors including:

(i) The synthesis route: In this work the graphene flakes were all mechanically exfoliated from the same HOPG parent material using the same exfoliation technique in a controlled environment;
(ii) The substrate material: The exfoliated graphene flakes were deposited on the same patterned PAA/Si substrate;
(iii) AFM testing: The same RHK-AFM equipment and testing conditions were utilised, and;
(iv) Data acquisition and post-processing: The same methods of acquiring and post-processing the force-distance curves were used.

Moreover, overall, although some variability between flakes can exist as these were prepared over a period of time, the Raman spectra of the graphene flakes confirm that the flakes were all of high crystalline quality. This is evidenced by the insignificant or entirely absent D peak, as shown in Chapter 3. Therefore, it is expected that since the same material is being investigated using the same set-up and technique, the measured elastic modulus of graphene should be relatively consistent. Thus, other factors must be causing significant variability in the measured elastic moduli.

A factor which may cause significant errors in the measured E value of the graphene membranes is the thickness of the graphene – or specifically the inconsistencies between the various membranes which is also subject to measurement error. As explained in Section 4.4, the 2D elastic modulus extracted from the fitting procedure, E^{2D} [N/m], is simply divided by the thickness, t_G, of the graphene membrane to obtain the bulk elastic modulus, E [TPa]. However, while the thickness of single-layer graphene is generally accepted to be 0.335 nm, the thickness of the mechanically exfoliated multi-layer graphene flakes in this study had to be measured for every flake using topography imaging via AFM. As such, the E^{2D} was divided by the average thickness found from the AFM topography scans as shown in Chapter 3. Nonetheless, it is believed that this method of obtaining the thickness value, t_G, is subject to significant error, up to ± 2.5 nm. This error significantly affects the resulting value of E. For instance, for graphene membrane M02 in Case Study 2, while the average elastic modulus calculated on a thickness of 25 nm was 3.43 TPa, increasing the thickness by 2.5 nm results in a decreased elastic modulus of 3.12 TPa. Therefore, comparing elastic moduli obtained for different flakes is subject to uncertainty originating from inaccurate membrane thickness measurement.

Additionally, as described in Chapter 3, the holes in the substrate were prepared using a masking technique which relies on the ability of semi-molten PS beads to act as a mask for the PAA deposition, and on the subsequent dissolution of the same PS beads. While imaging the clean substrate via SEM and AFM revealed adequately consistently sized holes, minor changes in the hole diameter and hence graphene membrane diameter, $2a$, can affect the measured value of the elastic modulus (refer to Equation 4.5). Moreover, the presence of relatively thick MLG flakes covering the holes make the measurement of the membrane diameter via AFM more prone to inaccuracy since the edges of the holes are not well-defined. The 'tip-broadening' effect and system nonlinearities in the X and Y directions further distort the topography image as discussed in Section 4.3.2.

The above, coupled with the fact that the mechanical exfoliation technique yields a small quantity of flakes each with different thicknesses, makes it very challenging to locate and indent multiple graphene membranes having the same thickness and geometry. This limits the ability to get repeated results or to study the effect of membrane thickness on the real value of its elastic modulus while being statistically robust.

To eliminate the problem of varying membrane thicknesses and diameters, the same membrane can be indented multiple times using different techniques, most specifically different AFM probes and different indentation depths. In fact, for both case studies presented in this section, each membrane was indented using at least two different probes having different spring constants, with each probe being used to indent the membranes to different depths.

The second major observation which could be made after analysing the indentation results from the mechanically exfoliated graphene membranes is that the measured elastic modulus appears to be inflated at the smallest indentation depths used in this work. The measured elastic modulus appears to stabilize to lower values at pre-set indentation depths ranging between 40 to 80 nm. Additionally, as evident in both case studies presented, it can be noted that for the same graphene membrane, the average measured elastic modulus is different when using different probes. However, the relationship between the probe spring constant and the measured elastic modulus is not a linear one; in Case Study 1, the Tap 190DLC having a middle-range spring constant produced the highest values for E, while the DTNCLR probe having the highest spring constant produced the lowest values for E. The softest FM50 probe produced a middle-range average value of elastic modulus of 1.66 ± 0.55 TPa. On the contrary, the use of the FM50 probe in Case Study 2 did not yield useful results as the membrane was too stiff for the cantilever to successfully indent, whereas the use of the Tap190DLC yielded more repeatable results. Once again, in order to be able to investigate the relationship between the measured elastic modulus and the probe's spring constant, more indentations need to be performed on very similar graphene membranes having verifiable identical thicknesses.

As such, the mechanical exfoliation technique used did not give enough yield of graphene membranes having consistent thicknesses to be able to investigate the reason behind the large deviations in the measured elastic modulus. Conversely, it was predicted that CVD-grown single-layer graphene can yield more reproducible results. As such, the procedures and methods established in Section 4.4, as well as the use of a variable sensitivity factor as described in Section 4.5.1.5, were applied to the CVD-grown SLG membranes as prepared in Chapter 3. The results will be discussed in Section 4.6.

4.6 INDENTATIONS OF AS-DEPOSITED CVD GRAPHENE

As explained in Chapter 3, the CVD-grown graphene membranes supported on the 0.45 μm silicon nitride filters were imaged in contact mode AFM. Once a suitable membrane without visible wrinkles or defects was found, the probe was located at the centre of the membrane with an accuracy of around 10 nm of the true centre. In an identical manner to the experiments performed on mechanically exfoliated graphene, the CVD-graphene membrane was then indented multiple times to different pre-set indentation depths, ranging from around 10 nm up to around 90 nm. In most cases, the final indentation depth was first increased (ramped-up) from 10 nm up to maximum, and then decreased (ramped-down) from maximum down to around 10 nm, in steps of ~10 nm. For each pre-set indentation depth, the membrane was indented three times. Using a variable sensor sensitivity factor, S_s, the resultant force curves were then converted to true force against indented depth following the procedure outlined in Section 4.4.

Once again three types of probes were used: the FM50 with a nominal force constant of 2.8 N/m, the Tap190DLC with a nominal force constant of 48 N/m, and the DTNCLR with a supplier-calibrated force constant of around 55 N/m. The spring constants of all FM50 and Tap190DLC probes used were determined using the geometrical method with trapezoidal cross-section correction (Section 4.4.3.1).

As opposed to the mechanically exfoliated graphene samples, a single layer of CVD-graphene was found to cover a significantly large area of the substrate. Optical microscopy and SEM evidenced only small regions of FLG and wrinkles which were subsequently easily identified during AFM imaging. In turn, most of the graphene membranes produced had a uniform single atomic thickness of 0.335 nm. Any graphene membranes which had predominant folds or wrinkles across them were not indented. Furthermore, in agreement with the microsieve product specification supplied by the manufacturer (Aquamarijn Micro Filtration BV, Zutphen, The Netherlands), SEM imaging ascertained that the resulting graphene membranes are consistently 0.45 μm in diameter.

The resultant larger number of virtually identical graphene membranes were therefore available for imaging and indentation, hence allowing the required quantity and quality of results which can be considered statistically significant to be acquired.

Unfortunately, however, the fact that all the graphene membranes are evenly spaced (due to the repetitive ordered arrangement of the pores in the microsieves) and because of the absence of identifying features on the sample, it was not possible to locate and indent the same graphene membrane twice, using different probes. Therefore, it is assumed that the mechanical properties of all the graphene membranes are truly identical so that the other factors which might affect the measurement of the membranes' elastic modulus – the indentation depth and especially the cantilever spring constant – could be investigated.

A total of twenty different graphene membranes were indented using a total of eight probes (three DTNCLR probes, three Tap190DLC probes, and two FM50 probes). Representative results using each type of probe are presented in Section 4.6.1.

4.6.1 RESULTS

Figure 4.35 to Figure 4.37 present representative results as obtained from indenting graphene membranes using FM50 probes (Figure 4.35), Tap190DLC probes (Figure 4.36), and DTNCLR probes (Figure 4.37).

A few trends can be noted upon analysing the results obtained from all 20 different membranes as represented by the above. These will be discussed separately in the following sections.

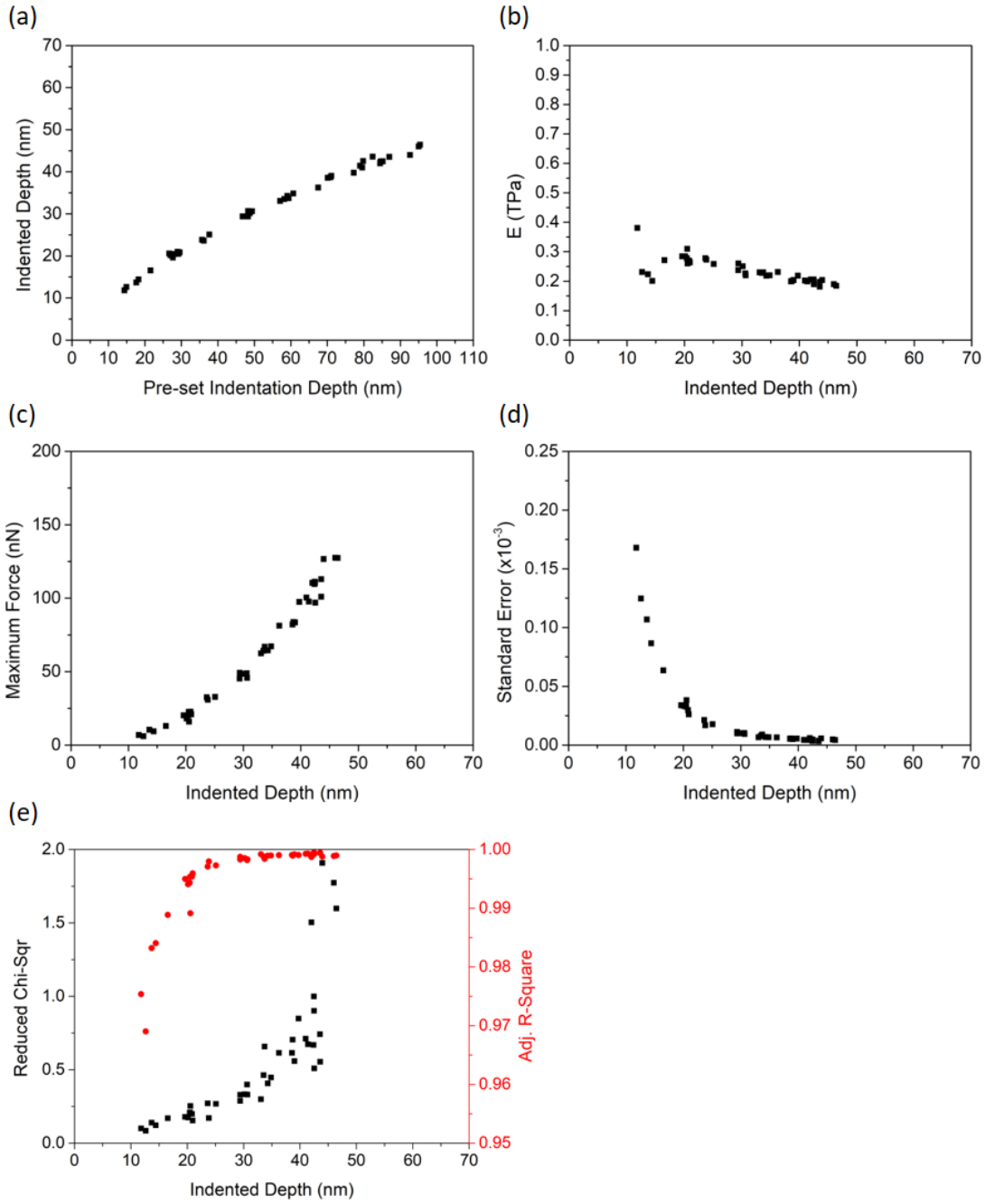

Figure 4.35: (a) Indented depth against pre-set indentation depth, and (b) elastic modulus, (c) maximum force, (d) standard error of the cubic term, and (e) reduced chi-squared and adjusted R-square against indented depth, for a representative graphene membrane using a FM50 probe with $k_{trapezoidal}$ *of 2.6 N/m.*

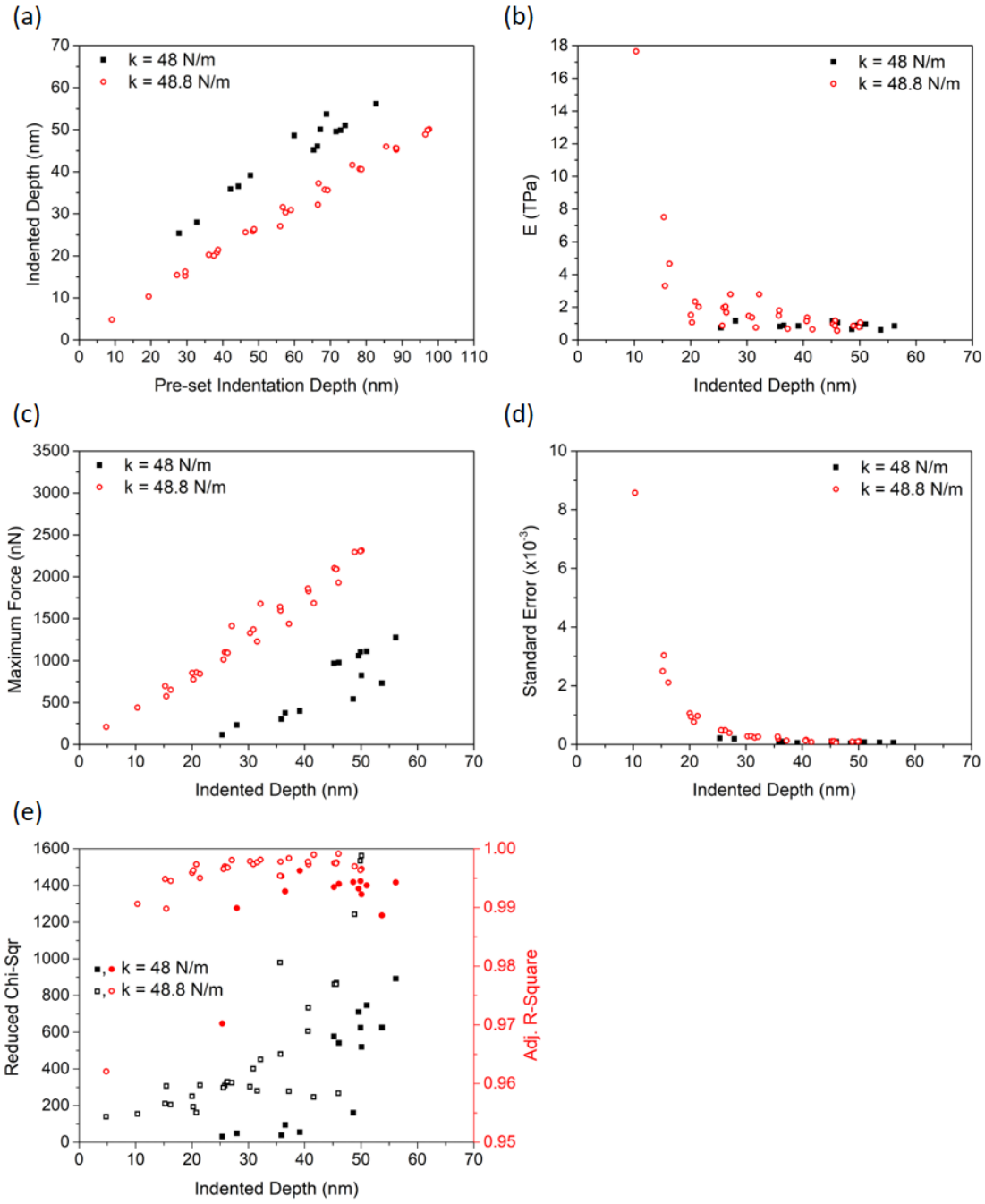

Figure 4.36: (a) Indented depth against pre-set indentation depth, and (b) elastic modulus, (c) maximum force, (d) standard error of the cubic term against indented depth, and (e) reduced chi-squared and adjusted R-square for two representative graphene membranes using two Tap190DLC probes with $k_{trapezoidal}$ *of 48 N/m and 48.8 N/m.*

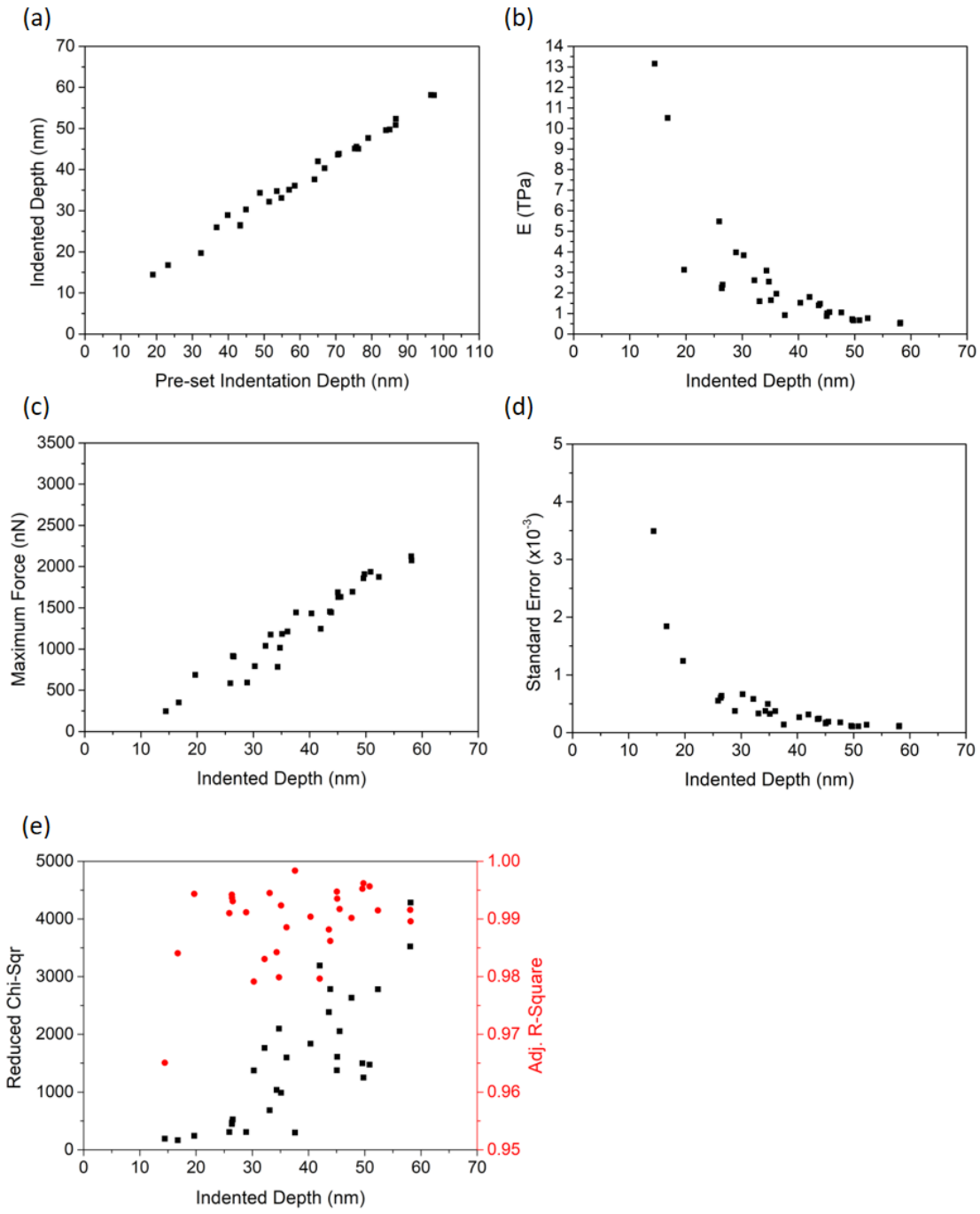

Figure 4.37: (a) Indented depth against pre-set indentation depth, and (b) elastic modulus, (c) maximum force, (d) standard error of the cubic term, and (e) reduced chi-squared and adjusted R-square against indented depth, for a representative graphene membrane using a DTNCLR probe with k of 54 N/m.

4.6.1.1 Effect of Indentation Depth

Figure 4.38 presents all the measured values for the elastic modulus obtained from all indented membranes using the (a) DTNCLR, (b) Tap190DLC, and (c) FM50 probes, against the true indented depth. It is important to note that the value obtained for the elastic modulus from each force-distance curve is dependent on the quality of the fit to Equation 4.14. Therefore, the standard error of the fitting parameter B (Figure 4.35 - Figure 4.37 (d)) is linearly proportional to the standard error, SE, of the elastic modulus by Equation 4.17.

$$\mathrm{SE}_{E^{2D}} = \frac{\mathrm{SE}_B a^2}{q^3}, \mathrm{SE}_E = \frac{\mathrm{SE}_{E^{2D}}}{t_G} \qquad \textit{Equation 4.17}$$

Using the student t-test with a confidence interval of 95% and the sample size being the number of data points within the force-distance curve beyond the zero-displacement point ($F = 0, \delta = 0$), the values of E with 95% confidence was calculated for each force-distance curve (Figure 4.38).

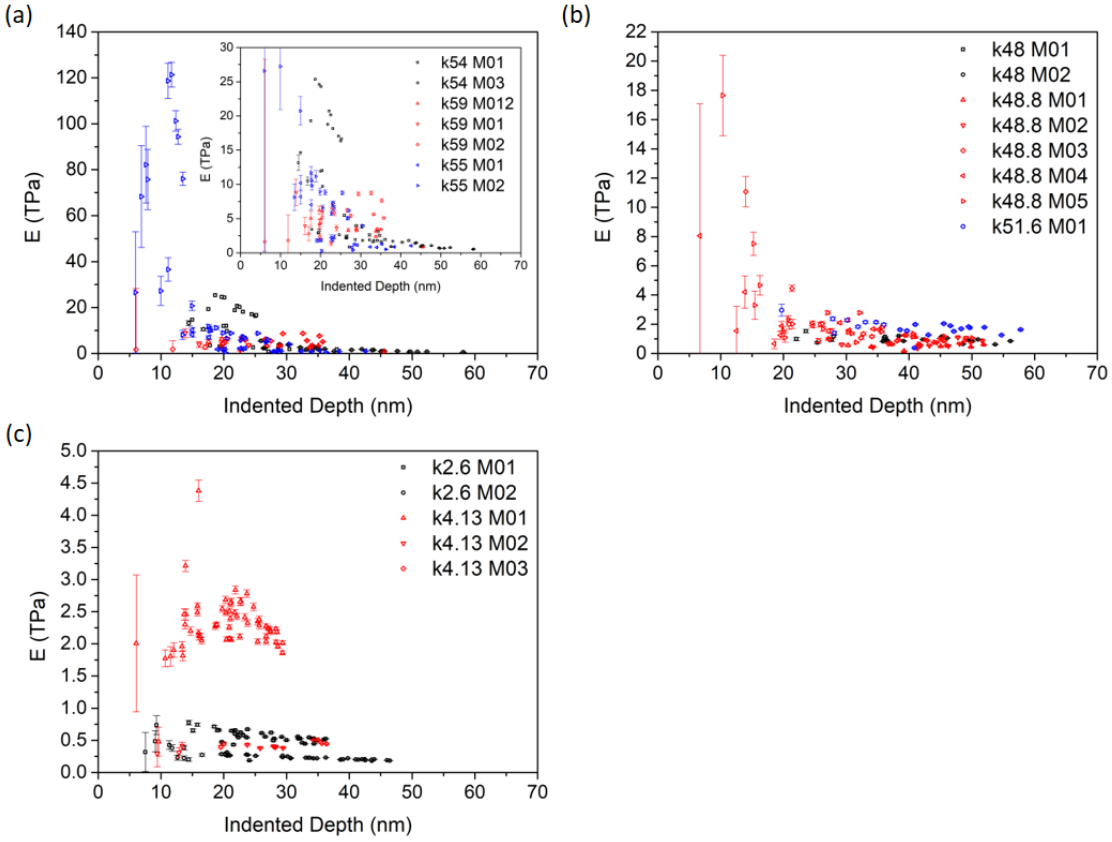

Figure 4.38: Values for the elastic modulus with the respective standard error against the indented depth, measured using the (a) DTNCLR, (b) Tap190DLC, and (c) FM50 probes. k is the spring constant of the cantilever used in N/m while M01, M02 etc. refer to different membranes. Note that each membrane is only indented with one probe.

As evident from Figure 4.38, a significant scatter and overestimation is observed at lower indented depths especially for the higher cantilever spring constants (DTNCLR in Figure 4.38 (a)). On the other hand, the values for the elastic modulus stabilize to lower values closer to the theoretical 1 TPa at higher indented depths. Furthermore, the elastic moduli obtained at small indented depths have significantly larger errors than those obtained from larger indentation depths, using all three different types of probes. This is akin to what was observed in the mechanically exfoliated graphene membranes. Due to the fitting error being introduced and the trend that the elastic modulus is being overestimated when measured from small indented depths, a cut-off indented depth of 25 nm was selected, above which all the results seem stable with small standard errors for a given membrane and cantilever. The selection of the 25 nm as the cut-off value was also made to reflect findings presented in Figure 4.35 to Figure 4.37 (d, e). In these plots the standard error of the cubic term (from which the elastic modulus is extracted) approaches zero beyond an indentation depth of 25 nm, the reduced chi-squared of the fit to the cubic equation saturates around 25 nm, while the adjusted R-square of the fitting procedure approaches 1 at higher indentation depths for all membranes and probes.

For each force-curve obtained, the pretension σ_0^{2D} in N/m was also extracted from parameter A of the fitting procedure (Equation 4.15). Figure 4.39 presents all the measured values for the pretension as obtained from all indented membranes using the (a) DTNCLR, (b) Tap190DLC, and (c) FM50 probes against the indented depth. Figure 4.40 and Figure 4.41 show the relationship between the pretension and the measured elastic modulus. In agreement with López-Polín et al. [61, 64], these plots show no apparent correlation between the elastic modulus and the pretension. Moreover, no correlation between the pretension and the indented depth can be observed. This confirms that the membrane is generally not modified by indentation since the pretension is relatively constant for each membrane. However, some exceptions can be noticed including membrane M01 indented via the FM50 probe with spring constant of 4.13 N/m (Figure 4.39 (c), Figure 4.40 (c) and Figure 4.41(c)). Interestingly however, just as observed for the elastic modulus, it can be noticed that the measured pretension is also significantly different when the membranes are indented using different cantilever spring constants. The pretension measured using stiffer cantilevers (DTNCLR) is higher than that measured using the less stiff cantilevers (FM50).

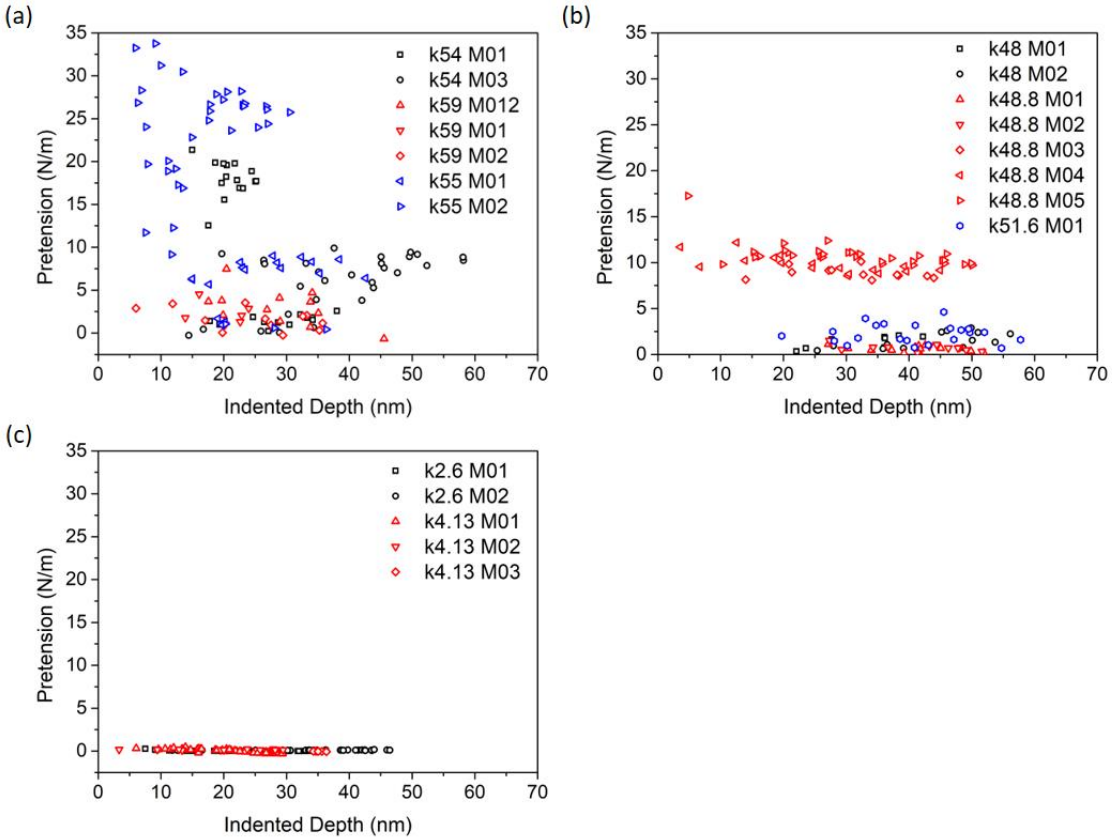

Figure 4.39: Values for the pretension against the indented depth, measured using the (a) DTNCLR, (b) Tap190DLC, and (c) FM50 probes. k is the spring constant of the cantilever used in N/m while M01, M02 etc. refer to different membranes. Note that each membrane is only indented with one probe.

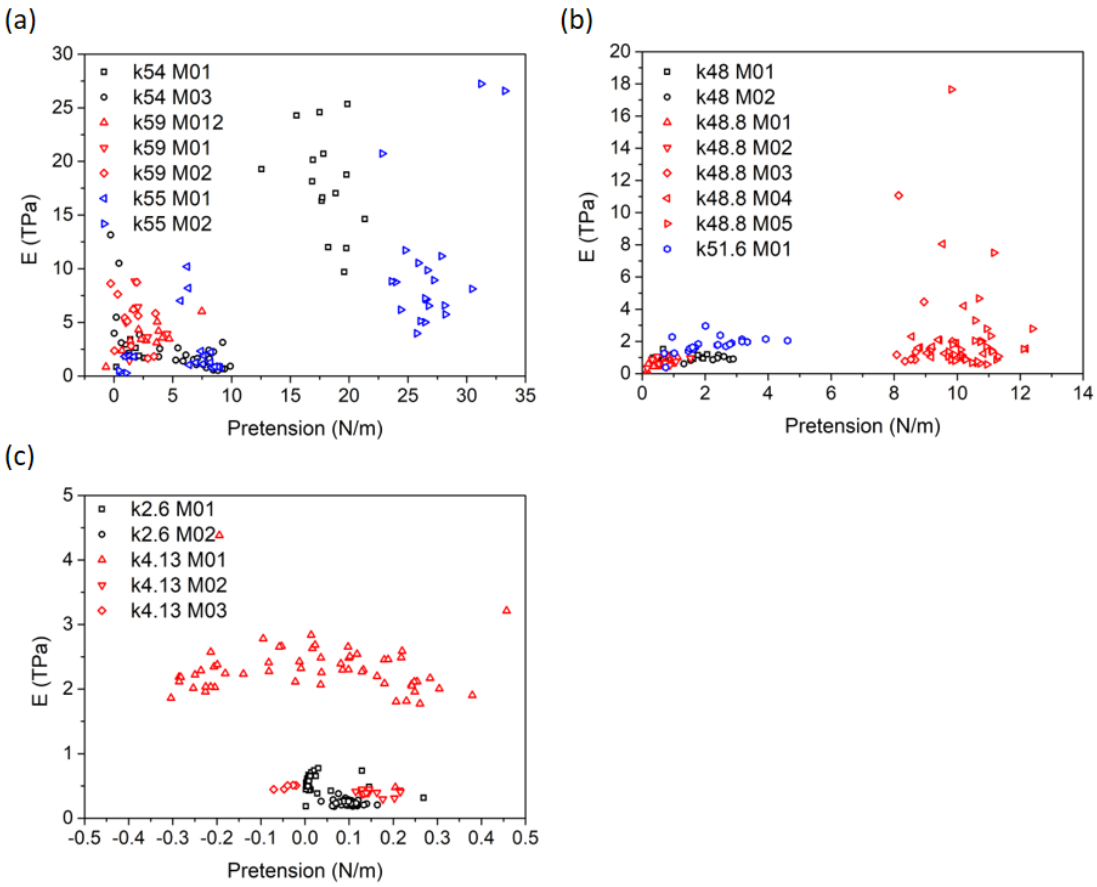

Figure 4.40: Values for the elastic modulus against the pretension, measured using the (a) DTNCLR, (b) Tap190DLC, and (c) FM50 probes. k is the spring constant of the cantilever used in N/m while M01, M02 etc. refer to different membranes. Note that each membrane is only indented with one probe.

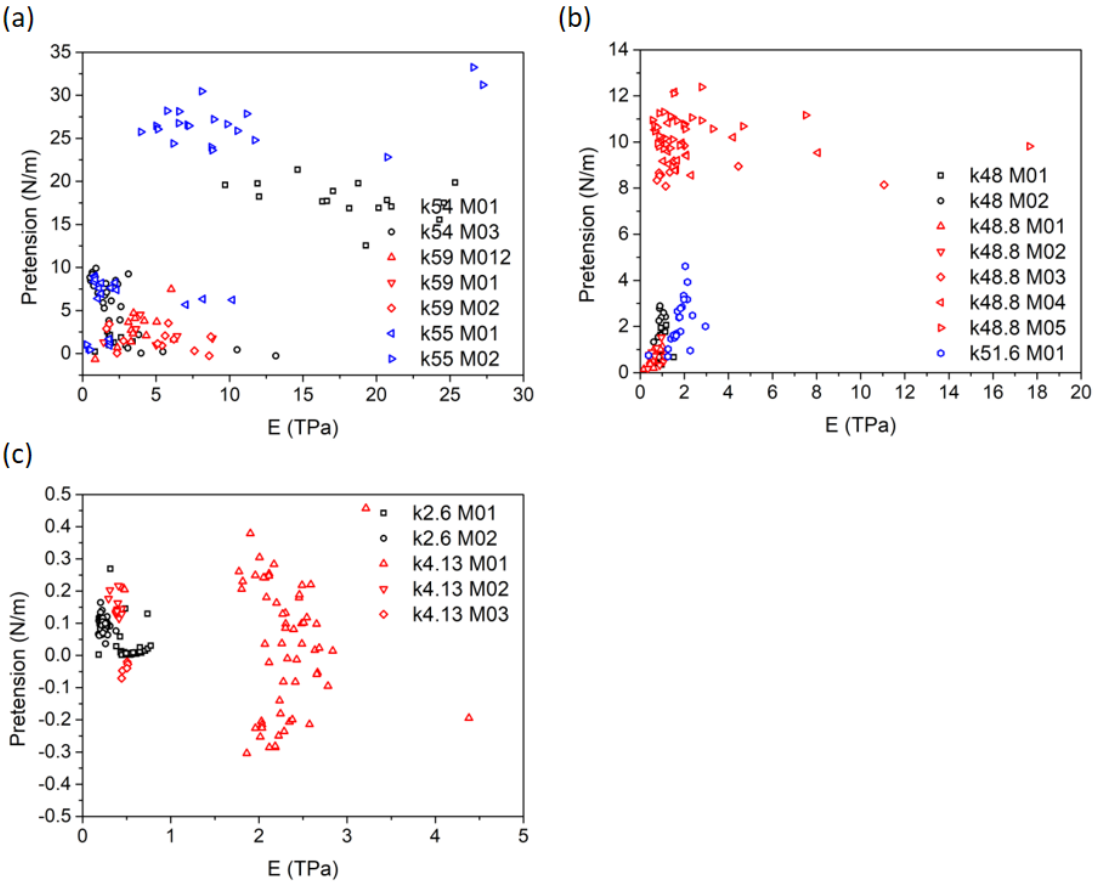

Figure 4.41: Values for the pretension against the elastic modulus, measured using the (a) DTNCLR, (b) Tap190DLC, and (c) FM50 probes. k is the spring constant of the cantilever used in N/m while M01, M02 etc. refer to different membranes. Note that each membrane is only indented with one probe.

4.6.1.2 Cantilever Spring Constant

The average elastic moduli obtained from indentation depths in excess of 25 nm were plotted against the spring constant of the cantilever used, as shown in Figure 4.42.

A few noteworthy observations can be made from the plots presented in Figure 4.42. Firstly, the DTNCLR probes, having the largest spring constants of the three probes, result in higher average values for the elastic modulus, ranging from just below 1 TPa up to around 7 TPa. This overestimation is coupled with a significant error as evidenced by the large error bars. On the other hand, both the Tap190DLC probes and the FM50 probes produce significantly smaller scatter in the results, coupled with more realistic elastic moduli of between 0.5 and 1.5 TPa.

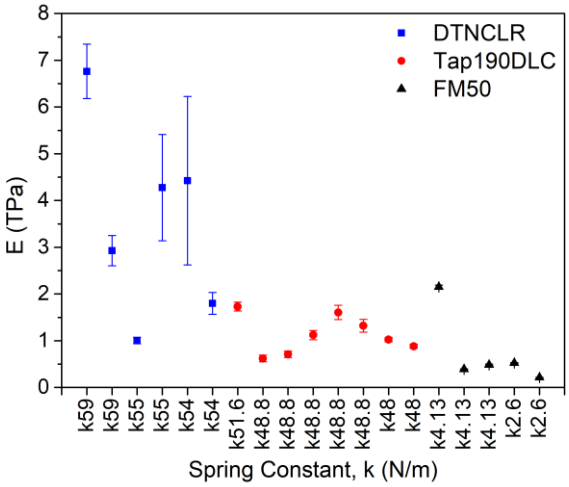

Figure 4.42: Average value of the elastic modulus omitting values obtained from indentation depths lower than 25 nm, against the spring constant of the probe used. The error bars represent the standard error.

Table 4.4: Statistical analysis of the elastic moduli as obtained using the three different types of probes.

Elastic Modulus (TPa)		**For $\delta > 25$ nm**			**All δ**		
		DT NCLR	**Tap190DLC**	**FM50**	**DT NCLR**	**Tap190DLC**	**FM50**
Average	$\bar{x} = \frac{\sum_{i=1}^{n} x_i}{n}$	3.03	1.18	0.75	17.79	0.49	1.07
Standard Error	$\sigma_{\bar{x}} = \frac{\sigma}{\sqrt{n}}$	0.38	0.05	0.09	4.44	0.89	0.08

Table 4.4 lists the average elastic modulus considering all membranes as obtained using different probes, together with the respective standard deviation and standard error. These results highlight that the values obtained using different probes are statistically different and thus, the choice of the cantilever spring constant significantly affects the measurements obtained for the elastic modulus of the graphene membranes.

Figure 4.43 presents histograms of all the obtained values for the elastic modulus for all indentation depths, i.e. including indentation depths lower than 25 nm. A log-normal distribution curve was fitted to each of these histograms. The resulting distribution curves highlight the skewness of the results whereby most of the elastic moduli lie close to 1 TPa (obtained from larger indentation depths) while some values are overestimated (obtained from smaller indentation depths). Therefore, irrespective of the scatter in E obtained at lower indentation depths, the elastic modulus is close to 1 TPa using all probes.

Figure 4.44 compares the distribution curves as obtained using the three different probes. This plot clearly highlights the fact that the values for the elastic moduli are much less scattered when using the FM50 probes, at all indentation depths.

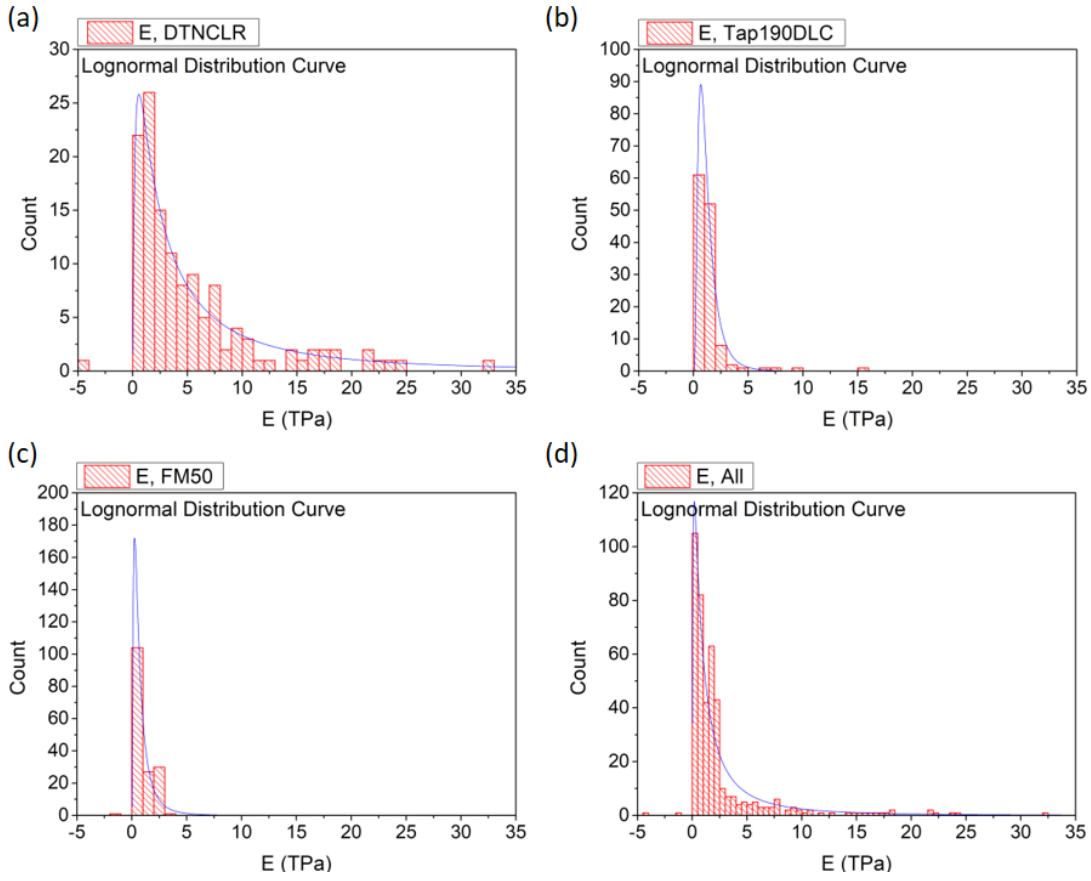

Figure 4.43: Histograms and log-normal distribution curves of the obtained values of the elastic modulus for all indented depths using the (a) DTNCLR, (b) Tap190DLC, (c) FM50, and (d) all probes.

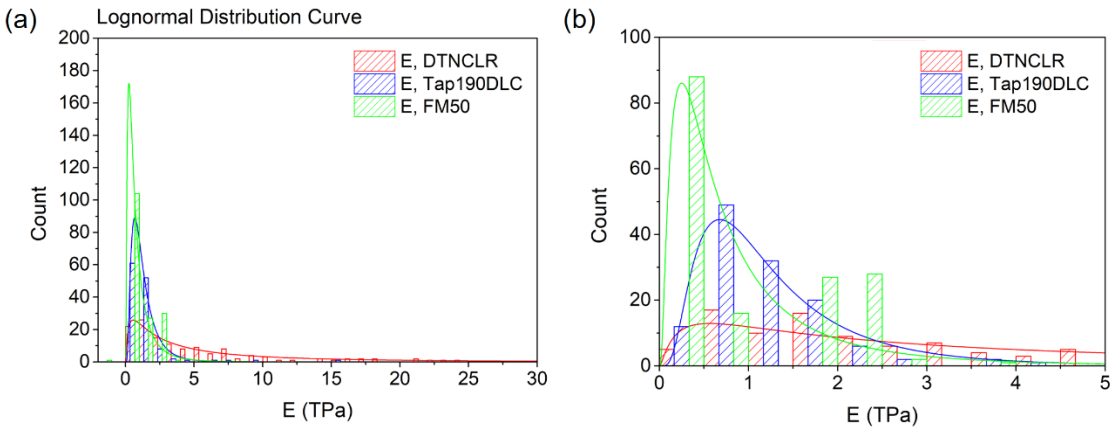

Figure 4.44: A comparison of the distribution curves for the elastic moduli obtained at all indentation depths using the DTNCLR, Tap190DLC, and FM50 probes, in red, blue, and green respectively. (a) and (b) have different scales.

4.6.2 DISCUSSION

The results presented in Section 4.6.1 can be organised into a number of observations:

1. Considering all probes used, the average measured elastic modulus of CVD-grown SLG membranes as obtained via AFM indentation to depths larger than 25 nm is 1.56 ± 0.13 TPa.
2. For indentation depths >25 nm, the measured elastic modulus using the DTNCLR probes ($k \approx 56$ N/m), the Tap190DLC probes ($k \approx 49$ N/m), and the FM50 probes ($k \approx 3$ N/m) was 3.03 ± 0.38 TPa, 1.18 ± 0.05 TPa, and 0.75 ± 0.09 TPa, respectively. Thus, higher cantilever spring constants resulted in higher elastic moduli and larger errors.
3. The scatter and uncertainty in the elastic modulus measurements increase significantly at lower indentation depths.
4. The elastic modulus is overestimated at lower indentation depths (<25 nm).

In the following sections, the above results and observations will be discussed.

4.6.2.1 Measured elastic modulus

The procedure outlined in Section 4.4, together with the use of a variable sensor sensitivity factor and indented depths larger than 25 nm, leads to an average measured elastic modulus of the CVD-grown SLG membranes of 1.56 ± 0.13 TPa. This value is higher than the typically referenced value of ~1.0 TPa [13, 22, 61, 64, 117, 149] for pristine mechanically exfoliated graphene. Some of the published experimentally derived values for the elastic modulus of graphene are listed in Chapter 2 Table 2.1 and Table 2.2. The average elastic modulus found in this study is furthermore significantly higher than that of CVD-grown graphene which has been reported to be as low as 0.16 TPa [83, 86, 151]. In such studies, the drop in the elastic modulus in CVD-graphene has been attributed to the presence of grain boundaries, ripples, small patches of bilayer graphene and other defects brought about by the CVD growth process and the subsequent transfer process/sample preparation [81, 86]. However, Lee et al. [82] report no statistical difference between the elastic modulus of mechanically exfoliated pristine SLG and CVD-grown SLG. The authors only mention that the presence of wrinkles and bilayer patches in the membranes increase the scatter in the results, yet not the average value [82].

Although it has been reported that defects within the graphene membrane have the potential of enhancing the stiffness of the material beyond 1 TPa [115], since the D peak in the Raman spectra obtained from the CVD-graphene membranes (Chapter 3) is very small to insignificant,

it can be deduced that there is no significant disorder in the graphene structure. Therefore, the increase in the elastic modulus measured in this study is not being ascribed to the presence of defects.

It is also commonly claimed in literature that in an un-strained membrane, the elastic properties of the membrane are dominated by out-of-plane thermal fluctuations or wrinkles trapped within the membrane which reduce the stiffness of the wrinkled CVD graphene. An applied strain irons out these fluctuations and the elasticity measured will be dominated by atomic-bond stretching [64]. Thus, an applied pre-strain is able to enhance the stiffness of the graphene membrane [64, 152]. In this study, membranes that had significantly large wrinkles or perturbations, identified in static contact mode AFM, were not sampled for indentation; however, smaller wrinkles, ripples or undulations were necessarily still present in the membranes. These smoothed out during AFM imaging. Evidence of these fine undulations can be seen from the tapping mode AFM images in Figure 4.45. As a side note, the cross-sectional data in Figure 4.45 (d) also demonstrates that the membranes also adhere to the vertical walls of the substrate holes for 2 to 5 nm, in agreement with [13]. As such, while the variations in the individual measurements of the elastic moduli from the average can be indeed attributed to these small ripples and non-uniformities, in agreement with [82], the presence of such small wrinkles confirm that the membranes were not pre-strained. The membranes were not actively strained by a non-indentation factor for example by an applied pressure difference [64], and so, it is not expected that the stiffness is enhanced in our membranes.

In conclusion, it is believed that the average modulus of 1.56 TPa is in fact an overestimation and can be attributed to the mismatch between the stiffness of the cantilever of choice, as will be discussed in the next section.

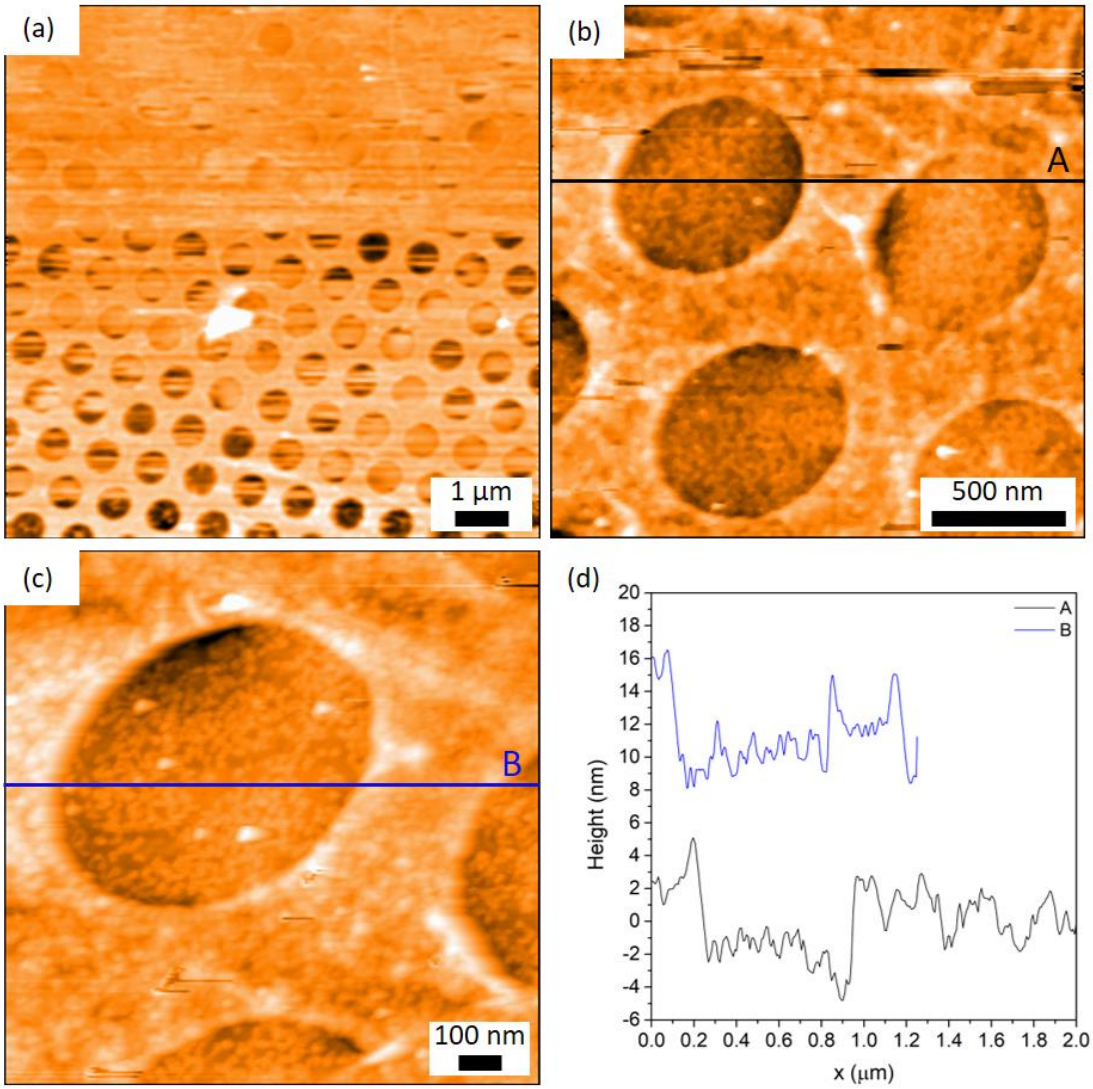

Figure 4.45: (a – c) Tapping mode AFM images obtained in ambient conditions using a Tap190DLC probe (k = 24 N/m using the Sader method) of the CVD-graphene membranes. (d) Cross-sectional height data across two typical graphene membranes.

4.6.2.2 Effect of cantilever spring constant on E

From the results presented in both Section 4.5 and Section 4.6, it can be noted that for the MLG membranes in Section 4.5 (Case Study 2), the FM50 cantilever was too soft to be able to indent the thicker membrane, yet the same type of cantilever resulted in the most stable measured elastic modulus in the CVD-grown SLG membranes in Section 4.6. On the other hand, while the stiffer cantilevers (Tap190DLC and DTNCLR) produced slightly more reproducible results upon indenting the MLG flakes, the use of these cantilevers caused much larger scatter in the results obtained from the SLG flakes. Furthermore, the results presented in Table 4.4 and plotted in Figure 4.46 clearly indicate that for CVD-grown SLG membranes, assuming that the true elastic modulus of the membranes used in this study is around 1 TPa, the DTNCLR probes

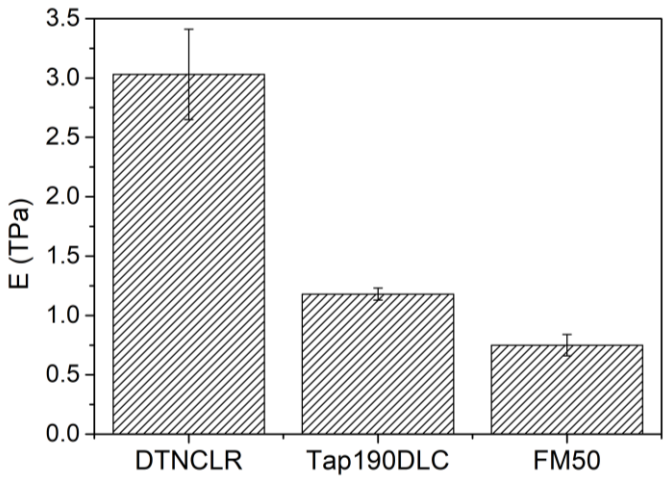

Figure 4.46: The average measured elastic modulus as measured using the DTNCLR, Tap190DLC and FM50 probes. The error bars represent the standard error.

overestimate the modulus, the Tap190DLC probes produce the most accurate and precise results, while the FM50 probes underestimate the modulus.

From the results presented in this study, it is being suggested that the Tap190DLC cantilever having the mid-range stiffness can be used for both MLG and SLG membranes. However, it is not as straightforward to select the most suitable spring constant as otherwise indicated by Frank et al. [52] and Kaman et al. [156], especially if the elastic modulus of the sample and/or the thickness of the sample membrane, both of which affect the E^{2D} [N/m], are not known beforehand. In fact, upon indenting SLG up to 5-layer graphene membranes using the same cantilever stiffness of 2.8 N/m, Annamalai et al. [60] report an elastic modulus of 1.12 TPa for SLG, yet an overestimated value of > 3 TPa for the thicker membranes. Similarly, Clark et al. [149] report that the force-displacement behaviour is indeed dependent on the number of layers, yet they claim that it is independent on the AFM probe used.

Other factors such as the diameter of the graphene membrane can also play a role in the cantilever selection process. The membrane diameter affects the force-distance curve, in agreement with [149]; a lower force would be needed to deflect a larger membrane. Even though the membrane diameter is considered upon finding E^{2D} from parameter B, the wrong choice of cantilever stiffness for the indented membrane might result in an artificial inflation of the material stiffness evidenced by a force-curve with a very high gradient. Thus, a different cantilever might also be required for differently sized suspended membranes. This means that nanoindentation of graphene membranes using an AFM set-up can only be used to obtain comparative data, and only if the same cantilever is used. Absolute values obtained must be

carefully scrutinized. Otherwise, the spring constant of the cantilever used must be well-defined and eventually standardized to allow studies by different research groups to be comparable.

4.6.2.3 Effect of indented depth on the elastic modulus

One of the most interesting set of results obtained in this study, which has not yet been extensively reported and discussed in literature, is the dependence of the measured elastic modulus on the indented depth of the obtained force curve, termed the skin effect [232]. The results presented show that the elastic modulus is often overestimated and displays significantly larger variance at lower indentation depths. In particular, the use of the DTNCLR probes resulted in higher modulus overestimation at lower indentation depths than the softer FM50 probes. A similar observation was made by Kaman et al. [156] who investigated the effect of the choice of spring constant relative to the elastic modulus of bulk H^+ irradiated PDMS samples. As mentioned in Chapter 2, the authors report that irrespective of the modulus of the sample and the cantilever of choice, the elastic modulus as calculated from smaller indentation depths is overestimated. However, no rationale for this phenomenon is presented.

Precise determination of the spring constant is a challenge. It is commonly accepted that the calibrated spring constant has an error of around 10 – 20 % [244, 246]. However, since the spring constant is multiplied to the cantilever deflection, any error in the spring constant determination is independent of the observed skin effect. That is, an error in the spring constant does not change the dependence of the modulus on the indentation depth [232].

Similarly, an error in the positioning of the probe relative to the centre of the membrane will affect the entire set of force curves obtained from a particular membrane. As such, this error should not increase the manifestation of the skin effect yet will directly affect the variation in the results obtained from one membrane to another.

4.6.2.3.1 Numerical error during fitting

The first potential source of higher errors at lower indentation depths is the fewer data points collected by the AFM to compile the force-distance curve. This leads to higher mathematical errors during fitting, as manifested in the larger standard errors of the fitting parameter B. Lopez-Polin et al. [64] report similar effects whereby a pressure difference across the membranes was first applied to flatten out any thermal wrinkles present within the membranes. The membranes were subsequently indented using an AFM probe. The authors report that the numerical fitting of indentation curves obtained at low indentation forces overestimated the

modulus, and constant values were only obtained at indentation forces above ~500 nN. Comparatively to this study, the 25 nm cut-off indentation depth roughly corresponds to indentation forces of ~50 – 100 nN using the FM50 probes, ~100 – 1000 nN using the Tap190DLC probes, and ~500 – 2000 nN using the DTNCLR probes. Furthermore, our results indicate that these errors are not dependent on the force applied (as suggested by Lopez-Polin et al. [64]) but rather on the indented depth. This is because the FM50 cantilevers produced much lower errors for lower indentation forces than the DTNCLR cantilevers.

Figure 4.47 shows a representative force curve obtained using a Tap190DLC probe. The curve was fit to Equation 4.5 using different indented depths. When the curve was fit to an indented depth of around 46 nm – almost the entire curve omitting the last few nanometres in which the curve appears to curve upwards – the elastic modulus was measured to be 0.64 ± 0.02 TPa. However, when the same mathematical model was fit to the same curve yet considering only an indented depth up to 20 nm, the measured elastic modulus was 1.54 ± 0.37 TPa. This confirms that fitting Equation 4.5 to shorter force curves (lower indentation depths) increases the uncertainty in the measured elastic modulus from ± 0.02 TPa to ± 0.33 TPa.

Nonetheless, while such errors in the numerical fitting are justifiable, it is still unclear why statistically these errors lead to an overestimation of the modulus. This can indicate that the model is only suitable for a set range of indented depths.

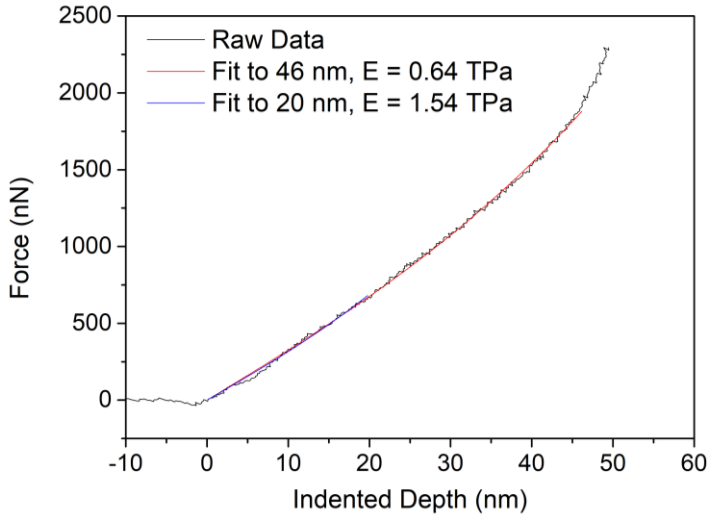

Figure 4.47: Typical FD curve obtained using Tap190DLC with Equation 4.5 being fit to different indented depths.

4.6.2.3.2 Selection of the zero-displacement point ($F = 0, \delta = 0$)

The proper selection of the zero-displacement point (ZDP), or the point where $F = 0, \delta = 0$, has been sufficiently discussed in literature as a main source of errors and uncertainties in the measured modulus. It is widely recognised that the cubic model $F = A\delta + B\delta^3$ to which the force-curve is fitted is highly sensitive to the selection of such ZDP or zero membrane deflection point [83, 149] possibly due to the restriction of the model to pass through the origin. It can also be presumed that the fitting will be more influenced by the ZDP region when the force-curve is restricted to lower indentation depths; fewer data points will lead to larger errors in the measured elastic modulus because of a poor selection of the ZDP.

On this, Lin et al. [83] emphasise that different selections of the ZDP can significantly affect the measured modulus. The authors used similar DTNCLR probes with a measured spring constant of 27 N/m to indent CVD graphene membranes 2.2 μm in diameter. The authors remark that moving the ZDP by 55 nm changes the modulus from 0.417 TPa to 0.935 TPa. The authors continue by saying that a 1 nm offset will change the measured modulus by 10 GPa. Although this discrepancy is significant, moving the ZDP by 55 nm is rather substantial. Given the data acquisition rate of the AFM equipment used in this work, the manual selection of the ZDP could only be off by a few nanometres (<5 nm). As such, this error is not large enough to attribute the significant overestimation in the data presented here.

Similar to Lin et al. [83], Lopez-Polin et al. [61] argue that an error of 2 nm to 5 nm in the selection of the ZDP can lead to a 10% error in the measured elastic modulus. Once again, this error has a much smaller magnitude than the errors that we observe, especially with using the DTNCLR probes (Figure 4.38).

Hence, while some of the scatter in the presented results can indeed be attributed to the uncertainty in the selection of the ZDP, this uncertainty is small in magnitude and does not support the statistical overestimation of the elastic modulus at lower indentation depth.

4.6.2.3.3 Relaxation of wrinkles

As previously mentioned, it is likely that the graphene membranes prepared in this study have a number of small wrinkles within them. Such wrinkles could be causing an instability during the initial indentation and hence particularly affecting the measured modulus at small indentation depths.

Ruiz-Vargas et al. [86] attributed the low elastic modulus measured for CVD SLG of around 0.16 TPa with large scatter in the results to the ripples in the graphene membrane. The authors argue that ripples can soften the membranes such that less energy would be required to flatten them out during indentation rather than activating the elastic response of the covalent bonds within the graphene sheet. This is however contrary to our findings. If the graphene membrane is initially soft, then at lower indentation depths the measured elastic modulus should be significantly lower than 1 TPa. Ruiz-Vargas et al. [86] also report that the presence of grain boundaries and ripples do not locally affect the elastic response of the graphene membranes. On the other hand, the presence of grain boundaries only affects the breaking strength.

Lin et al. [83] report that upon indenting the same CVD-graphene membrane multiple times to the same indentation depths (up to 7 indentations), the membrane stiffness increases. Via AFM imaging before and after indentation, the authors show how initially, the membranes are characterized by a large number of small wrinkles. After the first few indentations, a single larger wrinkle is formed at the expense of the smaller wrinkles. Upon indenting the membrane with the larger wrinkle, it was suggested that the large wrinkle immediately flattens out so the stiffness recorded is only of the interatomic elasticity (covalent bond stretching) rather than the flattening of the smaller wrinkles which would otherwise lead to a reduced stiffness. Therefore, they indicate that small wrinkles are easier to bend and unravel causing the stiffness to be lower than 1 TPa. Once again, this is in disagreement with the results in this work.

Cao et al. [150] who use diamond tips with spring constants of 34 N/m report that the elastic response is scattered upon initial contact but the GO membranes exhibit similar stiffening behaviour as the force-curves converge at higher loads. This is in partial agreement with our observations of significant scatter in the data at low indentation depths, once again indicating the presence of wrinkles which makes the indentation unstable. However, when superimposing all the force curves (Figure 4.21), the curves are seen to deviate more at larger loads, unlike reported in [150]. Furthermore, this still does not explain why at small indentation loads the average modulus is much larger than 1 TPa, assuming that wrinkles are softer than the covalent bonds.

Nicholl et al. [154] confirm using non-contact interferometric profilometry that out-of-plane wrinkles in CVD and exfoliated graphene membranes (7.5 to 30 μm in diameter) soften the stiffness of the membranes. Lopez-Polin et al. [64] induce strain (>0.25%) in the membranes to suppress thermal wrinkling and report an enhanced stiffness.

Therefore, the overestimation of the elastic modulus at lower indentation depths cannot be attributed to the presence of wrinkles in the graphene membranes since such wrinkles have been reported to reduce the stiffness.

4.6.2.3.4 Large local stresses under sharp tips

Dokukin et al. [232] study the qualitative accuracy of the measured elastic modulus of soft polymers using AFM nanoindentation. Similar to this study, the authors [232] attribute the observed skin effect (i.e. the overestimation of the elastic modulus at small indentation depths) to the fact that finer tips create large local stresses in the vicinity of the tip which exceed the linear stress-strain regime of the sample material [233]. Thus, they conclude that tips having a larger radius (810 nm and 1030 nm) are able to eliminate the skin effect. This is contrary to our observations whereby the overestimation is more manifested in the duller tips (DTNCLR with radii ~200 nm) rather than the sharp tips (FM50 with radii < 10 nm). This suggests that the skin effect phenomenon observed in this study is more dependent on the spring constant of the cantilever rather than the tip radius.

The tip was also seen to be damaged after the indentations. However, it was reported that this only affects tip-graphene adhesion, breaking force and hence intrinsic strength and nonlinear elastic behaviour, and not the modulus [149]. Moreover, the multiple force curves obtained in this study were repeatable so any changes in the tip morphology or membrane structure due to the indentations did not affect the modulus.

4.6.2.3.5 Uncertainty in defining the boundary conditions

Annamalai et al. [60] use Equation 4.18 to extract the elastic modulus from force-curves.

$$F = \left[\frac{4\pi E}{3(1-v^2)} \cdot \left(\frac{t^3}{R^2}\right)\right]\delta + (\pi T)\delta + \left(\frac{q^3 E t}{R^2}\right)\delta^3 \qquad \textit{Equation 4.18}$$

They note that the equation is very sensitive to boundary conditions, so a minimal variation in the clamping of the membranes can affect the scatter in the results obtained. However, the scatter in our results are detected in the same graphene membrane. Therefore, if a particular membrane had an irregular boundary due to a defect in the substrate or any inclusions between the substrate and graphene membrane, this should affect all the results in that membrane.

Lopez-Polin et al. [61] list the factors that might have added scatter between different membranes indented (scatter was small for the same membrane unlike what it is being reported in this study at different indentation depths). The authors [61] mention that scatter can be caused by irregular or different boundary conditions, inaccurate diameter measurement and

finite size of the indenter. While it is possible that these factors are present in this study, such inaccuracies still do not explain the different values of elastic modulus measured at different indentation depths. Neither do they explain the significant effect of the spring constant used on the skin effect and also the average "bulk" modulus (at δ > 25 nm).

4.6.2.3.6 Slipping of the membrane

Several research groups considered the possibility of the graphene flake slipping into the hole upon indentation. However, if the membrane was slipping from the edges, it can be assumed that the energy required for slipping is once again lower than that required for elastic deformation of the covalent bonds. Therefore, this would have produced lower moduli at low indentation depths. Otherwise, it is possible that initial indentation does evoke the elastic response, however upon further indentation, the membrane starts to slip. Yet, this will mean that E should be around 1 TPa at low indentation depths, and less for higher indentation depths. Slip is often recognised from the force-curve by the presence of hysteresis between the loading and unloading curves. However, the magnitude of the hysteresis observed in our force-curves is similar to that observed upon indenting the rigid silicon sample. Hence, such hysteresis was assigned to system nonlinearities (Section 4.4.1). If slip had to occur, successive indentations would not have been as reproducible as reported in this study. Finally, slip has also been characterised by small dips in the force-curves [82] which have not been observed in the curves obtained.

In Chapter 6, molecular dynamics simulations modelling nanoindentation of circular graphene membranes are presented with the aim of improving the understanding of the results obtained via experimental AFM nanoindentation.

Chapter 5 FOCUSED GALLIUM ION BEAM BOMBARDMENT

Some of the work and results presented in Section 5.2 were published in [253].

5.1 INTRODUCTION

Following sample preparation (described in Chapter 3) a select number of graphene samples were bombarded with a focused gallium ion beam (FIB) in order to introduce atomic defects in the graphene and hence modify its crystalline structure. Raman spectroscopy was primarily used to characterize the extent of damage imparted to the graphene. Treated graphene membranes were also indented via AFM to investigate the effect of gallium ion bombardment on the elastic mechanical properties of graphene.

The effects of gallium ion bombardment on both supported and suspended single-layer and multi-layer graphene as characterised via Raman spectroscopy is investigated in Section 5.2. These experiments were used to observe correlations between the FIB treatment parameters and the resultant damage in the graphene. Such studies are important for the development of nanostructured membranes and nanoelectronics, for which ion beam irradiation may be used to impart controlled defects or precise sputtering of the graphene. Knowledge of the effect of the substrate on the final crystalline quality of the disordered graphene will determine the process adopted in the fabrication of graphene-based technologies.

The effect of gallium ion bombardment on the elastic modulus of the treated graphene membranes is presented in Section 5.3. The same graphene samples were indented via AFM both before and after the ion beam bombardment following the same methods defined in Chapter 4.

5.2 Effect of Ion Bombardment on Raman Spectra

In order to study the relationship of ion beam dose with the resultant damage imparted to graphene, the following samples were irradiated with a focused gallium ion beam using a FEI Nova 600 Nanolab DualBeam™-SEM/FIB (FEI Company, Oregon, USA):

i) CVD-grown graphene supported on a SiO_2/Si substrate,

ii) Suspended CVD-grown graphene membranes on Quantifoil® TEM grids,

iii) Suspended CVD-grown graphene membranes on silicon nitride microsieve, and

iv) Mechanically exfoliated multi-layer graphene flakes on the patterned PAA/Si substrate.

Two methods for treating graphene samples using the same FIB equipment were used, as described below. Different ion beam parameters were used to alter the ion bombardment dose.

i) The *patterning* method involved scanning the focused ion beam in a raster motion to cover the specified area with a pre-defined shape. With this method, the ion dose is controlled by the 'pixel' density, and the dwell time of the focused ion beam (FIB) at each pixel. The resulting ion dose was calculated automatically by the FIB equipment software used.

ii) The *imaging* method involved using the FIB itself to image the graphene sample. With this method, the area to be treated is imaged for a pre-defined time such that the graphene is damaged by the scanning ion beam. The resulting ion dose (units of measurement C/μm^2) is calculated based on the imaging area (units of measurement μm^2), the number of pixels, dwell time of the beam on each pixel, t, current of the ion beam, I, and the number of scans performed, according to Equation 5.1 and Equation 5.2.

$$Dose\ \left[\frac{C}{\mu m^2}\right] = \frac{I\left[\frac{C}{s}\right] \times t[s]}{A_{pixel}[\mu m^2]} \times (Number\ of\ scans) \qquad \textit{Equation 5.1}$$

$$A_{pixel} = \frac{Area\ of\ image}{Total\ number\ of\ pixels} \qquad \textit{Equation 5.2}$$

The supported CVD graphene was irradiated using the patterning method at an accelerating voltage of 5 kV and ion beam current of 47 pA. Five different beam doses, ranging from 1.8×10^{-13} up to 1×10^{-10} C/μm^2 (equivalent to 1.12×10^{6} to 6.24×10^{8} Ga$^+$/μm^2) were used to pattern differently shaped areas in the graphene sample. The suspended CVD graphene membranes on TEM grids were also treated using the patterning method. To achieve different treatment doses, the pitch of the ion beam raster was changed. Out of a total of four TEM grids being available, only three were exposed to the gallium ion treatment, leaving the fourth sample untreated for control purposes. Different areas within each of the three treated TEM grids were then irradiated at a different dose. The various FIB parameters used for the CVD graphene treated with the patterning method are listed in Table 5.1.

The imaging method was used on the suspended CVD-graphene on the silicon nitride microsieve. The FIB parameters and hence ion doses used for the CVD graphene are listed in Table 5.2.

Table 5.1: Patterning Focused Gallium Ion Beam Treatments on Supported CVD Graphene on SiO_2/Si, and Suspended CVD Graphene on TEM Grids.

Sample	Energy (kV)	Current (pA)	Incidence Angle (°)	Dose (C/μm^2)	(Dose ID)
Supported CVD Graphene on SiO_2/Si	5.0	47	90	1.80×10^{-13}	(T0.18)
				5.00×10^{-13}	(T0.5)
				1.00×10^{-12}	(T1)
				5.00×10^{-11}	(T50)
				1.00×10^{-10}	(T100)
Suspended CVD Graphene on TEM Grids	5.0	1.6	90	5.28×10^{-7}	
				5.28×10^{-5}	
				2.11×10^{-4}	
				4.86×10^{-4}	
				5.28×10^{-3}	
	30.0	1.5	90	1.22×10^{-2}	
				3.27×10^{-7}	
				3.27×10^{-3}	
				1.31×10^{-2}	
	30.0	1.5	28	3.27×10^{-3}	
			53		
			68		
			83		

Table 5.2: Imaging Focused Gallium Ion Beam Treatments on Suspended CVD Graphene on Silicon Nitride Microsieves.

Sample	Energy (kV)	Current (pA)	Dose (C/µm^2)	(Dose ID)
Suspended CVD Graphene on Microsieve	30.0	10.5	6.86×10^{-16}	(T1)
		10.5	3.29×10^{-15}	(T2)
		92	6.61×10^{-13}	(T3)

Table 5.3: Focused Gallium Ion Beam Treatments on Mechanically Exfoliated Multi-layer Graphene on patterned PAA/Si Substrate.

Sample	Ion bombardment method	Flake ID	Dose (C/µm^2)
Mechanically Exfoliated MLG on patterned PAA/Si Substrate	Patterning	Flake E	6.62×10^{-13}
		Flake F	1.33×10^{-14}
	Imaging	Flake G	3.30×10^{-15}
		Flake H	3.30×10^{-15}
		Flake C	6.60×10^{-16}
		Flake I	6.60×10^{-16}
		Flake J	6.60×10^{-16}

Both the patterning and imaging methods were used on different mechanically exfoliated MLG flakes. For all treatments, an ion beam energy of 30 kV, current of 1.5 pA and an incidence angle of 90° were used. The resulting treatment doses are listed in Table 5.3.

5.2.1 Characterization Methods

Optical microscopy, scanning electron microscopy, Raman spectroscopy and atomic force microscopy, were once again used to study the graphene before and after bombardment via gallium ions.

Raman spectra using the Witec Alpha300 at an excitation wavelength of 633 nm, a 60× objective, and a 600 g/mm grating, were recorded from the untreated and treated areas to compare the quality of graphene before and after ion beam bombardment. The suspended CVD-graphene on the silicon nitride microsieve was similarly characterized using the Horiba Xplora Plus at an excitation wavelength of 532 nm, a 100x objective, and a 1200 g/mm grating. As noted in Chapter 3, to limit the damage induced by the 532 nm Raman laser itself, the laser

power was limited to 1% of the full power and single spectra were obtained with an integration time of 5 seconds for a total of 5 accumulations.

For the supported graphene, the damaged graphene surrounding the treated areas was also analysed, with the distance away from the edge of the 1×10^{-10} C/μm^2 treated area, D_T, ranging from 0 to 66 μm (denoted as $T100_0$ to $T100_{60}$, respectively), in steps of 6.6 μm.

For the suspended CVD-graphene membranes on the TEM grids, both single spectra and 2D spectral maps were gathered for each treated area. For the single spectra, an integration time of 10 seconds was used for a total of 10 accumulations. For the 2D spectral maps (a sample of which is included in Appendix E), an integration time of 5 seconds was used with an acquisition step size varying from 0.1 to 0.5 μm. For each map, sets of ten consecutive spectra obtained from circular areas of freely suspended graphene, and hence those featuring minimal substrate-generated background noise, were then selected and averaged.

Similar 2D Raman spectral maps were obtained for the mechanically exfoliated MLG flakes. Spectra obtained from distinct areas showing similar Raman features were averaged.

Each Raman spectrum was post-processed to remove the background noise and analysed using the same procedures explained in Chapter 3. Section 5.2.2 presents a set of detailed results extracted from the Raman spectra from the treated graphene samples.

5.2.2 RESULTS

5.2.2.1 Treated Supported CVD Graphene on SiO_2/Si

Figure 5.1 (a) shows an SEM image of the treated supported CVD graphene. A two-dimensional Raman spectral map was obtained to cover the entire treated area. Figure 5.1 (b – e) show the same spectral map with the intensity colour of each pixel corresponding to the intensity of part of the corresponding spectrum; Figure 5.1 (b) shows the combined intensity of the G and D peaks (between 1099.9 and 1754.4 cm^{-1}), (c) shows the intensity of the D peak (between 1290.8 and 1368.8 cm^{-1}), (d) shows the intensity of the G peak (between 1535.9 and 1652.9 cm^{-1}), and (e) shows the intensity of the 2D peak (between 2583.3 and 2717.0 cm^{-1}). Generally, the brighter the area is on the D peak map, the darker it is on the 2D peak map, yet in some instances, some brightness can be attributed to fluorescence. Representative Raman spectra of the graphene treated with 1×10^{-12} C/μm^2 (T1), 5×10^{-13} C/μm^2 (T0.5), and 1.8×10^{-13} C/μm^2 (T0.18) are shown in Figure 5.2.

The SEM image in Figure 5.1 (a), as well as Figure 5.2, shows that the areas treated with 1×10^{-12} C/µm^2 (T1) and 5×10^{-13} C/µm^2 (T0.5) are damaged, with the former appearing more damaged. The texture, while not entirely flat and featureless like in the case of the two higher doses (T50 and T100), is still different than the rest of the untreated graphene, mainly characterised by uneven brightness. The Raman spectra indicate that while the 2D peak is absent from both areas (T1 an T0.5), significantly broad (large FWHM) D and G peaks may appear in only some parts. In other areas, the broadened D and G peaks merge to form one plateaued peak. Finally, a dose of 1.8×10^{-13} C/µm^2 (T0.18) retained the texture of the untreated graphene and the SEM only registered a change in the brightness in the treated area. However, the 2D peak is still barely present while the D and G peaks are significantly large yet less broad and more defined than at higher doses.

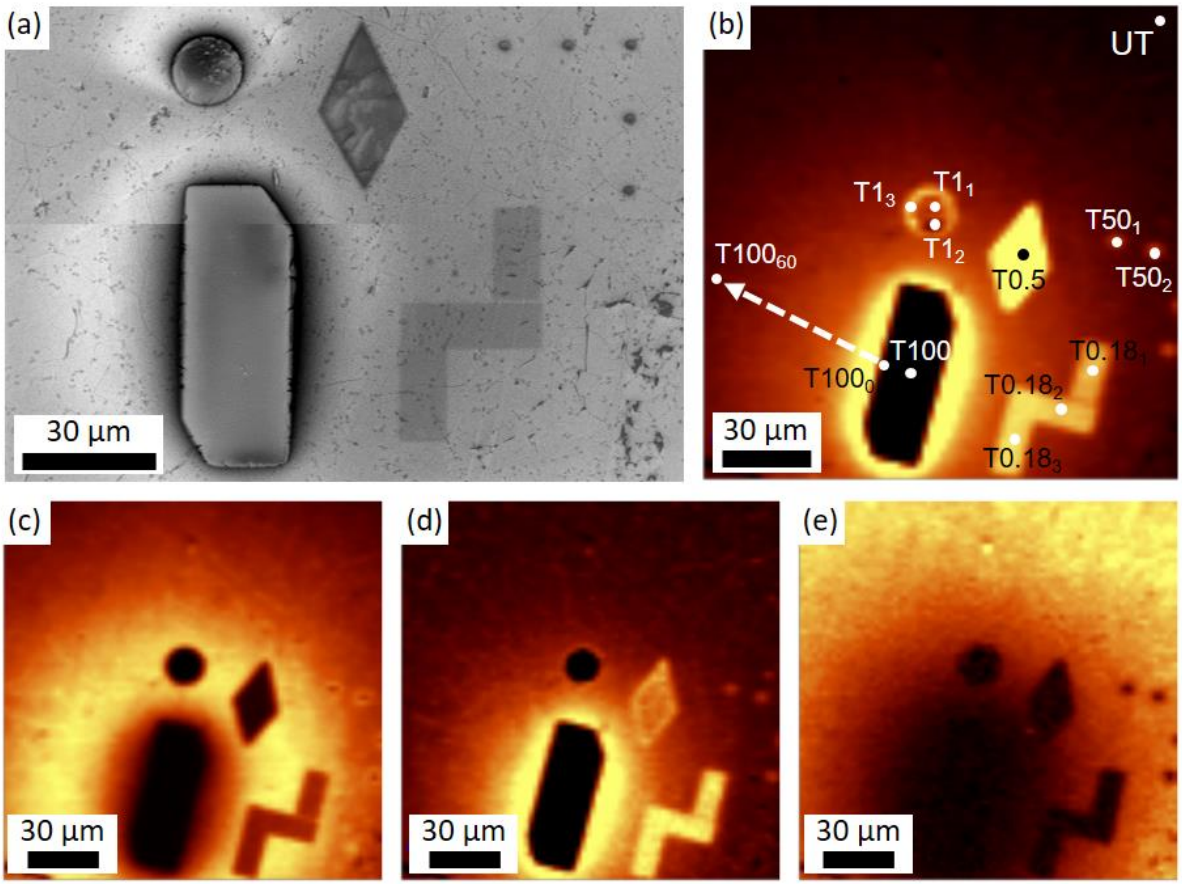

Figure 5.1: Treated supported CVD graphene patterned via a focused gallium ion beam. (a) SEM image. (b-e) 2D Raman spectral maps of the sum of parts of the spectrum depicting the intensity of the (b) G and D, (c) D, (d) G, and (e) 2D peaks.

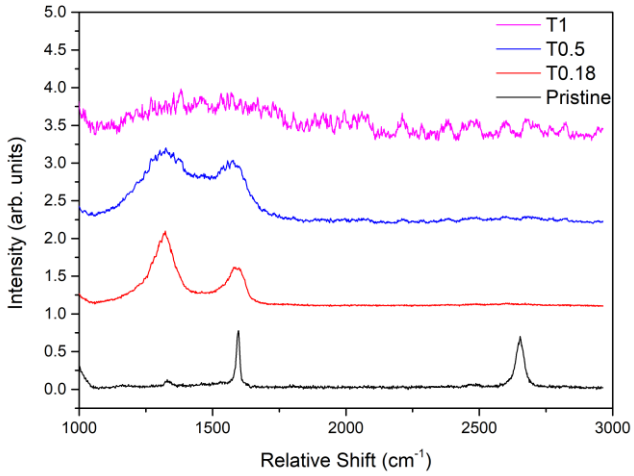

Figure 5.2: Representative Raman spectra from the supported CVD graphene treated with a dose of 1×10^{-12} C/µm² (T1), 5×10^{-13} C/µm² (T0.5), and 1.8×10^{-13} C/µm² (T0.18).

The Raman spectrum recorded from the directly irradiated area with an ion beam dose of 1×10^{-10} C/µm² (T100) is free from any peaks characteristic of graphene or other carbonaceous materials, signifying the complete removal of graphitic material during ion bombardment. The area surrounding the 1×10^{-10} C/µm² (T100) and 1×10^{-12} C/µm² (T1) treated areas also looks damaged in the SEM images by the presence of a dark ring followed by a bright ring around the target areas. Moreover, the 2D Raman maps reveal a larger radius of damage (up to around 70 µm from the target areas) caused by the treatment evident from a circular ring of low 2D peaks (Figure 5.1 (e)) and large D peaks (Figure 5.1 (c)). This surrounding area and the associated damage profile were investigated, and the recorded Raman spectra are presented.

At the edge of the bombarded area (D_T = 0 µm, $T100_0$ in Figure 5.1 (b)), the D+D" and 2D band disappear, while the Lorentzian D and G bands downshift by 16 cm^{-1} and 20 cm^{-1}, respectively. As the Raman spectra were taken further away from the irradiated area, the untreated graphene spectrum was progressively restored. Thus, as shown in Figure 5.3 and Figure 5.4, the position of the Lorentzian D, G, and 2D peaks upshift slowly converging toward the original positions in untreated graphene, in agreement with [54]. The intensity of the 2D peak linearly increases while the FWHM of the 2D peak decreases further away from the edge of the treated area. This combination causes the integrated area of the 2D peak to exhibit non-monotonic behaviour as shown in Figure 5.4.

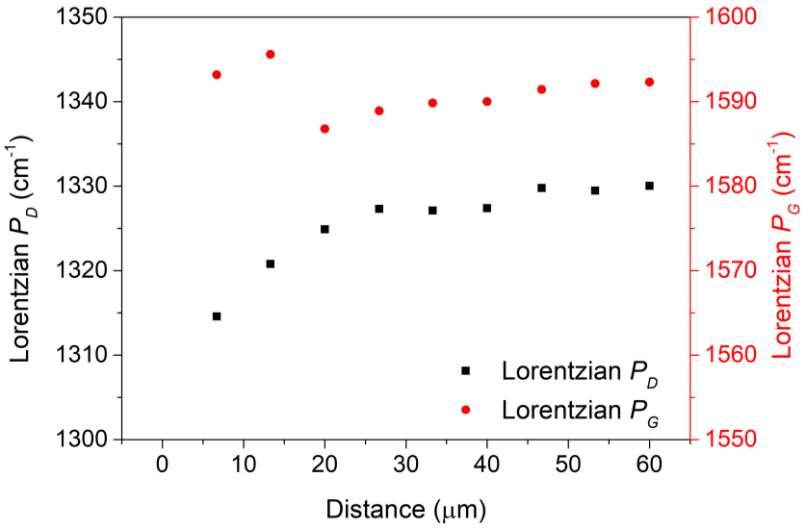

Figure 5.3: The position of the Lorentzian D band (P_D) and Lorentzian G band (P_G) in the damaged supported graphene.

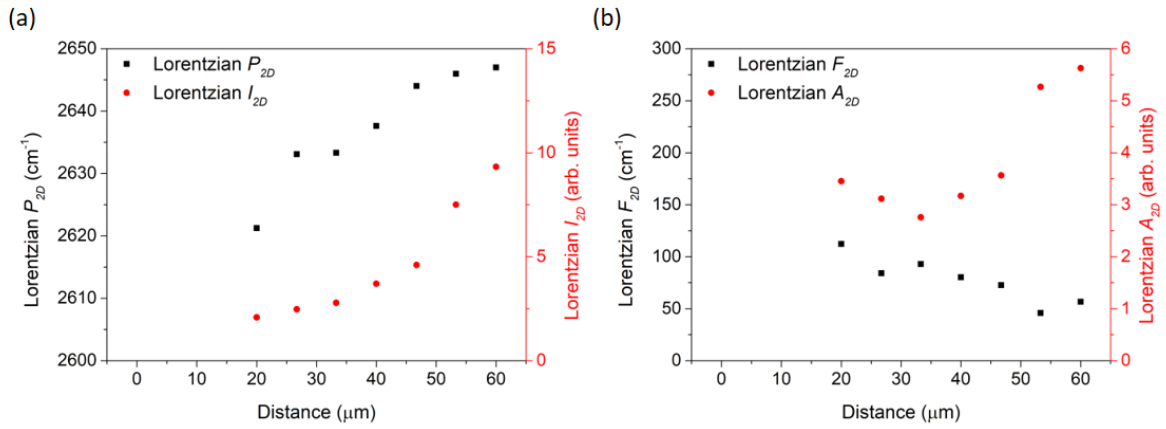

Figure 5.4: The 2D band in the damaged supported graphene.

Particularly in Raman spectra taken from areas closer to the directly treated area, it was noted that the profiles of both the D and G peak are not entirely Gaussian nor Lorentzian. As such, the D and G peaks of such spectra of supported highly-damaged graphene were fit with two components each; a Lorentzian peak for crystalline graphene and a Gaussian peak to represent the partial amorphization of graphene. In fact, the Raman spectrum corresponds to amorphous carbon at the very edge of the treated area, with the Gaussian G peak appearing at 1571 cm^{-1} and the Gaussian D peak appearing at 1320 cm^{-1}. For D_T smaller than around 20 μm, both the Gaussian D peak and the Gaussian G peak increase in intensity and broaden indicating the large degree of amorphization (Figure 5.5). Both Gaussian peaks reduce in intensity and width with an increase in the distance from the edge of the treated area. This indicates that the amount of amorphous carbon present is reducing. The position of both the Gaussian G peak and of the

Gaussian D peak is also observed to downshift further away from the directly treated area. This supports the assigning of these peaks to the amorphization of graphene, with an increase in the disorder of the sp^2 hybridized sites and an increase in the sp^3 hybridization resulting in a corresponding upshift of the Gaussian D and G peaks [254, 255]. Contrarily, the Lorentzian D peak and the intensity ratio between the Lorentzian D peak and the Lorentzian G peak (Lorentzian I_D/I_G) start to increase due to the larger presence of defected graphene rather than amorphous carbon (Figure 5.6).

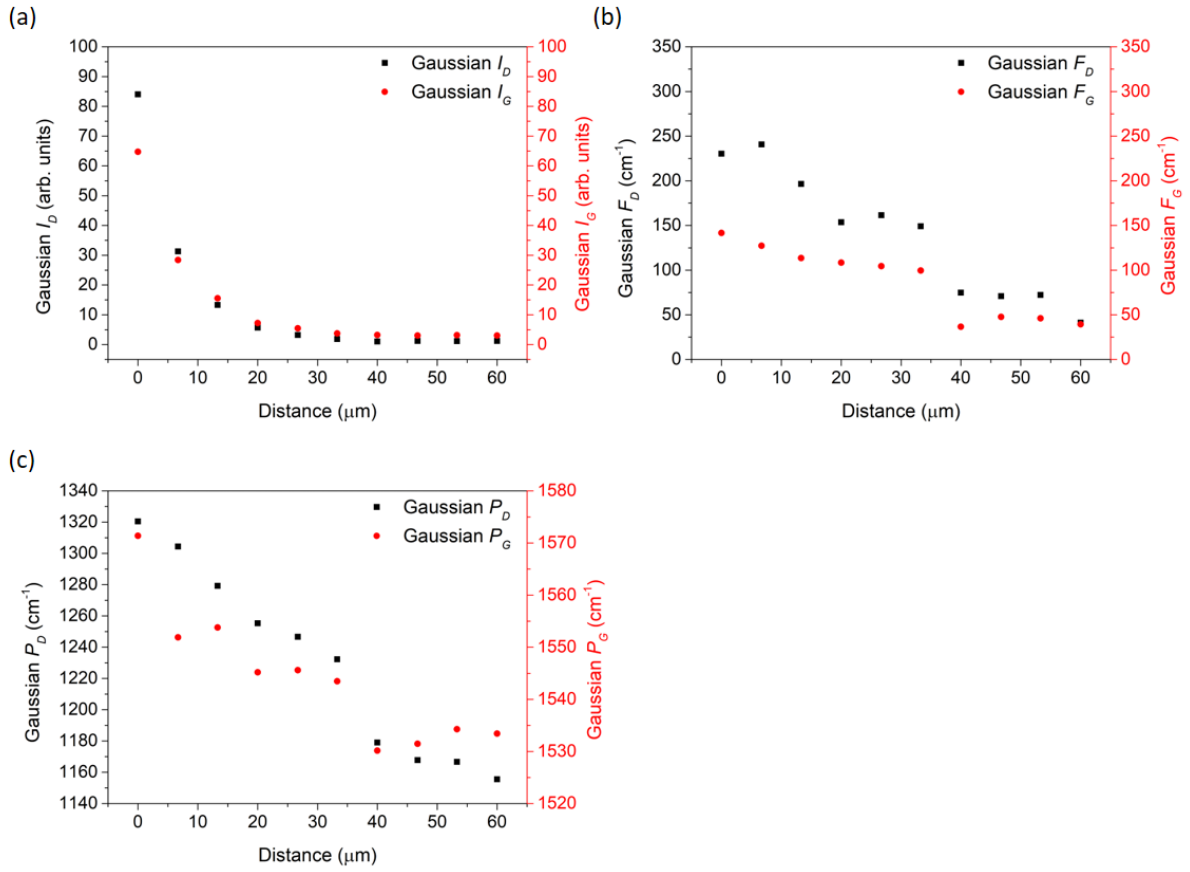

Figure 5.5: The (a) intensity, (b) FWHM, and (c) position of the Gaussian D and Gaussian G bands in the damaged supported graphene. (d) The intensity of the Lorentzian D band (I_D) and the intensity ratio between the Lorentzian D band and Lorentzian G band (I_D/I_G) in the damaged supported graphene.

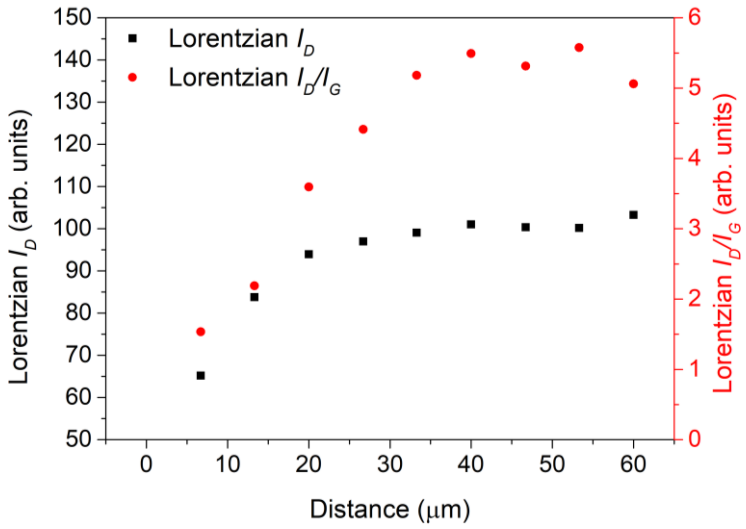

Figure 5.6: The intensity of the Lorentzian D band (I_D) and the intensity ratio between the Lorentzian D band and Lorentzian G band (I_D/I_G) in the damaged supported graphene.

As shown in Figure 5.7, the intensity ratio between the Gaussian D peak and the Lorentzian D peak (I_{DG}/I_{DL}) is around 0.3 as close as 6.7 μm away from the edge of the treated area, and exponentially decays to around 0.01 at a distance of around 35 μm, where the ratio seems to stabilize over the next few micrometres. It is expected that this ratio continues to fall further away from the treated area to approach that for untreated CVD graphene. Likewise, the intensity ratio between the Gaussian D peak and the Gaussian G peak (I_{GG}/I_{GL}) is around 0.4 at around 13 μm, exponentially decays, and finally stabilizes to around 0.16 at 45 μm. These two ratios are believed to be closely related to the degree of amorphization of graphene due to ion bombardment and the resulting high degree of disorder. Thus, it is suggested that in such cases of partial amorphization of graphene, the intensity ratios of the Gaussian D peak to the Lorentzian D peak (I_{DG}/I_{DL}) and the Gaussian G peak to the Lorentzian G peak (I_{GG}/I_{GL}) can be used to specify the degree of amorphization, with larger ratios indicating a higher degree of disorder.

Figure 5.8 shows the Raman spectrum recorded at D_T = 40 μm. Raman spectra with similar peaks were recorded at D_T = 20 to 60 μm. Apart from the large Lorentzian I_D/I_G ratio, the presence of a low-intensity 2D peak and the Gaussian G peak previously attributed to the amorphous carbon, the Lorentzian G band is seen to split into two peaks with the emergence of the D' peak at around 1620 cm^{-1}. Although the Gaussian G peak (at around 1530 cm^{-1}) was previously attributed to the presence of amorphous carbon, the peak shape develops from a Gaussian one at higher defect concentrations to a Lorentzian peak shape.

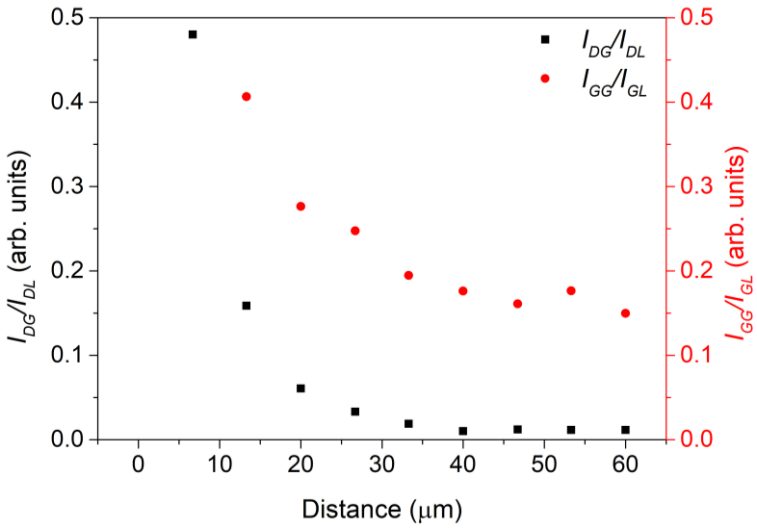

Figure 5.7: The intensity ratio between the Gaussian and Lorentzian D band (I_{DG}/I_{DL}) and the intensity ratio between the Gaussian and Lorentzian G band (I_{GG}/I_{GL}) in the damaged supported graphene.

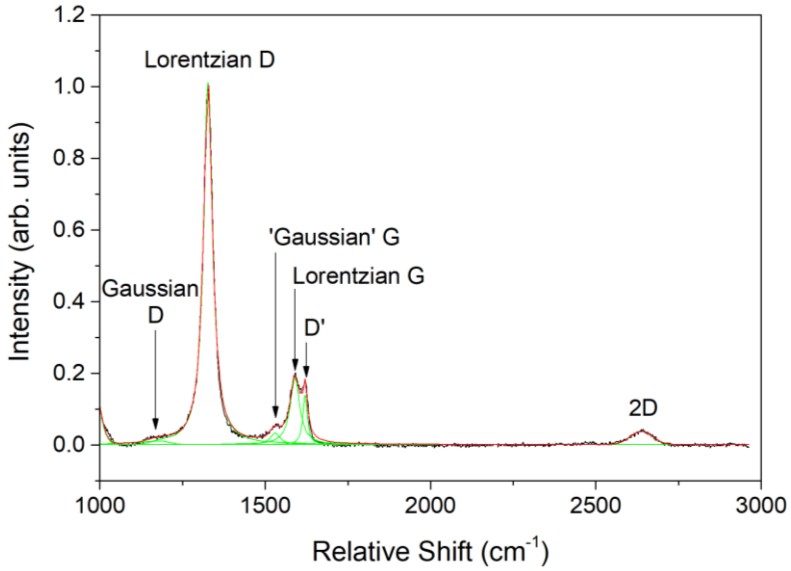

Figure 5.8: The Raman spectrum at D_T = 40 μm showing the D peak (1327.4 cm^{-1}), 'Gaussian G' peak (1530.1 cm^{-1}), Lorentzian G peak (1590.0 cm^{-1}), D' peak (1620.68 cm^{-1}) and 2D peak (2637.7 cm^{-1}).

Down to a distance of 60 μm, the D peak is not fully restored, unlike the G peak in which case the intensity, position and FWHM significantly approach the pristine state after 42 μm.

5.2.2.2 Treated Suspended CVD Graphene Membranes on TEM Grids

Figure 5.9 to Figure 5.11 show the peak parameters of interest for the Lorentzian and Gaussian D, G and 2D bands in treated suspended CVD graphene on TEM grids. As expected, the intensity of the Lorentzian D band increases linearly with an increase in treatment dose (Figure 5.9 (b)). The Lorentzian D peak is also seen to downshift nonlinearly from around 1355 cm^{-1}

to around 1325 cm^{-1} in an exponential decay (Figure 5.10 (a)). The frequencies at which the Lorentzian G band and 2D band occur do not shift significantly with the increase in treatment dose. However, both the Gaussian G band and Gaussian D band are seen to upshift with an increase in treatment dose, and downshift again at doses higher than 1.22×10^{-2} $C/\mu m^2$. The intensity of both the Lorentzian G and 2D bands linearly decrease with an increase in dose. However, changes in both parameters, especially the intensity of the 2D may not be statistically significant given the large variation in the untreated membranes. Since the intensity of the 2D peak decreases and the width of the same 2D peak exhibits no significant change, the integrated area of the 2D peak decreases with an increase in the treatment dose (Figure 5.11).

Figure 5.11 (b) shows the change in the Lorentzian I_D/I_G and F_D/F_G ratios of the suspended CVD graphene before and after gallium ion irradiation. The fact that the I_D increases while the I_G decreases enhances the linear increase of the I_D/I_G intensity ratio. The F_D/F_G follows an exponential decay mainly due to the changes of the same nature in the D peak.

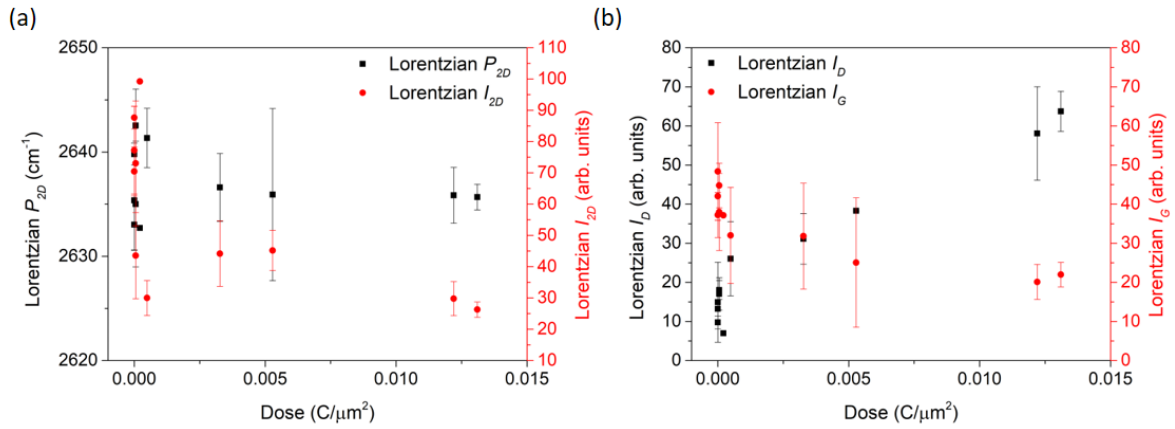

Figure 5.9: (a) The position and intensity of the Lorentzian 2D peak, and (b) the intensities of the Lorentzian D and G peaks, in suspended graphene.

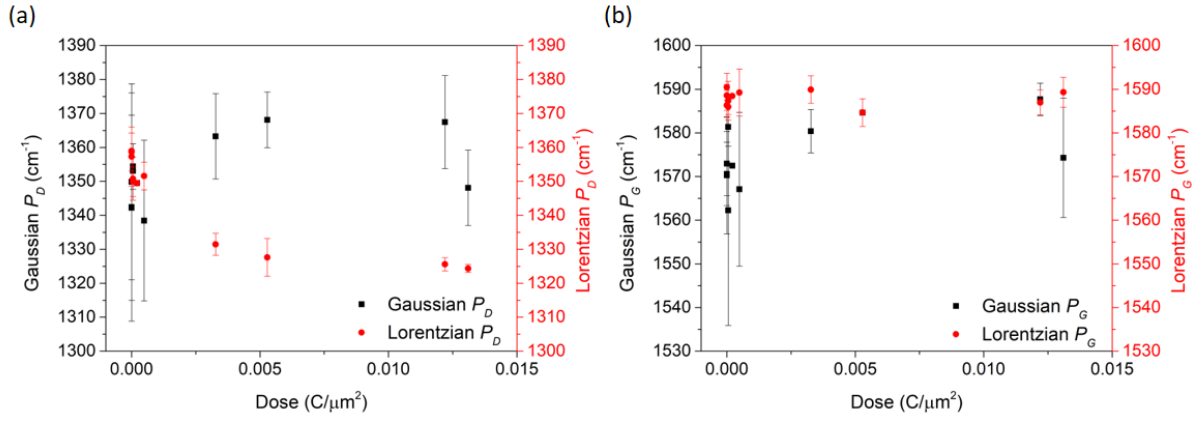

Figure 5.10: The position of the Lorentzian and Gaussian (a) D peak, and (b) G peak, in suspended graphene.

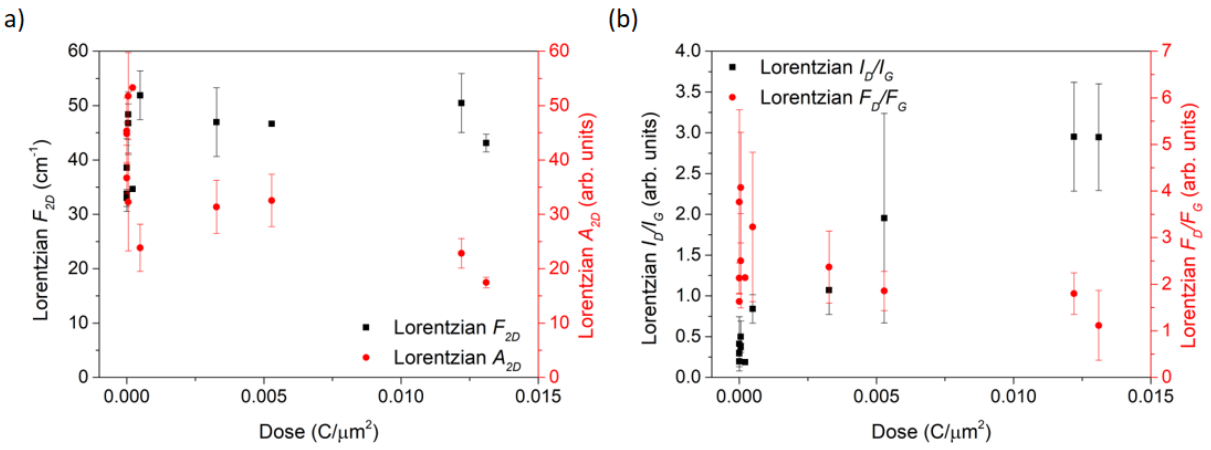

Figure 5.11: (a) The FWHM and integrated area of the Lorentzian 2D peak, and (b) the intensity ratio I_D/I_G *and FWHM ratio* F_D/F_G*, in suspended graphene.*

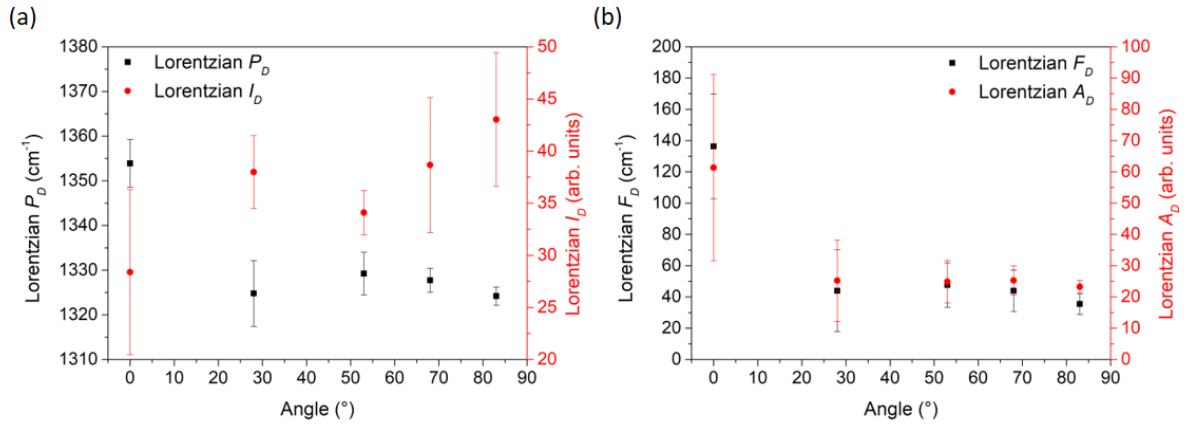

Figure 5.12: The Lorentzian D peak against ion beam incidence angle.

The effect of the incidence angle of the ion beam on the Raman spectrum was also investigated. Only the 2D peak was not affected by the incidence angle. Similar to an increase in treatment dose, an increase in the incidence angle to the surface downshifted the Lorentzian D peak in an exponential decay from around 1355 cm^{-1} to around 1325 cm^{-1} (Figure 5.12). Furthermore, while the I_D increases linearly with a higher incidence angle (i.e. closer to normal incidence), the F_D decreases linearly from around 40 cm^{-1} to 20 cm^{-1}, causing the overall area to decrease. Again, similar to the treatment dose, an increase in the angle of incidence reduces the F_G and hence the A_G (Figure 5.13). The abovementioned changes cause the I_D/I_G ratio in Figure 5.14 to increase linearly with an increase in incidence angle.

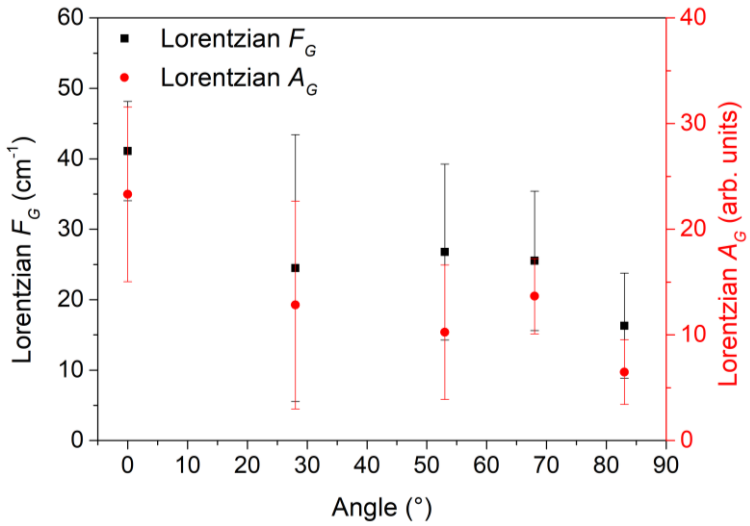

Figure 5.13: The FWHM and integrated area of the Lorentzian G peak against ion beam incidence angle.

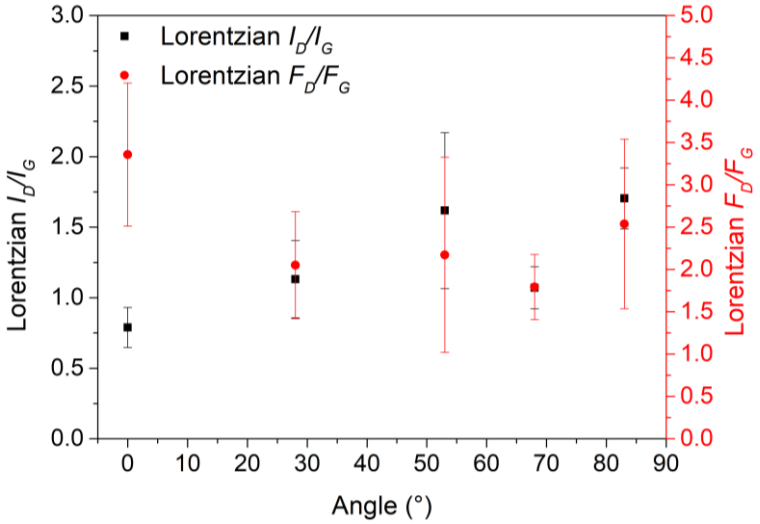

Figure 5.14: The intensity ratio I_D/I_G *and the FWHM ratio* F_D/F_G *against the incident angle.*

5.2.2.3 Treated Suspended CVD Graphene Membranes on Silicon Nitride Microsieve

Figure 5.15 shows optical micrographs of the CVD-graphene on silicon nitride microsieve before treatment, indicating the FIB treated areas . For each ion dose, two areas of graphene membranes were irradiated, denoted as T1-1 and T1-2 etc. Figure 5.16 presents the averaged Raman spectra obtained from the silicon nitride microsieve substrate, untreated (UT) graphene membranes, and the ion irradiated graphene membranes (T1, T2, and T3 as in Table 5.2), obtained using the 532 nm laser. The corresponding peak parameters obtained after post-processing the Raman spectra are listed in Appendix F.

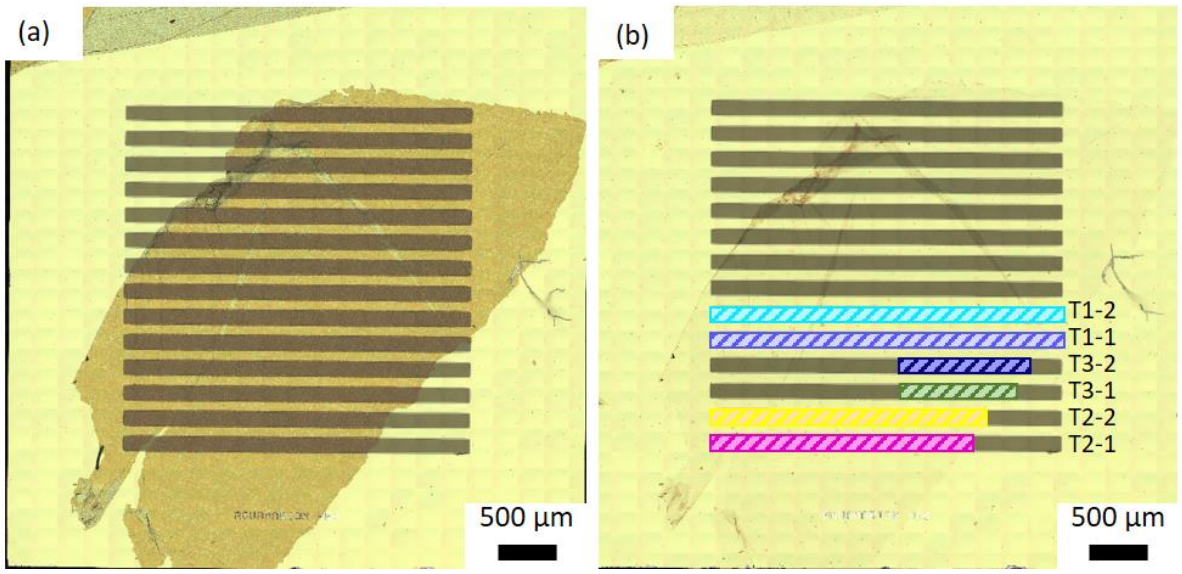

Figure 5.15: Optical micrographs of the CVD graphene on the silicon nitride microsieve (a) before, and (b) after removal of the sacrificial layer, showing the ion irradiated areas in (b).

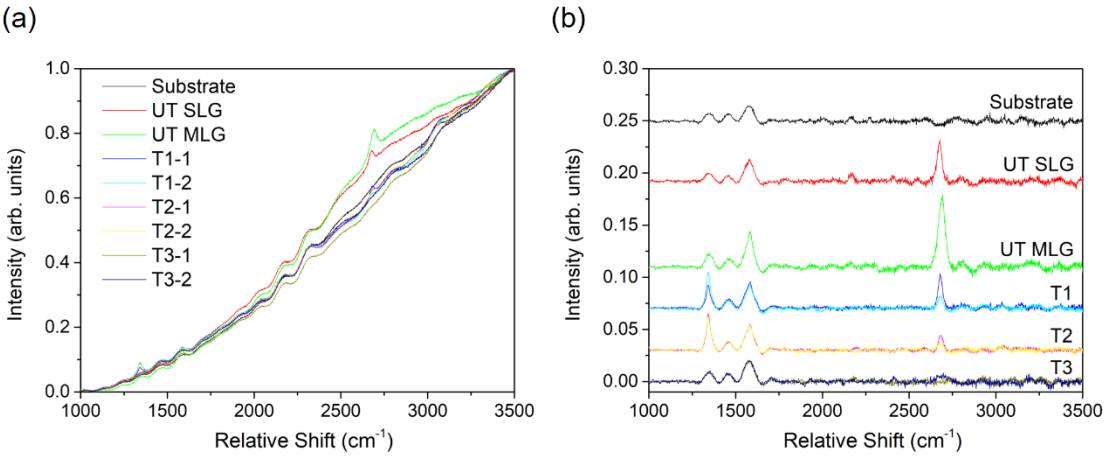

Figure 5.16: Raman spectra obtained of the CVD-graphene on the silicon nitride microsieve in the untreated (UT) and treated (T) regions. The spectra were (a) averaged and normalised, and (b) subtracted from the baseline.

As also noted in Chapter 3, the silicon nitride microsieve substrate coupled with the use of the 532 nm laser wavelength produces a significantly predominant baseline, with three peaks appearing in the same Raman shifts as the graphene D and G peaks. Thus, the 2D peak remains the main marker indicating the presence of graphene. However, upon irradiation with 6.86×10^{-16} C/µm^2 (T1) and 3.29×10^{-15} C/µm^2 (T2), the D peak is observed to intensify and reduces in FWHM. This is coupled with an increase in the I_D/I_G and I_D/I_{2D} ratios and a decrease in the I_{2D}/I_G and F_D/F_G ratios. The higher I_D/I_G and I_D/I_{2D} ratios in the T1-2 area indicate that area T1-2 is more similar to areas T2 rather than to area T1-1. This may be attributed to imperfect control of the irradiation process. As observed for the previously irradiated CVD

graphene samples, higher irradiation doses of 6.61×10^{-13} C/μm^2 (T3) once again reduce the intensity of the D and 2D peaks, and hence the I_D/I_G, I_D/I_{2D} and I_{2D}/I_G ratios. Optical imaging of the sample after treatment also showed that the areas treated with the highest dose (T3) were partially sputtered off.

5.2.2.4 Treated Mechanically Exfoliated Graphene Membranes on PAA/Si Substrate

Since mechanical exfoliation yielded a wide range of graphene flakes having different morphologies and number of layers, seven different flakes were chosen for ion irradiation. In the following sub-sections, the results obtained for each flake are presented separately.

5.2.2.4.1 Flake E – 6.62×10^{-13} C/μm^2 Patterning Method

Figure 5.17 shows the 2D Raman spectral maps of Flake E before (Figure 5.17 (a-c)) and after (Figure 5.17(d-f)) irradiation using the patterning method at a dose of 6.60×10^{-13} C/μm^2. A dose of 6.60×10^{-13} C/μm^2 was selected since the damage incurred in the CVD graphene was appreciable even at the lower doses of 1.8×10^{-13} C/μm^2 for the supported graphene (Section 5.2.2.1) and 5.28×10^{-7} C/μm^2 for the suspended graphene (Section 5.2.2.2).

The spectral maps taken before irradiation indicate various different areas within the graphene flake, labelled from A1 to A5. Averaged spectra obtained from such areas are presented in Figure 5.18 (a). The different intensities of the 2D (Figure 5.17 (a)) and G (Figure 5.17 (b)) peaks within these areas indicate that each area has a different number of layers, with the brighter areas having less layers. Moreover, the D peak map in Figure 5.17 (c) indicates that majority of the areas are pristine, with the D peak present only at the edges of the flake and absent from the averaged spectra in Figure 5.18 (a). The flake is also observed to cover a total of five patterned holes in the substrate creating the membranes labelled M01 to M05. Figure 5.18 (b) shows the averaged spectra for each membrane. Note that prior to obtaining the Raman spectra, M01 and M04 were imaged via AFM causing significant damage to the membranes, and hence the appearance of the D peak in such areas.

As shown in Figure 5.17 (d-f) and Figure 5.18 (c), irradiation caused a significant change in the Raman spectra obtained from Flake E. The 2D peak is absent while the D and G peaks increased in intensity and broadened into a broad band. This indicates that irradiating MLG with a dose of 6.62×10^{-13} C/μm^2 using the patterning method caused complete amorphization of the graphene.

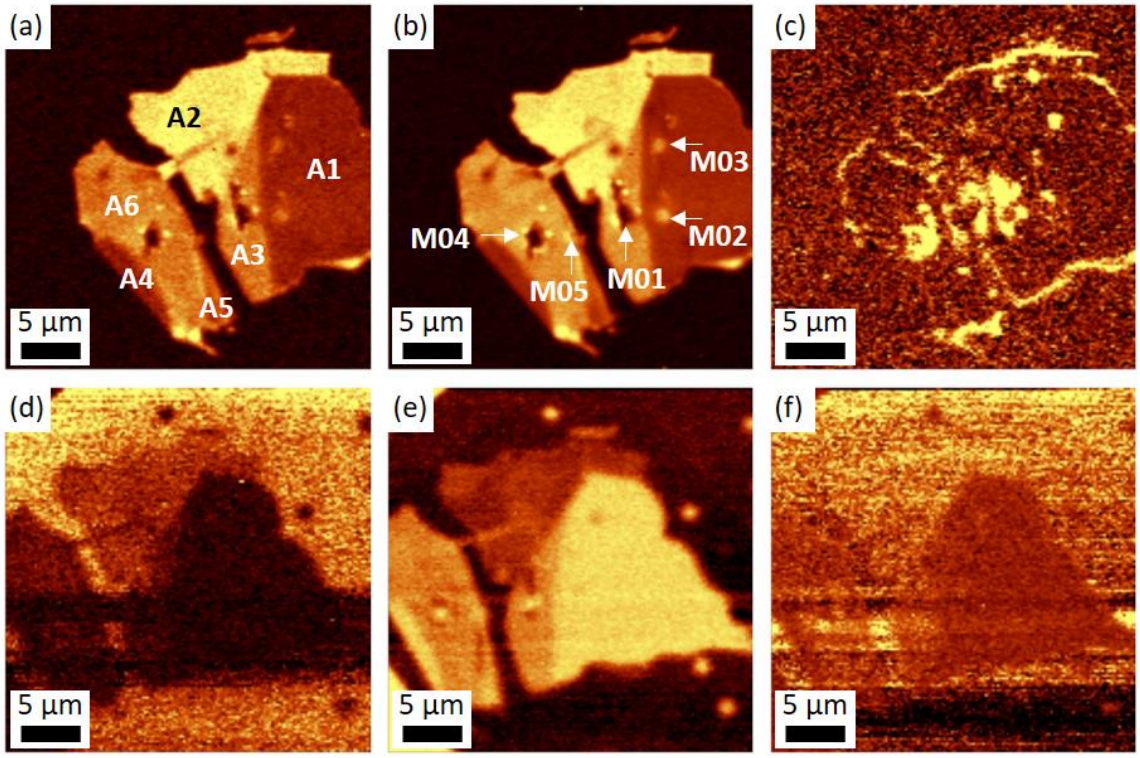

Figure 5.17: 2D Raman spectral maps of the sum of parts of the spectrum depicting the intensity of the (a, d) 2D, (b, e) G, and (c, f) D peaks of Flake E, (a – c) before and (d – f) after ion bombardment.

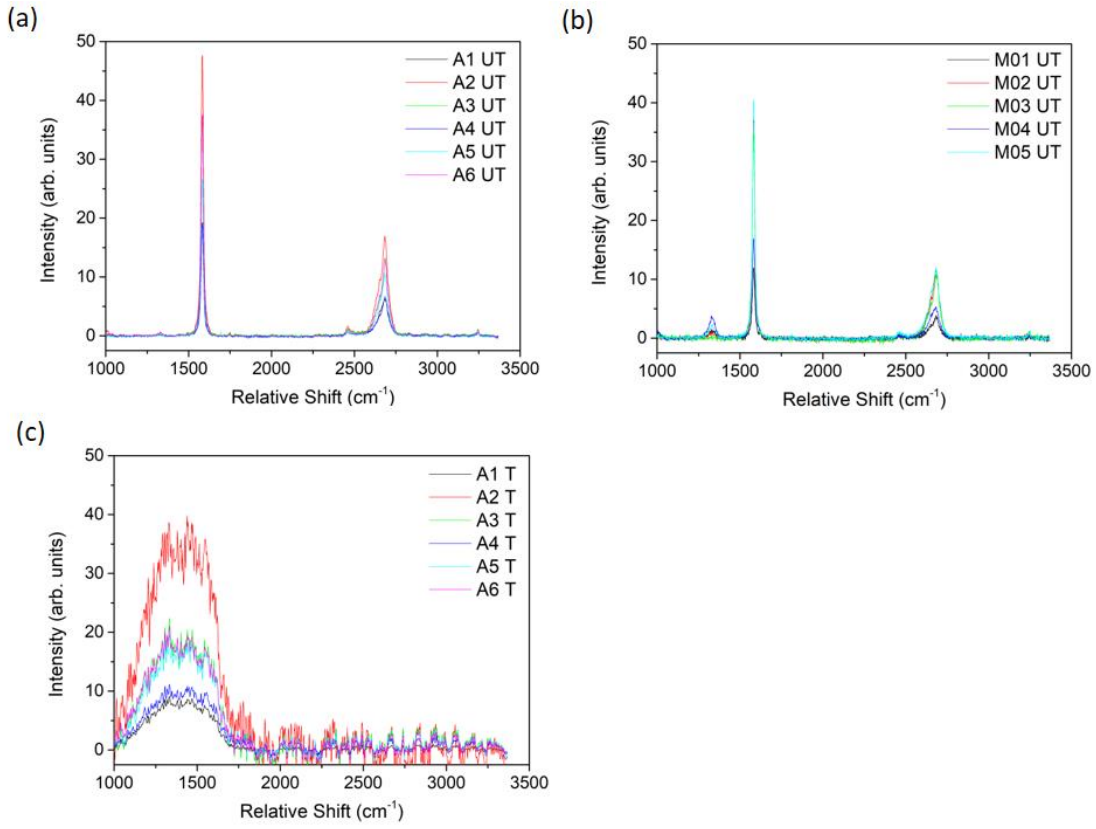

Figure 5.18: Raman spectra obtained from Flake E (a, b) before, and (c) after ion bombardment. In all spectra, an appropriate baseline was fitted and subsequently subtracted from the raw data.

5.2.2.4.2 Flake F – 1.33×10^{-14} C/µm^2 Patterning Method

Figure 5.19 shows optical micrographs of Flake F before and after irradiation. Compared to Flake E, Flake F was irradiated using a lower dose of 1.33×10^{-14} C/µm^2 using the same patterning method. Figure 5.20 and Figure 5.21 present the 2D Raman maps and averaged spectra, respectively, of Flake E before and after irradiation. For the untreated flake, two main areas, A1 and A2, were identified, with A2 being a folded region of the MLG. Flake F also covers a hole creating membrane M01. After irradiation, both the optical micrograph as well as the Raman spectral maps indicate that the flake has been subjected to different doses. As such, areas labelled as A1.1, A1.2, A2.1, A2.2, and A3 were further identified and examined.

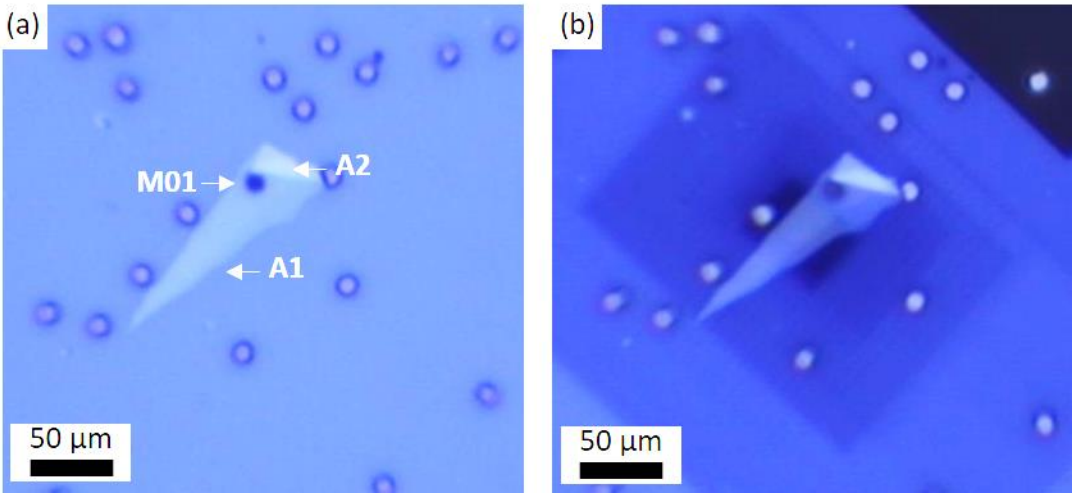

Figure 5.19: Optical micrograph of Flake F (a) before, and (b) after irradiation.

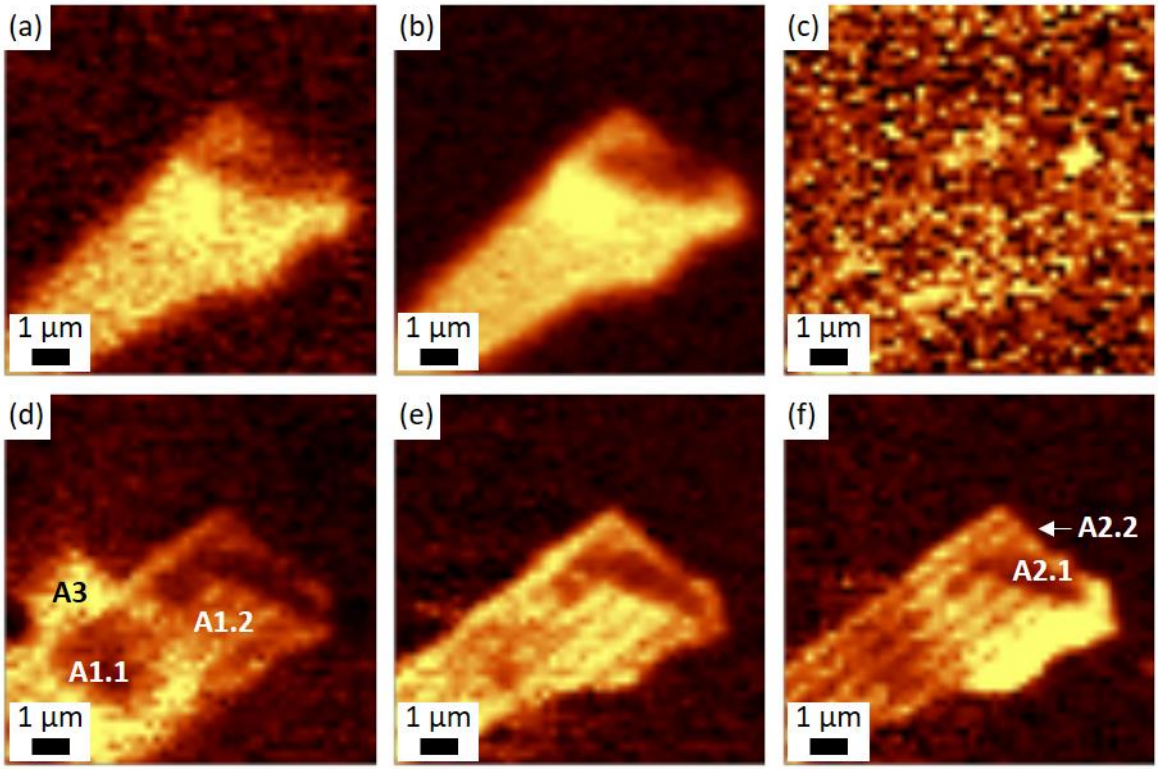

Figure 5.20: 2D Raman spectral maps of the sum of parts of the spectrum depicting the intensity of the (a, d) 2D, (b, e) G, and (c, f) D peaks of Flake F, (a – c) before and (d – f) after ion bombardment.

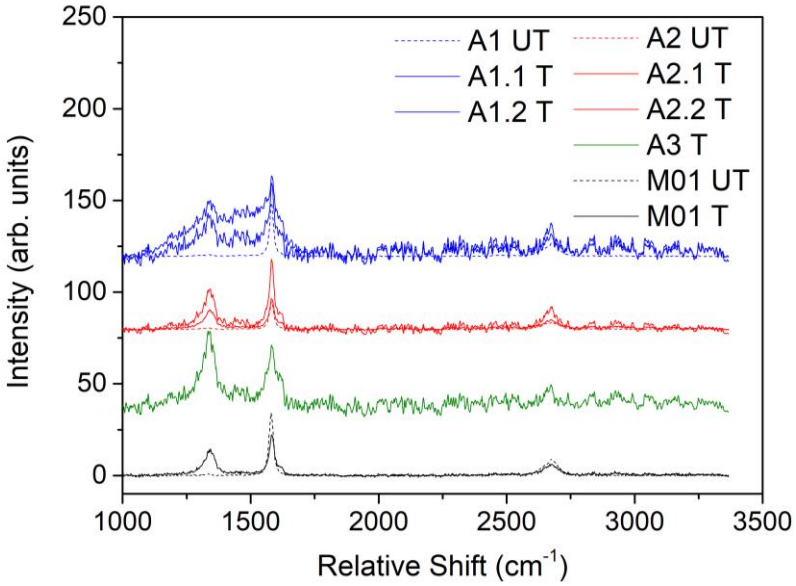

Figure 5.21: Raman spectra obtained from Flake F before (dashed), and after (solid) ion bombardment.

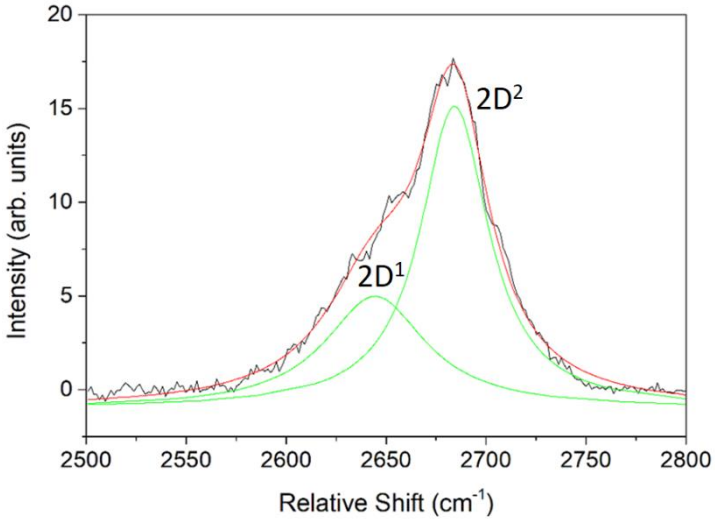

Figure 5.22: Representative 2D peak from the untreated Flake F.

Similar to Flake E, before ion irradiation Flake F exhibited a sharp G peak, and a very small D peak demonstrating the pristine nature of the graphene. Due to the multi-layer nature of the flake, the 2D peak was broad and was therefore fitted using two Lorentzian peaks, $2D^1$ and $2D^2$, as shown in Figure 5.22. The corresponding peak parameters are listed in Appendix F.

Upon irradiation, the G peak was noted to slightly broaden, especially for the thinner areas, while the D peak was observed to increase significantly. The D' peak also appeared as a shoulder to the G peak. With an ion dose of 1.33×10^{-14} C/μm^2, the I_D/I_G ratio was observed to increase from around 0.03 to a minimum of 0.42 and a maximum of 1.28. As noted earlier, both the optical micrographs and the spectral maps of the treated flake indicate that the flake was not homogeneously irradiated. In fact, area A1.1 was heavily damaged to an I_D/I_G ratio of 0.91. Furthermore, across the entire flake, linear markings can be noticed in the spectral maps, especially evident in the D peak map in Figure 5.20 (f). It is believed that these are related to the raster motion of the ion beam during patterning; the coarse step-wise motion of the beam leads to inhomogeneity of the treatment.

5.2.2.4.3 Flake G – 3.30×10^{-15} C/μm^2 Imaging Method

Figure 5.23 (a) and (b) show an optical micrograph and an AFM height micrograph of Flake G before treatment, while Figure 5.24 presents the 2D Raman maps of the flake before and after treatment. Flake G was irradiated using the imaging method – thereby circumventing the inhomogeneity observed in Flake F. The resulting ion dose was calculated using Equation 5.1 and Equation 5.2. More specifically, Flake G was imaged using an ion beam of 30 kV and

1.5 pA. The entire imaging area was of 98 × 84 μm^2 with 2048 × 1768 pixels. Using a pixel dwell-time of 1 µs and 5 total scans, a dose of 3.30×10^{-15} C/μm^2 was calculated.

Average spectra from the areas labelled A1, A2, and membrane M01 are shown in Figure 5.25, with the respective peak parameters listed in Appendix F.

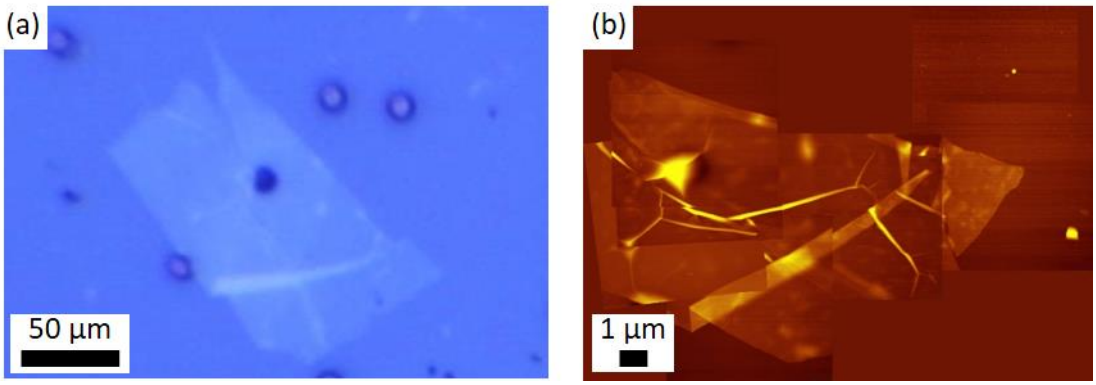

Figure 5.23: (a) Optical micrograph, and (b) AFM height micrograph of Flake G.

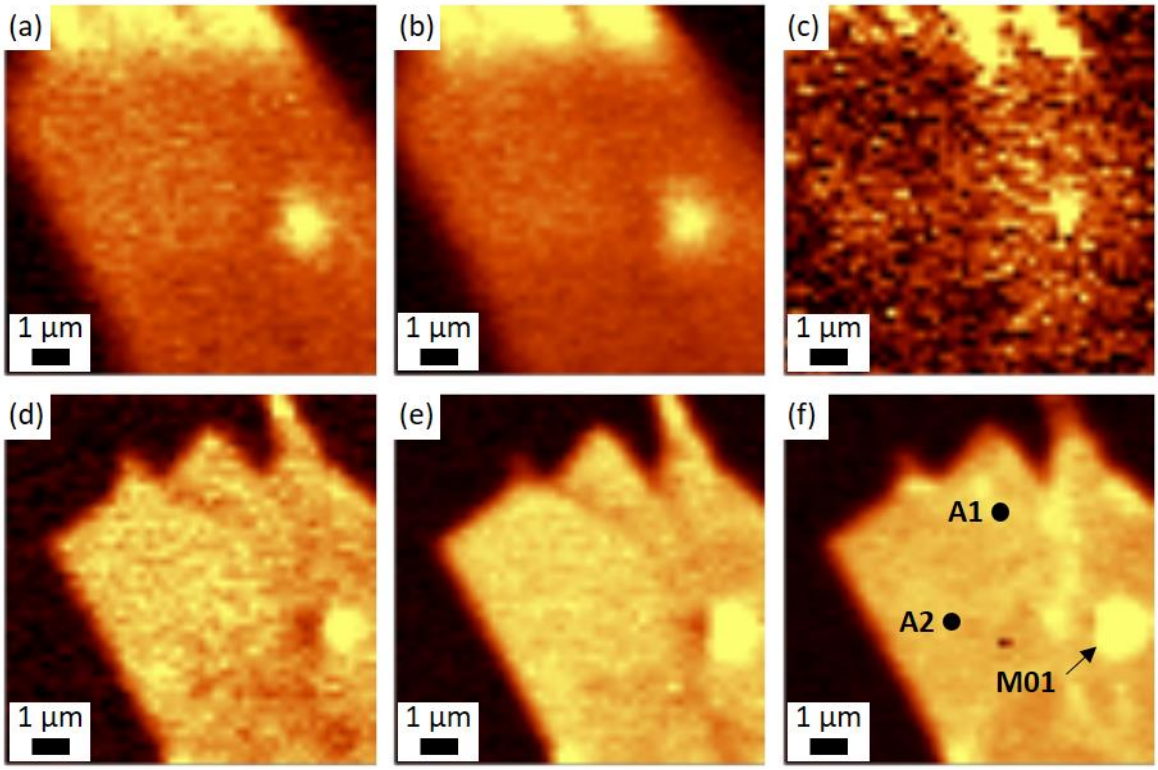

Figure 5.24: 2D Raman spectral maps of the sum of parts of the spectrum depicting the intensity of the (a, d) 2D, (b, e) G, and (c, f) D peaks of Flake G (a – c) before and (d – f) after ion bombardment.

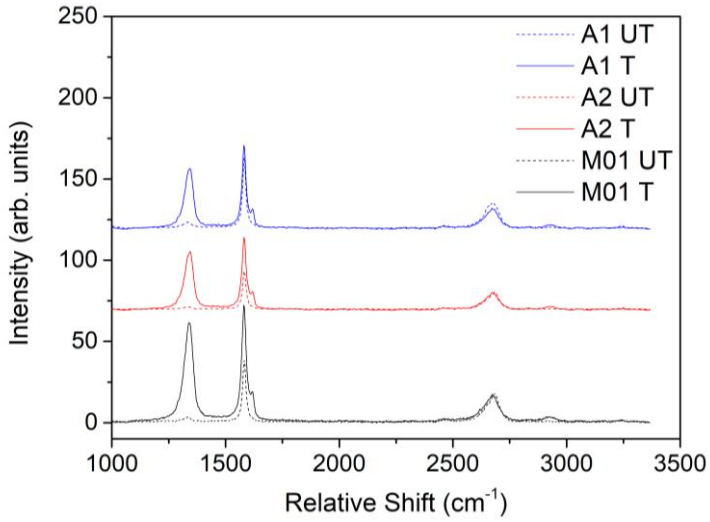

Figure 5.25: Raman spectra obtained from Flake G before (dashed), and after (solid) ion bombardment.

The spectral maps of the treated Flake G confirm the homogeneity of the ion irradiation using the imaging method. While the flake is noted to be damaged due to the increase in the D peak, widening of the G peak and the emergence of the D' peak, the 2D maps do not exhibit the same linear markings as in Flake F. The applied dose of 3.30×10^{-15} C/μm^2 increased the I_D/I_G ratio from 0.07 up to an average of 0.83. The relative consistency of the I_D/I_G ratio across the entire flake further proves the homogeneity of the treatment with this method.

5.2.2.4.4 Flake H – 3.30×10^{-15} C/μm^2 Imaging Method

The same dose used for Flake G was used to treat Flake H, shown untreated in the optical micrograph of Figure 5.26. Figure 5.27 and Figure 5.28 show the 2D Raman spectral maps and the corresponding average spectra after treatment, respectively. The corresponding peak parameters of the treated spectra are listed in Appendix F.

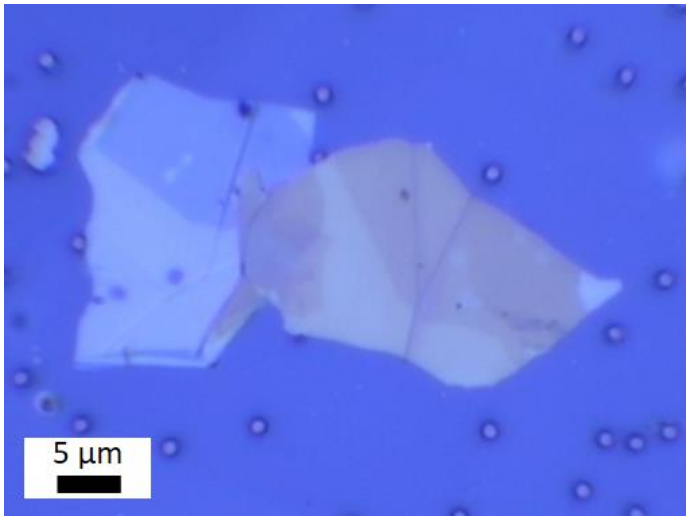

Figure 5.26: Optical micrograph of Flake H.

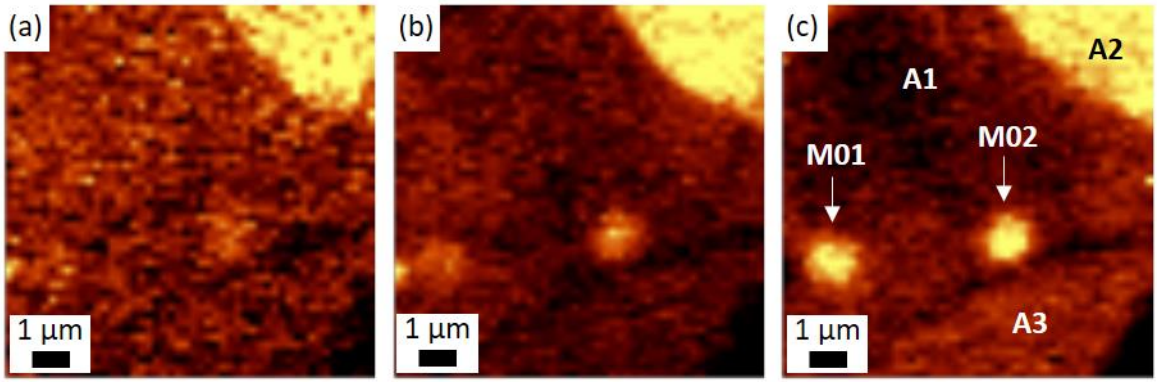

Figure 5.27: 2D Raman spectral maps of the sum of parts of the spectrum depicting the intensity of the (a) 2D, (b) G, and (c) D peaks of Flake H, after ion bombardment.

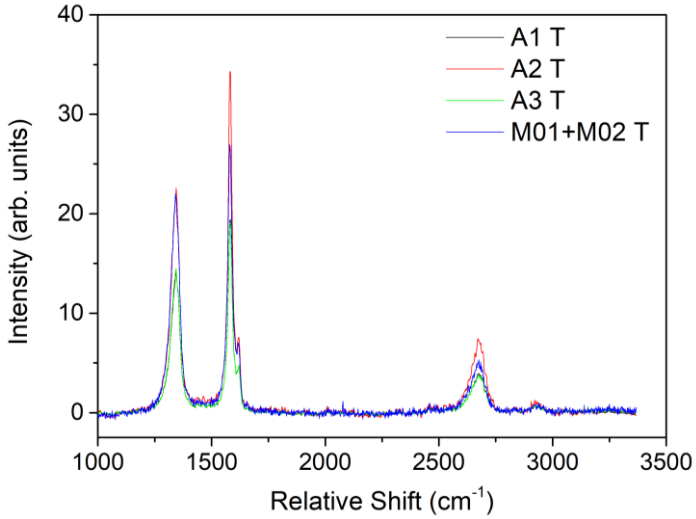

Figure 5.28: Raman spectra obtained from Flake H after ion bombardment.

The ion dose of 3.30×10^{-15} C/µm^2 produced an average I_D/I_G ratio of 0.75, slightly lower than that in Flake G (0.83). This slight discrepancy is attributed to the different thicknesses of both flakes. However, both the $I_D/I_{D'}$ and $I_{D'}/I_G$ ratios are very similar in both treated Flakes G and H.

5.2.2.4.5 Flake C – 6.60×10^{-16} C/µm^2 Imaging Method

Figure 5.29 shows the 2D Raman spectral maps obtained before (a – c) and after (d – f) ion bombardment of Flake C presented in Chapter 3. Flake C was irradiated with a lower ion dose of 6.60×10^{-16} C/µm^2 using the imaging method. While the 2D Raman maps depicting the intensity of the 2D peak and G peak show little change with ion bombardment, the 2D Raman map exhibiting the D peak is significantly different; the D peak was only present at the edges of the flake before irradiation (similar to what was observed in Flake E), whereas the D peak appeared across the entire flake after irradiation, with its intensity being the highest in area A2 and the membrane regions.

Figure 5.30 shows the averaged Raman spectra obtained from the various locations A1, A2, M01, and M02 (as labelled in Figure 3.28 (a)) before and after ion bombardment. The Raman corresponding peak parameters are listed in Appendix F. As evidenced by Figure 5.30, the

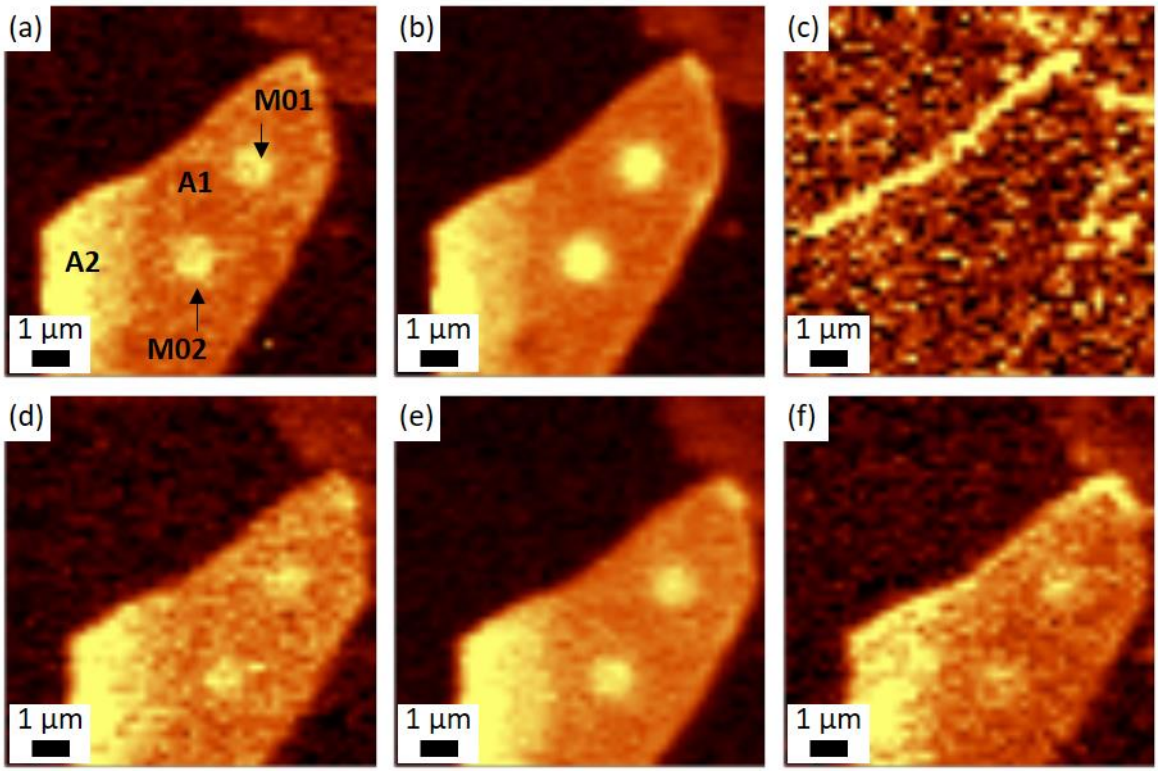

Figure 5.29: 2D Raman spectral maps of the sum of parts of the spectrum depicting the intensity of the (a, d) 2D, (b, e) G, and (c, f) D peaks of Flake C, (a – c) before and (d – f) after ion bombardment.

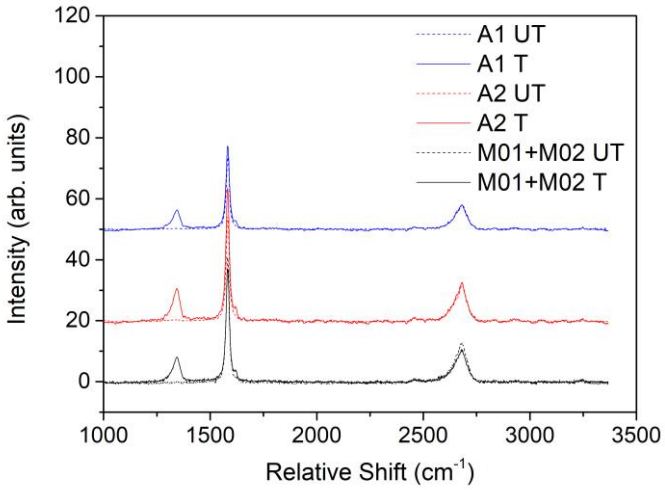

Figure 5.30: Raman spectra obtained from Flake C before (dashed), and after (solid) ion bombardment.

position of the G peak did not change with the treatment, while its FWHM marginally increased by < 2 cm^{-1}. Once again, treatment did not cause a significant change in the 2D peak.

As described in Chapter 3, the mechanically exfoliated flake was originally pristine as evidenced by the absence of the D peak in its Raman spectra. Conversely, and as expected, ion bombardment introduced defects within the MLG flake causing the D peak and the D' peak to appear in the obtained Raman spectra. The ion dose of 6.60×10^{-16} C/µm^2 on the 25 nm thick MLG flake caused the I_D/I_G ratio to increase from 0 (absent D peak) to approximately 0.23, significantly less than the I_D/I_G ratio obtained with the higher dose.

5.2.2.4.6 Flake I – 6.60×10^{-16} C/µm^2 Imaging Method

Similar to Flake C, Flake I, a 10 to 15 nm thick MLG flake, was treated with an ion dose of 6.60×10^{-16} C/µm^2 using the imaging method. The optical micrograph before treatment and the 2D Raman maps are shown in Figure 5.31 and Figure 5.32, respectively. The corresponding averaged spectra are shown in Figure 5.33 with the peak parameters listed in Appendix F.

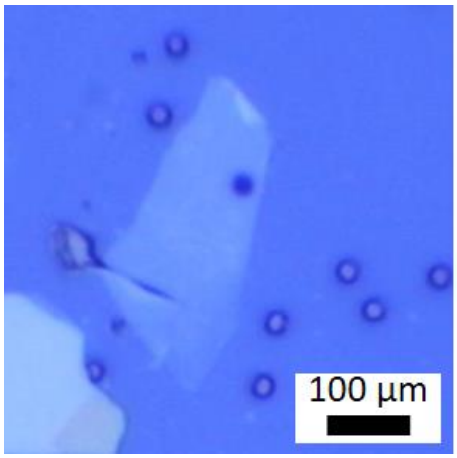

Figure 5.31: Optical micrograph of Flake I.

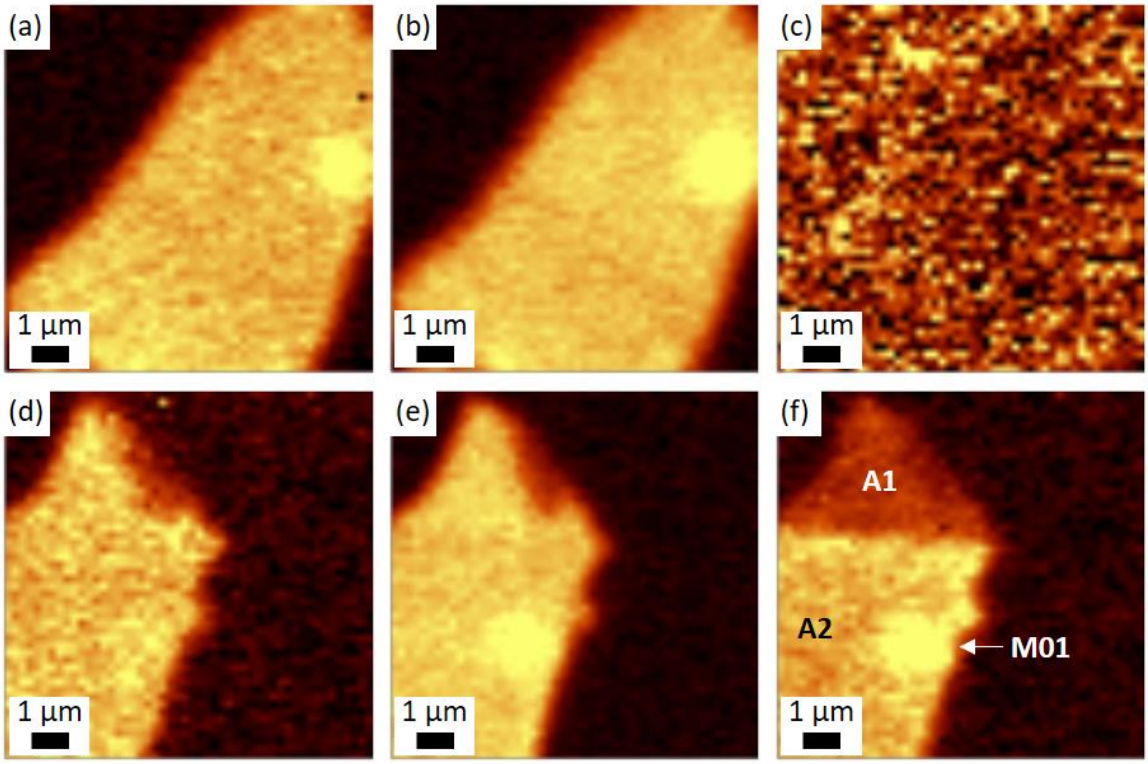

Figure 5.32: 2D Raman spectral maps of the sum of parts of the spectrum depicting the intensity of the (a, d) 2D, (b, e) G, and (c, f) D peaks of Flake I, (a – c) before and (d – f) after ion bombardment.

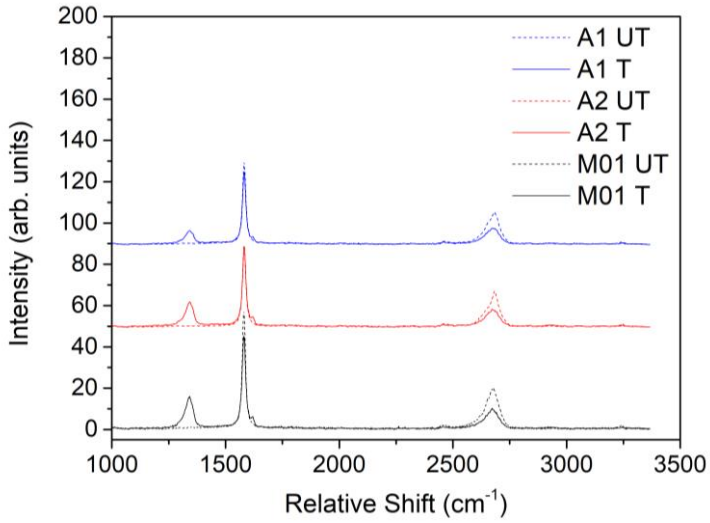

Figure 5.33: Raman spectra obtained from Flake I before (dashed), and after (solid) ion bombardment.

Similar to Flake C, the 2D spectral maps of the 2D and G peaks are very similar before and after irradiation. On the other hand, Figure 5.32 (c) suggests that the bottom half of the flake (A2) was damaged more than the top half of the flake (A1). Compared to the I_D/I_G ratio of 0.23 for Flake C, the I_D/I_G ratio varied from 0.18 to ~0.32 at A1 and A2, respectively. The inhomogeneous irradiation can be attributed to user error while aligning the ion beam image to

the flake. Although similar, the difference in the average I_D/I_G ratios in Flake C and Flake I can be attributed to the difference in thickness of the MLG, with the thicker flake (Flake C ~25 nm) exhibiting less damage.

5.2.2.4.7 Flake J – 6.60×10^{-16} C/µm^2 Imaging Method

Lastly, the same ion irradiation dose of 6.60×10^{-16} C/µm^2 was used to treat Flake J, shown in Figure 5.34. Figure 5.35 and Figure 5.36 show the 2D spectral maps and average spectra of the flake after irradiation. The peak parameters are listed in Appendix F. Once again, a similar I_D/I_G ratio of ~0.21 was obtained upon irradiation.

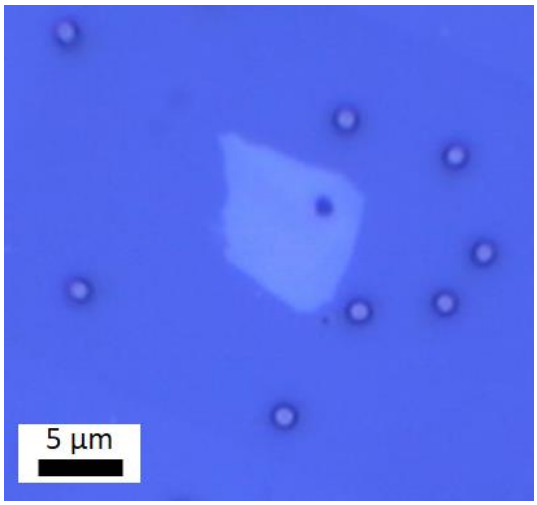

Figure 5.34: Optical micrograph of Flake J.

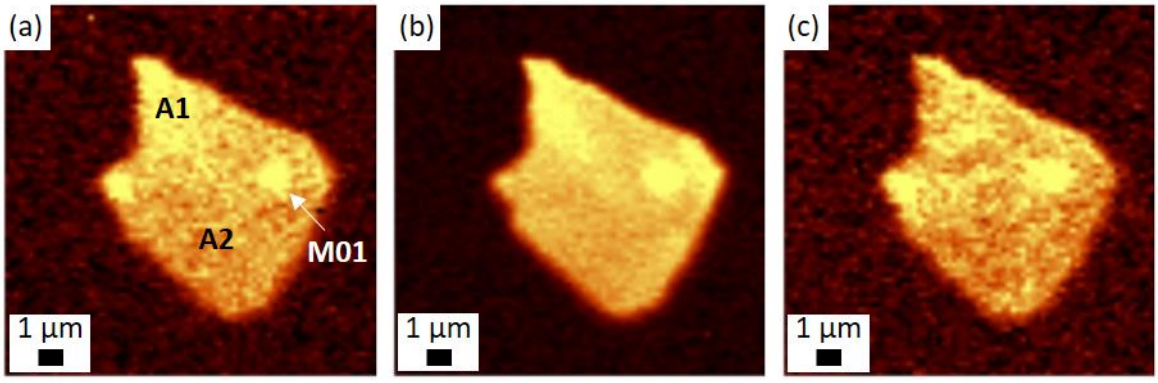

Figure 5.35: 2D Raman spectral maps of the sum of parts of the spectrum depicting the intensity of the (a) 2D, (b) G, and (c) D peaks of Flake J, after ion bombardment.

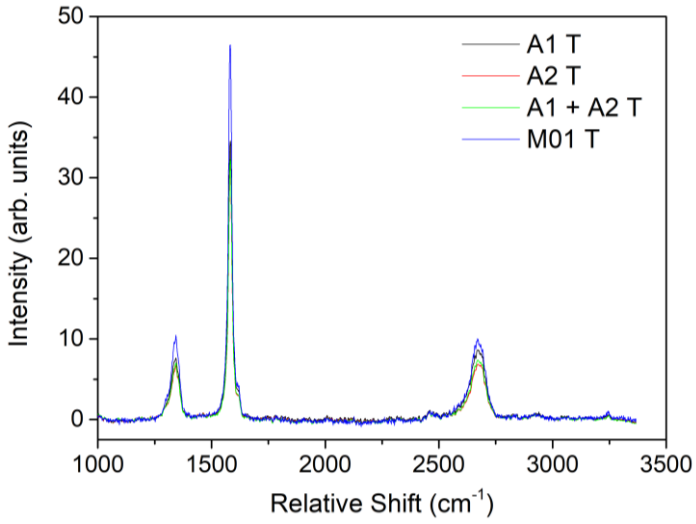

Figure 5.36: Raman spectra obtained from Flake J after ion bombardment.

5.2.3 DISCUSSION

5.2.3.1 Treated Supported CVD Graphene on SiO_2/Si

SEM imaging of supported graphene samples shows that graphene has been completely sputtered off from the areas treated with 1×10^{-10} C/µm^2 (T100) and 5×10^{-11} C/µm^2 (T50) as evidenced by the lack of texture in these areas. The characteristic D, G and 2D bands are also absent from the Raman spectra acquired from the mentioned areas.

Due to the relatively large size of the gallium ion, it is found that lower doses are required to sputter graphene then if, for example, helium ions were used [38, 56]. While helium ions pass right through the graphene with minimal damage and embed themselves in the SiO_2 substrate, gallium ions tend to transfer most of their kinetic energy to the surface of the sample and hence produce more damage in the top-most graphene layer [38]. Molecular dynamics work has shown that while heavier ions produce more damage, higher energies (on the order of 100 keV compared to 500 eV) induce less damage [163]. Thus, heavier ions with lower energies are more efficient to mill uniformly shaped pores i.e. causing full sputtering in confined areas.

At treatment doses of 1×10^{-12} C/µm^2 (T1) and 5×10^{-13} C/µm^2 (T0.5), the 2D peak which is associated with the breathing mode of the graphene hexagonal ring is lost, implying that the graphene was transformed into amorphous carbon [57, 126]. Raman spectra of carbon black (amorphous carbon) consist of broad D and G peaks and a small broad bump at the 2D peak location [132], similar to what is observed in the above-mentioned treated supported graphene.

Various mechanisms can be attributed to the amorphization of the supported graphene sample. Firstly, the energetic ions hitting the graphene sample create defects, mostly point defects such as vacancies [57]. At low doses, these defects are sparse and only give rise to the activation of the disorder-induced D peak while the 2D peak is retained as the hexagonal crystal structure of the graphene is still mostly present, defined as Stage 1 [57]. At higher ion doses, the point defects start to coalesce to form more complex defects which will ultimately destroy the crystal structure of the graphene and hence the de-activation of the 2D peak, defined as Stage 2 [57]. In this case, the G and D peaks are still both present. The substrate supporting the graphene sheet can also be affected by the energetic ions [38, 256]. The size of the gallium ions precludes structural effects to the bulk of the substrate and thus causes a lot of disruption in the sample top-surface, even just below the graphene layer, forming serrations or very rough topographies of the underlying SiO_2 [257]. In turn, the disorder and roughness induced in the surface of the substrate supporting the graphene may increase the possibility of cracking and the formation of other associated defects which will de-crystallize and amorphize the graphene. This might be especially true for the areas treated with 1×10^{-12} C/μm^2 (T1) and 5×10^{-13} C/μm^2 (T0.5) as the topography and texture changed significantly, as shown in Figure 5.1 (a).

Finally, the atoms which have been sputtered from the graphene crystal structure to create vacancies can jump to another location to form adatoms and hence induce sp^3 hybridization. Similarly, the ion beam may be also depositing more carbonaceous material which may be present either in the chamber atmosphere or as contamination on the sample itself onto the graphene layer increasing the sp^3 hybridization [133]. In fact, Hong et al. [132] attribute the broad peaks induced by annealing to amorphous carbon deposited on graphene through carbonization of hydrocarbons during the applied thermal treatments in inert atmosphere. In this work, the polymer transfer method used to transfer the CVD-grown graphene from the copper foil to the SiO_2 substrate is known to leave some polymer residue on the graphene sample – a precursor to carbonaceous material. Another contribution to the broad band at around 1300 cm^{-1} is the presence of organic contaminants which might be bound to the graphene causing chemical enhancement in the Raman spectrum [131, 258].

The ring of damaged graphene surrounding the 1×10^{-10} C/μm^2 (T100) area (Figure 5.1) can be attributed to energetic ions from the ion beam which may have strayed from the focused beam and hit the graphene outside the target area. The presence of the D' peak at 1615 to 1623 cm^{-1} is in fact often attributed to the presence of point defects, as also created by argon ion beam sputtering [57, 259]. As the gallium ions impinge the sample, some ions might be backscattered

and some atoms from both the graphene and the substrate might be sputtered inducing other defects, possibly away from the target area [56, 80, 256]. In fact, the majority of the total defects produced by an ion beam on supported graphene is attributed to indirect defect production [256].

The intensity ratio of $I_D/I_{D'}$ has been used to determine the defect type in graphene [127]. As shown in Figure 5.37, the $I_D/I_{D'}$ increases linearly from around 4.8 at a distance of around 20 µm when the peak can be first distinguished from the G peak, to around 8.6 at a distance of 60 µm. It is being proposed that closer to the treated area, the small $I_D/I_{D'}$ can be attributed more to boundary-like defects [127] brought about by extensive amorphization of the graphene and possible cracking due to the severe swelling of the substrate. As the distance away from the target area increases, these defects are replaced by vacancy-type defects caused by stray ions, and backscattering and sputtering actions resulting in a larger $I_D/I_{D'}$ [127]. The $I_D/I_{D'}$ is expected to vary gradually and the presence of the D′ peak at any point in the damaged zone can be attributed to a mixture of all the types of defects, from boundary defects to the presence of adatoms [56]. Song et al. [131] attribute peaks at relative shifts < 1550 cm^{-1} to materials bound to graphene which in this case could have originated from the polymer transfer process used or any other atmospheric contaminants. The $I_{D'}/I_G$ was also seen to increase closer to the target area until the D′ peak was no longer distinguishable from the G peak, as also reported in [68, 127].

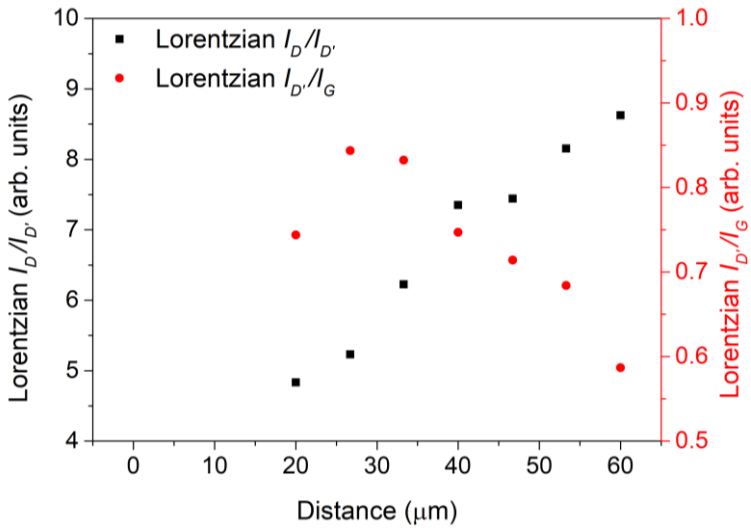

Figure 5.37: The evolution of the intensity ratio between the Lorentzian D and D' bands ($I_D/I_{D'}$) and the intensity ratio between the Lorentzian D' and G bands ($I_{D'}/I_G$).

One of the G peaks found at approximately 1530 cm^{-1}, previously attributed to the presence of amorphous carbon due to its Gaussian profile, evolves into a peak with a Lorentzian profile at lower defect concentrations. The G band is typically reported to split in two peaks with the presence of defects with the D' peak emerging at a higher frequency and often being attributed to the presence of point defects created by ion beam sputtering. The splitting of the G peak into two and the presence of multiple peaks in the wide region of 1150 to 1650 cm^{-1} was also related to strain in graphene, functionalization of graphene, and to the vibration of molecular oxygen [153, 258, 260-262].

5.2.3.2 Treated Suspended CVD Graphene Membranes on TEM Grids

Clear trends relating the treatment dose applied to monolayer graphene membranes suspended over Quantifoil TEM grids to the Raman spectra are evident. These include the increase in the intensity, in agreement with [57], yet narrowing of the Lorentzian D peak with an increase in dose, and a decrease in intensity and broadening of the 2D peak. Both the Gaussian D and G peaks, and the Lorentzian G peak show a slight decrease in intensity. The slight upshift of the Gaussian G peak can be attributed to an increase in the disorder [255]. Furthermore, the I_{GG}/I_{GL} ratio (Figure 5.38 (a)), which was previously used to determine the degree of amorphization, shows a non-monotonic trend with respect to the dose in the suspended graphene. On the other hand, contrary to what was observed for supported graphene, the I_{DG}/I_{DL} ratio (Figure 5.38 (a)) decreases with an increase in the treatment dose. This may be attributed to the increase in Lorentzian D peak intensity while the intensities of the Gaussian peaks do not significantly change. The intensity of the D peak and the Lorenztian I_D/I_G ratio increases linearly with an increase in the treatment dose, showing that defects are still being created in the graphene. MD simulations of suspended graphene under ion irradiation report that at low ion energies, comparable to those used in this study, the types of defects produced are most prominently single vacancies [140].

The two stages of low and high disorder as a result of ion bombardment mentioned previously have stemmed from a reported non-monotonic trend for the I_D/I_G [57]. While in Stage 1, the I_D/I_G ratio increases with an increase in the ion beam dose due to the introduction of defects, at higher doses, the graphene enters Stage 2 during which the defects start to coalesce, cause partial amorphization and hence a decrease in the I_D/I_G ratio. While it is reported that Stage 2 is reached with ion fluences as low as 10^{15} $Ar^+/\mu m^2$ [57], the I_D/I_G ratio in the present study is not observed to decrease even with a treatment fluence of at least 7.6×10^{16} $Ga^+/\mu m^2$, indicating that the suspended graphene is still at Stage 1 disorder. As will be further discussed hereunder,

this discrepancy can be mainly attributed to the fact that the graphene in this work is suspended and not supported by a substrate. Another contributing factor to the absence of the non-monotonic trend in the I_D/I_G is the presence of both the Gaussian and Lorentzian D and G peaks. In fact, on examination of the total integrated area under the D and G peaks by adding both the Gaussian and Lorentzian components of each peak, A_D and A_G respectively in Figure 5.38 (b), it can be noticed that both areas seem to peak at a fluence of 3×10^{15} $Ga^+/\mu m^2$ before they start to decay, in agreement with [57]. The laser used for the Raman measurements (633 nm or 1.96 eV) may also be a contributing factor to why this non-monotonic trend is not evidently observed as it has been reported that the non-monotonic trend of the I_D/I_G is less pronounced when using lower energy lasers [58].

It appears that while lower treatment ion doses from 1.80×10^{-13} $C/\mu m^2$ up to 1.00×10^{-10} $C/\mu m^2$ applied to supported graphene lead to partial amorphization or complete sputtering of graphene, higher ion doses from 3.27×10^{-7} $C/\mu m^2$ up to 1.31×10^{-2} $C/\mu m^2$ applied to suspended graphene do not induce extensive amorphization. This is in agreement with the work by Fox et al. [80] who observe that supported graphene has a greater defect density I_D/I_G ratio than freestanding graphene for the same helium ion dose. To be able to fairly compare the two cases, the accelerating voltage used must also be taken into consideration. In the suspended graphene, the same range of treatment dose was applied using both 5 kV and 30 kV (constant ion beam current of 1.5 pA), however, no discernible changes were seen in the Raman spectra. Therefore, it is determined that this difference in accelerating voltage is insufficient to affect the extent of damage done by the ion beam on the supported graphene for the same dose [256].

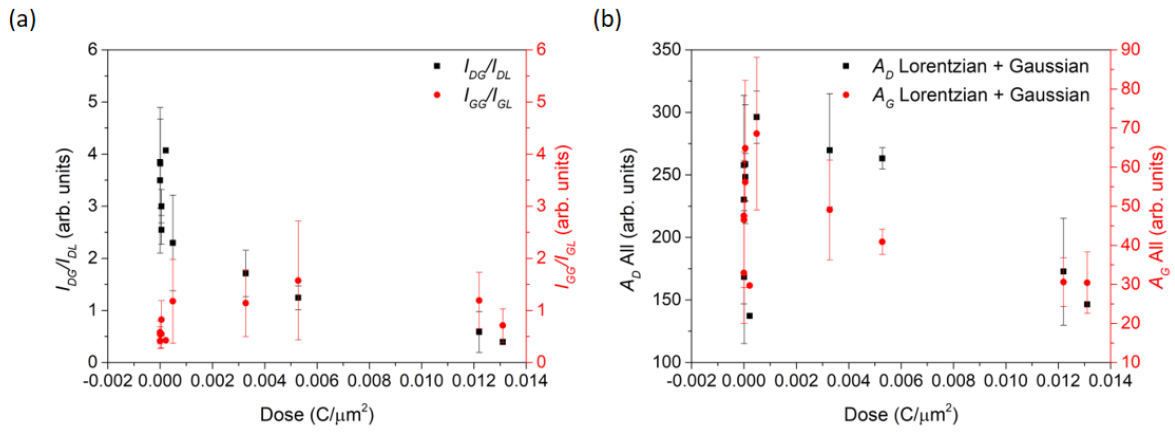

Figure 5.38: The evolution of (a) the intensity ratios I_{DG}/I_{DL} and I_{GG}/I_{GL}, and (b) the total integrated area A_D and A_G in suspended graphene.

This discrepancy in the effect of the same dose on different graphene samples is being attributed to the manner in which the graphene exists. The energetic ions impinging the supported graphene sample are able to pass through the graphene but are often trapped into the substrate causing swelling and roughening of the substrate. Some of the ions may also hit the substrate atoms and backscatter to the graphene from underneath causing double the damage [56, 80, 256]. On the other hand, the energetic ions impinging suspended graphene will only pass once through the graphene and then proceed to disperse in the atmosphere (or in the sample stage) with no backscatter. This means that the ions will only cause minimal damage mostly consisting of small vacancies. Furthermore, any carbon atoms from the graphene crystal structure which may have been knocked off the lattice will most likely be sputtered away into the atmosphere rather than implanted in the substrate or relocated as adatoms in the nearby graphene as expected in the supported graphene.

Similar results have been reported following MD simulations of argon and silicon ions hitting suspended and supported graphene [164, 256]. For a given dose at accelerating voltages lower than 5 keV, the energetic ions tend to produce more defects in suspended graphene rather than supported graphene since in the latter, the carbon atoms are supported by the substrate and more energy would be needed to sputter them. However, ions at higher accelerating voltages produce more defects in supported graphene [256].

The effect of the incidence angle on the damage imparted to the suspended graphene is also investigated. A treatment dose of 3.27×10^{-3} C/μm^2 was used and the incidence angle was changed from 28° to 83° to the sample surface. The Gaussian D and G peaks do not significantly change with the incidence angle. On the other hand, the intensity of the Lorenztian D peak and the Lorenztian I_D/I_G increase with an increase in the incidence angle. This indicates that as the incidence angle of the ion beam approaches 90° to the surface, more defects are being imparted in the graphene membrane, in agreement with simulation work [140]. This is attributed to the fact that at lower incidence angles the energetic ions graze the sample thus splitting their transferred energy between the in-plane and out-of-plane directions. Therefore, less energy is available to knock off the carbon atoms in the out-of-plane direction hence creating less vacancies. The grazing ions and any sputtered atoms may then bounce off the sample rather than pass through the graphene and so less indirect damage is produced. Grazing ions may create more Stone-Wales type defects since the carbon atoms would only be relocated or their bonds twisted.

5.2.3.3 Treated Suspended CVD Graphene Membranes on Silicon Nitride Microsieve

The imaging method of irradiating graphene was applied to the suspended CVD graphene on silicon nitride microsieve at lower doses. Albeit treating these samples with only three different doses – 6.86×10^{-16} C/μm^2, 3.29×10^{-15} C/μm^2 and 6.61×10^{-13} C/μm^2 – the results indicate that both Stage 1 and Stage 2 of disorder are reached, with the latter being reached with the highest dose of 6.61×10^{-13} C/μm^2. The fact that Stage 2 appears to be initiated at 6.61×10^{-13} C/μm^2, a significantly lower dose than those used for the CVD graphene on TEM grids, shows that the non-monotonic trend is indeed more pronounced when analysing the Raman spectra using a 532 nm laser.

5.2.3.4 Treated Mechanically Exfoliated Graphene Membranes on PAA/Si Substrate

As shown in Section 5.2.2.4.2, the Raman 2D maps obtained from treated MLG using the patterning method indicate that the resultant treated area is inhomogeneous with respect to the damage imparted on the sample. Therefore, the imaging method was preferred to treat other graphene flakes with the same FIB equipment. The latter method produced more homogeneous results with respect to the damage imparted throughout the treated area.

Figure 5.39 presents the evolution of different peak parameters upon ion irradiating mechanically exfoliated MLG. Each data point on the graphs represents the average obtained from all the areas within one flake, with the error bars reflecting the standard deviation. Furthermore, the data points having a dose of 0 C/μm^2 refer to the untreated flakes while the data points at the right-most side (dose of 133×10^{-16} C/μm^2) were obtained from Flake F using the patterning method. As evident in most plots, the averages obtained from flakes irradiated using the same dose are very similar. This suggests that while the MLG flakes had different thicknesses, the same ion dose induced a similar extent of damage.

In line with the results obtained on the CVD SLG, an increase in ion irradiation dose from zero up to 3.30×10^{-15} C/μm^2 linearly increased the I_D/I_G ratio from around 0.03 to around 0.75. This was accompanied by a linear decrease of the F_D/F_G ratio from around 2.5 to around 1.9, the emergence of the D' peak, and an increase of the $I_{D'}/I_G$ ratio. The significant and inhomogeneous damage imparted on Flake E using a dose of 1.33×10^{-14} C/μm^2 and the patterning method led to large error bars and an I_D/I_G average of 0.75, similar to that obtained at a dose of 3.30×10^{-15} C/μm^2. However, as shown in Figure 5.19 and Figure 5.20, the spectra obtained from the heavily damaged area (A1.1) had a significantly lower I_D/I_G ratio of 0.42, while other areas had an I_D/I_G ratio of up to 1.28 (A3). This indicates that the I_D/I_G ratio once

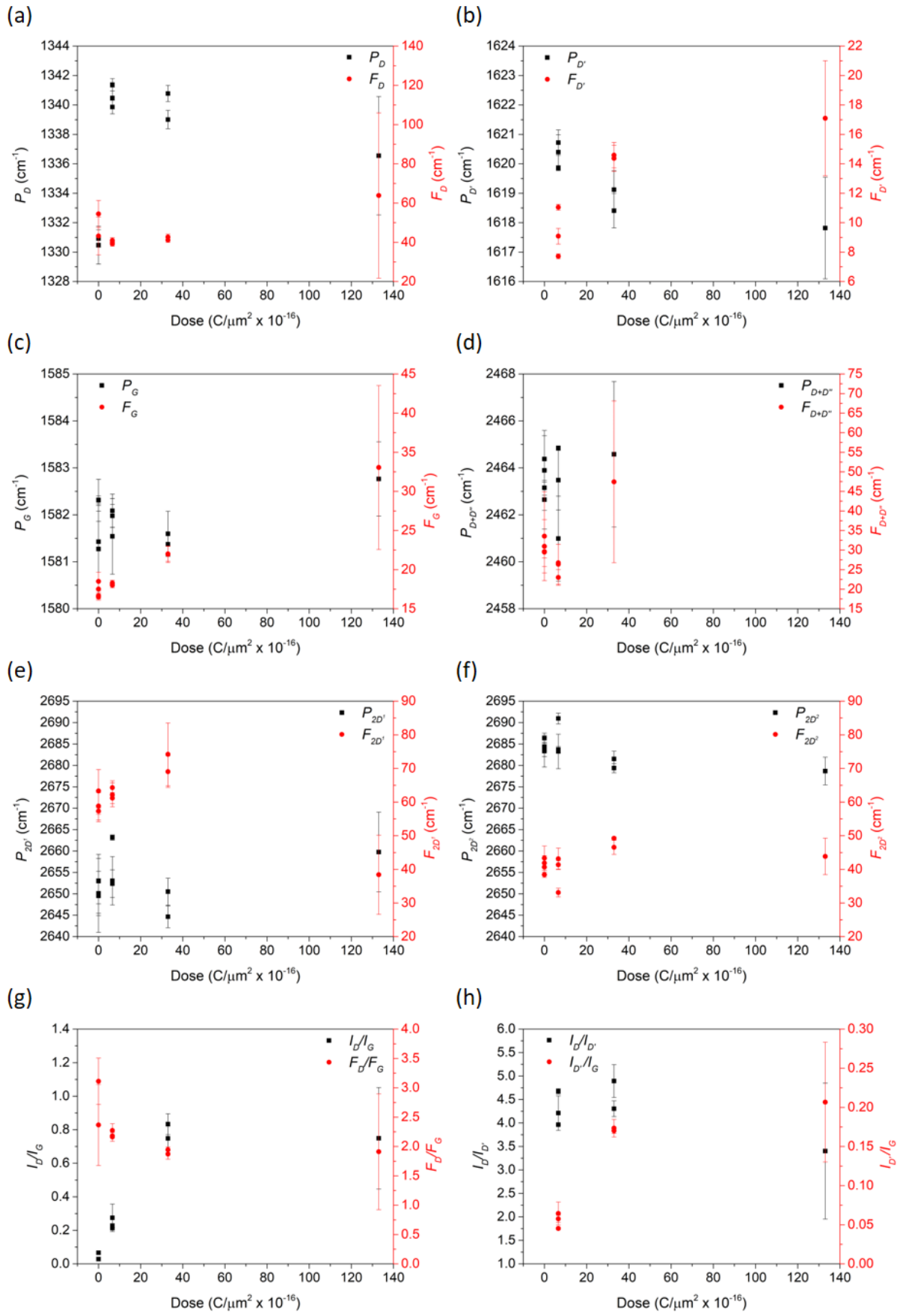

Figure 5.39: The peak parameters with increasing dose. Every data point represents the average obtained from one entire flake, with the error bars signifying the standard deviation.

again follows a non-monotonic trend on MLG, with the highest dosage reducing the I_D/I_G ratio due to partial amorphization. However, for the suspended CVD SLG (Figure 5.11), an I_D/I_G ratio of around 0.84 was obtained at a much higher dose of 4.86×10^{-4} C/μm^2 while the I_D/I_G ratio was observed to increase to up to 2.95 at a dose of 1.22×10^{-2} C/μm^2. The significant decrease in the dosage required to impart the same degree of damage on the mechanically exfoliated MLG deposited on the patterned PAA/SiO_2 substrate can be attributed to the mechanism discussed in Section 5.2.3.2; exposing supported graphene to ion bombardment subjects the graphene to backscattered ions, hence increasing the damage induced.

Irrespective of the absolute ion doses used, the FWHM of the G peak, F_G, increases with an increase in defect density similar to the behaviour observed in supported CVD graphene (Figure 5.5 (b)). The F_D/F_G ratio decreases in agreement with Figure 5.11 (b) for suspended CVD graphene. The position of the D peak, P_D, decreases in agreement with Figure 5.3 for supported CVD graphene, while both P_{2D1} and P_{2D2} decrease in agreement with P_{2D} of the supported CVD graphene in Figure 5.4 (a).

The emergence of the D' peak in most of the spectra obtained further allowed some trends to be noticed regarding this peak. With an increase in defect density, the position of peak was observed to decrease to lower Raman shifts while its FWHM increases. This results in the D' peak and the G peak to merge at higher defect densities, and hence the reason why the D' was not detected for the suspended CVD graphene with significantly larger defect densities (I_D/I_G ratios of up to 2.95).

In all of the 2D Raman spectral maps presented in Section 5.2.2.4, the suspended MLG membranes appear brighter than the surrounding supported flake, both before and after treatment. This is attributed to less background noise due to the underlying substrate, and hence more clarity and higher intensities in the individual spectra. However, no significant difference was detected between the effect and degree of damage that the same treatment imparted on the suspended MLG membranes compared to the adjacent supported MLG flake. This is contrary to the results between the supported CVD graphene and exfoliated MLG flakes, and the suspended CVD graphene. In this case, it is believed that although the membranes in the MLG flakes are technically freely suspended, the well over which they are suspended is not a through hole, yet around 100 nm deep. Therefore, it is thought that the energetic ions incident on the MLG membrane can go through the membrane, interact with the bottom substrate, and backscatter onto the underside of the membrane, inducing secondary defects. Moreover, unlike

the other CVD-graphene samples which are single layered, the multi-layer nature of the exfoliated membranes may also be the reason behind (i) the lower dose required to induce damage, and (ii) the less evident difference between damage in the supported vs. suspended graphene. Upon ion bombardment, the ion has the chance to go through much more graphene layers and induce damage in any of these layers – unlike a one-time through pass in suspended SLG.

5.3 Effect of Ion Bombardment on Elastic Modulus

Following the results presented in Section 5.2, the effect of ion beam bombardment on the elastic modulus of the graphene membranes was investigated.

Indentations were initially performed on the treated CVD graphene on TEM grids samples. However, the results were largely inconclusive with respect to any changes in the elastic modulus due to ion bombardment. Since it proved to be challenging to accurately locate different areas treated with different doses on these samples, mainly due to the nature of the TEM grids themselves and the AFM set-up – the repeated pattern of the TEM grid offers no visual markers within the small area that can be imaged with the AFM – it could not be ascertained that the indented membranes were in fact treated with the documented dose. As such, no conclusions could be drawn from any of the results obtained, and hence will not be presented in this thesis.

Conversely, the imaging method used to treat the CVD graphene on the silicon nitride microsieve as well as the geometry of the microsieve itself (Figure 5.15) allowed for indentations to be performed with high confidence that the membranes indented were indeed treated with the documented dose. However, only graphene membranes irradiated with treatment T2 (dose of 3.29×10^{-15} C/μm^2) were investigated for two reasons.

Firstly, optical imaging after treatment showed that the highest dose of 6.61×10^{-13} C/μm^2 (T3) caused most of the graphene to sputter off and thus, much less membrane area was available to indent with the AFM probe. Furthermore, upon imaging the remaining membranes with the AFM probe prior to indentation, most of the membranes were being ruptured during imaging itself even though lower force set-points were used. This indicates that severe disorder in the graphene structure is significantly detrimental to the mechanical integrity and strength of SLG.

Secondly, results obtained for the mid-range dose of 3.29×10^{-15} C/μm^2 (T2), showed that indentation of the membranes with the lowest dose of 6.86×10^{-16} C/μm^2 (T1) was futile. More details are given in Section 5.3.1.1.

The T2 treated membranes were thus indented via AFM following similar procedures to those explained in Chapter 4. A total of thirteen different treated graphene membranes were indented using a total of six AFM probes; one DTNCLR probe with a spring constant of 61 N/m, two Tap190DLC probes with spring constants of 64 N/m and 57.4 N/m, and three FM50 probes with spring constants of 5.3 N/m, 4.2 N/m and 3.6 N/m. The results of these nanoindentations are presented in Section 5.3.1.1 and are compared to the results obtained from the same CVD graphene sample before treatment (presented in Chapter 4 Section 4.6.1).

Similarly, the mechanically exfoliated MLG membranes in Flake D, which was treated at a dose of 6.62×10^{-13} C/μm^2 using the patterning method, and Flake C treated with a dose of 6.60×10^{-16} C/μm^2 using the imaging method, were indented both before and after the treatment. Table 5.4 lists the AFM probes used for the indentations. The same kind of probes were used in this study to allow a constant spring constant value. Once again, the same procedure outlined in Chapter 4 was used to post-process the obtained force-curves.

Table 5.4: Focused Gallium Ion Beam Treatments on Mechanically Exfoliated Multi-Layer Graphene indented via AFM.

MLG Flake	**Treatment Dose (C/μm^2)**	**AFM Probe**	
		Treated	**Untreated**
Flake D	Patterning Method, 6.62×10^{-13} C/μm^2	Tap190DLC $k = 49$ N/m	Tap190DLC $k = 51$ N/m
		DTNCLR $k = 54$ N/m	DTNCLR $k = 54$ N/m
Flake C, M01 and M02	Imaging Method, 6.60×10^{-16} C/μm^2	Tap190DLC $k = 49.20$ N/m	Tap190DLC $k = 62.13$ N/m

5.3.1 RESULTS

5.3.1.1 Treated Suspended CVD Graphene on Silicon Nitride Microsieve

Figure 5.40 and Figure 5.41 compare the average elastic moduli obtained from the CVD graphene membranes on silicon nitride microsieve before treatment (also shown in Chapter 4) with those obtained after treating the same membranes with a dose of 3.29×10^{-15} C/μm^2. In both cases, force curves obtained to indentation depths lower than 25 nm were omitted.

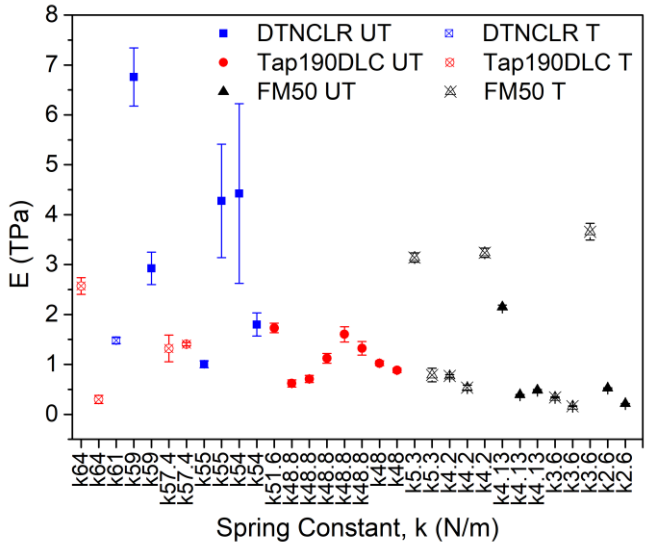

Figure 5.40: Average value of the elastic modulus before (UT) and after (T) treatment, against the spring constant of the probe used. The error bars represent the standard error.

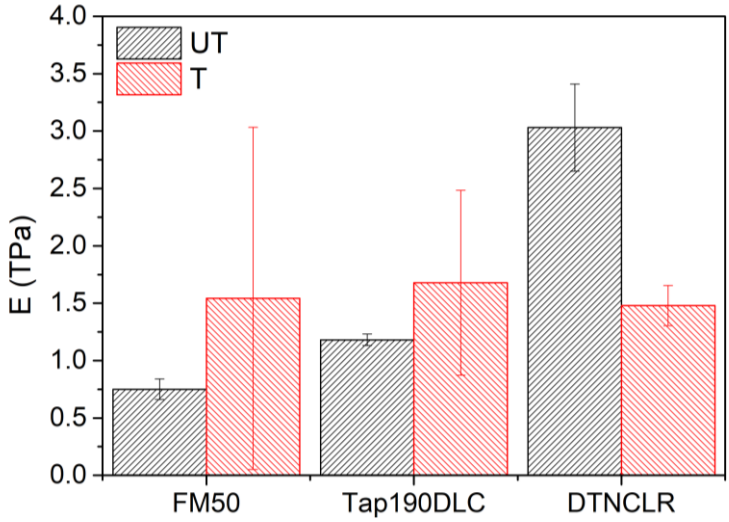

Figure 5.41: The average measured elastic modulus as measured using the FM50, Tap190DLC, and DTNCLR, probes before (UT) and after (T) treatment. The error bars represent the standard error.

As already discussed in Chapter 4, for the untreated membranes a clear trend can be noticed whereby higher and more scattered elastic moduli are obtained using probes with higher spring constants. However, this is not the case for the treated membranes. On the one hand, as shown in Figure 5.40, different force curves obtained from the same membranes produced an average elastic modulus with low error bars using all probes. This means that the method of measuring the elastic modulus for a given membrane is repeatable. However, the average elastic moduli vary significantly from one membrane to another, even using the same AFM probe. This is especially the case with the use of the FM50 probe and leads to significant scatter in Figure

5.41. These results indicate that the individual membranes exhibit different resultant mechanical properties, possibly due to the inhomogeneous treatment. It is also possible that while untreated CVD graphene may have very small defects which do not significantly affect the elastic modulus of the membrane, ion irradiation preferentially attacks such defects. Such preferential attack can be significant enough to alter the elastic modulus, hence amplifying any native difference in the previously untreated membranes. It is well-known that defect sites within a material, and hence sites with higher energy levels, are more prone to chemical or morphological alteration upon an applied treatment.

5.3.1.2 Treated Mechanically Exfoliated Graphene Membranes on PAA/Si Substrate

5.3.1.2.1 Flake D – 6.62×10^{-13} C/μm^2 Patterning Method

Flake D from Case Study 1 in Chapter 4 was irradiated at a dose of 6.62×10^{-13} C/μm^2 using the patterning method, similar to the treatment applied for Flake E. Raman analysis of the untreated flake shows no detectable D peak. On the other hand, upon treatment Flake D was at least partially amorphized with the treatment.

Flake D was indented using Tap190DLC (k = 51 N/m, 49 N/m), and DTNCLR (k = 54 N/m) probes both before and after treatment. Figure 5.42 presents the measured elastic modulus from each force curve against the indented depth, as well as the average elastic modulus obtained using each probe. Once again, only force curves obtained using pre-set indentation depths of between 40 to 80 nm as suggested in Chapter 4 were considered in Figure 5.42 (b).

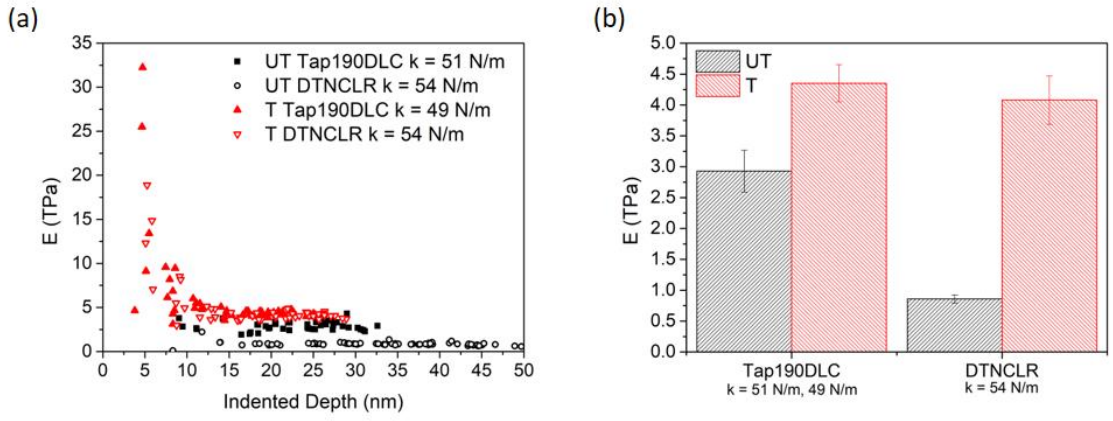

Figure 5.42: (a) The calculated elastic modulus against the indented depth, and (b) the average calculated elastic modulus, E, using a pre-set indentation depth of between 40 nm and 80 nm, before (UT) and after (T) ion bombardment.

From Figure 5.42 (a), the same trend observed in Chapter 4 for the untreated (UT) membrane is once again observed for the treated (T) membrane; the measured elastic modulus is overestimated at lower indentation depths and stabilizes to lower values beyond indented depths of around 10 nm. However, the data points obtained from the treated membrane are overall higher than those obtained from the untreated membrane (Figure 5.42 (b)).

5.3.1.2.2 Flake C – 6.60×10^{-16} C/µm^2 Imaging Method

Membranes M01 and M02 in Flake C, which was treated at a lower dose of 6.60×10^{-16} C/µm^2 using the imaging method inducing an I_D/I_G ratio of 0.22 at the membranes, were also indented before and after treatment using two Tap190DLC probes with a spring constant of 62 N/m and 49 N/m, respectively for the untreated and treated membranes.

Figure 5.43 presents the measured elastic modulus from each force curve against the indented depth, as well as the average elastic modulus obtained using each probe, considering only force-curves obtained using pre-set indentation depths of between 40 to 80 nm. Similar to the previous studies, the elastic modulus is once again overestimated at indentation depths lower than around 10 to 15 nm. However, no particular correlation between the application of the treatment and the resulting elastic modulus can be observed. This can be attributed to the fact that the spring constants of the probes used before and after treatment are significantly different.

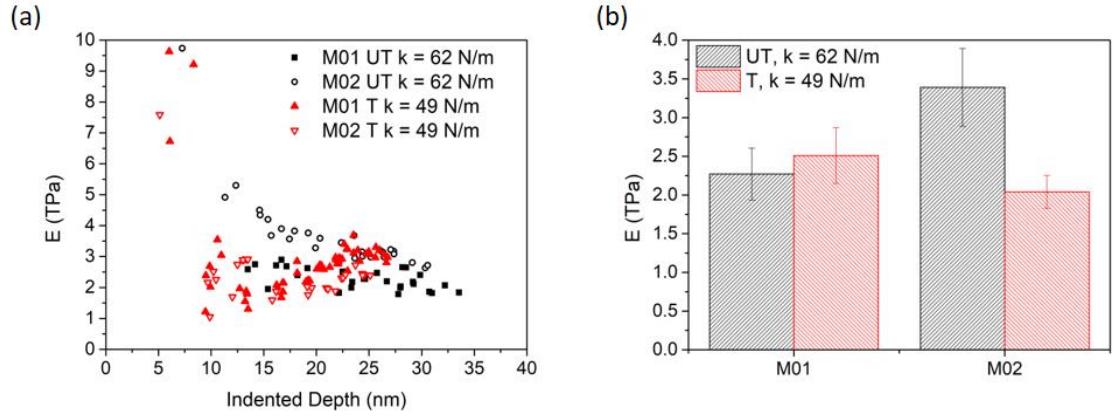

Figure 5.43: (a) The calculated elastic modulus against the indented depth, and (b) the average calculated elastic modulus, E, using a pre-set indentation depth of between 40 nm and 80 nm, using two Tap190DLC probes on both graphene membranes M01 and M02, before (UT) and after (T) ion bombardment.

5.4 CONCLUSION

In Section 5.2, the effect of ion irradiation on the Raman spectrum of graphene was investigated. A significant distinction between the response of the supported graphene and suspended graphene membranes to ion beam irradiation is reported, with the former experiencing more induced damage in response to lower beam doses. This is being attributed to indirect damage which is caused in the supported graphene due to backscattering and sputtering incidents, as well as substrate swelling. A similar response was observed in multi-layered graphene whereby the multiple layers induce backscattering, and hence lower doses were required to produce similar defect densities.

Full and partial amorphization of the supported SLG graphene was also observed in the areas surrounding the directly irradiated areas. The ratio between the Gaussian D and Lorentzian D peaks (I_{DG}/I_{DL}) and the Gaussian G and Lorentzian G peaks (I_{GG}/I_{GL}) are being suggested to be used to quantify the degree of amorphization. A higher incidence angle of the ion beam to the suspended graphene surface increases the damage imparted in the graphene.

In Section 5.3, the effect of ion irradiation on the measured elastic modulus was investigated. From the results presented in Section 5.3.1, it is indicated that bombarding both SLG and MLG membranes with a focused ion beam with doses varying from 6.60×10^{-16} C/μm^2 to 6.62×10^{-13} C/μm^2 may produce membranes with more scattered elastic moduli due to possible preferential attack in certain membranes. However, no clear trend can be seen whether the elastic modulus increases or decreases with such applied treatment. Any true variation in the elastic modulus is masked by the rather significant variation in the results caused by indenting the same membranes using AFM probes having different spring constants.

Having said that, when using similar AFM probes with very similar spring constants, such as shown in Flake D (Section 5.3.1.2.1), the elastic modulus of the MLG membrane was seen to increase. Studies [63, 164] report that this increase in the elastic modulus can be attributed to cross-linking between the multi-layers of the graphene flake induced by ion irradiation.

Furthermore, from the eight treated CVD SLG membranes indented with an FM50 probe, five membranes exhibited similar elastic moduli to the untreated membranes, while three of them exhibited a significantly higher elastic modulus upon treatment. Such an increase in elastic modulus cannot be attributed to cross-linking since only one graphene layer is present, and therefore other mechanisms might be in place.

Chapter 6 MOLECULAR DYNAMICS SIMULATIONS

The work and results presented in Section 6.3 were published in [25].

6.1 INTRODUCTION

Experiments with graphene can be laborious and demand accurate, precise and calibrated equipment, as evidenced by the results presented in Chapters 3 to 5. Molecular simulations can complement experiments and offer insights into the mechanical behaviour of graphene under nanoindentation, provided a suitable simulation model of graphene is used.

In this work, two different molecular dynamics (MD) simulation models of graphene were used. Section 6.2 briefly describes the background of MD simulations and the role of force fields. In Section 6.3, a simplified force field, which uses the Morse bond potential is implemented in-house within the OpenFOAM/mdFOAM software as an initial benchmark study. This model is used to simulate uniaxial loading of graphene sheets in order to measure their elastic modulus, fracture stress and fracture strain. The effects of graphene sheet size, temperature and presence of vacancy defects within the sheets on such mechanical properties are investigated. Dedicated visualisation software is also used to explore the fracture behaviour of such graphene sheets.

In Section 6.4, the Adaptive Intermolecular Reactive Empirical Bond Order (AIREBO) potential [263] within the more popular open-source LAMMPS (Large-scale Atomic/Molecular Massively Parallel Simulator) [264] MD simulation code, chosen due to its superior computational performance and modelling accuracy, is used to model the nanoindentation experiments performed via AFM, described in Chapter 4. This is done in order to understand better the interactions between the graphene membrane and the indenter during indentation, and the elastic response of the graphene membrane under point loading. More specifically, such simulations aim at unveiling any phenomena at play during indentation which would explain the results presented in Chapter 4; the overestimation of elastic modulus at low indentation depths, and the dependence of the measured elastic modulus on the stiffness of the AFM cantilever used.

6.2 MOLECULAR DYNAMICS

Molecular dynamics involves the use of Newton's equations of motion, presented in Equation 6.1 and Equation 6.2, to solve for the position $\boldsymbol{r}_i$, and velocity $\boldsymbol{v}_i$, of all N atoms in the system ($i = 1,2 \dots, N$), with mass m_i [265].

$$\boldsymbol{v}_i = \frac{d\boldsymbol{r}_i}{dt} \qquad \textit{Equation 6.1}$$

$$\boldsymbol{f}_i = m_i \frac{d\boldsymbol{v}_i}{dt} \qquad \textit{Equation 6.2}$$

$$\boldsymbol{f}_i = -\frac{\partial \mathcal{V}(r)}{d\boldsymbol{r}_i} \qquad \textit{Equation 6.3}$$

The net force $\boldsymbol{f}_i$, acting on the atoms is obtained from Equation 6.3 using a potential function $\mathcal{V}(r)$. Potential functions, or force fields, dictate the net force that acts on each atom during the simulation, due to the configuration of neighbouring atoms. These are normally a combination of intermolecular bonds (e.g. van der Waals bonds) and intramolecular bonds (e.g. covalent bonds). The Tersoff-Brenner [147, 183] and AIREBO [24, 148, 160, 174] potentials are amongst the most commonly used force fields to simulate graphene in MD. However, it was shown that the Morse bond potential function is also able to accurately simulate graphene at lower computational costs [168]. Hence, in this work, both the Morse bond potential as well as the more widely used AIREBO potential are used in Section 6.3 and Section 6.4, respectively.

The equations of motion are numerically integrated in space and time for all atoms in the sheet using the velocity Verlet algorithm. A flow chart of the algorithm is presented in Figure 6.1 and in Equation 6.4 to Equation 6.7. The velocity Verlet algorithm is computed for every time-step Δt, whereby the total simulated time is the total time-steps performed multiplied by the time-step size. For the algorithm to be stable and computationally efficient, the correct choice of Δt is required. A too large time-step will reduce the processing time, but will integrate the atomic positions within the high repulsive part of its neighbours, causing system heating and then simulation blow-up. A too small time-step will be wasteful of computational resource. In every problem, a careful identification of the time-step is carried out. Typically, literature provides a good starting point for Δt. In this work, a time-step of 0.43 fs using the Morse bond potential (Section 6.3) and 0.5 fs using the AIREBO potential (Section 6.4) were used.

$$\boldsymbol{v}_i\left(t+\frac{1}{2}\Delta t\right)=\boldsymbol{v}(t)+\frac{1}{2}\Delta t\frac{\boldsymbol{f}_i}{m_i} \quad \textit{Equation 6.4}$$

$$\boldsymbol{r}_i(t+\Delta t)=\boldsymbol{r}(t)+\boldsymbol{v}_i\left(t+\frac{1}{2}\Delta t\right) \quad \textit{Equation 6.5}$$

$$\boldsymbol{f}_i(t+\Delta t)=-\nabla\mathcal{V}\big(\boldsymbol{r}_i(t+\Delta t)\big) \quad \textit{Equation 6.6}$$

$$\boldsymbol{v}_i(t+\Delta t)=\boldsymbol{v}\left(t+\frac{1}{2}\Delta t\right)+\frac{1}{2}\Delta t\frac{\boldsymbol{f}_i\left(t+\frac{1}{2}\Delta t\right)}{m_i} \quad \textit{Equation 6.7}$$

All simulated atoms are initialised with a zero (Section 6.3) or pre-defined Maxwellian distributed (Section 6.4) velocities applied to all atoms, and then equilibrated for a pre-defined duration of time before loading is applied. This allows for all the atoms to interact with each other and for an equilibrium in their energies to be reached. For computational speed up, atoms interact only with their neighbours within a radius of r_{cut}, instead of the full system N. This is done using the standard neighbour list algorithm. The value of r_{cut} is chosen large enough to ensure that van der Waals interactions at such atom-atom distances are close to zero.

A thermostat can also be applied to set and control the temperature of the graphene sheet. Since the temperature of a system is proportional to its kinetic energy, the thermostat operates by regulating the molecular velocities to control the overall temperature of the system throughout the simulation.

In this work, MD simulations are run using either NVE (microcanonical) or NVT (canonical) ensembles. Running a simulation at NVE means that the number of atoms, the volume of the simulation box, and the net energy of the system are conserved throughout the simulation. On the other hand, running the simulation using the NVT ensemble means that the number of atoms, the volume of simulation box and the temperature are held constant. With the latter ensemble, the Nosé-Hoover algorithm is used as the thermostat.

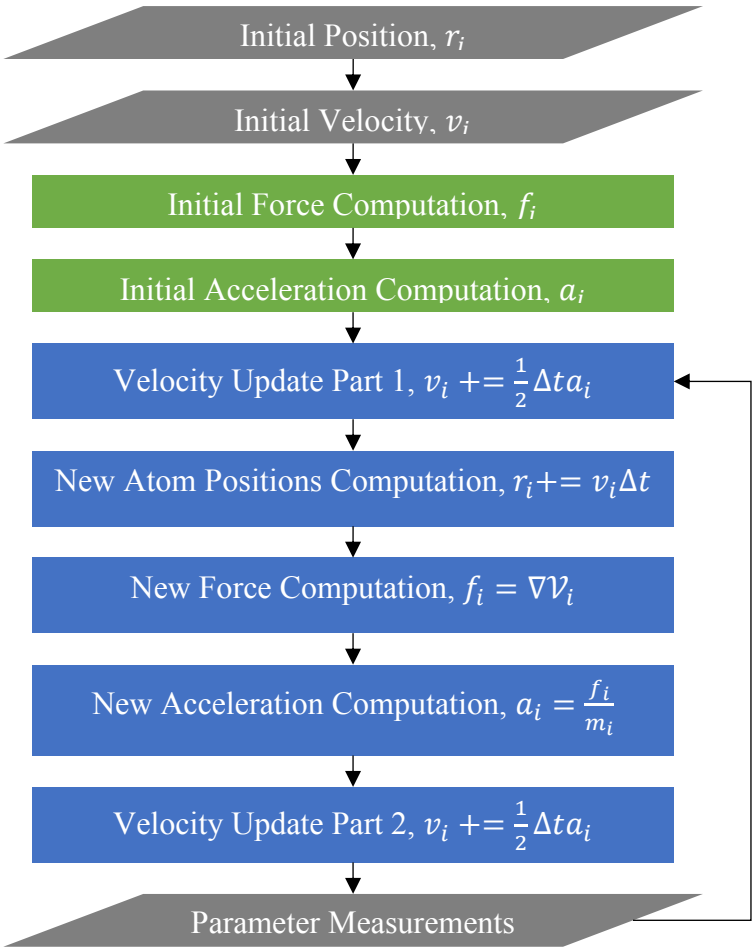

Figure 6.1: A flow chart showing the velocity Verlet algorithm in a typical MD simulation timestep.

6.3 A Simplified Model for Graphene on OpenFOAM

In this work, the Morse, bending angle, torsion and Lennard-Jones potential functions were first used concurrently, as described by Walther et al. [266]. These potentials were originally used to understand hydration effects of water with carbon nanotubes, and are tested here due to their simplicity and low computational cost. In this work, these potentials were implemented for the first time in the OpenFOAM software within the mdFOAM library. This simple force field was used to test pristine graphene under uniaxial loading and was validated with available studies. The aim of this study was to understand the dependence of mechanical properties on sheet size, temperature and orientation. Whenever possible, the obtained results were compared with experiments and literature MD simulation results that use different potential functions. These MD simulations were also used to study the fracture behaviour and mechanical properties of nanoporous graphene with increasing monovacancy defect concentration. This

was carried out to mimic graphene in the as-synthesised condition, and also intentionally porous sheets for applications that require non-pristine sheets such as filtration membranes.

Section 6.3.1 gives a detailed description of the molecular dynamics simulations and case setup. Section 6.3.2 describes the validation simulations for pristine graphene and presents results for nanoporous graphene, while Section 6.3.3 concludes the presented work.

6.3.1 METHODOLOGY

In this section, the mdFOAM molecular dynamics code [267, 268] was used, which is available in the OpenFOAM software [269]. OpenFOAM is an open-source C++ toolbox typically used for computational simulations. The mdFOAM library was extended to include the new potential functions, constraints and measurement tools described in the following.

6.3.1.1 Potential functions

During the MD simulation, the net force on all atoms in Equation 6.3 is determined via the spatial derivative of four potential functions [266]. These potentials are illustrated in Figure 6.2 and consist of; (i) a Morse stretching potential $\mathcal{V}_{ij}^{M}$ used to model the C-C covalent bond lengths, (ii) a harmonic potential $\mathcal{V}_{jik}^{BA}$ used to model the bending angle between bonds, (iii) a two-fold torsion potential $\mathcal{V}_{jikl}^{T}$ used to model out-of-plane stiffness, and (iv) a Lennard-Jones intermolecular potential $\mathcal{V}_{ij}^{LJ}$ used to model van der Waals and steric bonds. These are given, respectively, by Equation 6.8 to Equation 6.11.

$$\mathcal{V}_{ij}^{M} = K_{Cr}\left(e^{-\gamma(r_{ij}-r_C)} - 1\right)^2 \qquad \textit{Equation 6.8}$$

$$\mathcal{V}_{jik}^{BA} = K_{C\theta}\left(\cos\theta_{jik} - \cos\theta_C\right)^2 \qquad \textit{Equation 6.9}$$

$$\mathcal{V}_{jikl}^{T} = \frac{1}{2}K_{C\phi}\left(\cos\phi_C - \cos\phi_{jikl}\right) \qquad \textit{Equation 6.10}$$

$$\mathcal{V}_{ij}^{LJ} = 4\epsilon_{CC}\left[\left(\frac{\sigma_{CC}}{r_{ij}}\right)^{12} - \left(\frac{\sigma_{CC}}{r_{ij}}\right)^{6}\right] \qquad \textit{Equation 6.11}$$

The values for the constants in these equations are listed in Table 6.1, and the variables r_{ij}, θ_{jik}, and ϕ_{jikl} are shown in Figure 6.2. The total potential energy $\mathcal{V}^{MORSE}$ of the system is given as a sum of all four potentials over all carbon atoms as shown in Equation 6.12.

$$\mathcal{V}^{MORSE} = \sum_{i,j}\mathcal{V}^{M}(r_{ij}) + \sum_{i,j,k}\mathcal{V}_{jik}^{BA} + \sum_{i,j,k,l}\mathcal{V}_{jikl}^{T} + \sum_{i,j}\mathcal{V}_{ij}^{LJ} \qquad \textit{Equation 6.12}$$

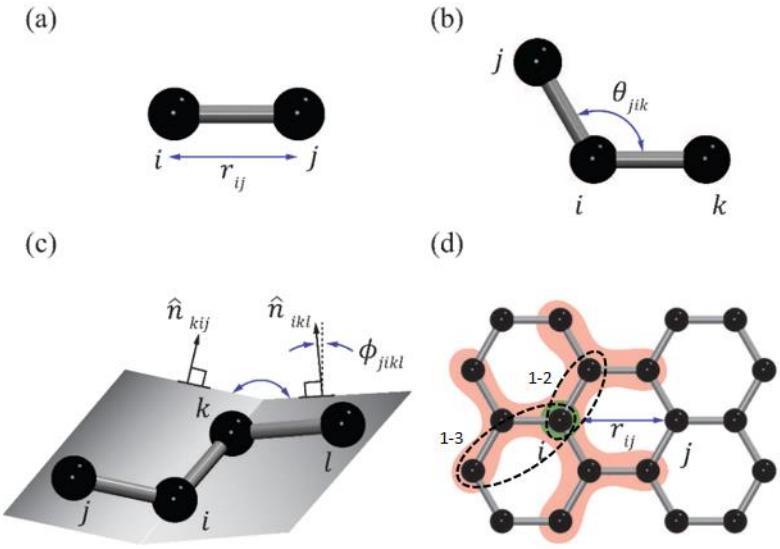

Figure 6.2: Schematics of (a) the Morse bond length r_{ij}, (b) the bond angle θ_{jik}, (c) the torsion angle ϕ_{jikl}, and (d) the Lennard-Jones pair interaction distance r_{ij}, where the highlighted region indicates the 1–2 and 1–3 atom interactions which are excluded for an arbitrary atom i.

Table 6.1: Parameter constants for the potential functions. [270]

$K_{Cr} = 478.9$ kJ mol^{-1}	$\theta_C = 120°$	$r_C = 1.418$ Å
$K_{C\theta} = 562.2$ kJ mol^{-1}	$\phi_C = 0°$	$\gamma = 2.1867$ Å^{-1}
$K_{C\phi} = 25.12$ kJ mol^{-1}	$\epsilon_{CC} = 0.4396$ kJ mol^{-1}	$\sigma_{CC} = 3.851$ Å

The Morse, bending angle and torsion potentials are applied to atom groups that are covalently bonded, while the Lennard-Jones potential excludes 1–2 and 1–3 interactions [266] as illustrated by the shaded region in Figure 6.2 (d) for an arbitrary atom, and excludes pair atom computations with separation r_{ij} greater than the cut-off radius r_{cut} = 1 nm. In the initialisation stage, the atomic bonds are established and saved in a bonds list. This list is accessed throughout the simulation to avoid unnecessary computational processing required to re-establish the bonds in every time-step.

During loading, the Morse, angle bending and torsion bonds are then permanently broken only when the Morse bond exceeds r_{ij} > 0.2 nm [271]. In such a case, the bonds list is repopulated. Given that this usually occurs towards the end of the simulation when the sheet fractures almost instantaneously, the bonds list remains constant throughout most of the simulation. As a result of the optimised bond selection, the resulting computational timings are approximately $O(C \times N)$ where $C \approx 1.5$. On the other hand, both the AIREBO and Tersoff-Brenner potentials

have a reactive bond-order term, with typically either 3- or 4-body potentials. These bond order terms are also adaptive, meaning they need to access atomic position information at every time-step (in contrast to the fixed bond lists used in this work), resulting in a major computational penalty. The cost of the AIREBO and Tersoff-Brenner potentials can however be reduced, although at the expense of numerical and programming complexity.

6.3.1.2 Atom Configuration

In this section, the mechanical properties of graphene are studied by simulating uniaxial tensile loading of a rectangular graphene sheet. As such, the atom positions in a hexagonal lattice with bond length 1.42 Å were created to represent the carbon atoms within a rectangular graphene sheet with a diagonal length L_D. The graphene sheets were also oriented such that their longer axis was either in the armchair or in the zigzag orientation, as shown in Figure 6.3.

To model vacancies in the graphene sheets, individual atoms were selected in a random manner or a uniform distribution and removed from the initial list of atoms.

6.3.1.3 Simulation Parameters

The velocity Verlet algorithm within an NVE ensemble with a time-step of 0.43 fs was used. All simulated graphene sheet atoms were initialised with a zero velocity, and then equilibrated for a duration of at least 20 ps (~46 500 time-steps) before loading was applied. During equilibration, the FADE algorithm [272] was applied to gradually introduce the intermolecular forces on the carbon atoms using a time-weighted function with time relaxation τ_T = 21 ps. This prevents a sudden increase in energy of the system which might otherwise result in a sudden expansion of the graphene sheet and hence possible premature sheet fracture. To prevent the sheet from drifting within the domain, the net velocity of the sheet was set to zero during equilibration using a simple velocity constraint [273]. A Langevin thermostat [274] was applied to control the temperature of the sheet during relaxation and loading.

6.3.1.4 Loading method and calculations

To simulate uniaxial tensile loading, hexagonal rings at opposite edges of the graphene sheet were constrained as shown in Figure 6.3. Constrained atoms were subjected to a quasistatic strain rate of 2.56×10^8 s^{-1} in accordance with [168]. Unless otherwise stated, armchair (AC) and zigzag (ZZ) graphene sheets with an aspect ratio of approximately 1:1.3 were considered, which are loaded along the longitudinal axis, as indicated in Figure 6.3 (b) and (c). The applied strain to the sheet ε at time t was found using $\varepsilon(t) = \frac{(l_x(t)-l_0)}{l_0}$, where l_0 and $l_x(t)$ are the

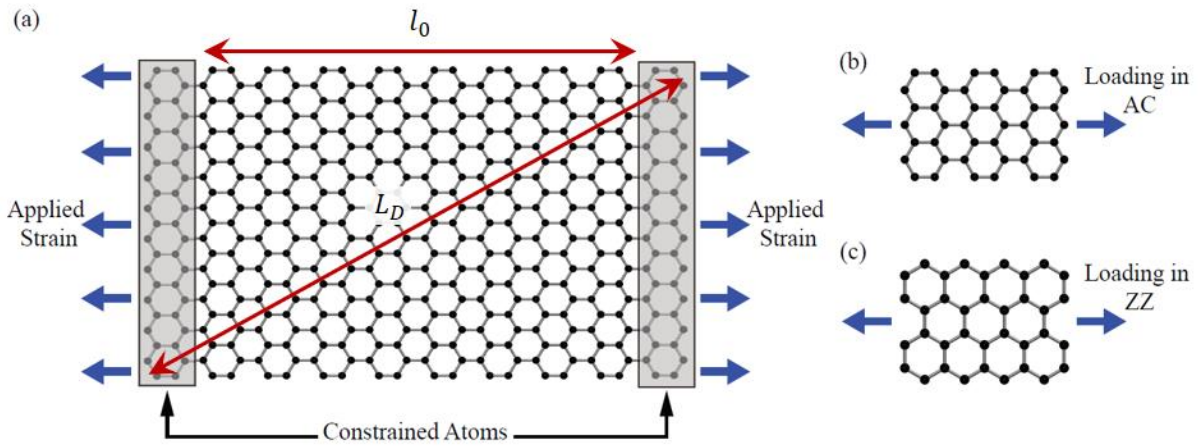

Figure 6.3: (a) A schematic illustration of a graphene sheet showing the edge atoms constrained (shaded in grey) for the application of the pre-defined strain-rate. (b) and (c) illustrate the loading direction of an armchair (AC) and zigzag (ZZ) sheet, respectively.

distances between two arbitrarily pre-selected atoms from the sheet (just outside the constrained region) before and during loading, respectively. The stress σ and elastic modulus E were computed using Equation 6.13 and Equation 6.14.

$$\sigma(\varepsilon) = \frac{1}{V_0}\frac{\partial U(\varepsilon)}{\partial \varepsilon} \qquad \textit{Equation 6.13}$$

$$E = \frac{1}{V_0}\frac{\partial^2 U(\varepsilon)}{\partial \varepsilon^2} \qquad \textit{Equation 6.14}$$

V_0 is the original volume of the sheet when assuming a thickness of 0.335 nm [13], and U is the strain energy of the sheet which is measured as the difference of the total system potential energy between a time t and the unloaded sheet. To solve Equation 6.13 and Equation 6.14, a similar method described by Le and Batra [168] was adopted, which involves fitting a cubic function to strain energy U against strain ε, and applying straightforward differentiation. The value of the elastic modulus reported in this work is E at zero strain.

6.3.2 Results and Discussion

In this section, the MD graphene model is validated by measuring the mechanical properties and investigating the fracture behaviour of pristine graphene for different orientations, sheet size and temperatures and comparing them to literature sources when available. Graphene with ordered and random vacancy defects are then investigated.

6.3.2.1 Sheet Size Dependence

Eleven different sheet sizes ranging from diagonal lengths L_D of 1.35 to 14.51 nm (42 to 4760 carbon atoms) were modelled at a temperature of 0 and 300 K. Each case was run using four

statistically independent realisations and an average of the mechanical properties was taken. To obtain statistically independent samples, each realisation of the same case was run for a different duration at the equilibration stage before loading was applied.

The effects of sheet size on elastic modulus, fracture stress and fracture strain are shown in Figure 6.4 (a – c) for 0 K. The results show that the mechanical properties assessed in this work decrease with an increase in sheet size from the smallest sheets considered up to a critical length of approximately 6 to 7 nm, beyond which the properties stabilise to that of bulk graphene. This behaviour is especially evident in ZZ sheets whereby an increase in diagonal length from 1.42 to 5.66 nm decreases the elastic modulus, fracture stress and fracture strain by 7.2%, 16.5% and 15%, respectively. On the other hand, the elastic modulus, fracture stress and fracture strain for AC graphene decrease by only 2%, 1.7% and 5.8%, respectively, for the same size range.

The results for sheets at 300 K are shown in Figure 6.4 (d – f), where the critical length at which the fracture stress and fracture strain approach that of bulk graphene observed at this temperature lies between 8 and 10 nm; this is in good agreement with the critical length of 10 nm indicated by Zhao et al. [24]. Furthermore, at 300 K a more pronounced behaviour is observed for the fracture stress and strain below this critical length. For ZZ graphene at 300 K, an increase in diagonal length from 1.42 to 5.66 nm results in a decrease of the fracture stress and fracture strain by 23.9% and 22.3%, respectively. On the other hand, the fracture stress and fracture strain for the AC graphene sheets decrease by 15.4% and 16.3%, respectively. This size dependency of fracture properties is in good agreement with Ni et al. [166] (Tersoff-Brenner) and Sakhaee-Pour [275] (finite-element modelling). For the smallest sheet when tested at a temperature of 300 K, a slight decrease in elastic modulus was also observed, which was not observed by Ni et al. [166] and Sakhaee-Pour [275], but was evident in the AIREBO MD simulations carried out by Zhao et al. [24].

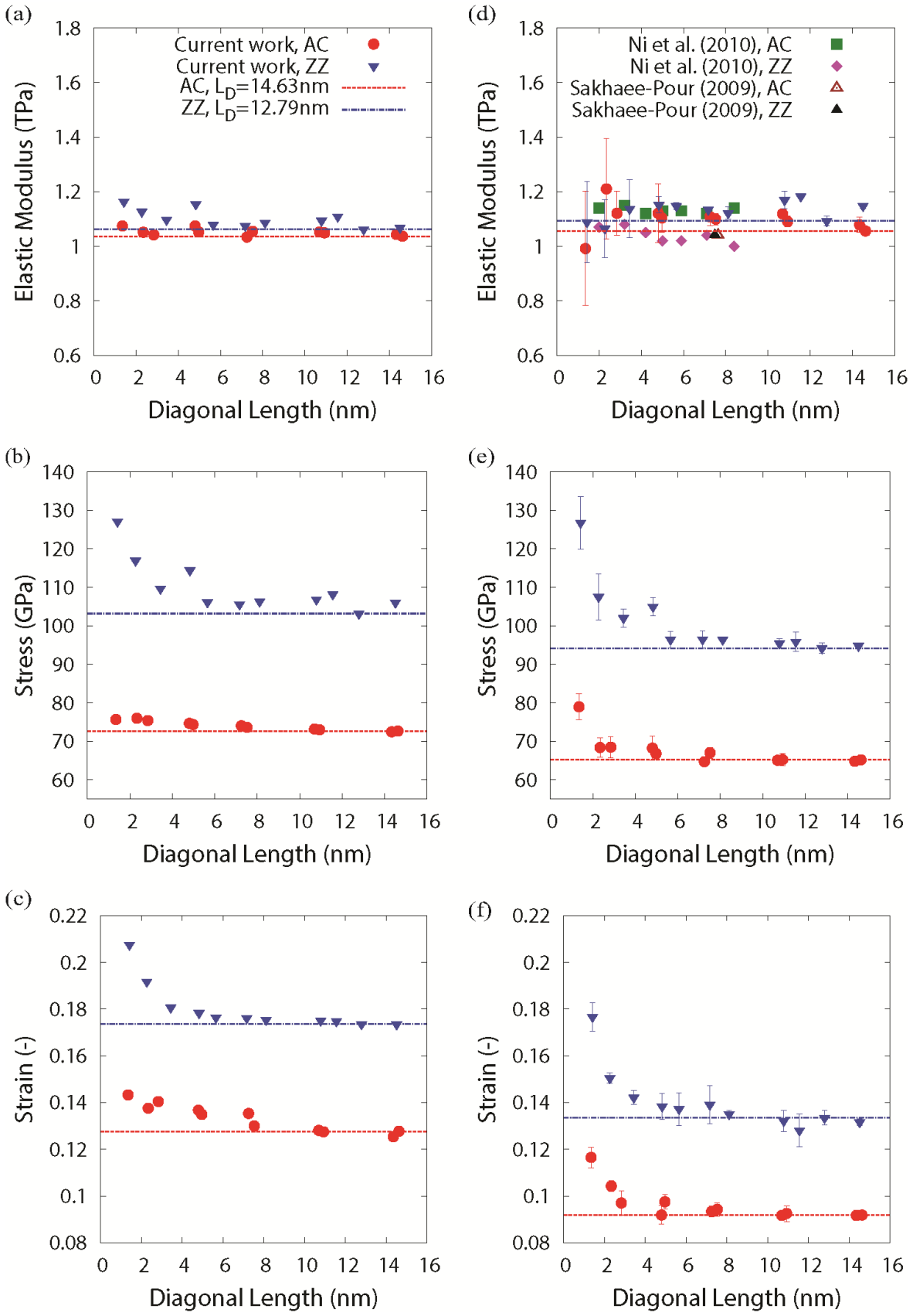

Figure 6.4: Results for elastic modulus, fracture stress and fracture strain for AC- oriented graphene (red solid circles) and ZZ-oriented graphene (blue inverted triangles) with increasing sheet size for two different temperatures: (a – c) 0 K, and (d – f) 300 K. The dashed lines represent bulk mechanical properties.

Table 6.2: Measured mechanical properties of pristine bulk graphene. Note that the error bars of the 0 K graphene sheet are negligible and have not been included.

	E (TPa)	σ (GPa)	ε
AC (0 K)	1.035	72.69	0.1278
ZZ (0 K)	1.061	103.19	0.1736
AC (300 K)	1.056 ± 0.011	65.19 ± 0.84	0.0919 ± 0.002
ZZ (300 K)	1.093 ± 0.175	94.19 ± 1.36	0.1335 ± 0.003
Nanoindentation Lee et al. [13]	1.0 ± 0.1	130 ± 10	0.25
AC (300 K) Zhao et al. [24]	1.01 ± 0.03	90	0.13
ZZ (300 K) Zhao et al. [24]	1.01 ± 0.03	107	0.20

Table 6.2 presents the resulting bulk mechanical properties of graphene as measured from the Morse bond MD simulations. The values for the elastic and fracture properties are in very good agreement with data found in [13, 24, 34, 275, 276]. Values for the elastic modulus agree very well with the experimental results of Lee et al. [13] (1.0 ± 0.1 TPa) and the MD simulations using the AIREBO potential of Zhao et al. [24] (1.01 ± 0.03 TPa). However, the fracture stress and fracture strain obtained are within 30% of the experimental [13] and AIREBO simulations [24] results available in literature. The differences between the presented results and those of Zhao et al. [24] may be attributed to the inability of the applied model to deal with changes in bond coordination which occurs just before and during fracture. In this respect, the adaptive bond-order term in the AIREBO potential performs better since it allows the bonds to change at fracture. A second possible contribution to the underestimation of fracture stress and strain values may be related to the fact that Zhao et al. [24] consider an infinite sheet in the transverse direction of loading by applying periodic boundary conditions, and constrain the dynamics of atoms at a fixed pressure using the NPT ensemble. On the other hand, the presented simulations consider a finite graphene sheet, with dangling bonds at the transverse edge of the graphene sheet in the NVT ensemble.

Stress versus strain graphs for bulk graphene are shown in Figure 6.5 (a). At small strains (up to about 2%), graphene exhibits a linear behaviour, while a non-linear stress-strain response is seen for larger strains up to fracture, in agreement with the simulation work in [24] and experimental work in [13, 104]. In this work, it is found that the ZZ direction is stronger and slightly stiffer than a graphene sheet loaded from the AC direction. This anisotropic dependence agrees with [24, 172, 174] which is attributed to the geometrical distribution of the

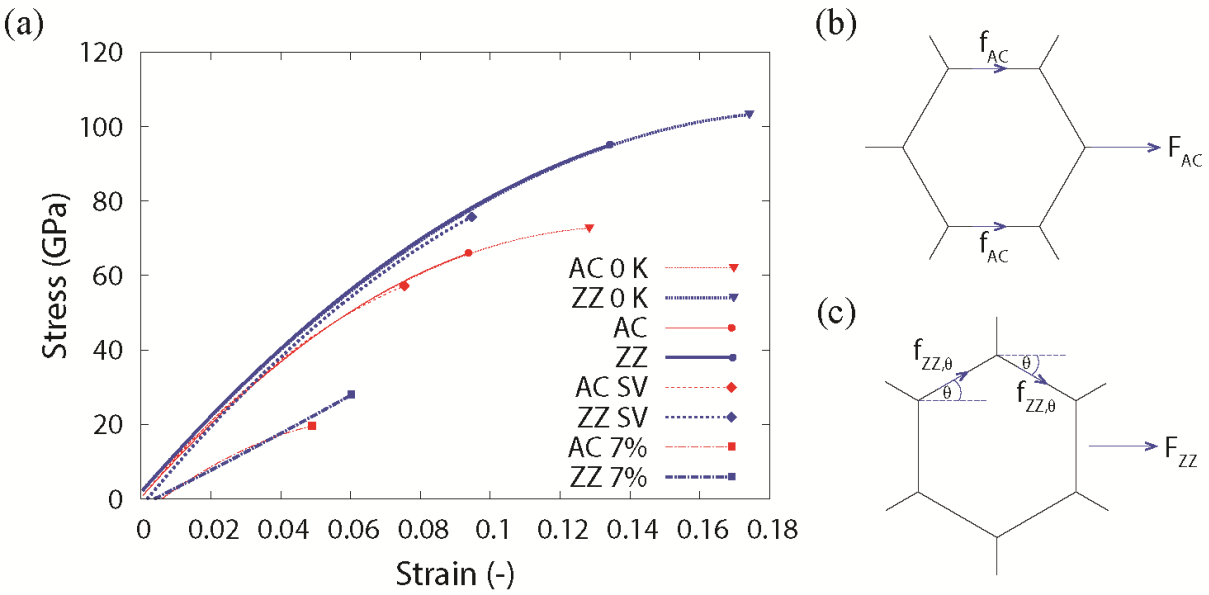

Figure 6.5: (a) Stress-strain plot of AC (red) and ZZ (blue) graphene sheets. All simulations were run at 300 K except the ones marked otherwise. Results from other simulations for sheets with a single vacancy (SV) defect, and nanoporous sheets with 7% defect density are also presented. (b) and (c) illustrate the resolved forces along selected covalent bonds during AC and ZZ loading, respectively.

covalent bonds in the hexagonal lattice, as illustrated in Figure 6.5 (b) and (c). When graphene is loaded along the AC direction, roughly a third of the bonds in the sheet are perfectly aligned to the loading direction (Figure 6.5 (b)), and thus the loading is directly transferred to these bonds. However, when the load is applied along the ZZ direction (Figure 6.5 (c)), none of the covalent bonds are aligned to the loading direction and therefore the actual force sustained by each covalent bond is in fact a component of the force acting along the bond angle, which results in less force than those sustained by the AC sheets. As such, this allows the ZZ-loaded sheet to elongate further and hence withstand more stress and strain along the ZZ direction prior to fracture.

Based on these results, sheets with diagonal length of approximately 13 nm and aspect ratio of 1:1.3 were used in the following studies (unless otherwise stated), such that all simulations represent graphene sheets having bulk-mechanical characteristics.

6.3.2.2 Fracture Behaviour of Pristine Graphene

Figure 6.6 and Figure 6.7 present the fracture process of pristine AC and ZZ graphene sheets, respectively, at 300 K. The fracture behaviour is mostly dependent on the alignment and position of the covalent bonds with respect to the loading direction. As such, the path of travel occurs perpendicular to aligned covalent bonds. For the AC-loaded sheet, a high percentage of covalent bonds are aligned with the loading direction and so the crack propagates perpendicular

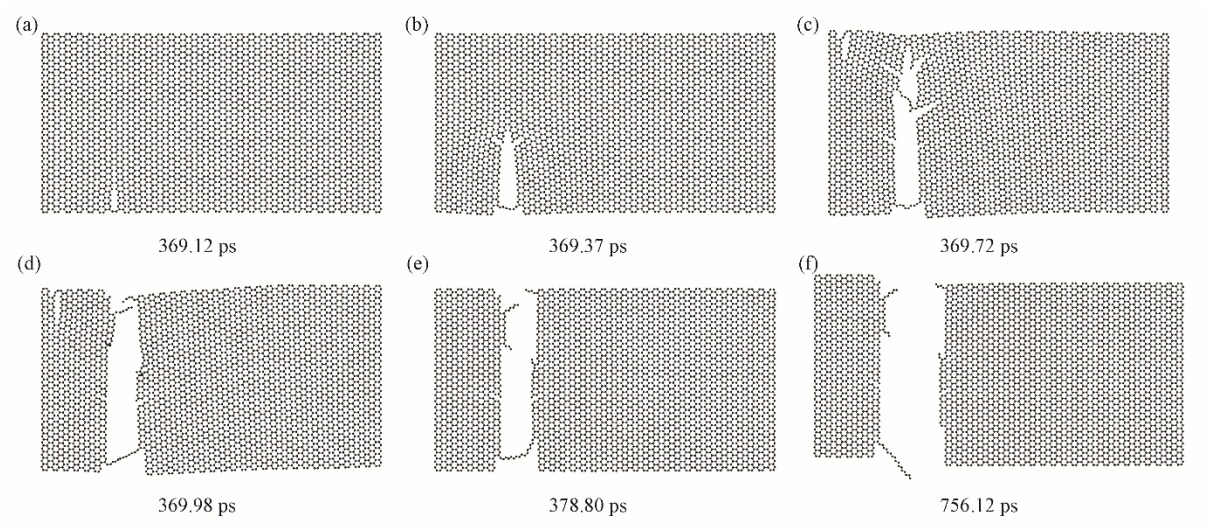

Figure 6.6: Fracture process of a pristine AC graphene sheet with a diagonal length of 14.63 nm at 300 K. (a – f) show snapshots of the sheet at different times of the simulation during the occurrence of fracture.

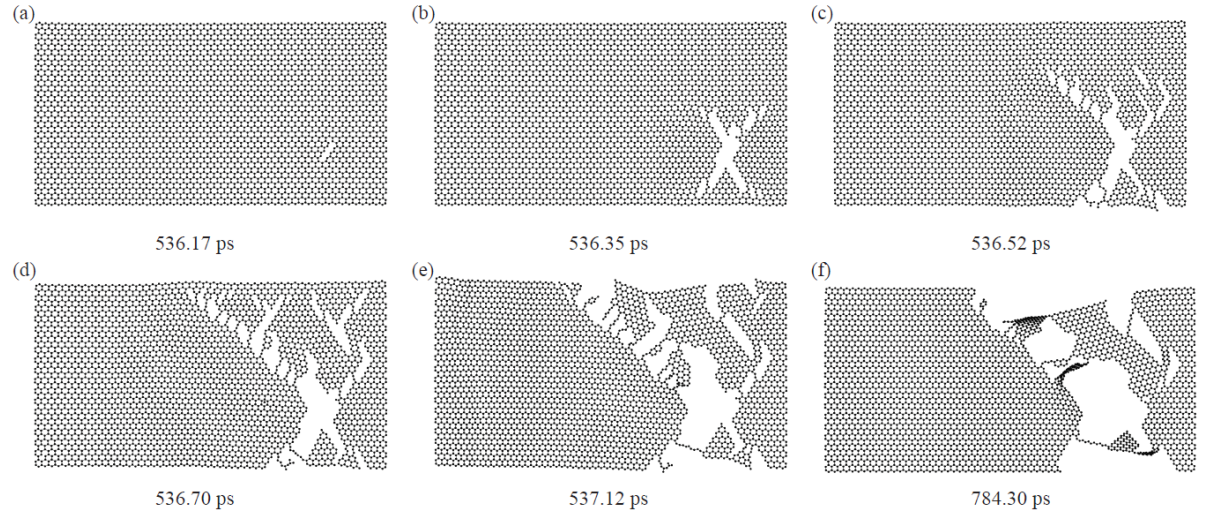

Figure 6.7: Fracture process of a pristine ZZ graphene sheet with a diagonal length of 14.84 nm at 300 K. (a – f) show snapshots of the sheet at different times of the simulation during the occurrence of fracture.

to loading. For the ZZ-loaded sheet, the covalent bonds are not oriented in the same direction as loading, and so crack propagation favours a diagonal travelling path (~60°) normal to the alignment of the bonds.

While pristine graphene supports high fracture strains, its mode of fracture under loading is brittle since cracks rapidly propagate when they form, resulting in catastrophic failure of the sheet. Similar fracture patterns to those presented in Figure 6.6 and Figure 6.7 have been also observed with the use of the AIREBO [174, 179, 180, 277] and Tersoff-Brenner [29, 278] potentials. AIREBO and Tersoff-Brenner potentials are known to model the fracture behaviour

accurately, thus the simulation results obtained in this study, albeit using a simpler set of potential functions, are in very good agreement with more established potentials.

6.3.2.3 Temperature dependence

Graphene is expected to be used in several different applications for which the environmental conditions vary considerably. In this study, the effect on the mechanical properties of pristine graphene at different temperatures, varying from 0 to 1100 K, is studied. For each case, five statistically independent simulations were carried out and an average was taken.

The variation of several mechanical properties with temperature is shown in Figure 6.8. It is evident from these graphs that the fracture stress and strain decrease substantially with an increase in temperature for both ZZ and AC loading configurations. For ZZ-loaded graphene at 1100 K, the fracture stress decreases to 53.3 GPa (48% decrease from 0 K), while the fracture strain decreases to 0.053 (70% decrease from 0 K), while for AC graphene fracture stress and strain reduce by 39 and 58%, respectively, from 0 K. The same dependence of stress and strain on temperature has been observed using the AIREBO potential in [34, 171, 175, 176, 180, 279]. For example, Zhang et al. [171] obtained a 50% decrease in intrinsic strength when the sheet temperature is increased from 0 to 1200 K.

The thermal fluctuations of atoms are the principal reason why graphene's fracture stress and strain are reduced at higher temperatures. Carbon atoms possess more kinetic energy at elevated temperatures, causing significantly high vibrations and, as a result, a large out-of-plane motion (in the z-direction) in equilibrium, resulting in overall sheet rippling, as shown inFigure 6.9. The distance covered by carbon atoms in the z-direction at equilibrium is shown in Figure 6.9 (a) as a function of temperature; assuming a sheet thickness of 0.335 nm at 0 K, the out-of-plane distance covered by molecules is 3 times larger for the 1100 K than the 0 K

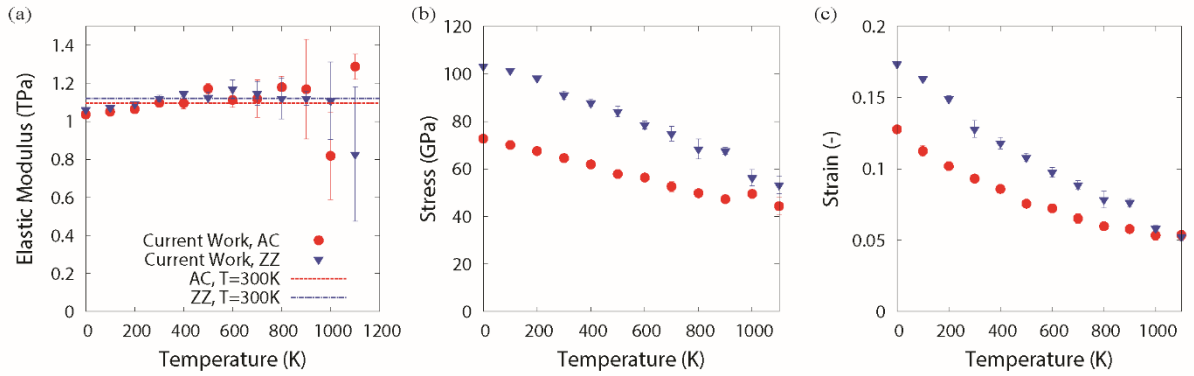

Figure 6.8: Results for (a) elastic modulus, (b) fracture stress, and (c) fracture strain of AC (red solid circles) and ZZ (blue inverted triangles) graphene sheets (L_D=14.7 nm), varying with sheet temperature.

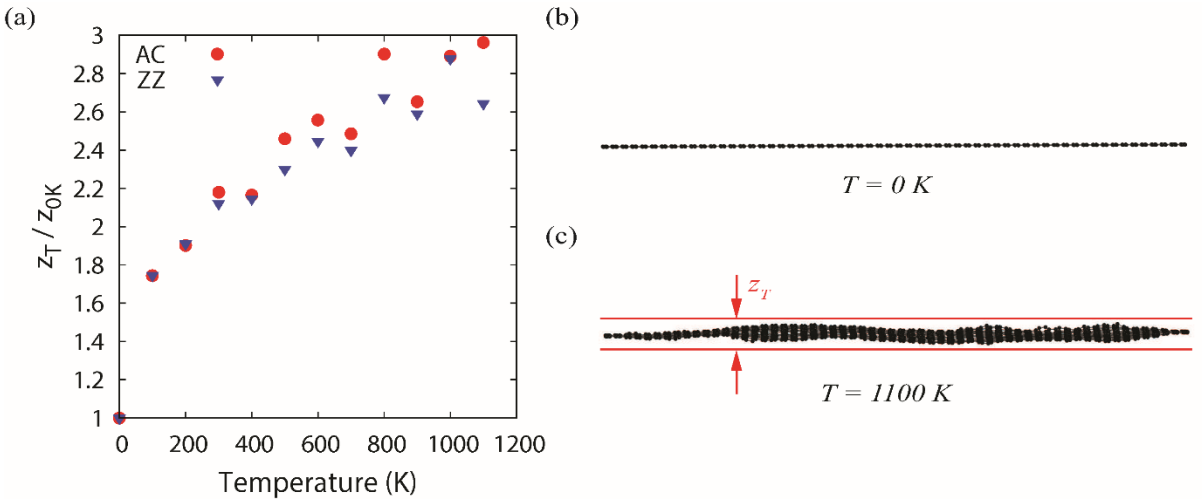

Figure 6.9: (a) Plot showing the increase in rippling in the z-direction with an increasing sheet temperature in AC and ZZ graphene sheets. The effective thickness has been normalized with respect to the original thickness of the pristine graphene sheets at 0 K i.e. z_{0K} = 0.335 nm. (b) and (c) illustrate a side view of pristine graphene sheets at 0 K and 1100 K, respectively, to highlight the rippling effect in the z-direction at higher temperatures.

sheet due to thermal motion. The perturbations in the sheet are gently ironed out during loading, but since thermal fluctuations still remain, covalent bonds are more susceptible to break prematurely, producing cracks at lower strain and stress. Conversely, the elastic modulus is largely unchanged within a large temperature range. The elastic modulus increases from 0 K to 500 K by 6% and 13 % for ZZ and AC graphene, respectively, and remains relatively constant until ~900 K. At higher temperatures (> 900 K), a decrease in the elastic modulus to ~0.8 TPa is observed, similar to that obtained in [279], but is still exceptionally high when compared to other conventional materials. The larger variation in results obtained at higher temperatures – evidenced by wider error bars – are expected due to the large thermal fluctuations.

6.3.2.4 Random and uniformly distributed vacancy defects

It is evident that the presence of atomic defects may affect the properties of graphene quite considerably. Although generally not desired, defects can originate from a fabrication process, but can also be intentionally introduced, for example, in the production of nanoporous graphene membranes for desalination [267] or filtration applications. In these applications, nanoporous graphene would need to contain a high level of porosity for there to be superior permeability over conventional membranes. The porosity might, however, affect the graphene's ability to withstand the high hydraulic pressures; ~5 MPa for typical reverse osmosis membranes. In this work, nanoporous graphene is simulated with randomly or uniformly distributed defects (single atoms removed from the sheet) varying in density from 0.1% up to 12% and its mechanical

properties and fracture behaviour are studied. For the following simulations, the graphene sheets were modelled with an aspect ratio that approximates a square with a diagonal length of 13.7 nm.

Figure 6.10 (a) shows the elastic modulus, fracture stress and fracture strain for randomly distributed vacancy defects, while Figure 6.10 (b) shows the same mechanical properties for uniformly distributed defects. In both cases, there is a considerable decrease in the calculated properties with increasing defect density. The introduction of a vacancy defect causes a significant drop in the fracture stress and fracture strain of around 15% and 23%, respectively. This reduction can also be seen in Figure 6.5 (a) (page 247) and has also been reported in [28, 35, 280]. We found that the elastic modulus remains relatively unaffected up to around 3% to 5% defects for random and uniform distributed defects, similar to the data found in [30, 281]. The elastic modulus then decreases roughly linearly with increasing defect density. This relationship was similarly found recently in [222] for nanoporous graphene with larger pore sizes. At the largest porosity considered in this dissertation (12%), the elastic modulus drops by around 80%. The stress–strain curve for a sheet with 7% defect density is shown in Figure 6.5 (a) which is compared with that of a pristine sheet.

An important outcome from these simulations, especially for use in filtration membranes is that a sheet with uniformly distributed defects has a fracture stress of up to 197% higher than that for randomly distributed defects in the case of AC graphene sheets with 12% defects. This is caused because the latter contains a wider range of defect sizes, having pores which are larger and more susceptible to fracture as noted in [222].

Another interesting outcome of these simulations is the behaviour of the fracture strain with increasing defect density above 3%. Unlike the fracture stress and elastic modulus, which continue to decrease with increasing vacancies, the fracture strain stabilises at around 3% defect density and starts to increase again above 6%. This is identified as a stage of improved ductility in graphene (above 6% defect density), and it is caused by large presence of vacancy defects that allow the sheet to stretch more under loading, and as such enabling larger fracture strains to be sustained. A similar behaviour was also observed by Xu et al. [35]. For the uniform distributed vacancy defects, however, the AC-loaded sheet seems to reach a saturation phase without signs of strain improvement.

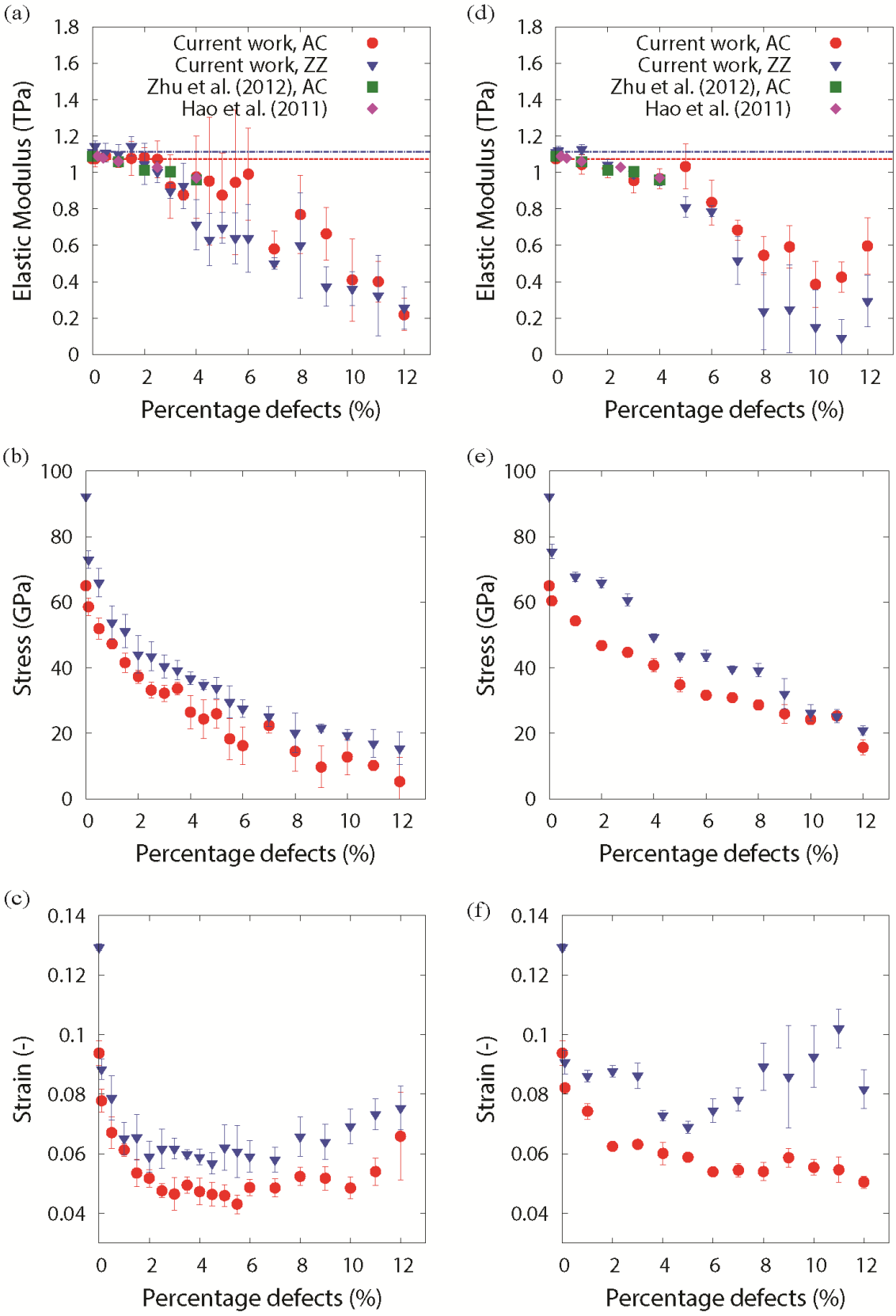

Figure 6.10: Graphs showing elastic modulus, fracture stress and fracture strain for AC- (red solid circles) and ZZ-loaded (blue inverted triangles) graphene sheets at 300 K with increasing defect density distributed (a – c) randomly, and (d – f) uniformly. The dashed lines represent bulk mechanical properties.

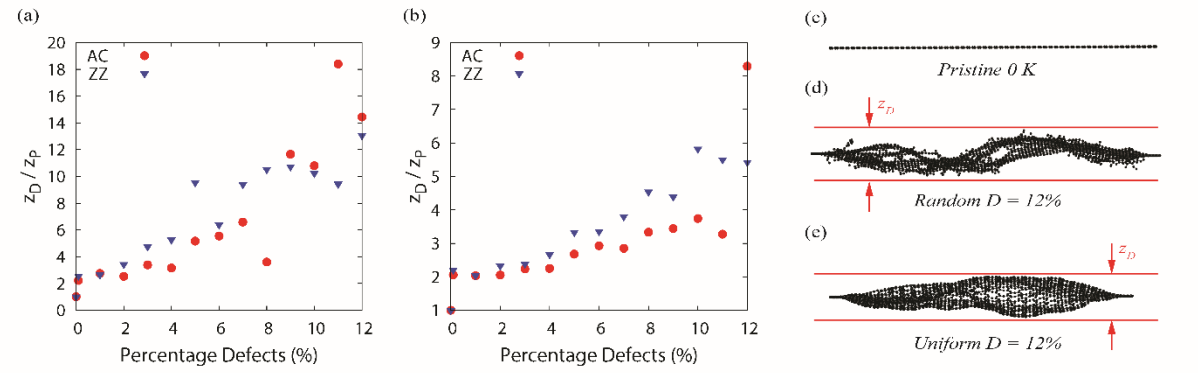

Figure 6.11: The increase in rippling in the z-direction with an increasing (a) random and (b) ordered defect density in AC and ZZ graphene sheets. The effective thickness has been normalized with respect to the original thickness of the pristine graphene sheets at 0 K. (c) A side view of a pristine graphene sheet at 0 K. (d, e) Side views of ZZ graphene sheets with a (d) random and (e) ordered defect density of 12% after 37 ps of relaxation.

Similar to the effect of higher thermal motion on sheet rippling in Section 6.3.2.3, it is also observed in this study that the introduction of defects promotes a similar rippling behaviour, as shown in Figure 6.11 (c – e) for a pristine sheet at 0 K and two sheets with 12% random and uniform defects. Figure 6.11 (a, b) shows the sheet thickness in the z-direction for both random and uniform defect density for a sheet at a temperature of 300 K. Sheets with large defect densities have an effective sheet thickness of up to 18 times larger than the pristine sheet, which is similarly an indication of a decrease in fracture strain.

The fracture processes of nanoporous graphene was also analysed in this work. Figure 6.12 and Figure 6.13 shows the fracture of AC and ZZ graphene sheets, respectively, containing a single vacancy at the sheet's centre. Their fracture behaviour is very similar to that of pristine graphene, with the only difference being that the crack nucleates at the vacancy and propagates in two opposing directions. This is in good agreement with the work in [35, 179, 180]. Figure 6.14 shows the fracture behaviour of a ZZ graphene sheet with 5.5% randomly distributed vacancies, while Figure 6.15 shows the fracture behaviour of a ZZ graphene sheet with 5% uniformly distributed defects. Unlike the equivalent ZZ-loaded pristine graphene simulation, where the crack propagates diagonally through covalent bonds, in this case the travel path is modified by the presence of defects, as such forming an almost perpendicular crack to the loading direction. This behaviour is similar to the fracture behaviour of an AC-loaded pristine sheet. In this work, it is found that this transition from a ZZ- to an AC-type fracture mode in nanoporous ZZ graphene sheets occurs at a defect density of around 4%, which is roughly equal to when the elastic modulus starts to decrease with increasing defect density. For AC graphene

sheets, the crack was observed to propagate perpendicular to the loading direction, similar to what happens in pristine AC sheets, for all the defect densities investigated in this work.

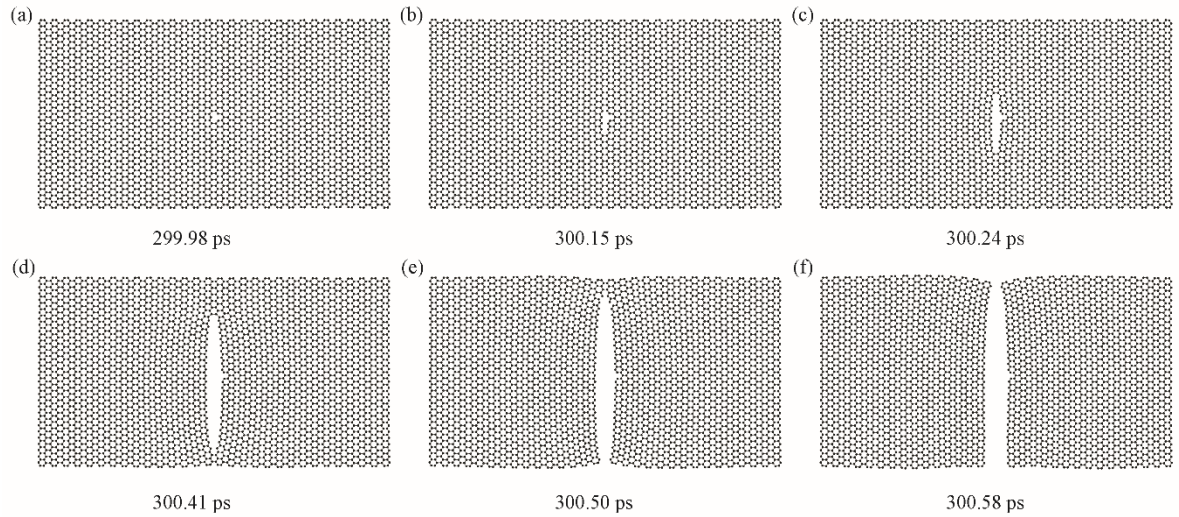

Figure 6.12: Fracture process of an AC graphene sheet with a diagonal length of 14.63 nm at 300 K and with a single vacancy defect at its centre; (a – f) show snapshots of the sheet at the corresponding time in picoseconds (ps) after initiation of loading.

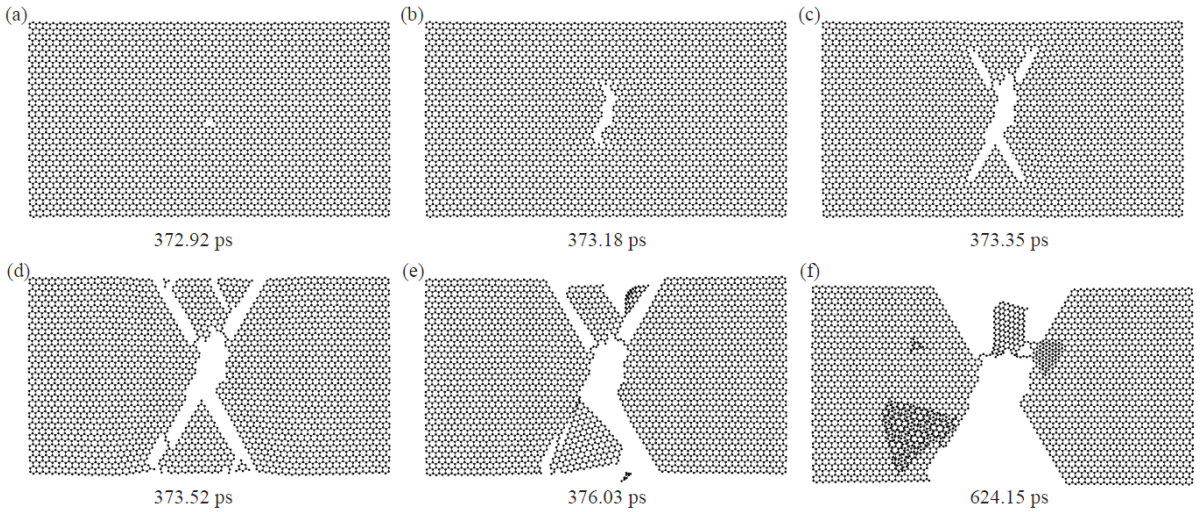

Figure 6.13: Fracture process of a ZZ graphene sheet with a diagonal length of 14.84 nm at 300 K and with a single vacancy defect at its centre; (a – f) show snapshots of the sheet at the corresponding time in picoseconds (ps) after initiation of loading.

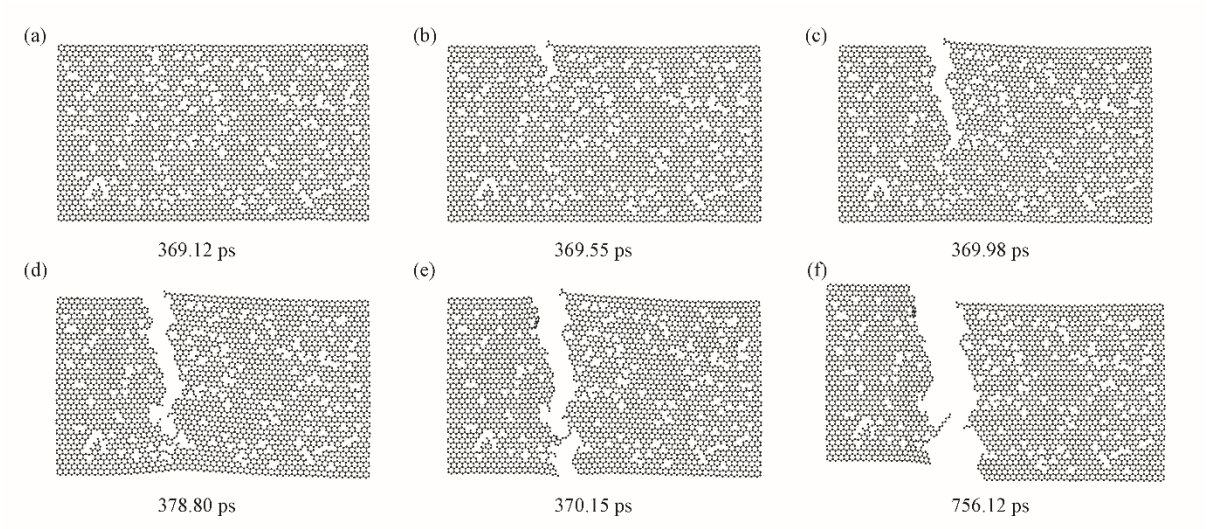

Figure 6.14: Fracture process of a ZZ graphene sheet with a diagonal length of 14.48 nm at 300 K and with 5.5% of the original atoms selected randomly and removed as vacancy defects; (a – f) show snapshots of the sheet at the corresponding time in picoseconds (ps) after initiation of loading.

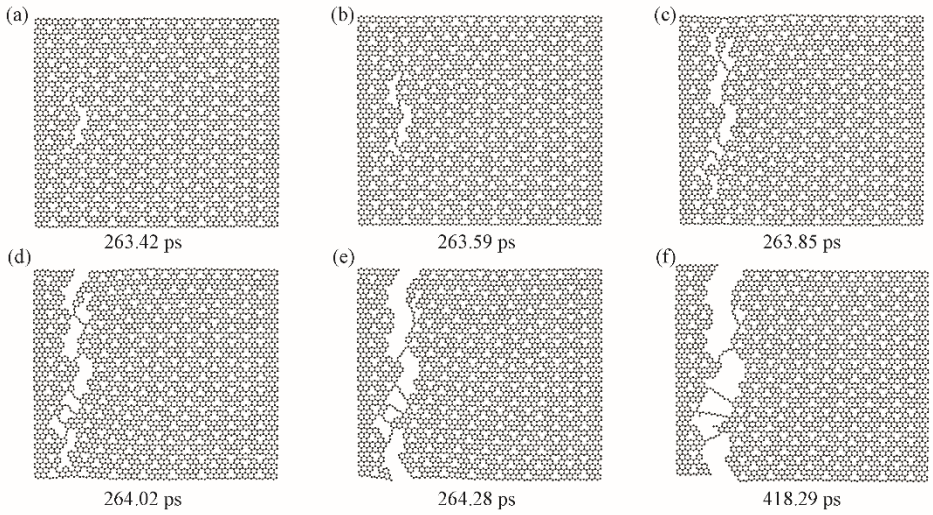

Figure 6.15: Fracture process of a ZZ graphene sheet with a diagonal length of 13.67 nm at 300 K and with 5% of the original atoms being removed as vacancy defects and distributed uniformly; (a – f) show snapshots of the sheet at the corresponding time in picoseconds (ps) after initiation of loading.

6.3.3 CONCLUSION

In this work, molecular dynamics simulations of monolayer graphene under uniaxial tensile loading were performed using the Morse, bending angle, torsion and Lennard-Jones potentials to describe the inter- and intra-molecular carbon interactions. This implementation of the model in OpenFOAM was found to scale with $O(C \times N)$, where N is the number of carbon atoms and $C \approx 1.5$. These simulations enabled the investigation of the elastic modulus, fracture stress and fracture strain of graphene with respect to the orientation, sheet size and sheet temperature.

Graphene exhibits anisotropy, with the ZZ loading direction being able to withstand higher loads and strain than the AC direction, in agreement with the AIREBO force field [24, 174]. Furthermore, size dependency is observed for graphene sheets smaller than 6 nm to 10 nm in diagonal length; the mechanical properties of larger graphene sheets rapidly approach those of bulk graphene above this size. A similar critical length had been reported in [24]. It was also found that higher temperatures tend to significantly decrease the fracture stress and strain almost linearly with temperature, in good agreement with [171]. The elastic modulus is however only affected at system temperatures higher than approximately 900 K. The introduction of randomly and uniformly distributed vacancy defects enabled the simulation of nanoporous graphene sheets, for which it was concluded that the fracture stress decreases substantially with increasing defect density. Nanoporous graphene sheets with uniformly distributed defects are able to withstand higher loads when compared to their counterparts with random defects. Although the model implemented tends to underestimate the quantitative results of the fracture strain and stress, the qualitative fracture behaviour of pristine AC and ZZ graphene sheets was still found to be in good agreement with those obtained by the AIREBO [174, 179, 180, 277] and Tersoff-Brenner [29, 278] potentials. Furthermore, the fracture behaviour of nanoporous graphene sheets exhibited a ZZ- to AC-type fracture transition occurring at roughly 4% defect density. For future work, it can be considered to investigate how this model can be improved to deal with rippling [282] and to investigate nanoporous graphene with larger pore sizes and shapes [222, 280].

6.4 AIREBO VIA LAMMPS

The results obtained from the MD simulations in the previous sections were part of an initial foundation study on graphene which tested a simplified model for graphene. The simplified model produced mechanical properties that matched well with the literature and offered new insights in how the introduction of defects required for membrane filtration applications affect these properties. The code was implemented in-house, and therefore only ran in serial on one processor core. As a result, the simulation size of the graphene sheet that could be modelled, i.e. the number of simulated atoms, was very limited.

LAMMPS [264] (Large-scale Atomic/Molecular Massively Parallel Simulator) is one of the most widely used molecular dynamics code, developed by Sandia National Laboratories in the United States. The LAMMPS code has a big community of users and developers, and is designed to run efficiently on the largest parallel computers in the world. In the rest of this

chapter, the LAMMPS code was used because it enabled the use of state-of-the-art models for graphene and much larger sheets to be modelled. When run in parallel, the computational domain is divided on many processor cores, meaning that the total processing time required to run large graphene sheets can be greatly reduced.

The MD model using the AIREBO potential in LAMMPS, described in Section 6.4.1, was initially validated by simulating a rectangular graphene sheet under uniaxial loading, similar to the simulations performed in Section 6.3, and comparing the results with those obtained from the previous simulations run using the Morse bond potential in OpenFOAM and with literature. The validation study is presented in Section 6.4.2. In Section 6.4.3, the AIREBO MD model was then used to simulate graphene membranes under nanoindentation in order to model and improve understanding of the experimental nanoindentations via AFM carried out in Chapter 4. To arrive towards an accurate simulation system at a reasonable cost, a number of simulations were run to investigate the effect each system parameter has on the final measured elastic modulus.

6.4.1 Potential Functions

In this section, the AIREBO potential [263] within the open-source LAMMPS [264] MD simulation code was used. LAMMPS is available free to download from http://lammps.sandia.gov. The larger simulations were run on the Albert supercomputing cluster at the University of Malta.

In this simulation model, the net force acting on all atoms is determined via the AIREBO potential $\mathcal{V}^{AIREBO}$, which consists of three terms as shown in Equation 6.15 [263]; (i) the REBO potential $\mathcal{V}_{ij}^{REBO}$ [283] which models the covalent bonds in graphene, (ii) the Lennard-Jones potential $\mathcal{V}_{ij}^{LJ}$ to model long-range interactions, similar to that used in Section 6.3 (Equation 6.11), and (iii) a four-body torsion potential $\mathcal{V}_{kijl}^{T}$ describing the torsion angle ϕ_{ijkl}.

$$\mathcal{V}^{AIREBO} = \frac{1}{2}\sum_{i}\sum_{j\neq i}\left[\mathcal{V}_{ij}^{REBO} + \mathcal{V}_{ij}^{LJ} + \sum_{k\neq i,j}\sum_{l\neq i,j,k}\mathcal{V}_{jikl}^{T}\right] \qquad \textit{Equation 6.15}$$

The REBO potential $\mathcal{V}_{ij}^{REBO}$ [283] can be further described by Equation 6.16 whereby $\mathcal{V}_{ij}^{R}$ and $\mathcal{V}_{ij}^{A}$ model repulsive and attractive contributions described by Equation 6.17 and Equation 6.18, respectively. Both the latter equations make use of a bond-weighting factor w_{ij}, which disables the REBO interactions when typical bonding distances are exceeded. The ratio between $\mathcal{V}_{ij}^{R}$

and $\mathcal{V}_{ij}^{A}$ is given by the bonding term b_{ij}, which specifies the "bond order" for the interaction between atoms i and j. The parameters Q_{ij}, A_{ij}, α_{ij}, $B_{ij}^{(n)}$ and $\beta_{ij}^{(n)}$ are given in Table 6.3.

$$\mathcal{V}_{ij}^{REBO} = \mathcal{V}_{ij}^{R} + b_{ij}\mathcal{V}_{ij}^{A} \qquad \textit{Equation 6.16}$$

$$\mathcal{V}_{ij}^{R} = w_{ij}(r_{ij})\left[1 + \frac{Q_{ij}}{r_{ij}}\right]A_{ij}e^{-\alpha_{ij}r_{ij}} \qquad \textit{Equation 6.17}$$

$$\mathcal{V}_{ij}^{A} = -w_{ij}(r_{ij})\sum_{n=1}^{3} B_{ij}^{(n)}e^{-\beta_{ij}^{(n)}r_{ij}} \qquad \textit{Equation 6.18}$$

The torsion potential $\mathcal{V}_{jikl}^{T}$ is described by Equation 6.19, where $\epsilon = 0.00284$ eV [263].

$$\mathcal{V}_{jikl}^{T} = \epsilon\left[\frac{256}{405}\cos^{10}\left(\frac{\phi_{jikl}}{2}\right) - \frac{1}{10}\right] \qquad \textit{Equation 6.19}$$

Table 6.3: Parameter constants for the AIREBO potential functions. [263]

$Q_{ij} = 0.313$ Å	$B_{ij}^{(1)} = 12\,388.792$ eV	$\beta_{ij}^{(1)} = 4.720$ Å^{-1}
$A_{ij} = 10\,953.544$ eV	$B_{ij}^{(2)} = 17.567$ eV	$\beta_{ij}^{(2)} = 1.433$ Å^{-1}
$\alpha_{ij} = 4.747$ Å^{-1}	$B_{ij}^{(3)} = 30.715$ eV	$\beta_{ij}^{(3)} = 1.383$ Å^{-1}

6.4.2 VALIDATION STUDY

6.4.2.1 Methodology

To validate the AIREBO MD model with previous work and literature, the first set of simulations involved a pristine graphene sheet modelled for uniaxial tensile loading similar to the simulations presented in Section 6.3.

To simulate uniaxial loading and hence calculate the mechanical properties of graphene, a pristine rectangular ZZ graphene sheet with a diagonal length, L_D, of around 16.4 nm (4780 carbon atoms) and an aspect ratio of approximately 1:1.3 was created. Note that such graphene sheet geometry corresponds to the largest ZZ sheet modelled in Section 6.3.2.1, hence it is presumed that this size of graphene sheet does not affect the measured mechanical properties.

The C-C bonding within the graphene sheet was modelled using the AIREBO potential with a cut-off distance of 2.0 Å. The simulations were run using an NVT ensemble with a time-step of 0.5 fs. A Berendsen thermostat [284] was used on the graphene sheet to maintain a

temperature of 300 K. The C atoms in the graphene sheet were initially given a velocity sampled randomly from a Maxwell Boltzmann distribution with mean speed of zero and a temperature of 300 K. The net linear momentum of the graphene sheet was set to zero throughout the simulation to prevent the graphene sheet from drifting through the simulation space.

For the uniaxial loading simulations, the simulations were initially run for 2000 time-steps (1 ps) to allow for the graphene sheet to reach an initial equilibrium state. To be able to apply a tensile load, the first couple of rows of carbon atoms at the sheet's edges were constrained as shown in Figure 6.16.

The constrained C atoms at both edges of the rectangular graphene sheet were first fixed in all three dimensions and the simulation was run for another 30 000 time-steps (15 ps) to ensure equilibration. The constrained atoms were then forced to move at a pre-defined velocity v of 0.015 Å/ps (1.5 m/s) in opposite directions to simulate a quasistatic strain rate of around 2.56×10^{8} s^{-1}, once again comparable to the strain rate used in Section 6.3. Loading was sustained until failure. A higher velocity of 0.5 Å/ps (50 m/s) to simulate dynamic loading with an effective strain rate of 8.55×10^{9} s^{-1}, and a low temperature of 1 K were also considered. Each loading condition was repeated three times for repeatability of the results.

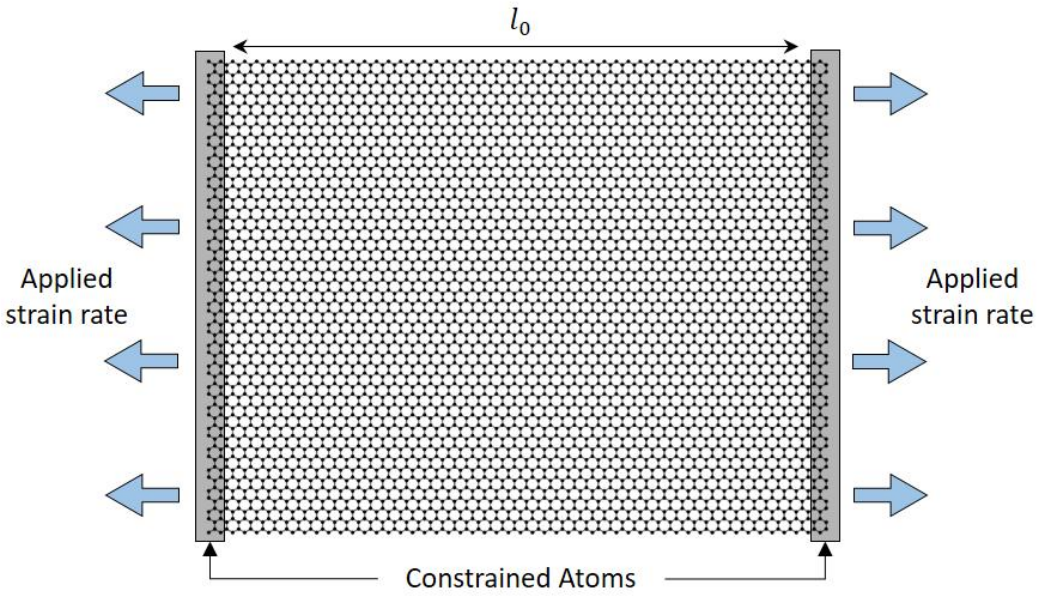

Figure 6.16: A schematic illustration of a graphene sheet showing the edge atoms constrained (shaded in grey) for the application of the pre-defined strain-rate.

The failure stress σ_f and the elastic modulus E were computed using a similar method to that explained in Section 6.3.1.4. Therefore, the strain energy U was computed by subtracting the total potential energy of the graphene sheet before loading from that at time t. The strain ε was derived from the original length of the graphene sheet just before loading l_0 and the imposed velocity v via Equation 6.20.

$$\varepsilon = \frac{t \times 2v}{l_0} \qquad \textit{Equation 6.20}$$

The curve of U against ε was then fitted to a cubic function while restricting the curve to pass through the origin $(0, 0)$. Straightforward differentiation was applied once to obtain the stress $\sigma(\varepsilon)$, and the second time to obtain the elastic modulus $E(\varepsilon)$ as a function of strain, according to Equation 6.21 and Equation 6.22.

$$\sigma(\varepsilon) = \frac{1}{V_0}\frac{\partial U(\varepsilon)}{\partial \varepsilon} \qquad \textit{Equation 6.21}$$

$$E(\varepsilon) = \frac{1}{V_0}\frac{\partial^2 U(\varepsilon)}{\partial \varepsilon^2} \qquad \textit{Equation 6.22}$$

V_0 is the original volume of the sheet assuming a thickness of 0.335 nm [13]. The values of the failure stress at the maximum strain ($\sigma_f = \sigma(\varepsilon_f)$) and elastic modulus at zero strain ($E = E(0)$) are reported in the results.

6.4.2.2 Results

Figure 6.17 shows representative strain energy U against strain ε curves of the ZZ graphene sheets, with diagonal length L_D of 16.4 nm, uniaxially loaded at strain rates of 2.56×10^8 s^{-1} (solid lines) and 8.55×10^9 s^{-1} (dashed lines), at temperatures of 1 K (black lines) and 300 K (red lines).

Simulations with each of the four loading conditions presented in Figure 6.17 were performed three times each to obtain the required repeated readings. As explained in Section 6.4.2.1, the strain energy against strain curves obtained were fitted to a cubic function to find the elastic modulus and failure stress at each loading condition. Examples of the fitting results for the sheets loaded at a strain rate of 2.56×10^8 s^{-1} at 1 K and 300 K are shown in Figure 6.18 (a) and (b), respectively. Figure 6.17 shows that the curves at both temperatures follow a very similar profile up until a strain of around 0.3. Beyond this strain, while the sheet at 300 K fails soon after, the curve obtained from the sheet at 1 K changes its trajectory. In fact, the 300 K curve closely follows a cubic function throughout as shown in Figure 6.18 (b) in red. However, fitting

a similar function to the entire 1 K curve results in a poor fit, as shown in Figure 6.18 (a) in blue. Therefore, to ensure accurate results for sheets loaded at 1 K, the cubic function was only fitted to the data up to a strain of 0.2 as shown in Figure 6.18 (a) in red. Note that since the elastic modulus at zero strain ($E = E(0)$) is reported, an accurate fit is mostly required at the start of the curve.

Table 6.4 lists the elastic modulus, failure stress and failure strain obtained from the simulations run to validate the AIREBO model by applying a uniaxial tensile load. The same results are presented in a bar chart in Figure 6.19.

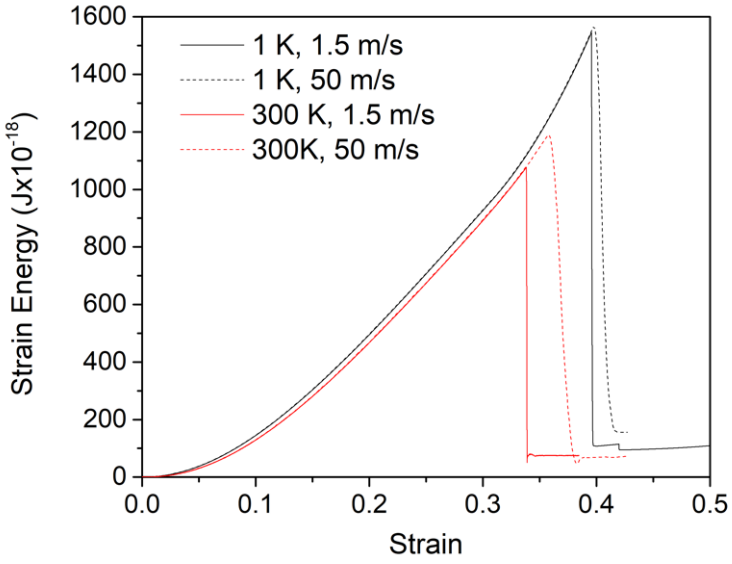

Figure 6.17: Representative strain energy against strain curves of the uniaxially loaded ZZ graphene sheets at 1 K (black) and 300 K (red), and strain rate of 2.56×10^{8} s^{-1} (solid lines) and 8.55×10^{9} s^{-1} (dashed lines).

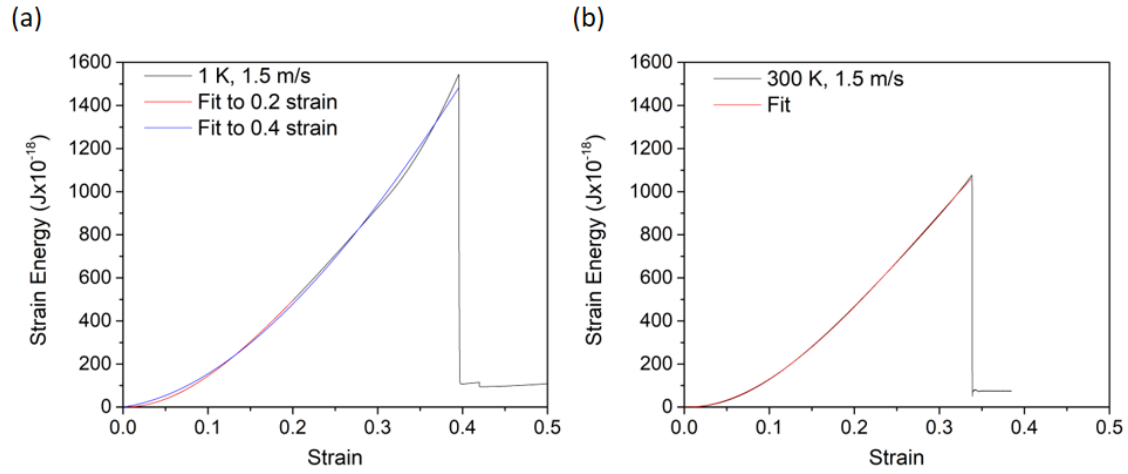

Figure 6.18: Strain energy against strain of the uniaxially loaded ZZ graphene sheet, together with the corresponding cubic fits.

Table 6.4: Simulation parameters and results obtained by uniaxial loading a ZZ graphene sheet with $L_D =$ 16.4 *nm. The errors represent the standard deviation across three repeated readings.*

Velocity (m/s)	Strain rate (s^{-1})	Temperature (K)	Elastic Modulus (TPa)	Failure Stress (GPa)	Failure Strain
1.5	2.56×10^{8}	1*	0.95 ± 0.004	63.265 ± 8.48	0.399 ± 0.007
1.5	2.56×10^{8}	300	0.82 ± 0.049	119.598 ± 5.525	0.343 ± 0.016
50	8.55×10^{9}	1*	0.95 ± 0.000	66.376 ± 0.946	0.397 ± 0.001
50	8.55×10^{9}	300	0.77 ± 0.025	125.61 ± 3.525	0.363 ± 0.005

* Cubic fit was restricted to strain of 0.02

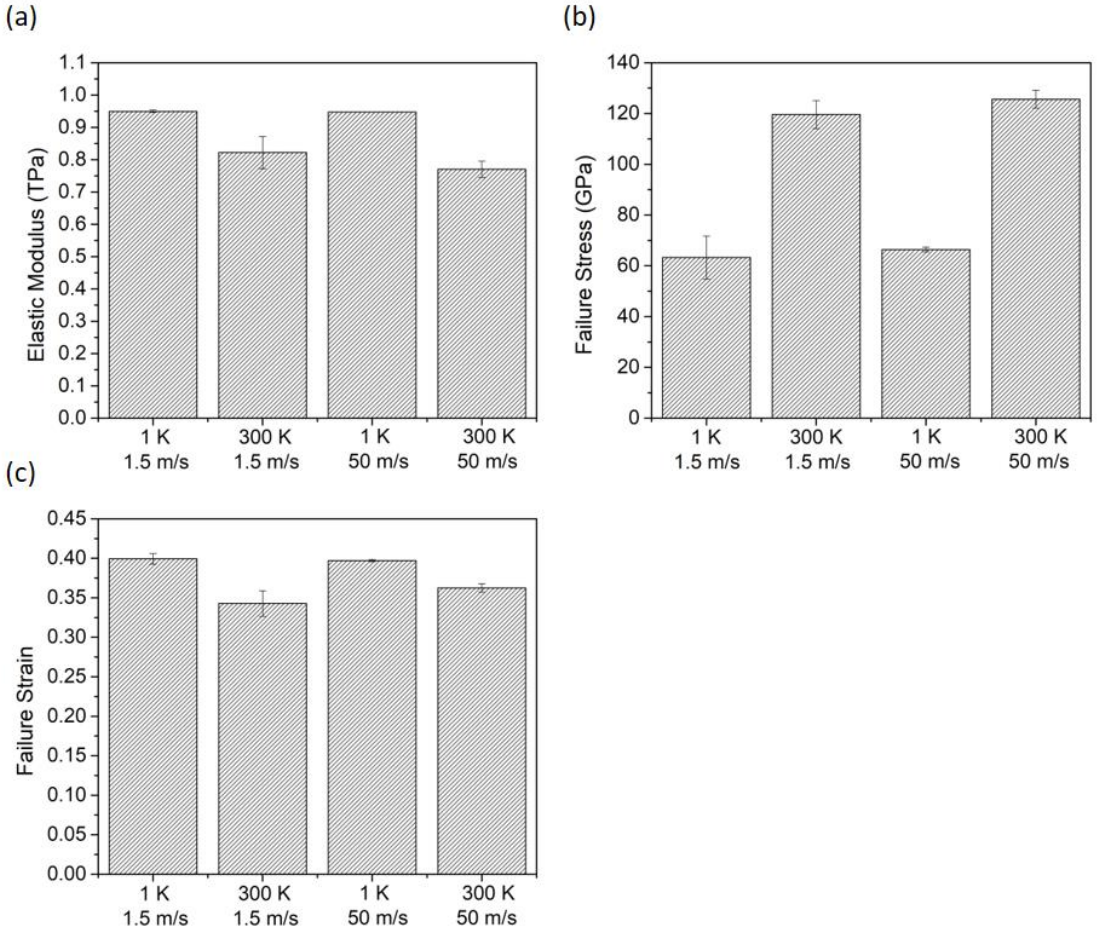

Figure 6.19: The average (a) elastic modulus, (b) failure stress, and (c) failure strain obtained from uniaxial loading at the four loading conditions. The error bars represent the standard deviation across three repeated readings.

At first glance, it is clear that the elastic modulus obtained, which varied from 0.77 ± 0.025 TPa using a strain rate of 8.55×10^{9} s^{-1} at 300 K up to 0.95 TPa using a strain rate of 2.56×10^{8} s^{-1} at 1 K, is in very good agreement with literature and slightly lower than the elastic modulus of around 1.08 TPa obtained in Section 6.3 using the Morse potential. The failure strains obtained

vary from 0.34 to 0.40, significantly larger than the ~0.15 failure strain obtained using the Morse potential. Furthermore, the failure stress varies significantly from 63.3 GPa using a strain rate of 2.56×10^{8} s^{-1} at 1 K up to 125.6 GPa using a strain rate of 8.55×10^{9} s^{-1} at 300 K. These values can be compared to those obtained using the Morse potential – 103.2 GPa at 0K and 94.2 GPa at 300 K.

The following subsections further discuss the presented results with respect to the effect of temperature and strain rate, compared to the results obtained using the Morse potential.

6.4.2.2.1 Effect of Temperature

The same ZZ graphene sheet was loaded at temperatures of 1 K and 300 K to study any effect of the temperature on the measured mechanical properties. As evident in Figure 6.17, the graphene sheets loaded at 1 K sustained higher strains and thus higher strain energies until failure when compared to the graphene sheets loaded at 300 K. Thus, irrespective of the strain rate, while the failure strain was found to be just under 0.40 at a temperature of 1 K, the failure strain decreased to around 0.35 at 300 K.

As already discussed, the strain energy against strain curves followed slightly different profiles especially at strains larger than 0.3 for 1 K. This necessitated the cubic function to be fitted to the first part of the curve only up to a strain of 0.2 for meaningful results. Considering the entire 1 K curve in the fitting procedure leads to an underestimated elastic modulus of around 0.44 TPa and consequential overestimation of the failure stress of 185.86 GPa.

Upon fitting the curves to the cubic functions and extracting the elastic modulus and failure stress, it resulted that under quasi-static loading conditions, the elastic modulus at 300 K is around 13.7 % lower than that measured at 1 K. On the other hand, the failure stress was measured at 119.6 GPa, 89 % higher than that measured at 1 K. A similar trend is observed for higher strain rates.

As expected, the variation in the results obtained from the simulations performed at 300 K is significantly larger than that at lower temperatures, as evidenced by the larger error bars in the 300 K cases. This is attributed to two main factors. Firstly, at higher temperatures, the individual atoms within the graphene sheet have higher kinetic energies. Therefore, the differences in the atoms' individual trajectories initialized at the beginning of the simulations are more pronounced and lead to a larger variance at higher temperatures. This can be visualised by the more prominent fluctuations of the graphene sheet at 300 K when compared to 1 K, as also described in Section 6.3. The second factor is related. The edge atoms are only

constrained and fixed in all 3 dimensions after the initial equilibration stage. This means that the thermal fluctuations would have been already manifested in the sheet, causing the to-be clamped regions to be not perfectly aligned with the loading axis. To minimize this effect, the first equilibration stage before constraining the atoms was limited to just 1 ps such that the sheet edges would not have moved as much. Naturally, at higher temperatures, the constrained atoms will be less aligned to the loading axis causing extra stresses to be introduced, thereby increasing the variance between one simulation and another and affecting the measurement of the mechanical properties.

6.4.2.2.2 Effect of Strain Rate

To validate the AIREBO MD model, uniaxial loading was initially carried out at a quasi-static strain rate of 2.56×10^{8} s^{-1}, similar to that used in Section 6.3. However, a larger strain rate to simulate 'dynamic' loading was also considered, primarily to understand its effect on the measured mechanical properties, recognizing its benefits of substantially decreasing the computational costs of the ensuing simulations. Thus, the same uniaxial loading simulations were also performed at a strain rate of 8.55×10^{9} s^{-1}.

At a temperature of 1 K, the increased strain rate did not markedly affect the elastic modulus or the failure strain. The average failure stress marginally increased from 63.265 ± 8.48 GPa to 66.376 ± 0.946 GPa.

A more pronounced effect was observed at 300 K. The average elastic modulus decreased from 0.82 ± 0.049 TPa to 0.77 ± 0.025 TPa. Similar to the 1 K case, the failure stress once again increased from 119.598 ± 5.525 GPa to 125.61 ± 3.525 GPa. The failure strain also increased markedly from 0.343 ± 0.016 to 0.363 ± 0.005.

The variance, or error bars, in the dynamic loading cases were slightly lower than those under quasi-static loading.

These results show that while the strain rate may affect the mechanical properties especially at 300 K, the difference is not so pronounced, meaning that ensuing simulations may be performed at slightly larger strain rates to decrease computational costs.

6.4.3 NANOINDENTATION

6.4.3.1 Methodology

Following validation of the model, the mechanical properties of graphene were studied by simulating nanoindentation similar to that performed experimentally via AFM. To model a simplified scenario using MD, unless otherwise stated, the atom configuration of the simulation system illustrated in Figure 6.20 was used.

As observed in Chapter 3 and mentioned in Chapter 4, even though grain boundaries and other defects are indeed present in the CVD-grown graphene used experimentally, membranes with visible grain boundaries were not indented. Furthermore, given the relatively small size of the graphene membranes indented experimentally ($a = 225$ nm) compared to the grain size of the CVD-graphene (~20 μm [99]), it was presumed that the probability of indenting grain-boundary-free graphene was significantly higher. Therefore, a pristine graphene lattice was considered to simplify and validate the simulation model. As such, a rectangular graphene sheet with dimensions $L \times b$ was initially created, where $L \approx b$.

In order to faithfully simulate the experimental indentations, the indenter tip would need to be modelled as (i) a hemispherical diamond tip with radius of around 100 to 200 nm with surface roughness of 10 nm to simulate the DTNCLR AFM probes, (ii) a hemispherical diamond-like carbon (DLC) tip with radius 15 nm to simulate the Tap190DLC AFM probes, or (iii) a hemispherical silicon tip with radius 10 nm to simulate the FM50 AFM probes. However, to simplify the MD model and reduce the computational cost, the size of the tips where made smaller than the experiments as these would be too prohibitive for even supercomputers. The atoms in the indenter are also modelled as rigid, that is, there are no intramolecular forces being computed between atoms on the indenter, but they retain the long-range van der Waals forces between the graphene atoms and individual atoms of the indenter that prescribes the indenting force. Furthermore, while the atomic crystal lattice is known for the diamond and the silicon tips, some assumptions need to be taken to model the diamond-like-carbon in the Tap190DLC tip. DLC is a synthetic diamond material whereby the carbon precursor is rapidly cooled and as such, the arrangement of the C atoms in DLC can be either amorphous or a mix of cubic and hexagonal lattices. Nevertheless, if the tip is modelled as a rigid body whereby the atoms within do not move relative to each other, it was expected that the atomic arrangement does not affect the nanoindentation response. As such, the indenter was modelled as a hemisphere consisting of carbon atoms in a diamond cubic crystal lattice (i.e. two interpenetrating FCC lattices) with

radius r, to simulate the diamond-coated AFM tips. The indenter was initially placed a distance $h^{DG} \sim 2$ nm above the graphene sheet (as shown in Figure 6.20), which is higher than the cut-off radius of the attractive long-range intermolecular forces, $r_{cut} = 1.4$ nm.

Following a similar logic to that presented for the indenter, the substrate was modelled as a rigid body consisting of atoms arranged in diamond cubic crystal lattice with a cube side of 5.431 Å, analogous to the crystal lattice of silicon. The substrate with dimensions $l \times b \times h^S$, having a pore of radius, a, was placed just below the graphene sheet, with h^S being the thickness of the substrate. The distance between the graphene sheet and the top atoms of the substrate was initially set to h^{SG} ~0.5 nm, slightly larger than the equilibrium height between the two bodies, yet close enough such that the long-range attractive Lennard-Jones potential attracts the graphene sheet to the rigid substrate to the equilibrium position.

While both the substrate and indenter were modelled as rigid bodies, the substrate-graphene (SG) and indenter-graphene (DG) interactions were modelled using the Lennard-Jones

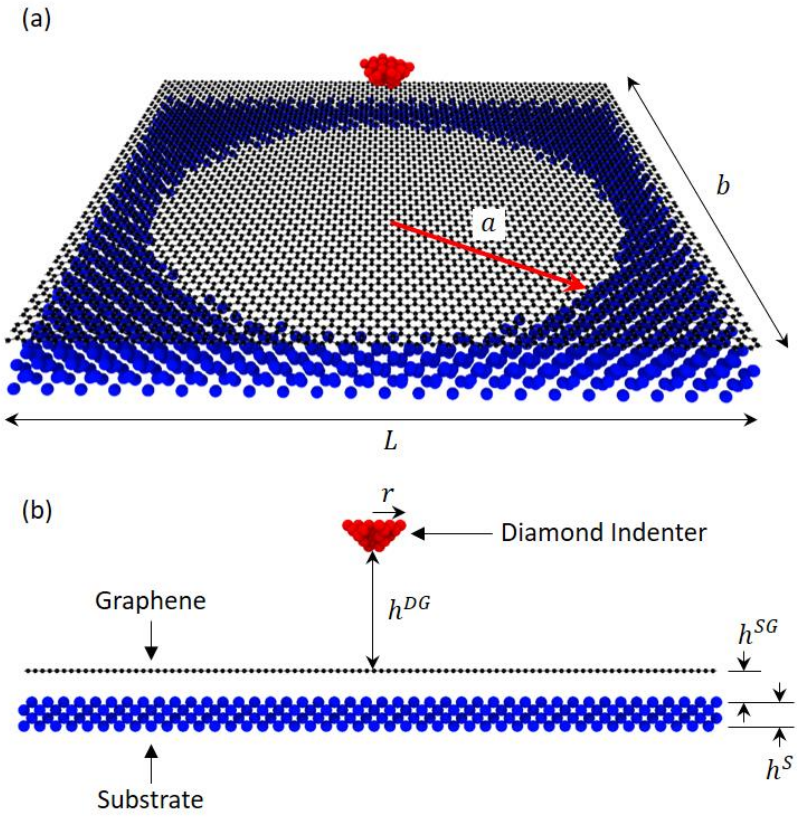

Figure 6.20: (a) Perspective and (b) side views of the system geometry of the nanoindentation simulations showing the hemispherical diamond indenter (red), graphene membrane (black), and the porous substrate (blue).

potential with the following parameters: ϵ_{SG} = 0.0089 eV, σ_{SG} = 3.629 Å, ϵ_{DG} = 0.00455 eV, σ_{DG} = 3.431 Å [285].

Unless otherwise stated, periodic boundaries [8] were applied to the graphene sheet. All simulations were run for at least 30 000 time-steps (15 ps) to allow for the system to reach equilibrium. After the equilibration time, the indenter was forced to move towards the graphene membrane at a pre-defined velocity v, until failure.

For the final set of simulations presented in Section 6.4.3.2.7, no periodic boundaries were applied to the graphene sheet and the sheet was allowed to move freely for the initial 180 000 time-steps. During indentation, the graphene edges were then held rigid and the indenter was moved 0.2 Å every ~900 timesteps to allow for the graphene sheet to reach a new equilibrium after each step-wise indentation.

To obtain the force-distance curve, the total force acting on all atoms of the indenter in the z-direction was considered, together with the position of the bottom-most atom of the indenter in the z-direction. Similar to the experimental methodology in Chapter 4, Equation 6.23 was then used to extract the pre-tension and elastic modulus of the simulated graphene sheet.

$$F = \sigma_0^{2D}(\pi a)\left(\frac{\delta}{a}\right) + E^{2D}(q^3 a)\left(\frac{\delta}{a}\right)^3 \qquad \textit{Equation 6.23}$$

Since in the simulations run, both the graphene membrane radius a and the indenter radius r were significantly scaled down yet with different scaling factors, the ratio between the two radii $\frac{r}{a}$ was sometimes used to apply a correction factor of $\left(\frac{r}{a}\right)^{\frac{1}{4}}$ on the calculated elastic modulus.

Since, unlike in the experimental indentations, the simulated graphene membranes were indented up to failure, the maximum stress, σ_m^{2D}, sustained just before fracture was also calculated using Equation 6.24.

$$\sigma_m^{2D} = \left(\frac{FE^{2D}}{4\pi R}\right)^{\frac{1}{2}} \qquad \textit{Equation 6.24}$$

[8] By using periodic boundaries, the atomic geometry described in Figure 6.20 is considered as a unit cell and is virtually repeated in the length, L, and breadth, b, directions. That is, the C atoms within the graphene sheet can interact across the boundary, whereby they can exit one end of the simulation space and re-enter the other end. This allows for the graphene sheet to be modelled as infinitely large.

6.4.3.2 Results and Discussion

6.4.3.2.1 Nanoindentation Simulation 1

The first nanoindentation simulation run consisted of a small graphene sheet with dimensions 12 × 12 nm ($L \times b$), having a total of 5800 carbon atoms. Note that such sheet size is already larger than the largest sheet considered in Section 6.3 with the Morse bond potential. The graphene sheet was placed on top of an FCC lattice with dimensions 12 × 12 × 0.5 nm having a pore radius a, of 5 nm (total of 1048 atoms). A hemispherical diamond indenter with radius r of 0.5 nm (68 atoms) was initially placed 1.5 nm above the graphene sheet. After equilibration, the indenter was forced to move towards the graphene at a velocity of 1 Å/ps (100 m/s) until failure. The simulation was run at 300 K.

Table 6.5 compares the dimensional parameters simulated in Simulation 1 to those used in the AFM experimental set-up. It is evident that the entire system was scaled down to limit the computational time penalty that is incurred with an increase in the number of simulated atoms. The indenter velocity was also considerably increased to reduce the total time-steps required and hence computational time.

Figure 6.21 shows the force-distance curve obtained together with the fit using Equation 6.23. The measured E^{2D} is 169.64 N/m, which translates to an elastic modulus E of 0.50 TPa assuming the thickness of graphene of 0.34 nm. However, it was noted that fitting the cubic curve to a smaller indentation depth, for example 1.5 nm, leads to a higher elastic modulus of 0.61 TPa. A maximum stress of 64.29 N/m was found, equal to a breaking strength of 189 GPa.

Table 6.5: Simulation dimensional parameters compared to the AFM experimental set-up.

	Simulation	**Experimental nanoindentation**	**Scaling factor**
Graphene	Pristine SLG	CVD-grown SLG	-
Tip Material	Diamond (Rigid Body)	Silicon, Diamond coated or DLC coated	-
Graphene Membrane Radius, a	5 nm	225 nm	0.022
Tip Radius, r	0.5 nm	10 – 100 nm	0.05 – 0.005
$\frac{r}{a}$	0.1	0.04 – 0.44	2.5 – 0.227
Indenter Velocity	100 m/s	23×10^{-9} m/s	4.35×10^{9}

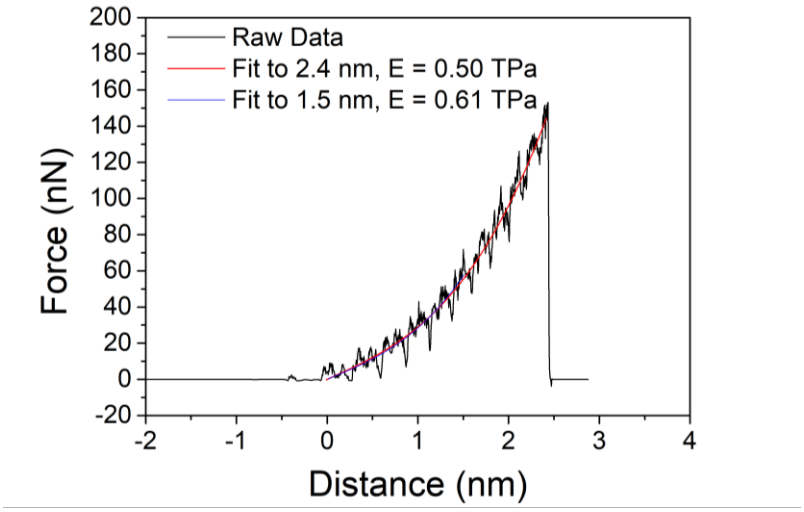

Figure 6.21: Force-distance curve for the benchmark case.

These results point to three observations. First, the measured elastic modulus is 50% lower than the theoretical value of 1 TPa for pristine single-layer graphene, and 35% lower than the E calculated in the validation model under dynamic loading at 300 K in Section 6.4.2. This decrease in the measured elastic modulus, especially when considering that the use of the same AIREBO potential in the validation studies gave much more accurate results, can be credited to a number of factors. Just as the high strain rate of 8.55×10^{9} s^{-1} (effective loading velocity of 100 m/s) in the uniaxial tensile loading simulation resulted in a slight decrease in the measured elastic modulus, the same unrealistic indentation velocity of 100 m/s could be influencing the dynamics of the graphene membrane in a similar manner and thus resulting in a low elastic modulus. The effect of the indentation velocity on the results is studied in Section 6.4.3.2.2. Moreover, although from the uniaxial tension tests in Section 6.3.2.1, the results indicate that the graphene sheet size does not significantly affect the measured elastic modulus, it is still possible the loading geometry used in this simulation – indentation of a circular membrane – introduces size-dependency. As such, to investigate this, a study on the effect of the membrane radius on the measured elastic modulus from indentation simulations is presented in Section 6.4.3.2.3. Finally, the decrease in the measured elastic modulus observed here can be directly related to the change in the loading method and more specifically the mathematical model used to extract the elastic modulus from the force-distance curve obtained.

The second observation that can be made from the force curve presented in Figure 6.21 is that several fluctuations can be seen in the force-distance curve. These are found to be surface waves induced in the graphene sheet due to the very high indentation velocities. Here, the high indentation velocity of 100 m/s invokes the ballistic properties of the graphene membrane that

cause ripples or waves to form within the membrane. Upon contact of the high-speed indenter with the graphene, a wave initiates from the centre of the membrane and travels radially outwards. Once this meets the membrane boundary, that is, the point where the graphene is attached to the substrate, the wave is reflected inwards. This is repeated periodically throughout the indentation. Whenever the crest of the wave reaches the centre of the membrane, where the indenter is in contact with the sheet, the raised graphene atoms apply an extra upward force on the indenter, forming the fluctuations in the force-distance curve in Figure 6.21. This effect introduces uncertainties upon fitting Equation 6.23 to the data and hence, errors in the measured elastic modulus. Therefore, the relatively low elastic modulus measured in this simulation is also being partly attributed to the high indentation velocity which is causing such fluctuations and hence errors in the fitting. It is also being presumed that the mechanical response of the material changes under dynamic loading conditions i.e. under high indentation velocities, as opposed to that displayed under quasi-static loading conditions. Similar surface waves were also observed by Fang et al. [187] upon modelling indentation.

To prevent such unrealistic surface waves, other research groups [165, 167] use a gradual or stepwise loading method whereby the indenter is moved for a number of time-steps, and kept fixed for the next few time-steps to allow for the graphene membrane to reach a new equilibrium state, thereby simulating quasi-static loading conditions. The force acting on the indenter is then recorded after the new equilibrium is reached. This methodology was adopted in the simulations presented in Section 6.4.3.2.7.

The third observation is that the measured breaking strength of 189 GPa is actually significantly higher than that reported in literature via other simulation work [24, 30, 34, 158, 167], experimental work [13] and 50 % higher than the failure stress measured in the validation studies. Once again, this discrepancy can be attributed to the dynamic loading conditions similar to the overestimation of the breaking stress measured in the validation studies where a breaking strength of 125.6 GPa was measured. Initial experimental studies have already been carried out indicating the promising use of graphene against supersonic projectiles [45].

6.4.3.2.2 Indenter Velocity

Since the very high indentation velocity used in the first simulation induced undesirable perturbations in the force-distance curve, the effects of such indentation velocity were investigated. As such, two similar cases were run with an indentation velocity of 10 m/s and 3 m/s.

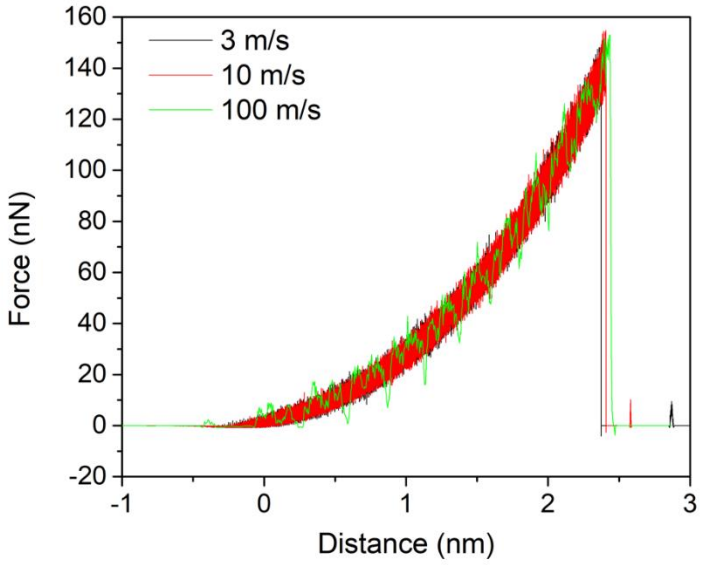

Figure 6.22: Force-distance curves for indentation velocities of 3 m/s, 10 m/s and 100 m/s.

Figure 6.22 shows the resulting force-distance curves upon indenting the graphene sheet at a velocity of 3 m/s and 10 m/s, compared to the one obtained at an indenter velocity of 100 m/s. The measured E^{2D} is 172.64 N/m (E = 0.51 TPa) at 10 m/s and 173.29 N/m (E = 0.51 TPa) at 3 m/s, while the maximum stress sustained was 62.65 N/m, equal to a breaking strength of 184.26 GPa at 10 m/s and 62.47 N/m, equal to a breaking strength of 183.74 GPa at 3 m/s. While the measured mechanical properties are almost equal to those measured using an indentation velocity of 100 m/s in Section 6.4.3.2.1, it can be noted that the fluctuations observed in the force-distance curves have higher frequency and lower magnitude. This indicates that the fluctuations are indeed being induced due to a sudden increase in energy in the graphene sheet due to the indenter. In fact, Fang et al. [187] note that when using high indentation velocities, the graphene does not have enough time to respond to the forces induced by the indenter, leading to higher breaking loads, elastic energy and plastic energy. As such, the lower indentation velocities allow for the generated energy to be dissipated more efficiently and effectively throughout the sheet without the formation of the radial surface waves.

As mentioned previously, simulating indentation at a lower indentation velocity increases the computational cost since more time-steps are required for the indenter to indent the same graphene membrane size up to fracture. Therefore, while indenting a 5 nm membrane at 100 m/s requires around 50 minutes of computer processing using an Intel® Core™ i7-3537U CPU @ 2.00 GHz ×4 processor, decreasing the indentation velocity by a factor of 10 to 10 m/s, increases the computational time by a similar factor of 10, i.e. to around 8 hours 25 minutes. Further reducing the indentation velocity to 0.1 m/s, which is still several orders of magnitude

larger than the experimental indentation speed of 23 nm/s, will require around 35 days of computational power. A more powerful processor utilising more cores in parallel further reduces the computational time required, and hence may make simulations at low indentation speeds more feasible.

6.4.3.2.3 Membrane Size

As noted in Table 6.5, the size of the graphene membrane simulated in the previous cases ($a = 5$ nm) is much smaller than that used in the experimental set-up ($a = 225$ nm). In order to investigate whether such difference in scale of the graphene membrane diameter influences the indentation simulation and hence the measured elastic modulus, a number of simulations with different membrane sizes were run. These simulations also allow some information to be obtained regarding the computational cost incurred with an increase in simulated atoms.

With similar geometry and simulation parameters to those used in Section 6.4.3.2.1, a total of seven simulations were run with the membrane radius a increased from 5 nm up to 50 nm, as listed in Table 6.6. Note that the membrane radius a and the substrate dimensions L and b were always scaled up with approximately the same factor such that the ratio $a: L$ was kept at around 0.44, with the exception of the membrane with radius 22.5 nm having the ratio $a: L$ set at 0.75.

The simulation temperature was once again fixed at 300 K via a Berendsen thermostat and the same indenter of radius 0.5 nm (39 atoms) was used for all simulations. For the majority of the simulations, an indenter velocity of 100 m/s was used, with the exception of one simulation with $a = 22.5$ nm run at 10 m/s. For the simulations having a membrane radius larger than 15 nm, a total of 50 000 time-steps (50 ps) were allowed for equilibration, instead of 30 000 time-steps.

Table 6.6 lists the simulations run with the relevant dimensional parameters together with the number of simulated atoms and total computational time required for every simulation using the same 4-core computer processor mentioned above. As clearly shown in Table 6.6, an increase in the membrane radius results in an increase in computational time. This increase in computational time is credited to two factors. First, a larger membrane radius leads to a greater number of simulated atoms, both belonging to the larger graphene sheet, as well as to the larger supporting substrate. Thus, more calculations need to be carried out during a single time-step, leading to a decrease in the number of time-steps computed per second. Secondly, a wider membrane sustains larger indentation depths until failure, and so, the simulated time also increases proportionally. In fact, using the same 4-core CPU mentioned in Section 6.4.3.2.2,

while the simulation with membrane radius of 5 nm ($5376 \approx 5 \times 10^3$ C atoms) took a total of 66 minutes to compute, the simulation with membrane radius of 50 nm ($411872 \approx 4 \times 10^5$ C atoms) took a total of 7 days and 5 hours to compute. Furthermore, the 4-core CPU was not capable of running a simulation with a membrane radius of 100 nm ($1617084 \approx 1 \times 10^6$ C atoms).

Figure 6.23 presents the relationship between the time-steps computed per second and the total computational time required for an increase in the total number of atoms.

Table 6.6: Simulation dimensional parameters to investigate the size-effect. All simulations were performed using the 4-core CPU using a 100 m/s indentation velocity, unless otherwise noted.

a (nm)	$L \times b$ (nm × nm)	Carbon atoms	Substrate atoms	Total atoms (including 39 indenter atoms)	Total computational time (hours)	Time-steps per second during indentation
5	12 × 12	5 376	1 743	7 158	1.10	33.052
5	406 × 406	6 289 800	4 461 943	10 751 782	**	**
6.5	15 × 15	8 400	2 239	10 678	1.62	22.963
8	18 × 18	12 264	3 263	15 566	4.04	15.835
9.5	21 × 21	16 660	3 567	20 266	3.24	12.227
15	34 × 34	43 608	11 563	55 210	18.96	4.382
22.5*	50 × 50	95 004	24 563	119 606	**	**
50	104 × 104	411 872	78 807	490 718	172.59	0.479

* 10 m/s

** Performed on a supercomputer

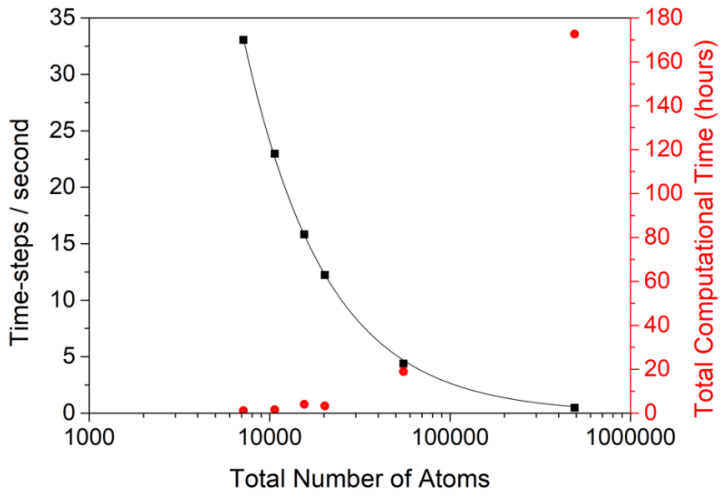

Figure 6.23: The dependency of the time-steps computed per second, and the total computational time with an increase in the total number of simulated atoms.

Figure 6.24 (a) shows all the force-distance curves of the simulated membranes with different radii that were indented at a velocity of 100 m/s. Similarly, Figure 6.25 (a) shows the force-distance curve of the 22.5 nm membrane indented at a velocity of 10 m/s as compared to Simulation 1 having a membrane radius of 5 nm indented at a velocity of 100 m/s. Since Equation 6.23 is a function of the membrane radius, a, the ratio of the force to membrane radius, F/a, was plotted against the ratio of the indentation distance to membrane radius, δ/a, as shown in Figure 6.24 (b) and Figure 6.25 (b). Table 6.7 presents the numerical results obtained.

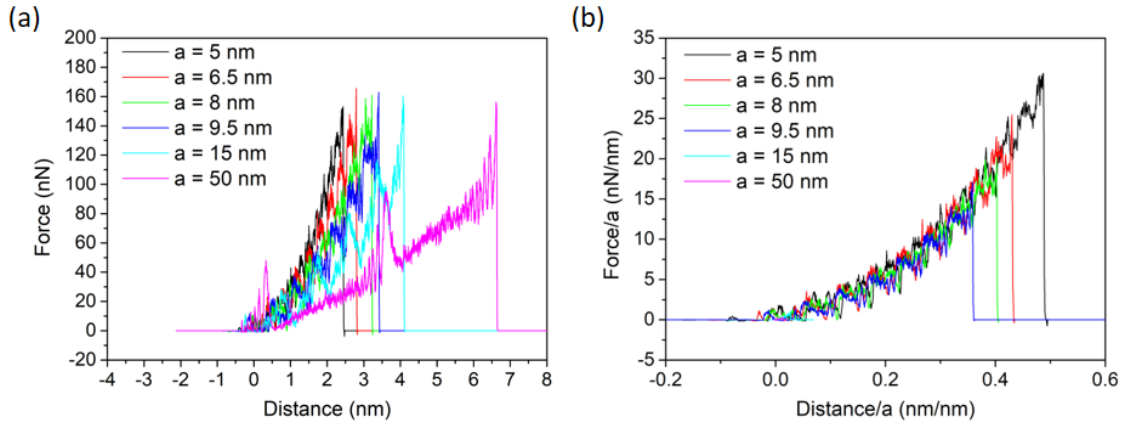

Figure 6.24: (a) Force-distance curves and (b) force/membrane radius vs distance/membrane radius curves for membrane radii of 5, 6.5, 8, 9.5, 15, and 50 nm.

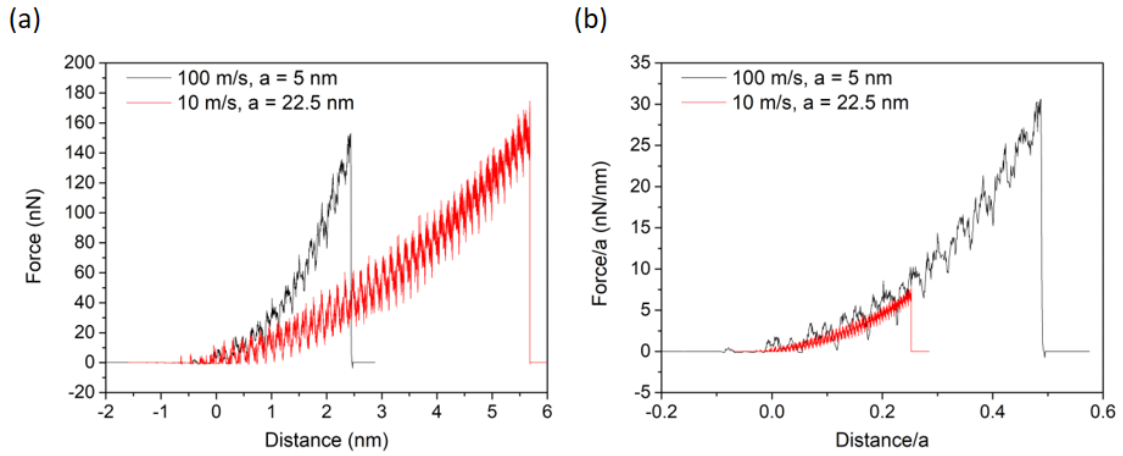

Figure 6.25: (a) Force-distance curves and (b) force/membrane radius vs. distance/membrane radius curves for indentation velocities of 100 m/s and 10 m/s, and membrane radius of 5 nm and 22.5 nm, respectively.

Table 6.7: The results comparing the elastic modulus, E, and breaking strength, σ_m, using different membrane radii, a. r is the indenter radius in nm while v is the indentation velocity.

a (nm)	v (m/s)	$\frac{r}{a}$	σ^{2D} (N/m)	E^{2D} (N/m)	E (TPa)	E^* (TPa)	σ_m (N/m)
5	100	0.1	7.16	150.46	0.50	0.89	64.29
6.5	100	0.08	6.88	148.65	0.49	0.94	66.42
8	100	0.06	6.11	157.77	0.52	1.05	67.50
9.5	100	0.05	5.80	157.49	0.52	1.09	67.83
15	100	0.03	4.80	189.78	0.63	1.47	73.90
22.5	10	0.02	4.40	202.85	0.67	1.74	78.80
50	100	0.01	3.60	238.57	0.79	2.50	72.61

*Calculated with the correction factor of $\left(\frac{r}{a}\right)^{\frac{1}{4}}$

While no significant difference is obtained in the elastic modulus for the membrane radii ranging from 5 nm to 9.5 nm, $E \approx 0.51$ TPa, the elastic modulus measured from the 22.5 nm membrane is slightly higher at 0.67 TPa, while that for membrane radius of 50 nm is measured at 0.77 TPa. Furthermore, the correction factor of $\left(\frac{r}{a}\right)^{\frac{1}{4}}$, as suggested by Tan et al. [147], was introduced resulting in the calculated elastic moduli to increase significantly to approach and even surpass 1 TPa, especially for the larger membranes.

Like in the previous cases, fluctuations are once again observed in all the force-distance curves presented in Figure 6.24 (a) and Figure 6.25 (a). However, it is noted that with an increase in membrane radius, the frequency and magnitude of such fluctuations decreases and increases, respectively. Furthermore, Figure 6.24 (b) shows that the period between fluctuations is proportional to the radius of the membrane whereby the fluctuations in all curves become comparable upon plotting F/a against δ/a.

The force-distance curve obtained for a membrane radius of 50 nm was selected for further investigation since the fluctuations are predominant and spaced apart. Upon visualising the atomic positions throughout indentation, it was understood that a wave was travelling radially across the graphene membrane. This confirms that the three peaks in the force-distance curve (Figure 6.24) are directly related to the movement of waves within the sheet. Similar to what was suggested in Section 6.4.3.2.1, the phenomenon can be compared to the radial waves induced in the surface of a body of water due to a spherical object dropped into the water. In

fact, at an indentation velocity of 100 m/s, which is close to the velocity of a bullet, shockwaves or ballistic pressure waves are indeed expected to radiate from the impact zone and be reflected back by the circular substrate boundary.

Figure 6.26 presents the average temperature of the graphene sheet superimposed on the force-distance curve of graphene membrane of radius 50 nm. This shows that during the force peaks, the average temperature of the entire graphene sheet was not affected. This can be partially attributed to the use of the thermostat set at 300 K. Nonetheless, the global graphene temperature is seen to spike up and drastically reduce upon failure. Thus, it can be concluded that the perturbations in the force-distance curve are not related to thermal fluctuations, but rather to the physical waves induced due to the extreme indentation velocities.

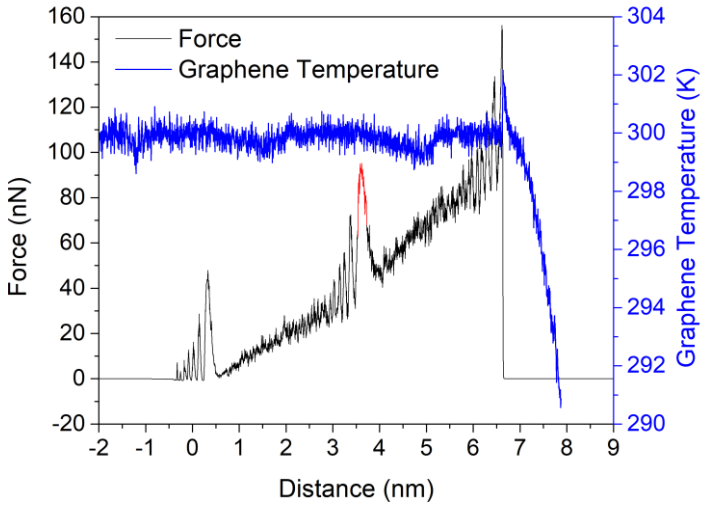

Figure 6.26: Force-distance curve and change in temperature of the graphene sheet with indentation distance.

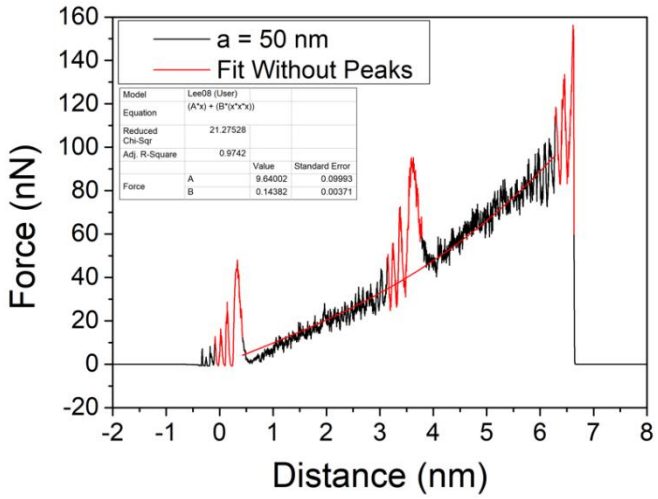

Figure 6.27: Force-distance curves for membrane radius of 50 nm, with fitting ignoring the data points within the peaks marked in red.

Figure 6.27 once again presents the force-distance curve of the 50 nm membrane, however with the data points within the substantial peaks being removed from the nonlinear fitting to Equation 6.23. With such fitting procedure, an elastic modulus of 1.12 TPa is obtained. This indicates that the fit has to consider only the lower data points and ignore the perturbations caused by the induced waves. This is in agreement with the work by [165] who only consider the force after equilibrium.

As mentioned previously, periodic boundaries were applied to the simulation space to mimic an infinitely large graphene sheet. This means that the simulation space modelled represents a unit cell which is repeated in a 3-dimensional lattice, effectively simulating the system shown in Figure 6.28. Therefore, it can be argued that during indentation, all the graphene membranes will be simultaneously indented and thus, the infinitely large graphene sheet would be point loaded from many different locations at once. Here, the ratio between the membrane radius a and the substrate dimensions L and b becomes more important, especially considering that typical microhardess tests have to be performed at least three indent lengths away from each other.

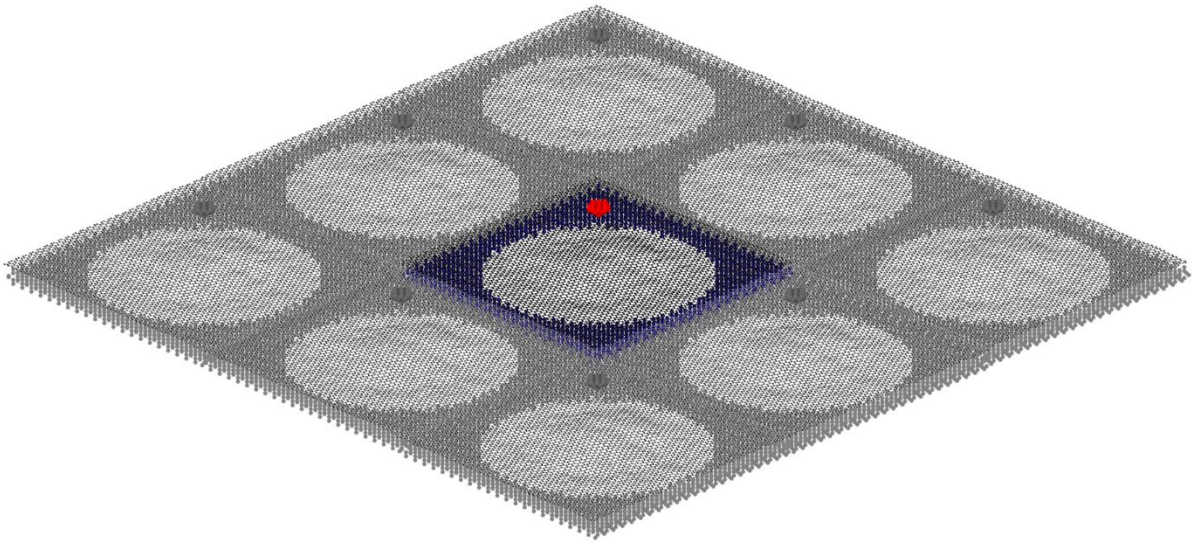

Figure 6.28: Illustration of the effect of periodic boundaries whereby one simulation box is a unit cell which is repeated in the adjacent cells.

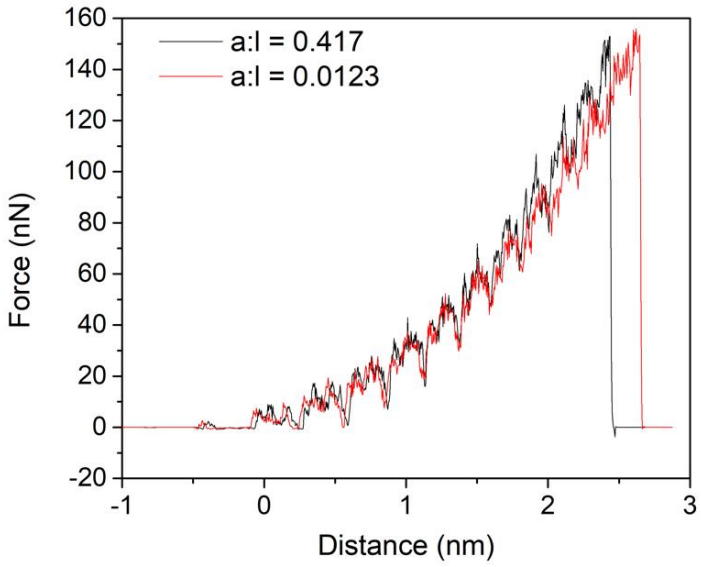

Figure 6.29: Force-distance curves for membrane radius of 5 nm at an indentation velocity of 100 m/s, with an a: L ratio of 0.417 (black line) and 0.0123 (red lime).

To investigate whether the ratio a: L is indeed too large, a simulation with a membrane radius a of 5 nm and substrate dimensions $L \times b$ of 406 × 406 nm, thus producing a ratio a: L of 0.0123, was run. The same indentation velocity of 100 m/s and temperature of 300 K were used.

Figure 6.29 shows the resulting force curve compared to that in Simulation 1, i.e. with a membrane radius of 5 nm and substrate dimensions of 12 × 12 nm. It can be noted that the membrane with the smaller a: l ratio sustained a slightly larger strain. Following the fitting procedure, an elastic modulus of 0.40 TPa and a breaking stress of 57.42 N/m were obtained, 20% and 10.7% lower, respectively, than those obtained with an a: L of 0.417. Thus, while such a modification of the model does affect the results, the elastic modulus obtained is even lower than expected.

6.4.3.2.4 Thermostat

In order to study the effect, if any, of the use of a different thermostat, the same simulation was run using two different thermostats; the Berendsen thermostat and the Nosé-Hoover thermostat [286]. A graphene membrane of radius 5 nm was indented at a velocity of 100 m/s and kept at a temperature of 300 K using the different thermostats.

Figure 6.30 presents the force-distance curves obtained using the two different thermostats. The curves are almost indistinguishable indicating that both thermostats were able to model the same simulation similarly.

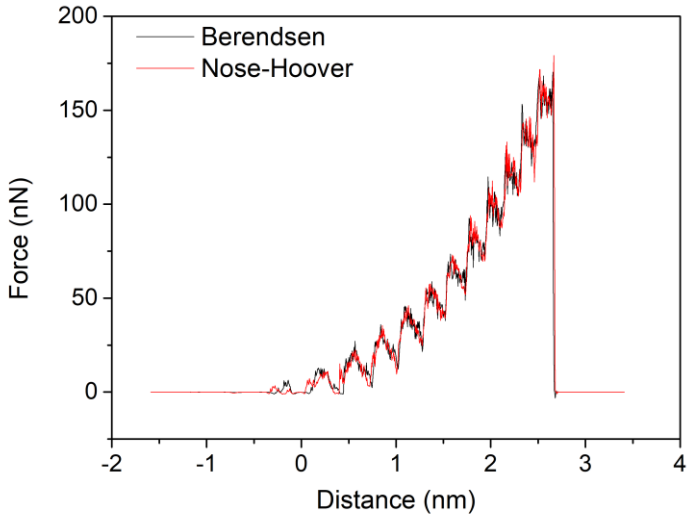

Figure 6.30: Force-distance curves as obtained using the Berendsen and Nosé-Hoover thermostats, both at 300 K.

6.4.3.2.5 Dynamic Substrate

In order to verify whether or not the substrate affects the indentation experiment and hence the measured elastic modulus of the graphene, the substrate was also modelled as a dynamic material rather than a rigid body. The hypothesis is that it is possible that during indentation of the graphene membrane, the surface atoms at the very edge of the supporting pore experience elastic deformation.

To test this hypothesis, the substrate was once again modelled as a silicon crystal with a diamond cubic lattice with a lattice constant of 5.43 Å, however applying the Stillinger-Weber potential [287] to model the interatomic interactions within the substrate material. The substrate was modelled with external dimensions of 12 × 12 × 2 nm and a pore radius of 5 nm. The same Berendsen thermostat set at 300 K and NVE ensemble were used to simulate the silicon substrate. The entire substrate was modelled as dynamic during the equilibration step, while the bottom 0.5 nm of the substrate was frozen and held rigid in the simulation space during indentation to support the overlying atoms.

Figure 6.31 presents a series of snapshots during indentation showing only a quasi-cross-section of the indented graphene membrane, that is, only a slice of width 13 Å is shown. Figure 6.31 shows that the atoms are evenly arranged before the simulation is started in (a), most of the surface atoms of the substrate lose their positions slightly throughout indentation in (b), and

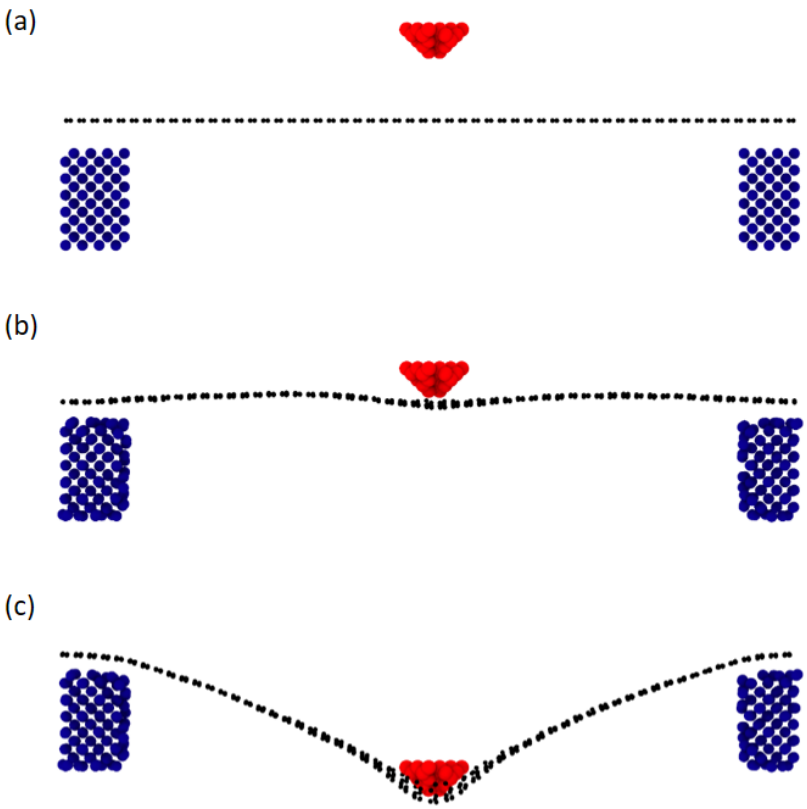

Figure 6.31: A series of snapshots during indentation with a dynamic substrate. Only a slice through the middle of the graphene membrane system of 13 Å width is shown.

in (c), the atoms at the pore edge are more displaced just before membrane failure. Although, the substrate does seem to slightly deform upon indentation (Figure 6.31 (c)), the extent of such deformation only applies to the first few atoms at the edge of the pore and thus, it is not deemed significant enough to affect the graphene's response to indentation. In fact, the measured elastic modulus of the graphene membrane in this simulation was not affected by the introduction of a dynamic substrate.

6.4.3.2.6 Dynamic and Spring-Loaded Indenter

Like the previous nanoindentation simulations in this work, most nanoindentation simulations reported in literature are performed by assigning a constant velocity to the indenter varying from 4 m/s up to 100 m/s [148, 162, 184, 187, 188]. Despite the large velocities compared to the experimental nanoindentation velocity of 23 nm/s, this simulation model may adequately approximate the indentation experiments especially if using a dedicated nanoindenter in the experimental set-up. However, the indenter tip in the AFM is fixed to a flexible cantilever, which is in turn moved at a constant velocity by a piezo actuator. Therefore, during indentation, both the graphene membrane and the cantilever elastically deform. This may induce a complex

system whereby the elastic properties of the graphene membrane compete against the elastic properties of the cantilever, hence possibly resulting in a variable membrane displacement rate. Furthermore, as discussed in Chapter 4, it is often the case that some tips are deformed or broken during indentation. This was observed via SEM imaging of the tip morphology before and after indentation, especially with the silicon FM50 and the diamond-like carbon Tap190DLC probes.

Investigating the effects of the elasticity of the indenter imposed by the flexible cantilever in AFM via MD simulations can potentially shed light on why the spring constant of the cantilever must match the spring constant of the sample material. As discussed in Chapter 4, a flexible cantilever is not able to indent the membrane, while a stiffer cantilever is not sensitive to the membrane deformation. As shown in the experimental results, choosing the correct AFM cantilever stiffness can be cumbersome as the optimal spring constant may vary depending on a number of factors that may affect the elastic response of the graphene membrane to indentation, such as the number of graphene layers indented, the size of the membrane, the presence of any defects or wrinkles in the graphene membrane, and the temperature. Furthermore, such study can shed light on the trend observed in some membranes, particularly with the use of the stiffer cantilevers, whereby the measured elastic modulus of the graphene membrane is overestimated at lower indentation depths.

In order to faithfully simulate nanoindentation via AFM, modelling the entire tip and cantilever would be ideal to replicate the elastic response of the flexible cantilever upon indentation. However, this is too costly to do via MD given that a typical cantilever is around 200 μm in length, 30 μm in width, and 3 μm in thickness. As such, to investigate the effects of the flexible cantilever and the potentially deformable tip on the indentation, the above scenario was simplified to a dynamic ‘spring-loaded’ indenter, as will be described next.

Similar to the work by Fang et al. [288], in which nanoscratching and nanoindentation on gold and platinum thin films were simulated via MD, in this work the indenter tip was coupled to a simplified cantilever via a virtual vertical spring to model the cantilever spring constant, as illustrated in Figure 6.32.

As shown in Figure 6.32, the indenter was modelled as a hemispherical diamond crystal with a diamond cubic lattice of cube size 3.567 Å. To better model the interactions between the graphene membrane and the tip, in addition to the Lennard-Jones potential applied between the graphene and the indenter atoms, the AIREBO potential was also applied to the carbon atoms

forming the diamond indenter, similar to the work carried out by Wang et al. [148]. The indenter was given a radius of 0.7 nm (127 atoms) to hold its crystalline shape during the simulation.

The cantilever was modelled as a cylinder of the same crystal lattice having the same radius of the hemispherical diamond tip (97 atoms), positioned a distance, d, above the indenter. The cantilever atoms were modelled as rigid atoms with no AIREBO or LJ potential applied to them, however these were coupled to the atoms in the diamond tip by a spring. The spring constant was initially set to 3.12 eV/Å^2 (50 N/m) and the equilibrium distance was set to be equal to the initial distance, d, between the centres of masses of the indenter and the cantilever atoms. The cantilever atoms were then moved at a fixed velocity of 100 m/s, pushing the indenter towards the graphene membrane. Two different spring constants of 3.12 eV/Å^2 (50 N/m) and 31.21 eV/Å^2 (500 N/m), each having an equilibrium distance ranging from 4.13 Å to 23.13 Å were initially investigated.

The indentation force was found by considering only the forces acting on the indenter due to the graphene atoms, while excluding the forces acting on the indenter due to the atoms within itself and the cantilever pushing down on it.

Figure 6.33 and Table 6.8 present the results obtained. Once again, the introduction of a spring and with different spring parameters did not result in a significant difference in the obtained force-distance curves and the measured elastic modulus.

The cantilever was also reduced to a single atom right on top of the indenter. The force acting on this single cantilever atom was compared to the total force acting on the indenter due to the graphene sheet. The force-distance curves obtained are presented in Figure 6.34, and show that these two methods of measuring the force lead to the same results.

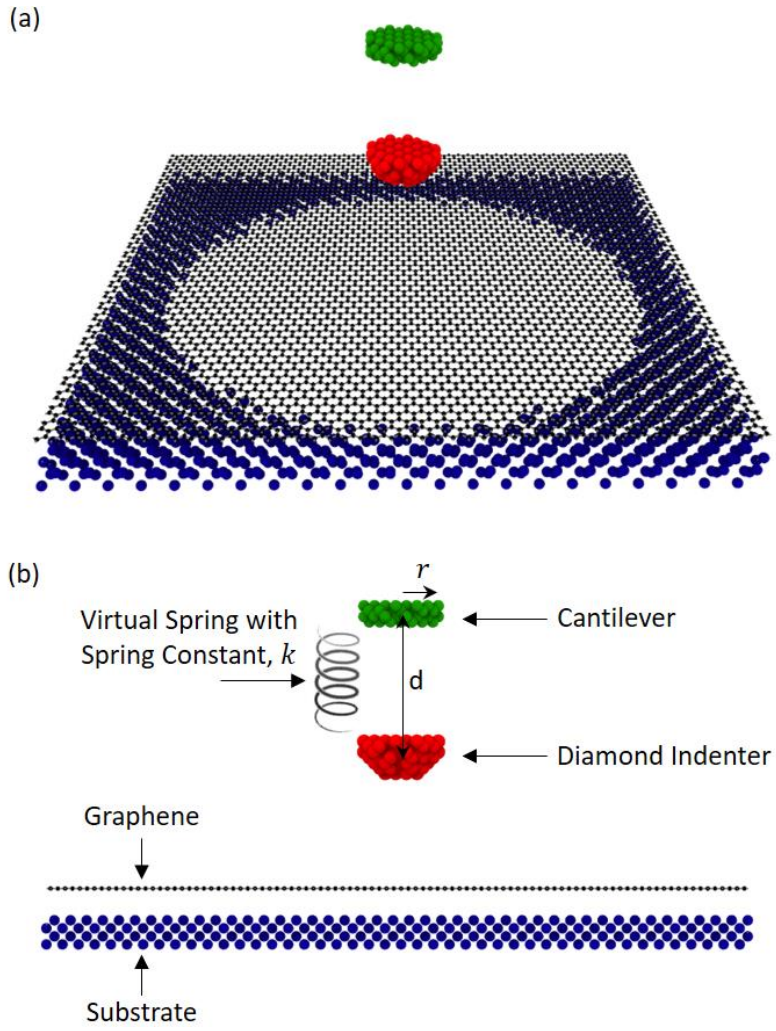

Figure 6.32: (a) Perspective and (b) side views of the system geometry of the nanoindentation simulations using a spring-loaded tip to simulate the effect of a flexible cantilever with a known spring constant, k. The hemispherical diamond indenter is coupled to a cylindrical cantilever by a virtual spring.

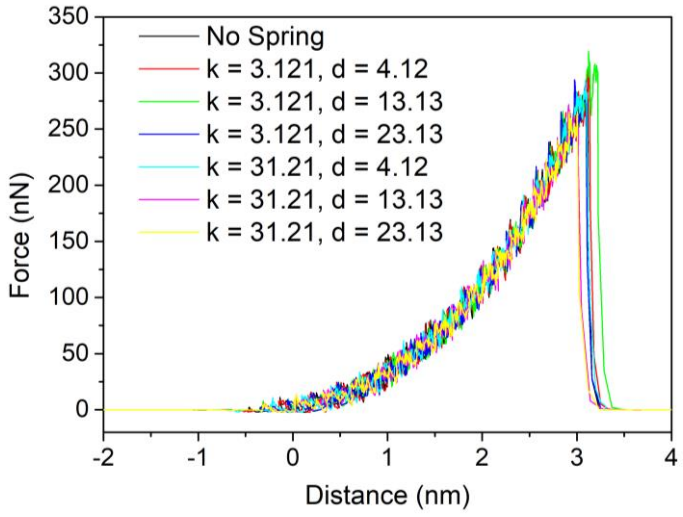

Figure 6.33: Force-distance curves of simulations utilizing different spring constants, k (eV/Å^2), and cantilever-to-indenter distance, d (Å).

Table 6.8: The results comparing different spring constants, k, and cantilever-to-indenter distance, d. The membrane radius is 5 nm, indenter radius 0.7 nm, temperature 300 K, and indentation velocity 100 m/s.

k (eV/Å^2)	d (Å)	σ^{2D} (N/m)	E^{2D} (N/m)	E (TPa)	E^* (TPa)	σ_m (N/m)
-	-	9.245	174.33	0.51	0.84	76.57
3.12	4.13	9.310	171.11	0.50	0.82	76.77
3.12	13.13	8.861	179.19	0.53	0.86	79.02
3.12	23.13	8.847	178.94	0.53	0.86	77.16
31.21	4.13	9.500	173.44	0.51	0.83	76.13
31.21	13.13	9.200	170.36	0.50	0.82	71.41
31.21	23.13	9.153	171.58	0.50	0.82	71.94

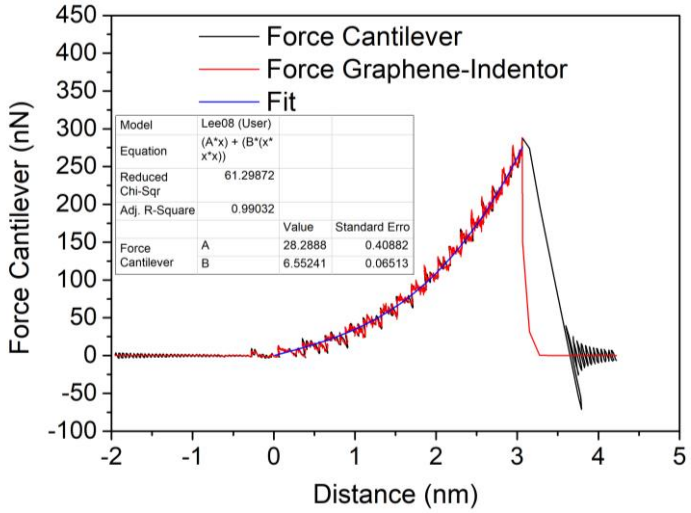

Figure 6.34: Force-distance curves of simulations utilizing different methods of calculating the force.

Figure 6.35 shows a series of snapshots during the indentation of a graphene membrane using a spring-loaded indenter with $k = 3.12$ eV/Å^2 and d$= 23.13$ Å. It can be noted how the equilibrium distance, d, between the indenter and the cantilever atoms decreases significantly during indentation as the force acting against the spring due to the graphene increases. For the same spring constant, a shorter equilibrium distance causes the indenter atoms to come in contact with the cantilever atoms during indentation, thereby rendering the effect of the virtual spring negligible compared to the contact forces induced. This indicates that for a given spring constant and graphene membrane radius, there is a minimum equilibrium distance, d, for which the spring remains active and significant throughout the simulation.

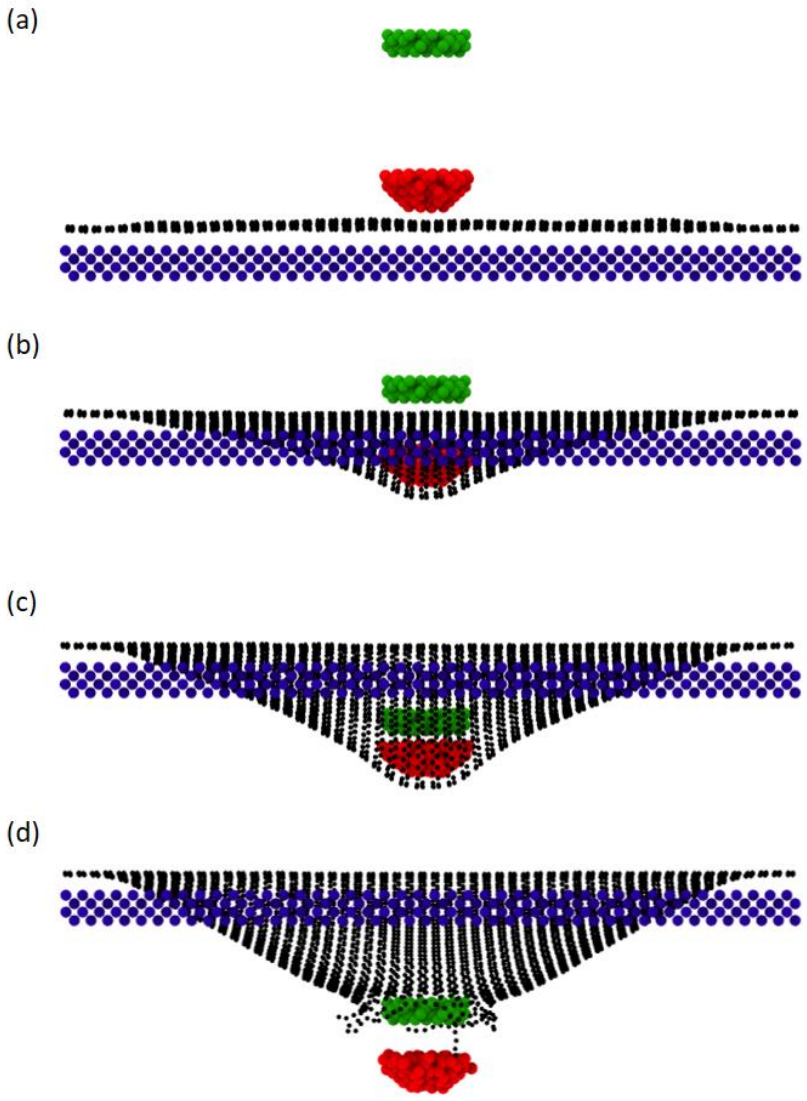

Figure 6.35: A series of snapshots obtained during indentation of the graphene membrane using the spring-loaded indenter with k = 3.12 eV/Å², d = 23.13 Å. (a) Before indenter-to-graphene contact, (b) during indentation, (c) when the virtual spring is fully compressed such that the cantilever atoms are in contact with the indenter atoms, and (d) after graphene membrane failure.

6.4.3.2.7 Non-periodic boundaries, step-wise indentation

As mentioned in the previous sections, the radial rippling during indentation, reflected as fluctuations in the force curves, are believed to be originating from the method of indenting; applying the same velocity to the indenter every time-step does not allow the graphene sheet to reach equilibrium. As such, similar to the work in [165, 167], another set of simulations were performed by moving the indenter by 0.1 Å or 0.2 Å in a step-wise manner whereby the indenter is held fixed for at least 800 time-steps to allow the graphene sheet to stabilize in between the individual indentation steps. Furthermore, periodic boundaries were not applied to the graphene sheet to allow it to form more natural wrinkles during the initial equilibrium stage,

and also prevent any effect from the neighbouring membranes (Figure 6.28). Instead, after at least 60 000 time-steps for equilibration, the graphene edges were clamped and held rigid throughout indentation.

Figure 6.36 shows a 50 × 50 nm graphene sheet suspended over a 15 nm radius pore after initialization and equilibration (60 000 time-steps), with significant wrinkling being observed in the membrane. Figure 6.37 shows the force curve obtained upon indenting the membrane with a step-wise indentation displacement of 0.2 Å, compared to the force curve obtained for a similar membrane indented at a velocity of 100 m/s. It is evident that the method employed for the step-wise indentation did not produce the unwanted radial rippling, and hence periodic fluctuations in the force curve, allowing for a better fit to Equation 6.23. The step-wise indentation resulted in a measured elastic modulus of 1.31 TPa and breaking strength of 86.40 N/m. The modulus is thus more than twice as high as that calculated in Section 6.4.3.2.3 for a similar 15 nm membrane (Table 6.7). For a pristine graphene sheet under indentation where an elastic modulus of around 1 TPa is expected, this method of indentation was therefore deemed more realistic.

A similar step-wise indentation methodology was used on different graphene membrane radii, ranging from 5 nm to 25 nm, to investigate any size effect. Figure 6.38 (a) shows the respective force curves. It can be noted that, once again, fluctuations are present in the larger membrane with radius 25 nm (green curve) presumably because a larger graphene sheet would require more time to effectively dissipate the imposed energy. To remove these unrealistic perturbations, the same simulation with a = 25 nm was run with a longer equilibration time of 1600 time-steps between each 0.2 Å indentation step – denoted as a = 25 nm* in Figure 6.38. Thus, by directly comparing the two force curves for the 25 nm membrane with and without fluctuations, it is indicated that, in case of rippling the data that needs to be considered for fitting are the upper-most crests of the curve, i.e. where the two curves in Figure 6.38 (a) overlap.

In order to be able to visually compare the different curves better, the force and indentation distance were both divided by the respective membrane radius, as shown in Figure 6.38 (c). This confirms that Equation 6.23, and hence the force-distance relationship during indentation, is indeed dependent on the radius of the graphene membrane. Upon eliminating this parameter (Figure 6.38 (c)), the curves overlap.

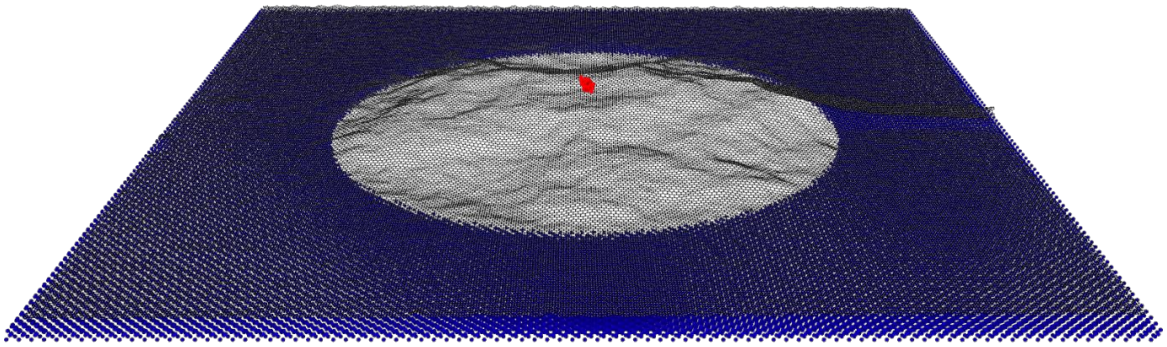

Figure 6.36: Wrinkling in a 15 nm radius membrane without periodic boundaries.

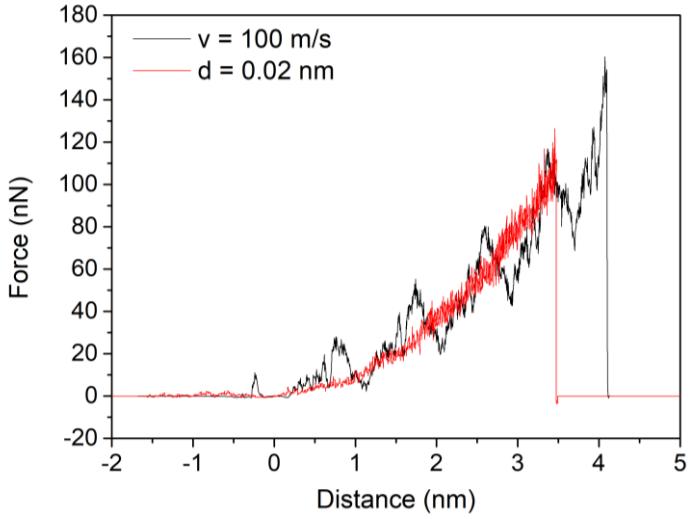

Figure 6.37: Force-distance curves for similar 15 nm radius membranes indented with an indentation velocity v of 100 m/s (black) and by a step-wise displacement d of 0.2 Å (red).

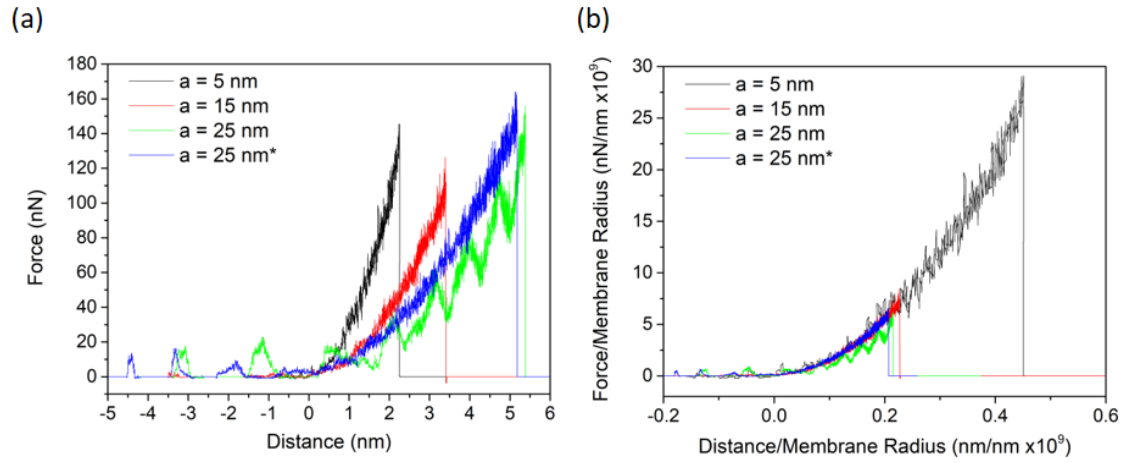

Figure 6.38: (a) Force-distance curves, and (b) force/membrane radius vs distance/membrane radius curves for membrane radii of 5, 15, and 25 nm. Simulation a = 25 nm was performed with longer equilibration time between indentation steps.*

Table 6.9: The results comparing the elastic modulus, E, and breaking strength, σ_m, using different membrane radii, a. r is the indenter radius equal to 0.5 nm, and an indenter displacement of 0.2 Å was used.

a (nm)	Time-steps between indentation	$\frac{r}{a}$	σ^{2D} (N/m)	E^{2D} (N/m)	E (TPa)	E^* (TPa)	σ_m (N/m)
5	800	0.1	6.72	203.11	0.61	1.08	65.71
15	800	0.03	3.50	437.28	1.31	3.057	86.40
25*	1600	0.02	3.70	436.37	1.30	3.46	100.38

*Calculated with the correction factor of $\left(\frac{r}{a}\right)^{\frac{1}{4}}$

Table 6.9 lists the obtained mechanical properties for each of the curves shown in Figure 6.38. Similar to Section 6.4.3.2.3, the size dependency is insignificant beyond a membrane radius of 15 nm. Furthermore, applying the correction factor of $\left(\frac{r}{a}\right)^{\frac{1}{4}}$ is once again only applicable to large $\frac{r}{a}$ ratios; applying the correction factor to $\frac{r}{a}$ ratios smaller than ~0.03 leads to an overestimation of the elastic modulus.

To verify the dependency of the measured elastic modulus on the chosen cantilever spring constant, a dynamic spring-loaded indenter similar to that used in Section 6.4.3.2.6 was used with a step-wise indentation methodology. A sample input script for these simulations is presented in Appendix G. Five different spring constants ranging from 0.3121 eV/Å^2 (5 N/m) up to 3121 eV/Å^2 (50 000 N/m) were used. In all simulations, the equilibrium distance between the cantilever and indenter was set to 63.13 Å to avoid the indenter from coming in contact with the cantilever atoms during indentation. Furthermore, since the indenter radius had to be increased to 0.7 nm to retain its shape during indentation, a graphene membrane radius of 25 nm was used to retain a low $\frac{r}{a}$ of 0.28. The graphene membranes were initially equilibrated for a total of 180 000 time-steps to ensure that equilibrium was reached and thus wrinkling was minimized again. Note that the same graphene initialization was used for all simulations such that any variability in the results cannot be attributed to different wrinkling configurations. Due to the presence of the spring, and hence increased complexity of the interatomic interactions at play, a step-wise indentation with a shorter indenter displacement of 0.1 Å followed by 2000 time-steps for equilibration were used.

Figure 6.39 (a) presents all the force curves obtained. In Figure 6.39 (b), the raw data was smoothed to improve discernability of the individual curves. The measured mechanical parameters are listed in Table 6.10. At first glance, it appears that spring-loading the indenter

increases the force that the graphene membrane can withstand, and hence the elastic modulus. However, no clear trend can be noted between the different spring constants used and the elastic modulus measured.

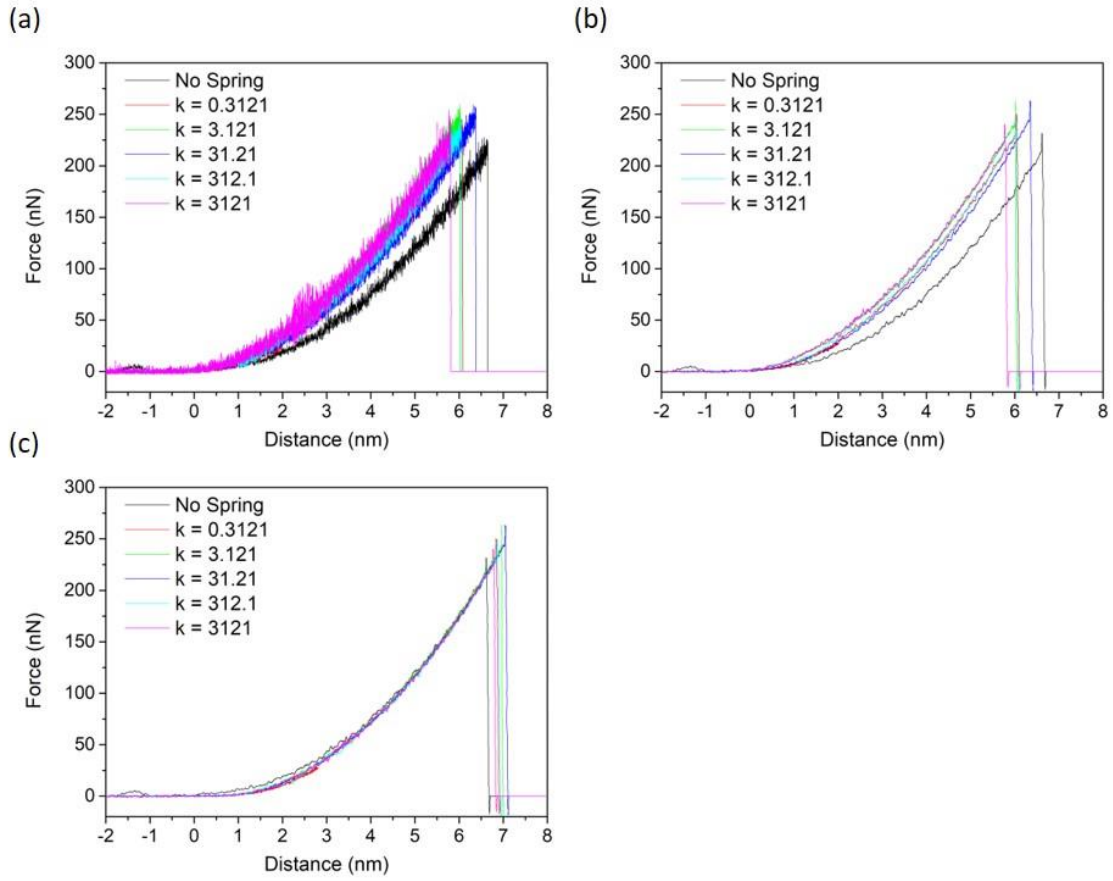

Figure 6.39: Force-distance curves of simulations utilizing different spring constants, k (eV/Å²), with the same cantilever-to-indenter distance of 63.13 Å; (a) raw data, (b) smoothed, and (c) shifted in the x-direction such that the curves overlap at higher indentation depths.

Table 6.10: The results comparing different spring constants, k. The cantilever-to-indenter distance is 63.12 Å, membrane radius 25 nm, indenter radius 0.7 nm, temperature 300 K, indentation step-wise displacement of 0.1 Å and 2000 time-steps equilibration after each indentation step.

k (eV/Å²)	σ^{2D} (N/m)	E^{2D} (N/m)	E (TPa)	σ_m (N/m)
-	2.96	367.24	1.10	94.69
0.3121	3.85	526.04	1.57	116.77
3.121	5.64	434.65	1.30	108.88
31.21	4.52	427.15	1.28	108.68
312.1	4.79	454.68	1.36	109.45
3121	5.53	453.91	1.35	108.57

Upon closer inspection, it is observed that at higher indentation depths the curves appear to be parallel to each other. In fact, in Figure 6.39 (c), the individual curves were shifted in the x-direction such that the second portion of the force curves overlap each other. The fact that the force curves at high indentation depths are similar using different cantilever spring constants and the curves only vary at lower indentation depths indicate that the cantilever spring mainly affects the initial part of indentation. This can be attributed to the fact that at lower indentation depths, the indenter will still be flattening out the wrinkles in the graphene sheet which presumably have a lower stiffness, and thus, the magnitude of the cantilever spring constant is comparable to, or more significant than, the stiffness of the out-of-plane wrinkles. On the other hand, at higher indentation depths, all the wrinkles are ironed out and only the true elastic stiffness of the graphene sheet will be acting on the indenter, thereby resulting in a true representation of the elastic modulus of graphene.

From these observations, a number of conclusions can be drawn.

Even though the force-curves may appear different when the zero-displacement point (ZDP) is set to the origin of the curve (0,0), the slope of the curves at higher indentation depths are nonetheless very similar. In fact, this portion of the graph is primarily characterised by the cubic term of Equation 6.23 which determines the elastic modulus of graphene – a material property that should remain constant and should not depend on any wrinkling in the sheet, pre-tension differences, cantilever spring constant, or otherwise.

Therefore, irrespective of the cantilever spring constant or wrinkling in the sheet, Equation 6.23 should only be fitted to the second portion of the force-curves to eliminate such external variations from affecting the measured elastic modulus. To test this hypothesis, Equation 6.23 was fit to the data at higher indentation depths of the force curves in Figure 6.39 (b), i.e. with the ZDP still at the (0,0) position. For simplicity, the fitted data was restricted to an indentation distance from 4 nm up to failure. Table 6.11 compares the elastic moduli obtained from higher indentation depths, to those obtained by fitting to the entire curve. The new method of fitting reduces the variation between the curves obtained using different spring constants, as graphically shown in Figure 6.40.

Table 6.11: The results comparing different spring constants, k upon fitting Equation 6.23 to the entire force curve or to indentation depths, $\delta > 4$ nm.

k (eV/Å^2)	σ^{2D} (N/m)	E^{2D} (N/m)	E (TPa)	σ^{2D} (N/m) $\delta >$ 4 nm	E^{2D} (N/m) $\delta > 4$ nm	E (TPa) $\delta > 4$ nm
-	2.96	367.24	1.10	3.75	317.66	0.95
0.3121	3.85	526.04	1.57	5.72	380.48	1.14
3.121	5.64	434.65	1.30	6.49	371.86	1.11
31.21	4.52	427.15	1.28	5.47	363.39	1.08
312.1	4.79	454.68	1.36	5.73	383.18	1.14
3121	5.53	453.91	1.35	6.43	381.24	1.14

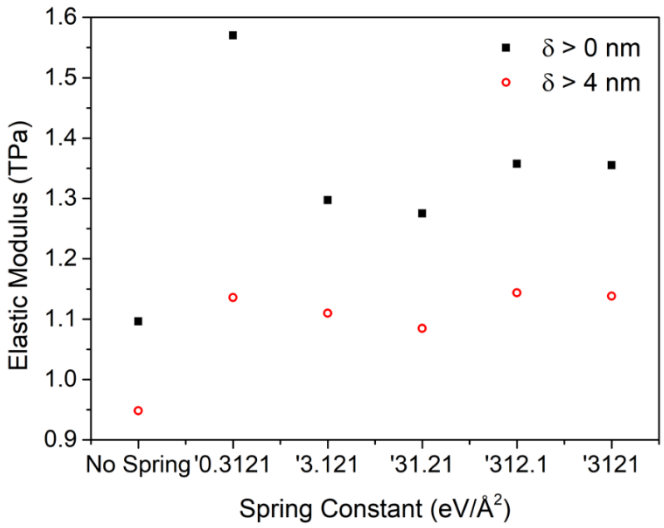

Figure 6.40: Elastic moduli as measured using different spring constants, and fitted to the entire force curve vs. to indentation depths higher than 4 nm.

A cumulative fit of Equation 6.23 was also applied to the force curve obtained using a membrane radius of 25 nm without the spring-loaded indenter. The time-cumulative fitting, corresponding to indentation depth-cumulative fitting, was continuously performed from the ZDP (initial point of indenter-graphene contact) up to the elapsed simulation time/indentation depth until membrane failure. A simple representation of the different fits performed is shown in Figure 6.41 (a), with the resulting measured elastic modulus by these different fits shown in Figure 6.41 (b). Figure 6.42 shows the entire data set obtained with the cumulative fitting. These results highlight the overestimation of the elastic modulus when Equation 6.23 is fitted to lower indentation depths, and the gradual decrease of the measured elastic modulus with increasing indentation depth. This is therefore the same trend observed in the experimental results (Chapter 4) whereby higher elastic moduli were found at lower indentation depths. For

this particular case, while the elastic modulus approaches the 1 TPa benchmark, it does not fully converge. As such, it can be thought that the force curve data set is not extensive enough to allow the cubic term – from which the elastic modulus is calculated – to be significant enough.

This suggests that Equation 6.23 may not be modelling the obtained force curves accurately. As already mentioned, the linear term is mainly responsible to fit the initial part of the curve (i.e. at low indentation depths), while the cubic term is mainly responsible to fit the second portion of the curve at higher indentation depths. Since the scope of the force curves as used in this work is to measure the elastic modulus of graphene, which is derived from the cubic term, it is therefore important to ensure that the force curve extends to larger displacements such that there are enough data points in the cubic regime.

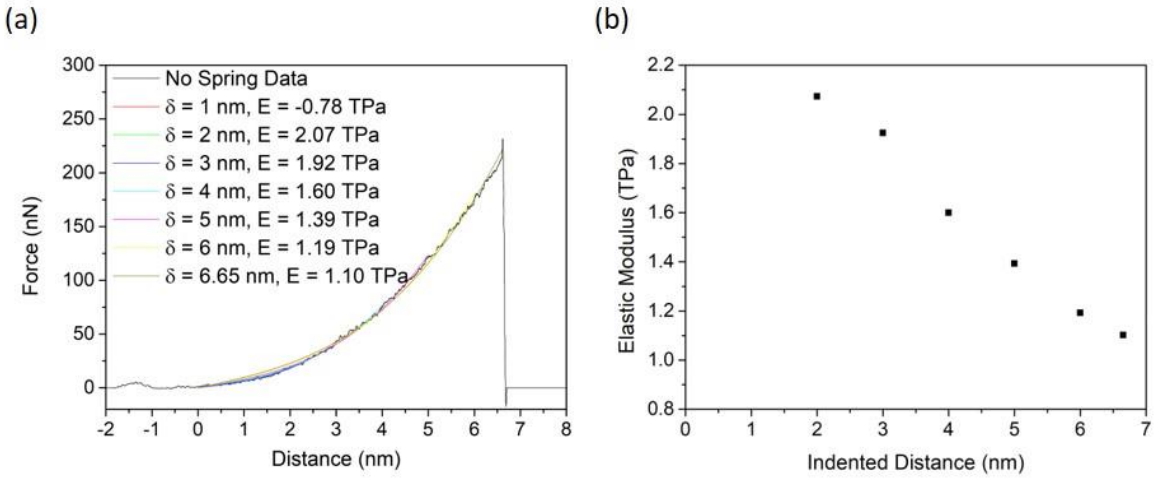

Figure 6.41: (a) Cumulative-fitting of the force distance curve to different indentation distances. (b) The resulting elastic moduli obtained for different indentation distances.

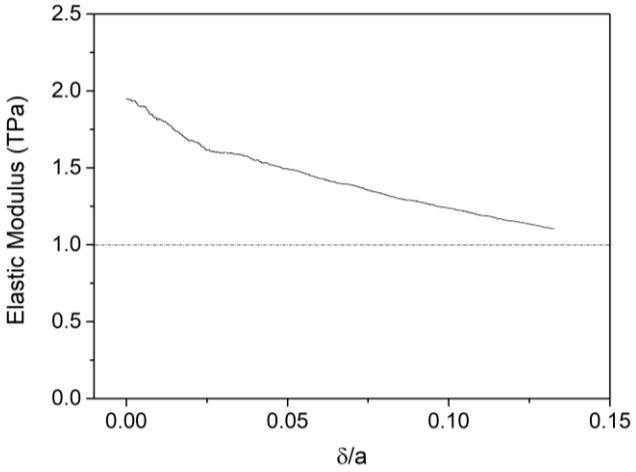

Figure 6.42: The values of elastic modulus obtained via cumulative fitting of the force curve. The x-axis is represented by the normalized displacement (δ/a).

To further eliminate the restrictive influence that both the choice of the zero-displacement point (0,0) and the linear term impose on the fitting procedure, the force F was plotted against the cube of the indentation depth divided by the membrane radius $\left(\frac{\delta}{a}\right)^3$ such that the curve assumes a linear relationship at higher indentation depths, as shown in Figure 6.43 (a). The gradient of the rolling-average of M data points, where $M = 1000$, of the F vs. $\left(\frac{\delta}{a}\right)^3$ curve at different indentation depths was then used to derive the elastic modulus at each point, plotted in Figure 6.43 (b). Once again, this shows that the force curve indeed approaches a cubic relationship at higher indentation depths. However, similar to Figure 6.42, the elastic modulus is short of converging, indicating that the force-distance data set is too limited.

The implications of these results are two-fold. Firstly, if the first method of cumulative-fitting is considered, it must be made sure that the final indentation depth reached during indentation is large enough to allow the force curve to assume a primarily cubic relationship. This will ultimately allow the cubic term in Equation 6.23 to reflect the true elastic modulus of the membrane. Secondly, it can be inferred that the extent of the force curve is directly related to the membrane radius; a larger membrane will be indented to larger indentation depths allowing for the cubic relationship to be pronounced. As such, the minimum indentation depth that has to be reached for the correct measurement of the elastic modulus has to consider the radius of the membrane. This explains why the MD simulations which made use of relatively small membrane radii, and hence low maximum indentation depths before failure, resulted in a slightly overestimated elastic modulus of around 1.2 TPa. The idea of considering the membrane radius to determine the minimum indentation depth required is especially important for experimental testing. While it is best to indent the membrane until failure to ensure that the

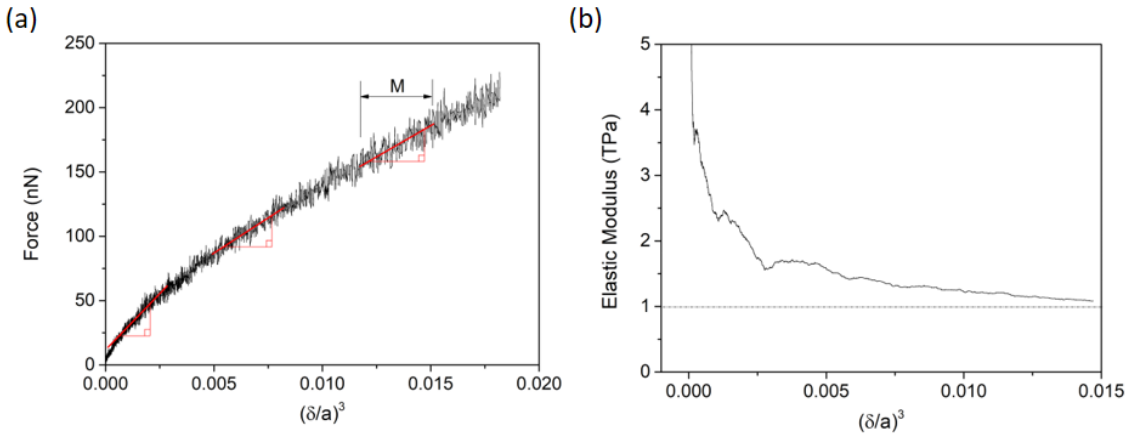

Figure 6.43: (a) F vs. $(\delta/a)^3$ showing examples of the rolling-average data set represented by M, and (b) the resulting elastic modulus at different indentation depths. M is not drawn to scale.

maximum potential of the force-distance relationship can be exploited, indenting up to failure can be problematic. Such approach is destructive in nature thereby not allowing multiple force curves to be obtained for the same membrane. Certain AFM set-ups, such as used in this work, are also limited in the maximum indentation depth that they can achieve. As such, the membrane radius has to be carefully selected such that it is small enough to ensure that the maximum indentation depth that the set-up can achieve is enough such that the cubic force-distance relationship is observed. However, the membrane radius cannot be too small such that the membrane fails before the entire cubic relationship is observed as happened in the MD simulations.

6.5 Conclusion - Comparing Experimental with Molecular Dynamics Results

In Figure 6.44, two force curves obtained via AIREBO MD simulations of 15 nm and 25 nm membrane radii without the use of the spring-loaded indenter are compared to typical experimental force curves obtained in Chapter 4. Both the force and the distance are divided by the membrane radius so that the curves become comparable and independent on the membrane size, as discussed in Section 6.4.3.2. Similar to what was observed in Section 6.4.3.2.7 with the use of different spring constants, the force curves resulting in the same elastic modulus are almost parallel to each other at higher indentation depths. On the other hand, curves representing a lower elastic modulus are significantly less steep while those resulting in a higher elastic modulus are steeper. The ability of directly comparing the force curves obtained via MD simulations to those obtain via experimentation confirms that molecular dynamics simulations can be successfully used to model nanoindentation of a circular graphene membrane.

Furthermore, from Figure 6.39, it is indicated that the indenter spring constant mainly affects the initial part of the force curve, which does not reflect the measured elastic modulus of the graphene membrane. Therefore, for experimental AFM indentations, the choice of spring constant will only affect the maximum force applied and hence graphene indentation distances for a given piezo extension – a stiffer cantilever will apply larger forces and hence larger graphene indentation distances for the same piezo displacement. As such, this difference in cantilever spring constant is then reflected into larger force curves and thus the ability of the cubic term in Equation 6.23 to faithfully represent the true elastic modulus of the graphene.

Figure 6.45 (a) shows the results obtained from the cumulative fitting procedure which was applied to all the force curves. The fact that the value of elastic modulus does not converge for most of the force-curves confirms that the raw data did not extend enough along the x-axis. For the radius of the graphene membranes being indented, the indentation depth should have been larger to allow for the cubic relationship to be more pronounced.

Any other effects that different spring constants may have on the initial part of the curve can be eliminated by fitting Equation 6.23 to the rolling-average of the force curve as shown in Figure 6.45 (b).

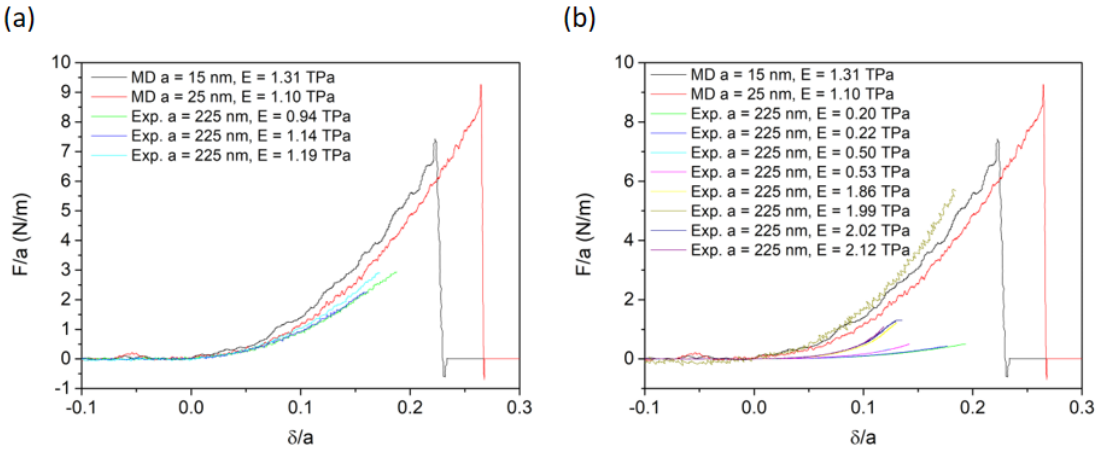

Figure 6.44: Selected (F/a) vs (δ/a) curves obtained via MD simulations and experimental AFM indentations. The elastic moduli in the legends were obtained by fitting Equation 6.23 to the entire force-curve.

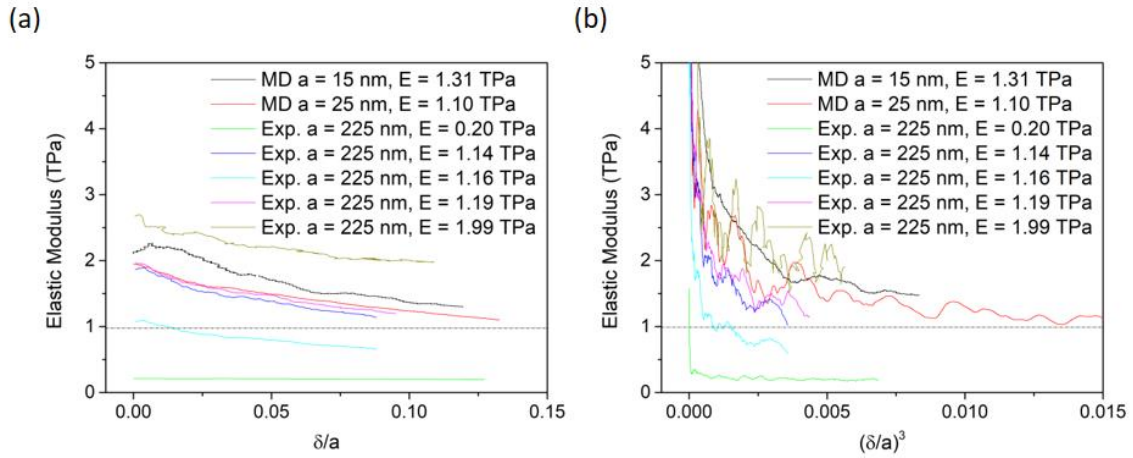

Figure 6.45: The elastic modulus at different indentation depths for selected force curves obtained via MD simulations and experimental AFM indentations. (a) using the cumulative fitting for increasing (δ/a), and (b) using rolling average at different $(\delta/a)^3$.

Chapter 7 CONCLUSIONS

Since its first discovery in 2004, graphene has emerged as a highly promising nanomaterial in various fields of application. Albeit the massive scientific research interest that graphene generated along these last few years, significant work is still being directed at fully understanding its material properties and in turn its expected behaviour under different conditions. Ultimately, successful integration of graphene in novel products and applications is dependent on the holistic understanding of the behaviours exhibited by graphene. The mechanical behaviour of graphene under different loads is deemed to be central in the design of a large portion of graphene-based devices including filtration membranes, biosensors, nanocomposites and MEMS. As part of this research effort, this work has focused on the measurement of the elastic modulus of graphene, specifically for pristine and defective membranes using a point-loading nanoindentation via atomic force microscopy.

Primarily, the techniques and methodologies employed to synthesise graphene and prepare samples for subsequent testing were explored. In this work, graphene was initially prepared in-house via mechanical exfoliation. This technique proved to be challenging to produce large-area single-layer graphene and hence high yields of SLG membranes. More repeatable results with higher yields of single-layer graphene membranes were obtained using CVD-grown graphene deposited on pre-fabricated microsieves. Characterization of the prepared graphene membranes was carried out using optical microscopy, scanning electron microscopy, Raman spectroscopy, and atomic force microscopy.

AFM was the primary tool of interest utilised to indent the graphene membranes and thereby measure the elastic modulus of graphene. The ability of introducing defects in the graphene membrane via gallium ion irradiation was also explored. The effect of ion bombardment on the elastic modulus exhibited by the treated graphene membranes was then investigated. Finally, molecular dynamics simulations were performed to support and provide insight to the experimental work carried out. These main aims were formulated into three research questions as presented in Chapter 2, and summarised in the following sections. The conclusions drawn from the work presented in this thesis are also outlined in the following sections.

Research Question 1

> *To what extent can nanoindentation via atomic force microscopy be used to accurately and repeatably measure the elastic modulus, fracture stress, and fracture strain of freely-suspended graphene membranes?*

The literature review presented in Chapter 2 indicates that indenting graphene membranes using the AFM probe and the general force spectroscopy set-up is a suitable method to measure the elastic modulus, fracture stress, and fracture strain of graphene. Furthermore, although different research groups used different AFM set-ups, different probes, and indented the graphene membrane with different parameters, most studies have obtained comparable elastic moduli for pristine graphene. As such, literature appears to suggest that such changes in the methodology parameters do not significantly affect the measurement results.

However, as evidenced in Chapter 4, this work reveals that some of the parameters of AFM nanoindentation do affect the measurements obtained. Firstly, this work revealed that the ability to measure the fracture stress and fracture strain of graphene membranes is highly dependent on the physical capabilities of the AFM set-up used. In this work, the AFM set-up had a limited nanoindentation depth range and thus, in the vast majority of the indented membranes, the maximum indentation depth was not sufficient to induce fracture, thereby making the technique unable to measure graphene's fracture properties.

With regards to the elastic modulus, this work shows that the spring constant of the cantilever used has a significant impact on the elastic modulus measured. For single-layer CVD-grown graphene, it is being reported that stiffer cantilevers with a spring constant of around 54 N/m may lead to overestimation of the elastic modulus, while conversely more flexible cantilevers with spring constants of around 3 N/m underestimate the modulus. As the spring constant is increased, the observed overestimation is further accompanied by significantly larger scatter in the results and associated error.

On the other hand, these trends have not been observed when indenting mechanically exfoliated few-layer and multi-layer graphene membranes. In particular, flexible cantilevers were unable to indent the thicker membranes thereby providing widely differing results. As such, this work attests that the spring constant of an AFM cantilever should be carefully tuned to the material under examination and specifically its mechanical properties. Furthermore, this work reveals that using the large range of spring constants employed by various authors in literature to obtain

a repeatable elastic modulus value for the graphene sample being indented is challenging. Additionally, the observations made in this work suggest that the selection of cantilevers should also be based on graphene membrane geometry, number of layers in the graphene sample, and presence of defects – which would be reflected in a change in stiffness of the membrane.

Furthermore, this work shows that the process of fitting a mathematical model to the obtained force curves once again affects the results. A clear overestimation is revealed when the fit is obtained at lower indentation depths for all AFM probes used. Moreover, this 'skin effect' is more pronounced using stiffer cantilevers. While other works have observed a similar skin effect [64, 156], this phenomenon has not yet been investigated for graphene membranes indented using AFM. Rather, some authors refer to the presence of wrinkles within the graphene membrane which were shown to reduce the elastic stiffness of the graphene, especially at lower indentation depths [83, 86, 150, 154], in direct contrast to the results presented in Chapter 4. Although the CVD-grown graphene membranes used in this work do have some undulations or wrinkles prior to indentation, the findings do not support the proposition that the presence of wrinkles reduces the elastic modulus.

In conclusion, this work highlights the challenges encountered when using nanoindentation via AFM to measure the elastic modulus of graphene membranes. The dependency of the results obtained on the exact methodology adopted point towards the need for an established set of guidelines to be followed such that the results across multiple research groups can be comparable. Similar guidelines are widespread across the heavily-researched material science fields – international standards for measuring particular material properties for a specific set of materials have been established along the years and are used consistently across the respective fields. Being a relatively newly discovered material in the novel nanomaterials field, such guidelines have not yet been established for graphene. To this end, this work attempts at providing a preliminary guideline for AFM testing of SLG membranes of 0.45 μm diameter including the recommended indentation depth of ~25 nm in order to surpass the skin effect. The results also indicate that a Tap190DLC cantilever having the mid-range nominal stiffness of 48 N/m can be reliably used. However, more work needs to be carried out to clearly determine the cantilever spring constant required to produce accurate results.

Research Question 2

How does the introduction of defects in graphene affect its elastic modulus?

Chapter 5 shows how different doses of gallium ion irradiation were used to modify the crystalline structure of single-layer and multi-layer graphene. Raman spectroscopy allowed for an assessment of the extent of damage induced by such irradiation. Primarily, it is reported that multi-layer graphene and supported single-layer graphene experience more induced damage due to ion irradiation than suspended single-layer graphene. This difference in response is attributed to backscattering and sputtering incidents caused by the multiple underlying graphene layers or the underlying substrate that increase the total damage induced in the graphene.

Although successfully characterizing the extent of damage imparted by the ion beam on the graphene membranes, nanoindentation of CVD SLG treated membranes revealed no clear trend as to whether the elastic modulus is affected by the applied treatment when compared to the untreated material. A significant increase in the scatter of the results is reported and is attributed to preferential attack of any pre-existing defects, such as grain boundaries, by the ion irradiation. However, it is noted that the sputtering appears to be mostly inconsequential compared to variation in the results induced by indenting the same membranes using AFM probes having different cantilever stiffnesses. Conversely, when utilising AFM probes with similar spring constants the elastic modulus of a MLG membrane and few CVD SLG membranes were noted to increase appreciably.

Research Question 3

Can molecular dynamic simulations adequately simulate the mechanical behaviour of graphene under nanoindentation?

The ability of a simpler and hence cheaper molecular dynamics force field to simulate graphene under tensile loading has been investigated. This work suggests that the use of a simplified model including the Morse stretching potential, a harmonic potential, a two-fold torsion potential, and a Lennard-Jones intermolecular potential, implemented in the OpenFOAM software within the mdFOAM library, is able to reproduce the mechanical behaviour in graphene in good agreement with literature. However, this model was deemed too expensive to scale-up due to the serial computation limitation offered by the implementation. Therefore,

it was not suitable to simulate nanoindentation of circular graphene membranes due to the larger number of atoms required.

As such, the AIREBO force field was used as the state-of-the-art graphene model, and was implemented in LAMMPS, which allows for parallel-processing and thereby overall more economical simulations on high performance computers. The MD simulations run confirm that, with the appropriate scaling, the force curves are in very good agreement with the force curves obtained experimentally via AFM. The similarity extends to the emergence of the skin effect discussed earlier at relatively small indentation depths. Furthermore, it is shown that the entire force curve up to failure does not reach a dominant cubic behaviour. As such, the elastic modulus cannot be accurately obtained from a cubic function fitted force curve.

Upon comparison of the force curves obtained experimentally via AFM to those obtained via MD simulation, it can be concluded that in order for the mathematical model used (Equation 2.1) to be adequately used to obtain the elastic modulus of the graphene membrane, the radius of the membrane has to be large enough to allow larger indentation depths up to failure and thus, for the cubic relationship between the force applied and the indentation depth to be pronounced.

7.1 FUTURE WORK

The conclusions outlined in this chapter necessarily highlight the scope for continued research work. In particular, the need to further investigate the suitability of AFM nanoindentation using a broader range of methodology variants is apparent. Other testing methodologies employed to measure the mechanical properties of graphene can also be further explored to establish a reliable and repeatable testing routine.

Furthermore, it is apparent that further investigation of the effect of ion bombardment on the elastic modulus of graphene is required. Such research can be followed by exploring the use of other energetic particles such as electrons, helium ions or oxygen plasma, or entirely other different treatment routes, such as chemical etching or variation in the growth parameters, to impart controlled defects in the crystalline lattice of graphene. The applicability of the emerging nanoporous graphene for filtration membranes can then be explored. Work on this has already been started by the author whereby the combined use of scanning electron microscopy coupled by chemical etching is being explored. Preliminary work on devising a

suitable method which allows for testing the ability of the treated graphene membranes to filter out contaminants has also been initiated.

Finally, the synthesis of three-dimensional networks of graphene to produce highly porous structures is also of interest and merits attention. Such graphene networks will possess ultra-low densities, thermal and electrical conductivity, and ultra-high specific surface areas. With the combination of these properties, these graphene networks can be used in oil sorption or filtration membranes, energy storage and energy conversion devices, and bioelectronics.

REFERENCES

[1] M. Fréchette, I. Preda, R. Veillette, and P. Moraille, "AFM as a tool for probing HV insulation systems involving nanodielectrics."

[2] K. Xu, P. Cao, and J. R. Heath, "Graphene visualizes the first water adlayers on mica at ambient conditions," *Science,* vol. 329, no. 5996, pp. 1188-1191, 2010.

[3] K. S. Novoselov and A. H. C. Neto, "Two-dimensional crystals-based heterostructures: materials with tailored properties," *Physica Scripta,* vol. 2012, no. T146, p. 014006, 2012.

[4] F. Banhart, J. Kotakoski, and A. V. Krasheninnikov, "Structural defects in graphene," *ACS nano,* vol. 5, no. 1, pp. 26-41, 2010.

[5] O. V. Yazyev and S. G. Louie, "Topological defects in graphene: Dislocations and grain boundaries," *Physical Review B,* vol. 81, no. 19, p. 195420, 2010.

[6] K. Novoselov *et al.*, "Two-dimensional atomic crystals," *Proceedings of the National Academy of Sciences,* vol. 102, no. 30, pp. 10451-10453, 2005.

[7] A. K. Geim and K. S. Novoselov, "The rise of graphene," in *Nanoscience and Technology: A Collection of Reviews from Nature Journals*: World Scientific, 2010, pp. 11-19.

[8] K. S. Novoselov *et al.*, "Electric field effect in atomically thin carbon films," *science,* vol. 306, no. 5696, pp. 666-669, 2004.

[9] K. S. Novoselov *et al.*, "Two-dimensional gas of massless Dirac fermions in graphene," *nature,* vol. 438, no. 7065, pp. 197-200, 2005.

[10] A. A. Balandin *et al.*, "Superior Thermal Conductivity of Single-Layer Graphene," *Nano Letters,* vol. 8, no. 3, pp. 902-907, 2008/03/01 2008.

[11] M. Freitag *et al.*, "Energy dissipation in graphene field-effect transistors," *Nano letters,* vol. 9, no. 5, pp. 1883-1888, 2009.

[12] D. Boukhvalov and M. Katsnelson, "Chemical functionalization of graphene with defects," *Nano letters,* vol. 8, no. 12, pp. 4373-4379, 2008.

[13] C. Lee, X. Wei, J. W. Kysar, and J. Hone, "Measurement of the Elastic Properties and Intrinsic Strength of Monolayer Graphene," *Science,* vol. 321, no. 5887, pp. 385-388, July 18, 2008 2008.

[14] (2018). *Graphene Flagship*. Available: http://graphene-flagship.eu

[15] P. R. Wallace, "The Band Theory of Graphite," *Physical Review,* vol. 71, no. 9, pp. 622-634, 05/01/ 1947.

[16] J. C. Slonczewski and P. R. Weiss, "Band Structure of Graphite," *Physical Review,* vol. 109, no. 2, pp. 272-279, 01/15/ 1958.

[17] N. D. Mermin, "Crystalline order in two dimensions," *Physical Review,* vol. 176, no. 1, p. 250, 1968.

[18] E. Fradkin, "Critical behavior of disordered degenerate semiconductors. II. Spectrum and transport properties in mean-field theory," *Physical Review B,* vol. 33, no. 5, pp. 3263-3268, 03/01/ 1986.

[19] The Royal Swedish Academy of Sciences, "Nobel Prize in Physics for 2010," ed. NobelPrize.org: Nobel Media AB 2018, 2018.

[20] C. Lee *et al.*, "Frictional Characteristics of Atomically Thin Sheets," *Science,* vol. 328, no. 5974, pp. 76-80, April 2, 2010 2010.

[21] P. Rivero, C. M. Horvath, Z. Zhu, J. Guan, D. Tománek, and S. Barraza-Lopez, "Simulated scanning tunneling microscopy images of few-layer-phosphorus capped by

graphene and hexagonal boron nitride monolayers," *Physical Review B,* vol. 91, no. 11, 2015.

[22] J. S. Bunch *et al.*, "Impermeable Atomic Membranes from Graphene Sheets," *Nano Letters,* vol. 8, no. 8, pp. 2458-2462, 2008/08/01 2008.

[23] C. Sun *et al.*, "Mechanisms of Molecular Permeation through Nanoporous Graphene Membranes," *Langmuir,* vol. 30, no. 2, pp. 675-682, 2014/01/21 2013.

[24] H. Zhao, K. Min, and N. Aluru, "Size and chirality dependent elastic properties of graphene nanoribbons under uniaxial tension," *Nano letters,* vol. 9, no. 8, pp. 3012-3015, 2009.

[25] A. Agius Anastasi, K. Ritos, G. Cassar, and M. K. Borg, "Mechanical properties of pristine and nanoporous graphene," *Molecular Simulation,* vol. 42, no. 18, pp. 1502-1511, 2016.

[26] S. Kiselev and E. Zhirov, "Molecular dynamics simulation of deformation and fracture of graphene under uniaxial tension," *Physical Mesomechanics,* vol. 16, no. 2, pp. 125-132, 2013.

[27] K. Min and N. Aluru, "Mechanical properties of graphene under shear deformation," *Applied Physics Letters,* vol. 98, no. 1, p. 013113, 2011.

[28] M. Dewapriya, R. Rajapakse, and A. S. Phani, "Molecular dynamics simulation of fracture of graphene," in *ICF13*, 2013.

[29] R. Ansari, B. Motevalli, A. Montazeri, and S. Ajori, "Fracture analysis of monolayer graphene sheets with double vacancy defects via MD simulation," *Solid State Communications,* vol. 151, no. 17, pp. 1141-1146, 2011.

[30] J. Zhu, M. He, and F. Qiu, "Effect of vacancy defects on the Young's modulus and fracture strength of graphene: a molecular dynamics study," *Chinese Journal of Chemistry,* vol. 30, no. 7, pp. 1399-1404, 2012.

[31] D. W. Kim, Y. H. Kim, H. S. Jeong, and H.-T. Jung, "Direct visualization of large-area graphene domains and boundaries by optical birefringency," *Nature nanotechnology,* vol. 7, no. 1, pp. 29-34, 2012.

[32] A. W. Robertson *et al.*, "Spatial control of defect creation in graphene at the nanoscale," *Nature communications,* vol. 3, p. 1144, 2012.

[33] A. Zandiatashbar *et al.*, "Effect of defects on the intrinsic strength and stiffness of graphene," *Nature communications,* vol. 5, p. 3186, 2014.

[34] M. Wang, C. Yan, L. Ma, N. Hu, and M. Chen, "Effect of defects on fracture strength of graphene sheets," *Computational Materials Science,* vol. 54, pp. 236-239, 2012.

[35] L. Xu, N. Wei, and Y. Zheng, "Mechanical properties of highly defective graphene: from brittle rupture to ductile fracture," *Nanotechnology,* vol. 24, no. 50, p. 505703, 2013.

[36] K. Celebi *et al.*, "Ultimate Permeation Across Atomically Thin Porous Graphene," *Science,* vol. 344, no. 6181, pp. 289-292, 2014.

[37] S. P. Surwade *et al.*, "Water desalination using nanoporous single-layer graphene," *Nature nanotechnology,* vol. 10, no. 5, pp. 459-464, 2015.

[38] D. C. Bell, M. C. Lemme, L. A. Stern, J. R. Williams, and C. M. Marcus, "Precision cutting and patterning of graphene with helium ions," *Nanotechnology,* vol. 20, no. 45, p. 455301, 2009.

[39] "First graphene-based flexible display produced," 5 Sep 2014. Available: https://www.cam.ac.uk/research/news/first-graphene-based-flexible-display-produced

[40] T.-H. Han *et al.*, "Extremely efficient flexible organic light-emitting diodes with modified graphene anode," *Nat Photon,* 10.1038/nphoton.2011.318 vol. 6, no. 2, pp. 105-110, 02//print 2012.

[41] A. Vaidyanathan, M. Mathew, S. Radhakrishnan, C. S. Rout, and B. Chakraborty, "Theoretical Insight on the Biosensing Applications of 2D Materials," *The Journal of Physical Chemistry B,* 2020/11/24 2020.
[42] G. Seo *et al.*, "Rapid Detection of COVID-19 Causative Virus (SARS-CoV-2) in Human Nasopharyngeal Swab Specimens Using Field-Effect Transistor-Based Biosensor," *ACS Nano,* vol. 14, no. 4, pp. 5135-5142, 2020/04/28 2020.
[43] M. Shokrieh, M. Hosseinkhani, M. Naimi-Jamal, and H. Tourani, "Nanoindentation and nanoscratch investigations on graphene-based nanocomposites," *Polymer Testing,* vol. 32, no. 1, pp. 45-51, 2013.
[44] M. A. Rafiee *et al.*, "Fracture and fatigue in graphene nanocomposites," *small,* vol. 6, no. 2, pp. 179-183, 2010.
[45] J.-H. Lee, P. E. Loya, J. Lou, and E. L. Thomas, "Dynamic mechanical behavior of multilayer graphene via supersonic projectile penetration," *Science,* vol. 346, no. 6213, pp. 1092-1096, 2014.
[46] K. D. Humfeld, "Graphene-augmented composite materials," ed: Google Patents, 2016.
[47] R. Atkinson, "University's Graphene Endeavours Rewarded with Partnership," 06/12/2018. Available: https://www.uclan.ac.uk/news/graphene-rewarded-with-partnership.php
[48] D. Cohen-Tanugi and J. C. Grossman, "Water desalination across nanoporous graphene," *Nano letters,* vol. 12, no. 7, pp. 3602-3608, 2012.
[49] J. M. Tour, "Top-down versus bottom-up fabrication of graphene-based electronics," *Chemistry of Materials,* vol. 26, no. 1, pp. 163-171, 2013.
[50] E. S. Agudosi, E. C. Abdullah, A. Numan, N. M. Mubarak, M. Khalid, and N. Omar, "A Review of the Graphene Synthesis Routes and its Applications in Electrochemical Energy Storage," *Critical Reviews in Solid State and Materials Sciences,* pp. 1-39, 2019.
[51] J. S. Bunch *et al.*, "Electromechanical resonators from graphene sheets," *Science,* vol. 315, no. 5811, pp. 490-493, 2007.
[52] I. Frank, D. M. Tanenbaum, A. Van der Zande, and P. L. McEuen, "Mechanical properties of suspended graphene sheets," *Journal of Vacuum Science & Technology B,* vol. 25, no. 6, pp. 2558-2561, 2007.
[53] D. Yoon *et al.*, "Interference effect on Raman spectrum of graphene on SiO2/Si," *Physical Review B,* vol. 80, no. 12, p. 125422, 09/23/ 2009.
[54] G. Compagnini, F. Giannazzo, S. Sonde, V. Raineri, and E. Rimini, "Ion irradiation and defect formation in single layer graphene," *Carbon,* vol. 47, no. 14, pp. 3201-3207, 2009.
[55] I. Childres *et al.*, "Effect of electron-beam irradiation on graphene field effect devices," *Applied Physics Letters,* vol. 97, no. 17, p. 173109, 2010.
[56] S. Hang, Z. Moktadir, and H. Mizuta, "Raman study of damage extent in graphene nanostructures carved by high energy helium ion beam," *Carbon,* vol. 72, no. Supplement C, pp. 233-241, 2014.
[57] M. M. Lucchese *et al.*, "Quantifying ion-induced defects and Raman relaxation length in graphene," *Carbon,* vol. 48, no. 5, pp. 1592-1597, 2010.
[58] L. G. Cançado *et al.*, "Quantifying Defects in Graphene via Raman Spectroscopy at Different Excitation Energies," *Nano Letters,* vol. 11, no. 8, pp. 3190-3196, 2011.
[59] M. Poot and H. S. van der Zant, "Nanomechanical properties of few-layer graphene membranes," *Applied Physics Letters,* vol. 92, no. 6, p. 063111, 2008.
[60] M. Annamalai, S. Mathew, M. Jamali, D. Zhan, and M. Palaniapan, "Elastic and nonlinear response of nanomechanical graphene devices," *Journal of Micromechanics and Microengineering,* vol. 22, no. 10, p. 105024, 2012.

[61] G. López-Polín *et al.*, "Increasing the elastic modulus of graphene by controlled defect creation," *Nature Physics,* vol. 11, no. 1, pp. 26-31, 2015.
[62] G. López-Polín, J. Gómez-Herrero, and C. Gómez-Navarro, "Confining Crack Propagation in Defective Graphene," *Nano letters,* vol. 15, no. 3, pp. 2050-2054, 2015.
[63] K. Liu *et al.*, "Self-passivation of defects: effects of high-energy particle irradiation on the elastic modulus of multilayer graphene," *Advanced Materials,* vol. 27, no. 43, pp. 6841-6847, 2015.
[64] G. López-Polín, M. Jaafar, F. Guinea, R. Roldán, C. Gómez-Navarro, and J. Gómez-Herrero, "The influence of strain on the elastic constants of graphene," *Carbon,* vol. 124, pp. 42-48, 2017.
[65] E. Stolyarova *et al.*, "High-resolution scanning tunneling microscopy imaging of mesoscopic graphene sheets on an insulating surface," *Proceedings of the National Academy of Sciences,* vol. 104, no. 22, pp. 9209-9212, 2007.
[66] S. P. Koenig, L. Wang, J. Pellegrino, and J. S. Bunch, "Selective molecular sieving through porous graphene," *Nature nanotechnology,* vol. 7, no. 11, p. 728, 2012.
[67] X. Z. Liu, Q. Li, P. Egberts, and R. W. Carpick, "Nanoscale adhesive properties of graphene: The effect of sliding history," *Advanced Materials Interfaces,* vol. 1, no. 2, 2014.
[68] Y.-B. Zhou *et al.*, "Ion irradiation induced structural and electrical transition in graphene," *The Journal of Chemical Physics,* vol. 133, no. 23, p. 234703, 2010.
[69] P. Blake *et al.*, "Making graphene visible," *Applied Physics Letters,* vol. 91, no. 6, p. 063124, 2007.
[70] T. Kim, "Large-Scale Assembly of Aligned Graphene Nanoribbons with Sub 30-nm Width," *Journal of the Korean Chemical Society,* vol. 58, no. 6, 2014.
[71] A. Castellanos-Gomez *et al.*, "Mechanical properties of freely suspended atomically thin dielectric layers of mica," *Nano Research,* vol. 5, no. 8, pp. 550-557, 2012.
[72] A. Castellanos-Gomez, M. Poot, G. A. Steele, H. S. van der Zant, N. Agraït, and G. Rubio-Bollinger, "Elastic properties of freely suspended MoS2 nanosheets," *Advanced Materials,* vol. 24, no. 6, pp. 772-775, 2012.
[73] A. Castellanos-Gomez, M. Poot, G. A. Steele, H. S. Van der Zant, N. Agraït, and G. Rubio-Bollinger, "Mechanical properties of freely suspended semiconducting graphene-like layers based on MoS 2," *Nanoscale research letters,* vol. 7, no. 1, p. 233, 2012.
[74] X. Li *et al.*, "Large-area synthesis of high-quality and uniform graphene films on copper foils," *science,* vol. 324, no. 5932, pp. 1312-1314, 2009.
[75] L. Ci *et al.*, "Atomic layers of hybridized boron nitride and graphene domains," *Nature materials,* vol. 9, no. 5, p. 430, 2010.
[76] S. Banerjee *et al.*, "Electrochemistry at the Edge of a Single Graphene Layer in a Nanopore," *ACS nano,* vol. 7, no. 1, pp. 834-843, 2012.
[77] P. Egberts, G. H. Han, X. Z. Liu, A. T. C. Johnson, and R. W. Carpick, "Frictional Behavior of Atomically Thin Sheets: Hexagonal-Shaped Graphene Islands Grown on Copper by Chemical Vapor Deposition," *ACS Nano,* vol. 8, no. 5, pp. 5010-5021, 2014/05/27 2014.
[78] C. Jia, J. Jiang, L. Gan, and X. Guo, "Direct Optical Characterization of Graphene Growth and Domains on Growth Substrates," *Scientific Reports,* vol. 2, no. 1, p. 707, 2012/10/04 2012.
[79] S. D. Costa *et al.*, "Resonant Raman spectroscopy of graphene grown on copper substrates," *Solid State Communications,* vol. 152, no. 15, pp. 1317-1320, 2012/08/01/ 2012.

[80] D. Fox *et al.*, "Helium ion microscopy of graphene: beam damage, image quality and edge contrast," *Nanotechnology,* vol. 24, no. 33, p. 335702, 2013.
[81] P. Y. Huang *et al.*, "Grains and grain boundaries in single-layer graphene atomic patchwork quilts," *Nature,* vol. 469, no. 7330, p. 389, 2011.
[82] G.-H. Lee *et al.*, "High-Strength Chemical-Vapor–Deposited Graphene and Grain Boundaries," *Science,* vol. 340, no. 6136, pp. 1073-1076, 2013.
[83] Q.-Y. Lin *et al.*, "Stretch-induced stiffness enhancement of graphene grown by chemical vapor deposition," *ACS Nano,* vol. 7, no. 2, pp. 1171-1177, 2013.
[84] J. H. Kim *et al.*, "No Tilt Angle Dependence of Grain Boundary on Mechanical Strength of Chemically Deposited Graphene Film," *Journal of the Korean Ceramic Society,* vol. 56, no. 5, pp. 506-512, 2019.
[85] V. Kochat *et al.*, "High contrast imaging and thickness determination of graphene with in-column secondary electron microscopy," *Journal of Applied Physics,* vol. 110, no. 1, p. 014315, 2011.
[86] C. S. Ruiz-Vargas *et al.*, "Softened elastic response and unzipping in chemical vapor deposition graphene membranes," *Nano letters,* vol. 11, no. 6, pp. 2259-2263, 2011.
[87] A. Martínez-Galera, I. Brihuega, A. Gutiérrez-Rubio, T. Stauber, and J. Gómez-Rodríguez, "Towards scalable nano-engineering of graphene," *Scientific reports,* vol. 4, 2014.
[88] Y. S. Park *et al.*, "Quasi-Free-Standing Graphene Monolayer on a Ni Crystal through Spontaneous Na Intercalation," *Physical Review X,* vol. 4, no. 3, p. 031016, 2014.
[89] P. Stojanov, E. Voloshina, Y. Dedkov, S. Schmitt, T. Haenke, and A. Thissen, "Graphene on Rh (111): combined DFT, STM, and NC-AFM studies," *Procedia Engineering,* vol. 93, pp. 8-16, 2014.
[90] C. Struzzi *et al.*, "High-quality graphene on single crystal Ir (111) films on Si (111) wafers: Synthesis and multi-spectroscopic characterization," *Carbon,* vol. 81, pp. 167-173, 2015.
[91] L. Zhao *et al.*, "Influence of copper crystal surface on the CVD growth of large area monolayer graphene," *Solid State Communications,* vol. 151, no. 7, pp. 509-513, 2011/04/01/ 2011.
[92] Z. Zhen, X. Li, and H. Zhu, "Synthesis of two dimensional materials on extremely clean surfaces," *Nano Today,* vol. 22, pp. 7-9, 2018.
[93] D. Lee *et al.*, "Significant enhancement of the electrical transport properties of graphene films by controlling the surface roughness of Cu foils before and during chemical vapor deposition," *Nanoscale,* vol. 6, no. 21, pp. 12943-12951, 2014.
[94] B. Huet, J.-P. Raskin, D. W. Snyder, and J. M. Redwing, "Fundamental limitations in transferred CVD graphene caused by Cu catalyst surface morphology," *Carbon,* vol. 163, pp. 95-104, 2020/08/15/ 2020.
[95] X. Li, L. Colombo, and R. S. Ruoff, "Synthesis of Graphene Films on Copper Foils by Chemical Vapor Deposition," *Advanced Materials,* vol. 28, no. 29, pp. 6247-6252, 2016.
[96] X. Li *et al.*, "Graphene films with large domain size by a two-step chemical vapor deposition process," *Nano letters,* vol. 10, no. 11, pp. 4328-4334, 2010.
[97] H. Kim *et al.*, "Activation energy paths for graphene nucleation and growth on Cu," *ACS nano,* vol. 6, no. 4, pp. 3614-3623, 2012.
[98] S.-H. Chan, S.-H. Chen, W.-T. Lin, M.-C. Li, Y.-C. Lin, and C.-C. Kuo, "Low-temperature synthesis of graphene on Cu using plasma-assisted thermal chemical vapor deposition," *Nanoscale research letters,* vol. 8, no. 1, p. 285, 2013.
[99] Graphenea Semiconductor SLU. (2019, 22/02/2019). *Easy Transfer: Monolayer Graphene on Polymer Film*. Available: https://www.graphenea.com/collections/buy-

graphene-films/products/easy-transfer-monolayer-graphene-on-polymer-film-1-cm-x-1-cm?variant=51789965715

[100] W. S. Hummers Jr and R. E. Offeman, "Preparation of graphitic oxide," *Journal of the American Chemical Society,* vol. 80, no. 6, pp. 1339-1339, 1958.

[101] F. Tavakoli, M. Salavati-Niasari, and F. Mohandes, "Green synthesis and characterization of graphene nanosheets," *Materials Research Bulletin,* vol. 63, pp. 51-57, 2015.

[102] Y. Si and E. T. Samulski, "Synthesis of water soluble graphene," *Nano letters,* vol. 8, no. 6, pp. 1679-1682, 2008.

[103] M. Hu and B. Mi, "Enabling graphene oxide nanosheets as water separation membranes," *Environmental science & technology,* vol. 47, no. 8, pp. 3715-3723, 2013.

[104] C. Gómez-Navarro, M. Burghard, and K. Kern, "Elastic properties of chemically derived single graphene sheets," *Nano letters,* vol. 8, no. 7, pp. 2045-2049, 2008.

[105] S. Stankovich *et al.*, "Synthesis of graphene-based nanosheets via chemical reduction of exfoliated graphite oxide," *carbon,* vol. 45, no. 7, pp. 1558-1565, 2007.

[106] V. Singh, D. Joung, L. Zhai, S. Das, S. I. Khondaker, and S. Seal, "Graphene based materials: past, present and future," *Progress in materials science,* vol. 56, no. 8, pp. 1178-1271, 2011.

[107] Y. Su, V. Kravets, S. Wong, J. Waters, A. Geim, and R. Nair, "Impermeable Barrier Films and Protective Coatings Based on Reduced Graphene Oxide," *arXiv preprint arXiv:1405.2360,* 2014.

[108] K. R. Paton *et al.*, "Scalable production of large quantities of defect-free few-layer graphene by shear exfoliation in liquids," *Nature materials,* vol. 13, no. 6, p. 624, 2014.

[109] C. Berger *et al.*, "Electronic Confinement and Coherence in Patterned Epitaxial Graphene," *Science,* vol. 312, no. 5777, pp. 1191-1196, May 26, 2006 2006.

[110] G. Rutter *et al.*, "Imaging the interface of epitaxial graphene with silicon carbide via scanning tunneling microscopy," *Physical Review B,* vol. 76, no. 23, p. 235416, 2007.

[111] L. B. Biedermann, M. L. Bolen, M. A. Capano, D. Zemlyanov, and R. G. Reifenberger, "Insights into few-layer epitaxial graphene growth on 4 H-SiC (000 1^{-}) substrates from STM studies," *Physical Review B,* vol. 79, no. 12, p. 125411, 2009.

[112] R. Yakimova *et al.*, "Analysis of the formation conditions for large area epitaxial graphene on SiC substrates," in *Materials Science Forum*, 2010, vol. 645, pp. 565-568: Trans Tech Publ.

[113] T. Burnett, R. Yakimova, and O. Kazakova, "Mapping of local electrical properties in epitaxial graphene using electrostatic force microscopy," *Nano letters,* vol. 11, no. 6, pp. 2324-2328, 2011.

[114] S. Tongay, M. Lemaitre, J. Fridmann, A. Hebard, B. Gila, and B. Appleton, "Drawing graphene nanoribbons on SiC by ion implantation," *Applied Physics Letters,* vol. 100, no. 7, p. 073501, 2012.

[115] G. López-Polín *et al.*, "Tailoring the thermal expansion of graphene via controlled defect creation," *Carbon,* vol. 116, pp. 670-677, 2017.

[116] C. Herbig *et al.*, "Interfacial Carbon Nanoplatelet Formation by Ion Irradiation of Graphene on Ir (111)," *ACS nano,* 2014.

[117] C. Lee, X. Wei, Q. Li, R. Carpick, J. W. Kysar, and J. Hone, "Elastic and frictional properties of graphene," *physica status solidi (b),* vol. 246, no. 11-12, pp. 2562-2567, 2009.

[118] Z. Deng, N. N. Klimov, S. D. Solares, T. Li, H. Xu, and R. J. Cannara, "Nanoscale Interfacial Friction and Adhesion on Supported versus Suspended Monolayer and Multilayer Graphene," *Langmuir,* vol. 29, no. 1, pp. 235-243, 2013/01/08 2013.

[119] D. H. Lee, M. J. Lee, Y. S. Kim, J. S. Choi, and B. H. Park, "Sample rotation angle dependence of graphene thickness measured using atomic force microscope," *Carbon,* vol. 81, pp. 210-215, 2015.
[120] D. L. Duong *et al.*, "Probing graphene grain boundaries with optical microscopy," *Nature,* vol. 490, no. 7419, pp. 235-239, 2012/10/01 2012.
[121] D. McMullan, "Scanning electron microscopy 1928–1965," *Scanning,* vol. 17, no. 3, pp. 175-185, 1995.
[122] M. Wall, "The Raman spectroscopy of graphene and the determination of layer thickness," *Madison, WI Thermo Fisher Scientific* 2011.
[123] A. C. Ferrari *et al.*, "Raman Spectrum of Graphene and Graphene Layers," *Physical Review Letters,* vol. 97, no. 18, p. 187401, 2006.
[124] Z. Ni, Y. Wang, T. Yu, and Z. Shen, "Raman spectroscopy and imaging of graphene," *Nano Research,* vol. 1, no. 4, pp. 273-291, 2008.
[125] A. C. Ferrari, "Raman spectroscopy of graphene and graphite: Disorder, electron–phonon coupling, doping and nonadiabatic effects," *Solid State Communications,* vol. 143, no. 1–2, pp. 47-57, 7// 2007.
[126] A. C. Ferrari and D. M. Basko, "Raman spectroscopy as a versatile tool for studying the properties of graphene," *Nature Nanotechnology,* Review Article vol. 8, p. 235, 2013.
[127] A. Eckmann *et al.*, "Probing the nature of defects in graphene by Raman spectroscopy," *Nano letters,* vol. 12, no. 8, pp. 3925-3930, 2012.
[128] E. M. Ferreira *et al.*, "Evolution of the Raman spectra from single-, few-, and many-layer graphene with increasing disorder," *Physical Review B,* vol. 82, no. 12, p. 125429, 2010.
[129] I. Childres, L. A. Jauregui, W. Park, H. Cao, and Y. P. Chen, "Raman spectroscopy of graphene and related materials," *New developments in photon and materials research,* vol. 1, 2013.
[130] H. Wang, Y. Wang, X. Cao, M. Feng, and G. Lan, "Vibrational properties of graphene and graphene layers," *Journal of Raman Spectroscopy: An International Journal for Original Work in all Aspects of Raman Spectroscopy, Including Higher Order Processes, and also Brillouin and Rayleigh Scattering,* vol. 40, no. 12, pp. 1791-1796, 2009.
[131] J. Song, T. Y. Ko, and S. Ryu, "Raman spectroscopy study of annealing-induced effects on graphene prepared by micromechanical exfoliation," *Bulletin of the Korean Chemical Society,* vol. 31, no. 9, pp. 2679-2682, 2010 2010.
[132] J. Hong, M. K. Park, E. J. Lee, D. Lee, D. S. Hwang, and S. Ryu, "Origin of New Broad Raman D and G Peaks in Annealed Graphene," *Scientific Reports,* vol. 3, p. 2700, 2013.
[133] K. N. Kudin, B. Ozbas, H. C. Schniepp, R. K. Prud'homme, I. A. Aksay, and R. Car, "Raman Spectra of Graphite Oxide and Functionalized Graphene Sheets," *Nano Letters,* vol. 8, no. 1, pp. 36-41, 2008.
[134] A. Felten *et al.*, "Single- and Double-Sided Chemical Functionalization of Bilayer Graphene," *Small,* vol. 9, no. 4, pp. 631-639, 2013.
[135] J. W. Suk, R. D. Piner, J. An, and R. S. Ruoff, "Mechanical properties of monolayer graphene oxide," *ACS nano,* vol. 4, no. 11, pp. 6557-6564, 2010.
[136] A. Turchanin *et al.*, "One nanometer thin carbon nanosheets with tunable conductivity and stiffness," *Advanced Materials,* vol. 21, no. 12, pp. 1233-1237, 2009.
[137] J. W. Suk, S. Murali, J. An, and R. S. Ruoff, "Mechanical measurements of ultra-thin amorphous carbon membranes using scanning atomic force microscopy," *Carbon,* vol. 50, no. 6, pp. 2220-2225, 2012.

[138] D. Yang *et al.*, "Chemical analysis of graphene oxide films after heat and chemical treatments by X-ray photoelectron and Micro-Raman spectroscopy," *Carbon,* vol. 47, no. 1, pp. 145-152, 2009/01/01/ 2009.
[139] A. Eckmann, A. Felten, I. Verzhbitskiy, R. Davey, and C. Casiraghi, "Raman study on defective graphene: Effect of the excitation energy, type, and amount of defects," *Physical Review B,* vol. 88, no. 3, p. 035426, 2013.
[140] O. Lehtinen, J. Kotakoski, A. V. Krasheninnikov, and J. Keinonen, "Cutting and controlled modification of graphene with ion beams," *Nanotechnology,* vol. 22, no. 17, p. 175306, 2011.
[141] V. Geringer *et al.*, "Intrinsic and extrinsic corrugation of monolayer graphene deposited on SiO 2," *Physical review letters,* vol. 102, no. 7, p. 076102, 2009.
[142] N. Rubio *et al.*, "Production of Water-Soluble Few-Layer Graphene Mesosheets by Dry Milling with Hydrophobic Drug," *Langmuir,* vol. 30, no. 49, pp. 14999-15008, 2014.
[143] H. C. Schniepp *et al.*, "Bending properties of single functionalized graphene sheets probed by atomic force microscopy," *ACS nano,* vol. 2, no. 12, pp. 2577-2584, 2008.
[144] Y. Zhang and C. Pan, "Measurements of mechanical properties and number of layers of graphene from nano-indentation," *Diamond and Related Materials,* vol. 24, no. 0, pp. 1-5, 4// 2012.
[145] S. Koch *et al.*, "Elastic Response of Graphene Nanodomes," *ACS Nano,* vol. 7, no. 4, pp. 2927-2934, 2013.
[146] S. Shivaraman *et al.*, "Free-Standing Epitaxial Graphene," *Nano Letters,* vol. 9, no. 9, pp. 3100-3105, 2009/09/09 2009.
[147] X. Tan, J. Wu, K. Zhang, X. Peng, L. Sun, and J. Zhong, "Nanoindentation models and Young's modulus of monolayer graphene: A molecular dynamics study," *Applied Physics Letters,* vol. 102, no. 7, pp. -, 2013.
[148] W. Wang, S. Li, J. Min, C. Yi, Y. Zhan, and M. Li, "Nanoindentation experiments for single-layer rectangular graphene films: a molecular dynamics study," (in English), *Nanoscale Research Letters,* vol. 9, no. 1, pp. 1-8, 2014/01/22 2014, Art. no. 41.
[149] N. Clark, A. Oikonomou, and A. Vijayaraghavan, "Ultrafast quantitative nanomechanical mapping of suspended graphene," *Physica Status Solidi (B),* vol. 250, no. 12, pp. 2672-2677, 2013.
[150] C. Cao, M. Daly, C. V. Singh, Y. Sun, and T. Filleter, "High strength measurement of monolayer graphene oxide," *Carbon,* vol. 81, pp. 497-504, 2015.
[151] I. R. Storch *et al.*, "Young's modulus and thermal expansion of tensioned graphene membranes," *Physical Review B,* vol. 98, no. 8, p. 085408, 2018.
[152] E. Khestanova, F. Guinea, L. Fumagalli, A. Geim, and I. Grigorieva, "Universal shape and pressure inside bubbles appearing in van der Waals heterostructures," *Nature communications,* vol. 7, p. 12587, 2016.
[153] O. Frank, J. Vejpravova, V. Holy, L. Kavan, and M. Kalbac, "Interaction between graphene and copper substrate: The role of lattice orientation," *Carbon,* vol. 68, no. Supplement C, pp. 440-451, 2014.
[154] R. J. Nicholl *et al.*, "The effect of intrinsic crumpling on the mechanics of free-standing graphene," *Nature communications,* vol. 6, p. 8789, 2015.
[155] M. Heuberger, G. Dietler, and L. Schlapbach, "Mapping the local Young's modulus by analysis of the elastic deformations occurring in atomic force microscopy," *Nanotechnology,* vol. 6, no. 1, p. 12, 1995.
[156] J. Kámán, R. Huszánk, and A. Bonyár, "Towards more reliable AFM force-curve evaluation: A method for spring constant selection, adaptive lever sensitivity calibration and fitting boundary identification," *Micron,* vol. 125, p. 102717, 2019/10/01/ 2019.

[157] L. Shen, H.-S. Shen, and C.-L. Zhang, "Temperature-dependent elastic properties of single layer graphene sheets," *Materials & Design,* vol. 31, no. 9, pp. 4445-4449, 2010.
[158] Y. Wei, J. Wu, H. Yin, X. Shi, R. Yang, and M. Dresselhaus, "The nature of strength enhancement and weakening by pentagon–heptagon defects in graphene," *Nature materials,* vol. 11, no. 9, p. 759, 2012.
[159] T. Zhang, X. Li, S. Kadkhodaei, and H. Gao, "Flaw insensitive fracture in nanocrystalline graphene," *Nano letters,* vol. 12, no. 9, pp. 4605-4610, 2012.
[160] Z. Yang, Y. Huang, F. Ma, Y. Sun, K. Xu, and P. K. Chu, "Size-dependent deformation behavior of nanocrystalline graphene sheets," *Materials Science and Engineering: B,* 2015.
[161] J. Zhang, T. Ragab, and C. Basaran, "The effects of vacancy defect on the fracture behaviors of zigzag graphene nanoribbons," *International Journal of Damage Mechanics,* vol. 26, no. 4, pp. 608-630, 2017.
[162] Z. D. Sha *et al.*, "On the failure load and mechanism of polycrystalline graphene by nanoindentation," *Scientific Reports,* Article vol. 4, p. 7437, 12/11/online 2014.
[163] W. Li, L. Liang, S. Zhao, S. Zhang, and J. Xue, "Fabrication of nanopores in a graphene sheet with heavy ions: A molecular dynamics study," *Journal of Applied Physics,* vol. 114, no. 23, p. 234304, 2013.
[164] X. Wu, H. Zhao, and J. Pei, "Fabrication of nanopore in graphene by electron and ion beam irradiation: Influence of graphene thickness and substrate," *Computational Materials Science,* vol. 102, pp. 258-266, 2015.
[165] M. Chen, A. M. Christmann, A. R. Muniz, A. Ramasubramaniam, and D. Maroudas, "Molecular-Dynamics Analysis of Nanoindentation of Graphene Nanomeshes: Implications for 2D Mechanical Metamaterials," *ACS Applied Nano Materials,* vol. 3, no. 4, pp. 3613-3624, 2020.
[166] Z. Ni, H. Bu, M. Zou, H. Yi, K. Bi, and Y. Chen, "Anisotropic mechanical properties of graphene sheets from molecular dynamics," *Physica B: Condensed Matter,* vol. 405, no. 5, pp. 1301-1306, 2010.
[167] R. Ansari, S. Ajori, and B. Motevalli, "Mechanical properties of defective single-layered graphene sheets via molecular dynamics simulation," *Superlattices and Microstructures,* vol. 51, no. 2, pp. 274-289, 2012.
[168] M.-Q. Le and R. C. Batra, "Single-edge crack growth in graphene sheets under tension," *Computational Materials Science,* vol. 69, pp. 381-388, 2013.
[169] Y. Zhang, C. Wang, Y. Cheng, and Y. Xiang, "Mechanical properties of bilayer graphene sheets coupled by sp3 bonding," *Carbon,* vol. 49, no. 13, pp. 4511-4517, 2011.
[170] K. I. Tserpes, "Strength of graphenes containing randomly dispersed vacancies," *Acta Mechanica,* vol. 223, no. 4, pp. 669-678, 2012.
[171] H. Zhang, Z. Duan, X. Zhang, C. Liu, J. Zhang, and J. Zhao, "Strength and fracture behavior of graphene grain boundaries: effects of temperature, inflection, and symmetry from molecular dynamics," *Physical Chemistry Chemical Physics,* vol. 15, no. 28, pp. 11794-11799, 2013.
[172] C. Wong and V. Vijayaraghavan, "Nanomechanics of free form and water submerged single layer graphene sheet under axial tension by using molecular dynamics simulation," *Materials Science and Engineering: A,* vol. 556, pp. 420-428, 2012.
[173] V. Vijayaraghavan and C. Wong, "Tensile loading characteristics of free-form and water submerged single layer graphene sheet," in *Nanotechnology (IEEE-NANO), 2012 12th IEEE Conference on*, 2012, pp. 1-4: IEEE.
[174] Y. I. Jhon, Y. M. Jhon, G. Y. Yeom, and M. S. Jhon, "Orientation dependence of the fracture behavior of graphene," *Carbon,* vol. 66, pp. 619-628, 2014.

[175] M. Dewapriya, A. S. Phani, and R. Rajapakse, "Influence of temperature and free edges on the mechanical properties of graphene," *Modelling and Simulation in Materials Science and Engineering,* vol. 21, no. 6, p. 065017, 2013.
[176] H. Zhao and N. Aluru, "Temperature and strain-rate dependent fracture strength of graphene," *Journal of Applied Physics,* vol. 108, no. 6, p. 064321, 2010.
[177] T. Shao, B. Wen, R. Melnik, S. Yao, Y. Kawazoe, and Y. Tian, "Temperature dependent elastic constants and ultimate strength of graphene and graphyne," *The Journal of chemical physics,* vol. 137, no. 19, p. 194901, 2012.
[178] S. Thomas and K. Ajith, "Molecular dynamics simulation of the thermo-mechanical properties of monolayer graphene sheet," *Procedia Materials Science,* vol. 5, pp. 489-498, 2014.
[179] A. Ito and S. Okamoto, "Molecular dynamics analysis on effects of vacancies upon mechanical properties of graphene and graphite," *Engineering Letters,* vol. 20, no. 3, pp. 271-278, 2012.
[180] M. Dewapriya, R. Rajapakse, and A. Phani, "Atomistic and continuum modelling of temperature-dependent fracture of graphene," *International Journal of Fracture,* vol. 187, no. 2, pp. 199-212, 2014.
[181] T. Zhang, X. Li, and H. Gao, "Fracture of graphene: a review," (in English), *International Journal of Fracture,* pp. 1-31, 2015/08/21 2015.
[182] K. Kim *et al.*, "Ripping graphene: preferred directions," *Nano letters,* vol. 12, no. 1, pp. 293-297, 2011.
[183] K. M. Fair, M. D. Arnold, and M. J. Ford, "Determination of the elastic properties of graphene by indentation and the validity of classical models of indentation," *Journal of Physics: Condensed Matter,* vol. 26, no. 1, p. 015307, 2014.
[184] M. Neek-Amal and R. Asgari, "Nano-indentation of circular graphene flakes," *arXiv preprint arXiv:0903.5035,* 2009.
[185] C. Y. Wang, K. Mylvaganam, and L. C. Zhang, "Wrinkling of monolayer graphene: A study by molecular dynamics and continuum plate theory," *Physical Review B,* vol. 80, no. 15, p. 155445, 10/23/ 2009.
[186] M. Neek-Amal and F. M. Peeters, "Nanoindentation of a circular sheet of bilayer graphene," *Physical Review B,* vol. 81, no. 23, p. 235421, 06/11/ 2010.
[187] T.-H. Fang, T. Wang, J.-C. Yang, and Y.-J. Hsiao, "Mechanical characterization of nanoindented graphene via molecular dynamics simulations," (in English), *Nanoscale Research Letters,* vol. 6, no. 1, pp. 1-10, 2011, Art. no. 481.
[188] M. Neek-Amal and F. Peeters, "Nanoindentation of a circular sheet of bilayer graphene," *Physical Review B,* vol. 81, no. 23, p. 235421, 2010.
[189] C.-r. Jin, "Large deflection of circular membrane under concentrated force," *Applied Mathematics and Mechanics,* vol. 29, no. 7, pp. 889-896, 2008/07/01 2008.
[190] X. Huang and S. Zhang, "Morphologies of monolayer graphene under indentation," *Modelling and Simulation in Materials Science and Engineering,* vol. 19, no. 5, p. 054004, 2011.
[191] F. Fornasiero *et al.*, "Ion exclusion by sub-2-nm carbon nanotube pores," *Proceedings of the National Academy of Sciences,* vol. 105, no. 45, pp. 17250-17255, November 11, 2008 2008.
[192] J.-L. Tsai and J.-F. Tu, "Characterizing mechanical properties of graphite using molecular dynamics simulation," *Materials & Design,* vol. 31, no. 1, pp. 194-199, 2010.
[193] Y. Zhang, Q. Pei, and C. Wang, "Mechanical properties of graphynes under tension: a molecular dynamics study," *Applied Physics Letters,* vol. 101, no. 8, p. 081909, 2012.

[194] X. Liu, M. Wang, S. Zhang, and B. Pan, "Application potential of carbon nanotubes in water treatment: a review," *Journal of Environmental Sciences,* vol. 25, no. 7, pp. 1263-1280, 2013.
[195] D. Cohen-Tanugi, S. H. Dave, R. K. McGovern, V. J. H. Lienhard, and J. C. Grossman, "Novel nanomaterials for water desalination technology," in *Technologies for Sustainability (SusTech), 2013 1st IEEE Conference on*, 2013, pp. 272-275: IEEE.
[196] L. Li, N. Liu, B. McPherson, and R. Lee, "Influence of counter ions on the reverse osmosis through MFI zeolite membranes: implications for produced water desalination," *Desalination,* vol. 228, no. 1–3, pp. 217-225, 8/15/ 2008.
[197] E. N. Wang and R. Karnik, "Water desalination: Graphene cleans up water," *Nat Nano,* 10.1038/nnano.2012.153 vol. 7, no. 9, pp. 552-554, 09//print 2012.
[198] M. D. Fischbein and M. Drndić, "Electron beam nanosculpting of suspended graphene sheets," *Applied Physics Letters,* vol. 93, no. 11, p. 113107, 2008.
[199] S. Dong, H. Yi, H. Lu, Z. Yi, and C. Yongsheng, "Investigation of gas storage properties of graphene material prepared by microwave-assisted reduction of graphene oxide," *Acta chimica sinica,* vol. 72, no. 3, pp. 382-387, 2014.
[200] S. C. O'Hern *et al.*, "Selective Ionic Transport through Tunable Subnanometer Pores in Single-Layer Graphene Membranes," *Nano Letters,* vol. 14, no. 3, pp. 1234-1241, 2014/03/12 2014.
[201] A. Du, Z. Zhu, and S. C. Smith, "Multifunctional porous graphene for nanoelectronics and hydrogen storage: new properties revealed by first principle calculations," *Journal of the American Chemical Society,* vol. 132, no. 9, pp. 2876-2877, 2010.
[202] O. Leenaerts, B. Partoens, and F. Peeters, "Graphene: A perfect nanoballoon," *Applied Physics Letters,* vol. 93, no. 19, p. 193107, 2008.
[203] S. C. O'Hern *et al.*, "Selective Molecular Transport through Intrinsic Defects in a Single Layer of CVD Graphene," *ACS Nano,* vol. 6, no. 11, pp. 10130-10138, 2012/11/27 2012.
[204] M. E. Suk and N. Aluru, "Water transport through ultrathin graphene," *The Journal of Physical Chemistry Letters,* vol. 1, no. 10, pp. 1590-1594, 2010.
[205] D. Konatham, J. Yu, T. A. Ho, and A. Striolo, "Simulation insights for graphene-based water desalination membranes," *Langmuir,* vol. 29, no. 38, pp. 11884-11897, 2013.
[206] Z. Wang, B. Dou, L. Zheng, G. Zhang, Z. Liu, and Z. Hao, "Effective desalination by capacitive deionization with functional graphene nanocomposite as novel electrode material," *Desalination,* vol. 299, no. 0, pp. 96-102, 8/1/ 2012.
[207] R. Joshi *et al.*, "Precise and ultrafast molecular sieving through graphene oxide membranes," *Science,* vol. 343, no. 6172, pp. 752-754, 2014.
[208] D.-e. Jiang, V. R. Cooper, and S. Dai, "Porous graphene as the ultimate membrane for gas separation," *Nano letters,* vol. 9, no. 12, pp. 4019-4024, 2009.
[209] S. Blankenburg, M. Bieri, R. Fasel, K. Müllen, C. A. Pignedoli, and D. Passerone, "Porous graphene as an atmospheric nanofilter," *Small,* vol. 6, no. 20, pp. 2266-2271, 2010.
[210] J. Schrier, "Helium separation using porous graphene membranes," *The Journal of Physical Chemistry Letters,* vol. 1, no. 15, pp. 2284-2287, 2010.
[211] A. W. Hauser and P. Schwerdtfeger, "Nanoporous graphene membranes for efficient 3He/4He separation," *The journal of physical chemistry letters,* vol. 3, no. 2, pp. 209-213, 2012.
[212] H. Du, J. Li, J. Zhang, G. Su, X. Li, and Y. Zhao, "Separation of hydrogen and nitrogen gases with porous graphene membrane," *The Journal of Physical Chemistry C,* vol. 115, no. 47, pp. 23261-23266, 2011.

[213] A. Tapia, R. Peón-Escalante, C. Villanueva, and F. Avilés, "Influence of vacancies on the elastic properties of a graphene sheet," *Computational Materials Science,* vol. 55, pp. 255-262, 2012.
[214] Y. J. Sun, F. Ma, D. Y. Ma, K. W. Xu, and K. C. Paul, "Stress-induced annihilation of Stone–Wales defects in graphene nanoribbons," *Journal of Physics D: Applied Physics,* vol. 45, no. 30, p. 305303, 2012.
[215] L. Yi, Z. Yin, Y. Zhang, and T. Chang, "A theoretical evaluation of the temperature and strain-rate dependent fracture strength of tilt grain boundaries in graphene," *Carbon,* vol. 51, pp. 373-380, 2013.
[216] J. Xiao, J. Staniszewski, and J. Gillespie Jr, "Fracture and progressive failure of defective graphene sheets and carbon nanotubes," *Composite structures,* vol. 88, no. 4, pp. 602-609, 2009.
[217] J. Kotakoski and J. C. Meyer, "Mechanical properties of polycrystalline graphene based on a realistic atomistic model," *Physical Review B,* vol. 85, no. 19, p. 195447, 2012.
[218] Z. Song, V. I. Artyukhov, B. I. Yakobson, and Z. Xu, "Pseudo Hall–Petch strength reduction in polycrystalline graphene," *Nano letters,* vol. 13, no. 4, pp. 1829-1833, 2013.
[219] Z. Sha *et al.*, "Inverse pseudo Hall-Petch relation in polycrystalline graphene," *Scientific reports,* vol. 4, 2014.
[220] A. Kvashnin, P. Sorokin, and D. Kvashnin, "The theoretical study of mechanical properties of graphene membranes," *Fullerenes, Nanotubes, and Carbon Nanostructures,* vol. 18, no. 4-6, pp. 497-500, 2010.
[221] Z. Song, Z. Xu, X. Huang, J.-Y. Kim, and Q. Zheng, "On the Fracture of Supported Graphene Under Pressure," *Journal of Applied Mechanics,* vol. 80, no. 4, p. 040911, 2013.
[222] D. Cohen-Tanugi and J. C. Grossman, "Mechanical Strength of Nanoporous Graphene as a Desalination Membrane," *Nano letters,* vol. 14, no. 11, pp. 6171-6178, 2014.
[223] A. Reina *et al.*, "Large Area, Few-Layer Graphene Films on Arbitrary Substrates by Chemical Vapor Deposition," *Nano Letters,* vol. 9, no. 1, pp. 30-35, 2009.
[224] C. A. Lieber and A. Mahadevan-Jansen, "Automated Method for Subtraction of Fluorescence from Biological Raman Spectra," *Applied Spectroscopy,* vol. 57, no. 11, pp. 1363-1367, 2003.
[225] B. Griffin, "A Comparison of Conventional Everhart-Thornley Style and In-Lens Secondary Electron Detectors-A Further Variable in Scanning Electron Microscopy," *Scanning,* vol. 33, pp. 162-73, 05/01 2011.
[226] C. Desmet, A. Valsesia, P. Colpo, and F. Rossi, "A 2D nanoparticle sorter: towards an on-chip quantification and full characterization of nanoparticles," in *Nanotechnology VII*, 2015, vol. 9519, p. 95190M: International Society for Optics and Photonics.
[227] Nano Carbon Sp. z o.o. (2016, 26/07/2018). *Graphene on conductive SiO_2 / Si*. Available: https://www.grapheneshop.pl/product/graphene-conductive-sio2-si/?wcmlc=EUR
[228] M. Pimenta, G. Dresselhaus, M. S. Dresselhaus, L. Cancado, A. Jorio, and R. Saito, "Studying disorder in graphite-based systems by Raman spectroscopy," *Physical chemistry chemical physics,* vol. 9, no. 11, pp. 1276-1290, 2007.
[229] Agar Scientific Ltd. (2018, 26/07/2018). *Suspended Monolayer Graphene on TEM Grids - Quantifoil*. Available: http://www.agarscientific.com/tem/support-films-graphene/suspended-monolayer-graphene-on-tem-grids-quantifoil.html
[230] S. M. Hues, C. F. Draper, and R. J. Colton, "Measurement of nanomechanical properties of metals using the atomic force microscope," *Journal of Vacuum Science &*

Technology B: Microelectronics and Nanometer Structures Processing, Measurement, and Phenomena, vol. 12, no. 3, pp. 2211-2214, 1994.

[231] M. Vanlandingham, S. McKnight, G. Palmese, R. Eduljee, J. Gillespie, and J. R. McCULOUGH, "Relating elastic modulus to indentation response using atomic force microscopy," *Journal of Materials Science Letters,* vol. 16, no. 2, pp. 117-119, 1997.

[232] M. E. Dokukin and I. Sokolov, "On the Measurements of Rigidity Modulus of Soft Materials in Nanoindentation Experiments at Small Depth," *Macromolecules,* vol. 45, no. 10, pp. 4277-4288, 2012/05/22 2012.

[233] M. E. Dokukin and I. Sokolov, "Quantitative mapping of the elastic modulus of soft materials with HarmoniX and PeakForce QNM AFM modes," *Langmuir,* vol. 28, no. 46, pp. 16060-16071, 2012.

[234] M. VanLandingham, "The effect of instrumental uncertainties on AFM indentation measurements," *Microscopy Today,* vol. 5, no. 10, pp. 12-15, 1997.

[235] G. Haugstad, *Atomic force microscopy: understanding basic modes and advanced applications*. John Wiley & Sons, 2012.

[236] M. S. Rana, H. R. Pota, and I. R. Petersen, "The design of model predictive control for an AFM and its impact on piezo nonlinearities," *European Journal of Control,* vol. 20, no. 4, pp. 188-198, 2014.

[237] C.-F. Yen and S. Sivasankar, "Minimizing open-loop piezoactuator nonlinearity artifacts in atomic force microscope measurements," ed: AVS, 2017.

[238] N. Gavara, "A Beginner's guide to atomic force microscopy probing for cell mechanics," *Microscopy research and technique,* vol. 80, no. 1, pp. 75-84, 2017.

[239] D. Croft, G. Shed, and S. Devasia, "Creep, hysteresis, and vibration compensation for piezoactuators: atomic force microscopy application," *Journal of Dynamic Systems, Measurement, and Control,* vol. 123, no. 1, pp. 35-43, 2001.

[240] M. Rakotondrabe, "Bouc–Wen modeling and inverse multiplicative structure to compensate hysteresis nonlinearity in piezoelectric actuators," *IEEE Transactions on Automation Science and Engineering,* vol. 8, no. 2, pp. 428-431, 2011.

[241] A. C. Fischer-Cripps, "Nanoindentation," (in English), 2011.

[242] J. E. Sader, J. W. M. Chon, and P. Mulvaney, "Calibration of rectangular atomic force microscope cantilevers," *Review of Scientific Instruments,* vol. 70, no. 10, pp. 3967-3969, 1999.

[243] J. L. Hutter and J. Bechhoefer, "Calibration of atomic-force microscope tips," *Review of Scientific Instruments,* vol. 64, no. 7, pp. 1868-1873, 1993.

[244] M. A. Poggi, A. W. McFarland, J. S. Colton, and L. A. Bottomley, "A method for calculating the spring constant of atomic force microscopy cantilevers with a nonrectangular cross section," *Analytical chemistry,* vol. 77, no. 4, pp. 1192-1195, 2005.

[245] M. S. Allen, H. Sumali, and P. C. Penegor, "DMCMN: Experimental/analytical evaluation of the effect of tip mass on atomic force microscope cantilever calibration," *Journal of dynamic systems, measurement, and control,* vol. 131, no. 6, p. 064501, 2009.

[246] J. Lübbe, L. Doering, and M. Reichling, "Precise determination of force microscopy cantilever stiffness from dimensions and eigenfrequencies," *Measurement Science and Technology,* vol. 23, no. 4, p. 045401, 2012.

[247] S. Belikov, J. Alexander, C. Wall, I. Yermolenko, S. Magonov, and I. Malovichko, "Thermal tune method for AFM oscillatory resonant imaging in air and liquid," in *2014 American Control Conference*, 2014, pp. 1009-1014.

[248] J. Cleveland, S. Manne, D. Bocek, and P. Hansma, "A nondestructive method for determining the spring constant of cantilevers for scanning force microscopy," *Review of scientific instruments,* vol. 64, no. 2, pp. 403-405, 1993.
[249] S. Timoshenko, "History of Strength of Materials McGraw-Hill Book Company," *Inc., New York/Toronto/London,* 1953.
[250] J. Wortman and R. Evans, "Young's modulus, shear modulus, and Poisson's ratio in silicon and germanium," *Journal of applied physics,* vol. 36, no. 1, pp. 153-156, 1965.
[251] Mikromasch. (24/10/2018). *Frequently Asked Questions*. Available: https://www.spmtips.com/AFM-probes-faq.afm#10
[252] D. R. Lide, *CRC handbook of chemistry and physics: a ready-reference book of chemical and physical data*. CRC press, 1995.
[253] A. Agius Anastasi, A. Valsesia, P. Colpo, M. K. Borg, and G. Cassar, "Raman spectroscopy of gallium ion irradiated graphene," *Diamond and Related Materials,* vol. 89, pp. 163-173, 2018.
[254] A. C. Ferrari and J. Robertson, "Interpretation of Raman spectra of disordered and amorphous carbon," *Physical review B,* vol. 61, no. 20, p. 14095, 2000.
[255] A. Ferrari and J. Robertson, "Resonant Raman spectroscopy of disordered, amorphous, and diamondlike carbon," *Physical Review B,* vol. 64, no. 7, p. 075414, 2001.
[256] Z. Shijun, X. Jianming, W. Yugang, and Y. Sha, "Effect of SiO 2 substrate on the irradiation-assisted manipulation of supported graphene: a molecular dynamics study," *Nanotechnology,* vol. 23, no. 28, p. 285703, 2012.
[257] R. Gago, L. Vázquez, R. Cuerno, M. Varela, C. Ballesteros, and J. M. Albella, "Nanopatterning of silicon surfaces by low-energy ion-beam sputtering: dependence on the angle of ion incidence," *Nanotechnology,* vol. 13, no. 3, p. 304, 2002.
[258] V. B. Mohan, M. Nieuwoudt, K. Jayaraman, and D. Bhattacharyya, "Quantification and analysis of Raman spectra of graphene materials," *Graphene Technology,* vol. 2, no. 3-4, pp. 47-62, 2017.
[259] P. Ahlberg *et al.*, "Defect formation in graphene during low-energy ion bombardment," *APL Materials,* vol. 4, no. 4, p. 046104, 2016.
[260] T. M. G. Mohiuddin *et al.*, "Uniaxial strain in graphene by Raman spectroscopy: G peak splitting, Gruneisen parameters, and sample orientation," *Physical Review B,* vol. 79, no. 20, p. 205433, 2009.
[261] M. Huang, H. Yan, C. Chen, D. Song, T. F. Heinz, and J. Hone, "Phonon softening and crystallographic orientation of strained graphene studied by Raman spectroscopy," *Proceedings of the National Academy of Sciences,* vol. 106, no. 18, pp. 7304-7308, 2009.
[262] A. Sadezky, H. Muckenhuber, H. Grothe, R. Niessner, and U. Pöschl, "Raman microspectroscopy of soot and related carbonaceous materials: spectral analysis and structural information," *Carbon,* vol. 43, no. 8, pp. 1731-1742, 2005.
[263] S. J. Stuart, A. B. Tutein, and J. A. Harrison, "A reactive potential for hydrocarbons with intermolecular interactions," *The Journal of Chemical Physics,* vol. 112, no. 14, pp. 6472-6486, 2000.
[264] S. Plimpton, "Fast Parallel Algorithms for Short-Range Molecular Dynamics," *J Comp Phys,* vol. 117, pp. 1-19, 1995.
[265] M. P. J. C. s. m. f. s. p. t. p. Allen, "Introduction to molecular dynamics simulation," vol. 23, no. 1, pp. 1-28, 2004.
[266] J. H. Walther, R. Jaffe, T. Halicioglu, and P. Koumoutsakos, "Carbon Nanotubes in Water: Structural Characteristics and Energetics," *The Journal of Physical Chemistry B,* vol. 105, no. 41, pp. 9980-9987, 2001/10/01 2001.

[267] W. D. Nicholls, M. K. Borg, D. A. Lockerby, and J. M. Reese, "Water transport through (7, 7) carbon nanotubes of different lengths using molecular dynamics," *Microfluidics and nanofluidics,* vol. 12, no. 1-4, pp. 257-264, 2012.
[268] K. Ritos, N. Dongari, M. K. Borg, Y. Zhang, and J. M. Reese, "Dynamics of nanoscale droplets on moving surfaces," *Langmuir,* vol. 29, no. 23, pp. 6936-6943, 2013.
[269] The OpenFOAM Foundation Ltd. (2016). Available: http://www.openfoam.org.
[270] J. H. Walther, R. L. Jaffe, E. Kotsalis, T. Werder, T. Halicioglu, and P. Koumoutsakos, "Hydrophobic hydration of C60 and carbon nanotubes in water," *Carbon,* vol. 42, no. 5-6, pp. 1185-1194, 2004.
[271] Y. Jin and F. Yuan, "Atomistic simulations of J-integral in 2D graphene nanosystems," *Journal of nanoscience and nanotechnology,* vol. 5, no. 12, pp. 2099-2107, 2005.
[272] M. K. Borg, D. A. Lockerby, and J. M. Reese, "The FADE mass-stat: A technique for inserting or deleting particles in molecular dynamics simulations," *The Journal of chemical physics,* vol. 140, no. 7, p. 074110, 2014.
[273] M. K. Borg, G. B. Macpherson, and J. M. Reese, "Controllers for imposing continuum-to-molecular boundary conditions in arbitrary fluid flow geometries," *Molecular Simulation,* vol. 36, no. 10, pp. 745-757, 2010.
[274] J. A. Izaguirre and A. I. Jes' us, "Langevin Stabilization of Multiscale Mollified Molecular Dynamics," 2001.
[275] A. Sakhaee-Pour, "Elastic properties of single-layered graphene sheet," *Solid State Communications,* vol. 149, no. 1-2, pp. 91-95, 2009.
[276] M. M. Shokrieh and R. Rafiee, "Prediction of Young's modulus of graphene sheets and carbon nanotubes using nanoscale continuum mechanics approach," *Materials & Design,* vol. 31, no. 2, pp. 790-795, 2010.
[277] Q. Lu, W. Gao, and R. Huang, "Atomistic simulation and continuum modeling of graphene nanoribbons under uniaxial tension," *Modelling and Simulation in Materials Science and Engineering,* vol. 19, no. 5, p. 054006, 2011.
[278] S. S. Terdalkar, S. Huang, H. Yuan, J. J. Rencis, T. Zhu, and S. Zhang, "Nanoscale fracture in graphene," *Chemical Physics Letters,* vol. 494, no. 4-6, pp. 218-222, 2010.
[279] Y. Y. Zhang and Y. Gu, "Mechanical properties of graphene: Effects of layer number, temperature and isotope," *Computational Materials Science,* vol. 71, pp. 197-200, 2013.
[280] Y. Liu and X. Chen, "Mechanical properties of nanoporous graphene membrane," *Journal of Applied Physics,* vol. 115, no. 3, p. 034303, 2014.
[281] F. Hao, D. Fang, and Z. Xu, "Mechanical and thermal transport properties of graphene with defects," *Applied physics letters,* vol. 99, no. 4, p. 041901, 2011.
[282] V. B. Shenoy, C. D. Reddy, A. Ramasubramaniam, and Y. W. Zhang, "Edge-Stress-Induced Warping of Graphene Sheets and Nanoribbons," *Physical Review Letters,* vol. 101, no. 24, p. 245501, 12/12/ 2008.
[283] D. W. Brenner, O. A. Shenderova, J. A. Harrison, S. J. Stuart, B. Ni, and S. B. Sinnott, "A second-generation reactive empirical bond order (REBO) potential energy expression for hydrocarbons," *Journal of Physics: Condensed Matter,* vol. 14, no. 4, p. 783, 2002.
[284] H. J. C. Berendsen, J. P. M. Postma, W. F. van Gunsteren, A. DiNola, and J. R. Haak, "Molecular dynamics with coupling to an external bath," *The Journal of Chemical Physics,* vol. 81, 1984.
[285] N. Inui and S. Iwasaki, "Interaction Energy between Graphene and a Silicon Substrate Using Pairwise Summation of the Lennard-Jones Potential," *e-Journal of Surface Science and Nanotechnology,* vol. 15, pp. 40-49, 2017.

[286] W. G. Hoover, "Canonical dynamics: Equilibrium phase-space distributions," *Physical Review A,* vol. 31, no. 3, pp. 1695-1697, 03/01/ 1985.
[287] F. H. Stillinger and T. A. Weber, "Computer simulation of local order in condensed phases of silicon," *Physical review B,* vol. 31, no. 8, p. 5262, 1985.
[288] T.-H. Fang, W.-J. Chang, and C.-I. Weng, "Nanoindentation and nanomachining characteristics of gold and platinum thin films," *Materials Science and Engineering: A,* vol. 430, no. 1-2, pp. 332-340, 2006.

Appendix A RAMAN POST-PROCESSING SCRIPT

```
% signalProcessingWeight Function
%   By Anthea Agius Anastasi, 2018

function signalProcessingWeight

sheet = 'SupportedGraphene';
num = xlsread('C:\RawRaman.xlsx',sheet);

for i = 2:29

    x = num(:,1);
    y = num(:,i);

    degree = 2; %polynomial fit order

    w = 1:length(x);
    w = w(:);
    w1 = 470;   %define the limits of the weighting function
    w2 = 590;
    w3 = 723;
    w4 = 783;

    w5 = 900;
    w6 = 1060;
    w7 = 1080;
    w8 = 1838;
    w9 = 2550;
    w10 = 2730;

    for j=1:length(w)
        if (x(j) > w1) && (x(j) < w2)
            w(j) = 1;
        elseif (x(j) > w3) && (x(j) < w4)
            w(j) = 1;
        elseif (x(j) > w5) && (x(j) < w6)
            w(j) = 1;
        elseif (x(j) > w7) && (x(j) < w8)
            w(j) = 1;
        elseif (x(j) > w9) && (x(j) < w10)
            w(j) = 1;
        else
            w(j) = 100000000;
        end
    end

    smoothdata=y; %initialize first smoothed data to raw spectrum
        oldL=10000000;
        newL=9999999;
        xn(1)=10000000;
        samevalue=0; %initialize counter
```

```
        count=2; %initialize counter

    while and((newL>1),and((newL<=oldL),samevalue<200)), %L is converging and
not diverging, and if no change in 50 iterations
        oldL=newL; %revalue L
        [mypoly, fitdata]=curfit2(smoothdata,degree,w); %curve fit data
%         p = polyfitweighted(x,smoothdata,degree,w);
        [tempdata,index]=min([fitdata';smoothdata']); %tempdata now holds the
lowest point of the two spectra
        xn(count)=sum((index-1)); %number of points unfiltered
        newL=xn(count)^(1/(count-1)); %calculate L according to the root test
of convergence
        smoothdata=tempdata(:); %assign smoothdata the tempdata points

        %calculate the number of points left unfiltered after each pass and
tally the streak
        if(xn(count)==xn(count-1))
            samevalue=samevalue+1;
            else
            samevalue=0;
        end
        disp(xn(count))
        count=count+1;
    end

    dif=y(:)-smoothdata(:); %subtract the smoothed data from the raw spectrum

    figure
    plot (x,y,'g',x,smoothdata,':b', x,dif +820,'b');

    legend ('raw data','baseline 1 ','subtracted 1')
    title ([num2str(sheet) ', ' num2str(i) ', n: '   num2str(degree) ',w1'
num2str(w1) ',w4' num2str(w4) ])

    saveas(gcf,['C:\Users\user\Google     Drive\PhD\Year     3\FINAL     Raman
Matlab\SupportedGraphene\' num2str(sheet) ',' num2str(i) ',n'  num2str(degree)
',w1'  num2str(w1)  ',w4'  num2str(w4)  ',w2'  num2str(w2)  ',w3'  num2str(w3)
'.png'])

    A(:,1) = x;
    A(:,i) = dif;
 end

    filename    =    'C:\Users\user\Google    Drive\PhD\Year    3\FINAL    Raman
Matlab\BaselineCorrectedLieberPoly.xlsx';
    xlswrite(filename,A,num2str(sheet),'A1')
end

%CURFIT2 Fit curve to data version2.. use with pmean_ajm
%   A = CURFIT(X,N) uses the POLYFIT function to find the
%   curve points A which best fit to the data points,
%   where X is the data to be fitted and N is the degree of
%   polynomial by which the fit is made.

%   By Chad Lieber, 1999
```

```
%mod by Alex Makowski 2010_03_18 to start monitoring polynomial fit
% now returns "a" and "b", respectively the polynomial coefficients and the
% error estimate matrix produced by matlab
% note that this change corresponds to changes in pmean_ajm
%

function [p,fit]=curfit2(ref,degree,w)
    ref=ref(:);
    lensamp=1:length(ref);
    lensamp=lensamp(:);
%     [a,b]=polyfit(lensamp,ref,degree);
    p = polyfitweighted(lensamp,ref,degree,w);
    fit=zeros(size(ref));
    for i=1:length(ref)
        fit(i)=0;
        for j=1:degree+1
            fit(i)=fit(i)+p(j)*(i^(degree+1-j));
        end
    end
end

function p = polyfitweighted(x,y,n,w)
% polyfitweighted.m
% -----------------
% Find a least-squares fit of 1D data y(x) with an nth order
% polynomial, weighted by w(x).
%
% By S.S. Rogers (2006), based on polyfit.m by The MathWorks, Inc. - see doc
% polyfit for more details.
%
% Usage
% -----
% P = polyfitweighted(X,Y,N,W) finds the coefficients of a polynomial
% P(X) of degree N that fits the data Y best in a least-squares sense. P
% is a row vector of length N+1 containing the polynomial coefficients in
% descending powers, P(1)*X^N + P(2)*X^(N-1) +...+ P(N)*X + P(N+1). W is
% a vector of weights.
%
% Vectors X,Y,W must be the same length.
%
% Class support for inputs X,Y,W:
%    float: double, single
%
% The regression problem is formulated in matrix format as:
%
%    yw = V*p    or
%
%          3    2
%    yw = [x w  x w  xw  w] [p3
%                           p2
%                           p1
%                           p0]
% where the vector p contains the coefficients to be found.  For a
% 7th order polynomial, matrix V would be:
% V = [w.*x.^7 w.*x.^6 w.*x.^5 w.*x.^4 w.*x.^3 w.*x.^2 w.*x w];
```

```
if ~isequal(size(x),size(y),size(w))
    error('X and Y vectors must be the same size.')
end

x = x(:);
y = y(:);
w = w(:);

% Construct weighted Vandermonde matrix.
%V(:,n+1) = ones(length(x),1,class(x));
V(:,n+1) = w;
for j = n:-1:1
   V(:,j) = x.*V(:,j+1);
end

% Solve least squares problem.
[Q,R] = qr(V,0);
ws = warning('off','all');
p = R\(Q'*(w.*y));    % Same as p = V\(w.*y);
warning(ws);
if size(R,2) > size(R,1)
   warning('polyfitweighted:PolyNotUnique', ...
       'Polynomial is not unique; degree >= number of data points.')
elseif condest(R) > 1.0e10
    if nargout > 2
        warning('polyfitweighted:RepeatedPoints', ...
            'Polynomial is badly conditioned. Remove repeated data points.')
    else
        warning('polyfitweighted:RepeatedPointsOrRescale', ...
            ['Polynomial is badly conditioned. Remove repeated data points\n'
...
            '             or try centering and scaling as described in HELP
POLYFIT.'])
    end
end
p = p.';          % Polynomial coefficients are row vectors by convention.
end

function [removedData,bg] = bglinprog(data,polyOrder,noiseSpan)
if nargin<3
    noiseSpan = 9;
end
if nargin<2
    polyOrder = 4;
end
[nData,len] = size(data);
removedData = zeros(nData,len);
bg = zeros(nData,len);
A = zeros(polyOrder+1,len);
x = linspace(0,1,len);
for i = 1:len
    A(:,i) = x(i).^(0:polyOrder);
end
f = -sum(A,2);
for i = 1:nData
    y = data(i,:);
```

```
    y = smooth(y,noiseSpan,'sgolay')';
    % linear programming
    w = linprog(f(1:polyOrder+1)',A(1:polyOrder+1,:)',y);
    % quadratic programming
    bg(i,:) = w'*A;
    removedData(i,:) = y-bg(i,:);
end
end
```

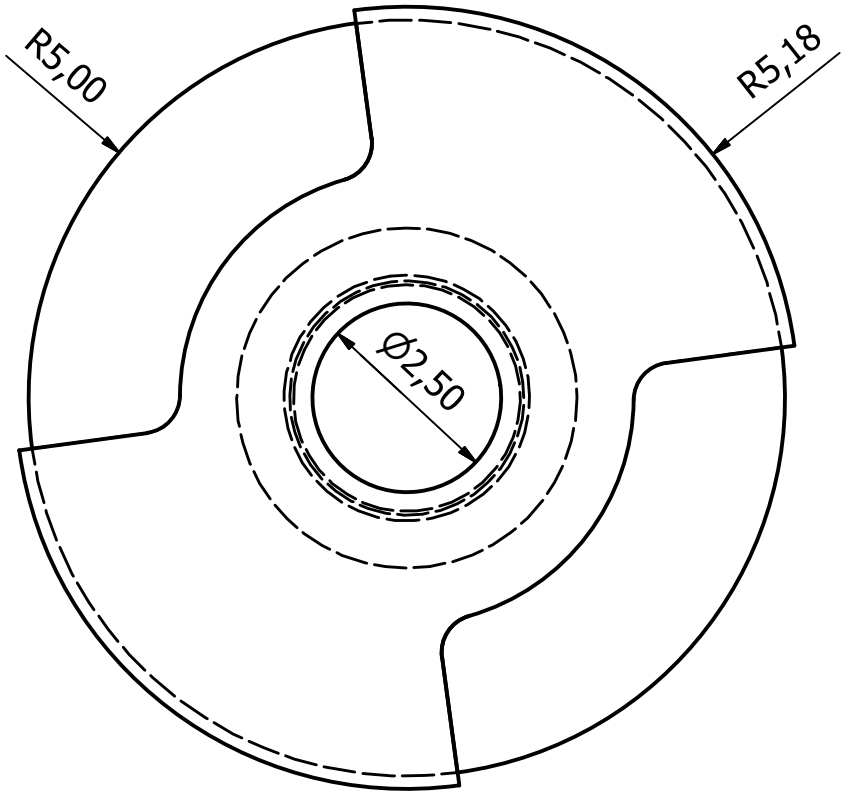

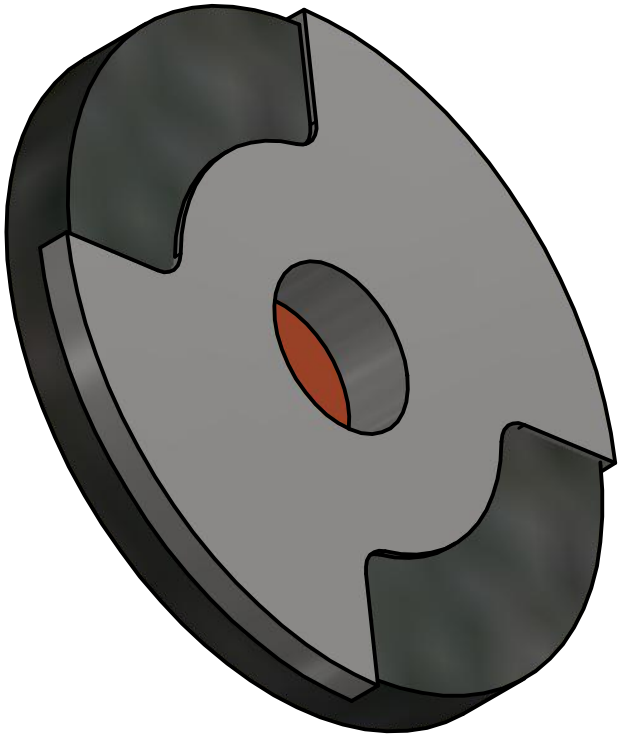

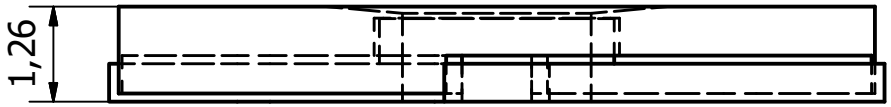

Designed by	Checked by	Approved by	Date		Date	
A Agius Anastasi					24/02/2017	

TEM Grid Sample Holder	Scale: 10:1		
	Appendix B	Edition	Sheet 1 / 3

D-D (10 : 1)

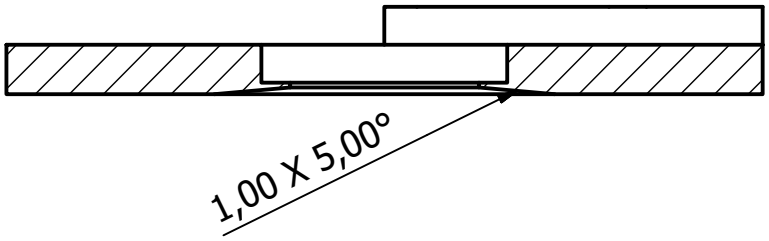

1,00 X 5,00°

0,50 ± 0,25

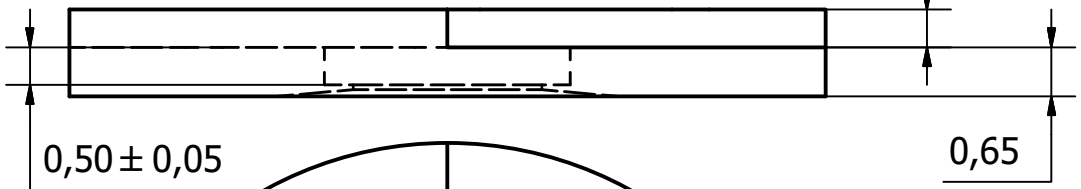

0,50 ± 0,05

0,65

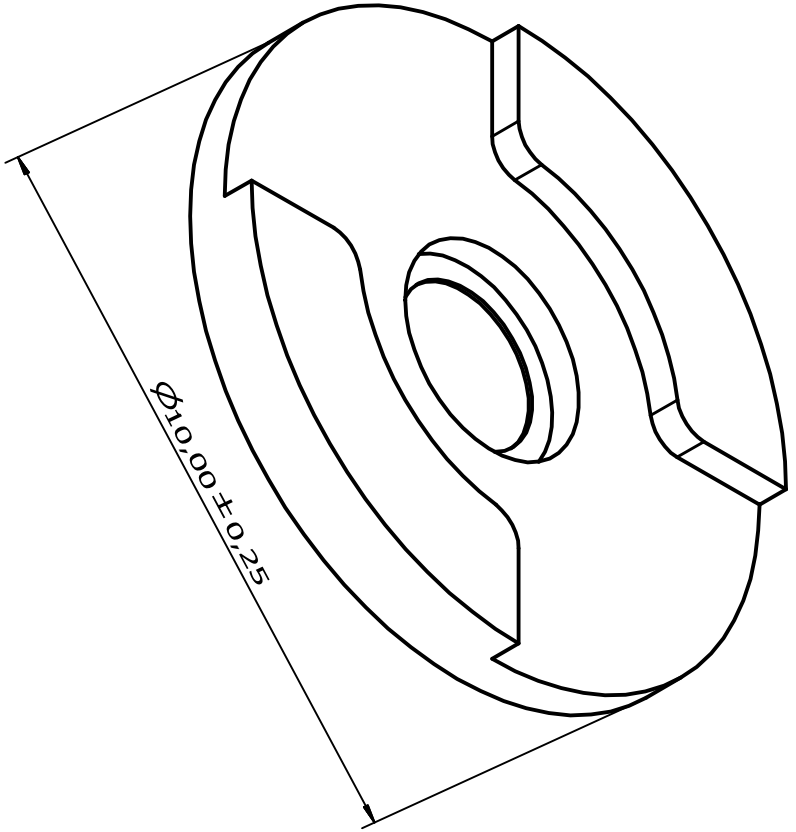

Ø10,00 ± 0,25

Ø3,25 +0,25 -0,05

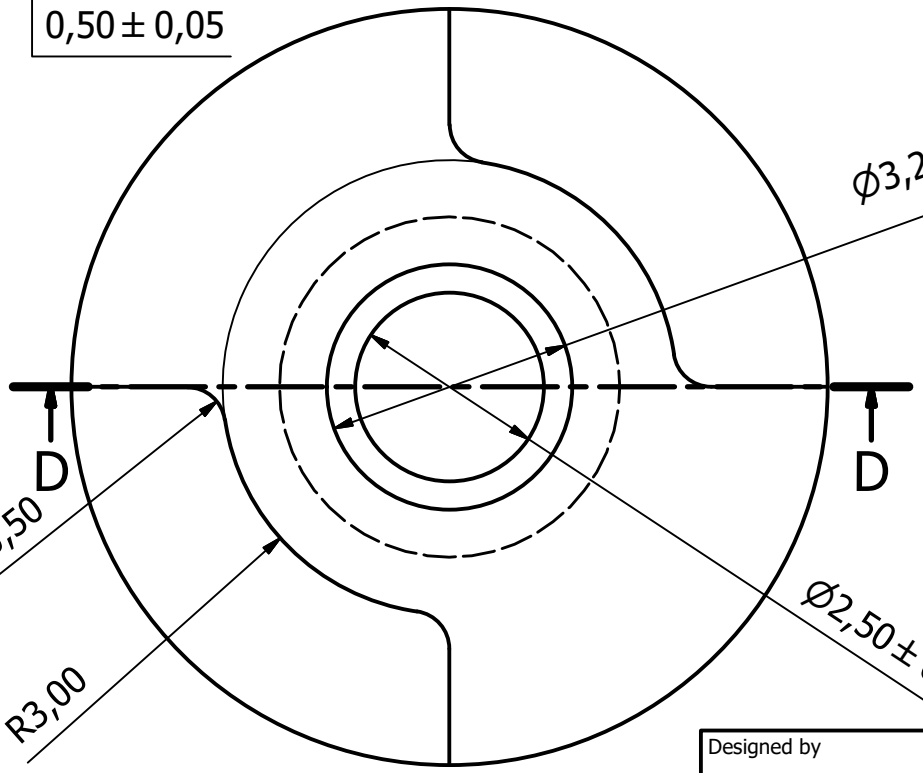

D

D

R0,50

R3,00

Ø2,50 ± 0,25

Designed by	Checked by	Approved by	Date		Date	
A Agius Anastasi					24/02/2017	

TEM Grid Sample Holder
Bottom Washer

Scale: 10:1

Appendix B

Edition	Sheet
	2 / 3

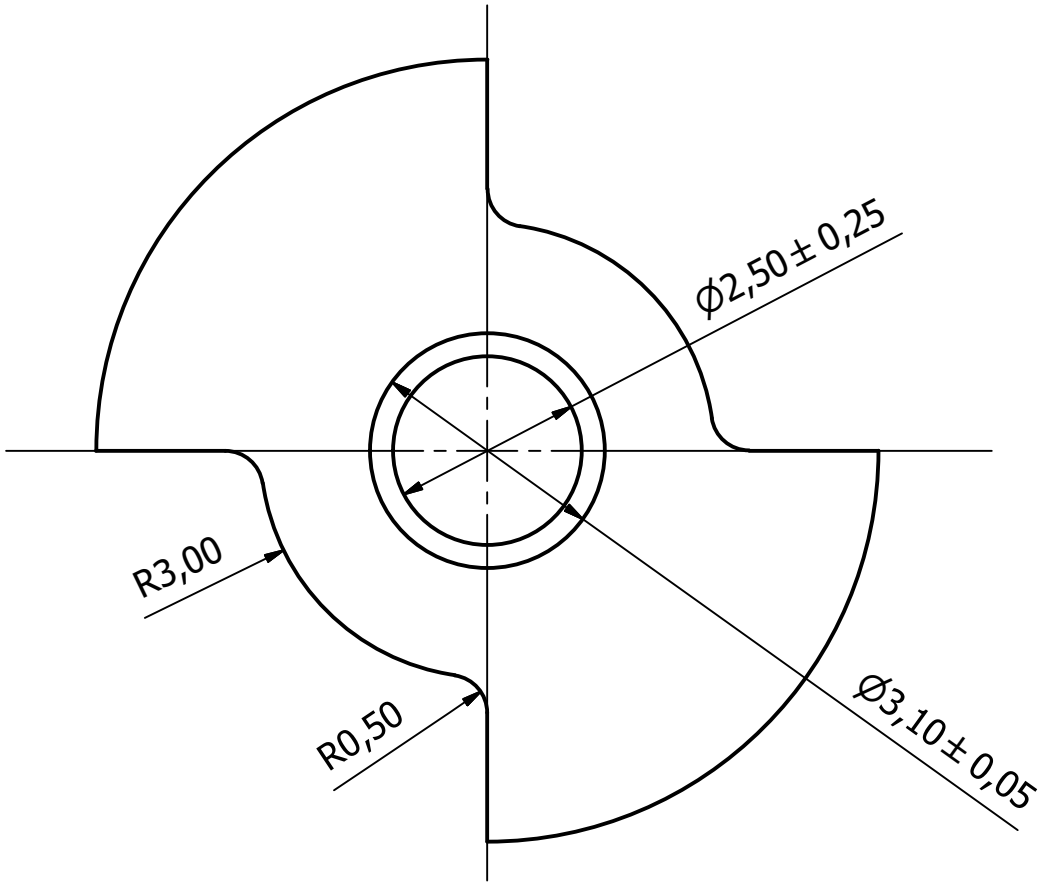

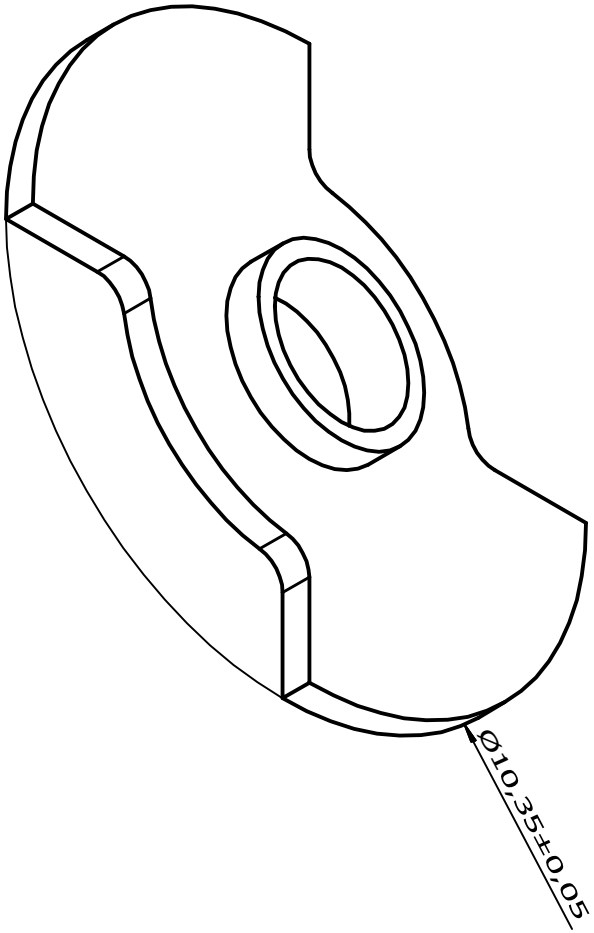

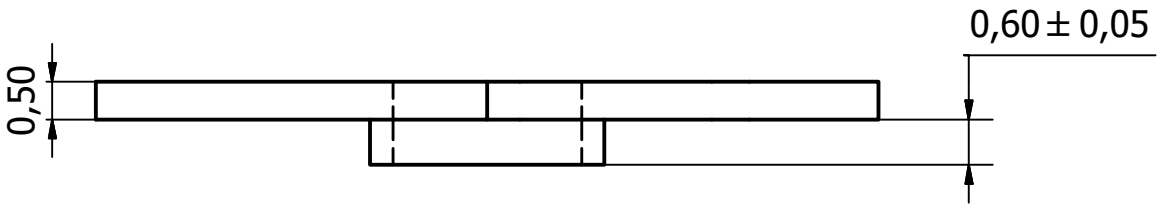

Designed by	Checked by	Approved by	Date		Date	
A Agius Anastasi					24/02/2017	

TEM Grid Sample Holder
Top Washer

Scale: 10:1

Appendix B

Edition

Sheet 3 / 3

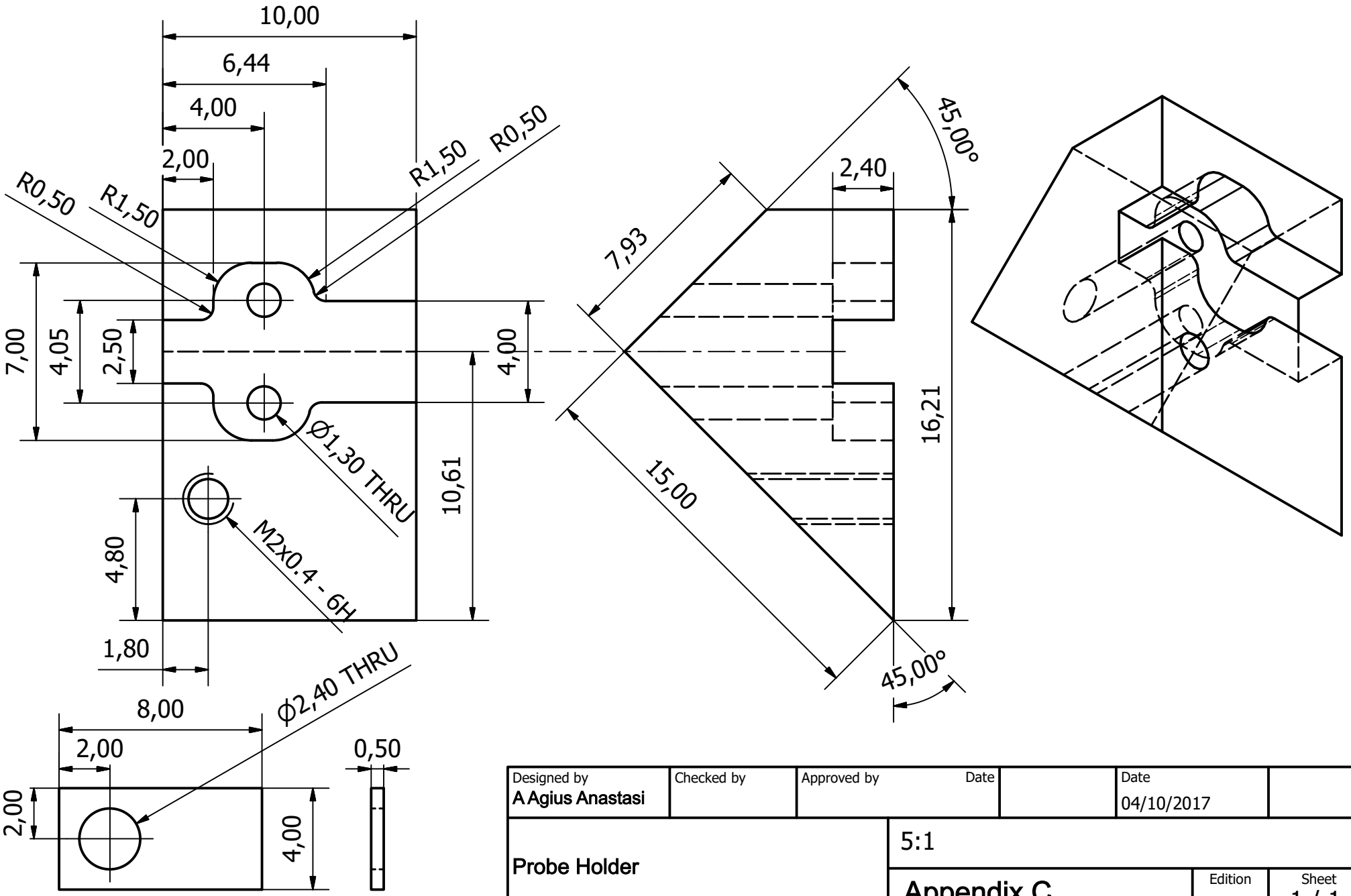

Designed by	Checked by	Approved by	Date		Date	
A Agius Anastasi					04/10/2017	

Probe Holder	5:1		
	Appendix C	Edition	Sheet 1 / 1

Appendix D SPRING CONSTANT CALIBRATION SCRIPT

```
function SpringConstantLubbe(f0,f1)

  %%%%%%%% INPUT %%%%%%%%

  f0 = 149.5e3; %160.3181e3;
  f1 = 956.01e3; %1000.849e3;

  L = 119.9e-6;
  w1 = 36.01e-6;
  w2 = 26.01e-6;

  rho = 2331;
  E = 169e9;

  freq_ratio=f1/f0;

  if (freq_ratio<6.266893); %6.266893
    disp('ratio f1/f0 out of range!')
    return;
  end
  mass_steps=1000;
  alpha_steps=10000;
  iterations=5;
  mass_sign=1; %change to -1 for negative tip mass

  format long;
  format compact;

  mass_ratio=linspace(0,mass_sign.*0.2,mass_steps);
  alpha0=linspace(1.61,2.60,alpha_steps);
  alpha1=linspace(4.26,6.51,alpha_steps);

  disp('first estimate:')
  [mu,alpha_0,alpha_1]=getMu(alpha0,alpha1,mass_ratio,freq_ratio)

  for i=1:iterations
    disp(sprintf('iteration(%i):',i));
    min_mass=mu-abs(mass_ratio(2)-mass_ratio(1));
    max_mass=mu+abs(mass_ratio(2)-mass_ratio(1));

    mass_ratio=linspace(min_mass,max_mass,mass_steps);

alpha0=linspace(getAlpha(alpha0,min_mass),getAlpha(alpha0,max_mass),alpha_ste
ps);
```

```
alpha1=linspace(getAlpha(alpha1,min_mass),getAlpha(alpha1,max_mass),alpha_ste
ps);
    [mu,alpha_0,alpha_1]=getMu(alpha0,alpha1,mass_ratio,freq_ratio)
  end

disp('Spring Constant (N/m):')
constant =
((36*sqrt(2)*(f0^3)*(pi()^3)*(L^3)*((w1+w2)^2))/((alpha_0^6)*sqrt((w1^2)+(4*w
1*w2)+(w2^2))))*(sqrt((rho^3)/E));
disp(constant)
end

function [mu,alpha_0,alpha_1]=getMu(alpha0,alpha1,mass_ratio,freq_ratio)
  freq_ratio_err=[];
  for i=1:length(mass_ratio)
    freq_ratio_err=[freq_ratio_err abs(getRatio(alpha0,alpha1,mass_ratio(i))-
freq_ratio)];
  end

  [no_output,massindex]=min(freq_ratio_err);
  mu=mass_ratio(massindex);
  alpha_0=getAlpha(alpha0,mu);
  alpha_1=getAlpha(alpha1,mu);
end

function mf=getRatio(alpha0,alpha1,mu)
  a0=getAlpha(alpha0,mu);
  a1=getAlpha(alpha1,mu);
  mf=(a1.^2)./(a0.^2);
end

function mf=getAlpha(alpha,mu)

[no_output,a]=min(abs(cos(alpha)+1./cosh(alpha)+mu.*alpha.*(tanh(alpha).*cos(
alpha)-sin(alpha))));
  mf=alpha(a);
end

function calcAlpha(f0,f1)

  if (freq_ratio<6.266893);
    disp('ratio f1/f0 out of range!')
    return;
  end
  mass_steps=1000;
  alpha_steps=10000;
  iterations=5;
  mass_sign=1; %change to -1 for negative tip mass

  format long;
  format compact;

  mass_ratio=linspace(0,mass_sign.*0.2,mass_steps);
  alpha0=linspace(1.61,2.60,alpha_steps);
  alpha1=linspace(4.26,6.51,alpha_steps);
```

```
  disp('first estimate:')
  [mu,alpha_0,alpha_1]=getMu(alpha0,alpha1,mass_ratio,freq_ratio)

  for i=1:iterations
    disp(sprintf('iteration(%i):',i));
    min_mass=mu-abs(mass_ratio(2)-mass_ratio(1));
    max_mass=mu+abs(mass_ratio(2)-mass_ratio(1));

    mass_ratio=linspace(min_mass,max_mass,mass_steps);

alpha0=linspace(getAlpha(alpha0,min_mass),getAlpha(alpha0,max_mass),alpha_ste
ps);

alpha1=linspace(getAlpha(alpha1,min_mass),getAlpha(alpha1,max_mass),alpha_ste
ps);
    [mu,alpha_0,alpha_1]=getMu(alpha0,alpha1,mass_ratio,freq_ratio)
  end
end

function [mu,alpha_0,alpha_1]=getMu(alpha0,alpha1,mass_ratio,freq_ratio)
  freq_ratio_err=[];
  for i=1:length(mass_ratio)
    freq_ratio_err=[freq_ratio_err abs(getRatio(alpha0,alpha1,mass_ratio(i))-
freq_ratio)];
  end

  [no_output,massindex]=min(freq_ratio_err);
  mu=mass_ratio(massindex);
  alpha_0=getAlpha(alpha0,mu);
  alpha_1=getAlpha(alpha1,mu);
end

function mf=getRatio(alpha0,alpha1,mu)
  a0=getAlpha(alpha0,mu);
  a1=getAlpha(alpha1,mu);
  mf=(a1.^2)./(a0.^2);
end

function mf=getAlpha(alpha,mu)

[no_output,a]=min(abs(cos(alpha)+1./cosh(alpha)+mu.*alpha.*(tanh(alpha).*cos(
alpha)-sin(alpha))));
  mf=alpha(a);
end
```

Appendix E 2D RAMAN SPECTRAL MAPS

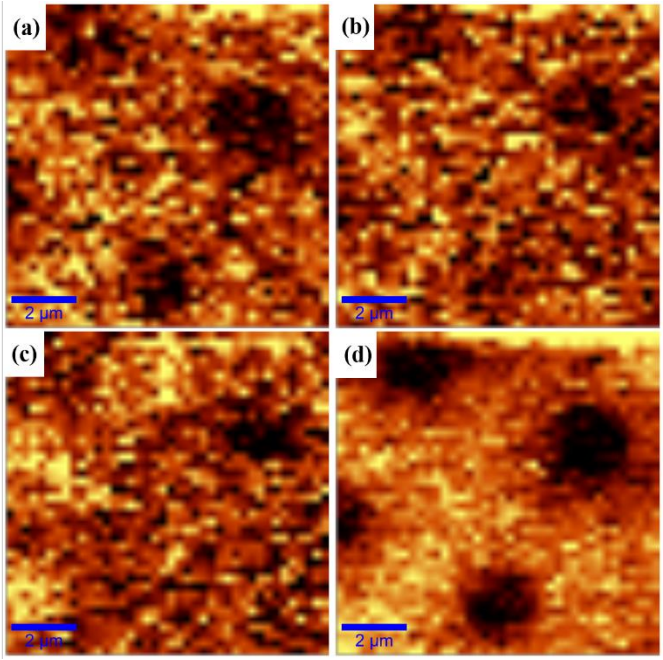

Figure E.0.1: 2D Raman spectral maps of the suspended graphene treated with a dose of 4.86×10^{-4} C/µm^2. The intensity colour of each map represents the intensity of the (a) D, (b) G, (c) 2D, and (d) G + D peaks.

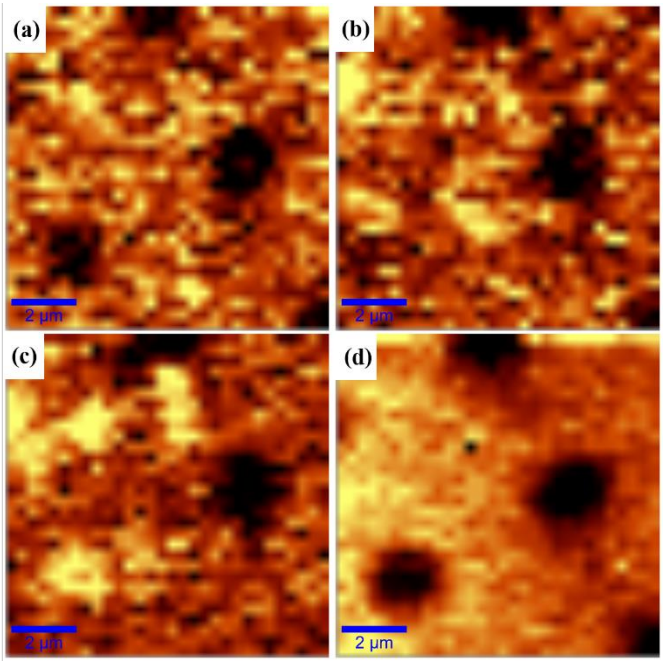

Figure E.0.2: 2D Raman spectral maps of the suspended graphene treated with a dose of 5.28×10^{-5} C/µm^2. The intensity colour of each map represents the intensity of the (a) D, (b) G, (c) 2D, and (d) G + D peaks.

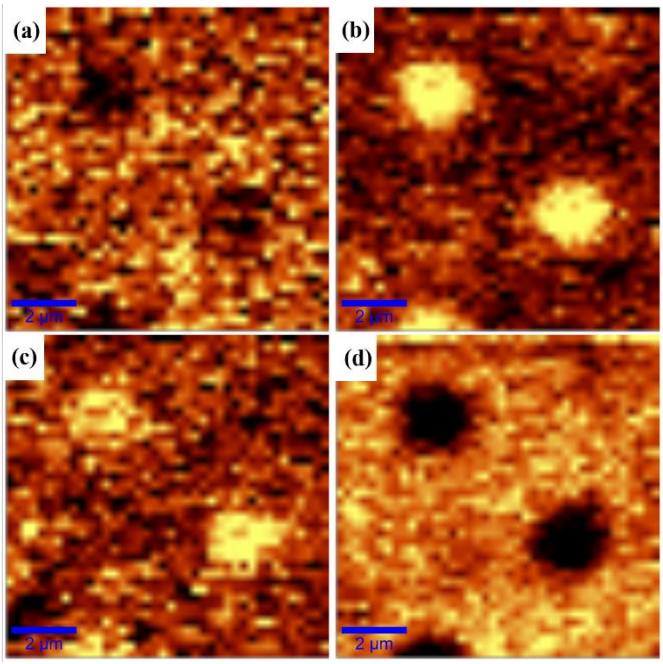

Figure E.0.3: 2D Raman spectral maps of the suspended graphene treated with a dose of 3.27×10^{-3} C/µm^2 at an incidence angle of 83°. The intensity colour of each map represents the intensity of the (a) D, (b) G, (c) 2D, and (d) G + D peaks.

Appendix F RAMAN PEAK PARAMETERS

F.1 TREATED SUSPENDED CVD GRAPHENE MEMBRANES ON SILICON NITRIDE MICROSIEVES

Table F.0.1: The relative shift (P) and the full width at half maximum (F) of the D, G, and 2D peaks obtained from untreated (UT) and irradiated (T) membranes.

Location	D Peak		G Peak		2D Peak	
	P (cm^{-1})	F (cm^{-1})	P (cm^{-1})	F (cm^{-1})	P (cm^{-1})	F (cm^{-1})
Substrate	1337.7	37.8	1576.2	50.9	-	-
UT SLG	1338.9	38.7	1577.9	48.6	2674.3	24.7
UT MLG	1340.7	39.1	1579.7	39.7	2679.9	32.4
T1-1	1339.2	22.6	1578.9	42.1	2673.0	22.7
T1-2	1339.4	29.0	1579.4	45.8	2674.7	26.3
T2-1	1340.5	23.8	1578.9	44.7	2674.8	31.2
T2-2	1339.4	25.6	1579.3	47.0	2668.8	33.5
T3-1	1338.7	38.0	1576.2	52.5	2710.3	44.7
T3-2	1340.4	40.7	1576.7	53.7	2668.8	46.2

Table F.0.2: The intensity (I) and width (F) ratios between the D, G and 2D peaks obtained from untreated (UT) and irradiated (T) membranes.

Treatment	I_D/I_G	F_D/F_G	I_D/I_{2D}	I_{2D}/I_G	F_{2D}/F_G
Substrate	0.32	0.75	-	-	-
UT SLG	0.38	0.80	0.20	1.88	0.51
UT MLG	0.41	0.99	0.23	1.84	0.82
T1-1	0.94	0.53	0.67	1.41	0.54
T1-2	1.54	0.64	2.27	0.91	0.58
T2-1	1.43	0.53	1.90	0.81	0.71
T2-2	1.45	0.54	3.73	0.40	0.72
T3-1	0.47	0.73	1.40	0.35	0.84
T3-2	0.50	0.76	1.34	0.33	0.82

F.2 TREATED MECHANICALLY EXFOLIATED GRAPHENE MEMBRANES ON PAA/SI SUBSTRATE

F.2.1 FLAKE F - 1.33×10^{-14} C/μM^2 PATTERNING METHOD

Table F.0.3: The relative shift (P) and the full width at half maximum (F) of the D, G, and D' peaks obtained from various locations in Flake F, before (UT) and after (T) irradiation.

Location	D Peak		G Peak		D' Peak	
	P (cm^{-1})	F (cm^{-1})	P (cm^{-1})	F (cm^{-1})	P (cm^{-1})	F (cm^{-1})
A1 UT	1329.5	53.8	1581.6	17.1	-	-
A2 UT	1331.9	34.7	1582.0	19.1	-	-
M01 UT	1330.0	41.2	1580.2	19.2	-	-
A1.1 T	1336.0	35.6	1582.3	31.6	-	-
A1.2 T	1329.5	146.4	1583.7	38.0	-	-
A2.1 T	1339.9	43.7	1582.1	26.5	1617.2	21.1
A2.2 T	1338.2	42.4	1582.0	26.3	1616.5	17.0
A3 T	1335.3	69.8	1583.7	51.8	-	-
M01 T	1340.5	45.1	1582.9	24.1	1619.8	13.2

Table F.0.4: The relative shift (P) and the full width at half maximum (F) of the 2D^1 and 2D^2 peaks obtained from various locations in Flake F, before (UT) and after (T) irradiation.

Location	2D^1 Peak		2D^2 Peak	
	P (cm^{-1})	F (cm^{-1})	P (cm^{-1})	F (cm^{-1})
A1 UT	2647.3	54.6	2683.9	41.2
A2 UT	2660.3	59.0	2686.7	41.2
M01 UT	2642.8	62.7	2679.4	47.52
A1.1 T	-	-	-	-
A1.2 T	2670.3	45.9	-	-
A2.1 T	2659.0	52.4	2681.7	45.7
A2.2 T	2650.9	25.9	2675.3	37.8
A3 T	2668.1	26.6	-	-
M01 T	2650.4	41.3	2679.0	48.1

Table F.0.5: The intensity (I) and width (F) ratios between the D, G and D' peaks obtained from various locations in Flake F, before (UT) and after (T) irradiation.

Location	I_D/I_G	F_D/F_G	$I_D/I_{D'}$	$I_{D'}/I_G$
A1 UT	0.02	3.14	-	-
A2 UT	0.04	1.82	-	-
M01 UT	0.02	2.14	-	-
A1.1 T	0.42	1.12	-	-
A1.2 T	0.91	3.85	-	-
A2.1 T	0.68	1.65	2.94	0.23
A2.2 T	0.60	1.61	2.25	0.27
A3 T	1.28	1.35	-	-
M01 T	0.61	1.88	5.02	0.12

F.2.2 FLAKE G – 3.30×10^{-15} C/μM^2 IMAGING METHOD

Table F.0.6: The relative shift (P) and the full width at half maximum (F) of the D, G, D' and D+D'' peaks obtained from various locations in Flake G, before (UT) and after (T) irradiation.

Location	D Peak		G Peak		D' Peak		D+D'' Peak	
	P (cm^{-1})	F (cm^{-1})	P (cm^{-1})	F (cm^{-1})	P (cm^{-1})	F (cm^{-1})	P (cm^{-1})	F (cm^{-1})
A1 UT	1331.5	61.3	1582.4	17.5	-	-	2465.6	30.9
A2 UT	1330.3	54.5	1582.2	17.4	-	-	2463.8	29.4
M01 UT	1331.0	47.6	1582.3	17.6	-	-	2462.2	28.0
A1 T	1339.3	40.8	1581.5	20.9	1618.9	14.2	2462.6	36.9
A2 T	1339.4	42.4	1581.6	22.6	1618.6	15.6	2463.0	34.1
M01 T	1338.3	40.1	1581.1	22.6	1617.8	14.0	2468.2	71.2

Table F.0.7: The relative shift (P) and the full width at half maximum (F) of the $2D^1$, $2D^2$ and 2D' peaks obtained from various locations in Flake G, before (UT) and after (T) irradiation.

Location	$2D^1$ Peak		$2D^2$ Peak		2D' Peak	
	P (cm^{-1})	F (cm^{-1})	P (cm^{-1})	F (cm^{-1})	P (cm^{-1})	F (cm^{-1})
A1 UT	2659.0	57.0	2687.7	38.1	3242.6	19.4
A2 UT	2651.2	56.6	2686.0	37.8	3244.0	24.3
M01 UT	2648.8	58.4	2685.4	39.3	3242.9	21.7
A1 T	2645.8	63.9	2679.9	48.8	-	-
A2 T	2646.4	70.2	2680.1	49.5	-	-
M01 T	2641.7	73.1	2678.1	49.5	-	-

Table F.0.8: The intensity (I) and width (F) ratios between the D, G, and D' peaks obtained from various locations in Flake G, before (UT) and after (T) irradiation.

Location	I_D/I_G	F_D/F_G	$I_D/I_{D'}$	$I_{D'}/I_G$
A1 UT	0.07	3.50	-	-
A2 UT	0.06	3.13	-	-
M01 UT	0.07	2.70	-	-
A1 T	0.76	1.95	4.56	0.17
A2 T	0.85	1.88	4.86	0.17
M01 T	0.89	1.78	5.26	0.17

F.2.3 FLAKE H – 3.30×10^{-15} C/μM^2 IMAGING METHOD

Table F.0.9: The relative shift (P) and the full width at half maximum (F) of the D, G, and D' peaks obtained from various locations in Flake H after (T) irradiation.

Location	D Peak		G Peak		D' Peak	
	P (cm^{-1})	F (cm^{-1})	P (cm^{-1})	F (cm^{-1})	P (cm^{-1})	F (cm^{-1})
A1 T	1341.2	43.8	1581.8	22.0	1619.5	14.3
A2 T	1341.0	40.5	1581.7	20.5	1619.3	13.2
A1+A2 T	1341.0	43.3	1582.0	22.3	1619.5	14.5
M01 T	1340.0	43.2	1580.9	23.0	1618.2	15.4

Table F.0.10: The relative shift (P) and the full width at half maximum (F) of the $2D^1$ and $2D^2$ peaks obtained from various locations in Flake H after (T) irradiation.

Location	$2D^1$ Peak		$2D^2$ Peak	
	P (cm^{-1})	F (cm^{-1})	P (cm^{-1})	F (cm^{-1})
A1 T	2650.8	60.8	2682.8	44.4
A2 T	2648.8	75.4	2680.8	48.2
A1+A2 T	2654.8	78.5	2683.2	45.1
M01 T	2647.6	82.1	2679.2	48.4

Table F.0.11: The intensity (I) and width (F) ratios between the D, G and D' peaks obtained from various locations in Flake H after (T) irradiation.

Location	I_D/I_G	F_D/F_G	$I_D/I_{D'}$	$I_{D'}/I_G$
A1 T	0.74	1.99	4.27	0.17
A2 T	0.65	1.98	4.13	0.16
A1+A2 T	0.77	1.94	4.29	0.18
M01 T	0.83	1.88	4.53	0.18

F.2.4 FLAKE C – 6.60×10^{-16} C/μM^2 IMAGING METHOD

Table F.0.12: The relative shift (P) and the full width at half maximum (F) of the D, G, D′ and D+D″ peaks obtained from various locations in Flake C, before (UT) and after (T) irradiation.

Location	D Peak		G Peak		D' Peak		D+D'' Peak	
	P (cm^{-1})	F (cm^{-1})	P (cm^{-1})	F (cm^{-1})	P (cm^{-1})	F (cm^{-1})	P (cm^{-1})	F (cm^{-1})
A1 UT	-	-	1582.8	16.7	-	-	2463.4	31.0
A2 UT	-	-	1582.4	16.7	-	-	2461.6	25.6
M01 & M02 UT	-	-	1582.1	15.9	-	-	2464.5	28.6
A1 T	1341.5	40.7	1582.4	18.6	-	-	-	-
A2 T	1340.9	40.1	1581.7	18.3	1620.4	8.7	-	-
M01 & M02 T	1341.7	38.8	1582.2	17.9	1621.0	9.5	2464.8	26.7

Table F.0.13: The relative shift (P) and the full width at half maximum (F) of the 2D^1, 2D^2 and 2D′ peaks obtained from various locations in Flake, before (UT) and after (T) irradiation.

Location	2D^1 Peak		2D^2 Peak		2D' Peak	
	P (cm^{-1})	F (cm^{-1})	P (cm^{-1})	F (cm^{-1})	P (cm^{-1})	F (cm^{-1})
A1 UT	2654.4	59.7	2685.8	40.3	3244.4	15.0
A2 UT	2647.2	59.4	2684.9	40.7	3244.4	16.7
M01 & M02 UT	2650.3	65.7	2683.6	44.8	3241.9	20.8
A1 T	2655.7	61.1	2684.3	41.4	-	-
A2 T	2649.3	59.6	2682.9	40.1	-	-
M01 & M02 T	2652.1	62.9	2683.8	42.7	3243.3	31.0

Table F.0.14: The intensity (I) and width (F) ratios between the D, G and D′ peaks obtained from various locations in Flake C, before (UT) and after (T) irradiation.

Location	I_D/I_G	F_D/F_G	$I_D/I_{D'}$	$I_{D'}/I_G$
A1 UT	-	-	-	-
A2 UT	-	-	-	-
M01 & M02 UT	-	-	-	-
A1 T	0.23	2.19	-	-
A2 T	0.24	2.19	3.97	0.06
M01 & M02 T	0.22	2.16	3.96	0.05

F.2.5 FLAKE I – 6.60×10^{-16} C/μM^2 IMAGING METHOD

Table F.0.15: The relative shift (P) and the full width at half maximum (F) of the D, G, D′ and D+D″ peaks obtained from various locations in Flake I, before (UT) and after (T) irradiation.

Location	D Peak		G Peak		D' Peak		D+D'' Peak	
	P (cm^{-1})	F (cm^{-1})	P (cm^{-1})	F (cm^{-1})	P (cm^{-1})	F (cm^{-1})	P (cm^{-1})	F (cm^{-1})
A1 UT	-	-	1581.9	16.7	-	-	2465.0	30.0
A2 UT	-	-	1581.7	17.1	-	-	2463.2	25.6
M01 UT	-	-	1580.7	16.3	-	-	2464.9	33.2
A1 T	1340.9	42.4	1581.9	17.8	1620.7	10.8	2461.1	25.3
A2 T	1340.9	40.7	1582.1	17.9	1620.7	11.1	2461.1	22.1
M01 T	1339.6	39.6	1580.6	18.4	1619.7	11.2	2459.1	21.6

Table F.0.16: The relative shift (P) and the full width at half maximum (F) of the 2D^1, 2D^2 and 2D′ peaks obtained from various locations in Flake I, before (UT) and after (T) irradiation.

Location	2D^1 Peak		2D^2 Peak		2D' Peak	
	P (cm^{-1})	F (cm^{-1})	P (cm^{-1})	F (cm^{-1})	P (cm^{-1})	F (cm^{-1})
A1 UT	2653.8	59.9	2686.2	39.9	3243.8	18.7
A2 UT	2644.2	53.7	2685.0	38.6	3244.7	18.1
M01 UT	2652.3	62.8	2681.8	43.5	3240.6	19.2
A1 T	2657.0	60.0	2685.8	40.9	3246.2	11.2
A2 T	2657.0	60.0	2685.3	41.7	3246.6	11.1
M01 T	2646.6	66.3	2678.6	46.8	3240.1	40.2

Table F.0.17: The intensity (I) and width (F) ratios between the D, D′ and G peaks obtained from various locations in Flake I, before (UT) and after (T) irradiation.

Location	I_D/I_G	F_D/F_G	$I_D/I_{D'}$	$I_{D'}/I_G$
A1 UT	-	-	-	-
A2 UT	-	-	-	-
M01 UT	-	-	-	-
A1 T	0.18	2.39	3.82	0.05
A2 T	0.30	2.28	4.25	0.07
M01 T	0.34	2.15	4.55	0.07

F.2.6 FLAKE J – 6.60×10^{-16} C/μM^2 IMAGING METHOD

Table F.0.18: The relative shift (P) and the full width at half maximum (F) of the D, G, D′ and D+D″ peaks obtained from various locations in Flake J, after (T) irradiation.

Location	D Peak		G Peak		D' Peak		D+D'' Peak	
	P (cm^{-1})	F (cm^{-1})	P (cm^{-1})	F (cm^{-1})	P (cm^{-1})	F (cm^{-1})	P (cm^{-1})	F (cm^{-1})
A1 T	1339.2	38.8	1582.1	18.5	1612.0	7.9	2465.3	31.1
A2 T	1340.2	40.7	1582.1	17.9	1619.8	7.5	2463.5	29.6
A1+A2 T	1339.9	39.0	1582.1	18.1	1619.8	7.7	2462.8	24.9
M01 T	1340.1	38.0	1581.6	17.9	-	-	2462.4	19.8

Table F.0.19: The relative shift (P) and the full width at half maximum (F) of the 2D^1 and 2D^2 peaks obtained from various locations in Flake J, after (T) irradiation.

Location	2D^1 Peak		2D^2 Peak	
	P (cm^{-1})	F (cm^{-1})	P (cm^{-1})	F (cm^{-1})
A1 T	2662.4	65.4	2690.0	33.6
A2 T	2663.1	65.6	2690.2	34.4
A1+A2 T	2663.4	65.0	2690.7	33.0
M01 T	2663.8	61.3	2692.8	31.4

Table F.0.20: The intensity (I) and width (F) ratios between the D, G, and D′ peaks obtained from various locations in Flake J, after (T) irradiation.

Location	I_D/I_G	F_D/F_G	$I_D/I_{D'}$	$I_{D'}/I_G$
A1 T	0.22	2.10	4.64	0.05
A2 T	0.20	2.27	4.65	0.04
A1+A2 T	0.21	2.15	4.74	0.04
M01 T	0.22	2.13	-	-

Appendix G AIREBO MD SCRIPT

```
################## GRAPHENE-SUBSTRATE POTENTIAL CASE ##################

log               log-init
echo              both

units             metal
dimension         3
boundary          p p p
atom_style        full

neighbor          3.0 bin
neigh_modify      every 10 delay 50 check no

processors        12 12 1
read_data         data.dat

################## Interactions

group             graphene    type 1
group             substrate   type 2
group             indentor    type 3
group             cantilever  type 4
group             Moving subtract all cantilever

pair_style        hybrid lj/cut 14.0 airebo 2.0
pair_modify       shift yes mix arithmetic

pair_coeff        * * airebo CH.airebo C NULL C NULL
pair_coeff        2 2 lj/cut 0.0 3.826 14
#pair_coeff       3 3 lj/cut 0.0 3 14
pair_coeff        4 4 lj/cut 0.0 3 14

pair_coeff        1 2 lj/cut 0.0089 3.629 14    ### G-S Nario Inui 2017
pair_coeff        1 3 lj/cut 0.00455 3.431 14   ### G-I Nario Inui 2017
pair_coeff        2 3 lj/cut 0.0 3 14           ### I-S
pair_coeff        3 4 lj/cut 0.0002 3.431 14    ###
pair_coeff        2 4 lj/cut 0.0 3 14           ###
pair_coeff        1 4 lj/cut 0.0 3 14           ###

################## Run paramters

### fix rigid the substrate ###
fix               subFix substrate setforce 0 0 0

### fix rigid the indentor ###
fix               cantFix cantilever setforce 0 0 0

compute           Gtemp graphene temp/com
velocity          graphene create 100 465754 dist gaussian mom yes
compute           Itemp indentor temp/com
velocity          indentor create 100 2345 dist gaussian mom yes
```

```
### thermostat ##
fix               gTemp graphene temp/berendsen 300.0 300.0 1
fix_modify        gTemp temp Gtemp
fix               iTemp indentor temp/berendsen 300.0 300.0 1
fix_modify        iTemp temp Itemp

compute           forceG indentor group/group graphene molecule inter

fix               cantspring cantilever spring couple indentor 312.1 NULL
                  NULL -13.1259 0
fix               indmom indentor momentum 1 linear 1 1 1 angular
fix               NVE Moving nve


timestep          0.0005                  ### 0.5 fs
thermo            100
thermo_style      custom step temp c_Gtemp c_Itemp c_forceG[3] pe ke

dump              1 all custom 1000 dump_init.lammpstrj id type x y z
minimize          1e-4 1e-6 1000 10000
run               60000 every 60000 "write_restart restart.*"

################## GRAPHENE-SUBSTRATE POTENTIAL CASE ##################

log               log-indent
echo              both

units             metal
dimension         3
boundary          p p p
#atom_style       full

neighbor          3.0 bin
neigh_modify      every 10 delay 50 check no

processors        12 12 1
read_restart      restart.*

################## Interactions

group             graphene    type 1
group             substrate   type 2
group             indentor    type 3
group             cantilever  type 4

region            bound block -237 236 -237 233 -200 200 side out
group             bound1 region bound

region            boundin block -237 236 -237 233 -200 200
group             bound2 region boundin
group             Moving subtract all bound1
pair_style        hybrid lj/cut 14.0 airebo 2.0
pair_modify       shift yes mix arithmetic

pair_coeff        * * airebo CH.airebo C NULL C NULL
pair_coeff        2 2 lj/cut 0.0 3.826 14
```

```
#pair_coeff       3 3 lj/cut 0.0 3 14
pair_coeff        4 4 lj/cut 0.0 3 14

pair_coeff        1 2 lj/cut 0.0089 3.629 14    ### G-S Nario Inui 2017
pair_coeff        1 3 lj/cut 0.00455 3.431 14   ### G-I Nario Inui 2017
pair_coeff        2 3 lj/cut 0.0 3 14           ### I-S
pair_coeff        3 4 lj/cut 0.00455 3.431 14   ###
pair_coeff        2 4 lj/cut 0.0 3 14           ###
pair_coeff        1 4 lj/cut 0.0 3 14           ###

##################  Run paramters

### fix rigid the substrate ###
fix               subFix substrate setforce 0 0 0

### fix rigid the indentor ###
fix               cantFix cantilever setforce 0 0 0

compute           Gtemp graphene temp/com
fix               gTemp graphene temp/berendsen 300.0 300.0 10
fix_modify        gTemp temp Gtemp

compute           Itemp indentor temp/com
fix               iTemp indentor temp/berendsen 300.0 300.0 10
fix_modify        iTemp temp Itemp

fix               cantspring cantilever spring couple indentor 31.21 NULL
                  NULL -13.1259 0
fix               indmom indentor momentum 1 linear 1 1 0 angular

fix               NVE Moving nve

timestep          0.0005                  ### 0.5 fs
thermo            100

compute           forceG indentor group/group graphene molecule inter
variable          ForceG equal c_forceG[3]

thermo_style      custom step temp c_Gtemp c_Itemp c_forceG[3] pe ke

variable          loopvar loop 600

label loop
fix               indFix indentor setforce 0 0 0
displace_atoms    cantilever move 0 0 -0.2
run               1
unfix             indFix
fix               springy cantilever spring/self 100

run               800  # run 100 timesteps - equilibration

fix               printForce all print 10 "${ForceG}" append
                  indentorforce.txt screen "no"

dump              1 all custom 100 dump_move.lammpstrj id type x y z fx fy fz
dump_modify       1 append yes
```

```
dump              2 indentor custom 10 dump_move_indentor.lammpstrj id type x
                  y z fx fy fz
dump_modify       2 append yes

run               100
undump            1
undump            2
unfix             printForce
unfix             springy
next              loopvar
jump              SELF loop

write_restart     restart.*
```